PERIODIC MATERIALS FOR SEISMIC BASE ISOLATION: THEORY AND APPLICATIONS TO SMALL MODULAR REACTORS

A Dissertation

Presented to

The Faculty of the Department of Civil and Environmental Engineering

University of Houston

In Partial Fulfillment

of the Requirements for the Degree

Doctor of Philosophy

in Civil Engineering

By

Witarto

December 2018

PERIODIC MATERIALS FOR SEISMIC BASE ISOLATION: THEORY AND APPLICATIONS TO SMALL MODULAR REACTORS

Witarto

Approved:

Chair of the Committee
Yi-Lung Mo, Professor,
Civil and Environmental Engineering

Co-chair of the Committee
Kalyana B. Nakshatrala, Associate Professor,
Civil and Environmental Engineering

Committee Members:

Thomas T. C. Hsu, Moores Professor,
Civil and Environmental Engineering

Alex Freundlich, Professor,
Physics

Jinghong Chen, Associate Professor,
Electrical and Computer Engineering

Egor Dontsov, HF Software Product Manager,
W.D. Von Gonten Laboratories, LLC.

Suresh K. Khator, Associate Dean,
Cullen College of Engineering

Roberto Ballarini, Thomas and Laura Hsu Professor and Chair of Department,
Civil and Environmental Engineering

ACKNOWLEDGEMENTS

I am profoundly grateful to my advisor, Prof. Yi-Lung Mo, for his guidance, encouragement, trust, and continuous support during my Ph.D. study at the University of Houston. I am also fortunate to have had this invaluable opportunity to learn from my co-advisor, Dr. Kalyana Babu Nakshatrala. They have strongly influenced my intellectual development and have exposed me to the academic and research cultures.

I am grateful to have Prof. Thomas T. C. Hsu, Prof. Alex Freundlich, Dr. Jinghong Chen, and Dr. Egor Dontsov as my dissertation committee members who have provided significant guidance, insightful comments, and suggestions for further improvement of this research.

I would also thank the research collaborators, Prof. Kuo-Chun Chang and Dr. Yu Tang, who have been involved in this research from the beginning to the end and have provided valuable input. My gratitude extends to the researchers at the National Center for Research on Earthquake Engineering (NCREE), Dr. Shiang-Jung Wang, Dr. Cho-Yen Yang, and Mr. Shieh-Kung Huang, as well as to the shake table operators, Mr. Chia-Hsin Hu and Mr. Chi-Hung Wu, and the laboratory technicians, Mr. An-Chih Chen and Mr. Chen-Hao Hsu, for their tireless support during the experimental program. I highly appreciate all graduate students in Prof. Kuo-Chun Chang's research group, especially I-Chen Chiu, Chueh-Ming Teng, and Shih-Sheng Chang who have helped significantly during the fabrication and the shake table tests.

My special thanks are also given to all colleagues in Prof. Yi-Lung Mo's research group, including Jamshaid Sawab, Mahadi Masud, Satyasapath Roy, Tianmin Zhou, Hsuan-Wen Huang, and Shalaka Dhonde who joined me on the graduate journey and accompanied me until its completion. In addition, the financial support from the US Department of Energy NEUP program (Project No. CFA-14-6446) and NCREE for my entire research study is acknowledged.

Above all I am grateful to my family, my parents and my sisters, who have always given me boundless love and everlasting support. It is because of them that this dissertation has come to completion.

PERIODIC MATERIALS FOR SEISMIC BASE ISOLATION: THEORY AND APPLICATIONS TO SMALL MODULAR REACTORS

An Abstract

of a

Dissertation

Presented to

The Faculty of the Department of Civil and Environmental Engineering

University of Houston

In Partial Fulfillment

of the Requirements for the Degree

Doctor of Philosophy

in Civil Engineering

By

Witarto

December 2018

ABSTRACT

Important structures such as nuclear power plants should experience very little vibrations in order to maintain the safety of the nuclear facilities during seismic events. Protection of these structures by seismic isolators requires the isolators to provide seismic isolation irrespective of the direction of excitations and to develop a stable response without rocking. Conventional seismic isolation systems, however, can only fulfill partial requirements for the seismic protection.

This study adopts the principle of periodic materials for seismic isolation. These materials exhibit unique properties of frequency band gaps, where incoming waves with frequencies falling inside the frequency band gaps are forbidden. The new isolation systems, known as periodic foundations, function both as a structural foundation to support the gravitational weight of the superstructure and also as a seismic isolator. The isolation mechanism, hypothetically, can easily fulfill all the requirements for seismic protection of the critical facilities.

This study focuses on the design of one-dimensional (1D) and three-dimensional (3D) periodic foundations for seismic isolation of small modular reactor (SMR) buildings. The theoretical study was first conducted to reveal the fundamental behavior of periodic foundations. Then global sensitivity analysis was utilized to study the effect of design parameters on the frequency band gaps. In addition, simple straight-forward design equations based on the sensitivity analysis are proposed for the design of periodic foundations. Utilizing the proposed equations, prototypes of 1D and 3D periodic foundations were designed to isolate an SMR building. Scaled models were fabricated and experimentally tested to validate the hypothesis and design. The periodic foundation structural systems were tested under various input waves, including seismic waves, in the horizontal and vertical directions and the torsional mode. The shake table test results show that the periodic foundations can reduce the acceleration response of the SMR building up to 90% in the horizontal direction and the torsional mode. As much as a 40% response reduction in the vertical direction is also observed. Moreover, the periodic foundation-isolated structure exhibited stable response with negligible rocking on the structure. This study proved the capability of periodic foundations to enhance the seismic safety of critical structures.

TABLE OF CONTENTS

LIST OF FIGURES

LIST OF TABLES

1 INTRODUCTION

1.1 Significance of Research

Important structures such as hospital buildings, fire, rescue, and other emergency response facilities, in general, are designed to withstand large earthquakes with minor damage or an immediate occupancy performance level as regulated by FEMA 273 [1]. Furthermore, structures housing sensitive equipment such as nuclear power plants should experience very little vibrations and therefore maintain the safety of the nuclear facilities. However, such high structural performance is often costly and difficult to achieve, especially in the high seismic regions.

One effective solution used to reduce the seismic demand on the structures is to equip them with seismic base isolation systems [2], such as rubber bearings and friction pendulum systems. The conventional base isolation systems work by introducing low lateral stiffness devices at the base of a superstructure, hence lengthening the natural period of the structural system and reducing the input acceleration accordingly. This concept of seismic base isolation has been developed over decades and has matured into practical applications around the world [3]. Although the developed base isolation systems had been proven to enhance the horizontal seismic performance of many isolated structural systems, they are incapable of isolating vertical earthquakes. Full-scale shake table tests conducted at the E-Defense facility in Japan show a great amplification in the vertical acceleration response of the isolated buildings when subjected to the vertical earthquakes [4, 5]. The vertical response amplification causes a wide variety of damage to the non-structural components inside the isolated buildings.

Various devices have been proposed to isolate earthquakes in both the horizontal and vertical directions. Devices such as the rolling seal type air spring [6, 7] and hydraulic isolation systems [8] can provide vertical isolation and are proposed to be combined with laminated rubber bearings for horizontal isolation. On the other hand, devices such as thick rubber layer bearings [9] and GERB systems [3] can simultaneusly provide seismic isolation in both the horizontal and vertical directions. All of the proposed devices are based on the same concept as the conventional isolation systems, i.e., introducing low lateral and vertical stiffness and subsequently lengthening the natural periods of the isolated structural systems to avoid damaging frequency content of the input earthquakes. However, researchers have found that these systems are prone to rocking when subjected to horizontal earthquakes [3, 10]. Consequently, rocking suppression devices are needed to control the rocking movement. So far the proposed systems have not been used in practical application except for the GERB system that was implemented in two houses in California. These houses, however, were severely shaken by the 1994 Northridge Earthquake due to the rocking motion introduced by the system [11]. Therefore, development of new seismic isolation systems that can provide seismic isolation in both the horizontal and vertical directions without rocking has become an attractive area of research.

The concept of periodic material-based seismic base isolation was introduced recently [12-15] to overcome the shortcomings of the above-mentioned isolation systems. The new isolation systems, better known as periodic foundations, adopt the concept of periodic materials or phononic crystals. These materials can manipulate incoming elastic waves by utilizing their frequency band gap property. According to the number of directions where the unit cell is repeated, periodic materials can be classified as one-dimensional (1D), two-dimensional (2D), and three-dimensional (3D) periodic materials, as shown in Figure 1-1. An infinite-layer of the phononic crystal lattice, in theory, can prevent the propagation of elastic waves having frequencies within the frequency band gaps to propagate through the crystal's medium [16, 17]. This concept is depicted in Figure 1-2(a) and Figure 1-2(b). It is shown in Figure 1-2(a) that the wave cannot propagate through the periodic material since the frequency of the wave falls within the range of the frequency band gap of the material. The opposite case is shown in Figure 1-2(b). The range of the frequency band gap can be engineered by design to cover any frequency of interest.

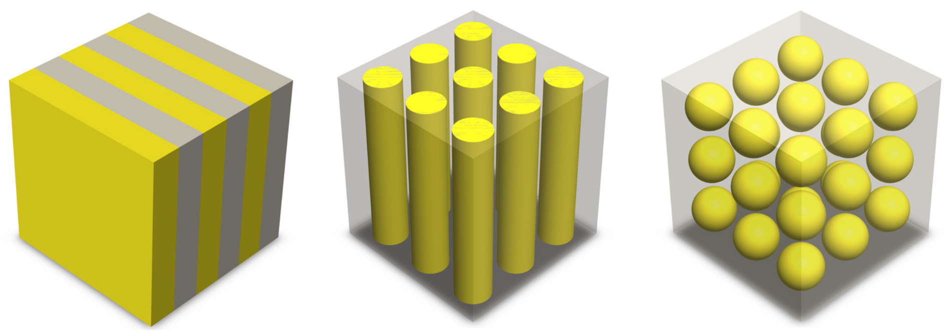

(a) 1D (b) 2D (c) 3D

Figure 1-1 Classification of periodic materials or phononic crystals

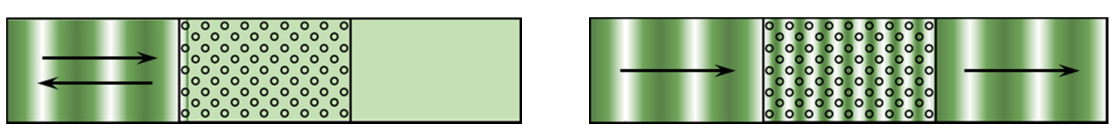

(a) (b)

Figure 1-2 Wave propagation with the wave frequency: (a) inside frequency band gap and (b) outside frequency band gap (Note: these figures were replicated from [18])

The term "periodic foundations" refers to the structural foundations that are made of periodic materials. These foundations are capable of both supporting any superstructure and isolating the superstructure from the incoming seismic waves by utilizing their frequency band gaps. Since this wave blocking mechanism is effective for both the vertically and horizontally propagating waves, periodic foundations can isolate the superstructure from seismic excitations in both the horizontal and vertical directions. The blocking mechanism, hypothetically, does not cause rocking to the structural systems. These advantages can easily solve the shortcomings of the above-mentioned seismic isolation systems.

Though the concept is still very new, a feasibility study of periodic foundations has been conducted to investigate the existence of frequency band gaps and their functionality in seismic isolation. At this level, researchers have conducted experimental tests of 1D [19], 2D [20], and 3D [21] periodic foundations. In each of the tests, a simple structure with a periodic foundation was tested simultaneously with a non-isolated counterpart. Although rocking of the structural systems was not investigated, the test results show that the structures isolated with periodic foundations have a much less acceleration response compared to the non-isolated structures.

Guided by results in the feasibility study, this research proceeds with the implementation of periodic foundations into a more specific engineering structure. In this study, the periodic foundations were designed for seismic protection of nuclear power plants, in particular small modular reactor (SMR) buildings. This research provides a complete study of periodic foundations from the basic behavior of periodic materials to the design and fabrication processes of large-scale periodic foundation structural systems to the experimental validation and numerical simulation. The research study would be beneficial for both academic and engineering communities as this study provides the baseline information to guide the communities in understanding and designing periodic foundations.

1.2 Research Objectives

This research aims to develop periodic foundations that can isolate an SMR building from incoming seismic waves. The designed periodic foundation should be able to isolate the SMR building using the novel concept of frequency band gaps. Specific research objectives considered in this research are the following:

1. The fundamental frequencies of seismic waves range from frequencies of 0 to 50 Hz, which corresponds well to the dominant frequencies of nuclear power plant structures. It is critical, therefore, to find a simple configuration of periodic foundations that have frequency band gaps covering frequencies from 0 to 50 Hz.
2. Periodic materials under development in the field of solid-state physics are typically configured with very small-size lattice constants and may utilize rare or expensive materials such as gold. The need for scale and economy in a building or other structural foundation systems, however, requires that a periodic foundation be limited to materials that will achieve the desired frequency band gaps, yet be commonly used materials in civil infrastructure applications and be familiar to both designers and contractors.
3. For the implementation of periodic foundations in real engineering structures, it is important to have the designed periodic foundation structural systems validated through experimental tests to critically investigate the actual behavior of the structural systems.

4. In-coming seismic waves have a wide variety of distribution of main frequency content, direction of excitation, and intensity. Investigation on the effects of ground motion excitations which include the distribution of main frequency content of the seismic waves, the intensity of shaking, and direction of excitations is necessary to assess the overall seismic performance of periodic foundation structural systems.

1.3 Scope of Research

This study focuses on the design of 1D and 3D periodic foundations for seismic isolation of an SMR building. A theoretical study of periodic materials was first conducted to understand the wave propagation in the periodic materials. Next, global sensitivity analysis was performed to investigate the affecting parameters on the first frequency band gap. Guided by the sensitivity analysis results, 1D and 3D periodic foundations were designed using existing construction materials to isolate an SMR building. Scaled models were then designed according to the similitude requirements [22] for experimental validation. The experimental validation on the 1D and 3D periodic foundation structural systems was conducted using a large shake table facility at the National Center for Research on Earthquake Engineering (NCREE). In addition, a reinforced concrete (RC) foundation was also designed for the shake table tests to represent a typical rough foundation on a non-isolated structure. The comparison of the test results between the SMR building model with both 1D and 3D periodic foundations and that with the RC foundation provides significant information on the effectiveness of the isolation systems. Finally, numerical simulation based on the finite element method was conducted to investigate to what extent a computer simulation can represent the actual behavior of periodic foundation structural systems.

1.4 Organization of Dissertation

This dissertation is divided into eight chapters. Chapter 1 presents the significance, objective, and scope of the research as well as the organization of the dissertation. Chapter 2 focuses on the literature review of the conventional seismic isolation systems and the previous development of periodic materials and their applications in various engineering fields. The test results of periodic foundations conducted in the feasibility stage were also discussed in this chapter. Chapter 3 presents the basic theory of periodic materials which include the dispersion relationship, vibration modes of waves propagating in periodic materials, and the frequency response of periodic materials that were obtained both analytically (by solving the wave equation) and numerically (through the finite element method). Chapter 4 discusses the global sensitivity analysis of periodic materials which led to the development of simplified design equations for the design of periodic materials. Chapter 5 presents the experimental program of periodic foundation structural systems which include the design of both the full-scale and the scaled model of each of the 1D and 3D periodic foundations and SMR building. In this chapter, the fabrication process of the test specimens is thoroughly explained and the shake table tests are elaborated. Chapter 6 presents the shake table test results and discusses the behavior of the test specimens according to the analyzed test data. Chapter 7 presents the numerical simulation of the test specimens and the comparison with the experimental outcomes. Lastly, Chapter 8 offers some concluding remarks on the research and proposes future research directions.

2 LITERATURE REVIEW

2.1 Conventional Seismic Isolation Systems

In the last fifty years, extensive research has been conducted on seismic isolation systems by a number of academic and research institutions around the world. The research effort has resulted in a matured concept of seismic base isolation systems that are well received and practically used in many countries [2, 3]. The basic idea of the seismic base isolation systems is quite simple. The systems provide a low lateral stiffness between a superstructure and its foundation to decouple the superstructure from horizontal components of ground motion. The decoupling action prevents the damaging input energy of an earthquake to reach the isolated superstructure.

In practice, there are two types of base isolation systems that are widely used: the elastomeric-based systems and the sliding-based systems. The earliest developed elastomeric bearings are the low damping natural rubber bearings (NRB) which are made of vulcanized natural rubber layers and reinforced with steel shims, as shown in Figure 2-1(a). The rubber layers have a low shear modulus that provides lateral flexibility. The steel shim plates are used between the rubber layers to prevent them from lateral bulge and to increase vertical stiffness and load bearing capacity of the NRB. In general, the lateral surface of NRB is covered by a thin layer of rubber to protect them from the UV light and oxidation. Two thick flange plates on the top and bottom are provided to connect the bearings to the structure. These bearings, however, possess a very low damping that is necessary to reduce seismic displacement demand and to suppress possible resonance at the isolation frequency. Variants of NRB were developed to incorporate damping to the rubber bearings. Invented in New Zealand in 1975 [23, 24], the structure of lead rubber bearings (LRB) is similar to that of NRB except for the addition of lead plugs at the center core, as shown in Figure 2-1(b). The shim plates and rubber layers confine the lead plug to develop a stable shear hysteresis behavior under lateral deformation which provides additional damping. Another variant was developed in 1982 [25], in which the rubber layers were treated with additives to increase their damping property. Such bearings are known as high damping rubber bearings (HDRB). The structure of HDRB, as shown in Figure 2-1(c) is exactly the same as NRB except the rubber layers have a much higher damping. The most commonly used sliding-based systems are the friction pendulum systems (FPS). The typical structure of FPS is depicted in Figure 2-2. The FPS combines a sliding and a re-centering mechanism by geometry. In principle, FPS has an articulated slider (moving disc) in between two stainless steel spherical surfaces (top and bottom sliding surfaces). The contact between the slider and the surfaces are coated with low-friction, low wear, and lubricated composite material. The concave geometry of the sliding surface allows the system to go back to the original state after seismic excitations. The friction between the sliding surfaces and the slider generates damping on the system.

Although the base isolation systems can isolate the superstructure from the horizontal components of ground motions, they are not capable of providing vertical isolation. Experimental studies conducted using shake table tests [4, 5] and field observation from seismic reconnaissance activities [26] show that the vertical earthquake can cause serious structural and non-structural damage. A few isolation systems were invented to provide vertical isolations. Devices such as the rolling seal type air spring [6, 7] and hydraulic isolation systems [8] were developed to provide isolation in the vertical directions. Both systems are proposed to be combined with laminated rubber bearings for horizontal isolation. The schematic layout of both devices are shown in Figure 2-3 and Figure 2-4. Other systems such as thick rubber layer bearings [9] were invented to provide seismic isolation in both the horizontal and vertical directions. The thick rubber layers, as shown in Figure 2-5, provide flexibility in both the horizontal and vertical directions simultaneously. Another similar system known as the GERB system [3], shown in Figure 2-6, consists of large helical springs that are flexible both horizontally and vertically. Researchers found that these proposed vertical isolation systems are prone to rocking when subjected to horizontal earthquakes [3, 10]. Consequently, rocking suppression devices are needed to control the rocking movement. So far the proposed systems have not been used in practical application except for the GERB system that was implemented in two houses in California. These houses, however, were severely shaken by the 1994 Northridge Earthquake due to the rocking motion introduced by the system [11].

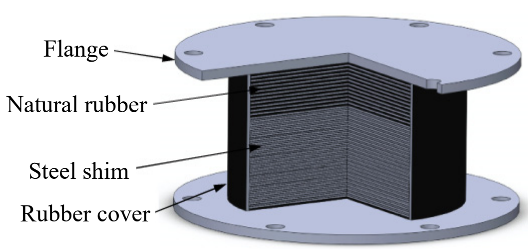

(a) Low damping natural rubber bearing (figure obtained from [27])

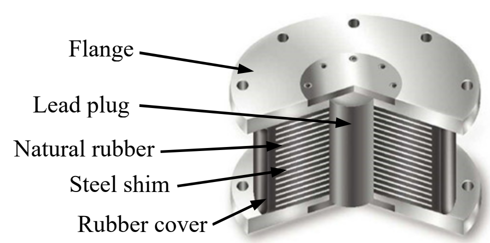

(b) Lead rubber bearing (figure obtained from [28])

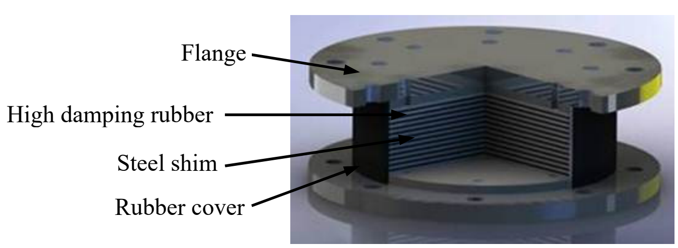

(c) High damping rubber bearing (figure obtained from [29])

Figure 2-1 Elastomeric-based base isolation systems

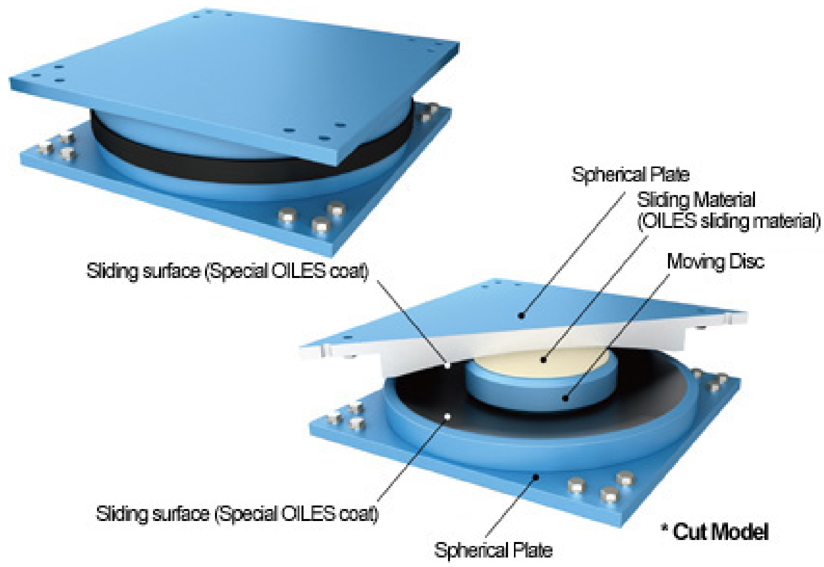

Figure 2-2 Friction pendulum system (figure obtained from [30])

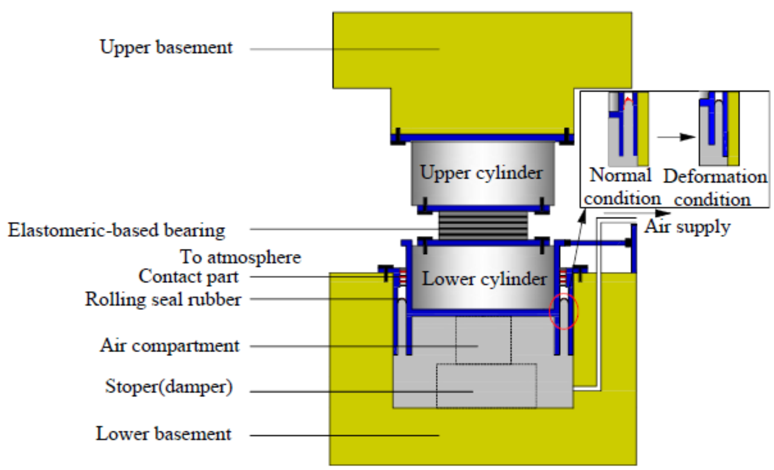

Figure 2-3 Rolling seal type air spring (figure obtained from [31])

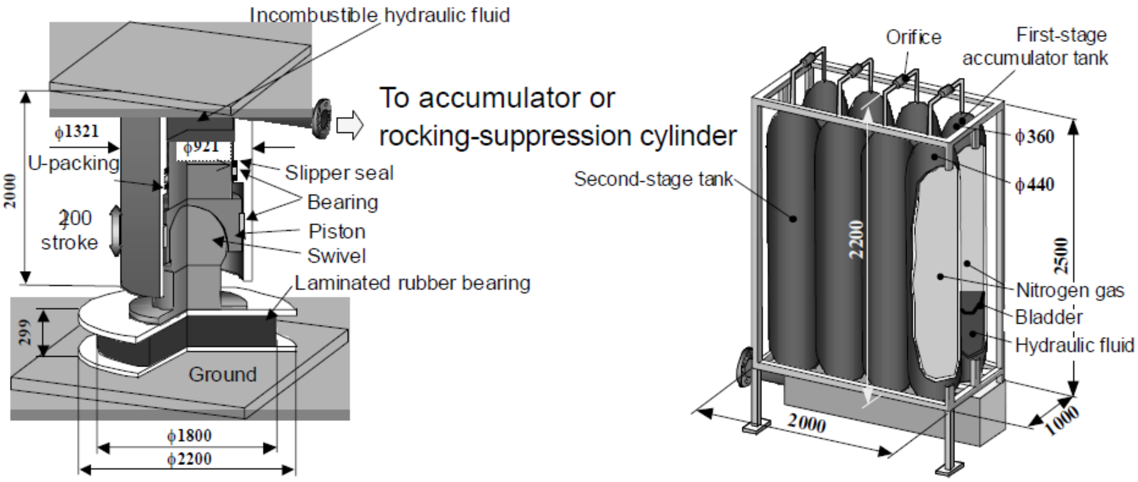

Figure 2-4 Hydraulic isolation system (figure obtained from [8])

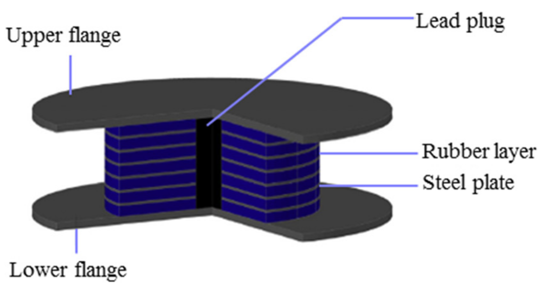

Figure 2-5 Thick rubber layer bearing (figure obtained from [31])

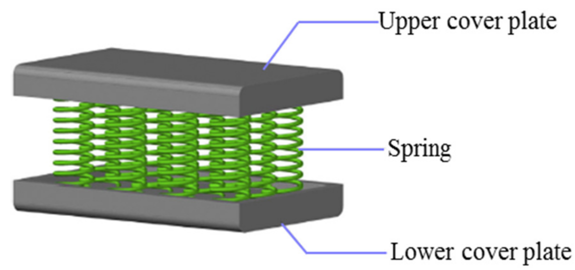

Figure 2-6 GERB system (figure obtained from [31])

2.2 Periodic Material-Based Seismic Isolation Systems

2.2.1 Overview of periodic materials

Periodic materials or phononic crystals are novel composites developed in the branch of solid state physics [32]. These materials possess a unique ability to manipulate the vibration of elastic waves. This is accomplished by deliberately structuring and arranging the material phase and/or geometry to take advantage of fundamental wave-material interactions, including interference and resonance [33]. Due to these interactions, the materials allow the propagation of elastic waves only in certain frequency regions (denoted as pass bands) and forbid the propagation of the waves in the other regions (denoted as band gaps) [18, 34-36]. The information of frequency band gaps can be obtained by construction of the dispersion curve of a certain unit cell with periodic boundary conditions. A typical dispersion curve for a 2D periodic material and the corresponding frequency band gap is shown in Figure 2-7.

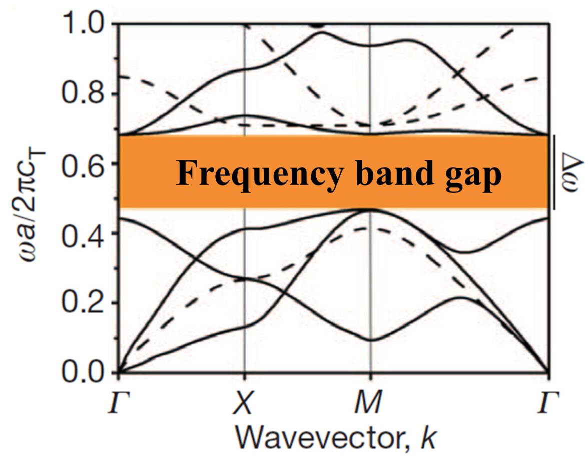

Figure 2-7 Typical dispersion curve of a 2D periodic materials (figure obtained from [36])

Ever since the first discovery in 1992 [37], many researchers have contributed toward the advancement of periodic materials. The research has resulted in the development of theoretical methods to obtain dispersion curves and subsequently to find the theoretical frequency band gaps. Among the available methods are transfer matrix (TM) [38-41], plane wave expansion (PWE) [16, 17, 42-45], finite difference time domain (FDTD) [46-48], multiple scattering theory (MST) [49-52], and finite element methods. Another aspect of the research was the development of different configurations of periodic materials in order to find the desired frequency band gaps. So far, two of the most well-known configurations are the Bragg scattering [53, 54] and Locally resonant [55-59].

The unique property of frequency band gaps has resulted in an immense potential engineering application of periodic materials. Depending on the coverage of the frequency band gaps that is inversely proportional to the structural scale, periodic materials can be utilized to control different types of waves across the phononic spectrum, as shown in Figure 2-8. At nanometer scales (see Figure 2-9), the periodic materials can effectively obstruct heat propagation as the heat vibration oscillates at frequencies of the order of terahertz [60]. At centimeter to micrometer scales, the periodic materials are mostly utilized to isolate acoustic waves that oscillate at relatively lower frequencies (kilohertz to megahertz) [36, 61, 62]. In addition to acoustic isolation, periodic materials have also been used to direct the propagation path of the acoustic waves, as shown in Figure 2-10. At decimeter scales and larger, periodic materials have been applied to isolate seismic waves [19-21, 63], which have frequencies lower than 50 Hz. Figure 2-11 shows a periodic material-based seismic isolation system in the form of a barrier. The periodic materials, therefore, can be engineered with different sizes and material constituents to cover any desired frequency ranges for different purposes.

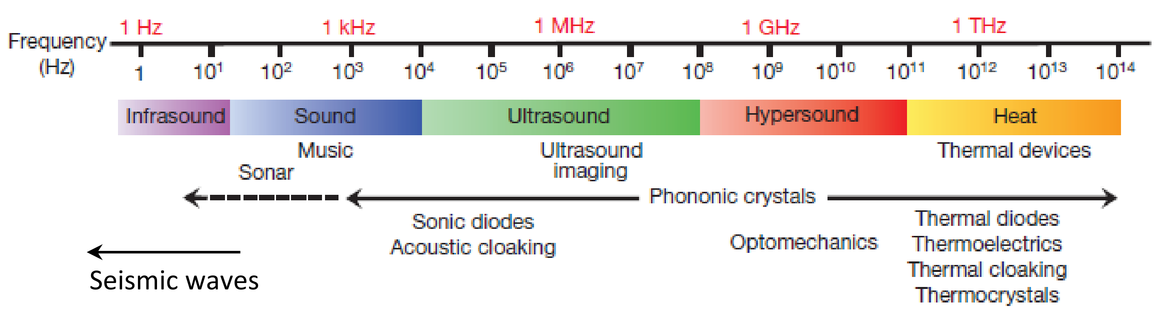

Figure 2-8 Phononic spectrum (figure obtained from [36])

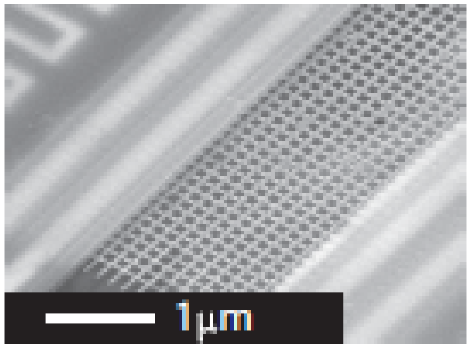

Figure 2-9 Nanomesh for thermal isolation (figure obtained from [60])

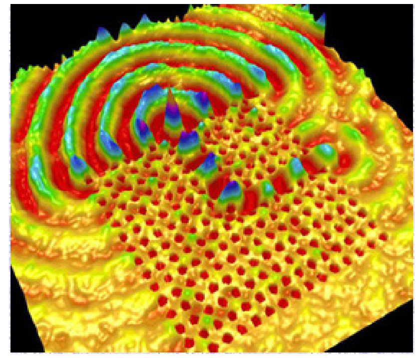

Figure 2-10 Sound wave guider (figure obtained from [64])

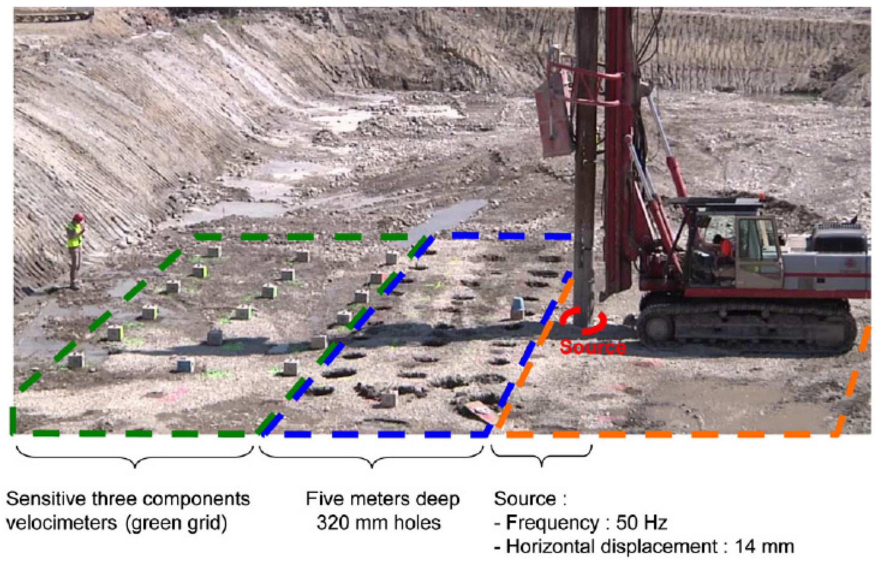

Figure 2-11 Seismic wave barrier (figure obtained from [63])

2.2.2 Feasibility study of periodic material-based seismic base isolation systems

This research focuses on the periodic-material based seismic isolation systems in the form of periodic foundations. Figure 2-12 illustrates the concept of periodic foundations as both a bearing support for a superstructure and seismic isolator. Similar to the classification of periodic materials, periodic foundations can also be classified into 1D, 2D, and 3D periodic foundations depending on the direction of periodicity, as shown in Figure 2-13.

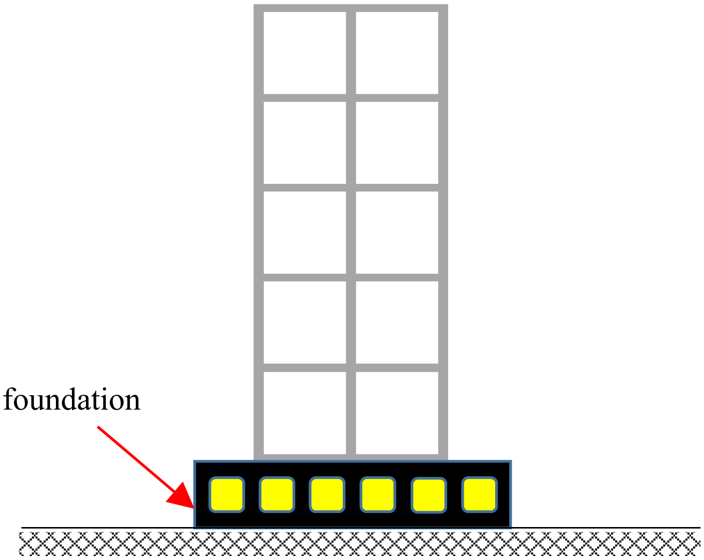

Figure 2-12 Periodic foundation supporting a building structure

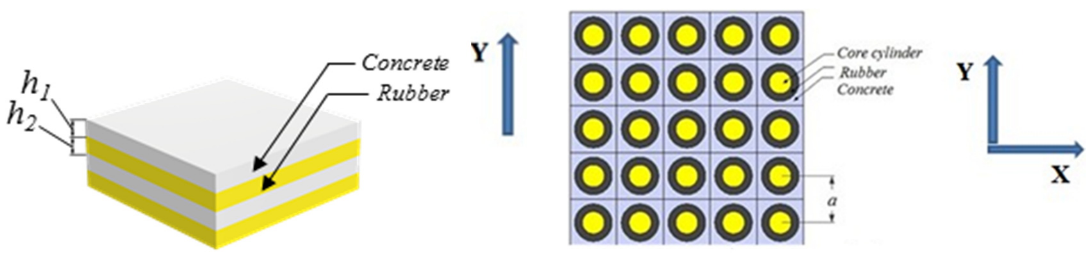

(a) 1D periodic foundation (b) 2D periodic foundation

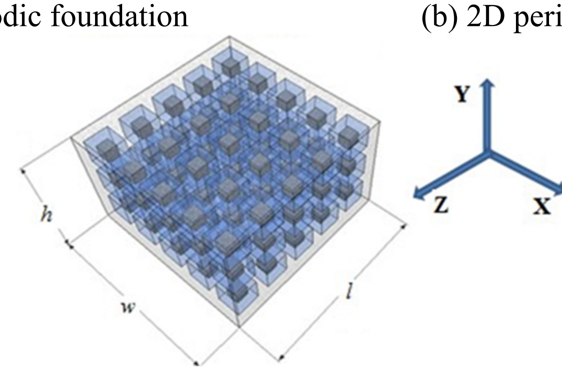

(c) 3D periodic foundation

Figure 2-13 Classification of periodic foundations (figures obtained from [15])

In the feasibility study stage, a few researchers have performed numerical studies of periodic foundations supporting simple structures [12-14]. The studies show a successful seismic isolation provided by periodic foundations. The concept of periodic foundations was then experimentally validated to investigate the existence of frequency band gaps in the real specimens. Xiang et al. [19] conducted tests to study 1D periodic foundations. The test specimens consisted of two identical three-story steel frames. The first specimen, designated as Specimen A, was fixed to the shake table while the second specimen, designated as Specimen B, was connected to the top of a 1D periodic foundation and placed on the shake table as shown in Figure 2-14(a). Following the tests by Xiang et al., Yan et al. [15, 20, 21] conducted tests on 2D and 3D periodic foundations. In the 2D periodic foundation tests, the response of two identical simple frames was compared. The first frame (Specimen C) was placed directly on a reinforced concrete (RC) base. In the second specimen (Specimen D), a 2D periodic foundation was placed between the frame and the RC base as shown in Figure 2-14(b). In the 3D periodic foundation tests, the response of a cantilever column connected to an RC foundation (Specimen E) was compared with the response of an identical cantilever column connected to a 3D periodic foundation (Specimen F).

The results from all of the above-mentioned tests are shown in Figure 2-15. The results in Figure 2-15(a) show that the acceleration at the top of Specimen B is significantly smaller in comparison to that of Specimen A under ambient vibrations. The main frequency of the ambient vibration was recorded at 50 Hz which is within the fourth frequency band gap (46.1-60 Hz) of the periodic foundation used in Specimen B. This proves that an input wave will be attenuated when its main frequency content is located inside the attenuation zone of the periodic foundation.

In the experimental test on the 2D periodic foundation, the specimens were subjected to a modified ground motion (BORAH.AS/HAU000 (1983/10/29)). The main frequency of the original seismic wave was recorded at 18 Hz. The seismic wave was then modified to shift its main frequency to 46 Hz to match the tested frequency band gap (38-100 Hz) of the 2D periodic foundation used in Specimen D. The test results shown in Figure 2-15(b) demonstrate that the maximum acceleration in Specimen D (with the 2D periodic foundation) was recorded at 0.64 g while the maximum acceleration in Specimen C (without the 2D periodic foundation) was recorded at 1.34 g. The 2D periodic foundation helped in reducing the response of the superstructure by more than 50% in comparison to the non-isolated counterpart.

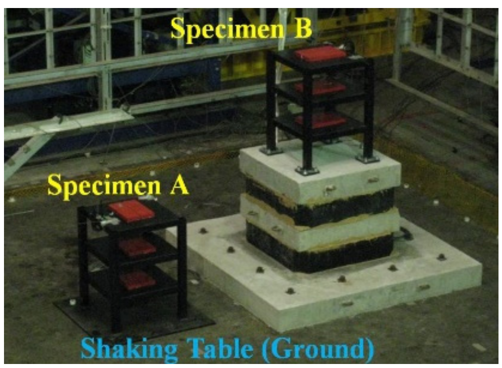

(a) 1D periodic foundation (figure obtained from [19])

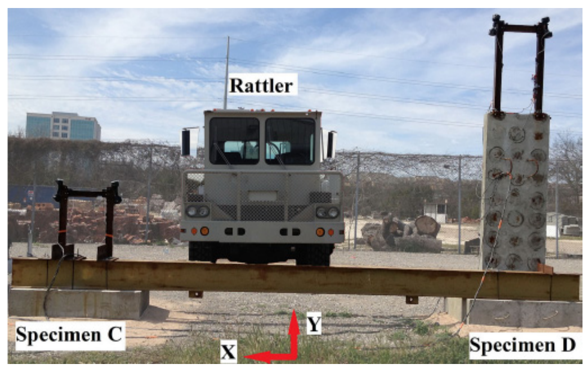

(b) 2D periodic foundation (figure obtained from [20])

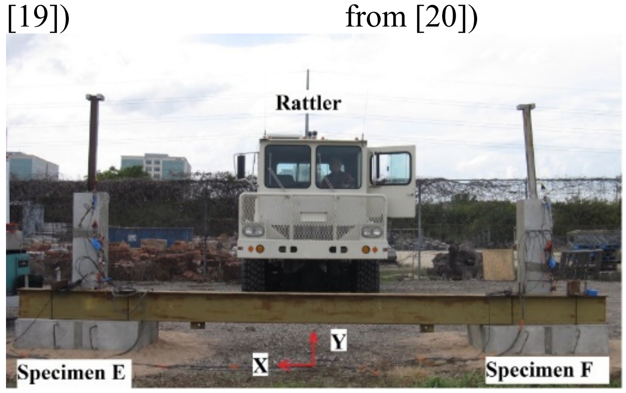

(c) 3D periodic foundation (figure obtained from [21])
Figure 2-14 Feasibility study of periodic foundations

The ground motion (BORAH.AS/HAU090 (1983/10/29)) was utilized as the input seismic wave to test Specimens E (with the RC foundation) and F (with the 3D periodic foundation). The seismic wave was modified so that the main frequency content is located at 35.1 Hz which corresponds with one of the tested frequency band gaps. Figure 2-15(c) shows that the maximum acceleration of Specimen E is 1.73 g while the maximum acceleration of Specimen F is 0.1 g. Thus, the 3D periodic foundation was able to reduce the response of the superstructure by more than 90 %. The test results show that significant response reduction can be achieved when the periodic foundations are used as the seismic isolator.

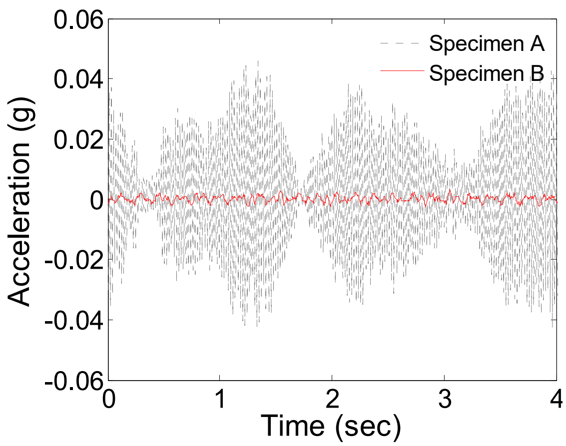

(a) 1D periodic foundation test results (figure obtain from [19])

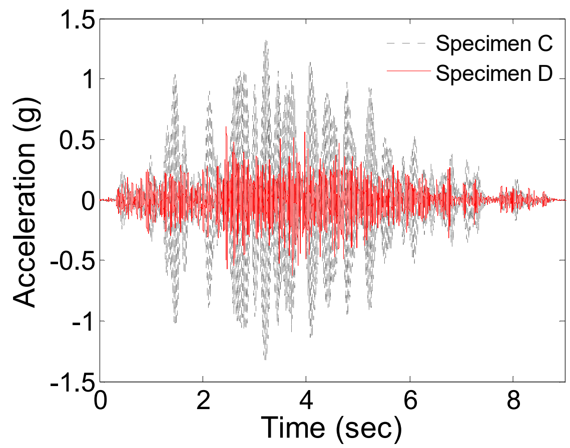

(b) 2D periodic foundation test results (figure obtained from [20])

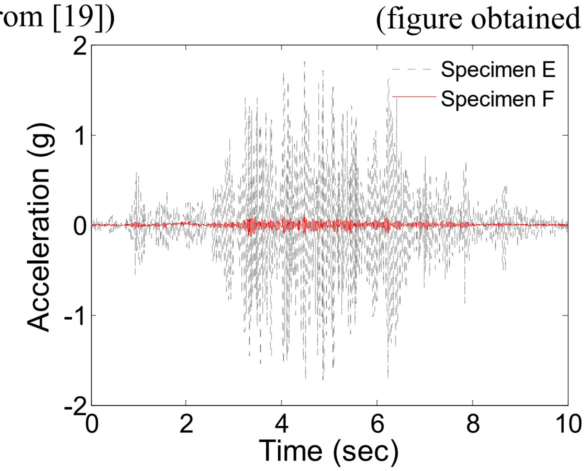

(c) 3D periodic foundation test results (figure obtained from [21])

Figure 2-15 Experimental test results in feasibility study stage

3 THEORY OF PERIODIC MATERIALS

3.1 Waves in Periodic Materials – Dispersion

The behavior of a wave field inside a domain or body can be explained through a dispersion relationship. The dispersion curve in general relates the frequency and the wave vectors which can reveal the wave's characteristic oscillations over space and exponential decay of the wave amplitude inside the frequency band gaps.

Following the Bloch-Floquet theorem [65, 66], the dispersion relationship can be obtained by solving the wave equation in a unit cell body with periodic boundary conditions. Among all the available methods mentioned in Section 2.2.1, the finite element method was utilized to solve the wave equation in this study because it can easily deal with any complex geometry. Moreover, the finite element method can be used to solve the wave equation for 1D, 2D, and 3D periodic materials. In addition to the finite element method, the transfer matrix method was also utilized to obtain the dispersion relationship in 1D periodic materials. This section presents the finite element and the transfer matrix methods for derivation of the dispersion relationship of 3D and 1D periodic materials, respectively, to be used in finding the frequency band gaps.

3.1.1 Finite element method

For a continuum body with isotropic elastic material and assuming small deformation without damping, the governing equation of motion is shown in Eq. (3-1)

$$\rho(\mathbf{r})\frac{\partial^2\mathbf{u}}{\partial t^2}=\nabla\left\{\left[\lambda(\mathbf{r})+2\mu(\mathbf{r})\right](\nabla\cdot\mathbf{u})\right\}-\nabla\times\left[\mu(\mathbf{r})\nabla\times\mathbf{u}\right], \tag{3-1}$$

where $\mathbf{r}$ is the coordinate vector, $\mathbf{u}$ is the displacement vector, $\rho(\mathbf{r})$ is the density, and $\lambda(\mathbf{r})$ and $\mu(\mathbf{r})$ are the Lamé constants. The relationship of the Lamé constants with Young's modulus $E(\mathbf{r})$ and Poisson's ratio $\nu(\mathbf{r})$ are shown in Eqs. (3-2) and (3-3):

$$\lambda(\mathbf{r}) = \frac{E(\mathbf{r})\nu(\mathbf{r})}{\left[1+\nu(\mathbf{r})\right]\left[1-2\nu(\mathbf{r})\right]} \quad \text{and} \tag{3-2}$$

$$\mu(\mathbf{r}) = \frac{E(\mathbf{r})}{2\left[1+\nu(\mathbf{r})\right]}. \tag{3-3}$$

The displacement solution that satisfies the Bloch-Floquet theorem is shown in Eq. (3-4)

$$\mathbf{u}(\mathbf{r},t) = \mathrm{e}^{\mathrm{i}(\mathbf{k}\cdot\mathbf{r}-\omega t)}\tilde{\mathbf{u}}(\mathbf{r}), \tag{3-4}$$

where $\mathbf{k}$ is the wave vector in the reciprocal space, i is the imaginary unit, ω is the angular frequency, t is the time, and $\tilde{\mathbf{u}}(\mathbf{r})$ is the wave amplitude. Although the coordinate vector $\mathbf{r}$ is defined over the full space $-\infty < \mathbf{r} < \infty$, based on the periodicity of the unit cell $\mathbf{a}$, the wave amplitude $\tilde{\mathbf{u}}(\mathbf{r})$ is periodic on $\mathbf{r} \in [0,\mathbf{a}]$, as shown in Eq. (3-5)

$$\tilde{\mathbf{u}}(\mathbf{r}+\mathbf{a}) = \tilde{\mathbf{u}}(\mathbf{r}). \tag{3-5}$$

Substituting Eq. (3-5) into Eq. (3-4), the periodic boundary conditions can be obtained as follows:

$$\mathbf{u}(\mathbf{r}+\mathbf{a},t) = \mathrm{e}^{\mathrm{i}\mathbf{k}\cdot\mathbf{a}}\mathbf{u}(\mathbf{r},t). \tag{3-6}$$

Then, by applying the periodic boundary conditions to the governing equation, Eq. (3-1), the wave equation can be reduced to the Eigenvalue problem, as shown in Eq. (3-7)

$$\left[\mathbf{\Omega}(\mathbf{k}) - \omega^2\mathbf{M}\right]\mathbf{u} = \mathbf{0}, \tag{3-7}$$

where $\mathbf{\Omega}$ is the stiffness matrix and $\mathbf{M}$ is the mass matrix of the unit cell. The Eigenvalue problem shown in Eq. (3-7) is the so-called dispersion equation. For each wave vector $\mathbf{k}$, a series of corresponding frequencies ω can be obtained. The relationship between the wave vector and the frequency forms the dispersion curve, which provides the information for the frequency band gaps.

An example of this method is shown as follows. Consider a periodic material with a simple cubic unit cell as shown in Figure 3-1(a). The unit cell consists of a cubic core inclusion (yellow) inside a matrix (grey). The unit cell length a is 1 m while the cubic core length is 0.9 m. The core and matrix were assigned with concrete and rubber materials, respectively, with the material properties shown in Table 3-1. The frequency band gap of the corresponding periodic material can be obtained by solving the Eigenvalue problem [Eq. (3-7)]. In the 3D periodic material, the coordinate vector $\mathbf{r}$ is three-dimensional which includes the x, y, and z directions. Owing to the high symmetry of the periodic structures under consideration, it is sufficient to calculate the frequencies for the wave vector varying along the boundary of the first irreducible Brillouin zone [32], the pyramid R-M-Γ-X-M, as shown in Figure 3-1(b).

Figure 3-2 shows the dispersion relationship of the corresponding periodic material. An absolute frequency band gap (yellow shaded area) is observed in the frequency region between 18.44 Hz and 27.09 Hz, which means any elastic waves with frequencies in the region cannot propagate in any direction.

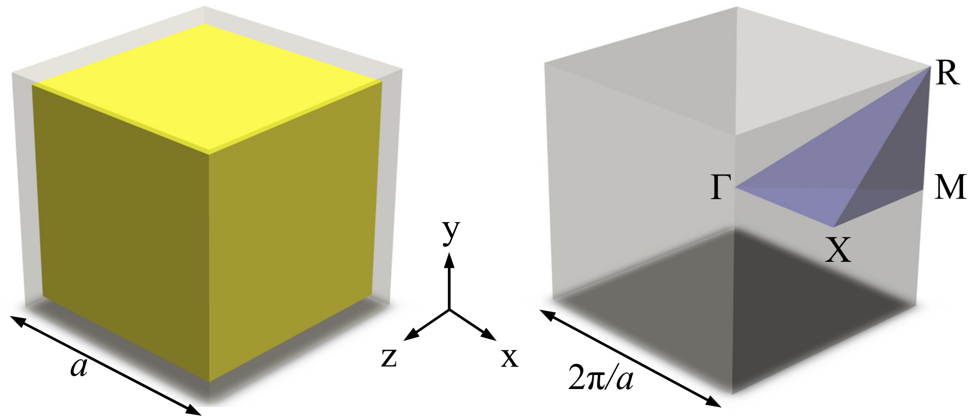

(a) (b)

Figure 3-1 Example of a 3D periodic material; (a) Unit cell (b) First Irreducible Brillouin zone

Table 3-1 Material properties for example of periodic material

Material	Young's modulus (MPa)	Density (kg/m^3)	Poisson's ratio
Concrete	40,000	2300	0.2
Rubber	0.1586	1277	0.463

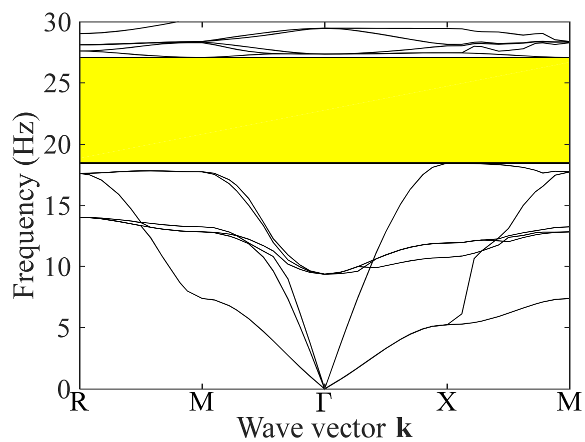

Figure 3-2 Dispersion curve of an example of a 3D periodic material

3.1.2 Transfer matrix method

In 1D periodic materials, the dispersion relationship of a unit cell can be constructed for each of the body waves, S-Wave and P-Wave. Suppose the unit cell is composed of N

layers stacked in the z direction, as shown in Figure 3-3. The wave oscillation in each layer n can be expressed using the elastic wave equation shown in Eq. (3-8)

$$\frac{\partial^2 u_n}{\partial t^2} = C_n^2 \frac{\partial^2 u_n}{\partial z_n^2}, \tag{3-8}$$

where u_n is the displacement at layer n, and z_n represents the position of interest within the layer with reference to the bottom of each layer n. This equation is a reduced form of that presented in Eq. (3-1). The speed constant C_n for each of S-Wave and P-Wave is shown respectively in Eqs. (3-9) and (3-10):

$$C_n = \sqrt{\mu_n / \rho_n} \text{ and} \tag{3-9}$$

$$C_n = \sqrt{(\lambda_n + 2\mu_n)/\rho_n}, \tag{3-10}$$

where λ_n and μ_n are the Lamé constants and ρ_n is the material density at layer n. For the S-Wave, the displacement u_n represents the lateral displacement or displacement along the y direction. For the P-Wave, the displacement u_n represents the axial displacement or displacement along the z direction.

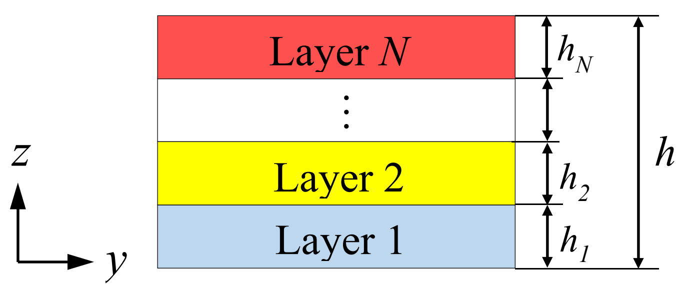

Figure 3-3 A unit cell with *N* layers

The 1D displacement solution that satisfies the Bloch-Floquet theorem is shown in Eq. (3-11)

$$u_n(z_n,t)=\mathrm{e}^{\mathrm{i}\omega t}u_n(z_n)\,, \tag{3-11}$$

Substitution of Eq. (3-11) to Eq. (3-8) yields the spatial wave equation, Eq. (3-12)

$$C_n^2\frac{\partial^2 u_n(z_n)}{\partial z_n^2}+\omega^2 u_n(z_n)=0\,. \tag{3-12}$$

The steady-state displacement that satisfies the spatial wave equation is shown in Eq. (3-13)

$$u_n(z_n)=A_n\sin(\omega z_n/C_n)+B_n\cos(\omega z_n/C_n)\,. \tag{3-13}$$

The terms A_n and B_n in Eq. (3-13) are the amplitudes of the steady-state displacement solution on layer n. In the elastic body of each layer n, the constitutive equations for normal (σ_n) and shear stresses (τ_n) are shown in Eqs. (3-14) and (3-15):

$$\begin{aligned}\sigma_n(z_n)&=(\lambda_n+2\mu_n)\partial u_n/\partial z_n\\&=(\lambda_n+2\mu_n)\omega\left[A_n\cos(\omega z_n/C_n)-B_n\sin(\omega z_n/C_n)\right]/C_n \text{ and}\end{aligned} \tag{3-14}$$

$$\begin{aligned}\tau_n(z_n)&=\mu_n\partial u_n/\partial z_n\\&=\mu_n\omega\left[A_n\cos(\omega z_n/C_n)-B_n\sin(\omega z_n/C_n)\right]/C_n\,.\end{aligned} \tag{3-15}$$

To obtain the dispersion curve of the S-Wave, Eqs. (3-13) and (3-15) are arranged into matrix form, as shown in Eq. (3-16)

$$\begin{Bmatrix}u_n(z_n)\\\tau_n(z_n)\end{Bmatrix}=\begin{bmatrix}\sin(\omega z_n/C_n) & \cos(\omega z_n/C_n)\\ \dfrac{\mu_n\omega}{C_n}\cos(\omega z_n/C_n) & -\dfrac{\mu_n\omega}{C_n}\sin(\omega z_n/C_n)\end{bmatrix}\begin{Bmatrix}A_n\\B_n\end{Bmatrix} \tag{3-16}$$

$$\text{or}\qquad \mathbf{w}_n(z_n)=\mathbf{H}_n(z_n)\boldsymbol{\psi}_n\,.$$

The C_n constant for the S-Wave propagation follows that presented in Eq. (3-9). The left-hand side vector of Eq. (3-16) at the bottom of layer n is defined as $\mathbf{w}_n^b$, as shown in Eq. (3-17)

$$\mathbf{w}_n^b \equiv \mathbf{w}_n\left(0\right) = \mathbf{H}_n\left(0\right)\boldsymbol{\psi}_n, \tag{3-17}$$

which gives information regarding the displacement and the stress at the bottom of layer n. As for the top of layer n, the left-hand side vector in Eq. (3-16) is defined as $\mathbf{w}_n^t$, as shown in Eq. (3-18)

$$\mathbf{w}_n^t \equiv \mathbf{w}_n(h_n) = \mathbf{H}_n(h_n)\boldsymbol{\psi}_n, \tag{3-18}$$

which gives the information of displacement and the stress at the top of layer n. Eq. (3-17) can be related to Eq. (3-18) through a transfer matrix $\mathbf{T}_n$, as shown in Eq. (3-19)

$$\mathbf{w}_n^t = \mathbf{T}_n\mathbf{w}_n^b. \tag{3-19}$$

Hence, the transfer matrix $\mathbf{T}_n$ for a single layer n is as denoted in Eq. (3-20)

$$\mathbf{T}_n = \mathbf{H}_n(h_n)\left[\mathbf{H}_n\left(0\right)\right]^{-1}. \tag{3-20}$$

Each layer's interface of the unit cell is assumed to be perfectly bonded; hence the displacement and shear stress need to satisfy continuity. Therefore, the displacement and shear stress of the top of layer n are equal to that of the bottom of layer $n+1$, as indicated in Eq. (3-21)

$$\mathbf{w}_{n+1}^b = \mathbf{w}_n^t. \tag{3-21}$$

Subsequently, the relationship of displacement and shear stress of the bottom and top surfaces of the unit cell containing the N layers can be expressed as in Eq. (3-22)

$$\mathbf{w}_N^t = \mathbf{T}_N\mathbf{w}_N^b = \mathbf{T}_N\mathbf{w}_{N\text{-}1}^t = \mathbf{T}_N\mathbf{T}_{N\text{-}1}\mathbf{w}_{N\text{-}1}^b = ... = \left(\mathbf{T}_N\mathbf{T}_{N\text{-}1}...\mathbf{T}_1\right)\mathbf{w}_1^b. \tag{3-22}$$

By changing the displacement and shear stress vector of the top and bottom surface of the unit cell as $\mathbf{w}^t = \mathbf{w}_N^t$ and $\mathbf{w}^b = \mathbf{w}_1^b$, respectively, Eq. (3-22) can be shortened into

$$\mathbf{w}^t = \mathbf{T}(\omega)\mathbf{w}^b. \tag{3-23}$$

The transfer matrix for a unit cell of the 1D periodic materials is $\mathbf{T}(\omega)=\mathbf{T}_N\mathbf{T}_{N-1}...\mathbf{T}_1$. Based on the periodicity of the unit cell, the displacement and stresses are periodic on $z\in[0,h]$, as shown in Eq. (3-24)

$$\mathbf{w}^t=\mathrm{e}^{ikh}\mathbf{w}^b, \tag{3-24}$$

where h is the unit cell thickness. Subtraction of Eq. (3-24) from Eq. (3-23) yields Eq. (3-25)

$$\left[\mathbf{T}(\omega)-\mathrm{e}^{ikh}\mathbf{I}\right]\mathbf{w}^b=\mathbf{0}. \tag{3-25}$$

The nontrivial solution can be achieved when the determinant is equal to zero, as shown in Eq. (3-26)

$$\left|\mathbf{T}(\omega)-\mathrm{e}^{ikh}\mathbf{I}\right|=\mathbf{0}. \tag{3-26}$$

Eq. (3-26) is the so-called Eigenvalue problem, with e^{ikh} equal to the Eigenvalue of the transfer matrix $\mathbf{T}(\omega)$. Thus the relationship between wavenumber k and frequency ω can be obtained by solving the corresponding Eigenvalue problem. The relationship between the wavenumber and frequency forms the S-Wave dispersion curve. The curves are related to real wavenumbers and the frequency band gaps are related to complex wavenumbers. Although the wavenumber k is unrestricted, it is only necessary to consider k limited to the first Brillouin zone [32], i.e., $k\in[-\pi/h,\pi/h]$, to obtain the frequency band gaps. Likewise, the P-Wave dispersion curve can be obtained through a similar approach by arranging Eqs. (3-13) and (3-14) into the matrix form of Eq. (3-16) and using the C_n constant for the P-Wave.

Although Eq. (3-26) can be solved directly, one can further simplify the form of the equation. It is known that the transfer matrix $\mathbf{T}(\omega)$ is a two-by-two matrix. Hence, the Eigenvalues L of the $\mathbf{T}(\omega)$ matrix can be obtained using the Cayley-Hamilton theorem, as shown in Eq. (3-27)

$$L^2 - I_1(\omega)L + I_2(\omega) = 0, \tag{3-27}$$

where $I_1(\omega) = \mathrm{tr}\left[\mathbf{T}(\omega)\right] = \mathrm{T}_{11} + \mathrm{T}_{22}$ and $I_2(\omega) = \left|\mathbf{T}(\omega)\right|$ are the first and second variants of the transformation matrix, respectively. From Eq. (3-20), the determinant of transfer matrix at each layer n is

$$\left|\mathbf{T}_n\right| = \left|\mathbf{H}_n(h_n)\right|\left|\mathbf{H}_n(0)\right|^{-1} = \left(\frac{-\mu_n\omega}{C_n}\right)\left(\frac{C_n}{-\mu_n\omega}\right) = 1. \tag{3-28}$$

Hence the second invariant becomes $I_2(\omega) = \left|\mathbf{T}(\omega)\right| = \left|\mathbf{T}_N\right|\left|\mathbf{T}_{N\text{-}1}\right|...\left|\mathbf{T}_1\right| = 1$. The polynomial equation shown in Eq. (3-27) can be written as

$$L + L^{-1} = I_1(\omega). \tag{3-29}$$

Note that $L + L^{-1} = \mathrm{e}^{ikh} + \mathrm{e}^{-ikh} = 2\cos(kh)$. Therefore, a simpler form of dispersion relationship is obtained, as shown in Eq. (3-30)

$$\cos(kh) = \frac{1}{2}I_1(\omega). \tag{3-30}$$

Eq. (3-30) can be expanded into Eq. (3-31) that works for both the S-Wave and P-Wave:

$$\cos(kh) = \cos\left(\frac{\omega h_1}{C_1}\right)\cos\left(\frac{\omega h_2}{C_2}\right) - \frac{1}{2}\left(\frac{\rho_1 C_1}{\rho_2 C_2} + \frac{\rho_2 C_2}{\rho_1 C_1}\right)\sin\left(\frac{\omega h_1}{C_1}\right)\sin\left(\frac{\omega h_2}{C_2}\right). \tag{3-31}$$

The subscripts one and two in Eq. (3-31) correspond to layers one and two, respectively.

Figure 3-4 shows the typical dispersion curves of a 1D periodic material subjected to both the S-Wave and P-Wave. The dispersion curves were constructed from a two-layer unit cell with the thickness of each layer set to 0.2 m. The two-layer unit cell was assumed to be made of concrete and rubber materials similar to that used in the 3D unit cell. The yellow shaded areas indicate the frequency band gaps, in which the wave propagation is forbidden. In general, the frequency band gaps of the S-Wave are located at a lower frequency because they have a lower wave speed than the P-Wave.

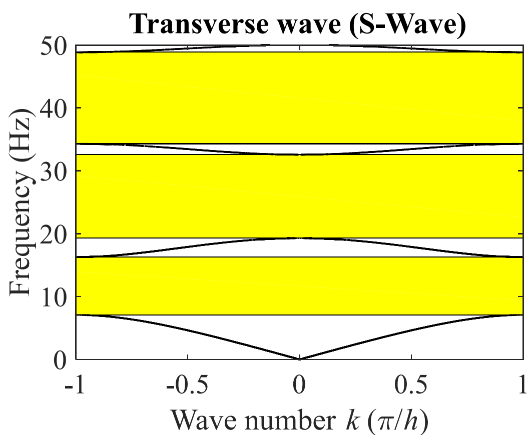

(a) S-Wave

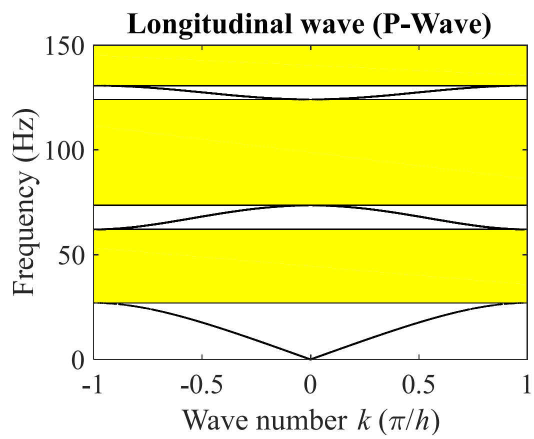

(b) P-Wave

Figure 3-4 Dispersion curve of an example of a 1D periodic material

3.2 Analytical Study of Periodic Materials

In this section, the focus of our interest is on the wave characteristics traveling on periodic materials. For the purpose of this study, S-Wave propagation in a 1D periodic medium is selected as the case study. The unit cell is the same as that discussed in Section 3.1.2. The results are obtained analytically through the transfer matrix method.

3.2.1 Periodic materials with infinite number of unit cells

By solving the Eigenvalue problem presented in Eq. (3-26) or the simplified Eq. (3-31), one can find a set of two complex wave numbers $(k = k_{\mathrm{RL}} + \mathrm{i}k_{\mathrm{IM}})$ for a given frequency, where k_{RL} indicates the real part of a wave number that represents the oscillation over space, and k_{IM} indicates the imaginary part that represents the exponential decay of the wave amplitude.

For a given frequency inside the pass bands (outside the frequency band gaps), each of the wave numbers only has the real part $(k_{\mathrm{IM}} = 0)$. This signifies that the waves propagate without any decay of the wave amplitude. Both wave numbers have the same value with different signs that represent the direction of propagation. Inside the frequency band gaps, the two complex wave numbers are conjugates to each other. Both real parts of the wave numbers have the same value. They are either 0 or π/h that indicates a standing wave form. The positive imaginary value indicates exponential decay in the positive direction. The negative value, on the other hand, shows an amplification in the positive direction. However, this can be seen as the wave amplitude decaying in the opposite direction.

Figure 3-5(a) shows the dispersion band diagram of the case study that put the real and imaginary parts together. This diagram only shows the results of the first wave number from each set. The dispersion diagram is the same as the dispersion curve shown in Figure 3-4(a) which only plots the wave numbers in the pass bands. It is observed from the diagram that the values in the imaginary part start from 0 near the boundaries of the frequency band gaps and become greater toward the middle of each frequency band gap. This indicates that the largest decay of wave amplitude occurs in the middle of the frequency band gaps and becomes less toward the boundaries, and ultimately the wave amplitude has no decay in the pass bands. The ratio of a wave amplitude after passing through the unit cell to the input wave amplitude is shown in Figure 3-5(b).

To have a better understanding of the vibration modes or the wave profiles inside the 1D periodic material, the wave profiles of selected frequencies are plotted. Figure 3-6(a) shows the wave profiles at two time instances at a frequency of 3.5 Hz (in the pass band). The wave number of this frequency is $0.3688\,\pi/h$ which tells that a sinusoidal wave is completed in 5.423 unit cells, as shown in the figure. Figure 3-6(a) also shows that a wave with a frequency falling in the pass bands propagates through the periodic material such that a phase difference develops between the profiles at any two instances in time, provided the time difference is not a whole number multiplication of period, T. Figure 3-6(b) shows the wave profiles at a frequency of 7.0794 Hz. This frequency is the boundary between the first pass band and the first frequency band gap with a wave number of π/h. Therefore, the sinusoidal wave is completed in two unit cells. This figure also indicates that the wave is neither propagating nor decaying, but rather is stationary, which signifies a standing wave form. Figure 3-6(c) shows the wave profiles at a frequency of 7.5 Hz, which is located inside the first frequency band gap. The real part of the complex wave number is π/h. Therefore, it has a similar standing wave form to that with a frequency of 7.0794 Hz. After passing though each unit cell the absolute wave amplitude is reduced to a factor of 0.5637, which is also indicated in Figure 3-5(b). As the wave travels through an infinite number of unit cells the wave amplitude goes to zero which essentially forbids the propagation of the wave.

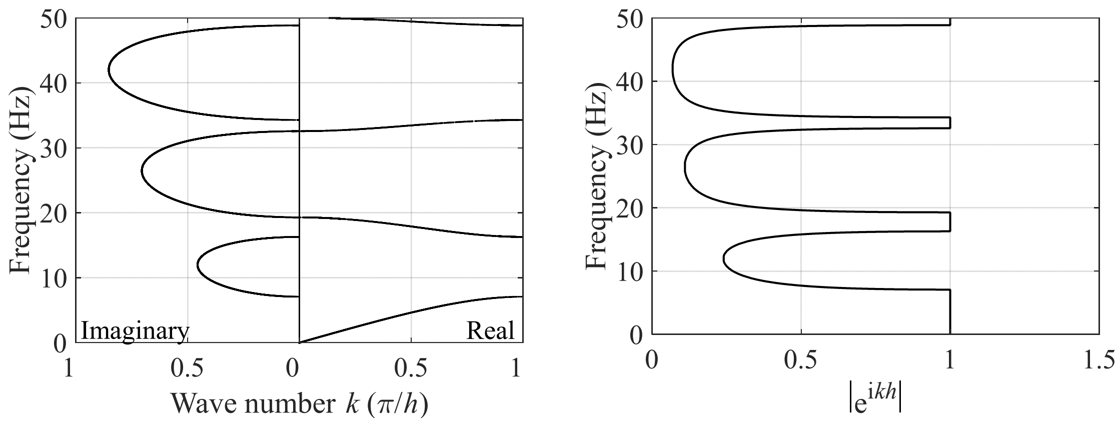

(a) (b)

Figure 3-5 (a) Dispersion diagram of S-Wave; (b) Wave amplitude ratio diagram

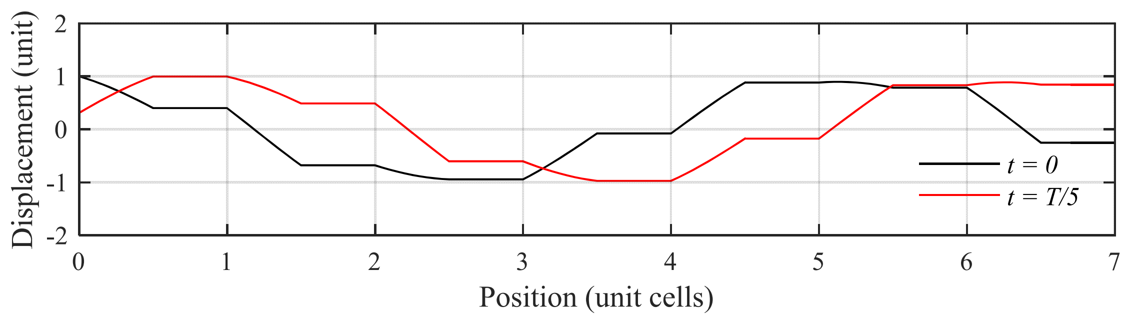

(a) Frequency 3.5 Hz (T=1/3.5 sec)

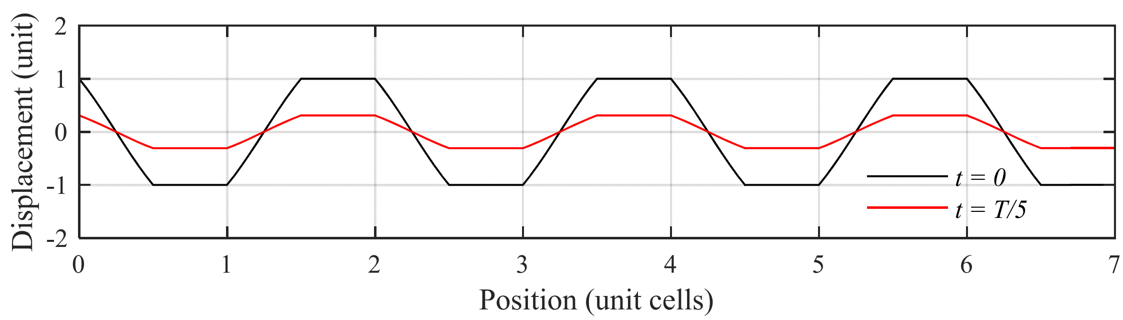

(b) Frequency 7.0794 Hz (T=1/7.0794 sec)

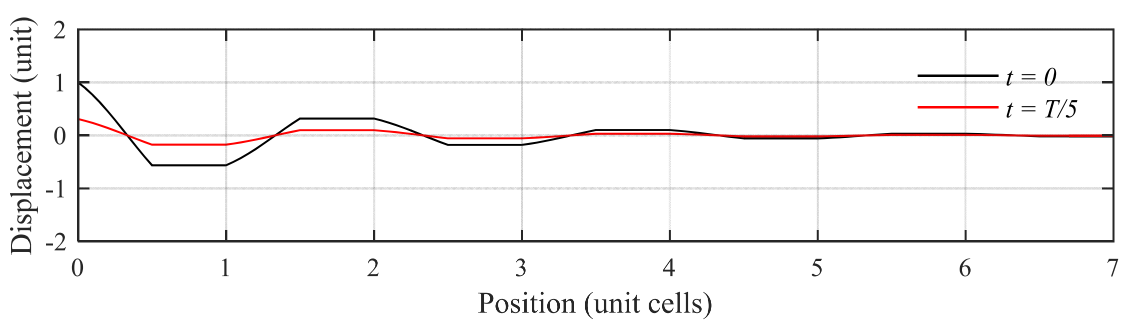

(c) Frequency 7.5 Hz (T=1/7.5 sec)

Figure 3-6 Wave profiles of seven unit cells with periodic boundary conditions

3.2.2 Periodic materials with finite number of unit cells

The study presented in the previous subsection considers periodic boundary conditions that assume an infinite number of unit cells. In reality, however, a constructed structure will consist of a finite number of unit cells. In this case, the periodic boundary conditions no longer apply. Instead, a stress free boundary condition at the top of the structure ($\tau^t = 0$) and an input displacement at the bottom of the structure ($u^b = \mathrm{e}^{i\omega t}$) are prescribed, as illustrated in Figure 3-7. The unknown variables [the stress at the bottom of the structure (τ^b) and the displacement at the top of the structure (u^t)] can be calculated from the transfer matrix equation [Eq. (3-23)], where the transfer matrix $\mathbf{T}$ contains all of the layers in the M unit cells. Knowing the displacement and the stress state at the boundaries, the displacement and the stress inside the body can also be calculated.

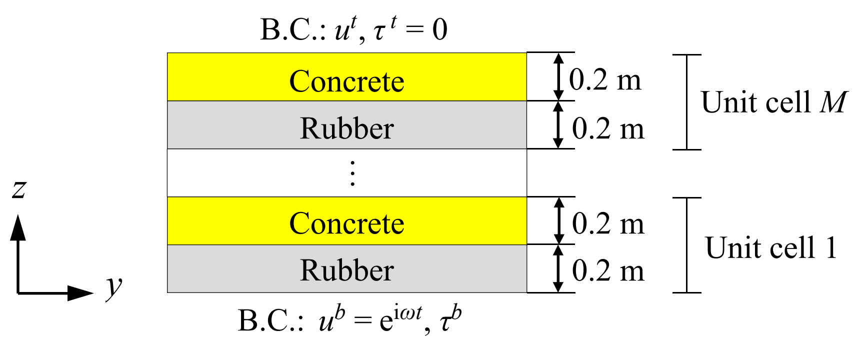

Figure 3-7 A 1D structure with M unit cells

This subsection presents a study on the wave characteristics in structures with a finite number of unit cells in comparison to the structures with an infinite number of unit cells. For brevity, the structures with a finite number of unit cells are referred to as finite structures while those with an infinite number of unit cells are referred to as infinite structures. The response of a finite structure is typically presented in the frequency response function (FRF), which can be calculated according to Eq. (3-32)

$$\text{FRF}=20\log\left(\frac{u_{out}}{u_{in}}\right), \tag{3-32}$$

where u_{in} is the input displacement or u^b in Figure 3-7 and u_{out} is the displacement at the other end boundary of the structure or u^t in Figure 3-7. Therefore, a negative value of FRF indicates a response reduction while a positive value indicates a response amplification. The regions in which the FRF values are negative are denoted as the attenuation zones. From the substitutions of the prescribed boundary conditions on Eq. (3-23), the displacement ratio $\left(u_{out}/u_{in}\right)$ can be related directly to the elements in the $\mathbf{T}$ matrix as follows: $u_{out}/u_{in} = \mathrm{T}_{(1,1)} - \mathrm{T}_{(1,2)}\mathrm{T}_{(2,1)}/\mathrm{T}_{(2,2)}$.

Consider two finite structures; each consists of one unit cell and seven unit cells. The FRF curves of both finite structures (dash-dot red curves) are compared to those of infinite structures (black curves), as shown in Figure 3-8. To construct the FRF curves of infinite structures, the displacement ratio for one unit cell is taken directly from the results presented in Figure 3-5(b) while that for seven unit cells is simply obtained by taking a power of seven from that of one unit cell. It is observed that the attenuation zones of the finite structures, shown by the dash-dot red curves, are consistent with the theoretical frequency band gaps (yellow shaded areas). It is also observed that the attenuation zones start at slightly lower frequencies than the frequency band gaps. The discrepancy, however, gets smaller as the number of unit cells increases. Inside the frequency band gaps, the attenuation feature of the finite structures is very close to that of infinite structures which also gets closer as the number of unit cells increases. Outside the frequency band gaps, the

FRF curves of finite structures show that a number of spikes equivalent to the number of unit cells are present in each of the pass bands. These spikes indicate amplification due to the resonance of wave frequencies with the natural frequencies of the finite structures.

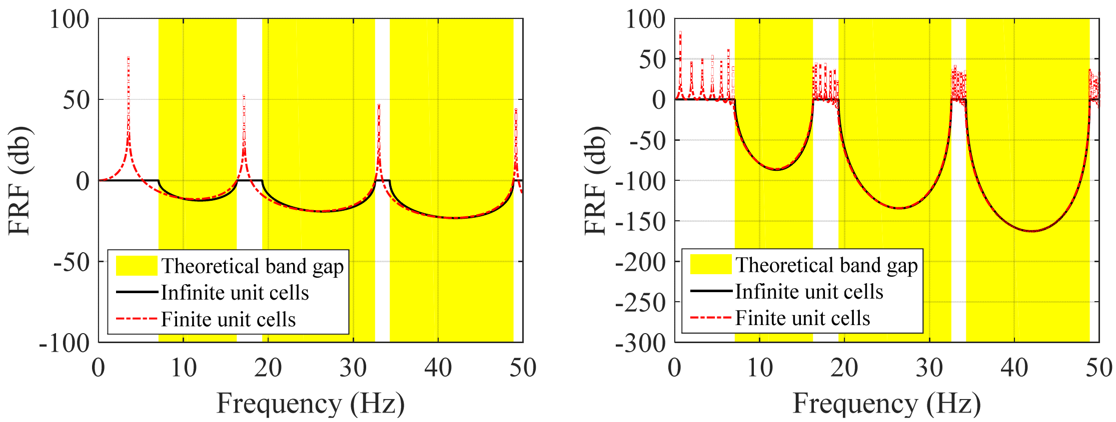

(a) One unit cell (b) Seven unit cells

Figure 3-8 Frequency response function comparison of structure with finite number of unit cells (finite structures) and structures with infinite number of unit cells (infinite structures)

Due to a few differences in the FRF curves of finite and infinite structures, one can expect a few differences in their wave profiles as well. Figure 3-9 shows the comparison of wave profiles of a finite structure with seven unit cells (dash-dot red curves) to those of an infinite structure (black curves). Figure 3-9(a) shows the wave profiles at a frequency of 3.5 Hz (in the pass band). Due to amplification in the pass band, the wave amplitude in the finite structure is observed to be larger than the input wave amplitude. In addition, the wave profiles in both structures are also found to have a phase difference. As observed from the FRF curves, the attenuation zones of periodic structures start at slightly lower frequencies than the frequency band gaps. Therefore, the wave amplitude decay is observed at the input frequency of 7.0794 Hz, as shown in Figure 3-9(b). Although an amplitude decay is observed in the finite structure, the standing wave form is displayed. The FRF curves show that the wave attenuation of both structures inside the frequency band gaps is very close to each other. The wave profile in the periodic structure at a frequency of 7.5 Hz (inside frequency band gaps) is similar to that of the infinite structure in terms of both the wave amplitude decay and the standing wave form, as shown in Figure 3-9(c).

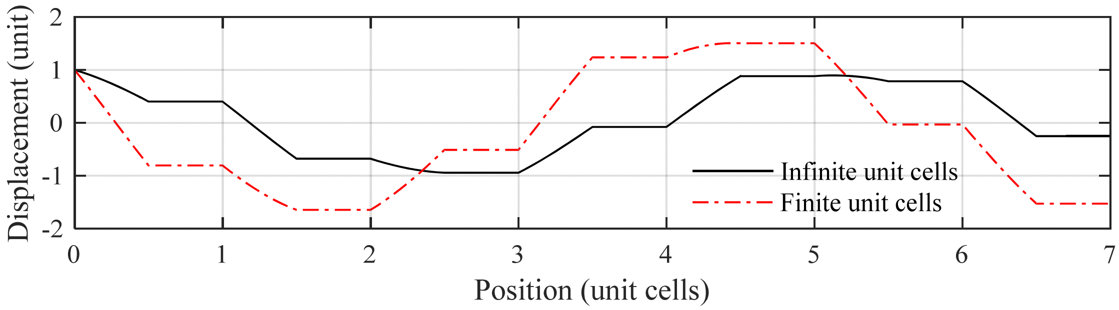

(a) Frequency 3.5 Hz

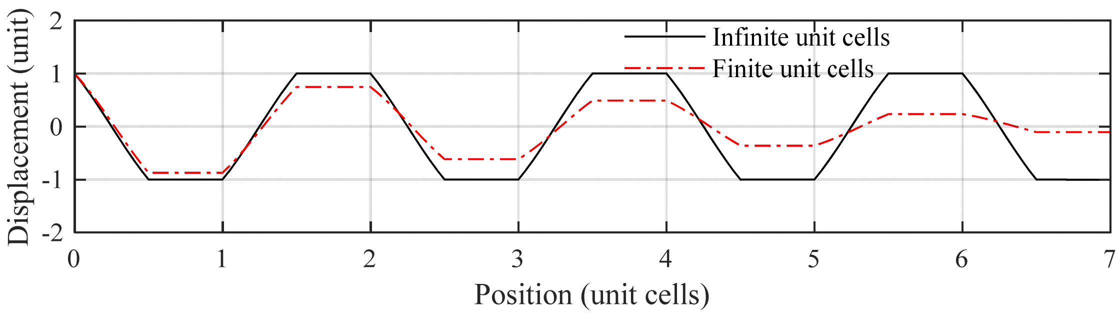

(b) Frequency 7.0794 Hz

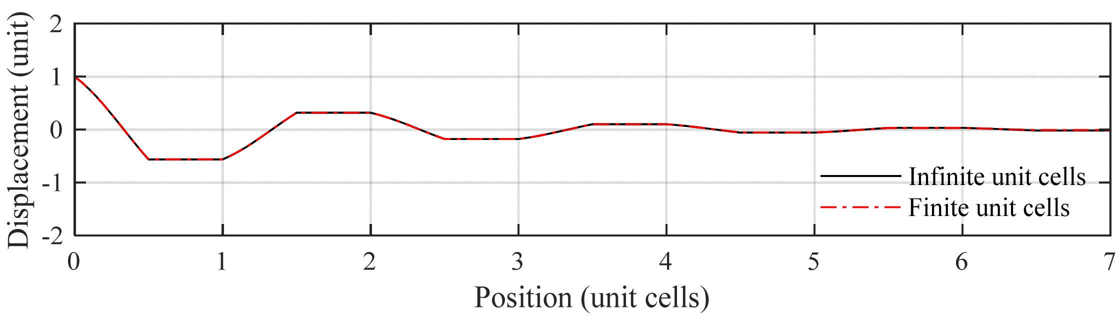

(c) Frequency 7.5 Hz

Figure 3-9 Comparison of wave profiles in a structure with finite number of unit cells (finite structures) and in a structure with infinite number of unit cells (infinite structures)

3.2.3 Periodic materials with damping

A real structure is not only finite in dimension but also possesses inherent material damping. Some materials, such as natural rubber, polyurethane, and other types of elastomers, are known to have a high amount of inherent damping. Employing these materials as one of the components of the unit cell in periodic materials makes the structure highly dissipative. This subsection explores the effect of material dissipation on the propagation of elastic waves. The discussion covers the damping effect in periodic materials from the aspect of the dispersion relationship to the response of finite structures.

In this study, the constitutive relationship of a viscoelastic material is represented using the Kelvin-Voigt model. As shown in Figure 3-10, the mechanical analog of this model is represented by a purely viscous damper and purely elastic spring connected in parallel. The mathematical formulation for this constitutive relationship is shown in Eq. (3-33)

$$\sigma = E\varepsilon + \eta\dot{\varepsilon}\,, \tag{3-33}$$

where σ is the stress, ε is the strain, $\dot{\varepsilon}$ is the strain rate, and η is the viscosity.

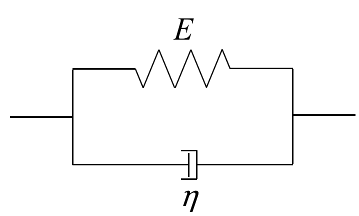

Figure 3-10 Mechanical analog of Kelvin-Voigt model

The implementation of the Kelvin-Voigt model in 1D periodic materials is as follows. Consider a 1D elasto-dynamic equation in each layer n as shown in Eq. (3-34)

$$\rho_n \frac{\partial^2 u_n}{\partial t^2} = \frac{\partial \sigma_n}{\partial z_n}. \tag{3-34}$$

The stress (σ_n) shown in Eq. (3-34) represents either normal stress or shear stress depending on the input wave. Based on the mechanical analog model, the constitutive equations for normal (σ_n) and shear (τ_n) stresses are shown in Eqs. (3-35) and (3-36):

$$\sigma_n = (\lambda_n + 2\mu_n)\frac{\partial u_n}{\partial z_n} + \eta_n \frac{\partial}{\partial t}\left(\frac{\partial u_n}{\partial z_n}\right) \text{ and} \tag{3-35}$$

$$\tau_n = \mu_n \frac{\partial u_n}{\partial z_n} + \eta_n \frac{\partial}{\partial t}\left(\frac{\partial u_n}{\partial z_n}\right), \tag{3-36}$$

respectively. To obtain the spatial wave equation for the S-Wave, the constitutive relationship for shear stress shown in Eq. (3-36) is first substituted into Eq. (3-34). The substitution results in a viscoelastic S-Wave equation, as shown in Eq. (3-37)

$$\rho_n \frac{\partial^2 u_n}{\partial t^2} = \mu_n \frac{\partial^2 u_n}{\partial z_n^2} + \eta_n \frac{\partial}{\partial t}\left(\frac{\partial^2 u_n}{\partial z_n^2}\right). \tag{3-37}$$

Substitution of Bloch-Floquet solution, Eq. (3-11), into Eq. (3-37) yields the spatial wave equation for the S-Wave, as shown in (3-38)

$$C_n^{*2} \frac{\partial^2 u_n(z_n)}{\partial z_n^2} + \omega^2 u_n(z_n) = 0, \tag{3-38}$$

where $C_n^* = \sqrt{(\mu_n + \eta_n \mathrm{i}\omega)/\rho_n}$ is the speed constant for the S-Wave in the viscoelastic medium. Following the same derivation using the constitutive relationship for normal stress, Eq. (3-35), one can find that the spatial wave equation for the P-Wave is the same as that presented in Eq. (3-38) with the speed constant for the P-Wave in the viscoelastic medium denoted as $C_n^* = \sqrt{(\lambda_n + 2\mu_n + \eta_n \mathrm{i}\omega)/\rho_n}$.

Since the difference between waves in viscoelastic and elastic materials only lies in the speed constants, the wave characteristic in viscoelastic periodic materials can also be solved using the transfer matrix method presented in Subsection 3.1.2. One only needs to change the speed constants to incorporate the damping effect.

Arbitrary values of viscosity η are selected to see the effect of damping in the dispersion relationship. The viscosity in each layer is taken as a fraction of the Young's Modulus E of the respective layer. Figure 3-11(a) shows the dispersion band diagrams of the S-Wave in medium with different viscosity values. When viscosity is included $(\eta \neq 0)$, all of the obtained complex wave numbers have a value in their imaginary parts $(k_{\mathrm{IM}} \neq 0)$. Therefore, an incoming wave with any frequency experiences wave amplitude reduction. Inside the frequency band gaps, the imaginary parts of the wave numbers with and without viscosity are very close. Viscosity mostly affects the wave reduction in the pass bands. The higher the pass bands the larger the wave amplitude reduction, as shown in Figure 3-11(b). The higher the viscosity value the larger the amplitude reduction on the pass bands. Whereas inside the frequency band gaps the response reduction remains similar to those without viscosity and with low viscosity value.

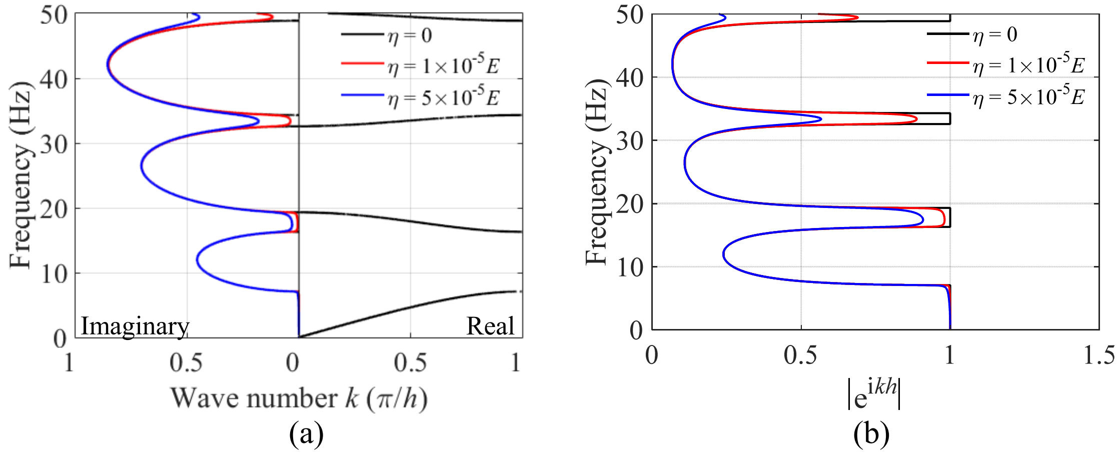

Figure 3-11 (a) Dispersion diagrams of S-Wave in viscoelastic mediums; (b) Wave amplitude ratio diagrams in viscoelastic mediums

When damping is applied to the finite structures, it is observed that damping can effectively control the amplifications that occur because of resonance in the pass bands. At higher pass bands, as shown in Figure 3-12, the spikes go below 0 db which makes the response amplification becomes response reduction. A higher viscosity causes the reduction to occur at lower pass bands. Inside the frequency band gap, the FRF curves with and without damping shows a very similar response. The results show that damping is very beneficial for wave isolation.

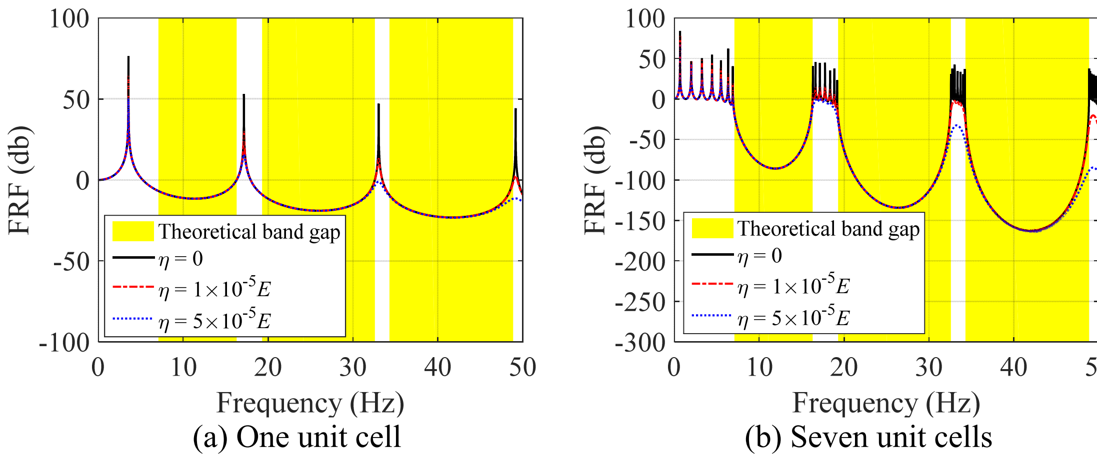

Figure 3-12 Frequency response function of structure with finite number of unit cells (finite structures) in viscoelastic mediums

3.3 Numerical Study of Periodic Materials

Although the number of unit cells is finite, the analytical study presented in the previous section still assumes infinite plane in the perpendicular direction to the layer thickness. This section extends the study using a numerical approach based on the finite element method to understand the behavior of periodic materials in a more realistic configuration. As this research focuses on the development of 1D and 3D periodic material-based seismic isolators for SMR building, both types of periodic materials were investigated.

3.3.1 Numerical verification

In order to ensure the finite element method is credible for this study, a numerical verification is first conducted. This subsection presents the verification of finite element models by comparing the numerical solution of a 1D finite structure subjected to the S-Wave with the analytical solution. In this section, the numerical solution refers to the results obtained from finite element simulation while the analytical solution refers to the theoretical (closed-form) solution obtained using the transfer matrix method.

Figure 3-13 shows the finite element model for the finite structure that was used in the analytical study section. The finite element model was built using a commercial finite element program ABAQUS. The thickness (length in *x* direction) for each of the rubber and concrete layers is 0.2 m and the width (length in *y* direction) of each layer is arbitrarily selected as 3 m. To mimic the 1D wave theory under the S-Wave, the upper and lower sides of the concrete layers as well as the left side of the structure were constrained to allow displacement only in the *y* direction. The provided constraints allow the periodic structure to have a simple shear deformation as prescribed in the 1D theory. In addition, these constraints eliminate the possibility of rocking in the structure allowing the width of the layers to be arbitrarily selected.

The finite element model of the structure was modeled in a 2D environment using plane elements. Each of the concrete layers was meshed with sixty elements along the width and two elements along the thickness. A 4-node bilinear quadrilateral element was assigned on each element on the concrete layers. On the other hand, each of the rubber layers was meshed with sixty elements along the width and three elements along the thickness. An 8-node biquadratic quadrilateral element was assigned on each element on the rubber layers. The rubber layers were assigned with a smaller size of element with a higher number of nodes because the results from the analytical study show that the displacement is concentrated on the rubber layers. A steady-state frequency sweeping analysis was conducted to obtain the FRF curve. The input displacement u_{in} is recorded at the left boundary of the structure and the output displacement u_{out} is recorded at the right boundary of the periodic structure. In addition to the two points on the left and right boundaries, displacement at the nodes inside the periodic structure were also recorded (see red dots in Figure 3-13) to see the form of the vibration modes. The analysis was carried out for each of the plane stress and plane strain conditions.

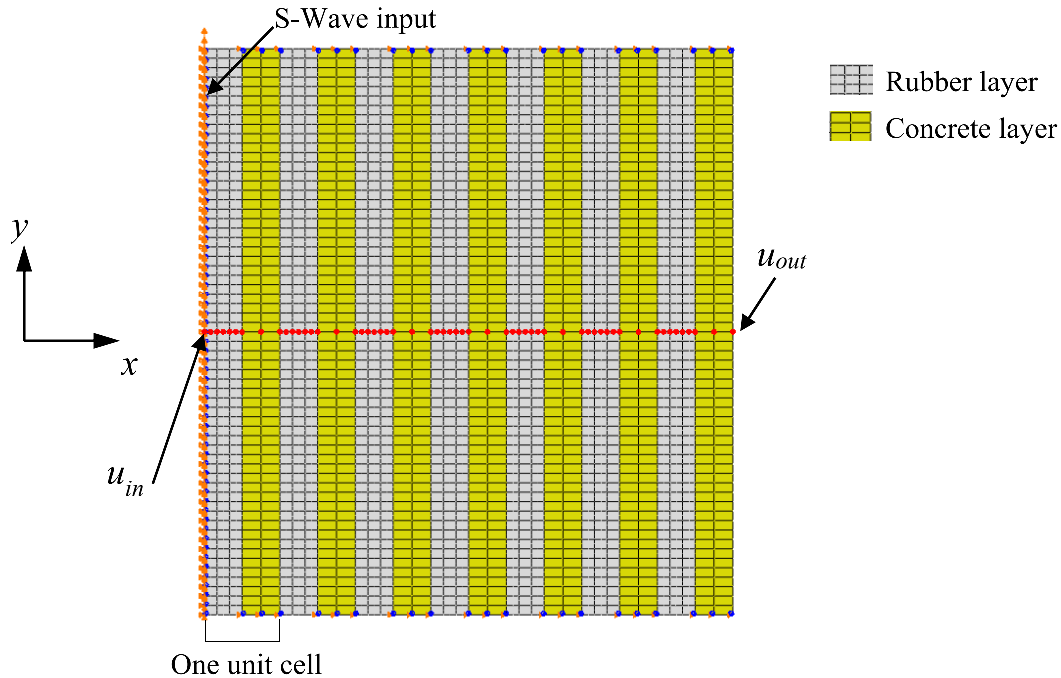

Figure 3-13 Finite element model with two-dimensional plane elements

The main problem in using the finite element method is that, in many cases, it exhibits severe stiffening near the incompressible limit, i.e., Poisson's ratio close to 0.5. This phenomenon is commonly referred to as *volumetric locking*. To eliminate the volumetric locking condition, a reduced integration scheme was assigned on each of the elements.

Figure 3-14 presents the FRF curves from the finite element simulation in comparison to the analytical solution. The FRF curves of both plane stress and plane strain conditions are similar to one another. They are also very close to the analytical solution. The results are very similar up to the third pass band. However, in the fourth attenuation zone, both curves from numerical solutions are slightly off from the analytical solution. This indicates that the size of elements in the rubber layers is not small enough to capture the response at the higher frequencies. However, the results are still acceptable considering the similar tendency and the small difference.

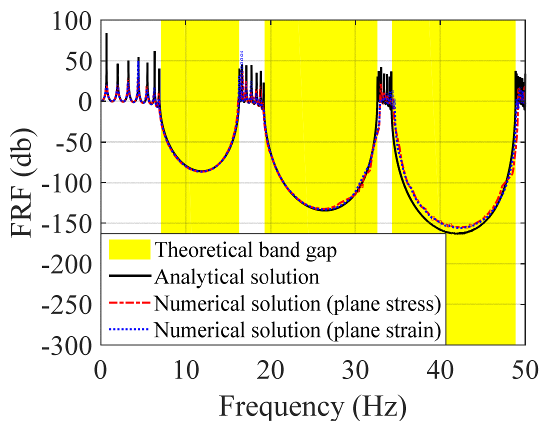

Figure 3-14 Frequency response function comparison of the numerical solutions with the analytical solution

In addition to the FRF, the wave profiles inside the body of the finite structure are also investigated. Figure 3-15 shows the wave profiles at frequencies of 3.5 Hz (in the first pass band) and 7.5 Hz (in the first frequency band gap). It is observed that the numerical solutions exhibit similar wave profiles as the analytical solution. Although results from both the plane stress and plane strain conditions are very close, the results from the plane strain condition are observed to be closer to the analytical solution. This is very reasonable considering that the plane strain assumes infinite length in the out-of-plane direction which is closer to the theory.

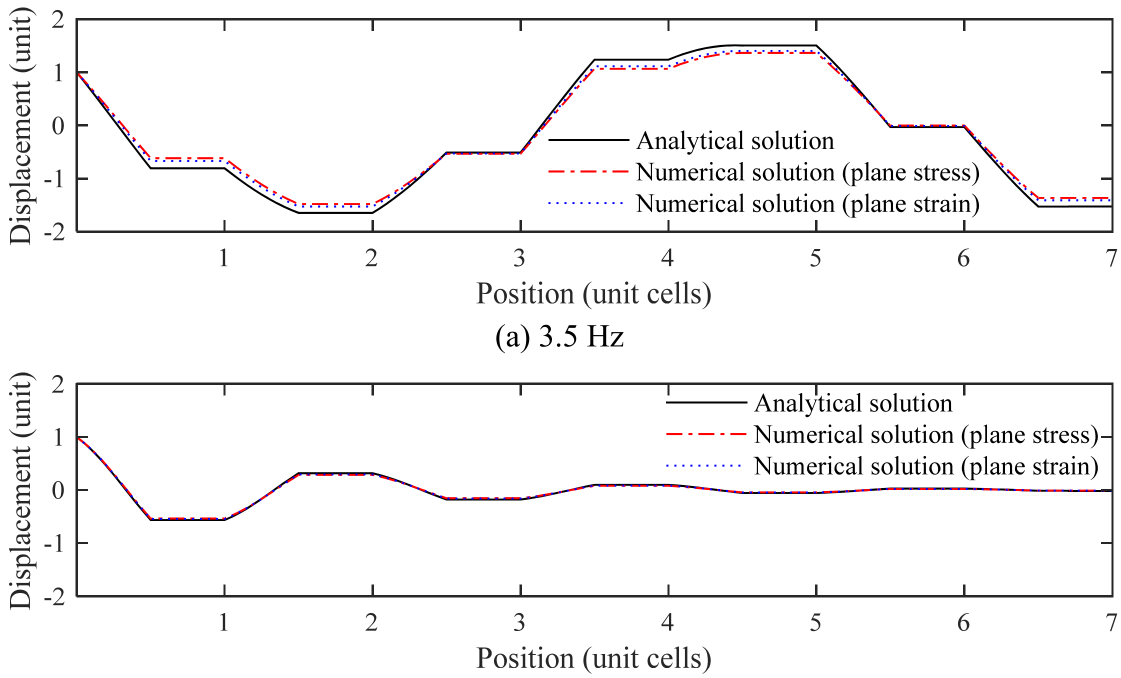

(a) 3.5 Hz

(b) 7.5 Hz

Figure 3-15 Wave profiles in the finite element models with different types of plane elements

The element size in a finite element model plays an important role in the accuracy of the simulation results. The higher the wave frequency gets, the shorter the wavelength becomes, and consequently, a smaller element size is needed to capture the wave response. A convergence study is conducted to understand what element size, in comparison to the wavelength, is needed for the finite element solution to converge to the analytical solution. In this study, the structure is modeled with the plane strain condition. Since the highest frequency considered in this study is 50 Hz, the element size is compared with the wavelength at that particular frequency. Based on the material properties, the wavelength for the S-Wave in each of the concrete and rubber layers at the frequency of 50 Hz is 53.8381 m and 0.1303 m, respectively. Since the concrete layers are relatively stiff in comparison to the rubber layers, the deformation of the periodic structure is concentrated on the rubber layers. Hence, the convergence study is conducted by changing the element sizes in the rubber layers in the thickness direction. Figure 3-16 shows the FRF results of finite element simulation with different element sizes in the rubber layers along the thickness. While the response is very similar up to a frequency of 40 Hz, the result with the element size of 0.1 m or 0.767 of the wavelength (dash green curve) shows deviation from the rest of the results at frequencies of 40-50 Hz. The results with element sizes of 0.067 m or 0.51 of the wavelength (dot blue curve) and 0.05 m or 0.3837 of the wavelength (dash-dot purple curve) are very close to the analytical solution. The results show that the element size needs to be at most a half of the wavelength to obtain an acceptable result. Note that this finding is for the quadratic type element.

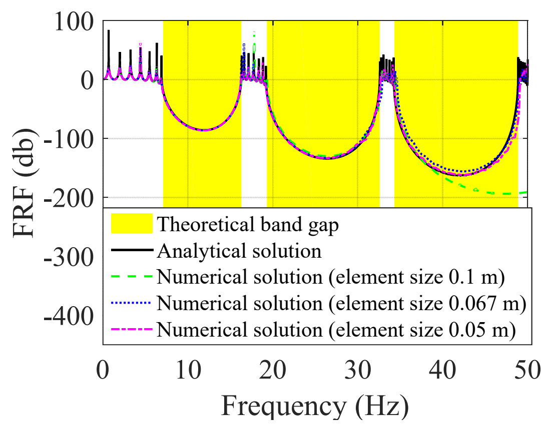

Figure 3-16 Frequency response function of finite element models with different element sizes in the rubber layers

The finite element verification conducted in this section showed that the finite element approach can simulate the behavior of the 1D finite structure very close to the theory. It is observed that the results of plane stress and plane strain conditions are very similar. However, the results from the plane strain condition are slightly closer to the analytical solution. The accuracy of the finite element model depends on the element size.

For a quadratic element type, an element size approximately a half of the wavelength is sufficient to capture the deformation.

3.3.2 Numerical study of 1D periodic materials

As the finite element method was verified to accurately model the wave characteristic in the structure with a finite number of unit cells, the study of periodic materials can be further carried out using the numerical approach. This subsection presents the study of 1D periodic materials with a finite geometry where the different plane sizes are considered. In addition, a method to eliminate pass bands using a four-layer unit cell was also studied. Finally, as the periodic material is designed as a structural foundation, the effect of the superstructure on the frequency band gaps was also investigated.

3.3.2.1 Plane size effect of 1D periodic materials

To study the plane size effect of 1D periodic materials on their behavior, three structures with different plane sizes were modeled and analyzed. Each of these structures consists of one unit cell. The thickness and material properties of each layer are the same as those used in the previous sections. Figure 3-17 shows all three case studies. In reality, the rubber layer will always sit on a base which receives input excitation. Therefore, a concrete base with a thickness of 0.2 m was modeled at the bottom of each unit cell to represent a foundation or base where the unit cell seats.

The FRF of all plane sizes are presented in Figure 3-18. It is observed that all of them have attenuation zones consistent with the theoretical frequency band gaps. Occasional spikes inside the frequency band gaps, such as those observed for the plane size of 1 m by 1 m, happen due to rocking modes. The rocking modes occur because the aspect ratio (length to the total thickness of all unit cells) is too small. The results clearly show that to eliminate the possibility of rocking, the aspect ratio needs to be large enough. The larger the plane size (aspect ratio), the closer it is to the theoretical infinite plane size and, therefore, the less spikes occur inside the frequency band gaps.

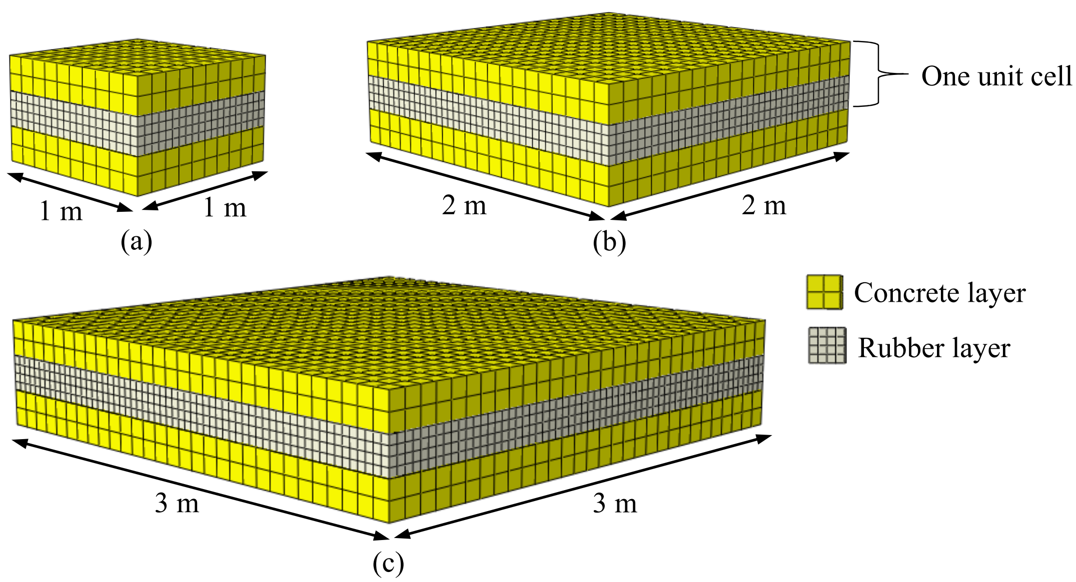

Figure 3-17 Case studies of finite structures with different plane sizes: (a) 1 m x 1 m (b) 2 m x 2 m, and (c) 3 m x 3 m

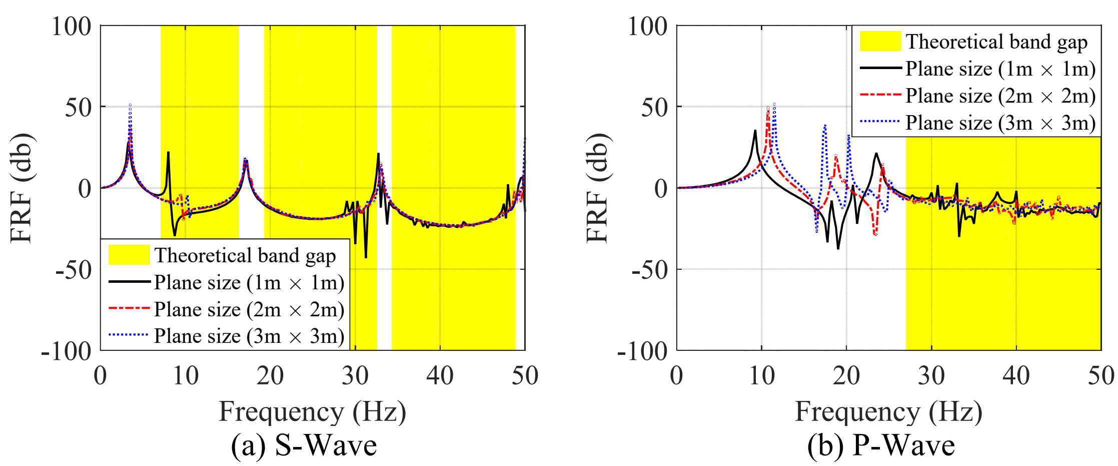

Figure 3-18 Frequency response function of 1D periodic material with different plane sizes

3.3.2.2 Multilayered unit cell on 1D periodic materials

Based on the study presented in Subsection 3.2.2, the addition of unit cells in a finite structure provides a larger response reduction inside the frequency band gaps. The attenuation zones, however, do not change much nor do the pass bands. Elimination or reduction of pass bands is an attractive subject given that one of the aims in this study is to design the frequency band gaps as wide as possible to cover a wide range of main frequency content of earthquakes. In this study two unit cells that have their frequency band gaps covering one another were put together as a four-layer unit cell to reduce the pass bands.

The first unit cell is the unit cell that has been the subject of analytical and numerical studies so far. For convenience, this unit cell is denoted as Unit cell A. The second unit cell, denoted as Unit cell B, is also composed of concrete and rubber layers as the first one. However, the thickness of the concrete layer was increased to 0.25 m and that of the rubber layer was decreased to 0.15 m. The frequency band gaps of these two unit cells are covering one another. Therefore, these two unit cells were combined into a four-layer unit cell denoted as Unit cell C. The finite element model for the structure with each of the above mentioned unit cells is shown in Figure 3-19.

The FRF and theoretical frequency band gaps of each of the unit cell structures subjected to the S-Wave wave are shown in Figure 3-20. The analyses were ceased at 50 Hz. The theoretical frequency band gaps of the finite structure with Unit cell A are 7.076-16.29 Hz, 19.29-32.58 Hz, and 34.3-48.87 Hz while those of the finite structure with Unit cell B are 7.56-21.72 Hz, 24.31-43.43 Hz, and 44.85-50 Hz. The frequency band gaps of both unit cells are overlapping one another. By combining these two unit cells, the frequency band gaps of Unit Cell C are found starting from 7.37 Hz to 50 Hz with thin pass bands at 17.35-17.85 Hz, 23.14-23.47 Hz, 33.32-33.44 Hz, 44.16-44.26 Hz, and 49.38-49.48 Hz. All these pass bands are smaller than 0.5 Hz. The FRF curves are observed to be very consistent with their respective theoretical frequency band gaps.

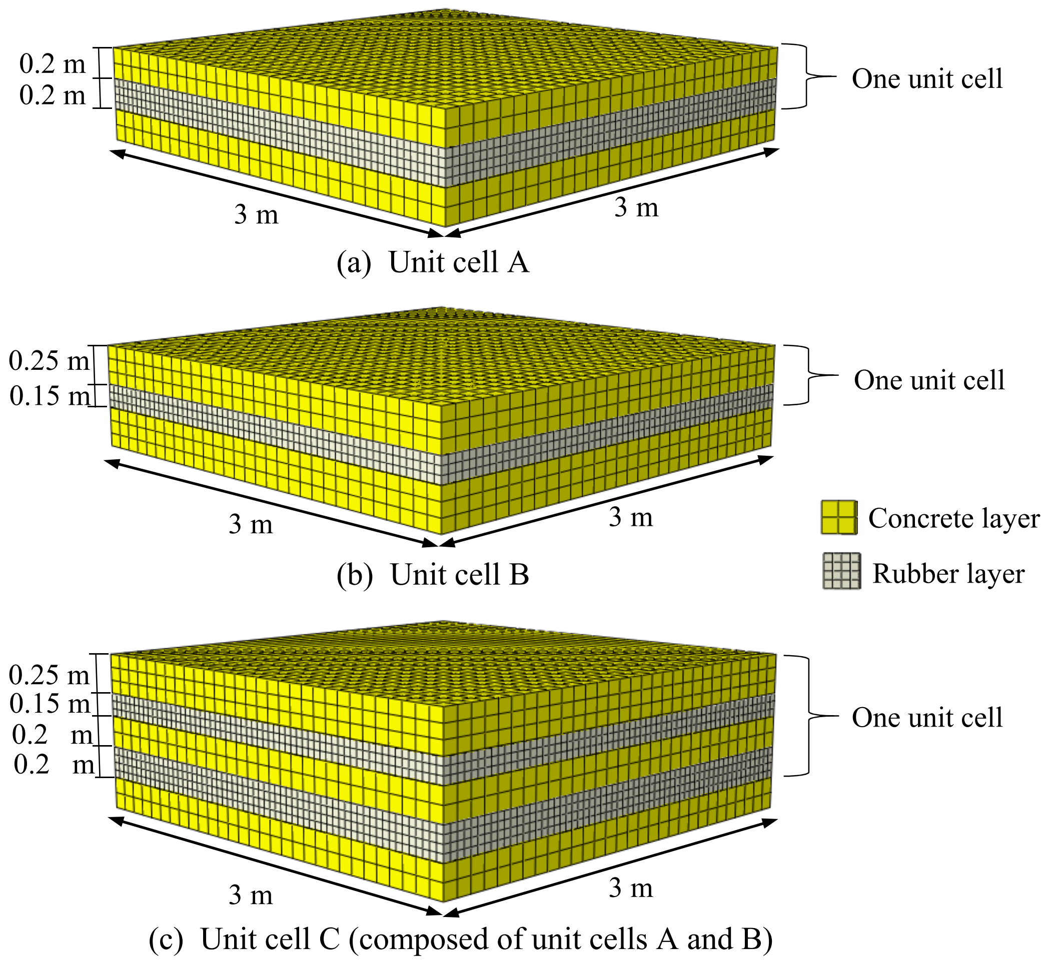

Figure 3-19 Finite structures with combined unit cells

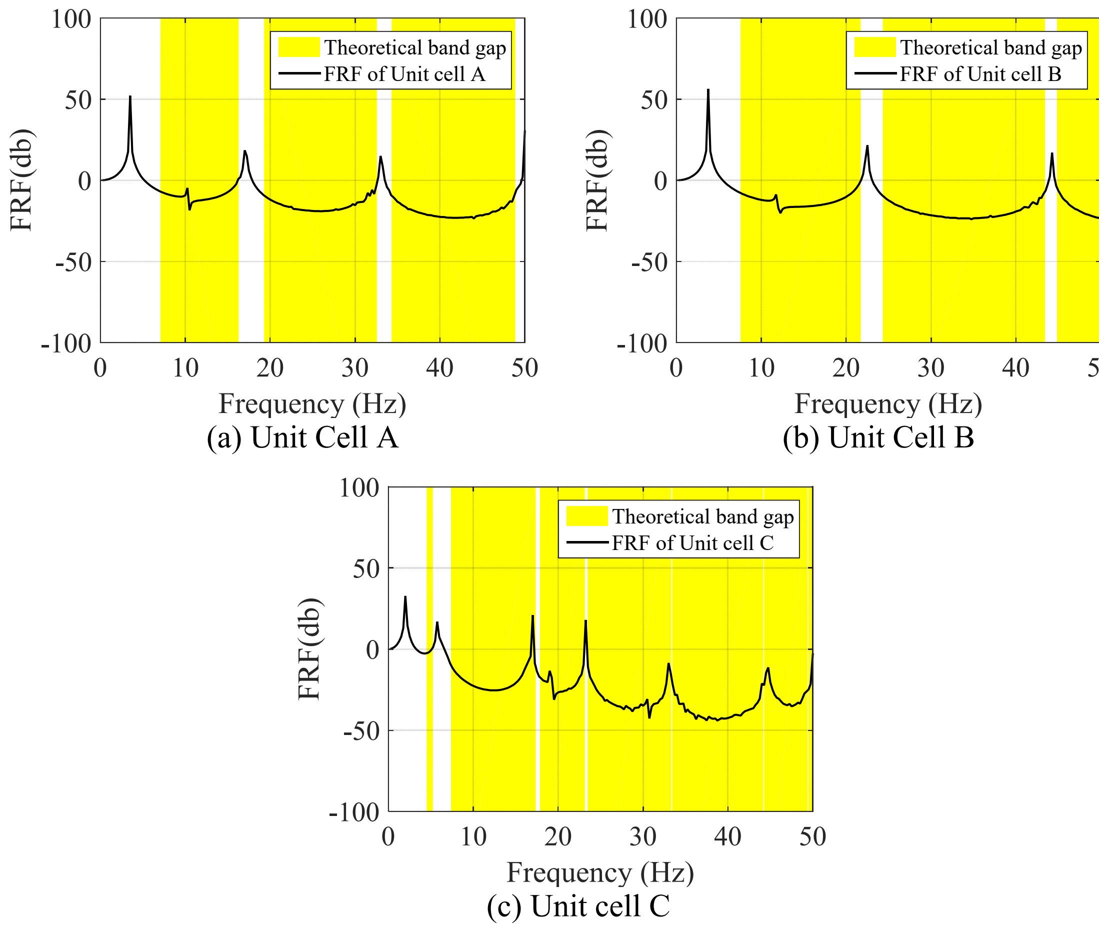

Figure 3-20 Frequency response function of 1D periodic material with different unit cells

3.3.2.3 Superstructure on 1D periodic foundation

In this study, the periodic materials will be designed at a larger scale as a foundation that supports a superstructure. The presence of the superstructure most likely will affect the attenuation zones of periodic foundations. Therefore, it is necessary that the effect of the superstructure on the attenuation zones be addressed. For that purpose, a finite element model of a superstructure seating on a one unit cell 1D periodic foundation was built, as illustrated in Figure 3-21(a). The entire 1D periodic foundation structural system seats on top of a concrete base where input is assigned. The mass and stiffness of the superstructure were tuned, so that the natural frequency of the superstructure alone is 10 Hz (typical natural frequency of a nuclear reactor building). Figure 3-21(b) shows the FRF curves of the 1D periodic foundation structural system in comparison to that of the 1D periodic foundation only. The response at the top of the superstructure (blue curve) and that at the bottom of the superstructure (red curve) is quite similar. This indicates that the superstructure is relatively stiffer and the movement is concentrated on the rubber layer. The responses, however, are quite different with that of the 1D periodic foundation only (black curve) especially in the first attenuation zone. It is observed that the first attenuation zone of the 1D periodic foundation structural system starts at a much lower frequency than that without the superstructure. However, each of the FRF curves has its first attenuation zone end at almost similar frequencies. In addition, the second and third attenuation zones are observed to be quite similar. Therefore, one can say that the presence of the superstructure lowers the starting of the first attenuation zone.

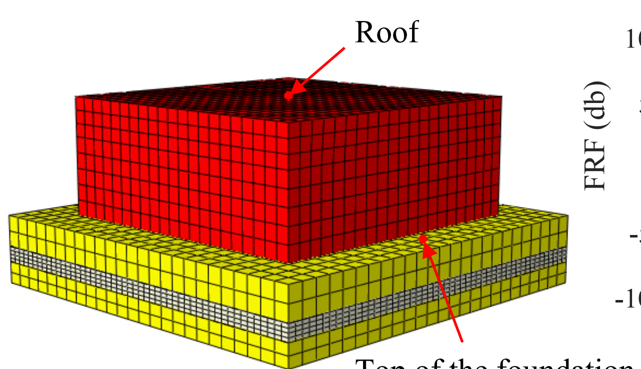

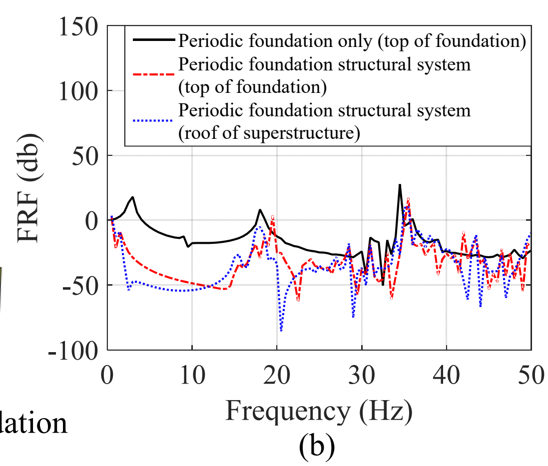

Figure 3-21 (a) A 1D periodic foundation structural system (b) FRF of a 1D periodic foundation structural system

Performing finite element analysis of the full superstructure with periodic foundation can be time consuming. Since the presence of the superstructure will alter the

FRF curve especially in the first attenuation zone, it is more convenient if one can predict the altered attenuation zone without having to model the entire superstructure. This is very advantageous especially during the preliminary design phase.

When the superstructure is stiff enough (such as a nuclear reactor building), it is proposed to transform the superstructure into an equivalent additional layer on the unit cell, as shown in Figure 3-22. The superstructure is assumed as an additional layer with a thickness h_{str}^{*}. The total weight of the superstructure is then transferred into an equivalent density by dividing the total weight with the multiplication of the designed cross sectional area (plane area) of the periodic foundation and the additional layer thickness.

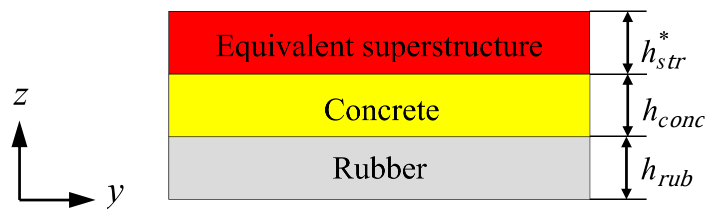

Figure 3-22 Unit cell with equivalent superstructure layer

Figure 3-23(a) and Figure 3-23(b) show the S-Wave dispersion curves of the unit cell with different equivalent superstructure layers. In Figure 3-23(a), the thickness of the equivalent superstructure layer was set equal to the thickness of the concrete layer $\left(h_{str}^{*} = h_{conc}\right)$. In Figure 3-23(b), it was set equal to ten times the thickness of the concrete layer $\left(h_{str}^{*} = 10h_{conc}\right)$. Both dispersion curves show very similar frequency band gaps. Figure 3-23(c) shows that the FRF curves coincide with the theoretical frequency band gaps of the unit cell with an equivalent superstructure layer. Based on these results, one can estimate the altered frequency band gaps due to the presence of the superstructure by using the proposed method. Since the superstructure is much stiffer than a component in the periodic foundation, the effect of the equivalent thickness on the predicted frequency band gaps is negligible. Therefore, it is proposed that the thickness of the equivalent superstructure layer be set the same as the uppermost concrete layer or the stiffer layer in the unit cell.

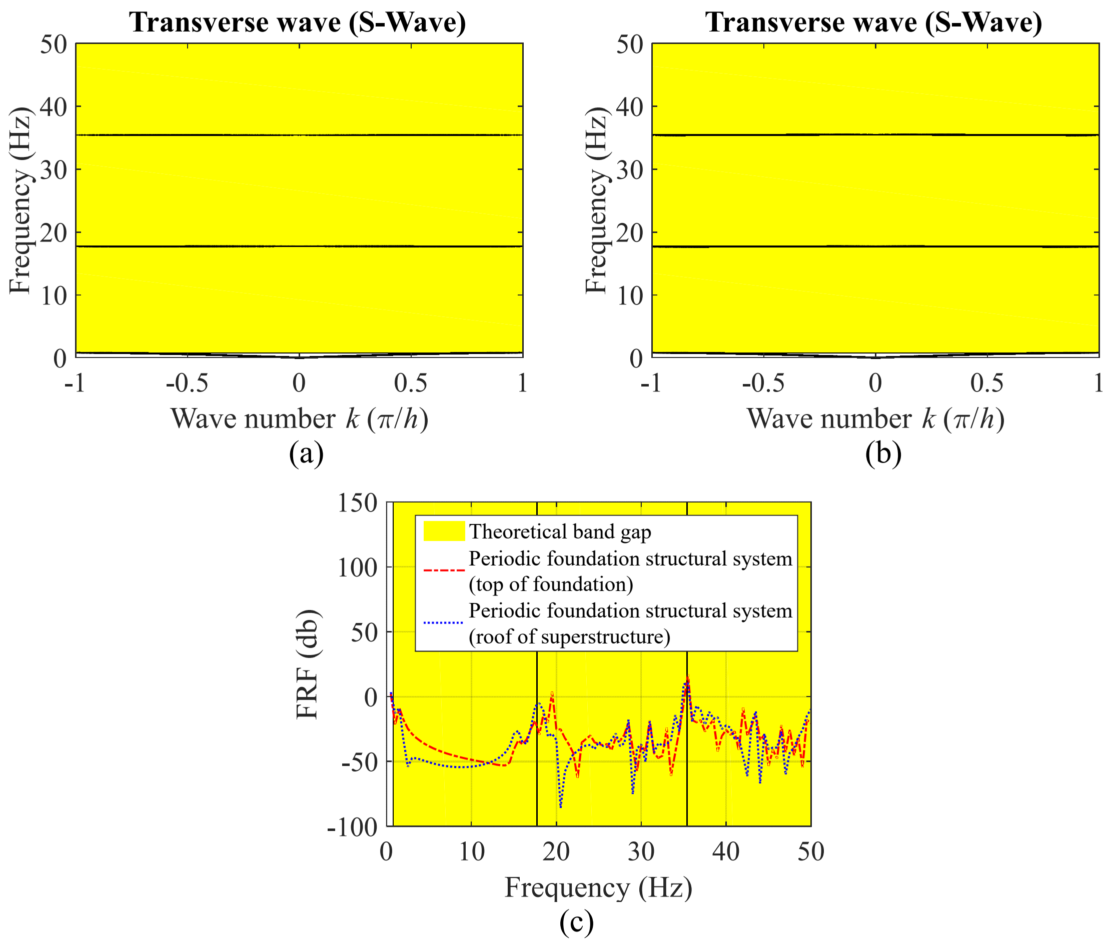

Figure 3-23 (a) Theoretical band gap for $\left(h_{str}^{*}=h_{conc}\right)$; (b) Theoretical band gap for $\left(h_{str}^{*}=10h_{conc}\right)$; (c) FRF of 1D periodic foundation structural system

3.3.3 Numerical study of 3D periodic materials

This subsection presents the study of 3D periodic materials with a finite geometry. Two types of unit cells were investigated, namely the Locally resonant type unit cell and the Bragg scattering type unit cell. Figure 3-24(a) shows a typical Locally resonant unit cell. The unit cell for this type is commonly composed of a stiff and dense core (red) enclosed by soft and light coating (grey) and contained in a stiff and dense matrix (yellow). The frequency band gaps of this type of unit cell arise from local vibration resonances of the coated core. In this study, the cubic core is made of steel with a length of 0.6 m while the coating is assumed to be made of rubber with a thickness of 0.1 m. The matrix is assumed to be made of concrete. The length of the cubic unit cell size was set as 1 m. The material properties for concrete and rubber are the same as those used in previous studies while those for steel are shown in Table 3-2. For convenience, all of the material properties are listed in Table 3-2. The corresponding dispersion curve is shown in Figure 3-25(a) with the FRF of the unit cell shown in Figure 3-25(b). It is observed that the minimum FRF value is -0.33 which corresponds to a response reduction of 3.73%. Such reduction is too small to economically protect the superstructure from incoming seismic waves.

Table 3-2 Material properties for numerical study

Material	Young's modulus (MPa)	Density (kg/m^3)	Poisson's ratio
Concrete	40,000	2300	0.2
Rubber	0.1586	1277	0.463
Steel	200,000	7850	0.3

Figure 3-24(b) shows a typical Bragg scattering unit cell. This type of unit cell is commonly composed of two different materials. A dense and stiff core (yellow) is usually embedded inside a light and soft matrix (grey). The frequency band gaps of this unit cell come from the scattering effect based on Bragg's law that was first proposed by two British physicists, Lawrence Bragg and his father William Henry Bragg, in 1913 [67]. In this study, the cubic core is made of concrete with a length of 0.9 m and the matrix is made of rubber with a unit cell length of 1 m. The dispersion curve and the FRF curve of the unit cell are shown in Figure 3-26. Unlike the Locally resonant one, the Bragg scattering unit cell possesses a large response reduction inside the frequency band gap which is very economical for use in seismic isolation. Therefore, the Bragg scattering type unit cell was selected for further investigation.

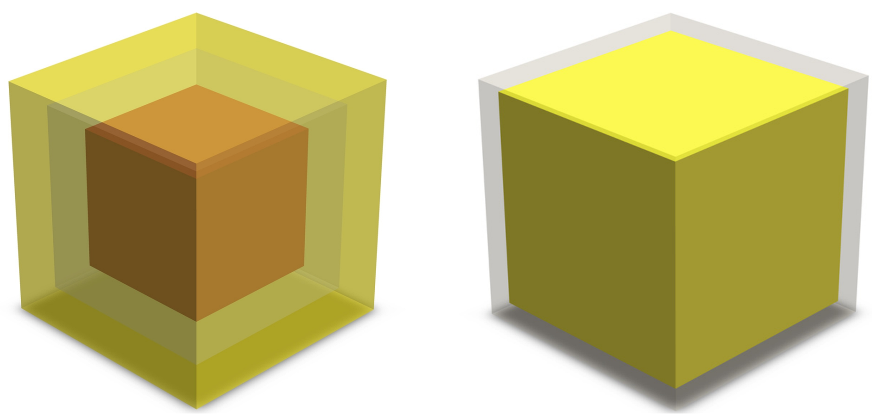

(a) Locally resonant (b) Bragg scattering

Figure 3-24 Types of unit cells of 3D periodic materials

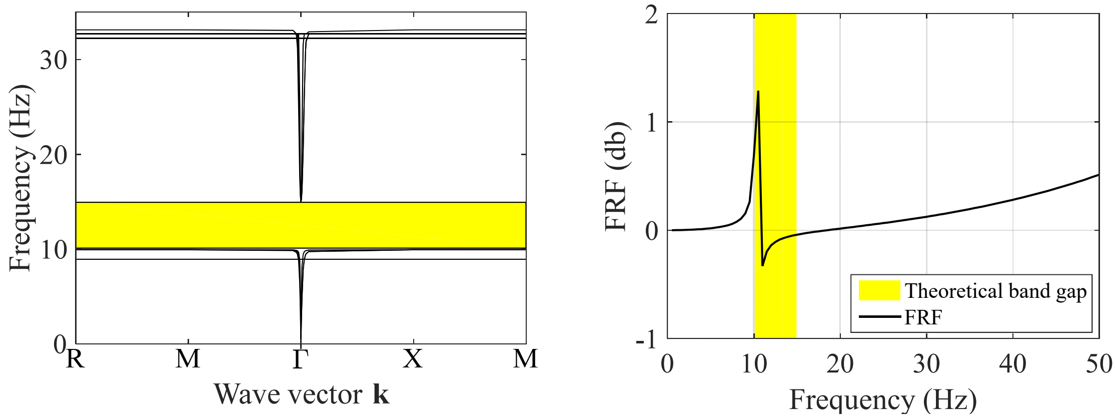

(a) Dispersion curve (b) FRF

Figure 3-25 Characteristic of Locally resonant unit cell

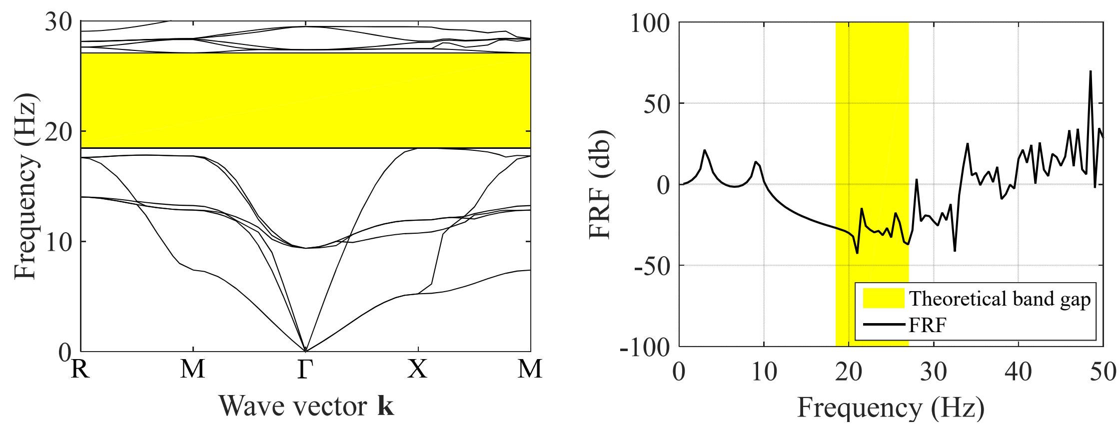

(a) Dispersion curve (b) FRF

Figure 3-26 Characteristic of Bragg scattering unit cell

3.3.3.1 Number of unit cells in the horizontal direction

The investigation on 3D periodic materials was first conducted to see the effect of the number of unit cells in the horizontal direction. For this study, three models are considered. Figure 3-27 shows the finite element models of one, nine, and twenty five unit cells where each was arranged as one layer in the vertical direction. The unit cell is the same as the Bragg scattering unit cell discussed in Subsection 3.3.3.

Figure 3-28 shows the FRF of each model where the output point is located at the top of the middle unit cell. The models were subjected to steady-state frequency sweeping of the S-Wave and P-Wave where the waves propagate from the bottom to the top of the unit cells. It is observed that the attenuation zones of the S-Wave start at a much lower frequency and end at a higher frequency in comparison to the theoretical frequency band gap. However, the attenuation zones of the P-Wave start at a frequency close to the theoretical band gap and end at a frequency similar to those of the S-Wave. The obtained theoretical frequency band gap is an absolute band gap where any type of incoming waves in any direction can be obstructed. Therefore, it is narrower but located within the attenuation zones. For the case of the S-Wave, the FRF curves of nine and twenty five unit cells show the starting frequency of their attenuation zones is slightly higher than that of one unit cell. The results show that the constraint from the surrounding unit cells provide a higher shear stiffness which pushes the starting of the S-Wave attenuation zones higher.

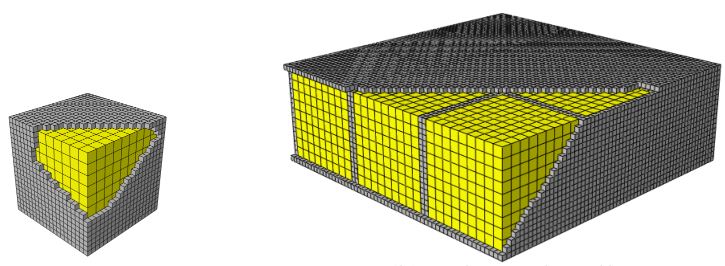

(a) One unit cell (b) Nine unit cells

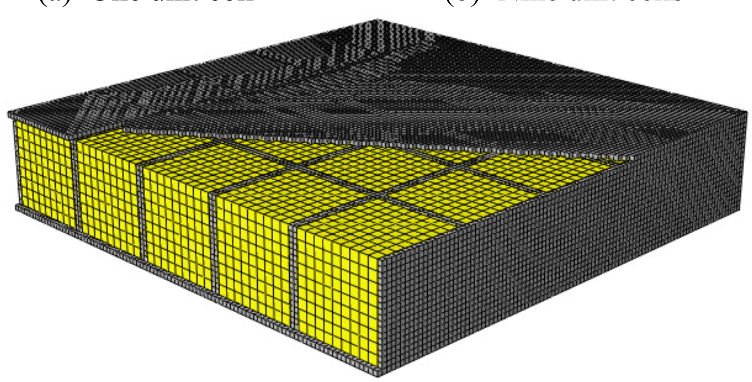

(c) Twenty five unit cells

Figure 3-27 Finite element models with different number of unit cells in the horizontal direction (some of the elements on the matrix are hidden)

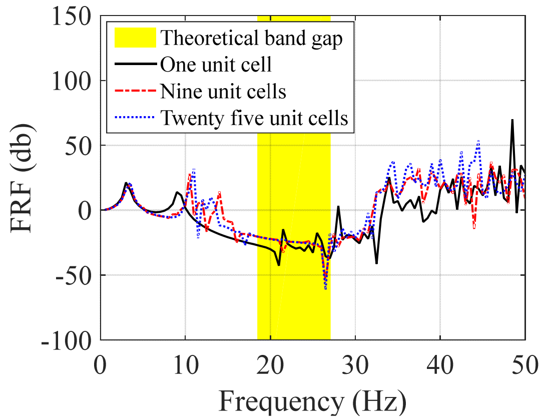

(a) S-Wave

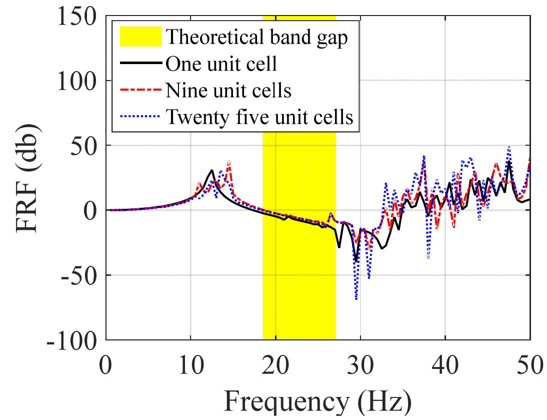

(b) P-Wave

Figure 3-28 Frequency response function of finite element models with different number of unit cells in the horizontal direction

3.3.3.2 Number of unit cells in the vertical direction

The effect of the number of unit cells in the vertical direction is also of interest and studied. Figure 3-29 shows the finite element models of one, two, and three layers in the vertical direction for this study. Each of the models consists of five-by-five unit cells in the horizontal direction. The unit cell is the same as the previously discussed Bragg scattering unit cell.

The top layer response of each model is depicted in Figure 3-30. Similar to the analytical study results of 1D periodic materials, more response reduction is observed inside the frequency band gap as more unit cells are placed in the vertical direction.

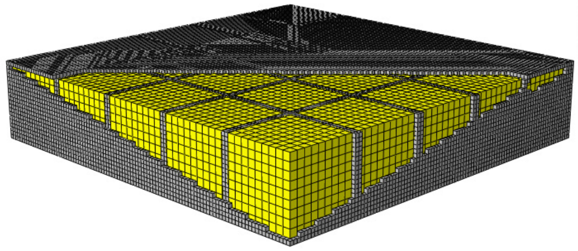

(a) One layer

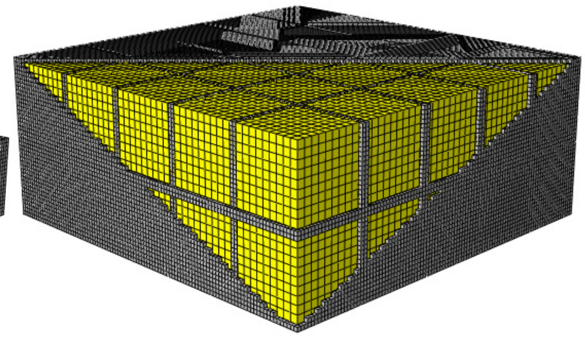

(b) Two layers

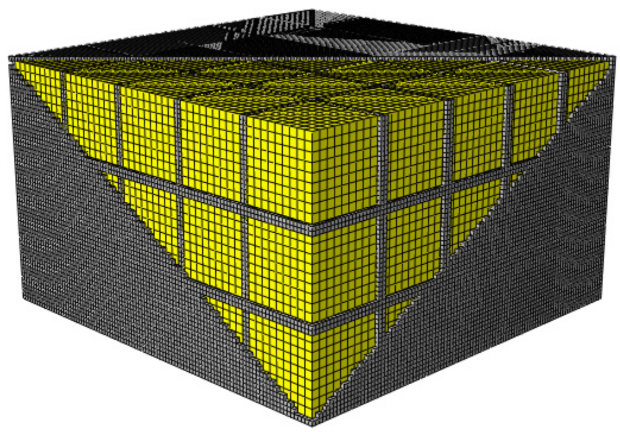

(c) Three layers

Figure 3-29 Finite element models with different number of unit cells in the vertical direction (some of the elements on the matrix are hidden)

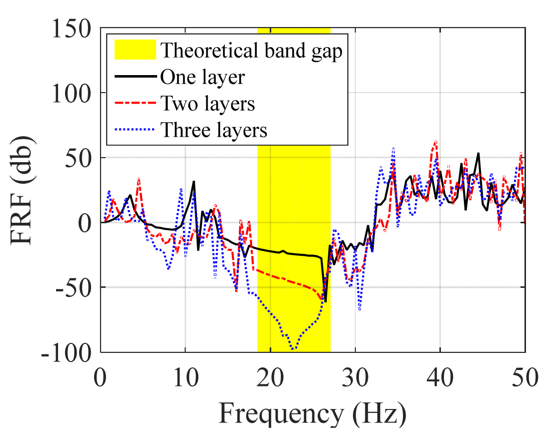

(a) S-Wave

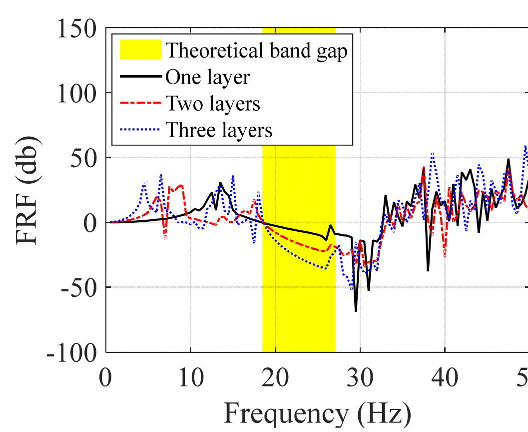

(b) P-Wave

Figure 3-30 Frequency response function of finite element models with different number of unit cells in the vertical direction

3.3.3.3 Comparison of FRF response of the 3D Bragg scattering unit cells with theoretical frequency band gaps of the layered 1D unit cell

The physical arrangement of the Bragg scattering unit cell is close to the unit cell of layered 1D periodic materials. Therefore, it is interesting to investigate how different the FRF results are from the Bragg scattering unit cell in comparison to the theoretical frequency band gap of layered 1D periodic materials. Assuming a three-layer 1D unit cell composed of two rubber layers, each with a thickness of 0.05 m, sandwiching a 0.9 m thick concrete layer, the theoretical frequency band gaps for each of the S-Wave and P-Wave are shown in Figure 3-31. Note that the analysis ceased at 50 Hz. It is observed that the first frequency band gap of the S-Wave is 5.098-32.58 Hz while that of the P-Wave is 19.42-50 Hz.

The results of the first frequency band gaps of the three-layer 1D unit cell, shown in Figure 3-31, are compared with the FRF curves of the 3D Bragg scattering unit cell, presented in Figure 3-28 and Figure 3-30. One can see that the end of the first frequency band gap of the S-Wave at 32.58 Hz is very close to the end of the attenuation zones of both the S-Wave and P-Wave. Meanwhile, the starting of the first frequency band gap of the P-Wave at 19.42 Hz is very close to the starting of the first attenuation zone of the P-Wave. Therefore, the attenuation zones in the Bragg scattering unit cell subjected to the S-Wave and P-Wave can be approximated from the theoretical frequency band gap of the layered 1D unit cell.

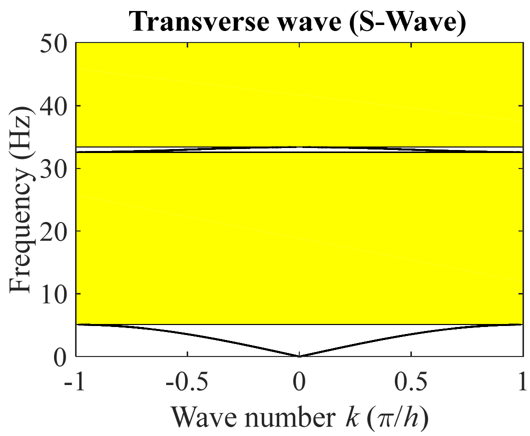

(a) S-Wave

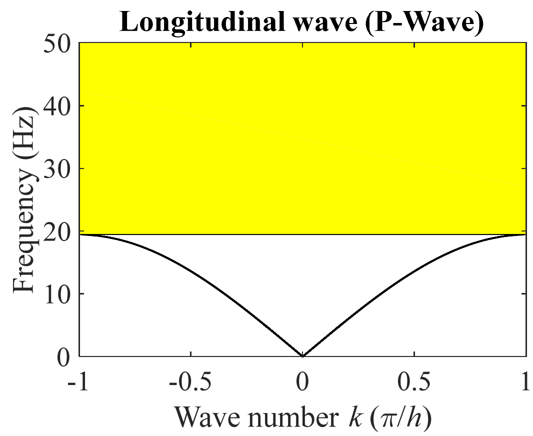

(b) P-Wave

Figure 3-31 Dispersion curve of three-layer 1D unit cell

3.3.3.4 Superstructure on 3D periodic foundation

In this study, the 3D Bragg scattering periodic materials will also be designed at a larger scale as a foundation that supports a superstructure. The presence of a superstructure most likely will also affect the attenuation zones of the 3D periodic foundations. Therefore, it is necessary that the effect of the superstructure on the attenuation zones be addressed. Figure 3-32(a) illustrates a single column seating on a concrete slab on top of a 3D periodic foundation. The mass and stiffness of the superstructure is tuned so that the natural frequency of the superstructure alone is 10 Hz (typical natural frequency of nuclear reactor building). The FRF curves of the 3D periodic foundation structural system (red and blue curves) are compared to that of the periodic foundation without the superstructure (black curve), as shown in Figure 3-32(b). It can be observed that the presence of the superstructure causes the response reduction to start at a slightly lower frequency than that without the superstructure. Moreover, the response reduction of the periodic foundation with superstructure continues up to 50 Hz which is very beneficial for seismic isolation.

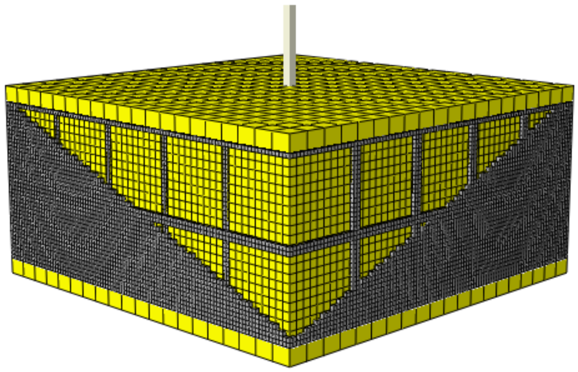

(a)

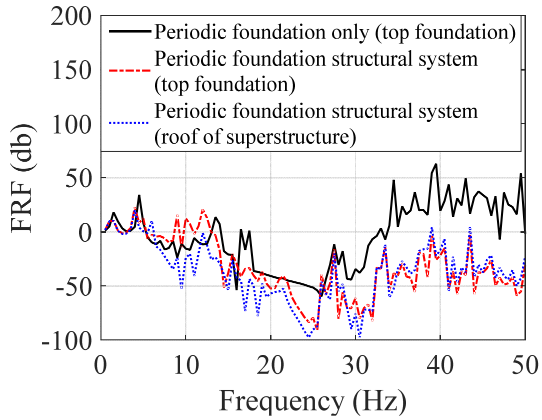

(b)

Figure 3-32 (a) A 3D periodic foundation structural system (b) FRF of a 3D periodic foundation structural system (some of the elements on the matrix are hidden)

4 GLOBAL SENSITIVITY ANALYSIS OF PERIODIC MATERIALS

One of the challenging issues in designing the periodic materials is the large number of random parameters as input variables, which makes the problem high-dimensional. The inherent uncertainties associated with the input parameters and the interaction between parameters can make the design process challenging and time-consuming. The generic approach to such problems is to identify the most influential input parameters and focus on those parameters in the design process. Although parametric studies based on a one-at-a-time technique have been performed to investigate how each of the material and geometric properties of periodic materials may affect the frequency band gaps [13, 14, 68], the studies do not quantitatively rank the influence of each parameter nor consider the interaction between the parameters.

Global sensitivity analysis or analysis of variance (ANOVA) based on Sobol' decomposition [69, 70] can quantify the amount of variance that each of the parameters and the interaction of two or more parameters contribute to the mathematical model output. This powerful method was developed by Ilya M. Sobol', a Russian mathematician known for his work on Monte Carlo methods. This chapter presents a global sensitivity analysis using Sobol' decomposition on 1D periodic materials that can be used for both 1D periodic materials and 3D Bragg scattering periodic materials. The sensitivity analysis focuses on the affecting parameters on the first frequency band gap, i.e., the lower bound frequency or the starting of the frequency band gap and the width of the frequency band gap, subjected to each of S-Wave and P-Wave excitations. Based on the most influential parameters, reduced models were derived as the simplified design equations to easily estimate the first frequency band gap of both the S-Wave and P-Wave. The design equations are derived in a dimensionless manner such that they can be applied for the design of the periodic materials at any scale.

4.1 Overview of The Sobol' Sensitivity Analysis

Sobol' sensitivity analysis is a global sensitivity analysis method using variance decomposition that can handle linear and nonlinear mathematical models. This section provides a brief formulation of Sobol' decomposition. Additional information about the theory and assumptions can be found in the original papers [69, 70].

Consider a mathematical model which is abstractly represented by Eq. (4-1)

$$Y = F(\mathbf{x}), \tag{4-1}$$

where $\mathbf{x} = (x_1, ..., x_n)$ is a set of input parameters on the *n*-dimensional unit hypercube domain $\Omega^n = \{\mathbf{x} | 0 \le x_i \le 1,\ i = 1, ..., n\}$. The mathematical model shown in Eq. (4-1) can be decomposed into a series of increasing order Sobol' functions as shown in Eq. (4-2).

$$F(\mathbf{x}) = F_0 + \sum_{i=1}^{n} F_i(x_i) + \sum_{i=1}^{n} \sum_{j=i+1}^{n} F_{ij}(x_i, x_j) + ... + F_{1...n}(x_1, ..., x_n). \tag{4-2}$$

For Eq. (4-2) to hold, the following three criteria must be satisfied:

a) The first term of the right-hand side in Eq. (4-2), F_0, must be a constant.

b) The integral of every summand over its own variables must be zero

$$\int_0^1 F_{i_1...i_s}(x_{i_1}, ..., x_{i_s}) dx_k = 0 \qquad \forall k = i_1, ..., i_s. \tag{4-3}$$

c) The summands are orthogonal, which means that if $(i_1, ..., i_n) \ne (j_1, ..., j_t)$ then

$$\int_{\Omega^n} F_{i_1...i_s} F_{j_1...j_t} d\mathbf{x} = 0. \tag{4-4}$$

Upon satisfying those three criteria, the individual member of the Sobol' functions in Eq. (4-2) can be calculated as follows

$$F_0 = \int_{\Omega^n} F(\mathbf{x})d\mathbf{x}, \tag{4-5}$$

$$F_i(x_i) = \int_{\Omega^{n-1}} F(x_i, \mathbf{x}_{\sim i})d\mathbf{x}_{\sim i} - F_0, \text{ and} \tag{4-6}$$

$$F_{ij}(x_i, x_j) = \int_{\Omega^{n-2}} F(x_i, x_j, \mathbf{x}_{\sim ij})d\mathbf{x}_{\sim ij} - F_i(x_i) - F_j(x_j) - F_0, \tag{4-7}$$

where $\mathbf{x}_{\sim i}$ is the vector corresponding to all variables except x_i in the input set $\mathbf{x}$. Similarly, $\mathbf{x}_{\sim ij}$ is the vector corresponding to all variables except x_i and x_j in the input set $\mathbf{x}$. The higher order Sobol' functions can be calculated in a similar manner.

The total variance of $F(\mathbf{x})$ can be defined as

$$D = \int_{\Omega^n} F^2(\mathbf{x})d\mathbf{x} - F_0^{\,2}, \tag{4-8}$$

which can be decomposed into partial variances as shown in Eq. (4-9)

$$D = \sum_{i=1}^{n} D_i + \sum_{i=1}^{n}\sum_{j=i+1}^{n} D_{ij} + \ldots + D_{i,\ldots,n}\,. \tag{4-9}$$

The partial variances are associated with the Sobol' functions and can be calculated by integrating the corresponding functions. The calculation of the first and second order variances are shown in Eqs. (4-10) and (4-11):

$$D_i = \int_{\Omega^1} F_i^2(x_i)dx_i \text{ and} \tag{4-10}$$

$$D_{ij} = \int_{\Omega^2} F_{ij}^2(x_i, x_j)dx_i dx_j\,. \tag{4-11}$$

The higher order variances can be calculated by integrating the higher order Sobol' functions.

Using the individual partial variance, one can calculate the contribution of each variance to the total output. The contribution, known as the Sobol' sensitivity indices, is characterized by the ratio of the partial variance relative to the total variance, as shown in Eqs. (4-12) and (4-13):

$$S_i = \frac{D_i}{D} \text{ and} \tag{4-12}$$

$$S_{ij} = \frac{D_{ij}}{D}. \tag{4-13}$$

The higher order Sobol' indices can be calculated in a similar approach. Therefore, the total Sobol' indices is

$$\sum_{i=1}^{n} S_i + \sum_{i=1}^{n} \sum_{j=i+1}^{n} S_{ij} + \ldots + S_{i,\ldots,n} = 1. \tag{4-14}$$

In many cases where the model functions are complex and nonlinear, the analytical solutions may not be available. Therefore, the integration can be approximated using the Monte Carlo-based numerical integration. In this numerical approach, the partial variances can be calculated without the need to evaluate Sobol' functions beforehand [69]. For this direct estimation, two sets of input need to be generated; the original input set $\mathbf{x}$ and the complementary input set $\mathbf{x}^{\mathbf{c}}$. The formulae for total, first order, and second order variances using the Monte Carlo estimation are shown in Eqs. (4-15)–(4-17):

$$\bar{D} = \frac{1}{N} \sum_{m=1}^{N} F^2(x_m) - \bar{F}_0^2, \tag{4-15}$$

$$\bar{D}_i = \frac{1}{N} \sum_{m=1}^{N} F(x_m) F(x_{im}, \mathbf{x}^{\mathbf{c}}_{\sim im}) - \bar{F}_0^2 \text{, and} \tag{4-16}$$

$$\bar{D}_{ij} = \frac{1}{N} \sum_{m=1}^{N} F(x_m) F(x_{im}, x_{jm}, \mathbf{x}^{\mathbf{c}}_{\sim ijm}) - \bar{D}_i - \bar{D}_j - \bar{F}_0^2. \tag{4-17}$$

The constant $\bar{F}_0$ can be estimated according to Eq. (4-18)

$$\bar{F}_0 = \frac{1}{N}\sum_{m=1}^{N} F(x_m), \tag{4-18}$$

where m represents the ordinal number of a test and N is the sample size of the Monte Carlo estimation. The $\mathbf{x}^{\mathbf{c}}_{\sim i}$ is the vector corresponding to all variables except x_i in the input set $\mathbf{x}^{\mathbf{c}}$. Similarly, $\mathbf{x}^{\mathbf{c}}_{\sim ij}$ is the vector corresponding to all variables except x_i and x_j in the input set $\mathbf{x}^{\mathbf{c}}$. The bar on the symbol, such as $\bar{D}$, denotes that the expression is numerically integrated. The Sobol' indices can then be evaluated with Eqs. (4-12) and (4-13) using the numerically estimated variances.

4.1.1 Application on simple mathematical model

In this subsection, the application of Sobol' sensitivity analysis is illustrated using a simple mathematical model. This model has been adopted from a journal article [71], which also provides an analytical solution. Herein, the adopted model is examined to investigate how the Sobol' functions and Sobol' indices that are estimated using the Monte Carlo simulation compare with the analytical solution. Such a study will be particularly relevant to this research, as the mathematical model for estimation of frequency band gaps does not have an analytical solution for Sobol' analysis and has to rely on the Monte Carlo simulation.

The simple mathematical model is given by the polynomial representation in Eq. (4-19)

$$F(x_1, x_2, x_3) = x_1^2 + x_2^4 + x_1 x_2 + x_2 x_3^4, \tag{4-19}$$

where x_1, x_2, and x_3 are independent variables, each of which is uniformly distributed in $[-4,4]$ input space. To perform Sobol' decomposition, the input space of each of the input variables needs to be rescaled to $[0,1]$. To this end, the variables x_1, x_2, and x_3 are expressed as $8y_1-4$, $8y_2-4$, and $8y_3-4$, respectively, where y_1, y_2, and y_3 are uniformly distributed in $[0,1]$.

The analytical solution of the Sobol' functions and the Sobol' indices of the problem posed in Eq. (4-19) are shown in Table 4-1 and Table 4-2.

Table 4-1 Analytically derived Sobol' functions

Sobol' functions	Function expression
F_0	56.533
F_1	$x_1^2-5.333$
F_2	$x_2^4+51.2x_2-51.2$
F_3	0
F_{12}	x_1x_2
F_{13}	0
F_{23}	$x_2x_3^4-51.2x_2$
F_{123}	0

Table 4-2 Analytically calculated Sobol' indices

Sobol' indices	Index number
S_1	0.0005
S_2	0.4281
S_3	0.0000
S_{12}	0.0007
S_{13}	0.0000
S_{23}	0.5708
S_{123}	0.0000

It is observed that S_2 and S_{23} are the dominant indices, which means that the individual variable x_2 and the interaction of variables x_2 and x_3 are the most influential to the model outcome. One can also find that there are no individual stands of x_3, combination (x_1, x_3), and correlation between all three variables (x_1, x_2, x_3) in the mathematical model. Therefore, it is expected to have their Sobol' functions F_3, F_{13}, and F_{123} and their corresponding Sobol' indices to be zero because there is no contribution of the single variable and the combination of the variables to the outcome.

Sobol' indices obtained using the Monte Carlo estimation with different sample sizes are shown in Table 4-3. The Latin Hypercube sampling scheme was applied when the input set for each sample size was generated. One can see that when the sample size is small, in this case 100 and 250 samples, the estimated Sobol' indices provide the wrong index value and wrong order of contribution. For example, the results with 100 samples show that x_3 is the most dominant variable while it is supposed to have no contribution. While the results using 250 samples show the domination of S_2 and S_{23}, the index of S_2 is shown larger than that of S_{23} the order of which is incorrect. From 500 samples onward, the indices show quite consistent results where S_2 and S_{23} dominate other variable's indices and also have the right order of contribution. The index values of S_2 and S_{23} are observed to be close enough to the analytical results with small variation. The small discrepancy may come from the nature of the Monte Carlo integration. For the very small indices, it is observed that some values are negative. The negative values may come from the inherent error in the Monte Carlo integration as the Sobol' indices are not supposed to have negative value. However, the absolute values of those negative indices are very small indicating that the contribution of the variables are negligible and thus can be ignored.

Figure 4-1 and Figure 4-2 show the comparison of the estimated Sobol' functions F_2 and F_{23} in comparison to the analytically obtained functions for dominant variables x_2 and combination variables (x_2, x_3). It is observed that even with a small number of sampling, the estimated functions are still very close to the analytical solutions as indicated by the coefficient of determination R^2 equal to 1. Although the Sobol' functions estimation is very accurate, the small number of sample sizes cannot fully populate the input space regions. The incomplete population, such as that with 100 samples shown in Figure 4-2(a), makes the estimation of the variances to be erroneous leading to the wrong Sobol' indices as shown in Table 4-3.

After all, once the converged indices are obtained, one can generate a new model function with reduced dimensions of the original mathematical model by selecting only the Sobol' functions that dominantly contribute to the outcome. Depending on the desired accuracy, one may choose to include as many Sobol' functions as needed. In this problem, based on the analytically obtained Sobol' index values, the summation of S_2 and S_{23} is 0.999. Therefore, the new function containing only x_2 and combination (x_2, x_3), as shown in Eq. (4-20)

$$F(x_1, x_2, x_3) \approx F(x_2, x_3) = F_0 + F_2(x_2) + F_{23}(x_2, x_3), \tag{4-20}$$

can have 99.9% accuracy of the original mathematical model. This advantage will be used to generate new design equations for 1D periodic materials presented in the next sections.

Table 4-3 Analytically and numerically obtained Sobol' indices

Sobol indices	Analytically obtained index	Monte Carlo estimated index with sample size of						
		100	250	500	1000	2000	3000	4000
S_1	0.0005	-0.0115	0.0742	-0.0266	0.0106	-0.0114	-0.0282	-0.0212
S_2	0.4281	0.4556	0.5524	0.4375	0.4432	0.4538	0.4281	0.4383
S_3	0.0000	0.6126	0.0547	-0.1432	0.0418	-0.0176	0.0165	-0.1024
S_{12}	0.0007	0.0113	-0.0705	0.0278	-0.0105	0.0131	0.0268	0.0234
S_{13}	0.0000	0.0140	-0.0751	0.0292	-0.0098	0.0107	0.0287	0.0219
S_{23}	0.5708	-0.0679	0.3892	0.7045	0.5149	0.5620	0.5568	0.6619
S_{123}	0.0000	-0.0140	0.0751	-0.0292	0.0098	-0.0107	-0.0287	-0.0219

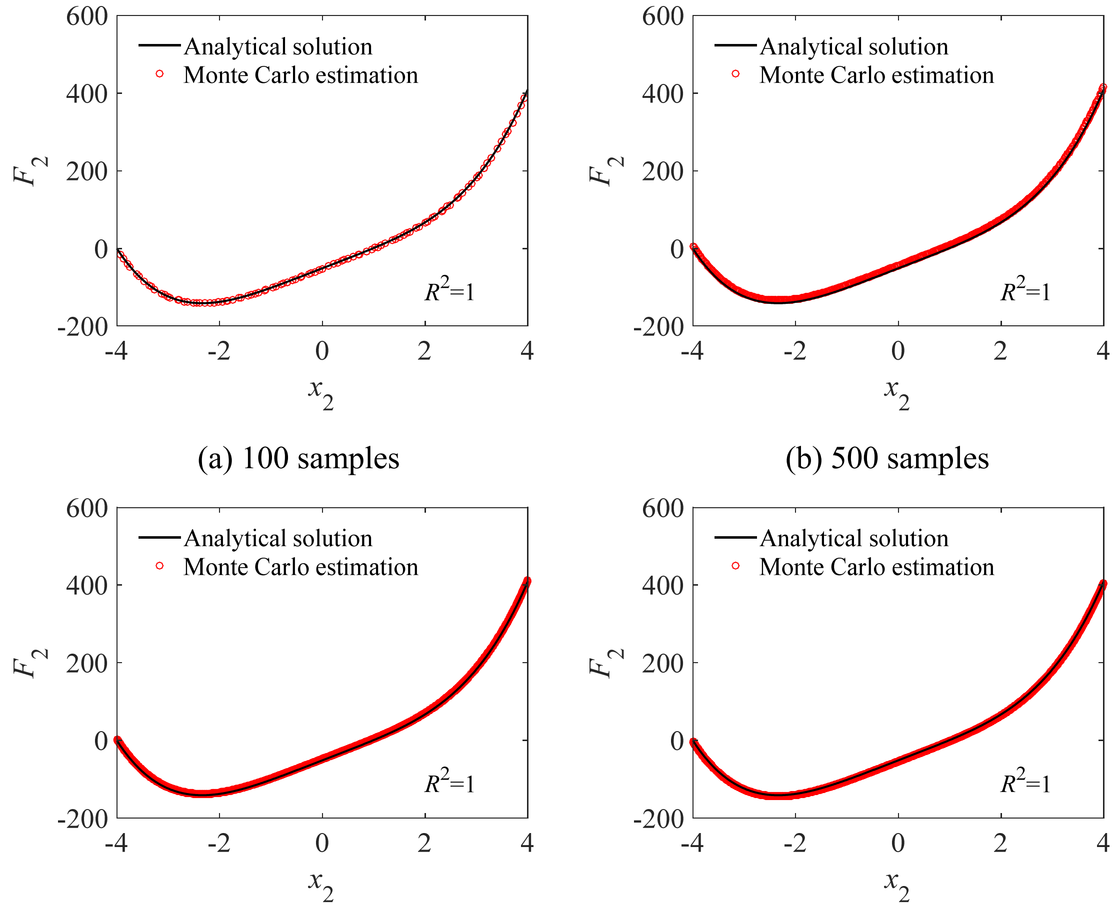

(a) 100 samples (b) 500 samples

(c) 2000 samples (d) 4000 samples

Figure 4-1 Comparison of Analytical solution and Monte Carlo estimation for Sobol' function F_2

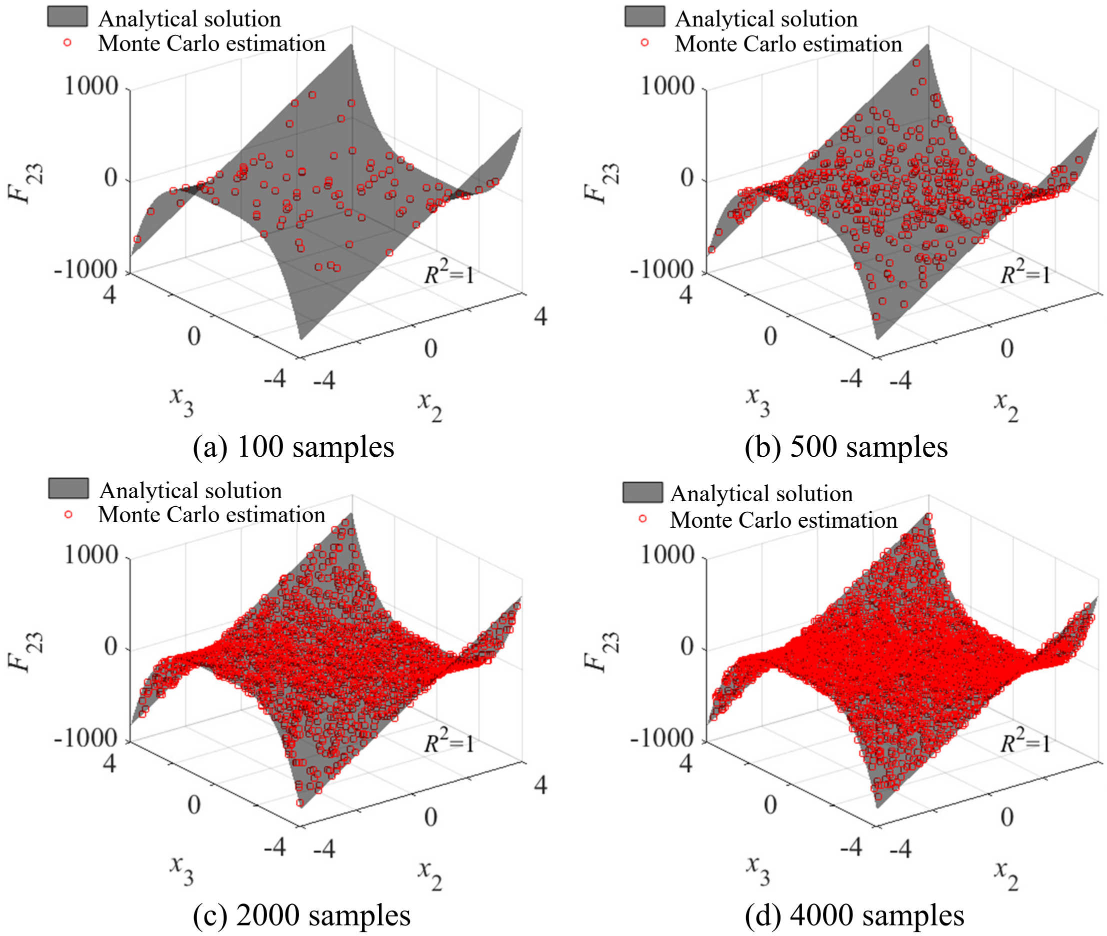

(a) 100 samples (b) 500 samples

(c) 2000 samples (d) 4000 samples

Figure 4-2 Comparison of Analytical solution and Monte Carlo estimation for Sobol' function F_{23}

4.2 Sensitivity Analysis of 1D Periodic Materials

This section presents the application of Sobol' sensitivity analysis on 1D periodic materials to characterize the influential parameters in obtaining the frequency band gaps. In this study, the objective functions are the first frequency band gaps subjected to each of the S-Wave and P-Wave. Since phononic crystals can be applied to vastly different scales, it is more convenient to analyze the property of the unit cell in a non-dimensional manner. Therefore, the formulation for dispersion relationship to obtain frequency band gaps, as presented in Section 3.1, is transformed into non-dimensional forms. The reference variables for the characteristic quantities of mass (M_*), length (L_*), and time (T_*) are selected from the power laws combination of total height or thickness of the unit cell (h) and density (ρ_1) as well as Young's modulus (E_1) of the first layer, as shown in Eqs. (4-21)–(4-23):

$$M_* = \rho_1 h^3 , \tag{4-21}$$

$$L_* = h \text{ , and} \tag{4-22}$$

$$T_* = h\sqrt{\rho_1/E_1} . \tag{4-23}$$

One can obtain the dimensionless variables by scaling the dimensional quantities with the reference variables. The dimensionless variables used in the derivation of dispersion relationship are summarized in the APPENDIX. Substitution of dimensionless variables into the original 1D wave equation [Eq. (3-8)] gives the dimensionless wave equation [Eq. (4-24)]

$$\frac{\partial^2 \hat{u}_n}{\partial \hat{t}^2} = \hat{C}_n^2 \frac{\partial^2 \hat{u}_n}{\partial \hat{z}_n^2} , \tag{4-24}$$

which retains the characteristic properties of the original wave equation. The dispersion relationship for dimensionless 1D periodic materials can then be obtained with the same transfer matrix method presented in Subsection 3.1.2 using the dimensionless variables.

Figure 4-3 shows the non-dimensional dispersion curves of 1D periodic materials that have the same characteristic as the dimensional ones. The dispersion curves were constructed from a unit cell consisting of two different materials with the following properties: $E_2/E_1 = 1000$, $\rho_2/\rho_1 = 2$, $h_2/h_1 = 1$, and $\nu_2 = \nu_1 = 0.2$.

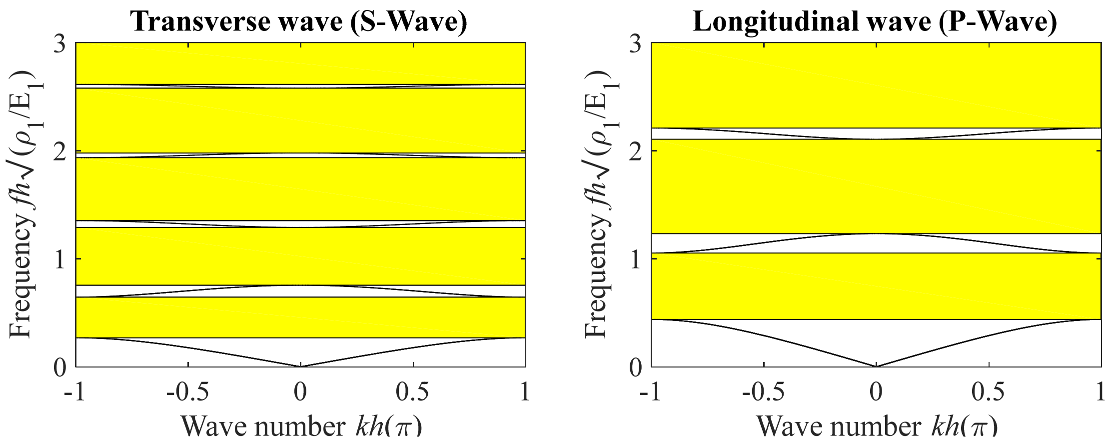

(a) S-Wave (b) P-Wave

Figure 4-3 Non-dimensional dispersion curves

Sobol' sensitivity analysis is strongly correlated to the input space. Since we performed our study in non-dimensional form, the input parameters are selected as the ratio of the material and geometric properties between the two layers in the unit cell with the softer and lighter layer set as the reference. For this study, the input parameters were varied as shown in Table 4-4. The parameters were generated using the Latin Hypercube sampling scheme. The first three parameters $\left(E_2/E_1, \rho_2/\rho_1, h_2/h_1\right)$ are uniformly distributed in the logarithmic scale while the Poisson's ratios are uniformly distributed in linear scale. The highest value of Poisson's ratio to be used in this study was selected as 0.463. The reason for such a selection is because as the Poisson's ratio gets closer to 0.5, the first Lamé parameter goes to infinity. This hypothetical condition is not applicable to any actual material [72] and therefore is omitted in this study.

Two objective functions are utilized to represent the first frequency band gap of two-layer 1D periodic materials, i.e., the starting frequency and the width. These two objective functions are employed to represent the first frequency band gap of each of the S-Wave and P-Wave, resulting in four objective functions in total.

Table 4-4 Parameters used in sensitivity analysis

Parameters	Value range
Young's modulus ratio $\left(E_2/E_1\right)$	$10-10000$
Density ratio $\left(\rho_2/\rho_1\right)$	$1-1000$
Thickness ratio $\left(h_2/h_1\right)$	$0.11-9$
Poisson's ratio of material in the first layer $\left(\upsilon_1\right)$	$0-0.463$
Poisson's ratio of material in the second layer $\left(\upsilon_2\right)$	$0-0.463$

Figure 4-4 shows the first and second order Sobol' indices with the starting of the first frequency band gap of the S-Wave (denoted by superscript "SS") as the objective function. The subscripts on each of the Sobol' indices and functions refer to the order of the parameters presented in Table 4-4. For example, subscript 1 refers to the Young's modulus ratio $\left(E_2/E_1\right)$ and so on. One can see that the sole dominant parameter that affects the starting of the frequency band gap is the density ratio $\left(\rho_2/\rho_1\right)$ of the two layers in the unit cell with a Sobol' index value around 0.9. The remaining parameters and the interaction between the parameters are shown to contribute very little to this objective function. Although not as significant as the density ratio, the second and third highest indices are shown by the combination of parameters $\left(\rho_2/\rho_1, h_2/h_1\right)$ and the thickness ratio $\left(h_2/h_1\right)$ parameter. The Sobol' indices values are reflected in their variation of Sobol' functions (derived from 2000 samples), as shown in Figure 4-5. For example, variation of $F_2^{\mathrm{SS}}\left(\rho_2/\rho_1\right)$ surrounding its mean value is much larger than $F_{23}^{\mathrm{SS}}\left(\rho_2/\rho_1, h_2/h_1\right)$ and $F_3^{\mathrm{SS}}\left(h_2/h_1\right)$. In addition, it is observed that the larger variation of $F_{23}^{\mathrm{SS}}\left(\rho_2/\rho_1, h_2/h_1\right)$ only occurs at the corner where the density ratio is small and the thickness ratio is high.

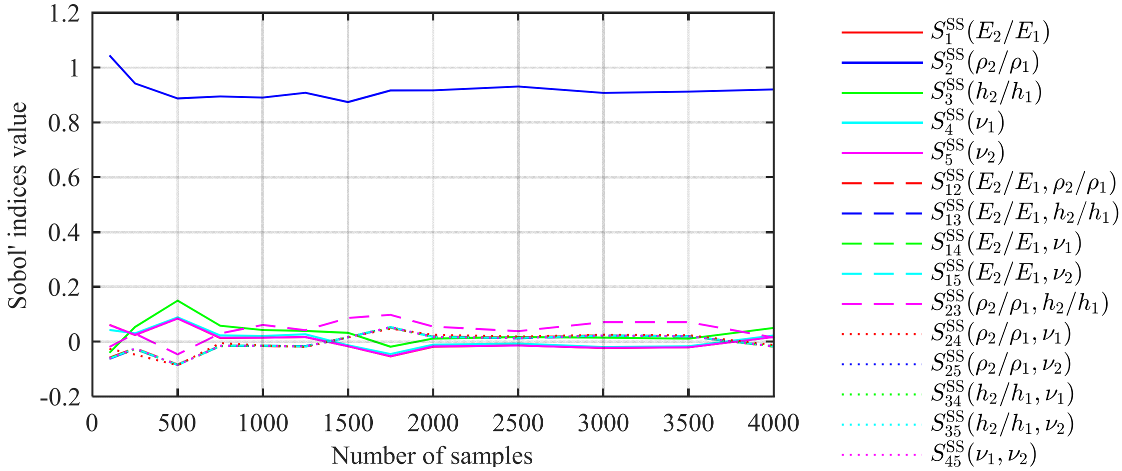

Figure 4-4 First and second order indices for the starting of the first frequency band gap of S-Wave

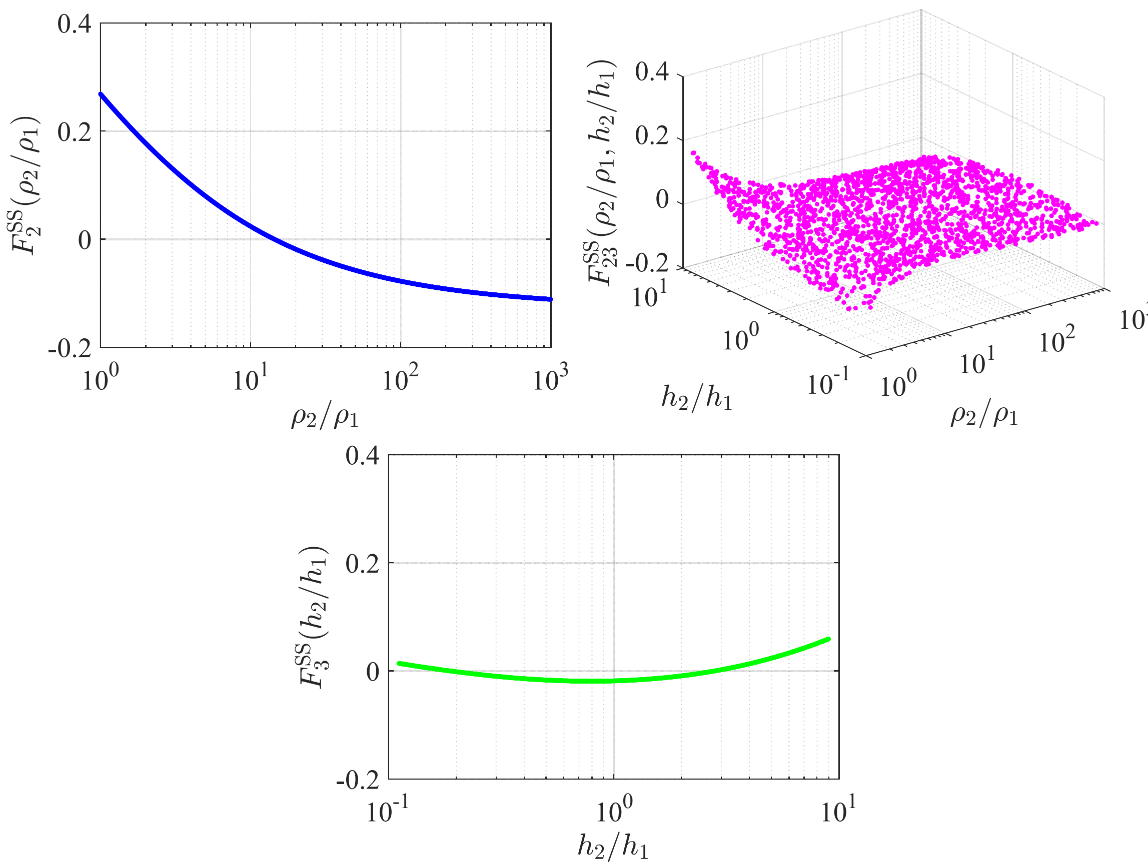

Figure 4-5 Influential Sobol' functions for the starting of the first frequency band gap of S-Wave

On the other hand, the width of the first frequency band gap of the S-Wave (denoted by superscript "WS") is affected by more parameters and their interaction. Figure 4-6 shows that the highest Sobol' index is only around 0.4 which is contributed by the thickness ratio (h_2/h_1) parameter. Closely below that, the next three indices that are located between index values of 0.1 to 0.2 are contributed by the combination of parameters $(E_2/E_1, h_2/h_1)$, $(\rho_2/\rho_1, h_2/h_1)$, and parameter (E_2/E_1). Therefore, the Sobol' functions associated with the respected parameters and the combination of parameters show a large variation as depicted in Figure 4-7. In fact, the variation in Sobol' functions shown in Figure 4-7 emphasize the importance of investigating the interaction between the parameters involved. For example, one may think that as the thickness ratio gets larger, the width of the first frequency band gap gets wider. The premise is only true when the Young's modulus ratio is high. As the Young's modulus ratio decreases, the opposite result is observed. For the parameters with a low Sobol' index value, such as that contributed by (ρ_2/ρ_1), the Sobol' function varies very little in comparison to other functions.

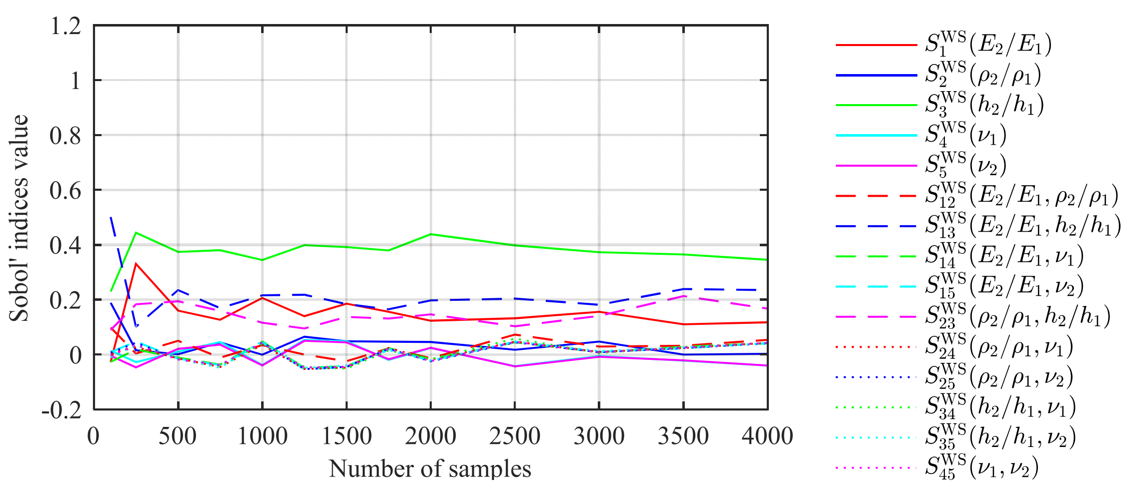

Figure 4-6 First and second order indices for the starting of the width frequency band gap of S-Wave

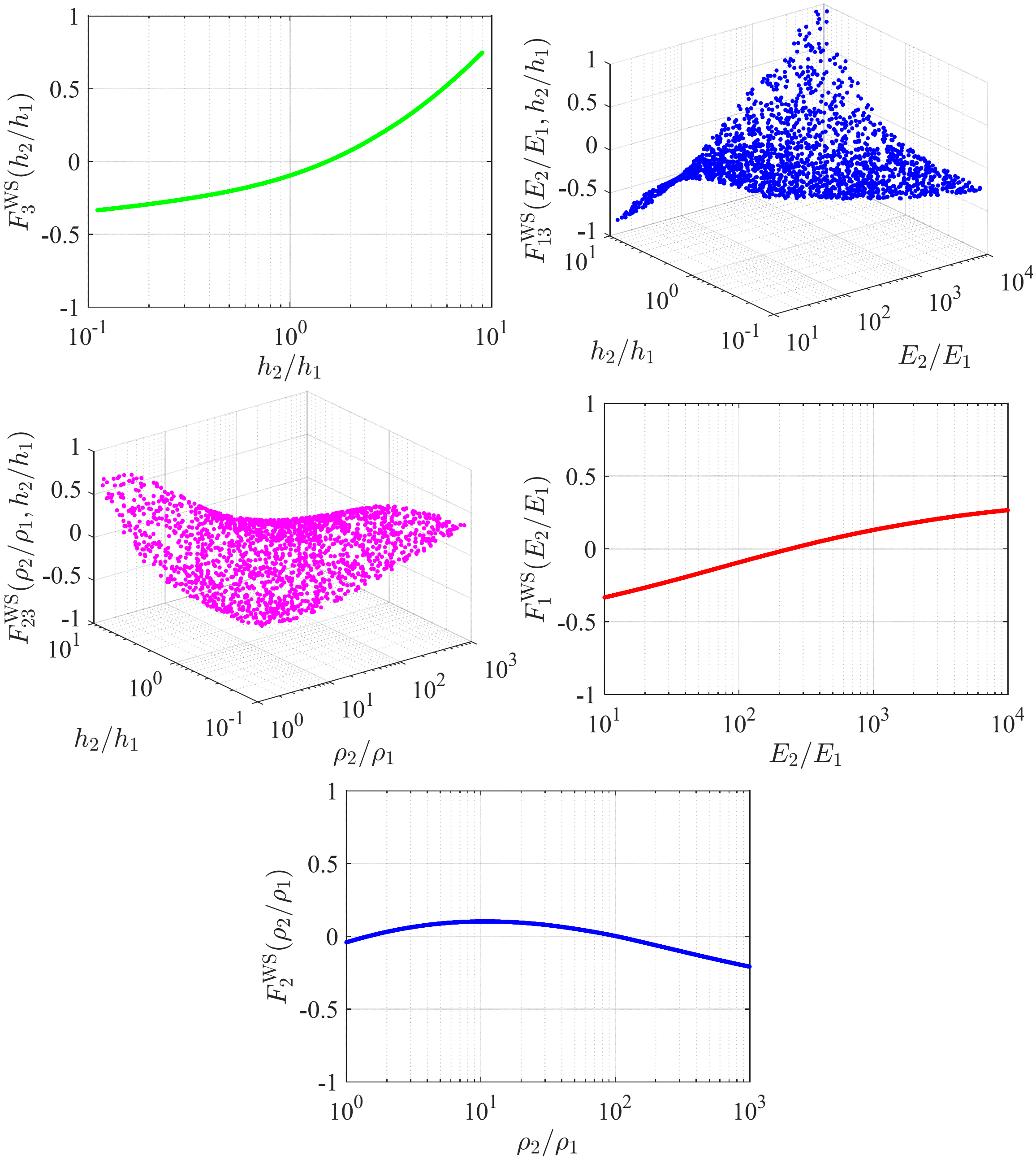

Figure 4-7 Influential Sobol' functions for the width of the first frequency band gap of S-Wave

For the objective function of the starting of the first frequency band gap of the P-Wave (denoted by superscript "SP"), similar results are observed as those of the S-Wave. The sole dominant parameter is contributed by the density ratio (ρ_2/ρ_1) parameter with the Sobol' index showing around 0.8 in Figure 4-8. However, Sobol' indices only represent the variation of the Sobol' function as a whole. A parameter or a correlation of parameters with small a Sobol' index value may have a Sobol' function with a large variation at a very minor portion of the input space. For example, the Poisson's ratio parameter only starts to affect the frequency band gaps of the P-Wave after 0.35. The five most important Sobol' functions that affect the starting of the first frequency band gaps of the P-Wave are shown in Figure 4-9.

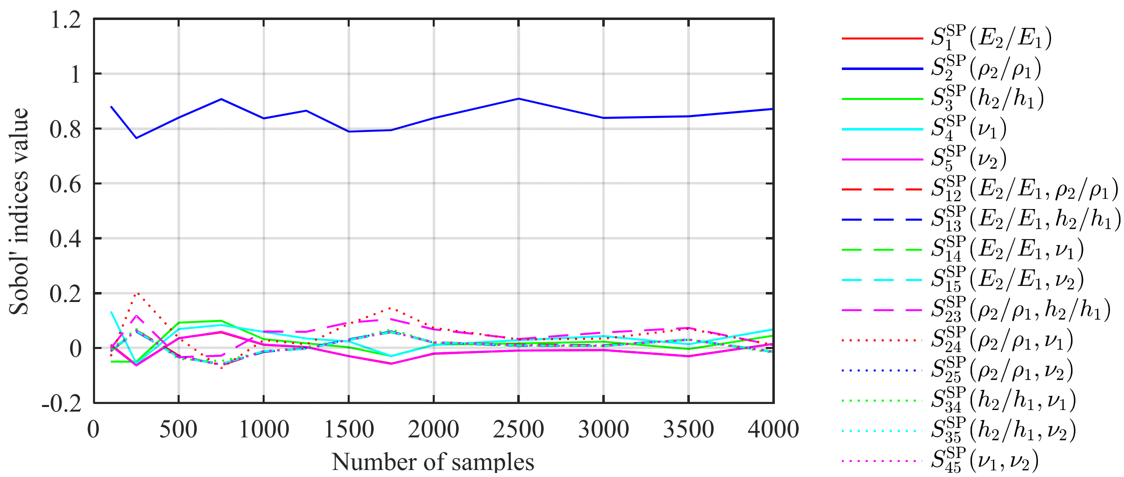

Figure 4-8 First and second order indices for the starting of the first frequency band gap of P-Wave

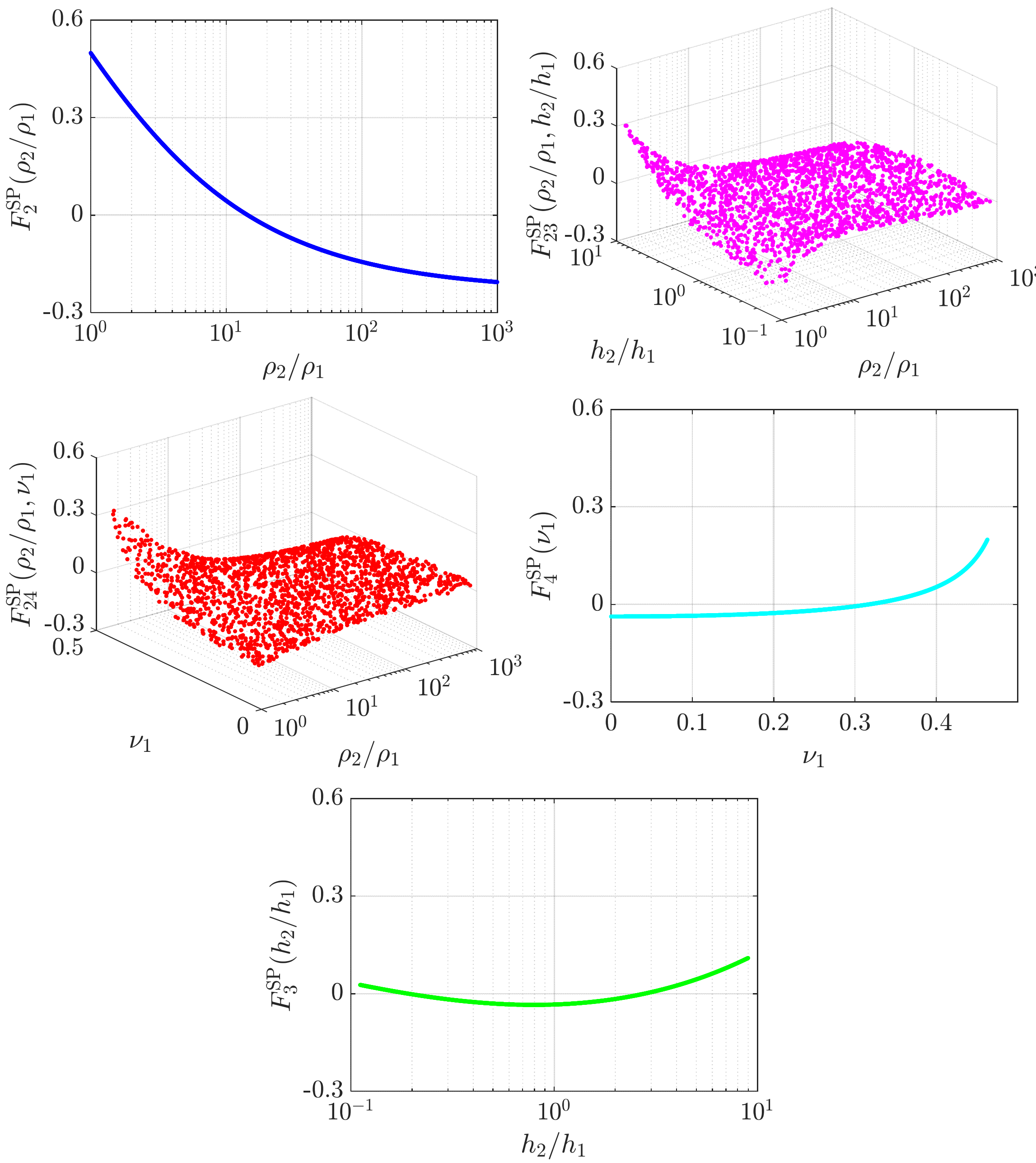

Figure 4-9 Influential Sobol' functions for the starting of the first frequency band gap of P-Wave

Similar to that of the S-Wave, the objective function for the width of the first frequency band gap of the P-Wave (denoted by superscript "WP") is also affected by more parameters and correlation of parameters. The Sobol' indices indicate that the thickness ratio $\left(h_2/h_1\right)$ is the most influential parameter followed by the correlation of parameters

$(E_2/E_1, h_2/h_1)$, $(\rho_2/\rho_1, h_2/h_1)$, individual parameters (E_2/E_1), (ρ_2/ρ_1), and (υ_1) in sequence as depicted in Figure 4-10. The Sobol' functions shown in Figure 4-11 describe how the parameters and the correlation of parameters affect the objective function. In order to get a wide frequency band gap, it is necessary to have a higher thickness ratio and a higher Young's modulus ratio with a lower density ratio.

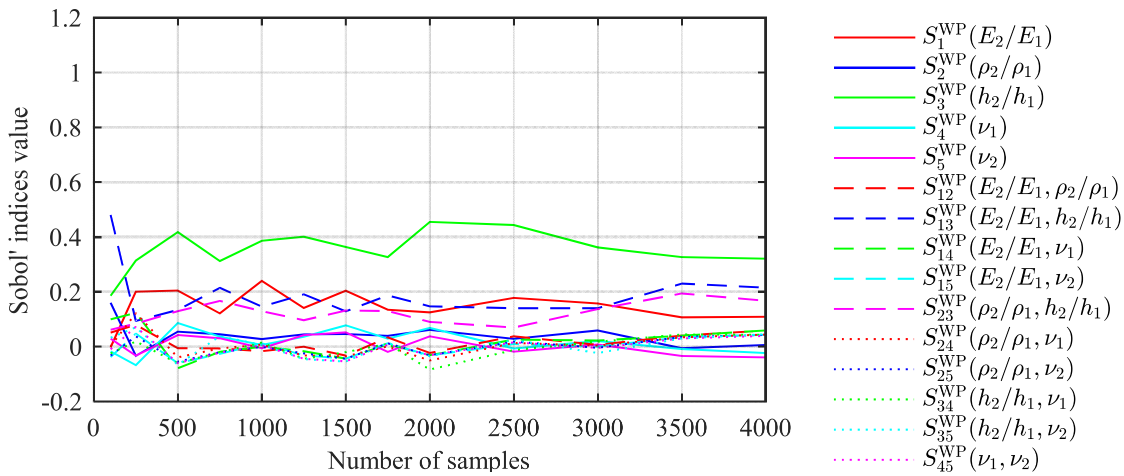

Figure 4-10 First and second order indices for the width of the first frequency band gap of P-Wave

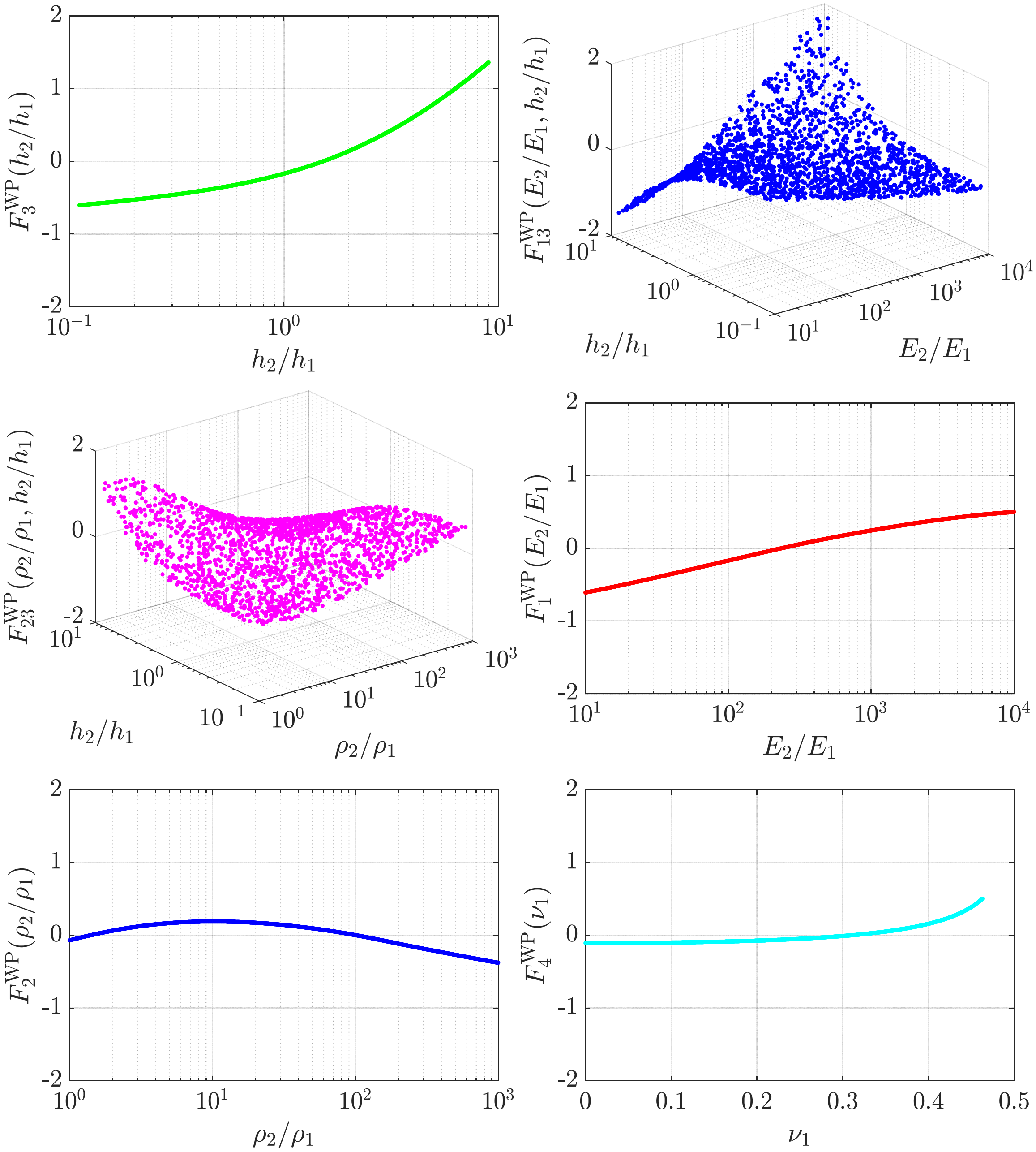

Figure 4-11 Influential Sobol' functions for the width of the first frequency band gap of P-Wave

4.3 Simplified Design Equations Based on Reduced Sobol' Functions

The advantage of Sobol' decomposition that allows the reduction of the dimension of the objective function is very beneficial for predicting the first frequency band gaps without the need to solve the wave equation. As previously mentioned in Subsection 4.1.1, the reduced objective function can be obtained by truncating the series of Sobol' functions up to the desired level of accuracy according to the Sobol' indices. In this section, a set of simplified design equations based on reduced order Sobol' functions is proposed to easily calculate the first frequency band gaps of 1D periodic materials under the S-Wave and P-Wave.

For the objective function of the starting of the first frequency band gap of the S-Wave, the summation of the first three Sobol' indices $\left(S_{(\rho_2/\rho_1)}, S_{(\rho_2/\rho_1, h_2/h_1)}, \text{ and } S_{(h_2/h_1)}\right)$ is roughly 0.98. Hence, using the summation of the Sobol' functions associated with those three indices, one can predict the objective function with 98% confidence. Figure 4-12 shows the regression curves and surface for those three Sobol' functions. An approximate objective function for the starting of the first frequency band gap of the S-Wave $\left(F^{\mathrm{SS}}\right)$ is shown in Eq. (4-25)

$$\begin{aligned} F^{\mathrm{SS}} &= 0.1265 + F_2^{\mathrm{SS}}\left(\log\left[\rho_2/\rho_1\right]\right) + F_{23}^{\mathrm{SS}}\left(\log\left[\rho_2/\rho_1\right], \log\left[h_2/h_1\right]\right) \\ &\quad + F_3^{\mathrm{SS}}\left(\log\left[h_2/h_1\right]\right), \end{aligned} \tag{4-25}$$

with the fitted Sobol' functions tabulated in Table 4-5.

Similarly, by fitting and summing up the dominant Sobol' functions as shown in Figure 4-13, the reduced objective function for the width of the first frequency band gap of the S-Wave $\left(F^{\mathrm{WS}}\right)$ can be obtained. The reduced objective function is shown in Eq. (4-26)

$$\begin{aligned} F^{\mathrm{WS}} &= 0.5484 + F_3^{\mathrm{WS}}\left(\log\left[h_2/h_1\right]\right) + F_{13}^{\mathrm{WS}}\left(\log\left[E_2/E_1\right], \log\left[h_2/h_1\right]\right) \\ &\quad + F_{23}^{\mathrm{WS}}\left(\log\left[\rho_2/\rho_1\right], \log\left[h_2/h_1\right]\right) + F_1^{\mathrm{WS}}\left(\log\left[E_2/E_1\right]\right) \\ &\quad + F_2^{\mathrm{WS}}\left(\log\left[\rho_2/\rho_1\right]\right). \end{aligned} \tag{4-26}$$

The fitted Sobol' functions for Eq. (4-26) are tabulated in Table 4-6.

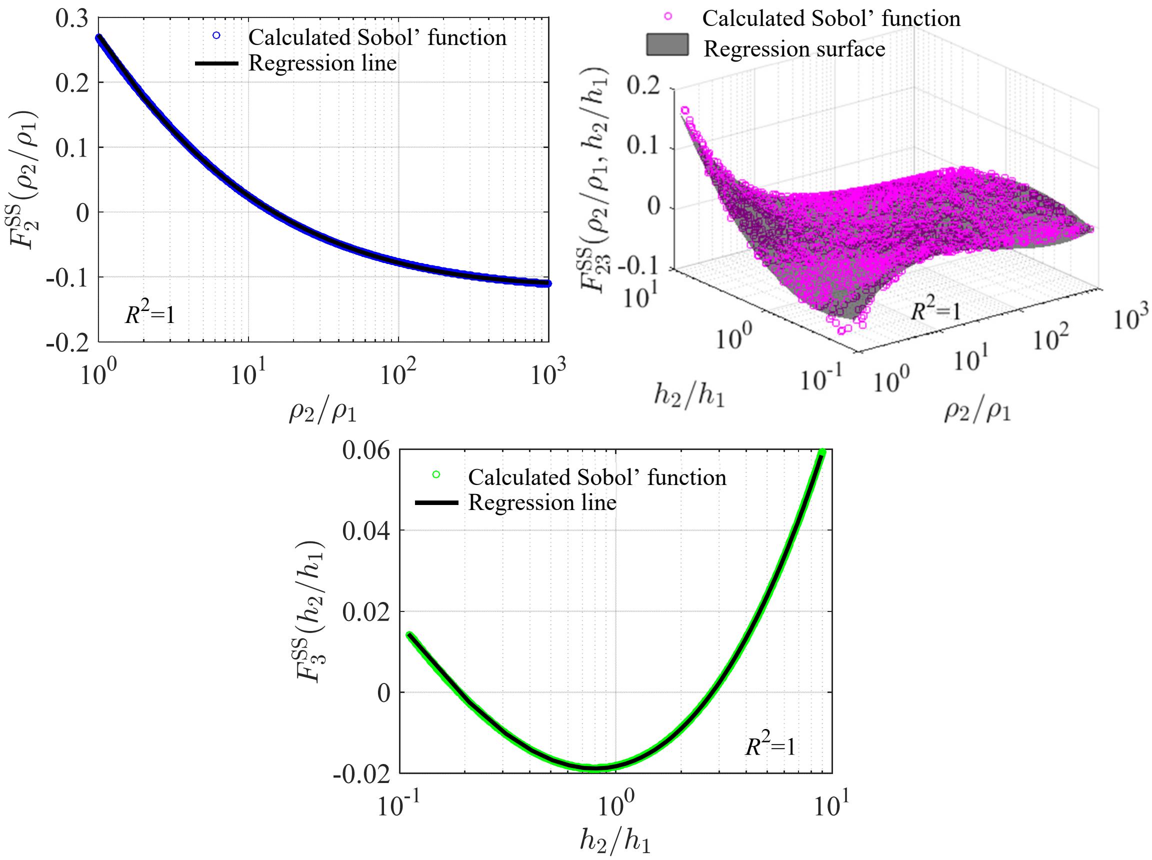

Figure 4-12 Curve fitting on Sobol' functions for the starting of the first frequency band gap of S-Wave

Table 4-5 Regression equation for Sobol' functions for the starting of the first frequency band gap of S-Wave

$F_2^{SS}(X) = 1239.088e^{-0.4557X} - 1238.816e^{-0.4555X}$
$F_{23}^{SS}(X,Y) = -0.02746 + 0.02426X + 0.1143Y - 0.001248X^2 - 0.2258XY + 0.09419Y^2 - 0.001116X^3 + 0.1204X^2Y - 0.09103XY^2 + 0.0001409X^4 - 0.02031X^3Y + 0.0142X^2Y^2$
$F_3^{SS}(Y) = -0.01822 + 0.0114Y + 0.06029Y^2 + 0.01339Y^3$

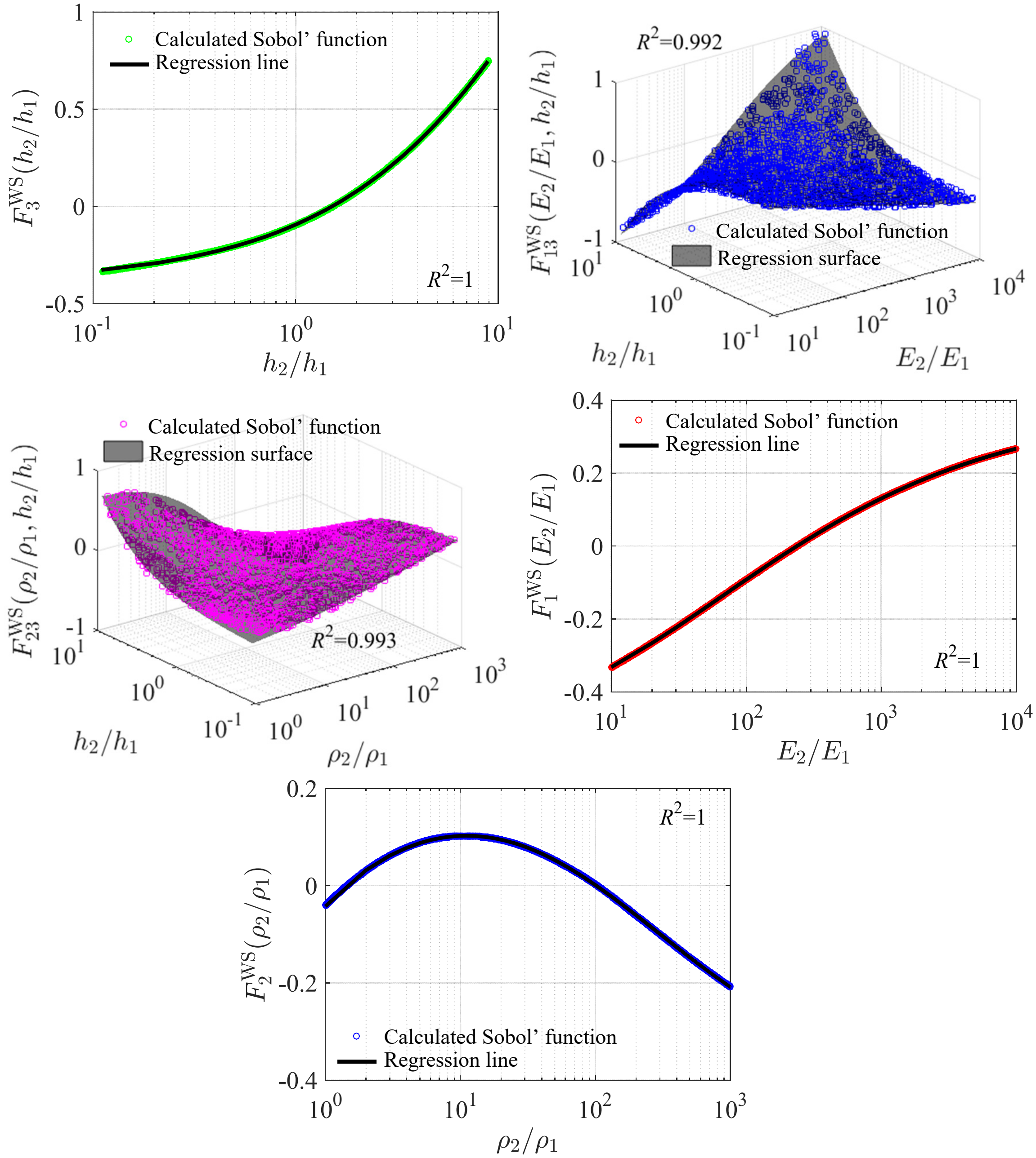

Figure 4-13 Curve fitting on Sobol' functions for the width of the first frequency band gap of S-Wave

Table 4-6 Regression equation for Sobol' functions for the width of the first frequency band gap of S-Wave

$F_3^{\mathrm{WS}}(Z)=\dfrac{-0.4961+2.7538Z}{5.2843-3.5212Z+Z^2}$
$F_{13}^{\mathrm{WS}}(X,Z)=\dfrac{0.2233\text{-}0.08928X-0.785Z+0.3128XZ}{1-0.2172X-0.7975Z+0.04177X^2+0.3198Z^2}$
$F_{23}^{\mathrm{WS}}(Y,Z)=\dfrac{-0.1193+0.0735Y+0.4151Z-0.2566YZ}{1-0.2974Y-0.8122Z+0.08275YZ+0.0607Y^2+0.1766Z^2}$
$F_1^{\mathrm{WS}}(X)=\dfrac{-5.1888+1.7591X+0.1783X^2}{11.1718-2.3914X+X^2}$
$F_2^{\mathrm{WS}}(Y)=\dfrac{-0.8474+5.817Y-2.6891Y^2}{19.9635+3.7597Y-2.4232Y^2+Y^3}$

The fitted functions for each of the starting and the width of the first frequency band gap subjected to the P-Wave is shown in each of Figure 4-14 and Figure 4-15, respectively. The reduced objective functions to predict the starting $\left(F^{\mathrm{SP}}\right)$ and the width $\left(F^{\mathrm{WP}}\right)$ of the first frequency band gap of the P-Wave are given in Eqs. (4-27) and (4-28):

$$\begin{aligned}F^{\mathrm{SP}}&=0.2348+F_2^{\mathrm{SP}}\left(\log\left[\rho_2/\rho_1\right]\right)+F_{23}^{\mathrm{SP}}\left(\log\left[\rho_2/\rho_1\right],\log\left[h_2/h_1\right]\right)\\&\quad+F_{24}^{\mathrm{SP}}\left(\log\left[\rho_2/\rho_1\right],\upsilon_1\right)+F_4^{\mathrm{SP}}\left(\upsilon_1\right)+F_3^{\mathrm{SP}}\left(\log\left[h_2/h_1\right]\right)\text{ and}\end{aligned}\tag{4-27}$$

$$\begin{aligned}F^{\mathrm{WP}}&=1.0021+F_3^{\mathrm{WP}}\left(\log\left[h_2/h_1\right]\right)+F_{13}^{\mathrm{WP}}\left(\log\left[E_2/E_1\right],\log\left[h_2/h_1\right]\right)\\&\quad+F_{23}^{\mathrm{WP}}\left(\log\left[\rho_2/\rho_1\right],\log\left[h_2/h_1\right]\right)+F_1^{\mathrm{WP}}\left(\log\left[E_2/E_1\right]\right)\\&\quad+F_2^{\mathrm{WP}}\left(\log\left[\rho_2/\rho_1\right]\right)+F_4^{\mathrm{WP}}\left(\upsilon_1\right),\end{aligned}\tag{4-28}$$

with each corresponding Sobol' function summarized in Table 4-7 and Table 4-8.

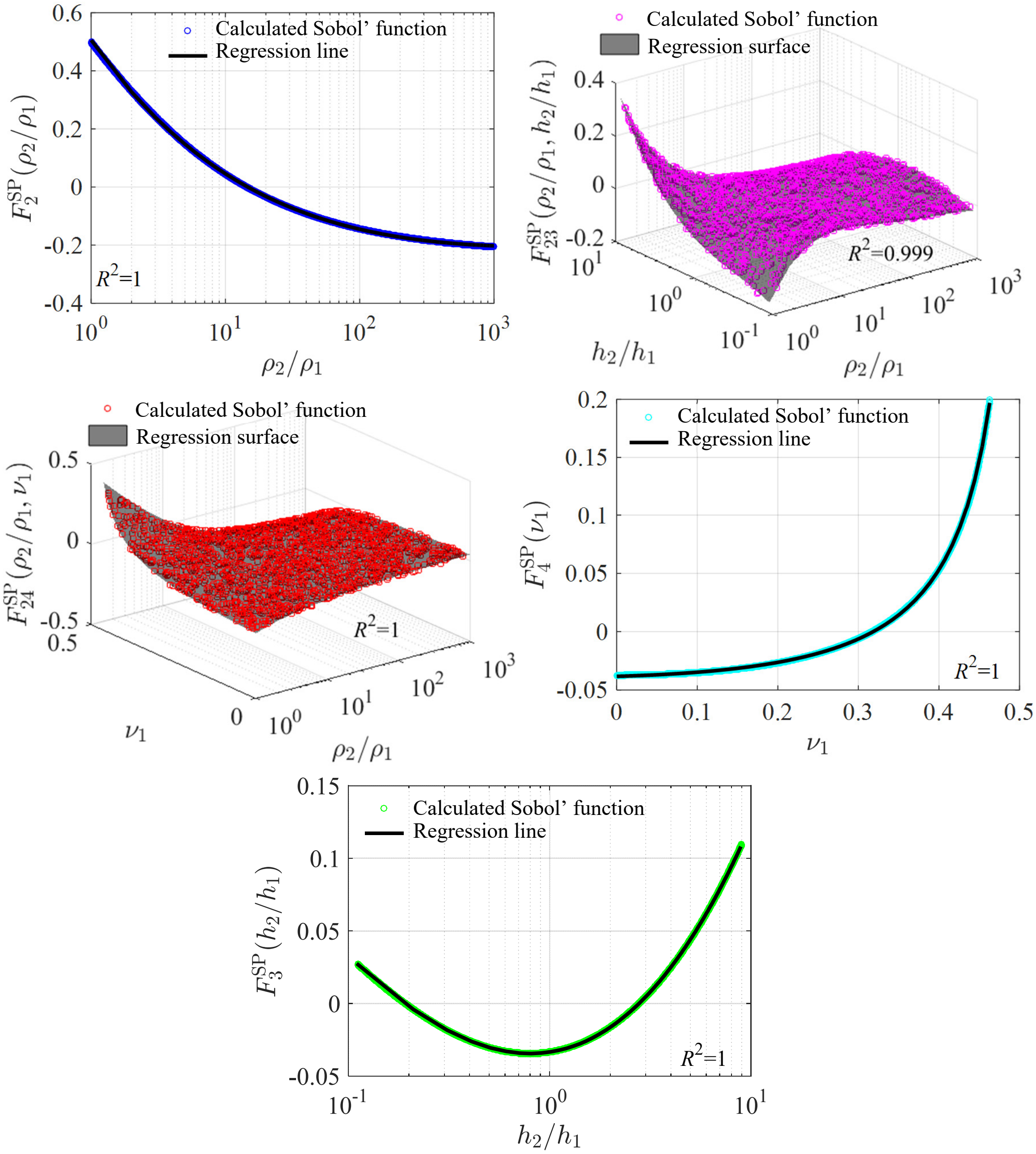

Figure 4-14 Curve fitting on Sobol' functions for the starting of the first frequency band gap of P-Wave

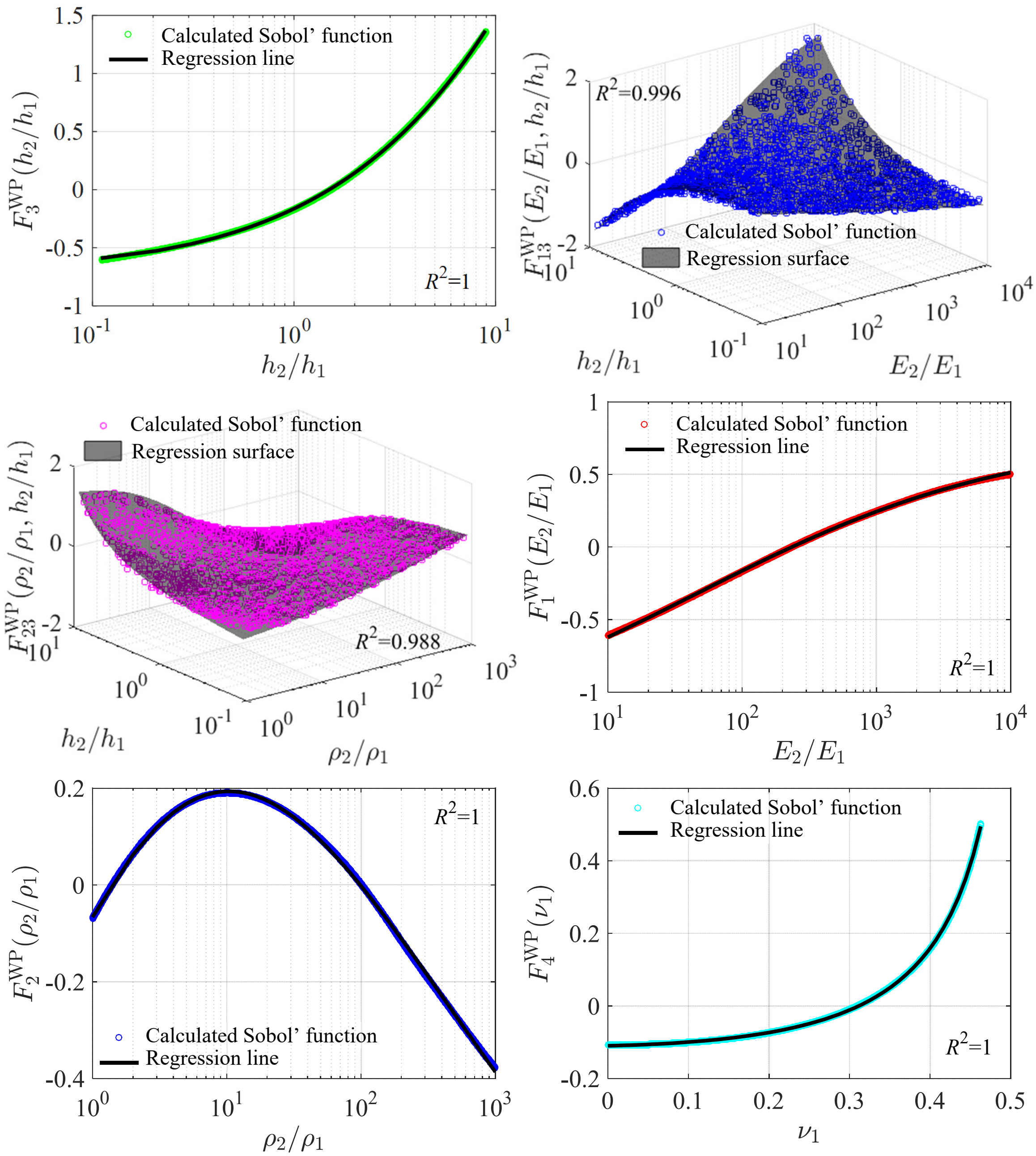

Figure 4-15 Curve fitting on Sobol' functions for the width of the first frequency band gap of P-Wave

Table 4-7 Regression equation for Sobol' functions for the starting of the first frequency band gap of P-Wave

$F_2^{\mathrm{SP}}(X) = 297.7911e^{-0.4565X} - 297.2854e^{-0.4551X}$
$F_{23}^{\mathrm{SP}}(X,Y) = -0.04856 + 0.03971X + 0.1815Y + 0.00122X^2 - 0.5028XY + 0.1629Y^2 - 0.003424X^3 + 0.4332X^2Y - 0.1377XY^2 + 0.1008Y^3 + 0.00077X^4 - 0.1538X^3Y + 0.004778(XY)^2 - 0.1301XY^3 - 0.000102X^5 + 0.01921X^4Y + 0.004352X^3Y^2 + 0.03148X^2Y^3$
$F_{24}^{\mathrm{SP}}(X,Z) = \dfrac{-0.0969 + 0.08431X + 0.3088Z - 0.2676XZ}{1 + 0.847X - 1.9226Z - 1.7922XZ + 0.02933X^2}$
$F_4^{\mathrm{SP}}(Z) = \dfrac{-209.3429 + 507.5532Z + 471.1006Z^2}{5462.1354 - 10408.7099Z + Z^2}$
$F_3^{\mathrm{SP}}(Y) = -0.03341 + 0.02097Y + 0.1116Y^2 + 0.02439Y^3$

Table 4-8 Regression equation for Sobol' functions for the width of the first frequency band gap of P-Wave

$F_3^{\mathrm{WP}}(Y) = 1.1042e^{1.0456Y} - 1.2681e^{0.2525Y}$
$F_{13}^{\mathrm{WP}}(W,Y) = \dfrac{0.4458 - 0.1779W - 1.5468Y + 0.6325WY - 0.06565Y^2}{1 - 0.2054W - 0.684Y - 0.067WY + 0.04826W^2 + 0.3312Y^2}$
$F_{23}^{\mathrm{WP}}(X,Y) = \dfrac{-0.1734 + 0.1082X + 0.6911Y - 0.4181XY - 0.04576Y^2}{1 - 0.2716X - 0.7256Y + 0.1226XY + 0.04735X^2}$
$F_1^{\mathrm{WP}}(W) = \dfrac{-26139.7298 + 11020.821W}{26761.2895 - 3942.3173W + 1499W^2 + W^3}$
$F_2^{\mathrm{WP}}(X) = \dfrac{-1383.2386 + 10241.098X - 4787.7159X^2}{20757.67 - 2034.7302X + 2324.8446X^2 + X^3}$
$F_4^{\mathrm{WP}}(Z) = \dfrac{-296.2129 + 679.2197Z + 871.5131Z^2}{2697.0582 - 4930.097Z + Z^2}$

The accuracy of the reduced objective functions depends on both the truncation of the Sobol's function series and the regression chosen to represent each function. To quantify the approximation error of the reduced objective functions, the scaled L_2 error (δ) as shown in Eq. (4-29)

$$\delta = \frac{1}{D}\int\left[F_{\text{response}}(\mathbf{x}) - F_{\text{predict}}(\mathbf{x})\right]^2 dx, \tag{4-29}$$

is used. The scaled L_2 error specifies how far the predicted or reduced objective function is from the real response function. If the crudest approximation $F_{\text{predict}} = F_0$, then $\delta = 1$. Hence, the best approximations are the ones with $\delta << 1$. The scaled L_2 error should be interpreted as the combination of truncation error and regression error. Figure 4-16 shows the evolution of the L_2 error with respect to the number of Sobol' functions included in the reduced objective functions. The L_2 error was evaluated using 2000 input samples. The sequence of the included Sobol' functions is as presented in Eqs. (4-25)–(4-28). Since the starting of the frequency band gap for both the S-Wave and P-wave are highly dependent on their respected first Sobol' functions, a huge drop in the L_2 error is observed after the inclusion of the first functions (see red and green curves in Figure 4-16). Inclusion of additional Sobol' functions can reduce the error but they are not particularly significant. As for the width of the first frequency band gaps of the S-Wave and P-Wave, the error can be seen to gradually decrease by the inclusion of more Sobol's functions. For the case of the S-Wave, the inclusion of the fifth Sobol' function only slightly reduces the error, as shown by the blue curve. Similarly for the case of P-Wave, the inclusion of the sixth Sobol' function also slightly reduces the error.

The reduced objective functions, therefore, can predict the starting frequency of the first frequency band gaps of the S-Wave and P-Wave very accurately, as the scaled L_2 error points to very small values of 0.0086 and 0.0036, respectively. For the case of the width of the first frequency band gap, the scaled L_2 error shows small values of 0.0994 and 0.1406, respectively, for the S-Wave and P-Wave, which is very acceptable from an engineering point of view. Depending on the level of accuracy, one may include more Sobol' functions in the reduced objective functions to further diminish the truncation error.

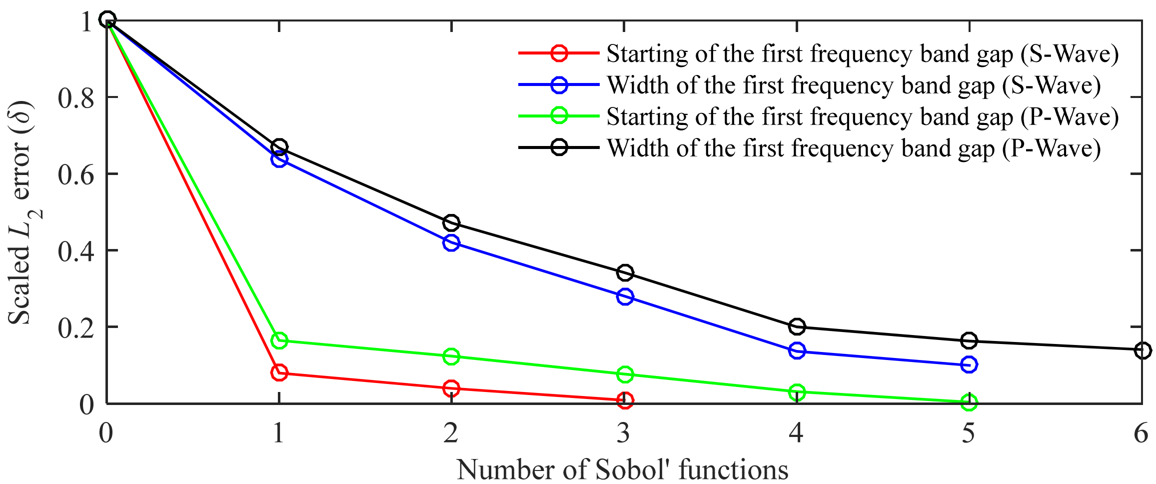

Figure 4-16 Scaled L_2 errors of the reduced objective functions

The reduced objective functions can be used as simplified design equations to easily obtain the first frequency band gaps for the S-Wave and P-Wave. Note that the design equations provide the frequencies in a non-dimensional unit. To obtain the dimension in Hz, the calculated non-dimensional frequencies need to be divided by the reference variable T_*.

5 EXPERIMENTAL PROGRAM

The study presented in Chapter 3 shows that 1D and 3D periodic materials with finite geometry are capable of reducing response of incoming elastic waves with frequencies inside their attenuation zones, which are consistent with their respective theoretical frequency band gaps. Based on the study, the 1D and 3D periodic materials are designed at a larger scale as periodic foundations to seismically isolate an SMR building. This chapter first presents the design of full-scale 1D and 3D periodic foundation structural systems. Then, the full-scale structural systems were scaled to fit a shake table facility for experimental validation. The fabrication process of the scaled structural systems as well as the shake table test program is also presented in this chapter.

5.1 Design of Full-Scale Structural Systems

This section elaborates the design process of 1D and 3D periodic foundations. In addition, detailed information on the full-scale SMR building is also presented.

5.1.1 Full-scale small modular reactor building

The information of an SMR building used as the superstructure in this study was obtained directly from NuScale. Shown in Figure 5-1 and Figure 5-2 are the notional sketches and render models of the SMR building provided by NuScale. As the dimension of the SMR building model comes in ranges, it offers a flexibility to choose the dimension of the SMR building that fits this study.

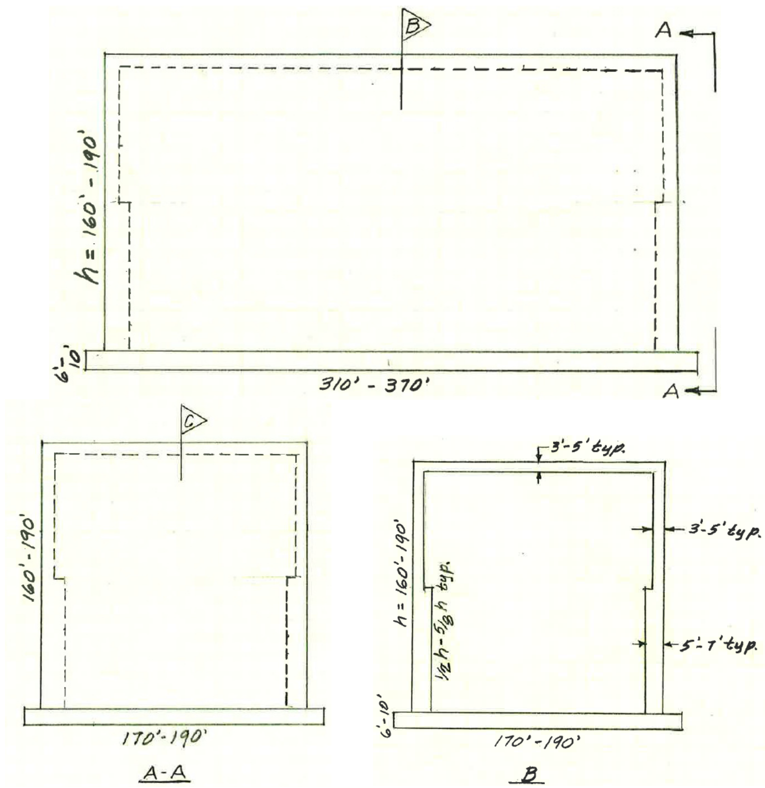

Figure 5-1 NuScale SMR building sketch (unit in ft)

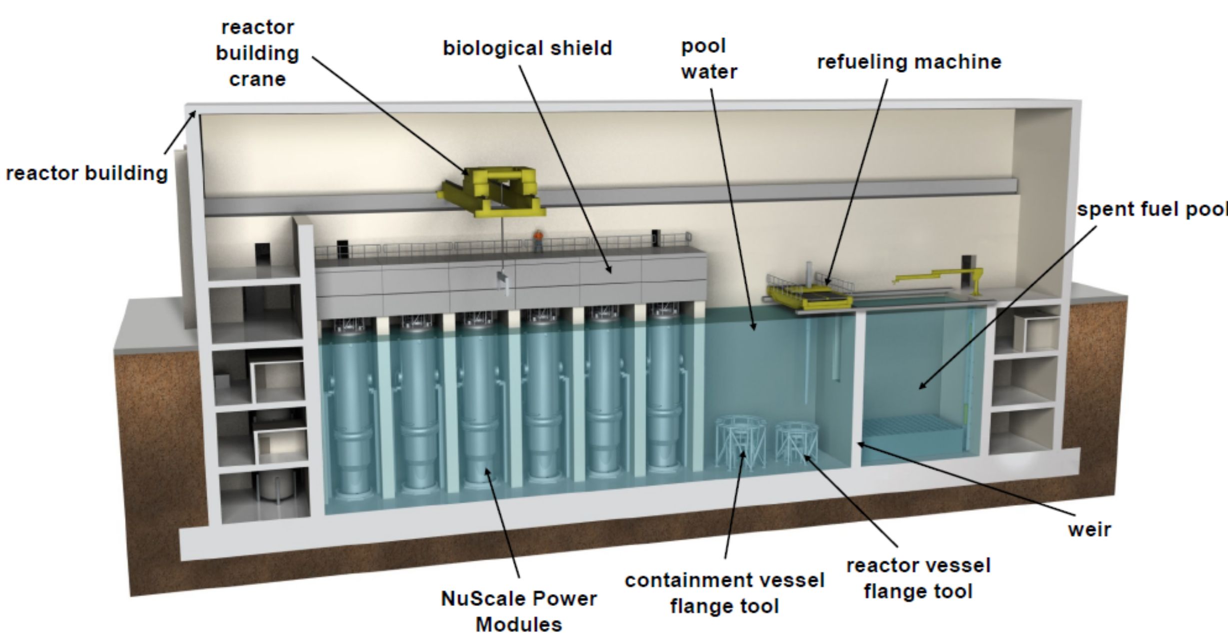

(a) Cutaway view

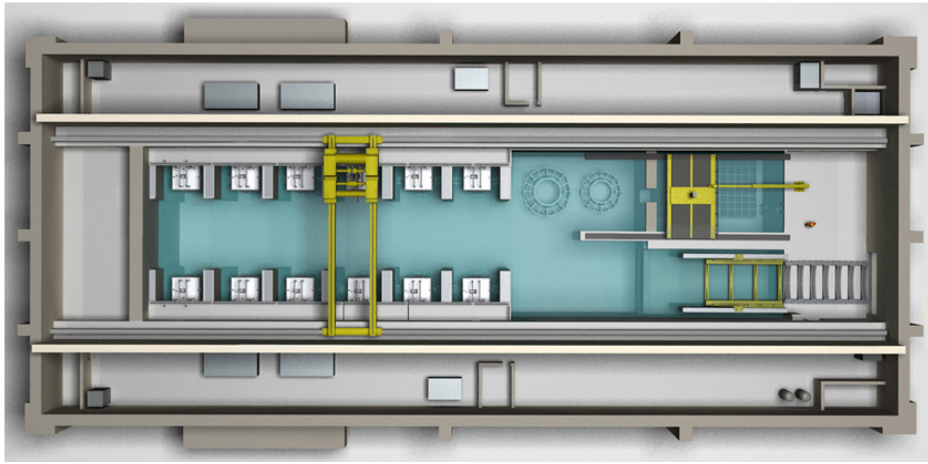

(b) Overhead view

Figure 5-2 Nu Scale Reactor Building (figures obtained from [73])

Based on the provided dimensions and building features, a finite element model of the full-scale SMR building was generated for this study. The SMR building structure used in this study is not an actual prototype of NuScale's SMR building, but rather a representation of its SMR building. The dimensions, masses, and volumes of the building structure were selected from the sketches and the rendering pictures provided by NuScale.

The SMR building was modeled as a rectangular shaped building. The building has a reactor pool in the middle of it with all of the structural components modeled in detail. The perspective view of the reactor building model is shown in Figure 5-3. Details of the plane view and the cuts are shown in Figure 5-4.

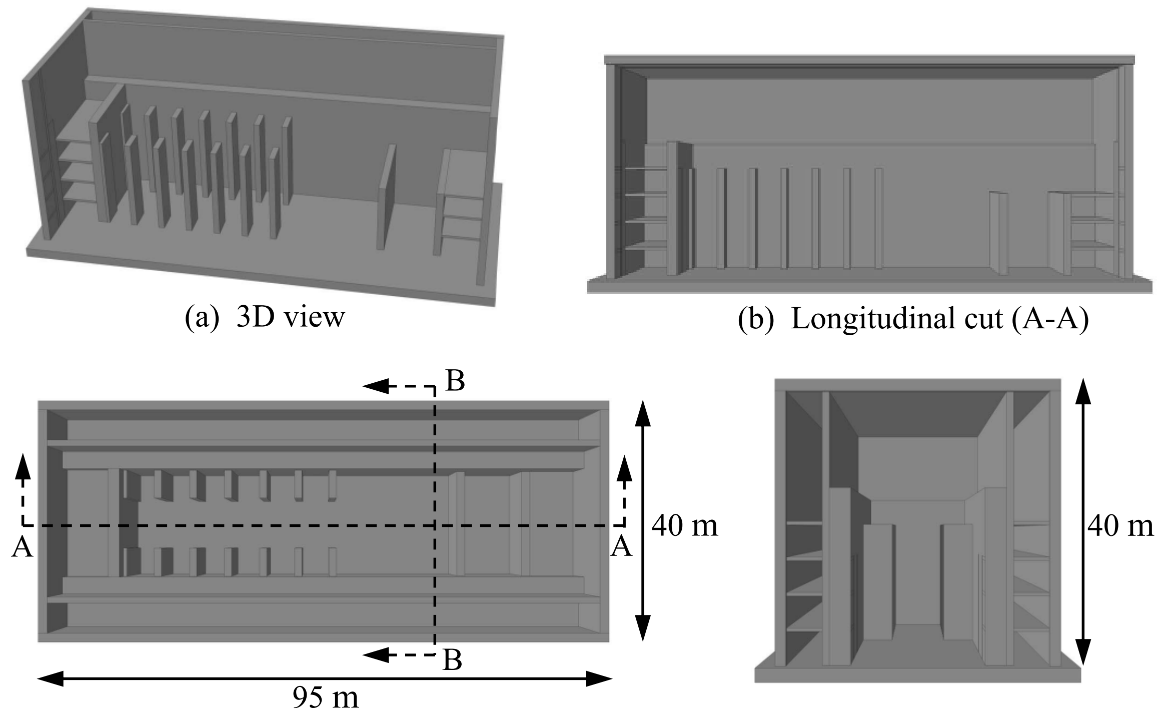

(c) Plan view

(d) Transverse cut (B-B)

Figure 5-3 Perspective view of SMR building

The building and its structural components shown in Figure 5-3 are assumed to be made of reinforced concrete (RC) with a Young's Modulus of 31400 MPa, a density of 2300 kg/m^3, and a Poisson's Ratio of 0.2. The roof is assumed to be rigid. The mass of non-structural elements that are considered for dynamics analysis are:

- Water in reactor pool = 5.09 million gallon = 19.28×10^6 kg
- Small modular reactors (12 units) = $12\times(8\times10^5)= 9.6\times10^6$ kg
- Crane and utilities = 8×10^5 kg

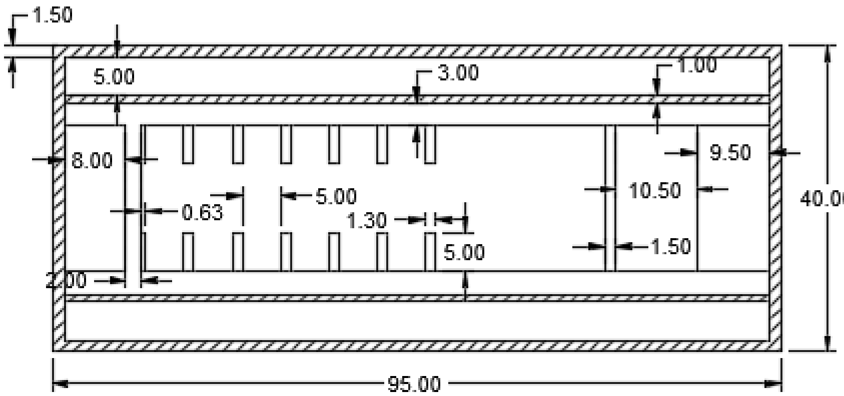

(a) Plane view

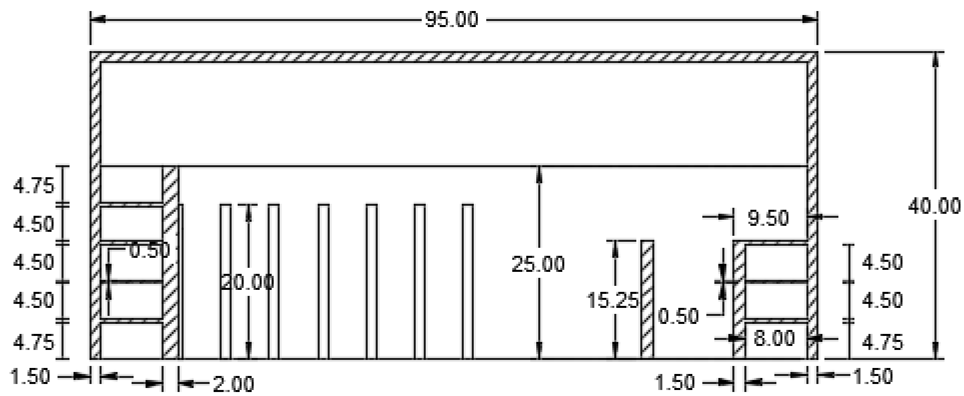

(b) Longitudinal cut (A-A)

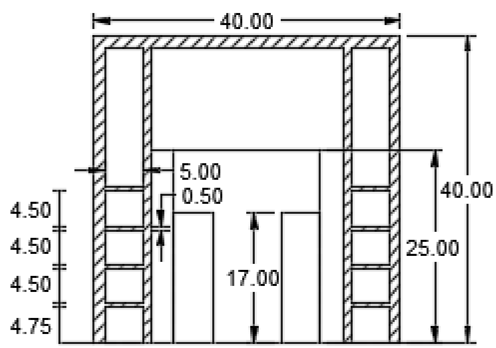

(c) Transverse cut (B-B)

Figure 5-4 Detail of SMR building (unit in m)

The first three mode shapes and natural frequencies of the structure are shown in Figure 5-5. The first mode is the translational mode in the transverse direction with a natural frequency of 6.77 Hz. The second mode is the rotational mode with a natural frequency of 11.14 Hz. The third mode is the translational mode in the longitudinal direction with a natural frequency of 11.98 Hz.

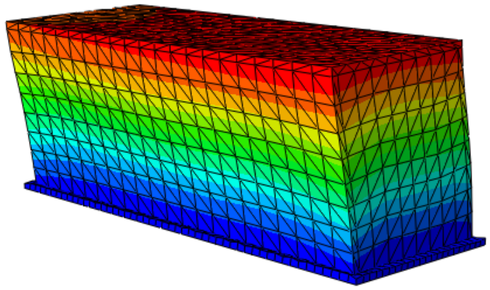

(a) Mode 1 (6.77 Hz)

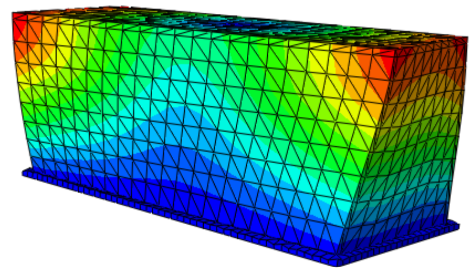

(b) Mode 2 (11.14 Hz)

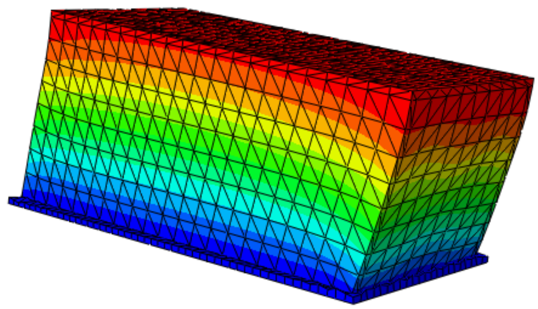

(c) Mode 3 (11.98 Hz)

Figure 5-5 Mode shapes and natural frequencies of SMR building

5.1.2 Full-scale 1D periodic foundation

5.1.2.1 Design of 1D periodic foundation unit cell

The study presented in Subsection 3.3.2 shows that the combination of the two sets of two-layer unit cells, with their frequency band gaps covering one another, as a four-layer unit cell can reduce the pass bands and create wide frequency band gaps. Although, the four-layer unit cell still possesses very thin pass bands, the response amplification can be easily damped out by material damping. Therefore, a four-layer unit cell was selected for the design of the 1D periodic foundation.

The first step in designing the four-layer unit cell is to design the two different two-layer unit cells that possess different frequency band gaps covering one another. After a series of trials, the first unit cell was designed using natural rubber and RC materials. Each of the natural rubber and RC layers has a thickness of 1.1 m. The material properties of the materials are shown in Table 5-1. By utilizing the proposed design equations presented in Section 4.3, the first frequency band gaps under the S-Wave and P-Wave are found to be at 6.64–19.03 Hz and 24.62–62.52 Hz, respectively. In comparison to the theoretical dispersion curves shown in Figure 5-6, the errors of the starting and ending frequencies of the first frequency band gap of the S-Wave are 8.7% and 27.18%, while those of the P-Wave are 5.8% and 9.7%. The highest error of 27.18%, which is the cutoff of the first frequency band gap of the S-Wave is off by only 4 Hz. Therefore, the calculated frequency band gaps using the design equation are considered sufficiently accurate from an engineering perspective.

Table 5-1 Material properties for designed 1D periodic foundation

Material	Young's Modulus (MPa)	Density (kg/m^3)	Poisson's Ratio
Reinforced concrete	31,400	2,300	0.2
Rubber	3.49	1,100	0.463
Equivalent Superstructure	31,400	24,247.2	0.2

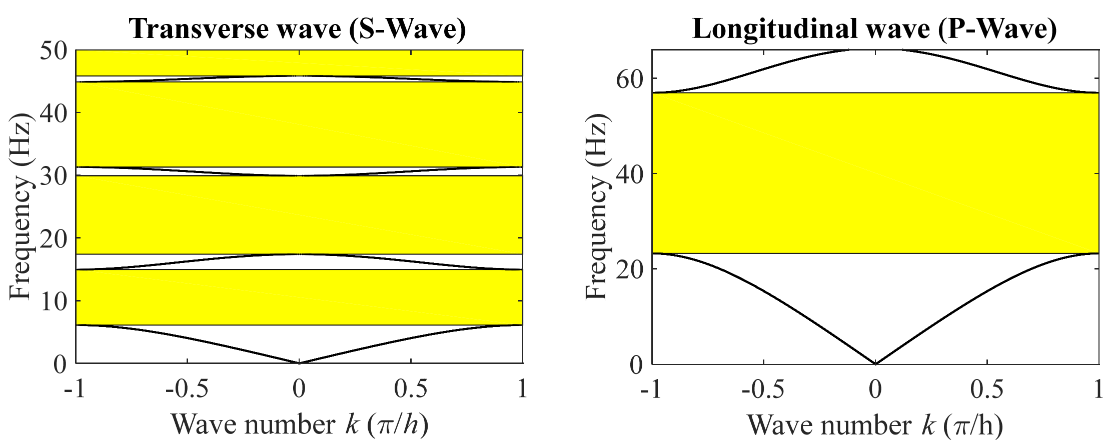

(a) S-Wave (b) P-Wave

Figure 5-6 Dispersion curves of the first two-layer unit cell

The second unit cell was also designed using the natural rubber and RC materials. However, the thickness of each of the natural rubber and RC layers is 0.88 m and 1.32 m, respectively. Using the proposed design equations for 1D periodic material, the first frequency band gaps under the S-Wave and P-Wave are found to be 7.03–25.48 Hz and 25.18–73.85 Hz, respectively. In comparison to the theoretical dispersion curves shown in Figure 5-7, the errors of the starting and ending frequencies of the first frequency band gap of the S-Wave are 10.12% and 36.19%, while those of the P-Wave are 3.51% and 3.69%. The highest error of 36.19%, which is the cutoff of the first frequency band gap of the S-Wave is off by 6.77 Hz. The calculated frequency band gaps using design equations are considered sufficiently accurate from an engineering perspective.

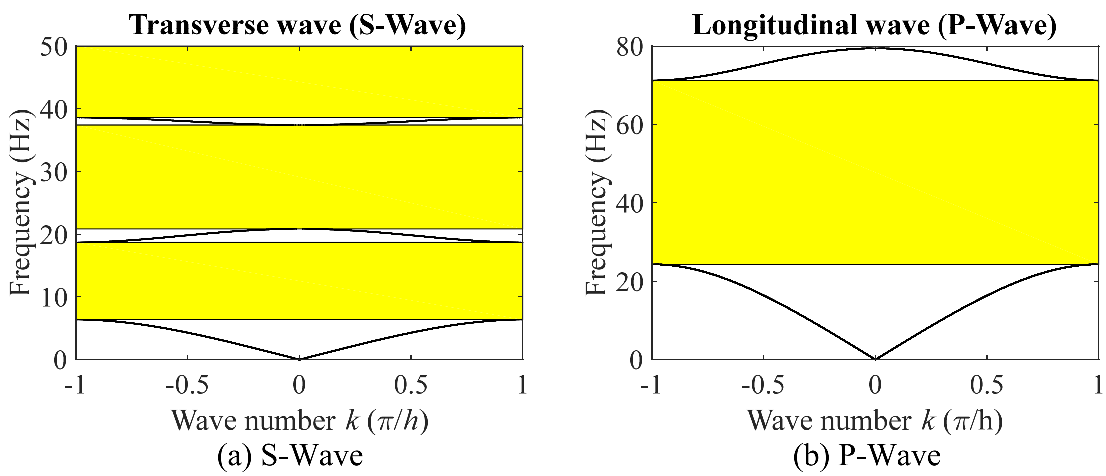

Figure 5-7 Dispersion curves of the second two-layer unit cell

The frequency band gaps of the first and second unit cells under the S-Wave can be seen covering one another. Therefore, the two unit cells were chosen for the 1D periodic foundation design. Considering a single four-layer unit cell that consists of the previous two unit cells, the dispersion curves are shown in Figure 5-8. Very thin pass bands are observed in 15.79–16.22 Hz, 19.89–20.18 Hz, 30.52–30.6 Hz, and 38.03–38.1 Hz. The response amplification in these thin passbands will be controlled by material damping. The obtained low and wide frequency band gaps are suitable to isolate seismic waves.

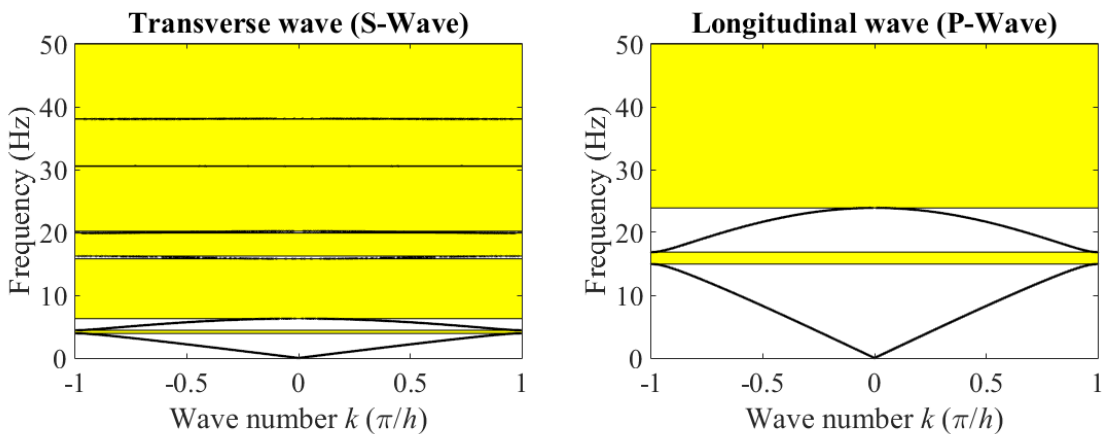

(a) S-Wave (b) P-Wave

Figure 5-8 Dispersion curves of full-scale four-layer unit cell

5.1.2.2 Design of 1D periodic foundation structural system

As reported in Chapter 3, the presence of the superstructure can affect the frequency band gaps. The shift in frequency band gaps can be predicted by converting the superstructure into an additional equivalent structure layer on the unit cell and subsequently by finding the dispersion curves of the corresponding unit cell.

According to Figure 5-4, the length and width of the reactor building are 95 m and 40 m, respectively. The periodic foundation was designed with a slightly larger plane size. A length (l) of 99 m and a width (t) of 44 m were chosen as the plane size of the periodic foundation. The thickness of the equivalent structure layer was selected to be equal to the thickness of the top concrete layer as shown in Figure 5-9. By knowing the exact total weight of the superstructure as 1366311100 N, the density of the equivalent superstructure layer can be calculated, as shown in Eq. (5-1)

$$\rho_s^* = \frac{m_s}{l \times t \times h_s^*} = \frac{139419500}{99 \times 44 \times 1.32} = 24247.207 \, \text{kg/m}^3 \, . \tag{5-1}$$

The unit cell with an additional equivalent superstructure layer is shown in Figure 5-9 with the material properties for each of the materials shown in Table 5-1. Figure 5-10 shows the corresponding dispersion curves. The frequency band gaps of the corresponding unit cell subjected to S-Wave and P-Wave are observed to be even lower and wider as compared to the frequency band gaps without considering the superstructure. As shown in Figure 5-10, the frequency band gaps of the unit cell subjected to the S-Wave are observed to start from 1.3 Hz all the way to 50 Hz with two very thin pass bands located at 4.34–4.57 Hz and 19.5–19.53 Hz. Meanwhile, the frequency band gaps of the unit cell subjected to the P-Wave are found to be at 4.97–16.51 Hz and 17.41–50 Hz.

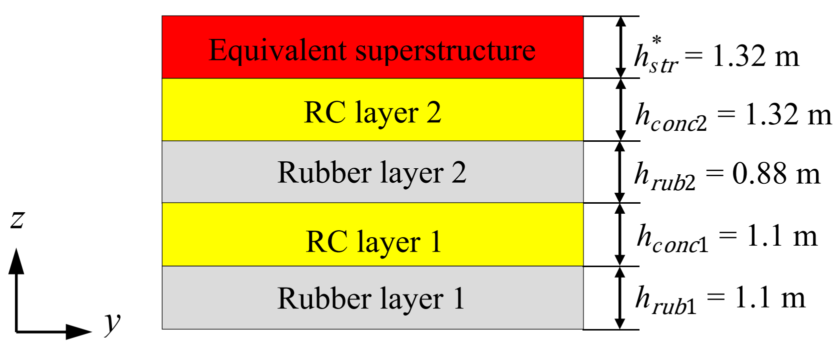

Figure 5-9 Full-scale 1D periodic foundation unit cell with additional equivalent structure layer (figure not to scale)

The designed 1D periodic foundation structural system is shown in Figure 5-11. The 1D periodic foundation is placed underneath the reactor building. The periodic foundation consists of a four-layer unit cell and is placed on top of an RC base. In practice, there is no specific requirement for the thickness of the RC base. The ground surface is paved with RC so that there is a flat surface to place the foundation. In this analysis, the base was assumed to have a thickness of 1.1 m. The color of each of the materials in the figure is presented as close as possible to the real materials' color with grey color for the RC and black color for the natural rubber.

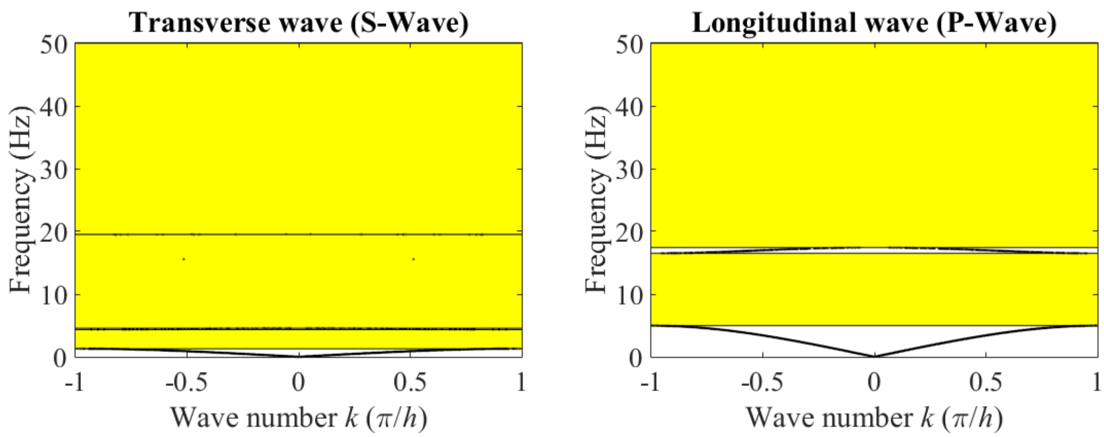

(a) S-Wave (b) P-Wave

Figure 5-10 Dispersion curves of full-scale 1D periodic foundation unit cell with equivalent superstructure layer

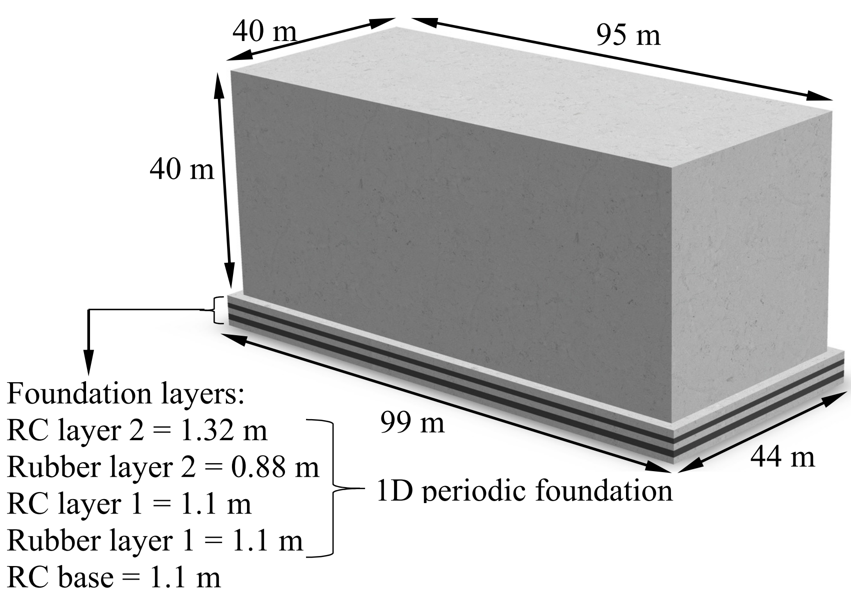

Figure 5-11 Designed full-scale 1D periodic foundation structural system

5.1.2.3 Modal analysis of 1D periodic foundation structural system

Based on the finite element analysis, the natural frequencies of the first three modes and the corresponding mode shapes are shown in Figure 5-12. It is observed that the mode shapes of the structural system are slightly different from the mode shapes of the superstructure only. Since the superstructure is considerably stiffer compared to the 1D periodic foundation, the superstructure acts as a rigid body and mass provider for the structural system. Therefore, the movement is concentrated on the periodic foundation. The first mode shape is the most flexible movement. In this case, it is a translational movement with a natural frequency of 0.59 Hz. The second and third modes, which are longitudinal and rotational modes, respectively, are observed to be very close to one another with natural frequencies of 0.63 Hz and 0.64 Hz, respectively.

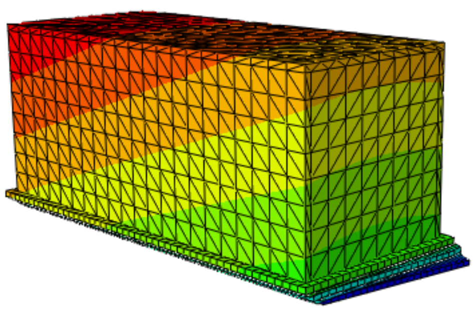

(a) Mode 1 (0.59 Hz)

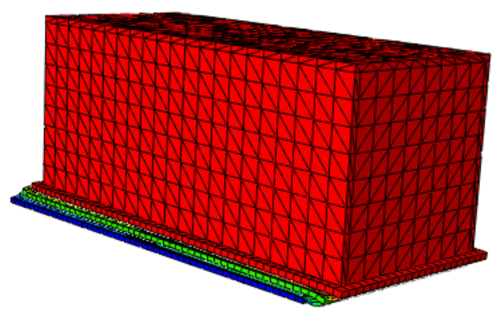

(b) Mode 2 (0.63 Hz)

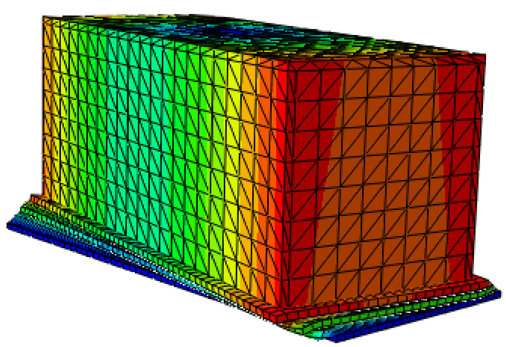

(c) Mode 3 (0.64 Hz)

Figure 5-12 Mode shapes and natural frequencies of full-scale 1D periodic foundation structural system

5.1.2.4 Frequency sweeping analysis of 1D periodic foundation structural system

The 1D periodic foundation structural system was subjected to steady-state frequency sweeping analysis in order to obtain the attenuation zones of the system. The response of the structural system was investigated from one point on the roof and two points on top of the 1D periodic foundation (points A and B), as shown in Figure 5-13. In the analysis, a commonly used damping model in structural engineering, the Rayleigh damping, was assigned on each of the materials. The mass proportional damping coefficient (α) and stiffness proportional damping coefficient (β) for a particular material can be calculated according to Eq. (5-2)

$$\begin{Bmatrix} \alpha \\ \beta \end{Bmatrix} = \frac{2\zeta}{\omega_i + \omega_j} \begin{Bmatrix} \omega_i \omega_j \\ 1 \end{Bmatrix}, \tag{5-2}$$

where ζ is the damping ratio for the particular material, ω_i corresponds to the first natural frequency of the structural system (in rad/sec), and ω_j is selected as the maximum angular frequency of interest. In this study the maximum angular frequency is selected as 314.159 rad/sec (50 Hz), which is the maximum frequency content in seismic waves. This selection was made to avoid an over damping condition in the finite element models. Damping ratios of 4% and 10% were assigned to the RC and rubber materials, respectively. The damping coefficients for each of the materials are shown in Table 5-2.

Table 5-2 Rayleigh damping coefficient for full-scale 1D periodic foundation structural system

Material	Damping ratio (ζ)	α	β
Reinforced concrete	4%	0.29	0.000252
Natural rubber	10%	0.73	0.000629

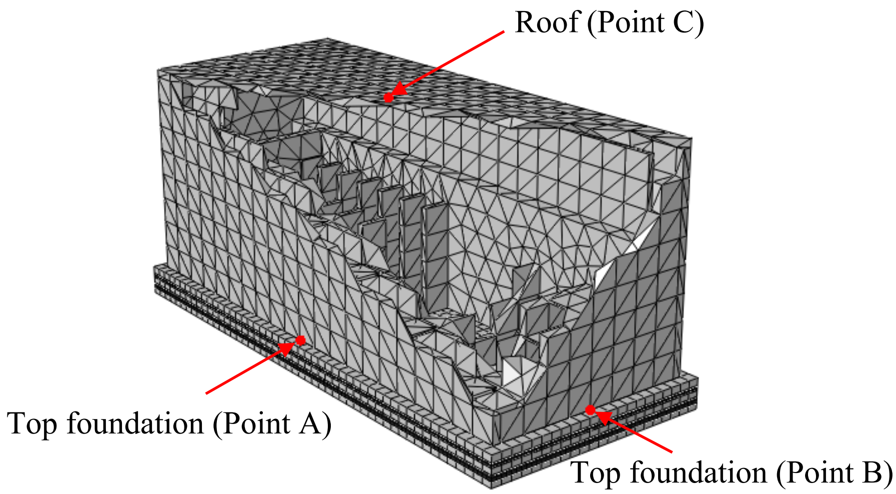

Figure 5-13 Finite element model of full-scale 1D periodic foundation structural system with location of the output points (some of the elements on the structural system are hidden)

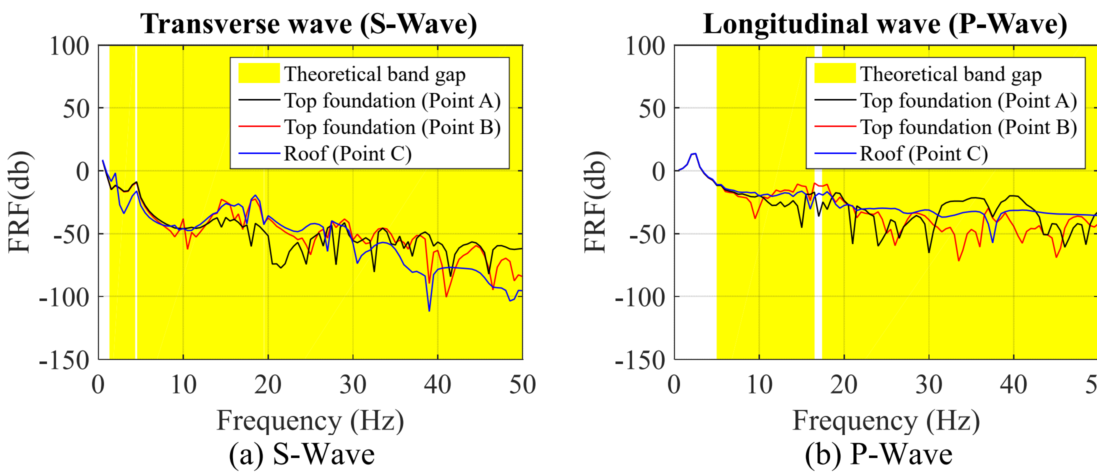

Figure 5-14 Frequency response function of full-scale 1D periodic foundation structural system

The input excitation for the frequency sweeping of the S-Wave was assigned in the horizontal (short) direction while that of the P-Wave was assigned in the vertical direction. It can be seen that the attenuation zones in each of three output points are consistent with the theoretical frequency band gaps, as shown in Figure 5-14. The response at the higher pass bands are attenuated owing to the damping in materials. The frequency sweeping results show that the designed periodic foundation is capable of isolating the reactor building from the majority of the incoming horizontal and vertical seismic waves.

5.1.2.5 Stress analysis on rubber under gravity load

The bottom rubber layer, i.e., rubber layer 1 in Figure 5-11, is subjected to the highest stresses under the gravity load. The principal stress fields in rubber layer 1 are shown in Figure 5-15. The majority of the rubber layer is subjected to compression stress with minor tensile stress observed on the perimeter elements. The maximum compression stress is observed to be 0.463 MPa, and the maximum tensile stress is observed to be 0.0745 MPa. The stresses are small enough and typically still within the elastic range of natural rubbers.

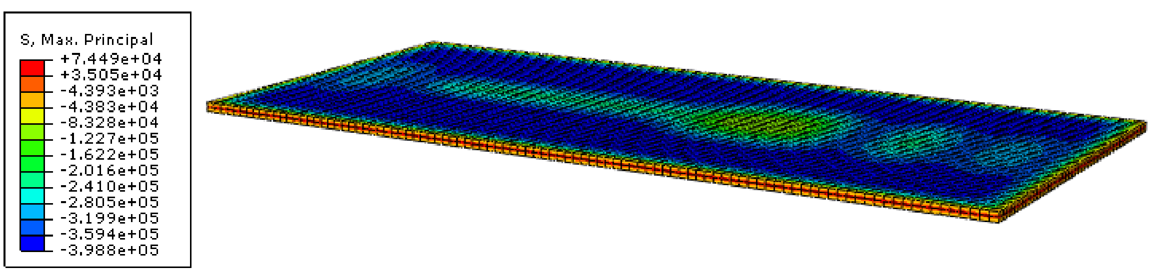

(a) Maximum principal stress

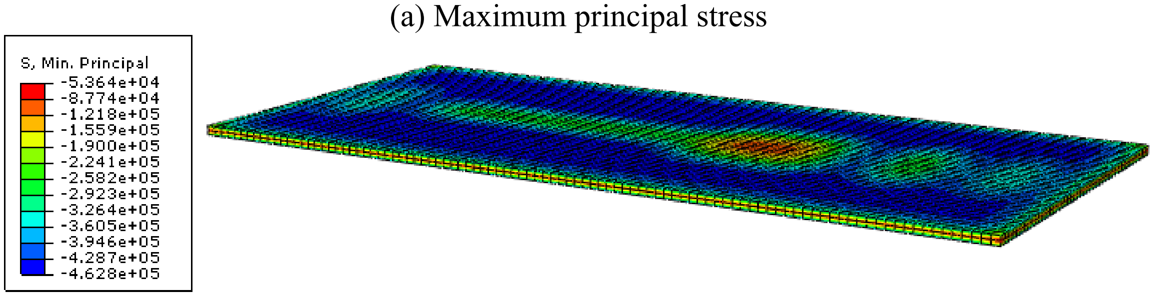

(b) Minimum principal stress

Figure 5-15 Principal stress fields on the rubber layer 1 in full-scale 1D periodic foundation structural system (unit in Pa)

Material tests on natural rubbers conducted by the National Center for Research on Earthquake Engineering (NCREE) are summarized in Table 5-3. The test data is obtained from direct correspondence with NCREE. The compressive stress-strain curves are shown in Figure 5-16. The material properties of the tested natural rubber are very similar to those used in the design of the 1D periodic foundation. The tensile strength of this rubber is found to be at 8.4 MPa. The tensile capacity is much higher than the maximum tensile stress in the analysis result. The maximum compression stress in the analysis is observed to be at 0.463 MPa, which is still within the elastic range on the stress-strain curve.

Table 5-3 Summary of natural rubber test results

Item	Test standard	Results
Specific gravity	ASTM D792-08	1.157
Tensile strength (MPa)	ASTM D412-06a	8.434
Elongation (%)	ASTM D412-06a	535
Compressive stress at 50% strain (MPa)	ASTM D575-91	3.24

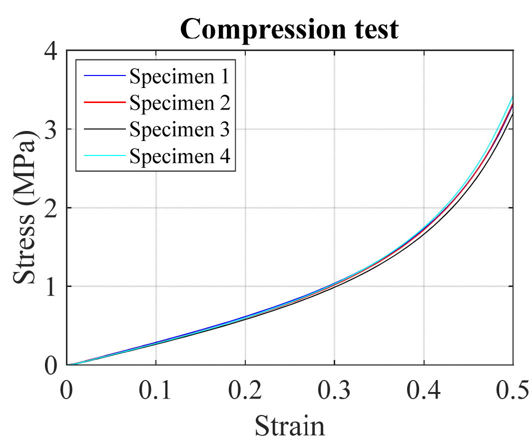

Figure 5-16 Compressive stress-strain curves of natural rubber

5.1.3 Full-scale 3D periodic foundation

5.1.3.1 Design of 3D periodic foundation unit cell

The study presented in Subsection 3.3.3 shows that the Bragg scattering type unit cell is relatively efficient in reducing the response of elastic waves in comparison to the Locally resonant unit cell. Therefore, the 3D periodic foundation for seismic isolation of the SMR building was designed with the Bragg scattering type unit cell. The unit cell is a cube with a length of 8 m encasing a cubical core with a length of 7.2 m, as shown in Figure 5-17. Regular RC material is used as the material for the core component and the natural rubber is used for the matrix component. The material properties for the RC and natural rubber are the same as those used in the design of the 1D periodic foundation which are shown in Table 5-1.

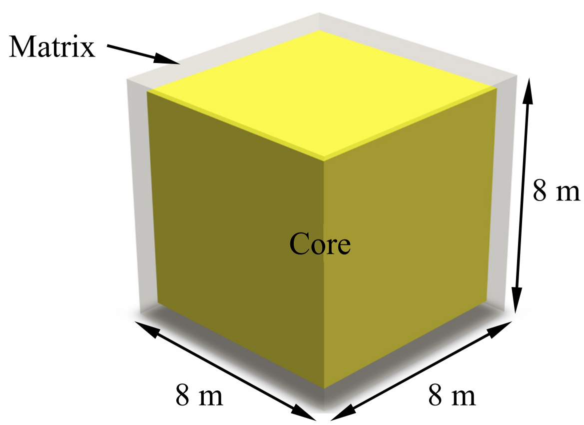

Figure 5-17 Unit cell of full-scale 3D periodic foundation

The dispersion curve for the designed unit cell is shown in Figure 5-18. An absolute frequency band gap is observed in the frequency range of 10.93–17.1 Hz. As mentioned in Sub-subsection 3.3.3.3, the absolute frequency band gap is an intersection of frequency band gaps from different waves. As a periodic foundation, the 3D unit cells are placed in between the ground and the superstructure. This mechanism leads to seismic waves' propagation only in one direction, the vertical direction. Therefore, steady-state frequency sweeping analysis is conducted to obtain the real attenuation zones subjected to the S-Wave and P-Wave. Figure 5-19 shows the FRF curves of the designed Bragg scattering unit cell which are lower and wider than the theoretical absolute frequency band gap.

According to the study presented in Sub-subsection 3.3.3.3, the attenuation zones of the Bragg scattering unit cells can also be approximated using the design equations for 1D periodic materials presented in Section 4.3. The end of the first attenuation zones of a Bragg scattering unit cell subjected to both the S-Wave and P-Wave are close to the end frequency of the layered 1D periodic material subjected to S-Wave. The predicted end frequency is 25.8 Hz which is close to the end attenuation zones in Figure 5-19. Moreover, the starting of attenuation zone under the P-Wave can be predicted by the starting of the P-Wave frequency band gap. The predicted frequency for the start of the P-Wave attenuation zone is 9.33 Hz which is also very close to that in the P-Wave FRF curve.

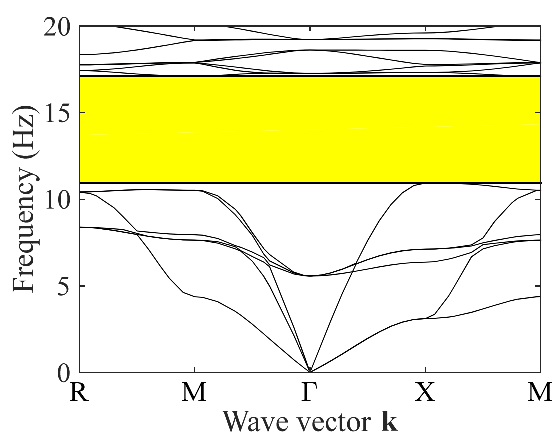

Figure 5-18 Dispersion curve of full-scale 3D periodic foundation unit cell

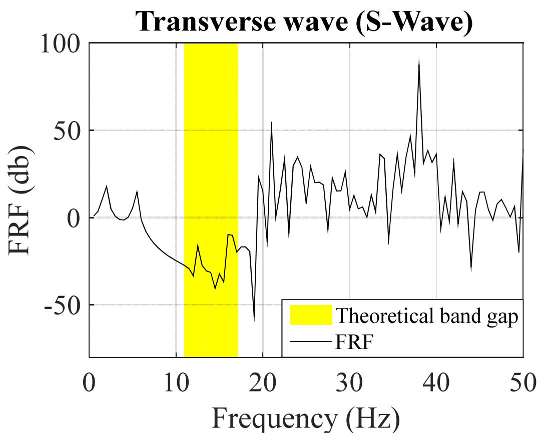

(a) S-Wave

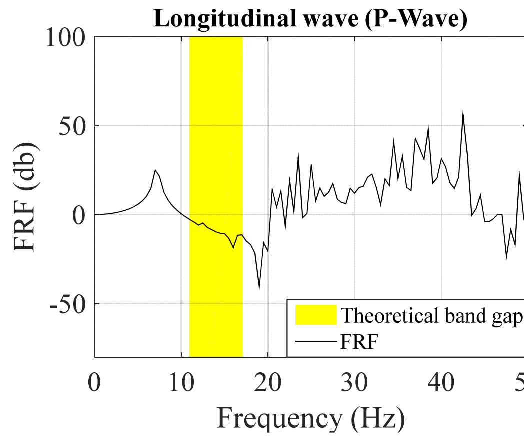

(b) P-Wave

Figure 5-19 Frequency response function of full-scale 3D periodic foundation unit cell

5.1.3.2 Design of 3D periodic foundation structural system

The 3D periodic foundation was designed with 54 unit cells that are separated into three blocks. Each block consists of 18 units with the arrangement of three units by six units in the horizontal plane and one unit in the vertical direction. Such arrangement eases the construction process and minimizes the error during construction. Figure 5-20 shows the design of the 3D periodic foundation supporting the SMR building. A 1.32 m thick RC slab was designed on top of the periodic foundation to provide a uniform stress distribution on the top surface of the 3D periodic foundation. The RC slab also serves as the ground floor of the reactor building. At the bottom of the periodic foundation, an RC base with a thickness of 1.1 m was also designed to provide uniform stress distribution on the bottom surface of the 3D periodic foundation.

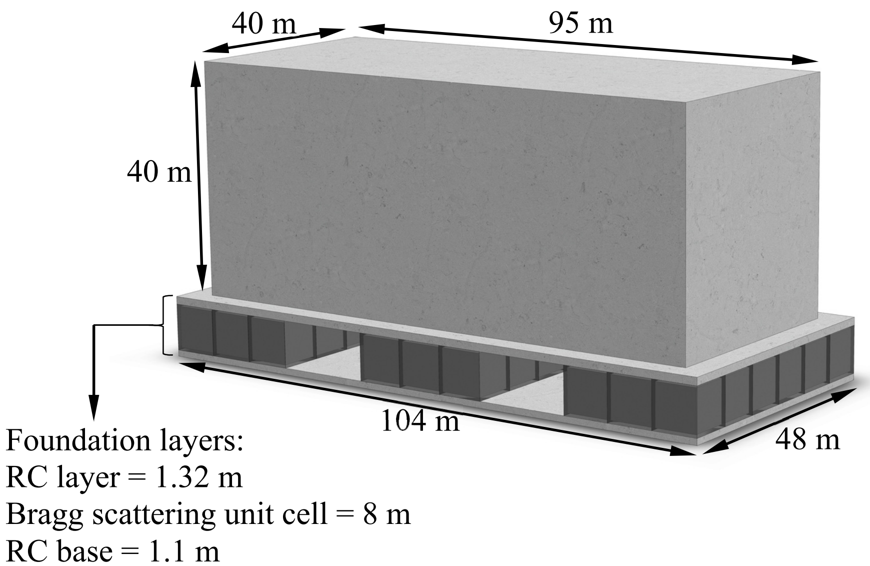

Figure 5-20 Designed full-scale 3D periodic foundation structural system

5.1.3.3 Modal analysis of 3D periodic foundation structural system

The natural frequencies of the first three modes and the corresponding mode shapes obtained from the finite element analysis are shown in Figure 5-21. Since the superstructure is considerably stiffer in comparison to the periodic foundation, the superstructure acts as a rigid body and mass provider to the structural system. The first mode shape is a translational movement with a natural frequency of 0.707 Hz. The natural frequencies of the second and third modes, which are the longitudinal translation and torsional modes, are observed to be of 0.739 Hz and 0.844 Hz, respectively.

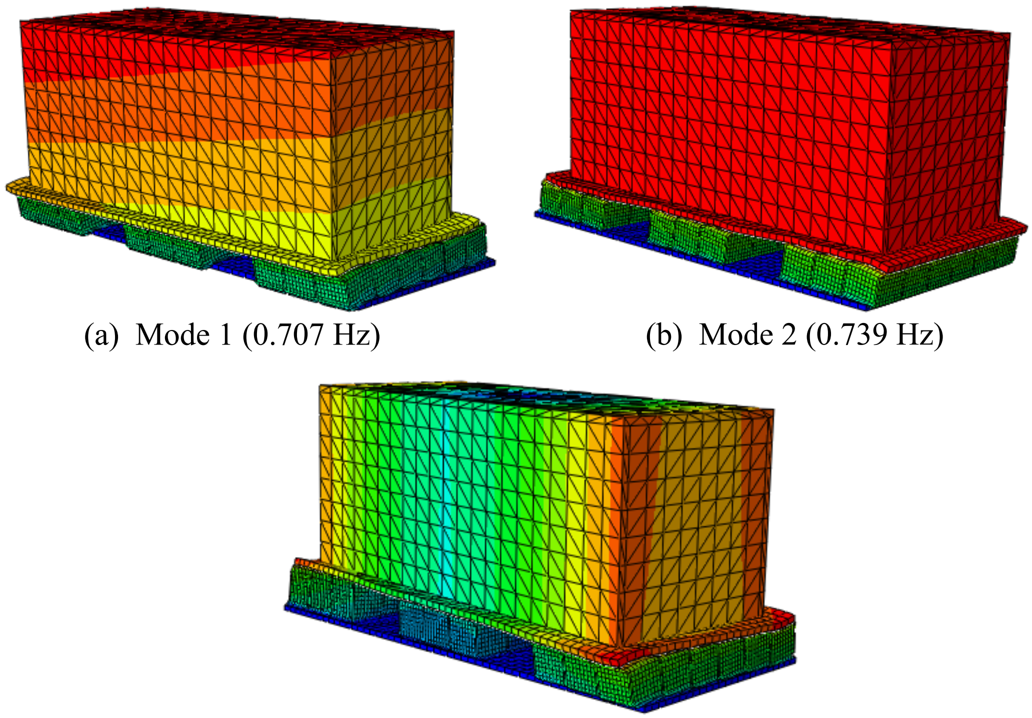

(a) Mode 1 (0.707 Hz)

(b) Mode 2 (0.739 Hz)

(c) Mode 3 (0.844 Hz)

Figure 5-21 Mode shapes and natural frequencies of full-scale 3D periodic foundation structural system

5.1.3.4 Frequency sweeping analysis of 3D periodic foundation structural system

Similar to the 1D periodic foundation, the presence of the superstructure affects the original frequency band gaps of the unit cell in the 3D periodic foundation. In general, the frequency band gaps or attenuation zones of the structural system will be lower than those of the periodic foundation without the superstructure. The frequency sweeping analysis was conducted on the 3D periodic foundation structural system to obtain the real attenuation zones of the structural system. Damping ratios of 4% and 10% were assumed for the RC and natural rubber materials, respectively. The damping model utilizes the Rayleigh damping which is explained in Sub-subsection 5.1.2.4. Table 5-4 shows the Rayleigh damping coefficient used in the analysis of the full-scale 3D periodic foundation structural system. Three points on the top of the 3D periodic foundation and one point on the roof of the superstructure were selected as the output points to see the response of the structural system (see Figure 5-22). Points A and C are located on the RC layer at the top of the 3D periodic foundation directly above the unit cells while Point B is located on the RC layer at the top of the 3D periodic foundation in between two blocks of unit cells.

Table 5-4 Rayleigh damping coefficient for full-scale 3D periodic foundation structural system

Material	Damping ratio (ζ)	α	β
Reinforced concrete	4%	0.35	0.000251
Natural rubber	10%	0.88	0.000628

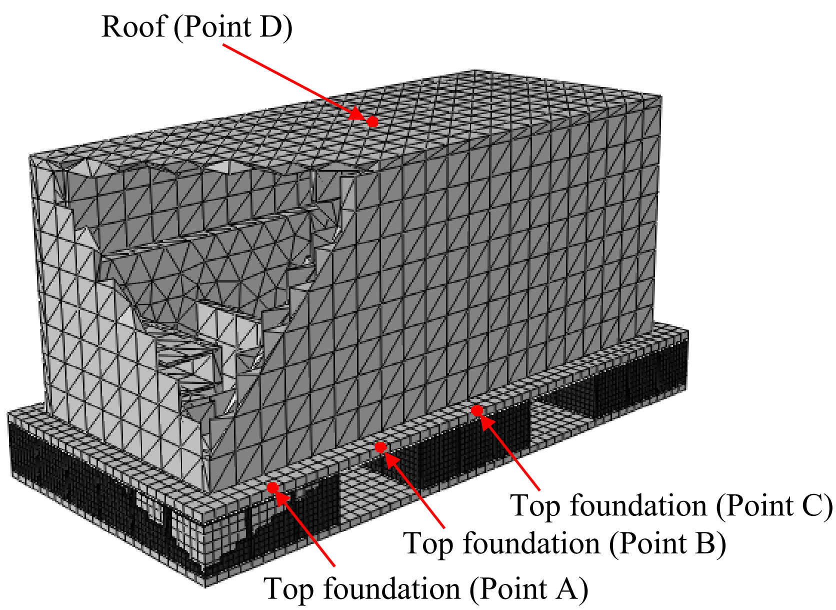

Figure 5-22 Finite element model of full-scale 3D periodic foundation structural system with location of the output points (some of the elements in the structural system are hidden)

The input excitation for the frequency sweeping of the S-Wave was assigned in the horizontal (short) direction while that of the P-Wave was assigned in the vertical direction. The frequency sweeping analysis results are presented in Figure 5-23. The attenuation zones of the S-Wave are observed to be in 1–1.76 Hz and 3.5–50 Hz. The attenuation zones of the P-Wave effectively start from 17 Hz to 50 Hz. The frequency sweeping results show that the designed 3D periodic foundation is capable of isolating the reactor building from the majority of the incoming horizontal and vertical waves.

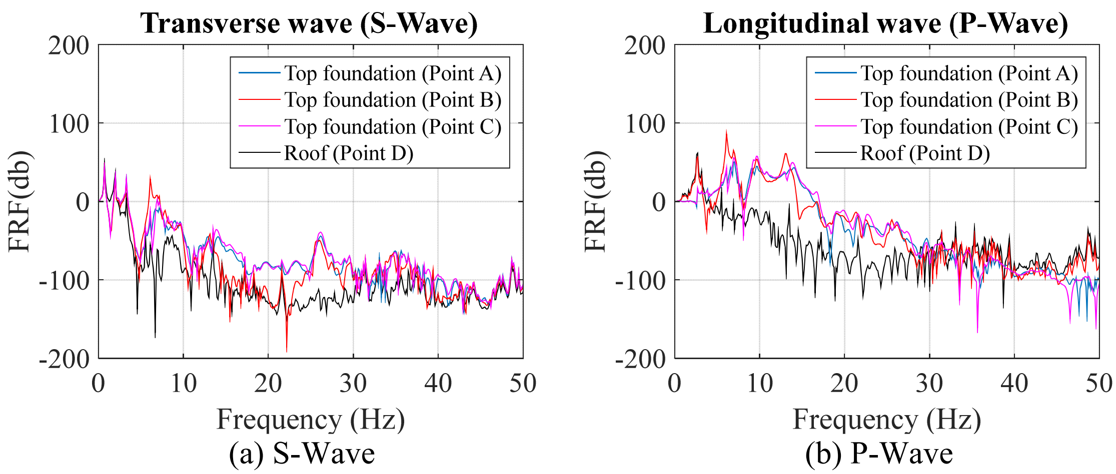

Figure 5-23 Frequency response function of full-scale 3D periodic foundation structural system

5.1.3.5 Stress analysis on rubber under gravity load

Stress analysis was conducted under the gravity load to investigate at which stage the stress of the rubber is. The principal stresses on the rubber under gravity load are shown in Figure 5-24. The maximum compression is observed to be 1.07 MPa while the maximum tensile is observed to be 0.575 MPa. Although the maximum compression stress seems to be large, this only applies to a small portion of elements. The majority of the elements in the rubber matrix have a maximum compression stress of 0.7 MPa which is still within the linear elastic range of natural rubber, as shown in Figure 5-16.

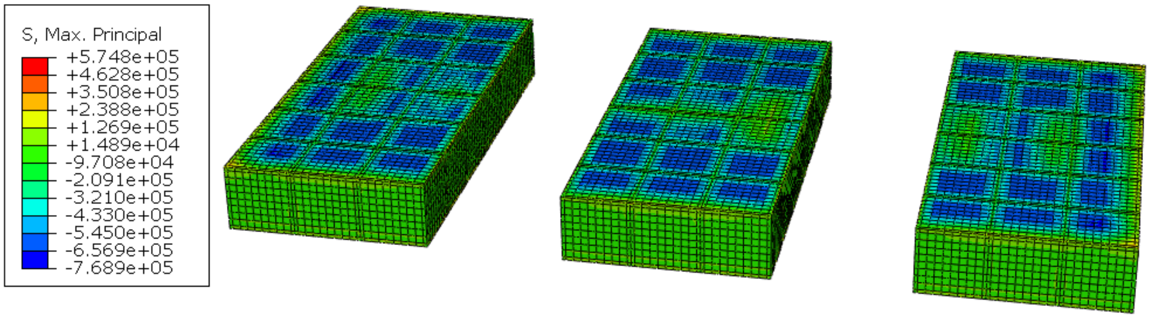

(a) Maximum principal stress

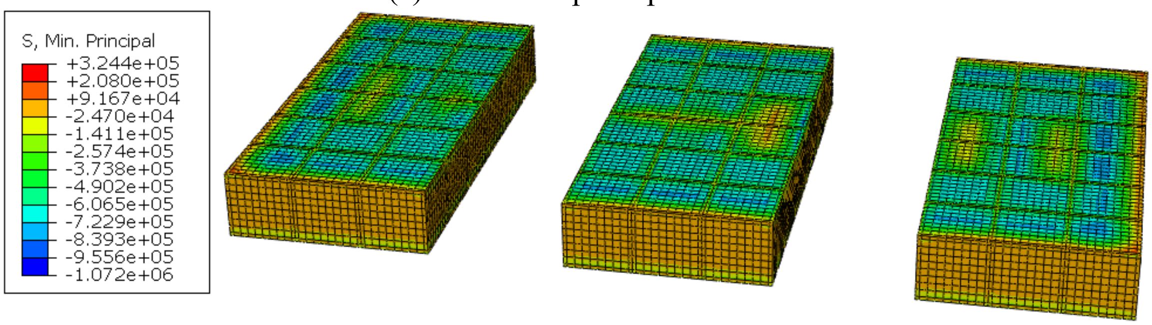

(a) Minimum principal stress

Figure 5-24 Principal stress fields on the matrix layer in full-scale 3D periodic foundation structural system (unit in Pa)

5.2 Design of Scaled Structural Systems

To fit the shake table, the designed structural systems were scaled by a length scale $l_r = 1/22$ of the original size. The scaling process follows the similitude requirements for true ultimate strength [22], as shown in Table 5-5. The subscript "*r*" in Table 5-5 refers to the ratio between the scaled model and the full-scale property. In the similitude requirements of dynamic models, if all of the requirements are satisfied, the scaled model is regarded as the true model. However, in many cases, not all of the requirements can be or need to be satisfied. As long as the essential scaled parameters are satisfied and serve the scaling purposes, the nonessential scaled parameters can be violated. The goal in this scaling is to obtain the scaled periodic foundation structural system models that have frequency band gaps corresponding to that of the prototype and fulfill the frequency scale requirement.

Table 5-5 Similitude requirements for dynamic models

Scaling Parameters		True ultimate strength model scale
Length	l_r	l_r
Time	t_r	$l_r^{1/2}$
Frequency	ω_r	$l_r^{-1/2}$
Velocity	v_r	$l_r^{1/2}$
Gravitational acceleration	g_r	1
Acceleration	a_r	1
Mass density	ρ_r	E_r/l_r
Strain	ε_r	1
Stress	σ_r	E_r
Modulus of elasticity	E_r	E_r
Specific stiffness	$(E/\rho)_r$	l_r
Displacement	δ_r	l_r
Force	F_r	$E_r l_r^2$
Energy	$(EN)_r$	$E_r l_r^3$

5.2.1 Small modular reactor building model

5.2.1.1 Scaling of small modular reactor building model

Analysis on the full-scale structural systems shows that the SMR building is considerably stiff as compared to the periodic foundations; therefore, the SMR building behaves as a rigid body and a mass provider to the periodic foundations. For experimental validation purposes, the superstructure can be scaled separately without the need to follow the dimension and the material properties scales, as long as the natural frequencies of the model superstructure and the model structural systems (superstructure with periodic foundations) satisfy the frequency scale $\omega_r = l_r^{-1/2} = \sqrt{22} = 4.69$. In addition, the frequency band gaps of the model structural systems also have to satisfy the frequency scale.

For the ease of construction and sensor installation, a steel frame structure was chosen as the model of the superstructure. The final design of the steel frame superstructure is shown in Figure 5-25 to Figure 5-28 with details of the structural members' dimension tabulated in Table 5-6. ASTM A36 steel was chosen as the material for the frame since the standardized A36 steel is widely used. The minimum yield strength of A36 steel is 36 ksi or 250 MPa [74]. A weld-type connection was selected for the assembly of the structural members.

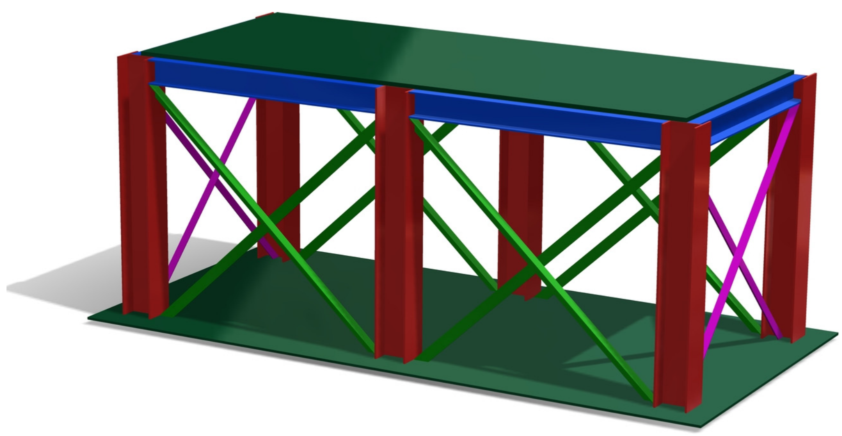

Figure 5-25 Steel frame structure

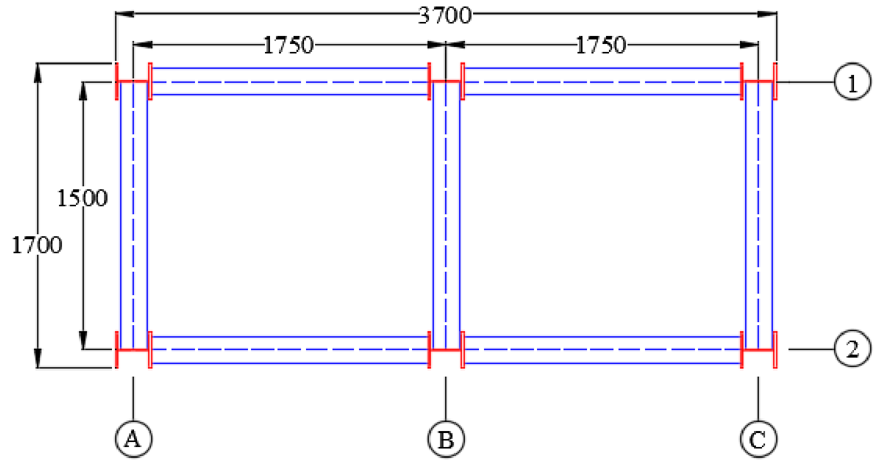

Figure 5-26 Plan view of steel frame structure (unit in mm)

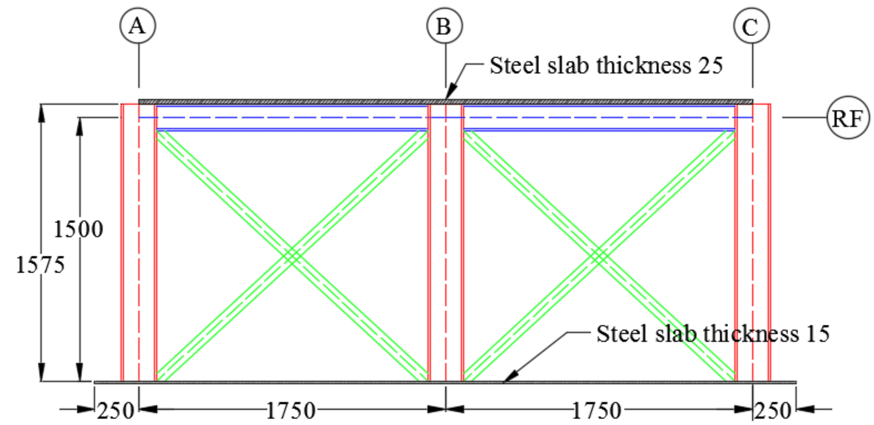

Figure 5-27 Elevation view of steel frame structure in the longitudinal direction (unit in mm)

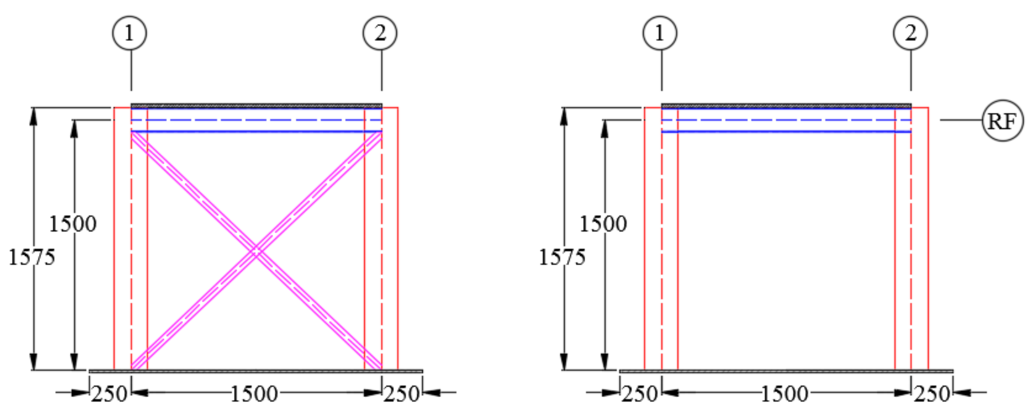

(a) Frame along lines A and C (b) Frame along line B

Figure 5-28 Elevation of steel frame structure in the transverse direction (unit in mm)

Modal analysis using the finite element model was first conducted to obtain the natural frequencies of the steel frame structure. Figure 5-29 shows the meshed finite element model of the structure. A two-node linear beam element type was assigned on each element in the beams, columns, and braces. A four-node doubly curved shell element was on each element in the roof and floor steel plates. A tie connection was utilized to connect the beams, columns, and the plates. A pin connection was utilized to connect the braces to the frame. A fixed boundary condition was assigned on each node at the steel floor. An additional mass of 1750 kg was provided on the roof of the superstructure to reach the frequency scale requirement.

Table 5-6 Detail of steel frame structural members (unit in mm)

Element	Dimension	Number
Column	Section profile: I section 200X200X8X12 (close to W8X35 in AISC) Length = 1575	6
Longitudinal beam	Section profile: I section 150X150X7X10 (close to W6X20 in AISC) Length = 1550	4
Transverse beam	Section profile: I section 150X150X7X10 (close to W6X20 in AISC) Length = 1492	3
Longitudinal brace	Section profile: angle section 65X65X6 Length: 2105	8
Transverse brace	Section profile: angle section 50X50X5 Length: 2063	4
Roof steel plate	Size 3500X1500 Thickness 25	1
Floor steel plate	Size 4000X2000 Thickness 15	1

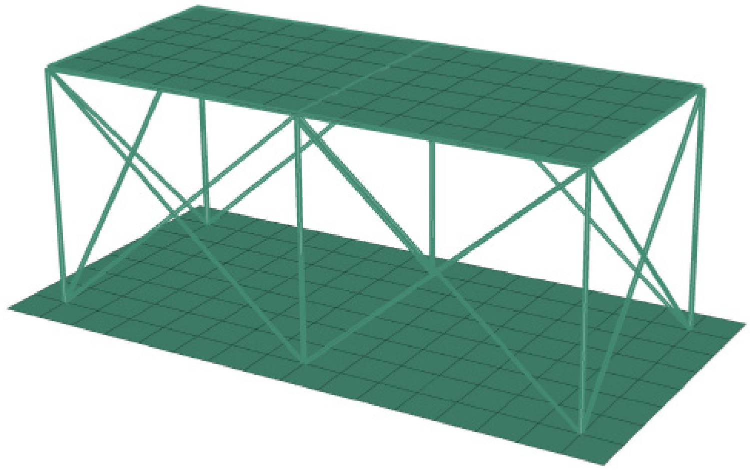

Figure 5-29 Finite element model of steel frame structure

The first three natural frequencies of the superstructure are shown in Figure 5-30. The first mode is the translational mode in the transverse direction with a natural frequency of 31.1 Hz. The second and third modes are the translational mode in the longitudinal direction and the torsional mode, respectively, each with a natural frequency of 53.55 Hz and 56.73 Hz.

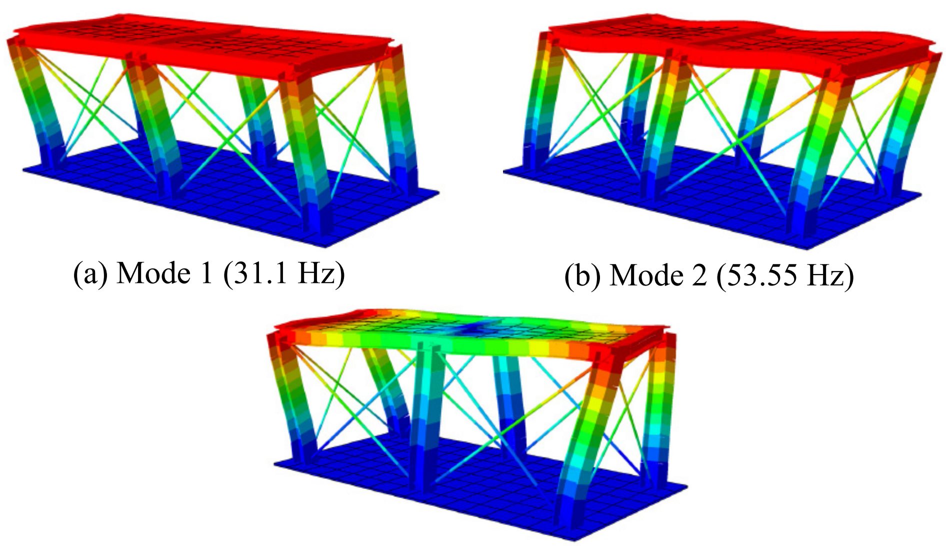

(a) Mode 1 (31.1 Hz) (b) Mode 2 (53.55 Hz)

(c) Mode 3 (56.73 Hz)

Figure 5-30 Mode shapes and natural frequencies of designed steel frame structure

Compared to the first natural frequency of the full-scale SMR building, the first natural frequency of the steel frame structure satisfies the frequency scale $\omega_r = l_r^{-1/2} = \sqrt{22} = 4.69$. The second and third modes of the model superstructure are the opposite of the second and third modes of the full-scale superstructure. However, in both model and full-scale superstructures, the natural frequencies of the second and third modes are very close to each other. Moreover, the model-to-prototype frequency ratios of the longitudinal and torsional modes are still close to the required frequency scale and still within the acceptable range ($\pm$10%). Therefore, the full-scale SMR building is representable by the steel frame structure. In the experimental study, the steel frame structure is also subjected to vertical excitations. The natural frequency of the structure in the vertical direction is observed to be 31.12 Hz with the mode shape shown in Figure 5-31.

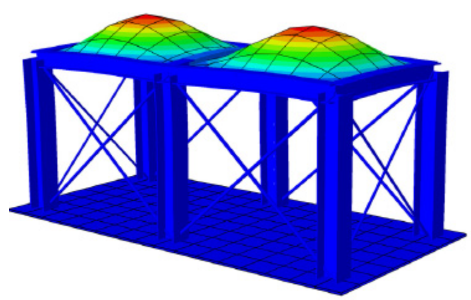

Figure 5-31 Vertical mode shape of model superstructure

In the periodic foundations scaling, described in the later sections (Sections 5.2.2 and 5.2.3), the density scale ρ_r is selected as 1. Therefore, the density of the superstructure, in theory, has to be consistent with the density scale of the periodic foundations. Based on the selected density scale, the total mass of the superstructure model can be calculated as

$$m_m = m_p \rho_r l_r^3 = m_p \times 1 \times \left(1/22\right)^3 . \tag{5-3}$$

The total mass of the full-scale superstructure $\left(m_p\right)$ is 139,419,500 kg. From Eq.(5-3), the total mass of the superstructure model $\left(m_m\right)$ is calculated as 13,093.49 kg. However, since the superstructure is scaled separately, the mass that needs to be put on the scaled superstructure $\left(m_s\right)$ might be different from the mass that is supposed to be on the scaled superstructure m_m. If $m_s \neq m_m$, the additional mass that needs to be provided on the top of the periodic foundation is $m_{add} = 13,093.49 - m_s$.

5.2.1.2 Connection detail of small modular reactor building model

A weld-type connection was selected for the assembly of the structural components except for the roof steel plate component. The roof steel plates will be connected to the beams on the frame using bolts. It was designed to create an opening for transportation and placement of the mass blocks on the floor steel plate.

To connect the mass blocks to the floor steel plate, 24 threaded holes with a diameter of 16 mm (M16) were designed on the steel plate. The holes are shown in blue in Figure 5-32. In addition, to connect the steel frame to the periodic foundations, non-threaded holes with a diameter of 34 mm (ϕ34) were provided. The 34 of ϕ34 holes are located along the center line of the columns, as shown in Figure 5-32.

Figure 5-33 shows the holes designed on the roof steel plates. As mentioned in Sub-subsection 5.2.1.1, mass blocks with a total mass of 1750 kg will be placed on the roof of the steel frame. In order for the mass blocks to be properly connected to the roof plate, 28 non-threaded holes with a diameter of 20 mm (ϕ20) were provided on the roof steel plates. Another 28 non-threaded holes with a diameter of 24 mm (ϕ24) were provided so that the plates can be bolted to the beams of the steel frame. Figure 5-34 shows the 28 $\phi 24$ holes on the beams.

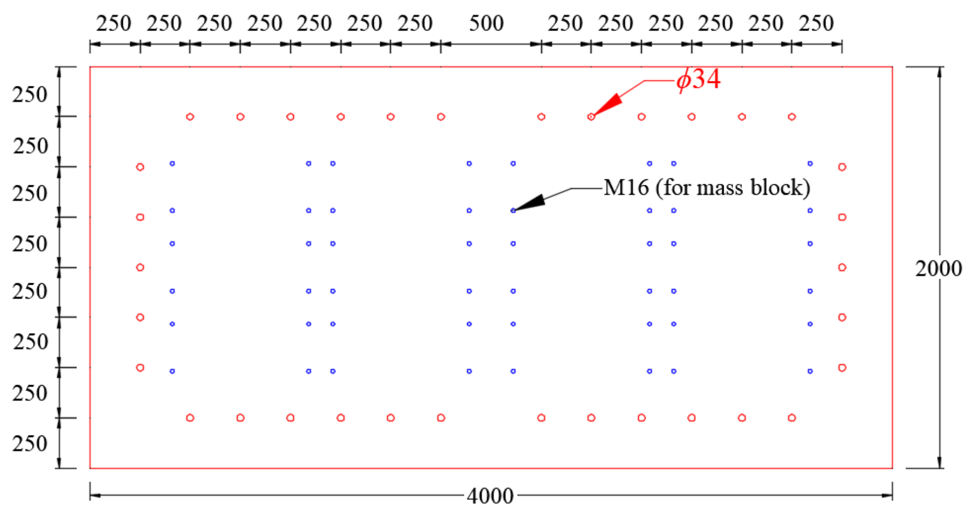

Figure 5-32 Holes on floor steel plate (unit in mm)

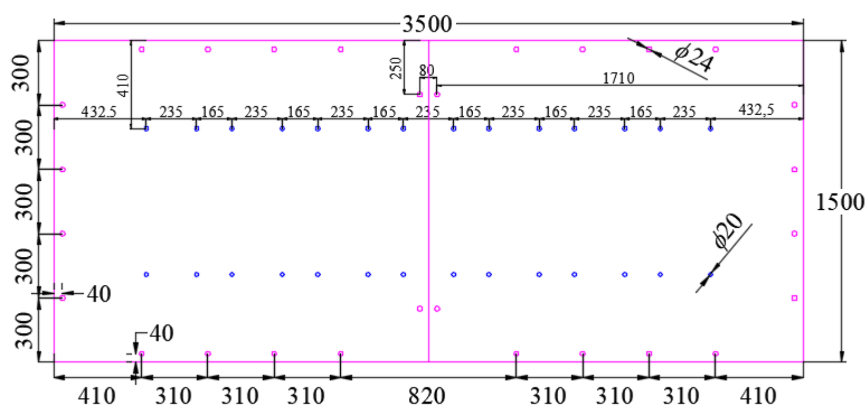

Figure 5-33 Holes on roof steel plate (unit in mm)

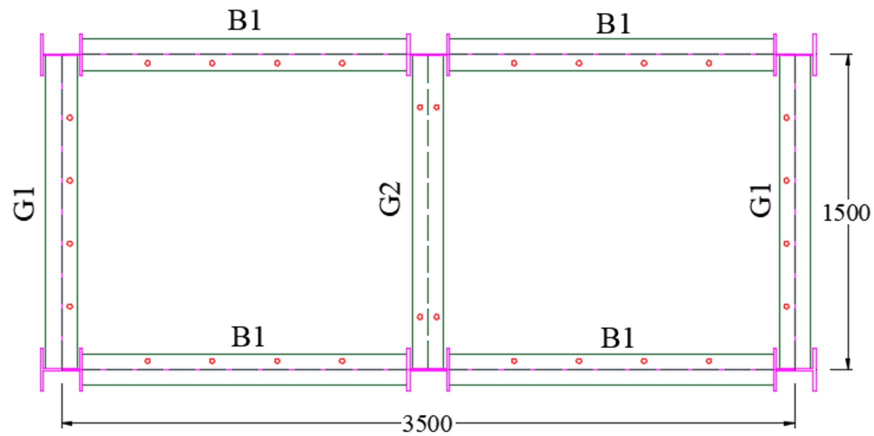

(a) Plan view of beams

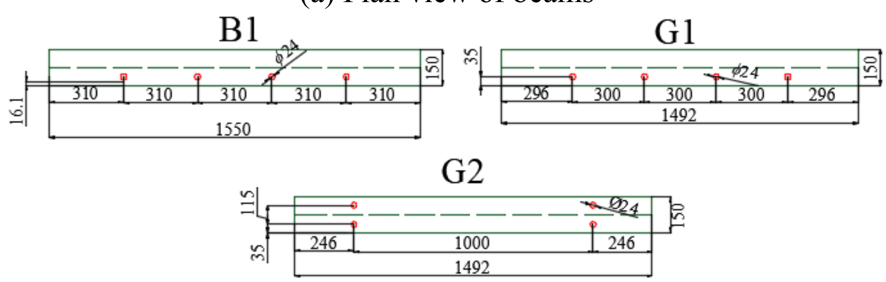

(b) Hole details on beams

Figure 5-34 Holes on beams (unit in mm)

5.2.2 Scaled 1D periodic foundation

5.2.2.1 Design of scaled 1D periodic foundation unit cell

Since the length scale is selected to be $1/22$, the thickness of each layer in the four-layer unit cell is reduced by 22 times. Figure 5-35 shows the comparison of the full-scale unit cell with the scaled unit cell. Based on the similitude requirements, the specific stiffness scale follows the length scale $(E/\rho)_r = l_r = 1/22$. In general, rubber material has a wide variety of hardness levels which correspond to different elastic Young's modulus. However, most of the rubber types have a similar density. Therefore, the density of the rubber in the scaled model is chosen to be equal to the density of the rubber in the prototype, i.e., $\rho_r = 1$. Thus, to satisfy the specific stiffness scale, the Young's modulus scale follows the length scale $E_r = l_r = 1/22$. The type of rubber-like material which has a very soft

Young's modulus at $1/22$ times the Young's modulus of the natural rubber is the ultra-soft polyurethane with a durometer OO20. The polyurethane material is made of polymer and has rubber-like properties.

Since the density scale of the rubber is chosen as 1, the density scale of the RC material needs to be kept at 1 for consistency. In theory, Young's modulus of RC needs to be scaled down to satisfy the specific stiffness scale. However, based on the sensitivity study shown in Section 4.2, the effect of Young's modulus ratio on the starting of the first frequency band gap is negligible. In addition, at such a high Young's modulus ratio, with the thickness ratio close to 1, the increase in Young's modulus ratio does not affect the width of the first frequency band gap. Therefore, in the scaled model, the RC material need not be scaled. The material properties for each of the scaled model and the full-scale unit cell are shown in Table 5-7.

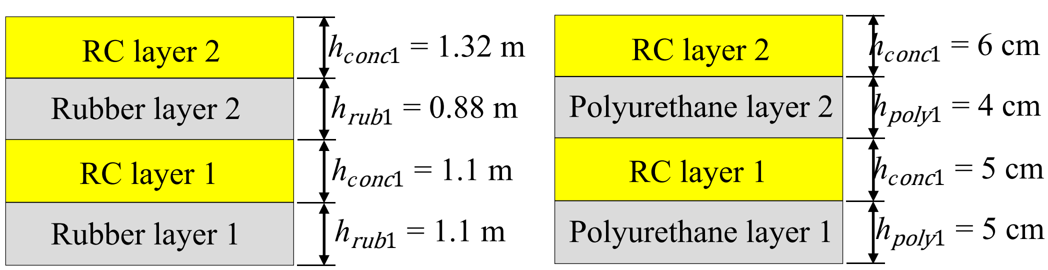

(a) Full-scale (b) Scaled model

Figure 5-35 Thickness of unit cell layers

Table 5-7 Material properties of full-scale and scaled 1D periodic foundation unit cells

Material	Material for full-scale unit cell			Material for scaled unit cell		
	Young's modulus (MPa)	Density (kg/m^3)	Poisson's ratio	Young's modulus (MPa)	Density (kg/m^3)	Poisson's ratio
Reinforced concrete	31400	2300	0.2	31400	2300	0.2
Rubber/Polyurethane	3.49	1100	0.463	0.1586	1100	0.463

The theoretical frequency band gaps of the scaled unit cell can be seen from the dispersion curves shown in Figure 5-36. It is observed that the frequency band gaps are shifted by a scale of $\omega_r = l_r^{-1/2} = \sqrt{22} = 4.69$ as compared to the frequency band gaps of the full-scale unit cell, shown in Figure 5-8.

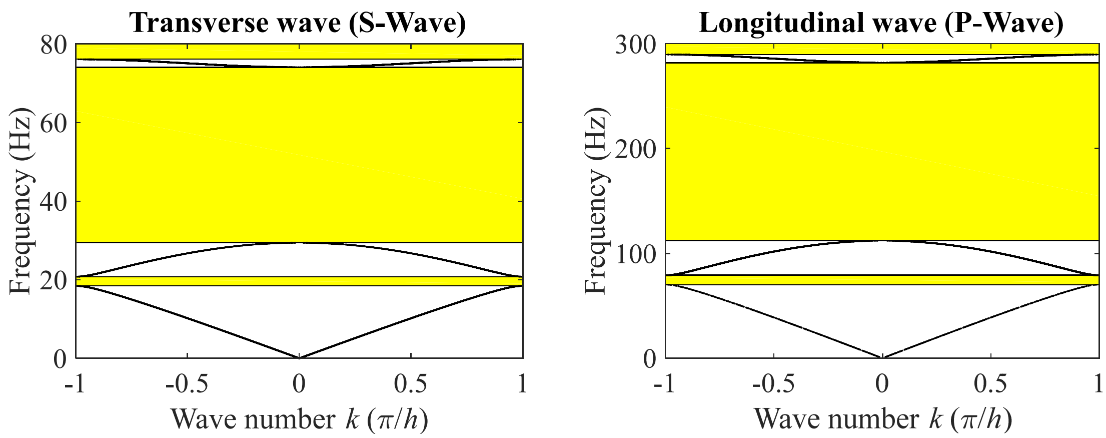

(a) S-Wave (b) P-Wave

Figure 5-36 Dispersion curves of scaled 1D periodic foundation unit cell

5.2.2.2 Design of scaled 1D periodic foundation structural system

Sub-subsection 3.3.2.3 shows that the attenuation zones of the 1D periodic foundation structural system are lower than those of the 1D periodic foundation only. The attenuation zones of the structural system can be approximated from the theoretical frequency band gaps of 1D periodic foundation with an equivalent superstructure layer. Therefore, the theoretical frequency band gaps of the scaled 1D periodic foundation structural system is first obtained to investigate if the frequency band gaps of the structural system are within the capacity of the shake table. Figure 5-37 shows the comparison of the full-scale unit cell with the scaled unit cell.

The density of the equivalent superstructure layer in the scaled unit cell still follows that in the full-scale unit cell. The theoretical frequency band gaps of the scaled 1D periodic foundation structural system are shown in Figure 5-38. The frequency band gaps are clearly lower than those of the scaled periodic foundation only, as shown in Figure 5-36, and satisfy the frequency scale of $\omega_r = l_r^{-1/2} = \sqrt{22} = 4.69$ as compared to the frequency band gaps of the full-scale unit cell, as shown in Figure 5-10. The dispersion curves are plotted up to 50 Hz since the maximum capacity of the shake table is up to 50 Hz. The frequency band gaps are within the capacity of the shake table. Therefore, the structural system can be experimentally validated.

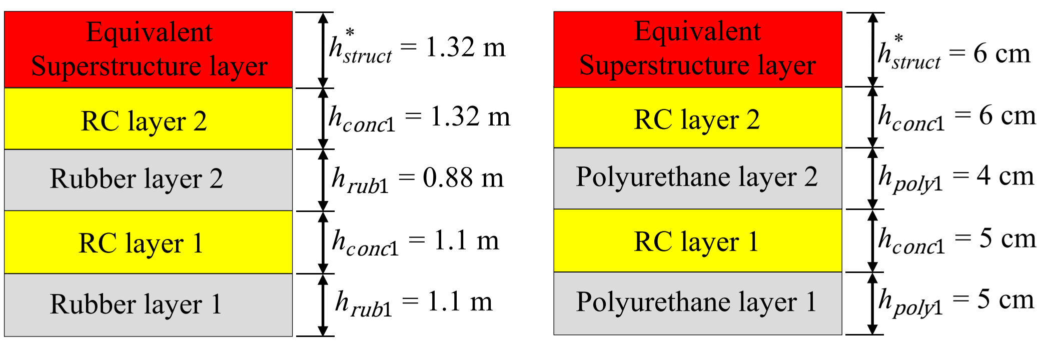

(a) Full-scale (b) Scaled model

Figure 5-37 Thickness of unit cell with equivalent superstructure layer

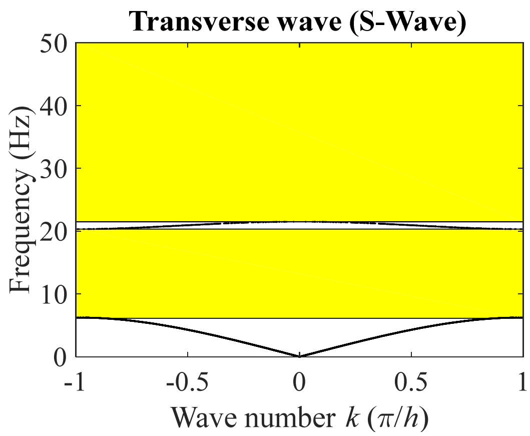

(a) S-Wave

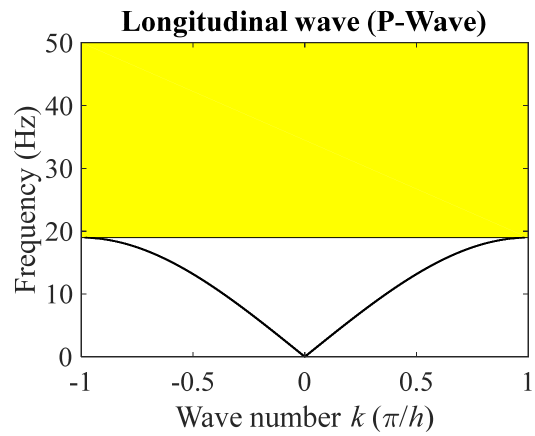

(b) P-Wave

Figure 5-38 Dispersion curves of scaled 1D periodic foundation unit cell with equivalent superstructure layer

5.2.2.3 Preliminary analysis of scaled 1D periodic foundation structural system

The scaled 1D periodic foundation structural system is shown in Figure 5-39. Complying with the length scale of $1/22$, the length and width of the scaled 1D periodic foundation should be 4.5 m and 2 m, respectively. However, since the polyurethane pads are only produced in certain sizes, the size of the scaled 1D periodic foundation becomes slightly larger at 4.6 m long and 2.06 m wide. The thickness of each of the layers in the periodic foundation still follows the scale factor, as shown in Figure 5-35(b). Therefore, the scale factor of $1/22$ is still valid and the frequency band gaps still fulfill the similitude requirements. The scaled periodic foundation is placed on top of a 0.2 m thick RC slab with a length and a width of 5.12 m and 3 m, respectively. This slab is designed with holes near the perimeter to connect to the shake table.

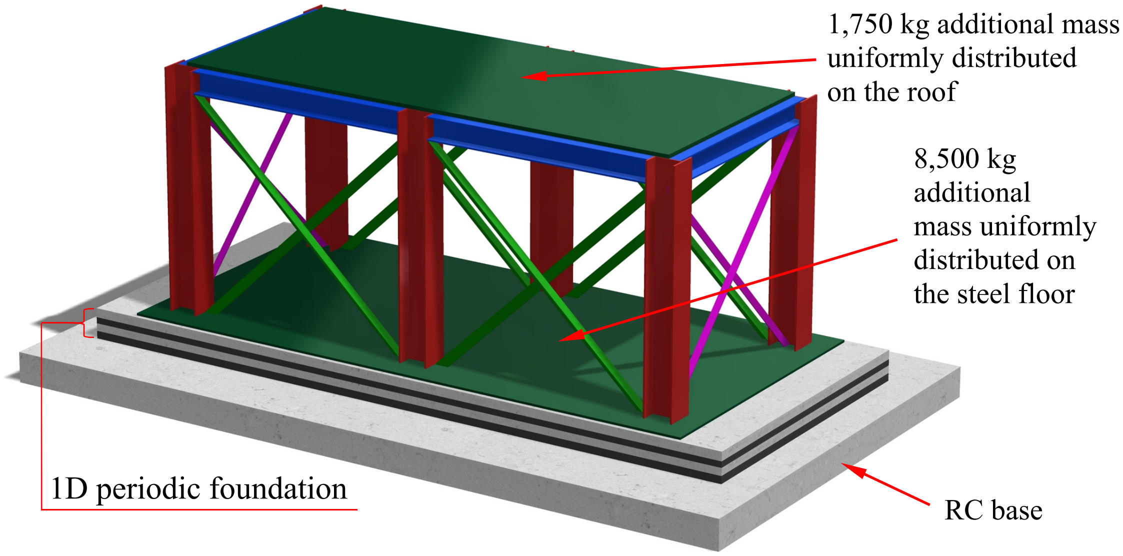

Figure 5-39 Designed scaled 1D periodic foundation structural system

As explained in Sub-subsection 5.2.1.1, the total mass that needs to be placed on top of the periodic foundation model is 13,093.49 kg. A mass of 1,750 kg has been placed on the roof of the superstructure to obtain the desired natural frequency of the superstructure only. Taking into account the self-weight of the steel frame, the remaining mass of 8,500 kg is uniformly distributed on the floor of the superstructure to reach the required total mass.

The preliminary analysis was conducted by utilizing the finite element method. The finite element model of the scaled structural system is shown in Figure 5-40. Each of the solid elements on the RC layers and RC base was assigned using an eight-node linear brick element while that on the polyurethane layers was assigned using a twenty-node quadratic brick element. A tie connection was utilized to connect each layer in the 1D periodic foundation and to connect the periodic foundation to the steel floor of the superstructure. In this preliminary analysis, the materials were assumed to be linear elastic with the properties of each material listed in Table 5-8.

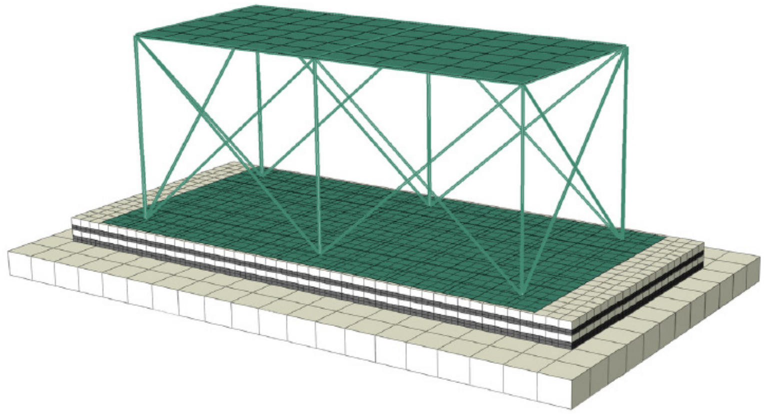

Figure 5-40 Finite element model of scaled 1D periodic foundation structural system

Table 5-8 Material properties for preliminary analysis of scaled 1D periodic foundation structural system

Material	Young's modulus (MPa)	Density (kg/m^3)	Poisson's ratio
Steel	200,000	7850	0.3
Reinforced concrete	31,400	2300	0.2
Polyurethane	0.1586	1100	0.463

5.2.2.3.1 Modal analysis

In the preliminary analysis, modal analysis was first conducted to obtain the natural frequencies of the scaled 1D periodic foundation structural system. The natural frequencies of the first three and the sixth modes as well as their corresponding mode shapes are shown in Figure 5-41. The order of the first three modes in the model structural system is the same as that of the full-scale structural system. The frequency ratio of the scaled model to full-scale structural system for each of the first three modes is:

- Mode 1 (translation in transverse direction)

$$f_{\text{full-scale}} / f_{\text{scaled model}} = 3/0.59 = 5.08,$$

- Mode 2 (translation in longitudinal direction)

$$f_{\text{full-scale}}/f_{\text{scaled model}} = 3.08/0.63 = 4.89\text{, and}$$

- Mode 3 (Torsion)

$$f_{\text{full-scale}}/f_{\text{scaled model}} = 3.47/0.64 = 5.42\,.$$

The frequency ratio of each mode is close to the required frequency scale, $\sqrt{22} = 4.69$, in the similitude requirements. The highest offset of the frequency ratio is 15.57%, which is observed in the torsional mode. The vertical mode of the 1D periodic foundation structural system occurs in the sixth mode with a natural frequency of 11.17 Hz.

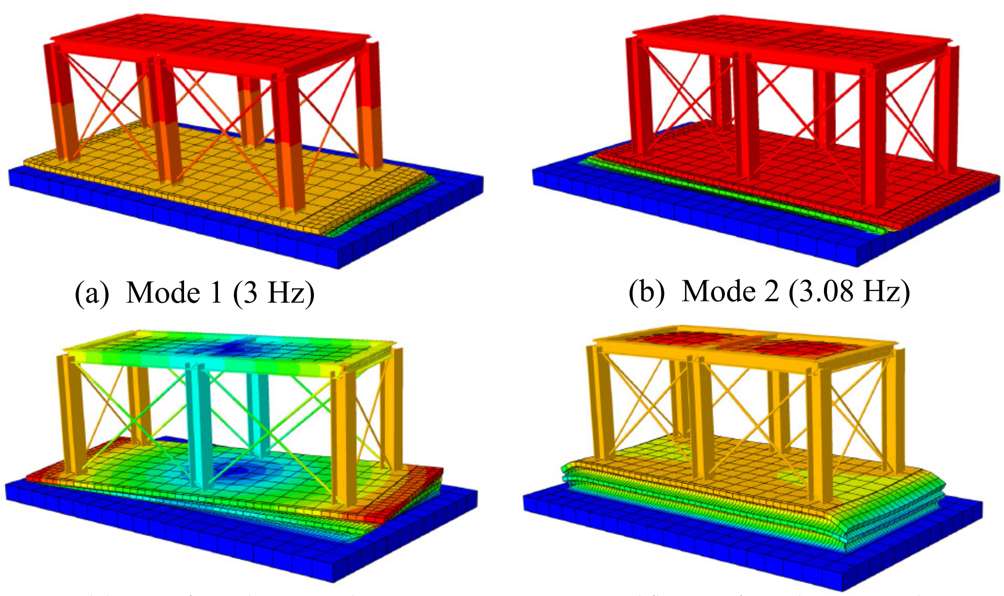

(a) Mode 1 (3 Hz) (b) Mode 2 (3.08 Hz)

(c) Mode 3 (3.47 Hz) (d) Mode 6 (11.17 Hz)

Figure 5-41 Mode shapes and natural frequencies of scaled model 1D periodic foundation structural system

5.2.2.3.2 Frequency sweeping and time history analyses

Steady-state frequency sweeping analysis was conducted to predict the actual attenuation zones of the scaled 1D periodic foundation structural system. Damping ratios of 2%, 4%, and 10% were assumed for steel, polyurethane, and RC materials, respectively. The Rayleigh damping coefficients used for the material damping are tabulated in Table

5-9. Two critical output points, the top of the 1D periodic foundation and the roof of the superstructure were selected to observe the behavior of the scaled structural system, as shown in Figure 5-42. The FRF curves obtained from the steady-state frequency analysis are shown in Figure 5-43. The S-Wave input was assigned in the transverse horizontal direction of the structural system while the P-Wave input was assigned in the vertical direction. The results show that the attenuation zones overlap with the theoretical frequency band gaps. The analysis results show that the scaled structural system can be experimentally validated using the shake table.

Table 5-9 Rayleigh damping coefficient for scaled 1D periodic foundation structural system

Material	Damping ratio (ζ)	α	β
Steel	2%	0.7113	0.00012
Reinforced concrete	4%	1.4226	0.00024
Polyurethane	10%	3.5565	0.0006

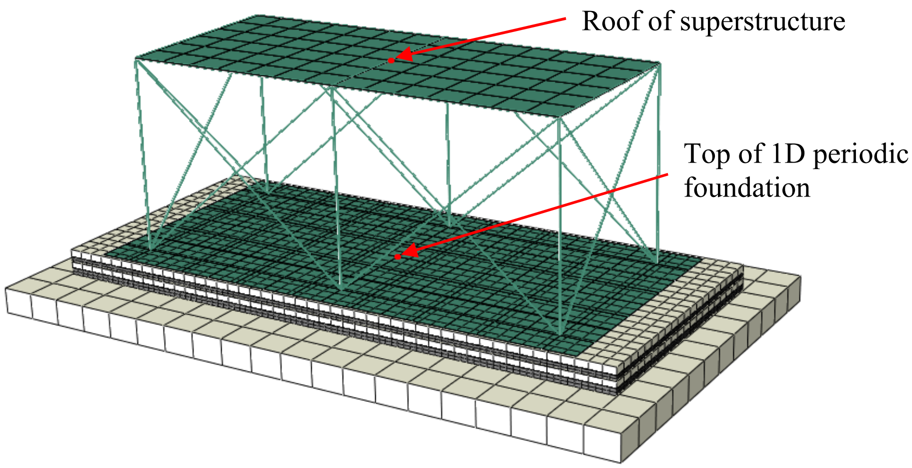

Figure 5-42 Finite element model of scaled 1D periodic foundation with location of the output points

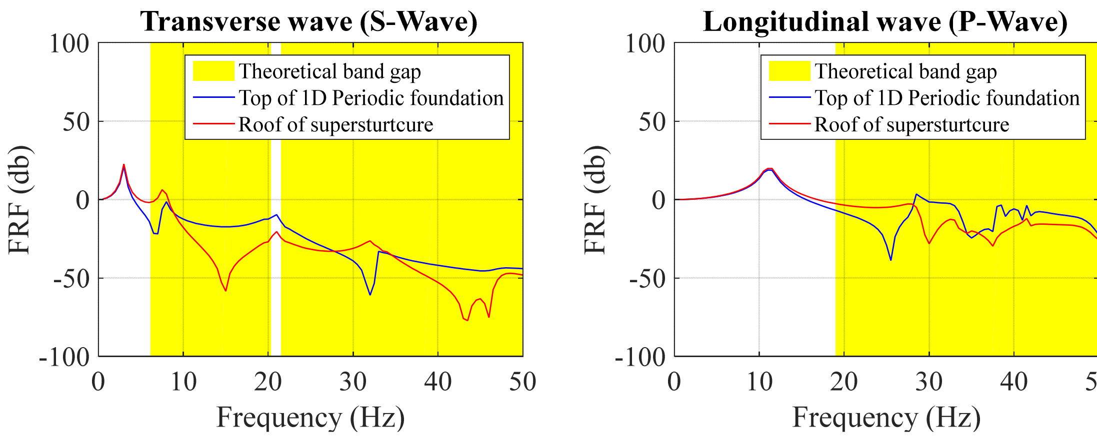

(a) S-Wave (b) P-Wave

Figure 5-43 Frequency response function of scaled 1D periodic foundation structural system

Time history analysis was conducted on the scaled 1D periodic foundation structural system to investigate the response of the structural system under seismic excitations. Here, the time history analysis results of the scaled structural system subjected to seismograms or ground motions from two seismic events are discussed. Table 5-10 shows the selected ground motions from the two seismic events. The ground motion in each of the horizontal and vertical directions was assigned on the finite element model separately to understand the response of the structural system in each direction. The horizontal ground motions were assigned to the RC base in the transverse direction which corresponds to the first natural frequency of the structural system.

Table 5-10 Selected ground motions for preliminary analysis

Event	Date	Station	Orientation
Anza	10/31/2001	Anza Fire Station	360 and Up
Bishop (Round Valley)	11/23/1984	MCGEE Creek Surface	360 and Up

For analysis purposes, the peak ground acceleration (PGA) of each seismogram was scaled to 1 g. In addition, the time was scaled a factor of $\sqrt{l_r} = 1/22$ to comply with the similitude requirements. Figure 5-44 and Figure 5-45 show the time history analysis results under the Anza and Bishop Earthquake ground motions in the horizontal direction. The accelerations on the top of the 1D periodic foundation and the roof of the superstructure were recorded and compared with the input excitation. It is observed that the peak acceleration responses on the output points are significantly smaller in comparison to the input acceleration. The reduction is mainly due to the wave filtering effect of the frequency band gaps which can be seen from the results in the frequency domain. The acceleration response of the structural system subjected to the Bishop Earthquake is smaller than that subjected to the Anza Earthquake. This is because a small portion of Anza's main frequency content is located outside the frequency band gaps and gets amplified while the main frequency content of the Bishop Earthquake is completely located inside the frequency band gap and effectively filtered out. A similar tendency is observed when the structural system is subjected to vertical ground motions. Figure 5-46 and Figure 5-47 show the time history analysis results under the Anza and Bishop Earthquakes in the vertical direction.

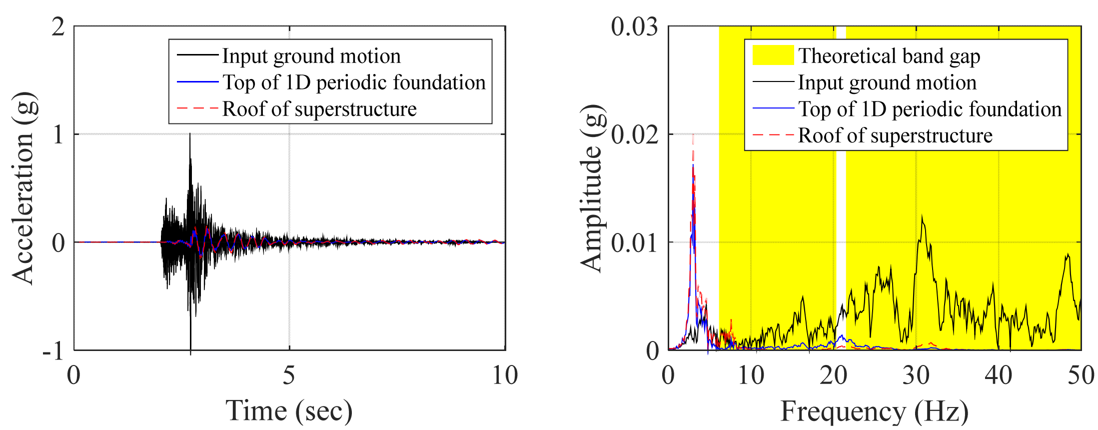

(a) Time domain (b) Frequency domain

Figure 5-44 Acceleration responses due to Anza ground motion in the horizontal direction

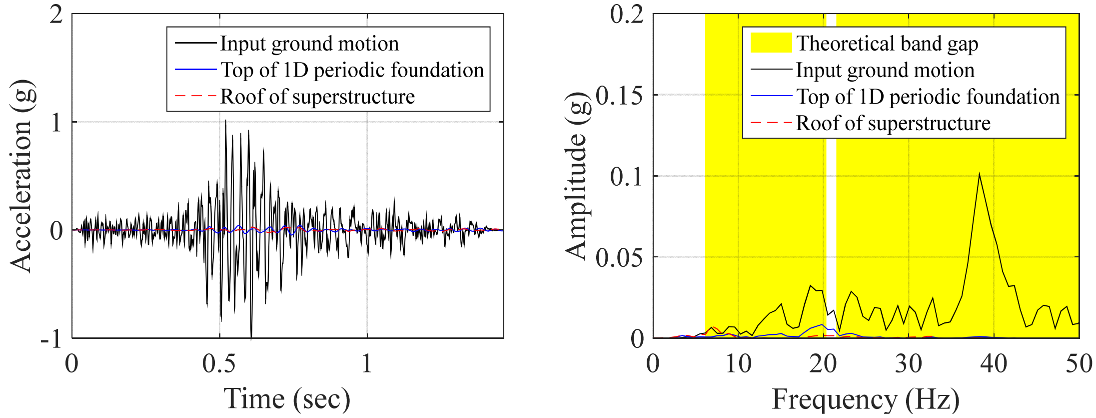

(a) Time domain (b) Frequency domain

Figure 5-45 Acceleration responses due to Bishop ground motion in the horizontal direction

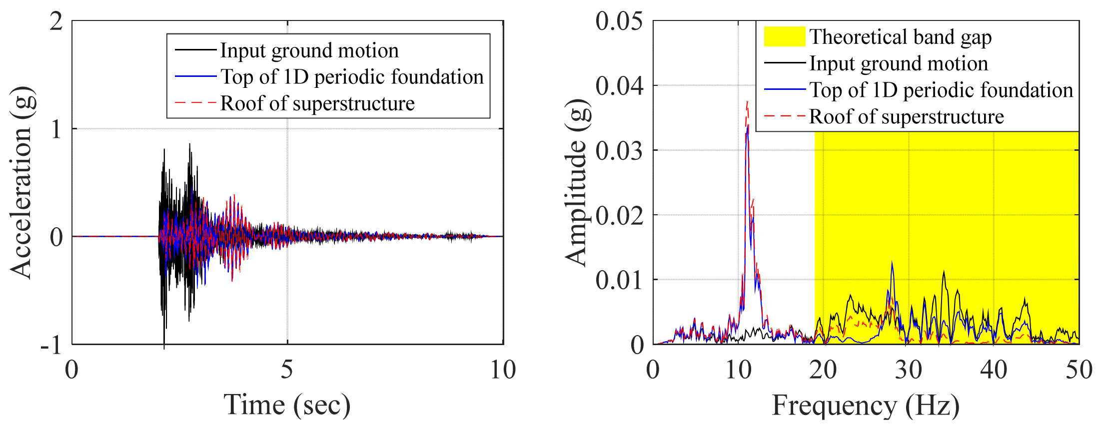

(a) Time domain (b) Frequency domain

Figure 5-46 Acceleration responses due to Anza ground motion in the vertical direction

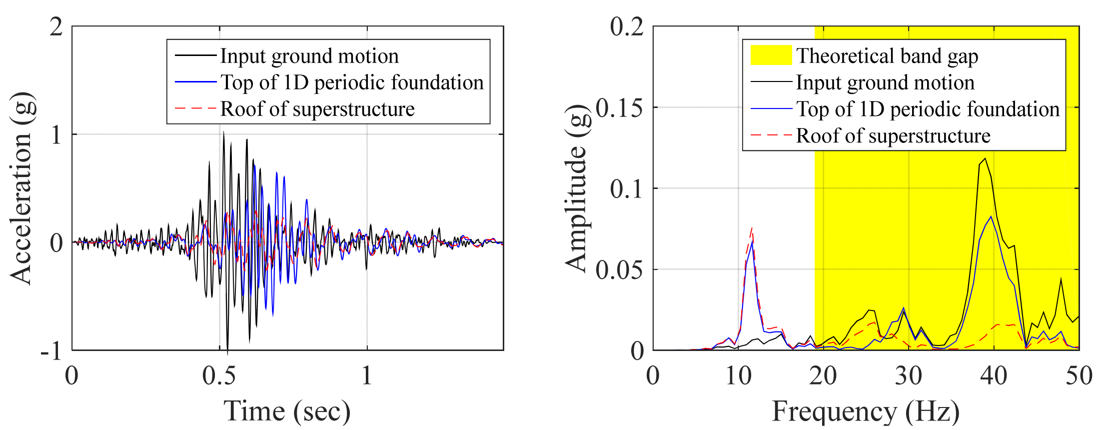

(a) Time domain (b) Frequency domain

Figure 5-47 Acceleration responses due to Bishop ground motion in the vertical direction

Table 5-11 provides the response summary of the scaled 1D periodic foundation structural system under the horizontal earthquake ground motions. The drift of the 1D periodic foundation can be observed to be quite small even though the input PGA is 1 g. Table 5-12 provides the response summary of the 1D periodic foundation structural system under the vertical earthquake ground motions. In general, the response reduction due to vertical earthquakes is not as large as that due to the horizontal earthquakes. This is due to the fact that frequency band gaps of the S-Wave are located at lower frequencies and also cover wider frequencies than those of the P-Wave. In addition, the frequency sweeping analysis results also show that response attenuation of the P-Wave inside the frequency band gaps is smaller than that of the S-Wave, as shown in Figure 5-43. Regarding the relative displacement, minor vertical displacement is observed when the structural system is subjected to vertical ground motions.

Table 5-11 Response summary of scaled 1D periodic foundation structural system under horizontal ground motions

Earthquake event	Peak acceleration on top of 1D periodic foundation (g)	Max acceleration on roof (g)	Max drift on 1D periodic foundation (%)
Anza	0.130	0.163	1.742
Bishop	0.047	0.027	0.147

Table 5-12 Response summary of scaled 1D periodic foundation structural system under vertical ground motions

Earthquake event	Peak acceleration on top of 1D periodic foundation (g)	Max acceleration on roof (g)	Max relative displacement on 1D periodic foundation (mm)
Anza	0.442	0.428	0.793
Bishop	0.708	0.292	0.485

5.2.2.3.3 Stress analysis on polyurethane under gravity load

Under the gravity load, the maximum and minimum principal stress fields on the polyurethane layer 1 are shown in Figure 5-48. The maximum compression stress is observed at 0.01905 MPa and maximum tension is at 0.00297 MPa. However, the tension only occurs on the elements located on the perimeter of the polyurethane layer. The majority of the elements are still subjected to compression.

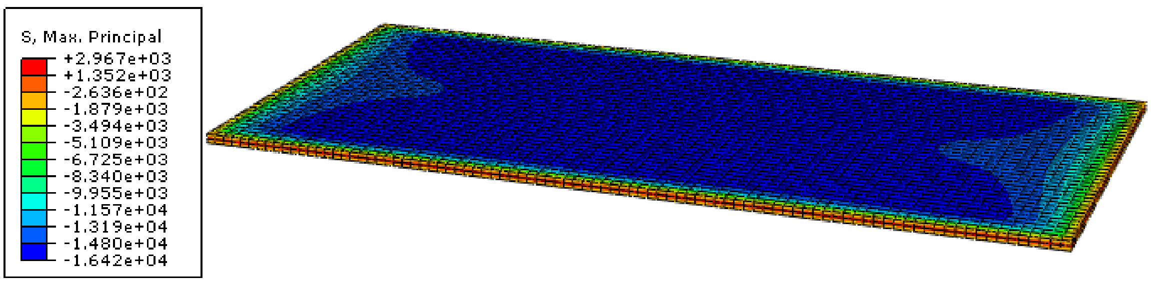

(a) Maximum principal stress

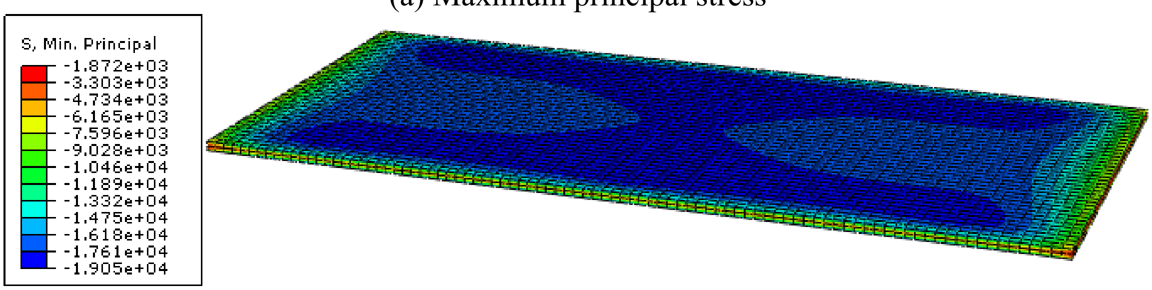

(b) Minimum principal stress

Figure 5-48 Principal stress fields on the rubber layer 1 in scaled 1D periodic foundation structural system (unit in Pa)

The material tests on the polyurethane samples are shown in Figure 5-49. The Young's modulus of the linear portion is observed to be 0.1586 MPa. The tested material has very close material properties to the material properties used for analysis and design of the scaled 1D periodic foundation. Referring to Figure 5-49, under the maximum compression stress, the polyurethane is still within the linear elastic range of the stress-strain curve.

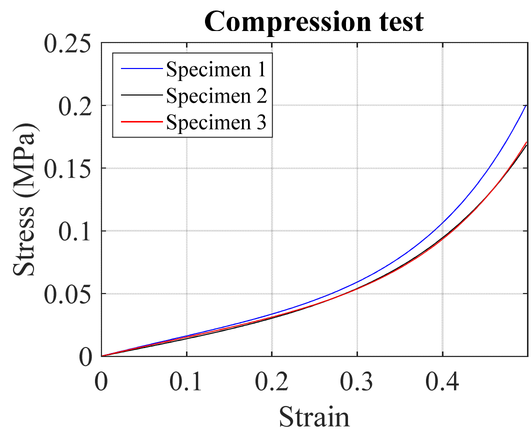

Figure 5-49 Compressive stress-strain curves of polyurethane

5.2.2.4 Reinforcement detail on reinforced RC base and layers

This Sub-subsection presents the reinforcing details on the RC base and layers and their compliance with the ACI 318-14 requirements [75]. The symbols used in this Sub-subsection follow the nomenclature in the ACI 318-14 provisions which may have a different meaning than those used in the previous chapters and sections. Figure 5-50 shows the reinforcing detail and the holes on the RC base. Sixty non-threaded holes with a diameter of 47 mm (ϕ47) were designed to connect the base to the shake table. Reinforcing bars (rebars) number 4 (#4) with a spacing of 250 mm were designed in both the transverse and the longitudinal directions. Two layers of rebar in each direction were provided to ensure sufficient strength of the RC base during transportation inside the laboratory.

According to provision number 24.4.3.2 in ACI 318-14, the minimum reinforcement ratio to resist shrinkage and temperature stress is 0.002 for a deformed bar with a yield strength of 60 ksi or 420 MPa and less. The spacing of the rebar should not exceed the lesser of 5h and 18 inches or 450 mm.

The reinforcement ratio on the RC base in the longitudinal and transverse directions are shown in Eqs (5-4) and (5-5):

$$\rho_{\text{long}} = \frac{A_s \times n}{b \times h} = \frac{129 \times 26}{3000 \times 200} = 0.00559 \text{ and} \tag{5-4}$$

$$\rho_{\text{trans}} = \frac{A_s \times n}{l \times h} = \frac{129 \times 42}{5120 \times 200} = 0.00529\,, \tag{5-5}$$

where ρ represents the reinforcement ratio, A_s is the area of a single rebar, n is the number of rebars and l, b, and h represent the length, width, and thickness of the RC base, respectively. The reinforcement ratio in each direction is larger than 0.002 which satisfies the minimum reinforcement provision. The maximum spacing according to provision number 24.4.3.3 in the ACI 318-14 provisions is the lesser of $5h = 5 \times 200 = 1000\,\text{mm}$ and 450 mm. Since the spacing of the rebar in Figure 5-50 is 250 mm, it satisfies the maximum spacing requirement.

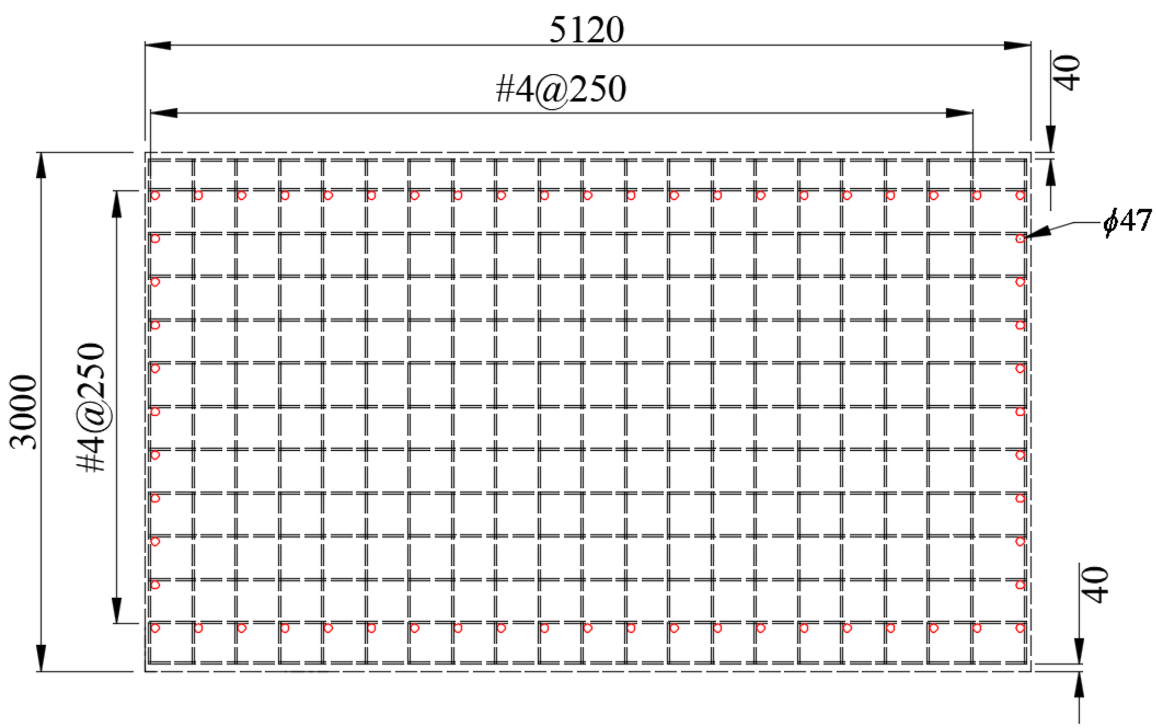

Figure 5-50 Reinforcement detail and holes on RC base (unit in mm)

Figure 5-51 shows the reinforcing detail and the holes on the RC layer 1. The six non-threaded holes with a diameter of 50 mm ($\phi 50$) were designed to inspect the glue underneath the RC layer during the fabrication process. Rebars number 3 (#3) with a spacing of 250 mm were designed in both the transverse and longitudinal directions. The reinforcement ratio on the RC layer in the longitudinal and transverse directions are shown in Eqs (5-6) and (5-7):

$$\rho_{\text{long}} = \frac{A_s \times n}{b \times h} = \frac{71 \times 9}{2060 \times 50} = 0.0062 \text{ and} \tag{5-6}$$

$$\rho_{\text{trans}} = \frac{A_s \times n}{l \times h} = \frac{71 \times 19}{4600 \times 50} = 0.00587\,. \tag{5-7}$$

The reinforcement ratio in each direction is larger than 0.002 which satisfies the minimum reinforcement provision. The maximum spacing according to provision number 24.4.3.3 in the ACI 318-14 provisions is the lesser of $5h = 5 \times 50 = 250\,\text{mm}$ and 450 mm. Since most the spacing of the rebars in Figure 5-51 are 250 mm, they satisfy the maximum spacing requirement. However, one side in each of the longitudinal and transverse directions has a spacing of 270 mm to accommodate the placement of the non-threaded holes. Since the RC layer is too slender, the transportation process might damage the concrete layer. Therefore, to protect the RC layer, all four edges of the RC layer were designed to be protected by a thin steel cover. The steel cover was designed as a channel section made of two angle sections, each with a size of $25 \times 25 \times 3\,\text{mm}^3$.

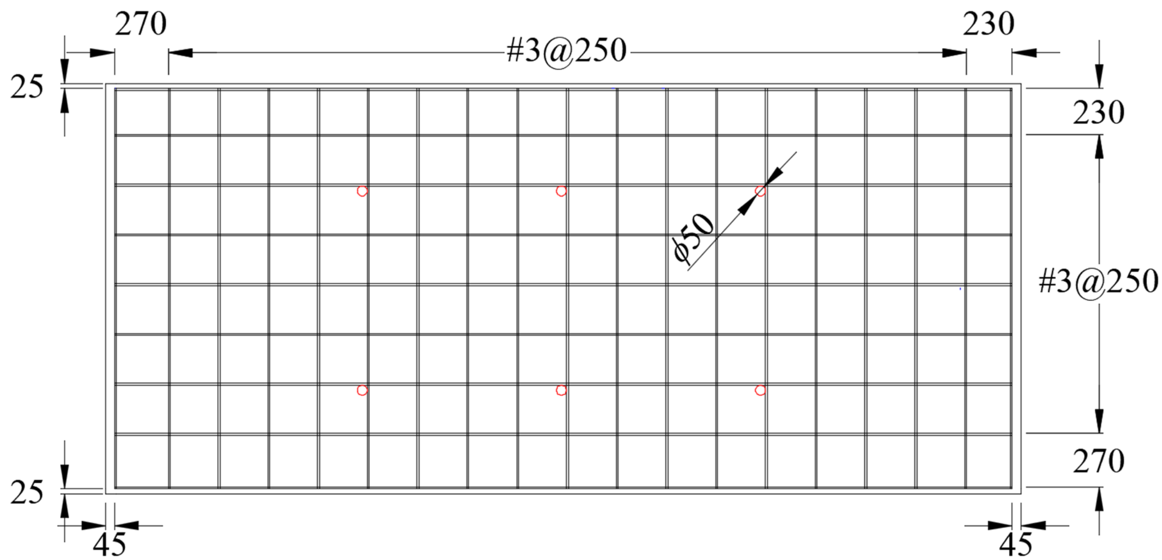

Figure 5-51 Reinforcement detail and holes on RC layer 1 (unit in mm)

Figure 5-52 shows the reinforcing detail and the holes on the RC layer 2. The six non-threaded holes with a diameter of 50 mm (ϕ50) were also provided for glue inspection. In addition, 34 threaded holes with a diameter of 30 mm (M30) were provided so that the steel frame can be bolted to the RC layer. Rebars number 3 (#3) with a spacing of 250 mm were designed in both the transverse and longitudinal directions. The reinforcement ratio on the concrete layer in the longitudinal and transverse directions is shown in Eqs. (5-8) and (5-9):

$$\rho_{\text{long}} = \frac{A_s \times n}{b \times h} = \frac{71 \times 9}{2060 \times 60} = 0.00517 \text{ and} \tag{5-8}$$

$$\rho_{\text{trans}} = \frac{\mathrm{A_s \times n}}{\mathrm{1 \times h}} = \frac{71 \times 19}{4600 \times 60} = 0.00489\,. \tag{5-9}$$

The reinforcement ratio in each direction is larger than 0.002 which satisfies the minimum reinforcement provision. The maximum spacing according to provision number 24.4.3.3 in the ACI 318-14 provisions is the lesser of $5h = 5 \times 60 = 300\,\text{mm}$ and 450 mm. All of the spacing of the rebars in Figure 5-52 are less than 300 mm, satisfying the maximum spacing requirement. All four edges of RC layer 2 were also designed to be protected by a steel cover. The steel cover was designed as a channel section made of two angle sections, each with a size of $30\times30\times3\,\mathrm{mm}^3$.

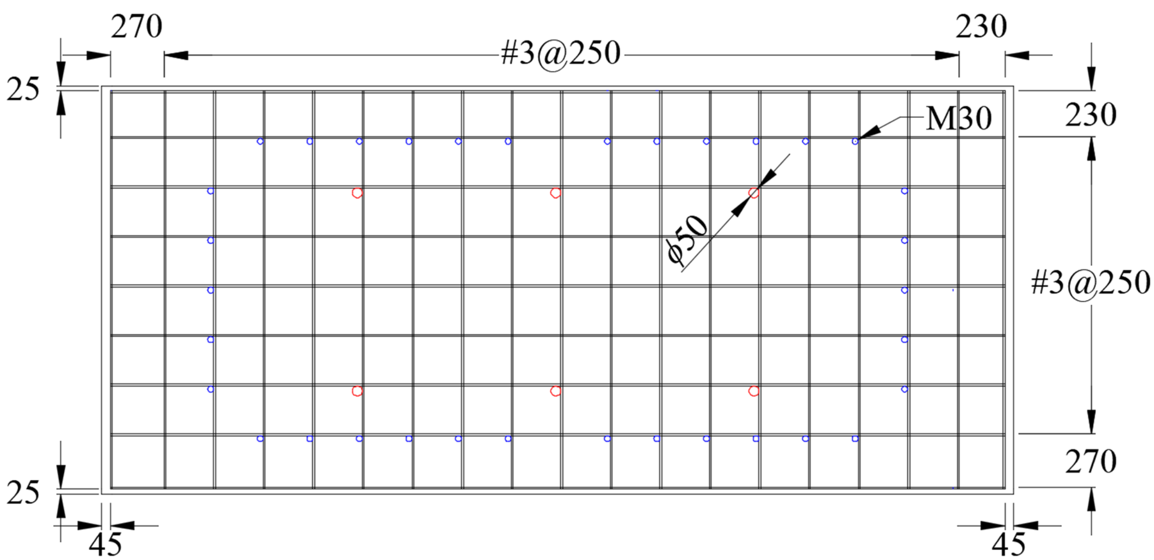

Figure 5-52 Reinforcement detail and holes on RC layer 2 (unit in mm)

5.2.3 Scaled 3D periodic foundation

5.2.3.1 Design of scaled 3D periodic foundation

To fit the shake table test facility, the designed full-scale 3D periodic foundation was also scaled down by following the similitude requirements. The same length scale (l_r) of $1/22$ was applied on the 3D periodic foundation. Using this scale factor, the full-scale unit cell of 8 m was scaled to 36.36 cm. Similarly, the full-scale cubical core with a length of 7.2 m needs to be scaled to 32.73 cm. However, for ease of fabrication the length of the core was slightly reduced to 32.5 cm. Both the full-scale and the scaled unit cells are shown in Figure 5-53. Material wise, the specific stiffness scale should follow the length scale $(E/\rho)_r = l_r = 1/22$. Similar to the scaling of the 1D periodic foundation, the material density is not subjected to the scaling effect. Instead, the Young's Modulus of material is. Therefore, the same polyurethane material is utilized to construct the matrix component of the unit cell of the 3D periodic foundation. However, since the top surface area of the 3D periodic foundation is smaller than that of the 1D periodic foundation, the matrix component in the 3D periodic foundation experiences higher stresses, which goes to the nonlinear portion of the tested polyurethane OO20 material. Iterative design was conducted to select the secant stiffness of the material. The converged secant stiffness of the polyurethane is shown in Table 5-13. The scaled Young's modulus of the core, however, does not affect the frequency band gaps. Hence, the core component is still designed to be made of RC material. The material properties of the scaled 3D periodic foundation can be obtained in Table 5-13.

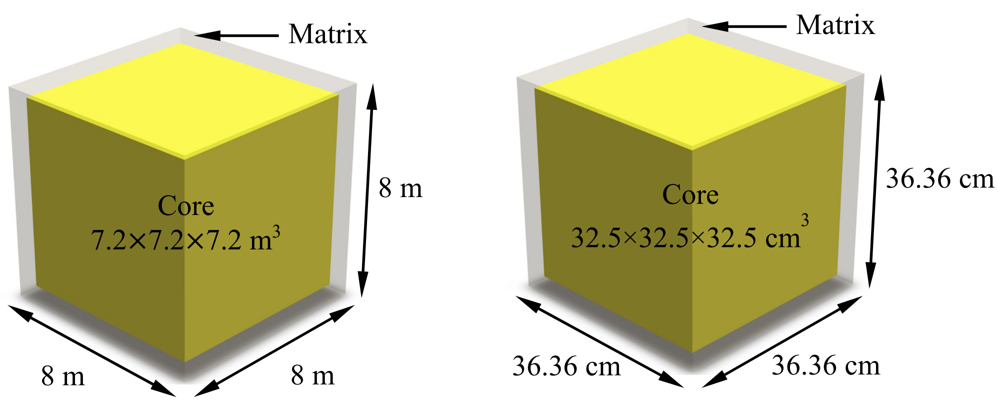

(a) Full-scale (b) Scaled model

Figure 5-53 Designed Bragg scattering unit cell

Table 5-13 Material properties of full-scale and scaled 3D periodic foundation unit cells

Material	Material for full-scale unit cell			Material for scaled unit cell		
	Young's modulus (MPa)	Density (kg/m^3)	Poisson's ratio	Young's modulus (MPa)	Density (kg/m^3)	Poisson's ratio
Reinforced concrete	31400	2300	0.2	31400	2300	0.2
Rubber/Polyurethane	3.49	1100	0.463	0.1695	1100	0.463

The dispersion curves of the scaled Bragg scattering unit cell is shown in Figure 5-54. An absolute frequency band gap is observed in the frequency range of 51.48–77.95 Hz. In comparison to the frequency band gap of the full scale unit cell at 10.93–17.1 Hz (see Figure 5-18), the frequency band gap of the scaled unit cell with slight adjustments still satisfies the frequency scale requirement. The attenuation zones of the scaled unit cell subjected to each of the S-Wave and P-Wave is shown in Figure 5-55. It is observed that the attenuation zone overlaps with the predicted theoretical band gap. The unit cell has shown sufficient response reduction inside the theoretical frequency band gap with average FRF values of -30 for S-Wave and -10 for P-Wave, which corresponds to 97% and 68% response reduction, respectively.

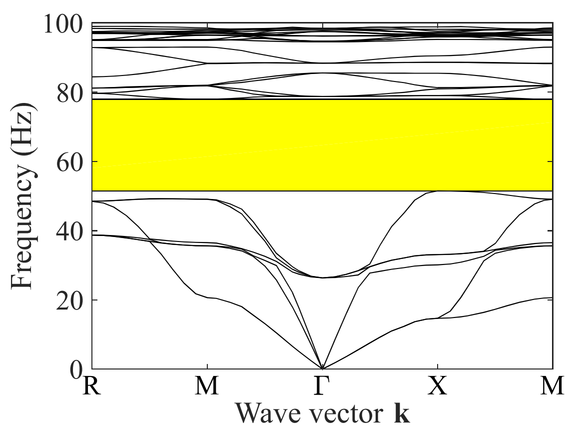

Figure 5-54 Dispersion curve of scaled 3D periodic foundation unit cell

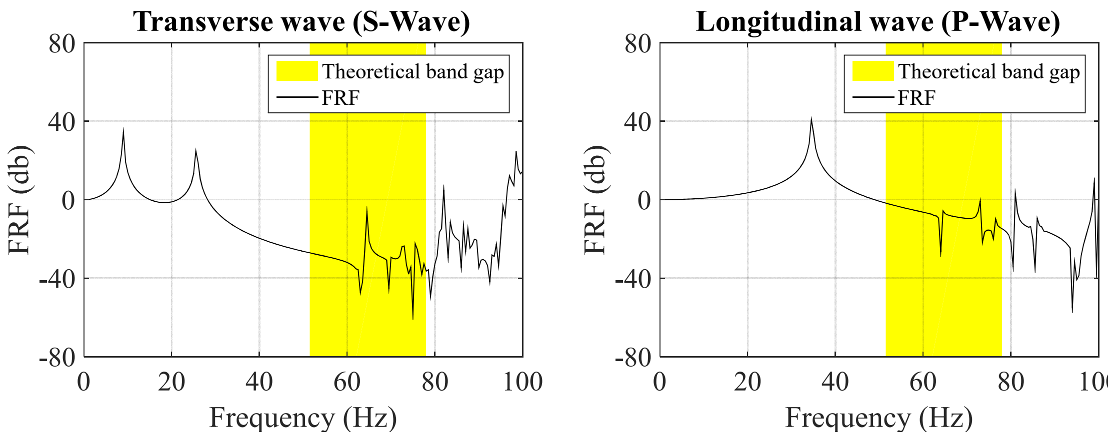

(a) S-Wave (b) P-Wave

Figure 5-55 Frequency response function of the scaled 3D periodic foundation unit cell

5.2.3.2 Preliminary analysis of scaled 3D periodic foundation structural system

The scaled 3D periodic foundation structural system is shown in Figure 5-56. The scaled periodic foundation is placed on the top of a 0.2 m thick RC slab with a length and a width of 5.12 m and 3 m, respectively. This slab is the same as the slab designed as the base for the scaled 1D periodic foundation structural system to connect the structural system to the shake table.

As explained in Sub-subsection 5.2.1.1, the total mass of the superstructure model is 13,093.49 kg. In the scaled 1D periodic foundation structural system, additional masses of 1,750 kg and 8,500 kg were provided on the roof and the steel floor of the superstructure, respectively. Therefore, these masses were supposed to be considered in the design and preliminary analysis of the scaled 3D periodic foundation structural system. However, the design and analysis of this structural system was conducted simultaneously with the experimental tests of the scaled 1D periodic foundation structural system. During the actual test of the 1D system, the mass blocks placed on the steel frame were not as exact as the original design. Instead, total masses of 1830 kg and 8368 kg were provided on the roof of the superstructure and the floor of the superstructure, respectively. Therefore, in the design and analysis of the 3D periodic foundation structural system, the actual masses on the superstructure were used.

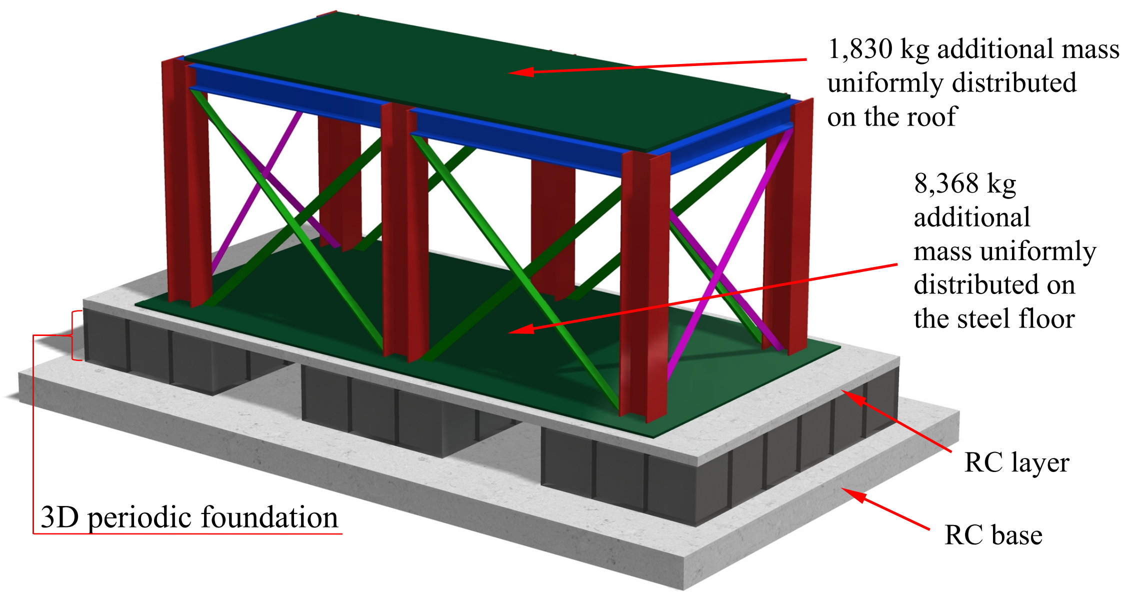

Figure 5-56 Designed scaled 3D periodic foundation structural system

The finite element model of the scaled structural system is shown in Figure 5-57. Each of the solid elements on the RC cores and RC base was assigned using an eight-node linear brick element while that on the matrix was assigned using a twenty-node quadratic brick element. A tie connection was utilized to connect the interfaces on the 3D periodic foundation, i.e., between the RC core and the matrix, between unit cells, between the periodic foundation and the RC layer, and between the periodic foundation and the RC base. In this preliminary analysis, the materials were assumed to be linear elastic with the properties of each material listed in Table 5-14.

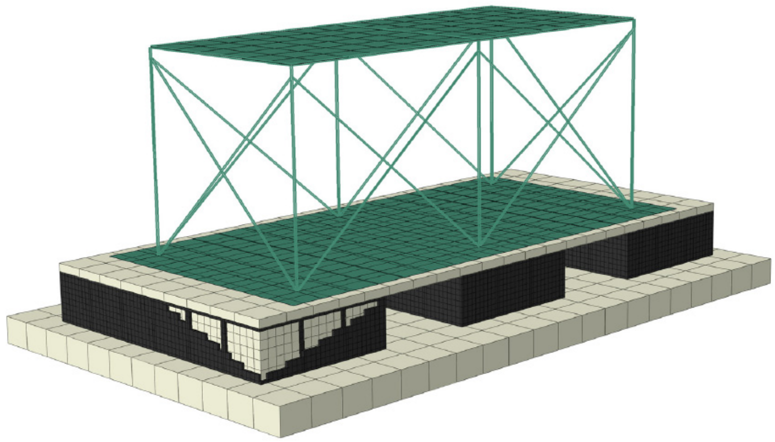

Figure 5-57 Finite element model of scaled 3D periodic foundation structural system (some of the elements on the periodic foundation are hidden)

Table 5-14 Material properties for preliminary analysis of scaled 3D periodic foundation structural system

Material	Young's modulus (MPa)	Density (kg/m^3)	Poisson's ratio
Steel	200,000	7850	0.3
Reinforced concrete	31,400	2300	0.2
Polyurethane	0.1695	1100	0.463

5.2.3.2.1 Modal analysis

The natural frequencies of the first three and the sixth modes as well as their corresponding mode shapes are shown in Figure 5-58. The order of the modes in the model structural system is the same as that in the prototype structural system. The frequency ratio of the scaled model to the full-scale structural system for each mode is:

- Mode 1 (translation in transverse direction)

$$f_{\text{full-scale}} / f_{\text{scaled model}} = 3.557/0.707 = 5.03,$$

- Mode 2 (translation in longitudinal direction)

$$f_{\text{full-scale}} / f_{\text{scaled model}} = 3.639/0.739 = 4.924, \text{ and}$$

- Mode 3 (torsion)

$$f_{\text{full-scale}} / f_{\text{scaled model}} = 4.532/0.844 = 5.369\,.$$

The frequency ratio of each mode is slightly larger than the target frequency scale of $\omega_r = l_r^{-1/2} = \sqrt{22} = 4.69$, in the similitude requirements. The difference may come from the actual redistributed mass on the steel frame structure. Considering the scale of the specimen, the difference is still tolerable. The vertical mode of the 3D periodic foundation structural system occurs in the sixth mode with a natural frequency of 12.389 Hz.

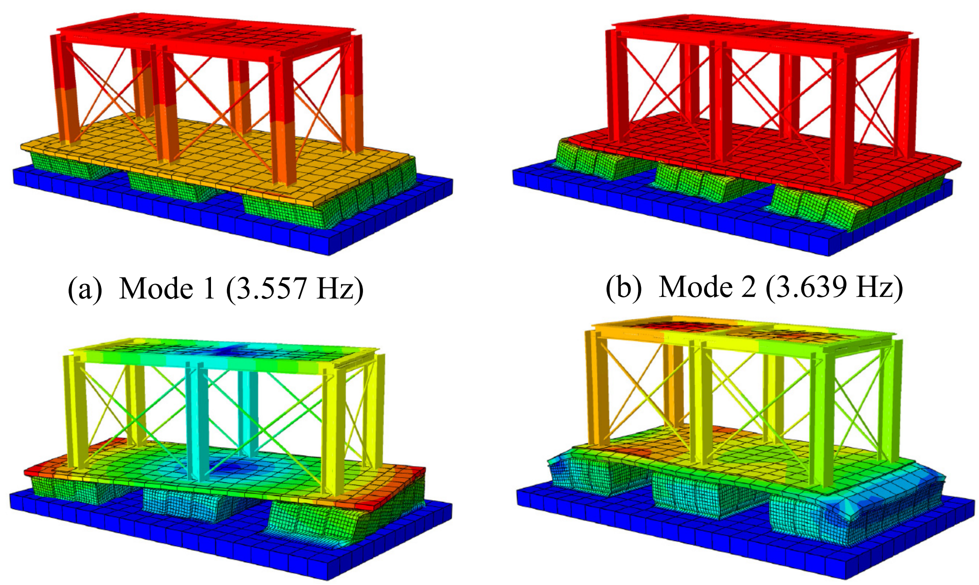

(a) Mode 1 (3.557 Hz) (b) Mode 2 (3.639 Hz)

(c) Mode 3 (4.532 Hz) (d) Mode 6 (12.389 Hz)

Figure 5-58. Mode shapes and natural frequencies of scaled model 3D periodic foundation structural system

5.2.3.2.2 Frequency sweeping and time history analyses

Steady-state frequency sweeping analysis was conducted to predict the actual attenuation zones of the scaled 3D periodic foundation structural system. Damping ratios of 2%, 4%, and 10% were assumed for steel, polyurethane, and RC materials, respectively.

The Rayleigh damping coefficients used for the material damping are tabulated in Table 5-15. Similar to the frequency sweeping analysis of the prototype structural system, three points on the top of the 3D periodic foundation and one point on the roof of the superstructure were selected as the reference outputs in order to investigate the response of the model structural system. Figure 5-59 shows that the output points A and C are located on the RC layer at the top of the 3D periodic foundation directly above the unit cells while point B is located on the RC layer at the top of the 3D periodic foundation in between two blocks of unit cells. The output point D is located on the beam-column joint.

Table 5-15 Rayleigh damping coefficient for scaled 3D periodic foundation structural system

Material	Damping ratio (ζ)	α	β
Steel	2%	0.8346	0.00012
Reinforced concrete	4%	1.6692	0.00024
Polyurethane	10%	4.1730	0.00059

The frequency sweeping results in the form of FRF are shown in Figure 5-60. The S-Wave input was assigned in the transverse horizontal direction of the structural system while the P-Wave input was assigned in the vertical direction. The attenuation zones from the output points on the top of the 3D periodic foundation are observed to be in 5–9 Hz and 9.8–50 Hz while that on the roof of the superstructure is observed to be 10–50 Hz. Under the P-Waves excitation, the attenuation zone from points A and C are observed to be at 15–28 Hz. Although there is a slightly different attenuation zone on the output point B, the result is still very close to the remaining two output points. On the roof of the superstructure, the vertical attenuation zone is observed to be at 17.58–50 Hz. These results are within the capacity of the shake table. Therefore, the scaled structural system can be experimentally validated using the shake table.

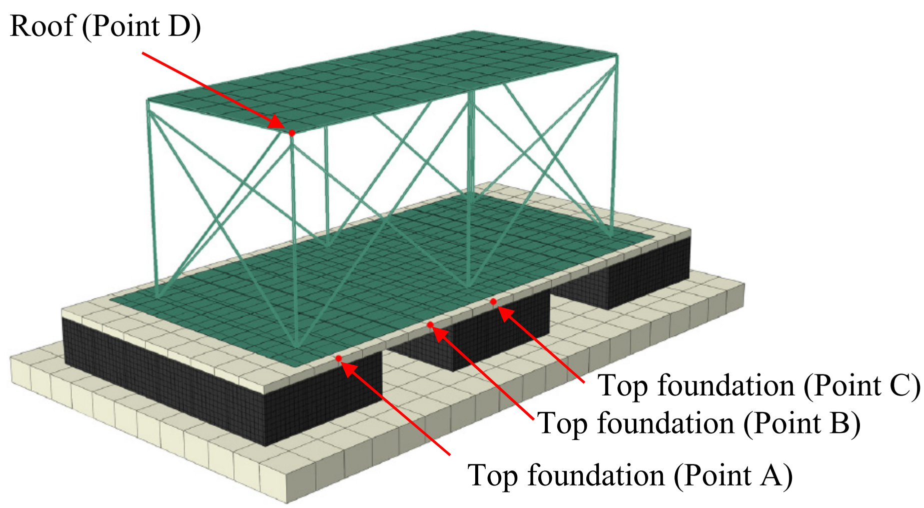

Figure 5-59 Finite element model of scaled 3D periodic foundation with location of the output points

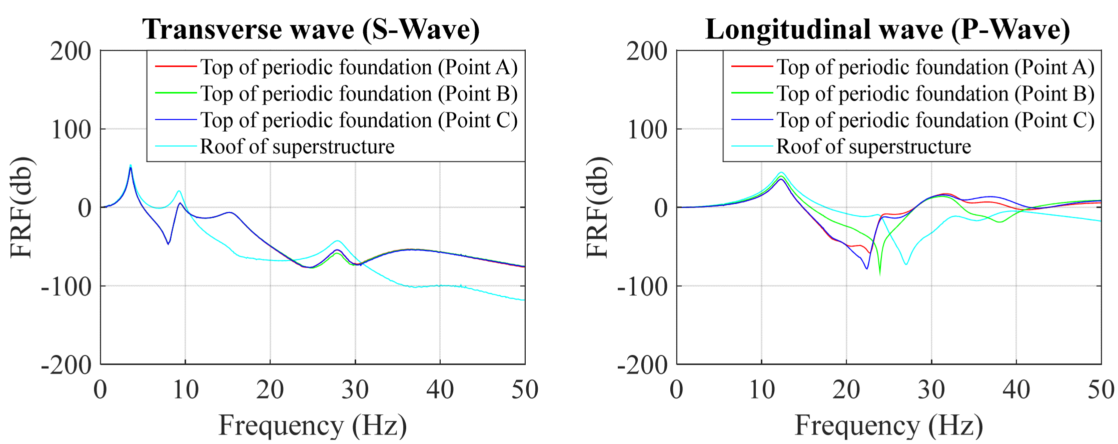

(a) S-Wave (b) P-Wave

Figure 5-60 Frequency response function of scaled 3D periodic foundation structural system

Time history analysis was also conducted on the scaled 3D periodic foundation structural system to investigate the response of the structural system under seismic excitations. The input excitations are the same as those used in the time history analysis of the scaled 1D periodic foundation, as shown in Table 5-10. Figure 5-61 shows the time history analysis results under the Anza Earthquake in the horizontal direction. The accelerations at the top of the periodic foundation (point A in Figure 5-59) and the roof were recorded and compared with the input excitation. It is observed that the peak acceleration responses on the top of the periodic foundation and the roof are reduced tremendously to 0.201 g and 0.232 g, respectively, as compared to the peak input acceleration of 1 g. The reduction is mainly due to the wave filtering effect which is shown in the frequency domain. Similarly, the peak acceleration on both output points is reduced to minuscule acceleration when subjected to the Bishop Earthquake in the horizontal direction, as shown in Figure 5-62. This is because almost all of the main frequency content of the ground motion is located in the attenuation zone. The same behavior is observed when the structural system is subjected to the vertical ground motions. However, since the attenuation zone of the P-Wave is not as low and as wide as that of the S-Wave, less frequency contents get filtered out. Therefore, less acceleration response reduction is observed in the vertical direction. Figure 5-63 shows the time history analysis results under the Anza Earthquake in the vertical direction. The peak acceleration on each of the top of the periodic foundation and the roof of the superstructure is found to be 0.744 g and 0.406, respectively. These peak accelerations, although still smaller than the peak input acceleration, are much larger than those in the horizontal direction. In addition, response amplification is observed when the structural system is subjected to the Bishop Earthquake in the vertical direction, as shown in Figure 5-64. This is because the main frequency content is located outside the attenuation zone which creates amplification.

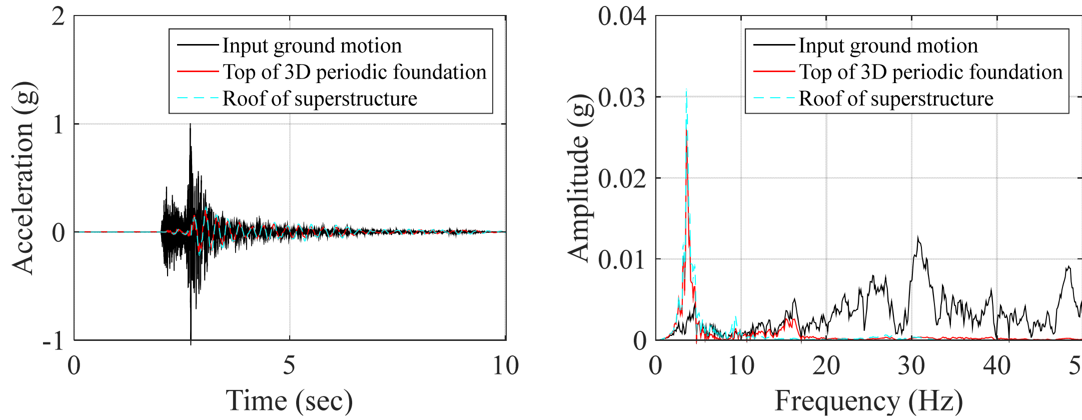

(a) Time domain (b) Frequency domain

Figure 5-61 Acceleration responses due to Anza ground motion in the horizontal direction

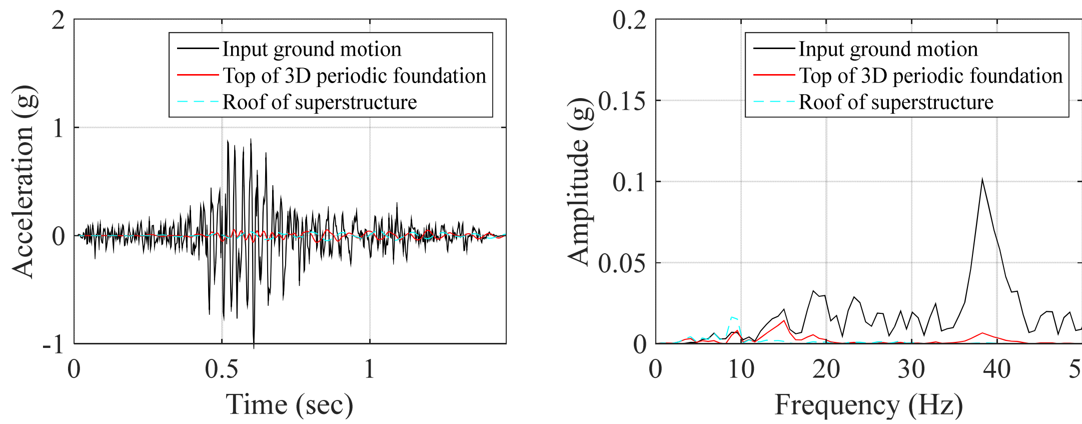

(a) Time domain (b) Frequency domain

Figure 5-62 Acceleration responses due to Bishop ground motion in the horizontal direction

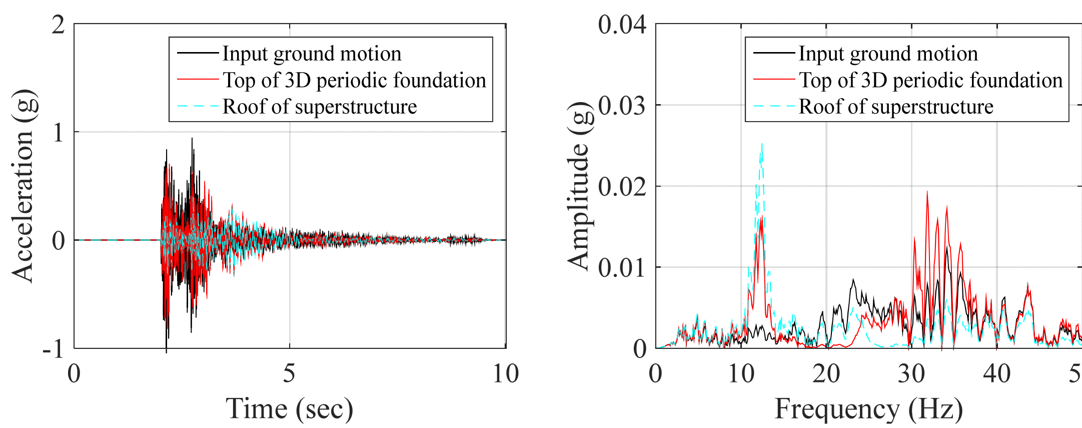

(a) Time domain (b) Frequency domain

Figure 5-63 Acceleration responses due to Anza ground motion in the vertical direction

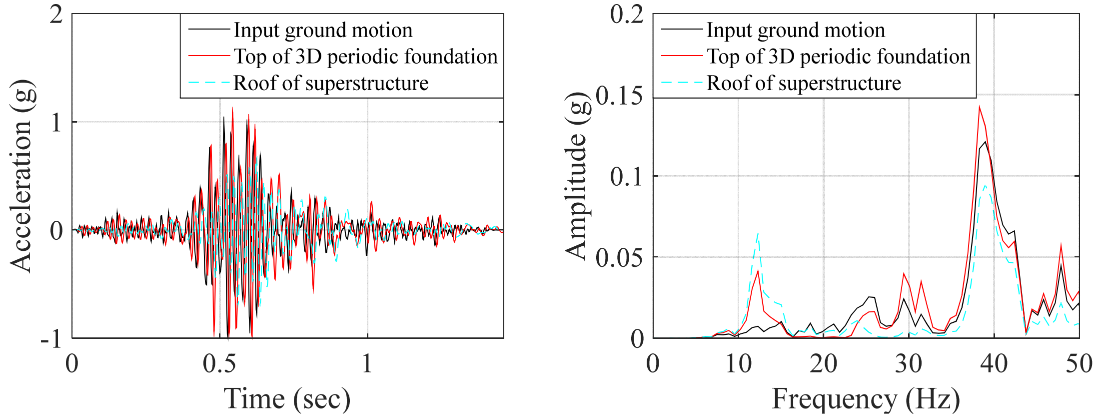

(a) Time domain (b) Frequency domain

Figure 5-64 Acceleration responses due to Bishop ground motion in the vertical direction

Table 5-16 provides the response summary of the scaled 3D periodic foundation structural system under the horizontal earthquake ground motions. The drift of the 3D periodic foundation can be observed to be quite small even though the input PGA is 1 g. Table 5-17 provides the response summary of the 3D periodic foundation structural system under the vertical earthquake ground motions. In general, the response reduction due to vertical earthquakes is not as large as that due to the horizontal earthquakes. This is due to the fact that attenuation zones of the S-Wave are located at lower frequencies and also cover wider frequencies than those of the P-Wave, as shown in Figure 5-60. As for the relative displacement, minor vertical displacement is observed when the structural system is subjected to vertical ground motions.

Table 5-16 Response summary of scaled 3D periodic foundation structural system under horizontal ground motions

Earthquake event	Peak acceleration on top of 3D periodic foundation (g)	Max acceleration on roof (g)	Max drift on 3D periodic foundation (%)
Anza	0.201	0.232	0.925
Bishop	0.062	0.052	0.086

Table 5-17 Response summary of scaled 3D periodic foundation structural system under vertical ground motions

Earthquake event	Peak acceleration on top of 3D periodic foundation (g)	Max acceleration on roof (g)	Max relative displacement on 3D periodic foundation (mm)
Anza	0.774	0.406	0.301
Bishop	1.091	0.715	0.413

5.2.3.2.3 Stress analysis on polyurethane under gravity load

Under the gravity load, the maximum and minimum principal stress fields on the matrix of the unit cells are shown in Figure 5-65. The maximum compression is observed at 0.0454 MPa, and the maximum tension is observed at 0.0268 MPa. The maximum compression stress corresponds to the assigned secant stiffness.

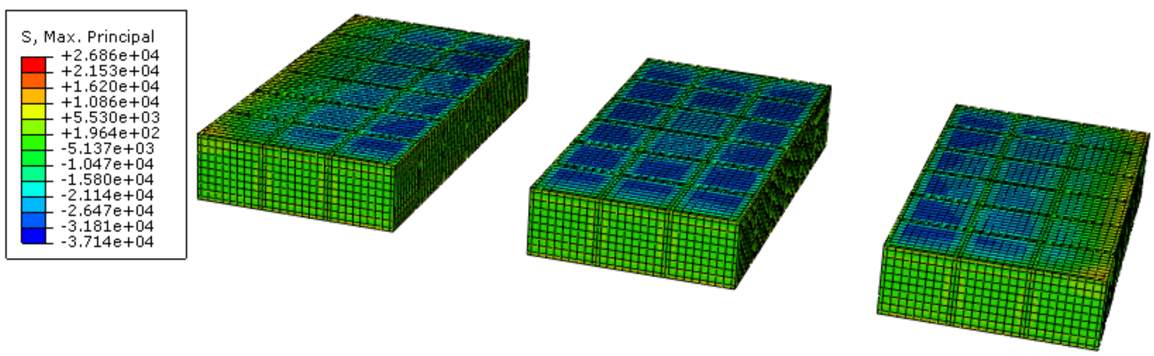

(a) Maximum principal stress

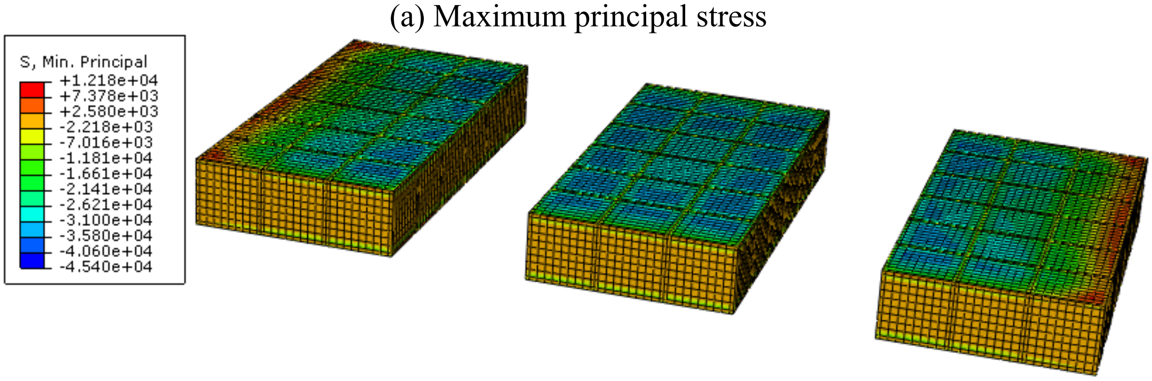

(b) Minimum principal stress

Figure 5-65 Principal stress fields on the matrix in scaled 3D periodic foundation structural system (unit in Pa)

5.2.3.3 Reinforcement detail on RC base, layer, and core

The RC base designed for the scaled 3D periodic foundation is the same as that designed for the scaled 1D periodic foundation. Therefore, the reinforcement detail of the RC base is not repeated. The RC layer designed on the top of the 3D periodic foundation has a similar reinforcement detail as the RC layer 2 in the scaled 1D periodic foundation. However, since the dimensions of both layers are slightly different, the reinforcement detail of the RC layer is presented. Figure 5-66 shows the reinforcing detail of the RC layer. The six non-threaded holes with a diameter of 50 mm ($\phi 50$) were provided for glue inspection. In addition, 34 threaded holes with a diameter of 30 mm (M30) were provided so that the steel frame can be bolted to the RC layer. Rebars number 3 (#3) with a spacing of 250 mm were designed in both transverse and longitudinal directions. The reinforcement ratio on the concrete layer in the longitudinal and transverse directions is shown in Eqs. (5-8) and (5-9):

$$\rho_{\text{long}} = \frac{A_s \times n}{b \times h} = \frac{71 \times 9}{2180 \times 60} = 0.00489 \text{ and} \tag{5-10}$$

$$\rho_{\text{trans}} = \frac{A_s \times n}{l \times h} = \frac{71 \times 19}{4730 \times 60} = 0.00475\,. \tag{5-11}$$

The maximum spacing according to provision number 24.4.3.3 in the ACI 318-14 provisions is the lesser of $5h = 5 \times 60 = 300\,\text{mm}$ and 450 mm. The spacing of most of the rebar in Figure 5-66 is 250 mm with the largest spacing of 300 mm. Therefore, the designed rebar spacing satisfies the maximum spacing requirement in the ACI provisions. Since the RC layer is too slender, the transportation process may damage the RC layer. Hence, to protect the RC layer, all four edges of the RC layer are designed to be protected by a thin channel section steel cover.

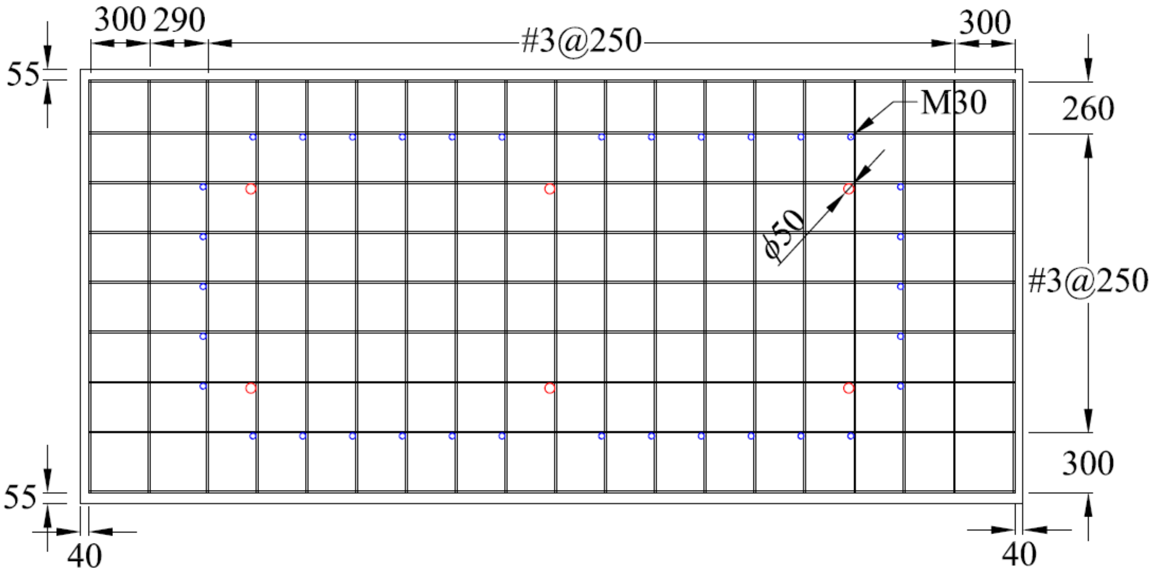

Figure 5-66 Reinforcement detail and holes on RC layer (unit in mm)

The function of the RC layer is to connect the superstructure to the 3D periodic foundation and also to provide uniform stress distribution to the unit cells. Therefore, the majority of the force resisted by the RC layer is the gravity load. Figure 5-67 shows the maximum principal strain on the RC layer under gravity load. The maximum strain is observed to be 0.00002241 which is less than a quarter of the cracking strain of a normal concrete at 0.00008 [76], which means that the RC layer will experience no crack under the gravity load. Therefore, a concrete compressive strength of 28 MPa is sufficient for the RC layer.

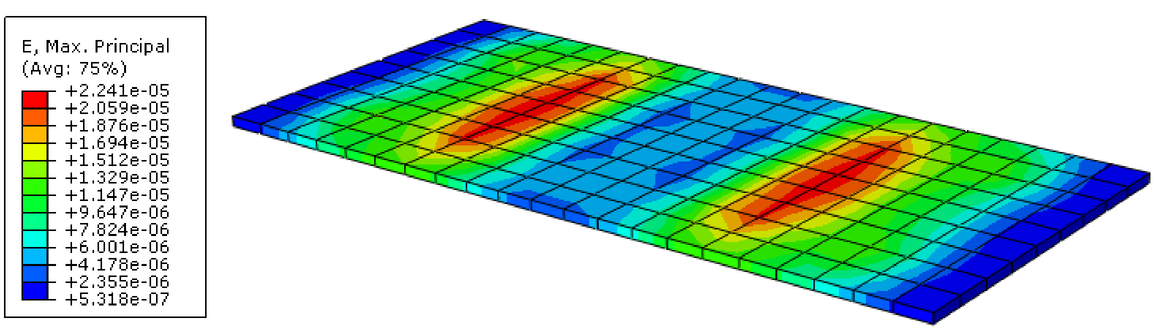

Figure 5-67 Maximum principal strain on RC layer

Figure 5-68 shows the reinforcing detail of the RC core of the scaled Bragg scattering unit cell. Minimum shrinkage reinforcement is provided on the RC core. The reinforcement is designed as a skeleton of a smaller cube with a size of 265 mm to allow 30 mm concrete cover on each side. For transportation purposes, a threaded hole with a size of 25 mm (M25) was designed on each RC core.

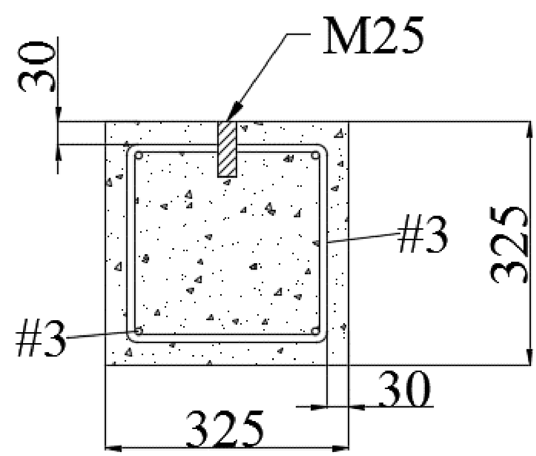

Figure 5-68 Reinforcement detail and anchorage hole on RC core (unit in mm)

5.3 Fabrication Process of Test Specimens

This section presents the fabrication process of the designed scaled structural systems, which include the steel frame structure, the 1D periodic foundation, and the 3D periodic foundation. The fabrication process covers the construction of the structural components and the assembly process of the structural components to form the designed test specimens.

5.3.1 Fabrication of steel frame structure

The single story two-bay steel frame was constructed frame by frame. Figure 5-69 shows the first constructed transverse frame or the frame along line A shown in Figure

5-28. Once the remaining two transverse frames (frames along lines B and C) were constructed, the three transverse frames were connected by the longitudinal beams and braces. Figure 5-70 shows the completely constructed steel frame structure.

As mentioned in Subsection 5.2.1, the frame was designed using a weld-type connection. Figure 5-71 shows the detail of one of the joints on the steel frame. The structural members were welded along all of the meeting lines. In order for the two cross braces to not run into one another at the center of the crossing, a space in between two cross braces was provided, as shown in Figure 5-72. In this way, each of the braces can effectively carry the axial load without interrupting the adjacent brace.

Figure 5-69 Transverse frame

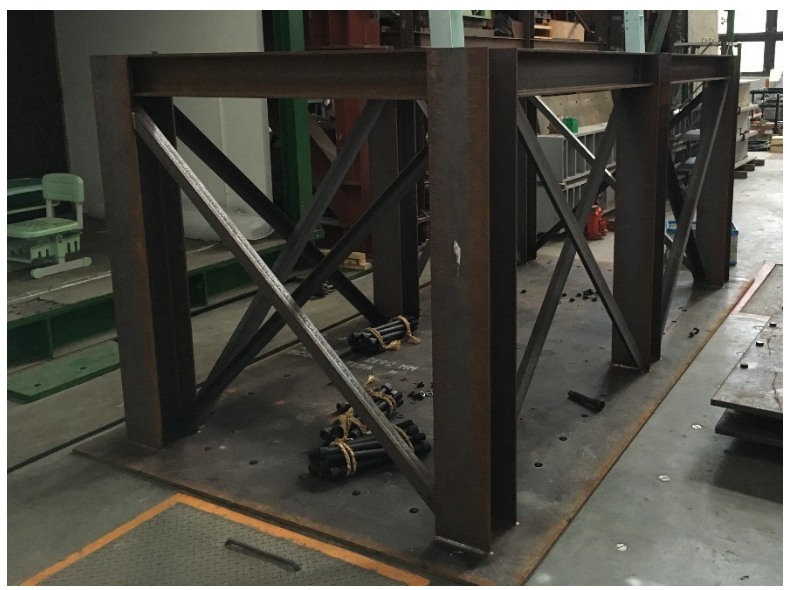

Figure 5-70 Completed steel frame

Figure 5-71 Beam–column–brace joint

Figure 5-72 Cross brace

5.3.2 Fabrication of scaled 1D periodic foundation

5.3.2.1 Construction of RC base and layers of scaled 1D periodic foundation

Figure 5-73 shows the formwork preparation for the RC base. A large wooden board was prepared for the base. Lines were drawn on the board to mark the position of the rebars and holes. To make non-threaded holes on the concrete, plastic pipes were placed on the formwork before the casting of the concrete. The plastic pipe will prevent the fresh concrete from filling the designated holes therefore creating the holes as the concrete hardens. Figure 5-74 shows the placement of rebars on the RC base inside the completed formwork. Ready mix concrete was used for the casting. During pouring, a vibrator was also used to vibrate the fresh concrete in order to remove the entrapped air void, as shown in Figure 5-75. Removing the air void ensures that the concrete is finished properly and that it will have the required strength once it reaches its 28-day life. Figure 5-76 shows the appearance of the concrete a few days after the casting.

(a) (b)

Figure 5-73 (a) Formwork of RC base; (b) Plastic pipe

Figure 5-74 Rebars on RC base


Figure 5-75 Casting of RC base


Figure 5-76 Cast RC base

A similar construction method was also applied to cast RC layers 1 and 2. Figure 5-77 shows the prepared formwork for RC layer 2. It has a wooden board at the bottom, rebars and plastic pipes lying on designated positions, a steel cover on all four edges, and steel strips to keep the threaded nuts in position. Figure 5-78 shows the cast RC layers 1 and 2.

Figure 5-77 Form works and rebars of RC layer 2

(a) (b)

Figure 5-78 (a) Cast RC layer 1; (b) Cast RC layer 2

5.3.2.2 Polyurethane sheets of scaled 1D periodic foundation

In the designed scaled 1D periodic foundation, each of the polyurethane layers has a length and width of 4600 mm and 2060 mm, respectively. However, producing a single polyurethane sheet of such a large size would be very challenging for the manufacturer. Moreover, it is prone to accidental damage during the transportation and construction process. Therefore, smaller polyurethane sheets were purchased. Figure 5-79 shows the purchased durometer OO20 polyurethane sheets. Each of the polyurethane sheets has a length of 45.25 inches or 1150 mm and a width of 20.25 inch or 515 mm. In total, there are 32 pieces of polyurethane that were purchased. Sixteen of them have a thickness of 2 inches or 50 mm, that would be assembled into polyurethane layer 1, and the remaining sixteen have a thickness of 1.58 inches or 40 mm, that would be assembled into polyurethane layer 2.

Figure 5-79 Polyurethane sheets

5.3.2.3 Assembly process of scaled 1D periodic foundation

Once the RC base and layers reached their designated strength, the assembly process was conducted. To ensure a perfect bond between the polyurethane layers and the RC layers, two products from Sika [77] were used. Figure 5-80 shows the first product, which is a solvent-based polyurethane compound resin solution (Sika Primer-215). It is a transparent, pale yellow liquid with low viscosity that dries by reaction with atmospheric moisture. This product is used to prime various plastic, timber, and other porous materials prior to bonding with the other SIKA product. The second product, as shown in Figure 5-81, is a polyurethane-based glue or sealant (Sikaflex-11FC+). It has strong adhesion to most clean and sound substrates. When dried, the glue becomes rubbery with a classification of shore durometer A hardness 37. The tensile and tear strength of the hardened glue are 1.5 MPa and 8 MPa, respectively, with a Young's modulus of 0.6 MPa.

Figure 5-80 Resin solution

Figure 5-81 Polyurethane glue

Prior to the assembly of the 1D periodic foundation, the RC base and layers were cleaned from dust by blowing high-pressure air on them. After that, lines were drawn to mark the position of the polyurethane sheets on the RC base and layers. Once the preparation was done, the assembly process was started. To make sure the polyurethane glue bonded perfectly with the RC surface, the resin solution was first applied on the RC surface. When the resin solution dried, the RC surface became glittery as shown in Figure 5-82. On top of the primed RC base, polyurethane glue was applied. Because the polyurethane glue dried fast, the glue was applied grid by grid. On each completed grid, a polyurethane sheet was placed, as shown in Figure 5-83. Figure 5-84 shows polyurethane layer 1 glued to the RC base.

Figure 5-82 Applying polyurethane glue on resin covered RC base

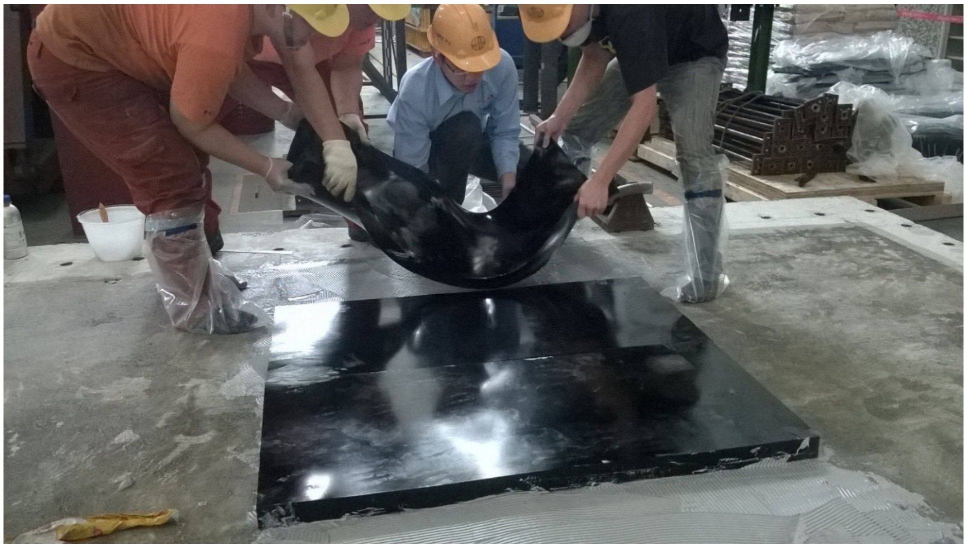

Figure 5-83 Placing of polyurethane sheets

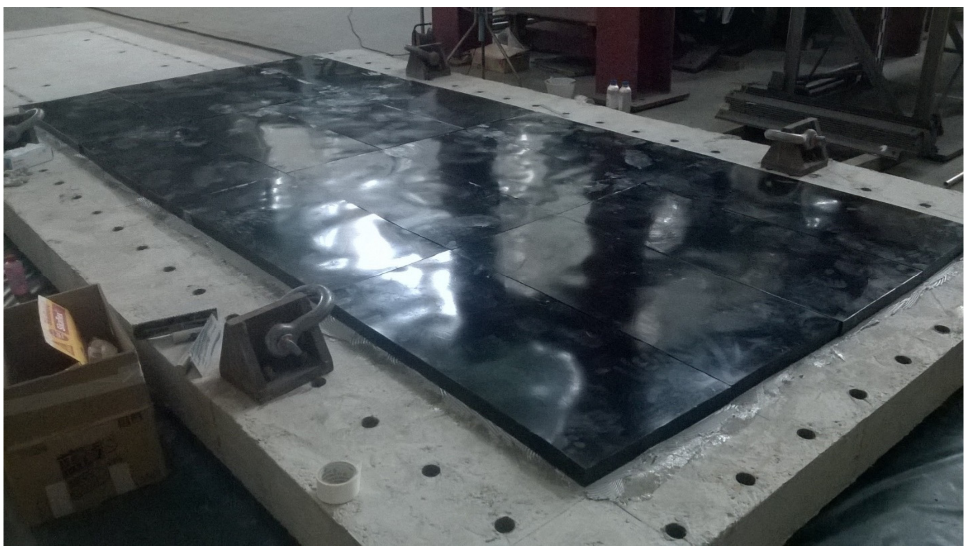

Figure 5-84 Polyurethane layer 1 on RC base

After polyurethane layer 1 was laid down and glued to the RC base, the next step was connecting polyurethane layer 1 and RC layer 1. Since RC layer 1 is on the top of polyurethane layer 1, the gluing process is somewhat different from gluing polyurethane layer 1 to the RC base. The RC layer 1 was lifted up, and the resin solution was applied to its bottom surface. While waiting for the resin solution to dry, the polyurethane glue was applied on top of the polyurethane layer 1. Figure 5-86 shows the process of putting polyurethane glue on polyurethane layer 1. By the time the whole surface of polyurethane 1 was covered with glue, the resin solution on RC layer 1 dried and was ready to attach. Figure 5-87 shows that RC layer 1 was lowered down carefully and placed on top of polyurethane layer 1. To ensure perfect contact between polyurethane layer 1 and RC layer 1, the half completed 1D periodic foundation was prestressed by applying a uniform distributed load on top of RC layer 1, as shown in Figure 5-88. The prestress was carried out for three days until the glue completely dried.

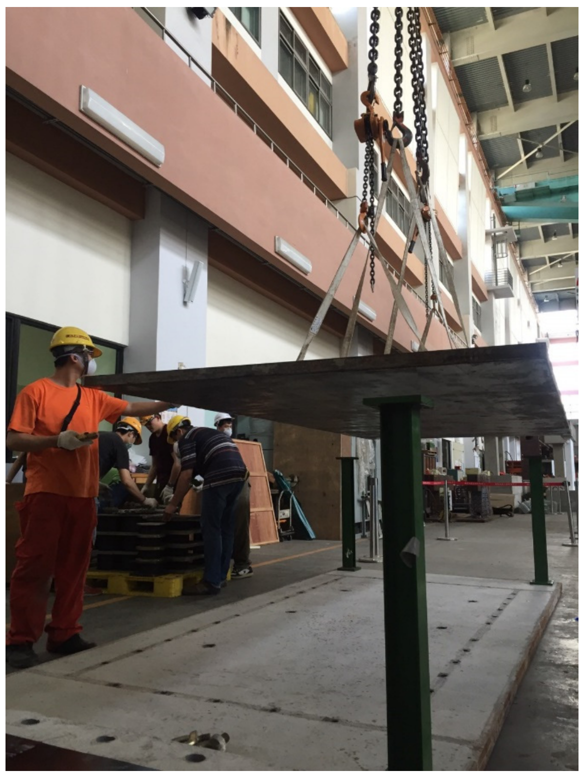

Figure 5-85 Resin coated RC layer 1

Figure 5-86 Applying polyurethane glue on top of polyurethane layer 1

Figure 5-87 Attaching RC layer 1 to polyurethane layer 1

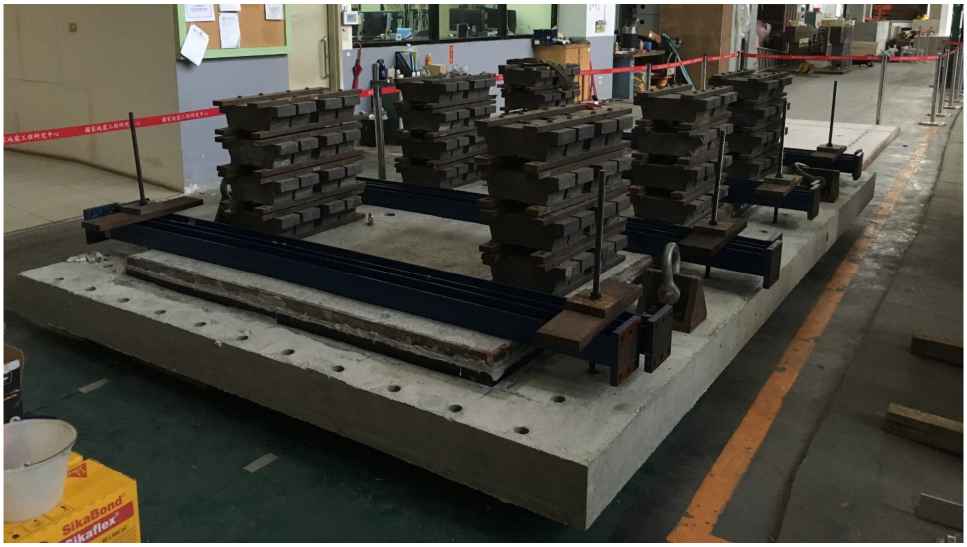
Figure 5-88 Prestress on half assembled 1D periodic foundation

After three full days of prestressing the half constructed 1D periodic foundation, the weights were removed, and the assembly of the remaining layers was resumed. The resin solution was applied to the top surface of RC layer 1. After the solution dried, the polyurethane glue was applied grid by grid on the primed surface. On each completed grid, a polyurethane sheet for polyurethane layer 2 was placed. After polyurethane layer 2 was securely located on top of RC layer 1, the resin solution was applied to the bottom surface of RC layer 2. While letting the resin solution on RC layer 2 dry, polyurethane glue was applied on the top of polyurethane layer 2, as shown in Figure 5-89. After polyurethane glue was applied on polyurethane layer 2 and the resin solution on RC layer 2 dried, RC layer 2 was carefully placed on top of polyurethane layer 2. To ensure perfect contact between the layers of the 1D periodic foundation, prestressing was applied, as shown in Figure 5-90. The prestress weights were removed once the glue had completely dried. Figure 5-91 and Figure 5-92 show the fully constructed 1D periodic foundation on the shake table ready to be tested.

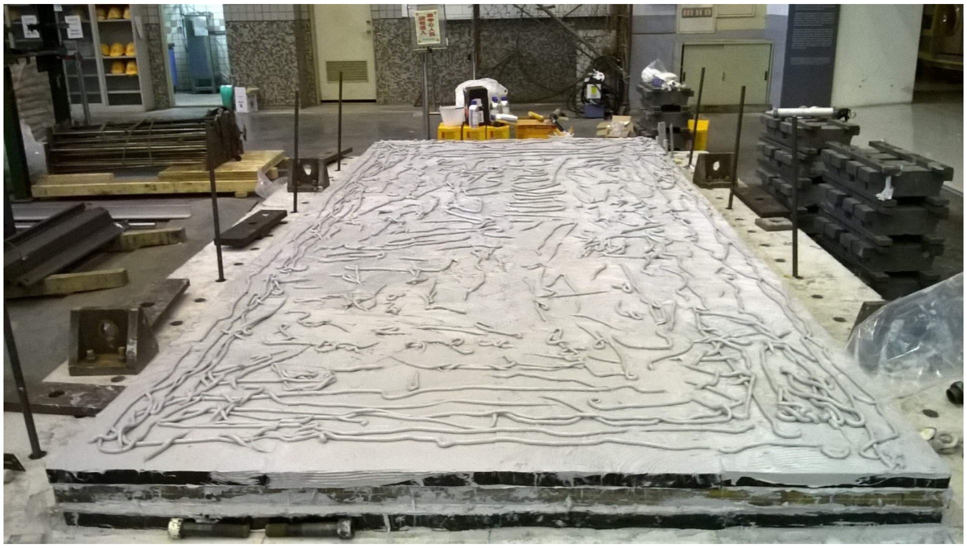

Figure 5-89 Polyurethane glue on top of polyurethane layer 2

Figure 5-90 Prestress on fully assembled 1D periodic foundation

Figure 5-91 Scaled 1D periodic foundation on shake table (East view)

Figure 5-92 Scaled 1D periodic foundation on shake table (South view)

5.3.3 Fabrication of scaled 3D periodic foundation

5.3.3.1 Construction of RC base and layer of scaled 3D periodic foundation

The construction process of the RC base and layer in the scaled 3D periodic foundation is exactly the same as that for the scaled 1D periodic foundation. Therefore, the description of the construction process is not repeated in this section.

5.3.3.2 Construction of RC cores of scaled 3D periodic foundation

The accuracy of the RC cores is very important to ensure the scaled 3D periodic foundation specimen will perform according to the design. To have high geometric precision RC cores, steel formworks were specially designed and constructed for casting the cores. Figure 5-93 shows the design drawing of the formwork. The formwork consists of removable panels to make the release of the cured RC cores easier without damaging them. Three formworks were constructed where each unit of the formworks can hold up to six RC cores. Therefore, eighteen RC cores can be cast at once.

Rebar and threaded nuts were first prepared and installed inside the formworks, as shown in Figure 5-94. Then fresh concrete mix was poured into the formworks and vibrated to eliminate any entrapped air void, as shown in Figure 5-95. The RC cores were left for seven days inside the formworks (see Figure 5-96) for initial curing until they reached sufficient strength. Then the RC cores were removed from the formworks, as shown in Figure 5-97. The formworks were then prepared for casting the next batch of the RC cores. The size of each of the RC cores was measured to be exactly 32.5 cm (see Figure 5-98).

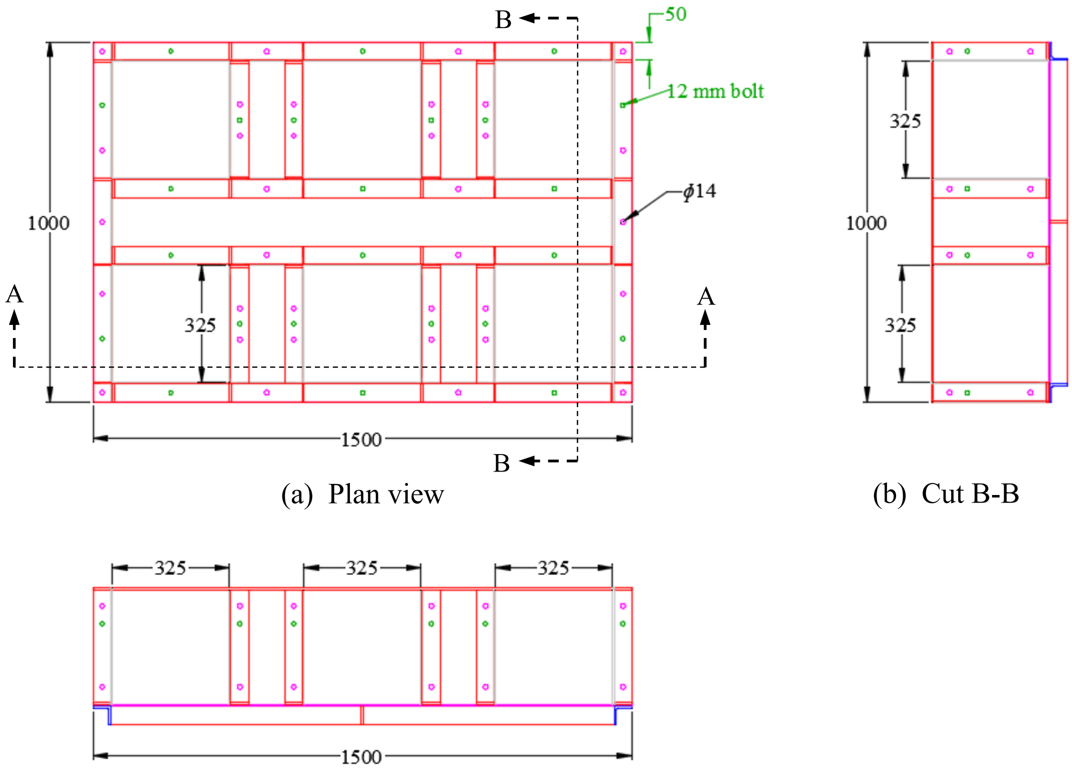

(a) Plan view (b) Cut B-B

(c) Cut A-A

Figure 5-93 Formwork for RC cores

Figure 5-94 Steel formworks with rebars and threaded nuts installed

Figure 5-95 Casting of RC cores

Figure 5-96 RC cores under curing

Figure 5-97 Cast RC cores

Figure 5-98 Size of a cast RC core

5.3.3.3 Polyurethane sheets of scaled 3D periodic foundation

To fully encase an RC core, two pieces of each of three different sizes of polyurethane sheets are needed, as shown in Figure 5-99. The custom made polyurethane sheets were purchased directly from a manufacturer specializing in manufacturing synthetic rubber. To encase all 54 RC cores, 108 pieces of polyurethane layers were purchased for each size.

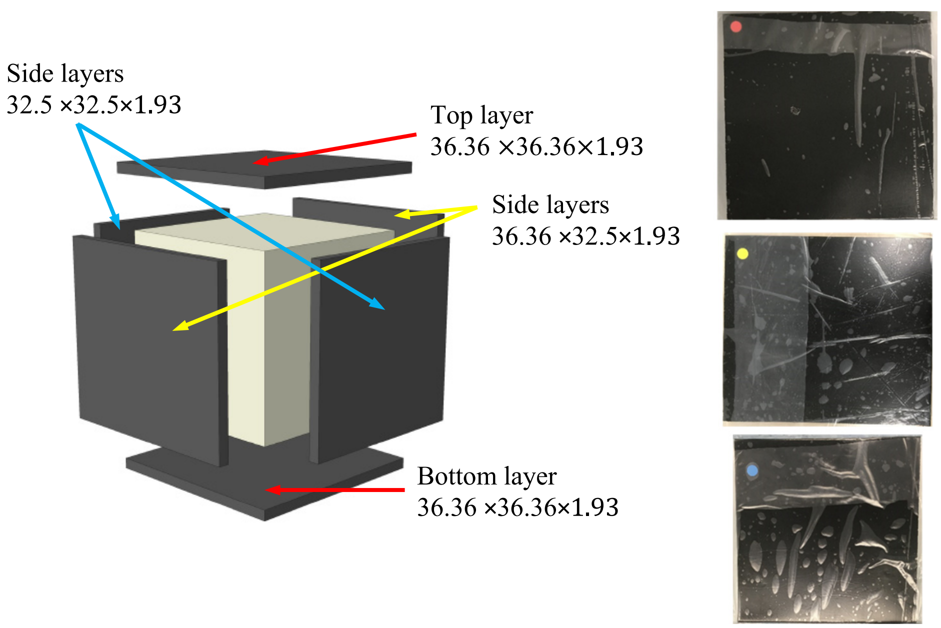

Figure 5-99 Polyurethane sheets of scaled 3D periodic foundation (unit in cm)

5.3.3.4 Assembly process of scaled 3D periodic foundation

Once the RC base, layer, and cores reached their designated strength, the assembly process was started. The same bonding agents used in the assembly of the scaled 1D periodic foundation were used for the scaled 3D periodic foundation.

In the first step, four sides of the RC cores (excluding bottom and top sides) were glued with polyurethane layers. Two pieces of each of sizes $36.36 \times 32.5 \times 1.93$ cm and $32.5 \times 32.5 \times 1.93$ cm were used in this step. Before the gluing process, the RC cores were laid on the gluing site (see Figure 5-100) and were cleaned from dust by blowing high-pressure air onto them. Once the surfaces were clean enough, the resin solution was applied on the four sides. When the resin solution dried, the RC surface became glittery and had a better bond with the polyurethane glue. After the resin solution dried, polyurethane glue was applied, as shown in Figure 5-101. Then, piece by piece the polyurethane layers were attached to the glued surface of the RC core, as shown in Figure 5-102. Fresh polyurethane glue, however, has an insufficient bond strength and may cause detachment of the connected substances. To prevent the polyurethane layers from sliding down due to their self-weight, wood plates were placed on the outer sides of the polyurethane layers and were tied with a rope, as shown in Figure 5-103. Figure 5-104 shows the RC cores with polyurethane layers on their four sides after curing.

Figure 5-100 RC cores for gluing

(a) Front view

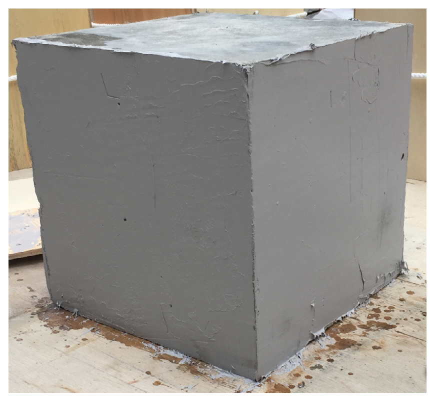

(b) Corner view

Figure 5-101 RC core with polyurethane glue

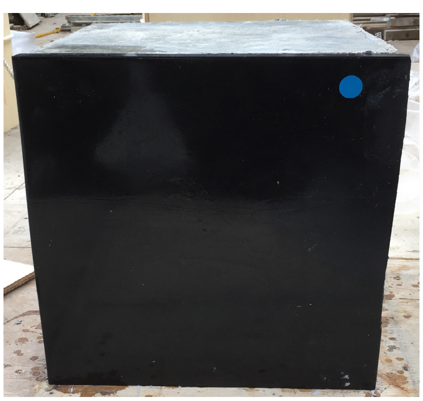

(a) Front view

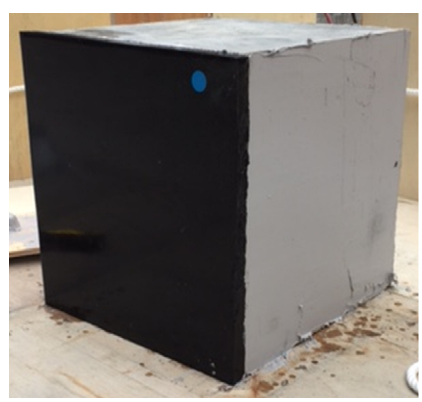

(b) Corner view

Figure 5-102 RC core with polyurethane layer on one side

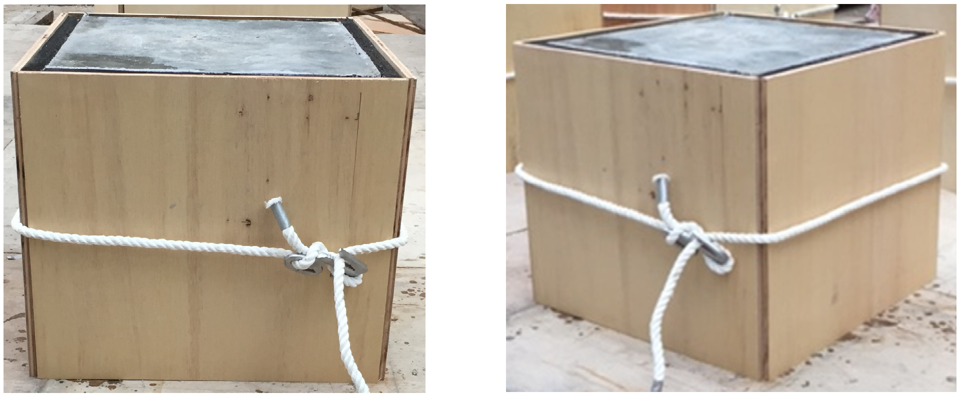

(a) Front view (b) Corner view

Figure 5-103 RC core with polyurethane layers on four sides supported by wood plates

Figure 5-104 RC cores with polyurethane layers on four sides after curing

In the second step, 54 polyurethane layers were glued to the RC base. These polyurethane layers were those that needed to be pasted to the bottom side of the RC cores. However, construction-wise, it is much easier to glue the polyurethane layers to the RC base first and then glue the cores on top of the polyurethane layers rather than to glue the polyurethane layers directly to the bottom side of the RC cores. Therefore, the easier way was chosen for construction.

Similar to the gluing process of the RC core, the RC base was first cleaned from dust and primed with the resin solution. Figure 5-105 shows the glittery area on the RC base where the resin solution was applied. After the resin solution dried, polyurethane glue was applied. To avoid the glue being hardened by long exposure to air, polyurethane layers were pasted immediately, as shown in Figure 5-106. Figure 5-107 shows all the 54 polyurethane sheets on the RC base.

Figure 5-105 Primed RC base

Figure 5-106 Applying polyurethane glue and pasting polyurethane sheets on RC base

Figure 5-107 Polyurethane layers pasted on RC base

In the third step, the RC cores were pasted on top of the polyurethane layers on the RC base. The RC cores were first hung on a frame so that the bottom side of the cores could be cleaned and primed with the resin solution. After the resin solution had dried, the RC cores were moved to the designated position one by one. Before the RC cores were attached to the polyurethane layers on the RC base, polyurethane glue was first applied on the adjacent polyurethane layers. To guide the RC cores into the right position, large steel beams were placed on the perimeter of the 3D periodic foundation, as shown in Figure 5-110. Prestress was applied on each of the unit cell blocks to make the adjacent polyurethane layers well bonded. The prestress was left for three days to allow the polyurethane glue to become fully cured. The prestress was released, and the beams on the perimeter were removed once the polyurethane glue was cured. The result after the curing process is shown in Figure 5-111.

Figure 5-108 Concrete cubes hung on a frame

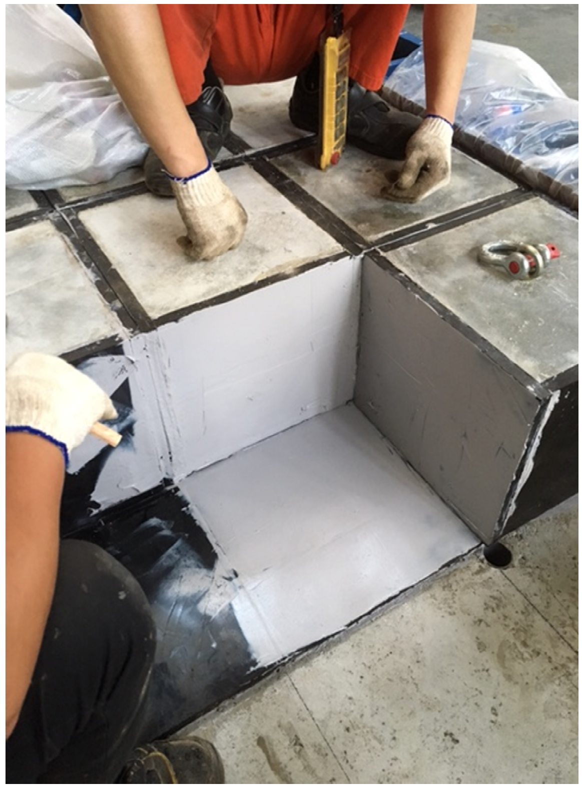
Figure 5-109 Polyurethane glue was applied on adjacent polyurethane layers


Figure 5-110 RC cores pasted on RC base

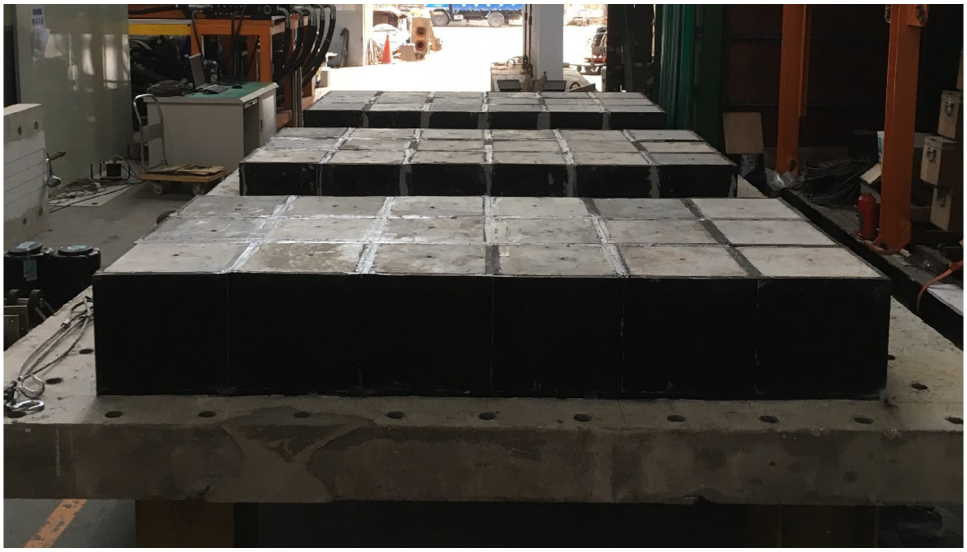

Figure 5-111 RC cores on RC base after curing

In the fourth step, the last side of each of the RC cores was covered with the final piece of the polyurethane layers. The top sides of the RC cores were cleaned and primed with the resin solution. After the solution had dried, polyurethane glue was applied on the top sides of the RC cores, as shown in Figure 5-112. Then the polyurethane layers were attached to the glued top sides of the RC cores. Figure 5-114 shows the completed 3D periodic foundation unit cells sitting on the RC base.

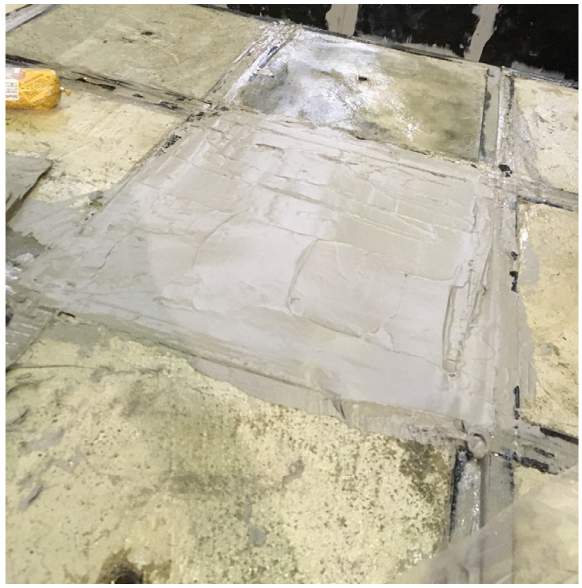
Figure 5-112 Polyurethane glue was applied on top of RC cores

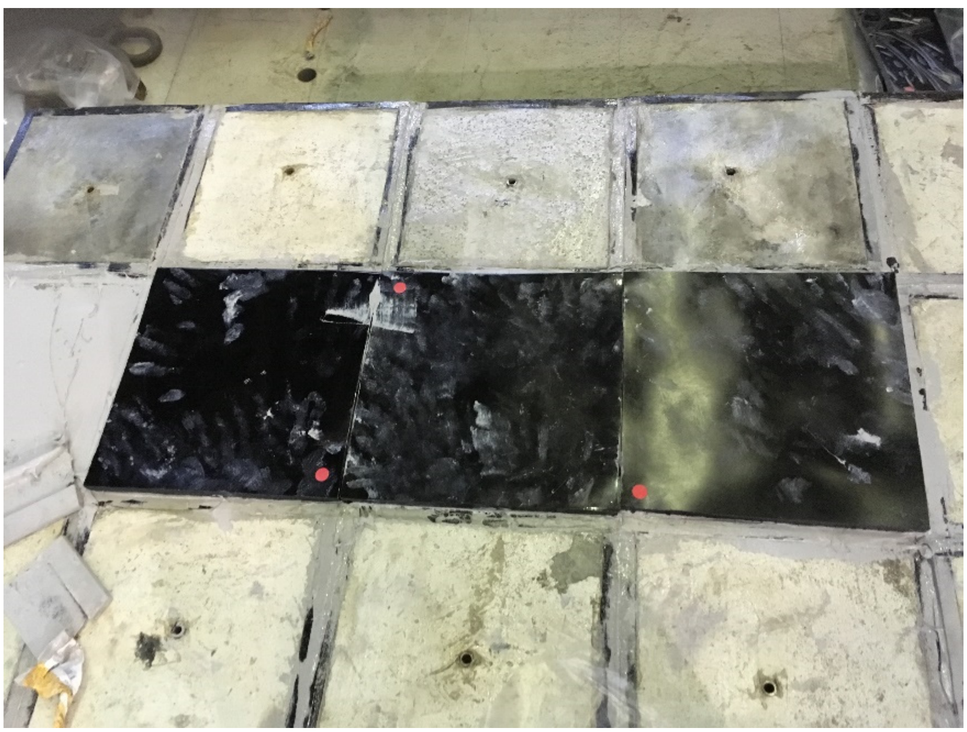
Figure 5-113 Polyurethane layers were attached to the top sides of RC cores

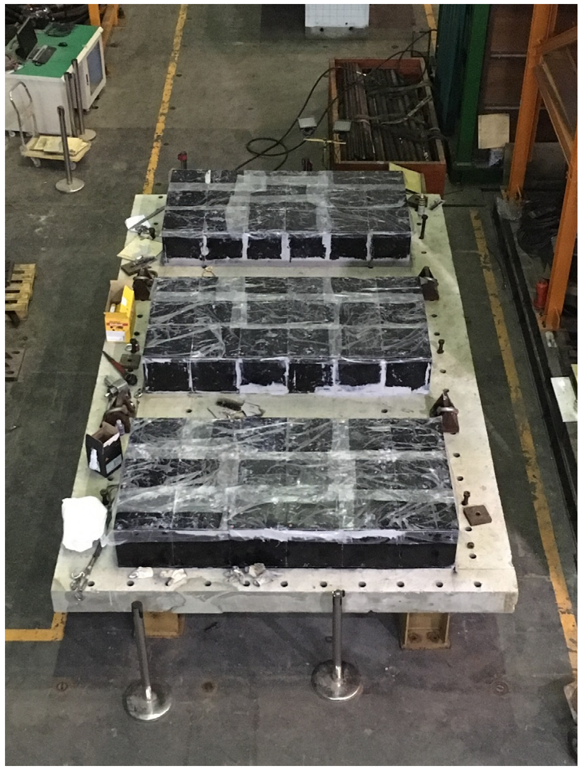

Figure 5-114 Scaled 3D periodic foundation unit cells on RC base

In the last step, the RC layer was connected to the unit cells. The RC layer was lifted up, and the resin solution was applied to its bottom surface. Once the resin solution dried, the polyurethane glue was applied to the top of the polyurethane layers. Figure 5-115 shows the process of putting polyurethane glue on the polyurethane layer. After the whole top surface of the polyurethane layers was covered in polyurethane glue, the RC layer was placed. Figure 5-116 shows that the RC layer was lowered down carefully and placed on top of the polyurethane layer. To ensure perfect contact between the unit cells and the RC layer, the 3D periodic foundation was prestressed, as shown in Figure 5-117. The prestress was carried out for three days until the glue completely dried. The prestress beams were removed once the glue completely dried.

Figure 5-115 Polyurethane glue applied on unit cells

Figure 5-116 Placement of RC layer

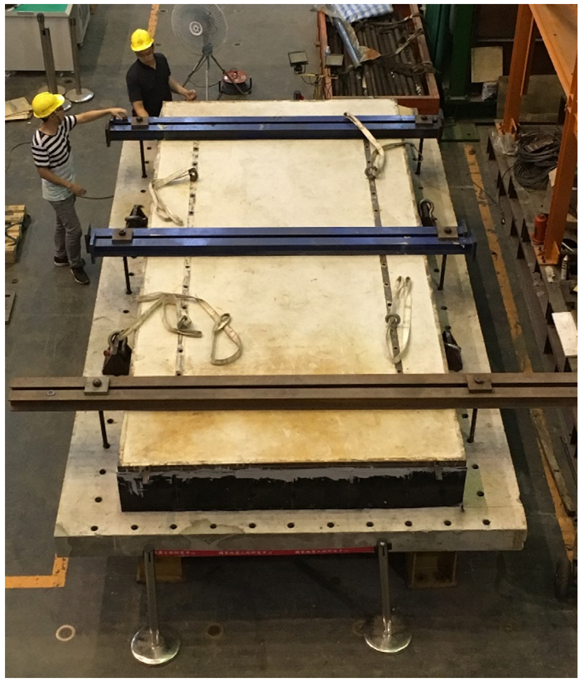

Figure 5-117 Prestress on fully assembled 3D periodic foundation

5.4 Shake Table Tests of Foundations and Structural Systems

This research aims to develop periodic foundations to isolate SMR buildings from the incoming seismic waves using the frequency band gap property. The designed scaled periodic foundation structural systems need to be experimentally validated to investigate the actual seismic performance of the structural systems. Table 5-18 shows the designed test cases for the experimental tests. A benchmark foundation made of RC (Case 1) was designed to show the wave propagation in a relatively homogeneous medium. The RC foundation is 4.6 m long, 2.06 m wide, and 0.2 m thick and seats on an RC base. The tests on the Case 3 specimen are intended to validate the frequency band gaps on the 1D periodic foundation only. Similarly, tests on Case 5 are for validation of the theory in the 3D periodic foundation. Tests on Cases 4 and 6 provide insight into the behavior of the 1D and 3D periodic foundation structural systems compared to the behavior of the benchmark structural system (Case 2) that represents a non-isolated SMR structure.

Table 5-18 Test cases

Test Case	Specimen	Description
1		RC foundation only
2		RC foundation supporting an SMR building
3		1D periodic foundation only
4		1D periodic foundation supporting an SMR building
5		3D periodic foundation only
6		3D periodic foundation supporting an SMR building

5.4.1 Test setups

Figure 5-118 shows the full test setup for each of Cases 2, 4, and 6. There is not much difference on the test setup between each of the test cases. In general, two identical steel frames (painted in blue), each on the north and south sides, were erected as reference frames to hold all temposonics in the horizontal direction and four vertical temposonics connected to the shake table. Two green steel columns on each of the east and west sides were erected to support two steel beams (blue color) crossing above the structure. The two beams, referred to as the main beams, were stiffened by two crossbeams (also blue color). The crossbeams held four vertical temposonics that were connected to the roof of the superstructure. Angle section steel beams were used to stiffen the two columns on each of the east and west sides. The angle section steel beams also held the remaining vertical temposonics that connect to the RC base and the top of the foundations as well as the steel floor of the superstructure in Case 6. The test setup for Cases 1, 3, and 5 are the same as the test setup for their respective structural systems; however, with a fewer number of sensors.

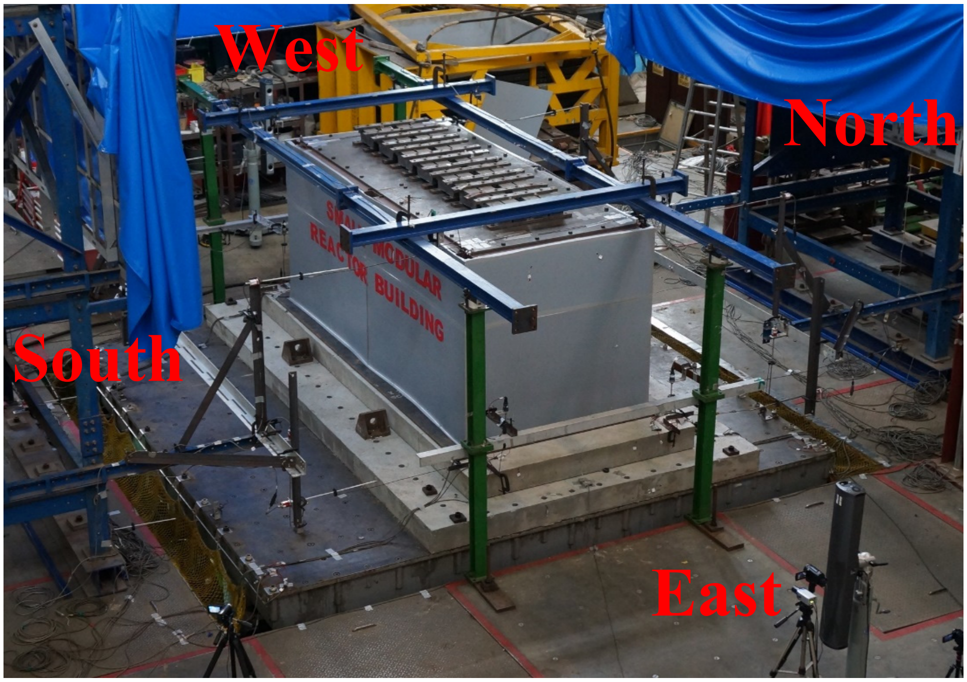

(a) Case 2

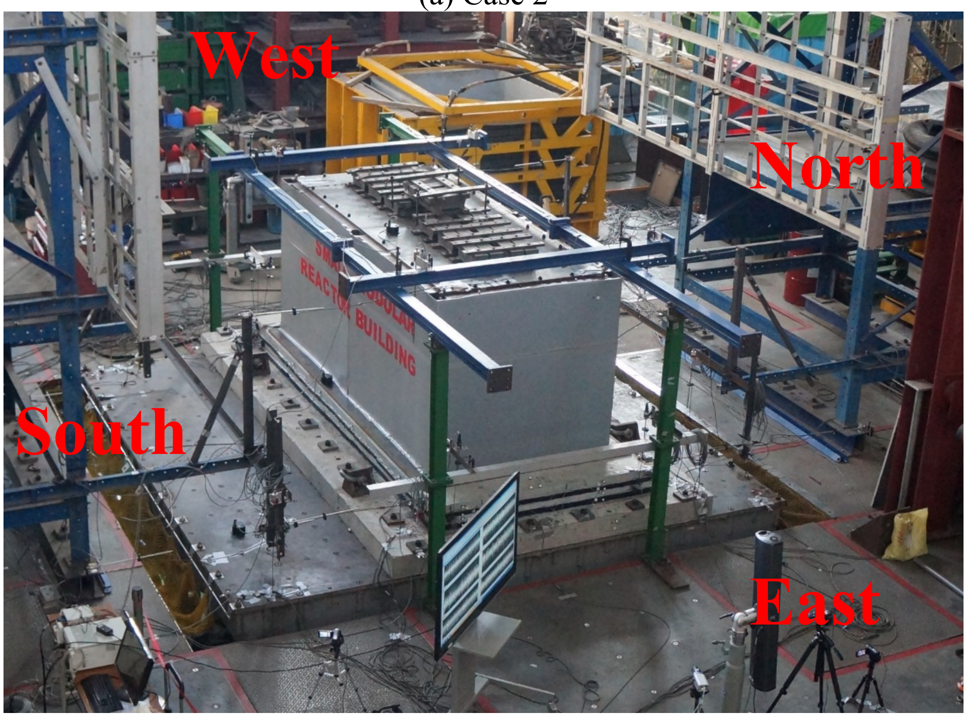

(b) Case 4

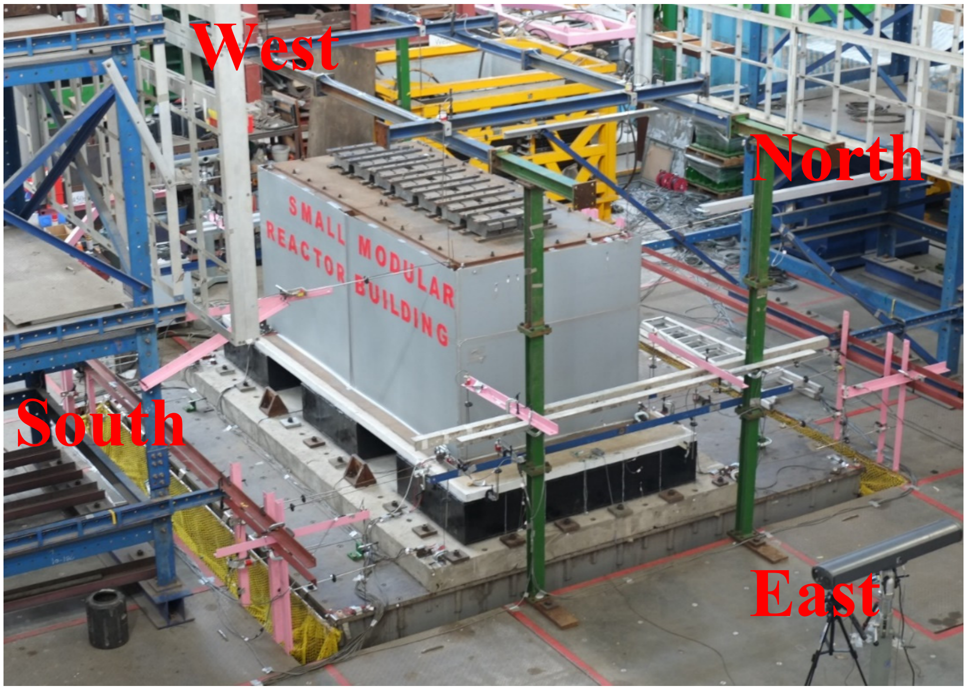

(c) Case 6
Figure 5-118 Test setup of structural systems

To capture the response of the test specimens, three types of sensors were installed on the specimens. The three types of sensors measure two important response variables, acceleration and displacement. Accelerometer sensors measure acceleration while both the traditional displacement transducer (temposonic) and vision-aided measurement system (NDI optotrak optical measurement) sensors measure displacement. Details of the sensors are explained in Subsection 5.4.2.

Figure 5-119 shows both the plan and elevation views of the sensors located on the Case 1 specimen. Each of the letters refers to a single sensor. Letter A refers to the accelerometer, letter T refers to the temposonic, and letter N refers to the NDI marker. The arrows on the accelerometers and temposonics indicate the direction of the measurement. The NDI markers are not marked with arrows because each marker can measure the displacement in three directions. The sensors were placed on all four corners of the specimen and the shake table to ensure that there was no additional rocking or twisting on the specimen and the table during the tests. Similar to the temposonic that can only measure displacement in one direction, a single accelerometer also can only measure acceleration in one direction. Therefore, two accelerometers and two temposonics (each for the horizontal and the vertical directions) were placed at each corner of the shake table and the top of the RC foundation. Due to the limitation of the optical receiver in the NDI system, the NDI markers were not put on the shake table. Instead, they were placed on the RC base.

Figure 5-120 shows the schematic layout of the sensors attached to Case 2. The location of the sensors on the shake table and the RC foundation are the same as those in Case 1. In addition to those, two more accelerometers and temposonics and one additional NDI marker were placed at each corner of the roof of the superstructure.

Figure 5-121 shows the sensors location for Case 3. For this case, two accelerometers and two temposonics were attached to each corner of the shake table, RC layer 1, and RC layer 2. The accelerometers and temposonics were not connected to the polyurethane layers because they cannot be connected without damaging the polyurethane material. The NDI markers, on the other hand, can be attached to any soft surface without damaging the material. Therefore, they were placed at each corner of the RC base, polyurethane layer 1, RC layer 1, polyurethane layer 2, and RC layer 2. For the Case 4 specimen, two more accelerometers and temposonics and one additional NDI marker were placed at each corner at the roof of the superstructure, as shown in Figure 5-122.

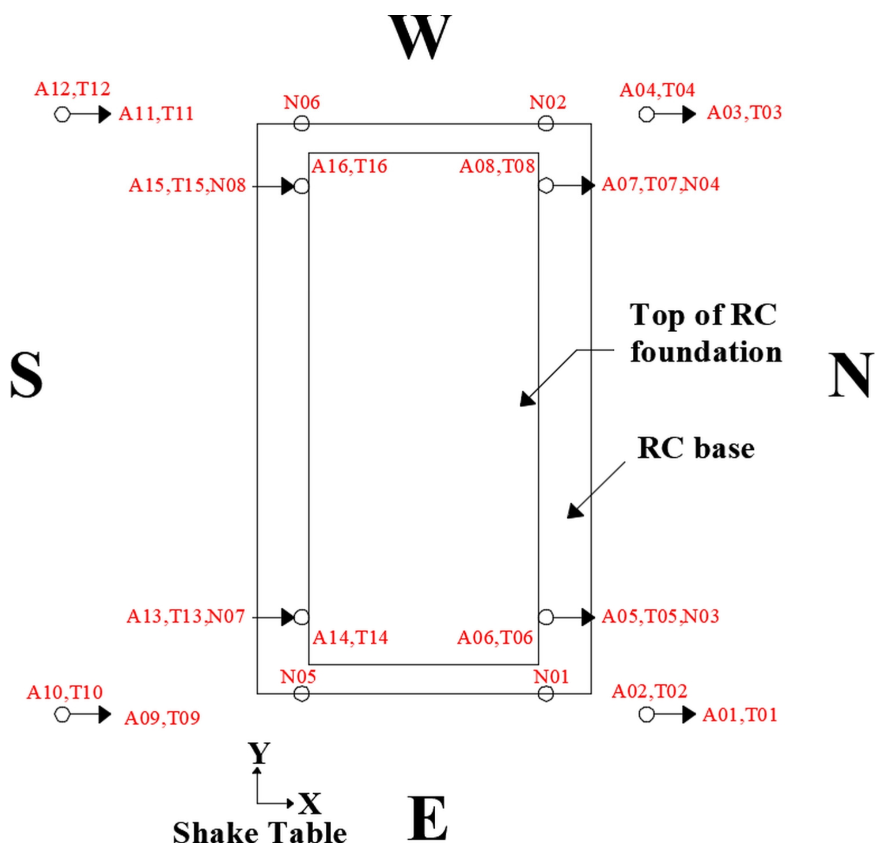

(a) Plan view

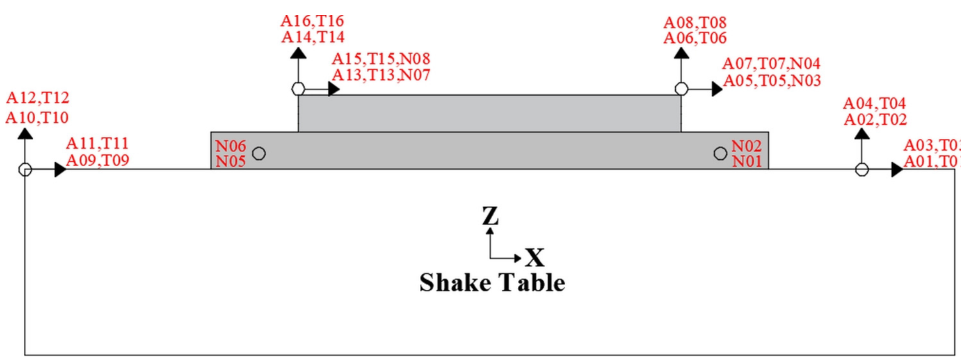

(b) Elevation view

Figure 5-119 Sensors location on Case 1

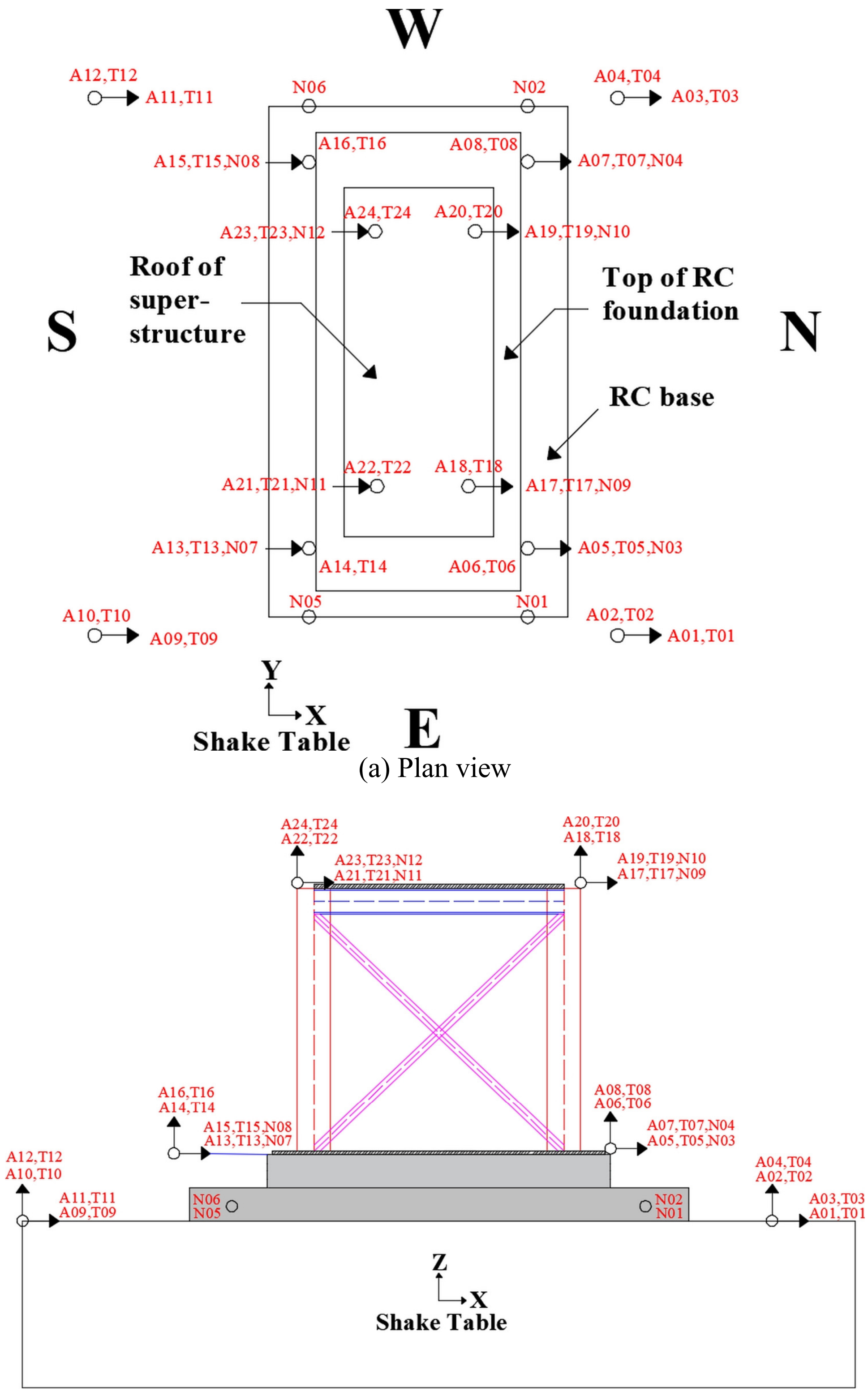

(a) Plan view

(b) Elevation view

Figure 5-120 Sensors location on Case 2

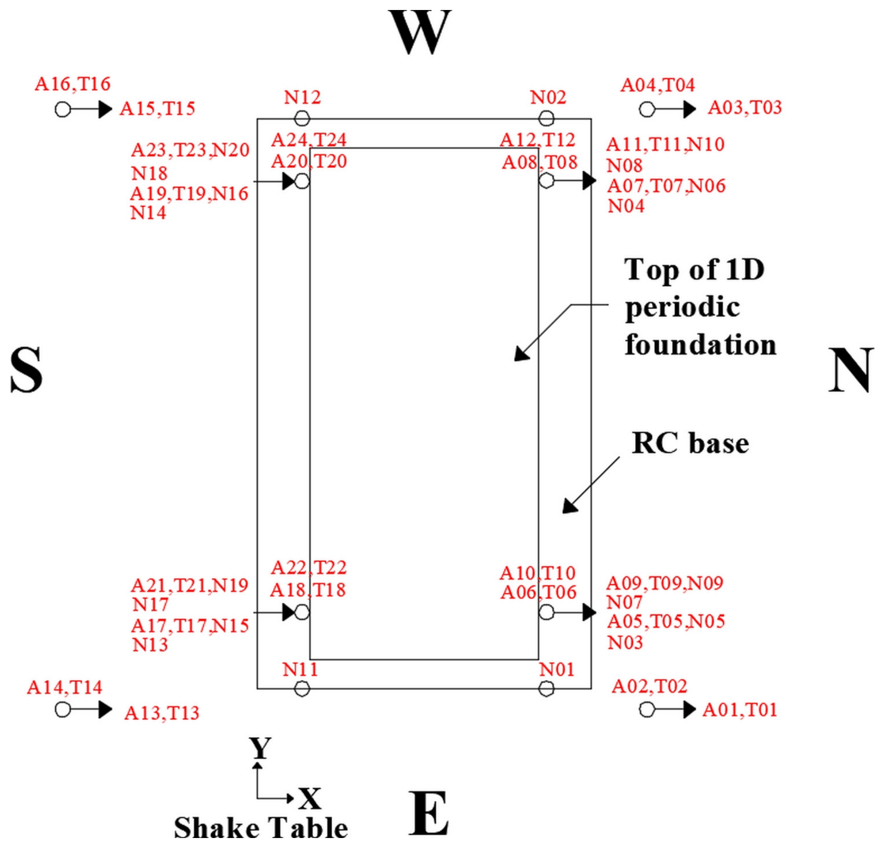

(a) Plan view

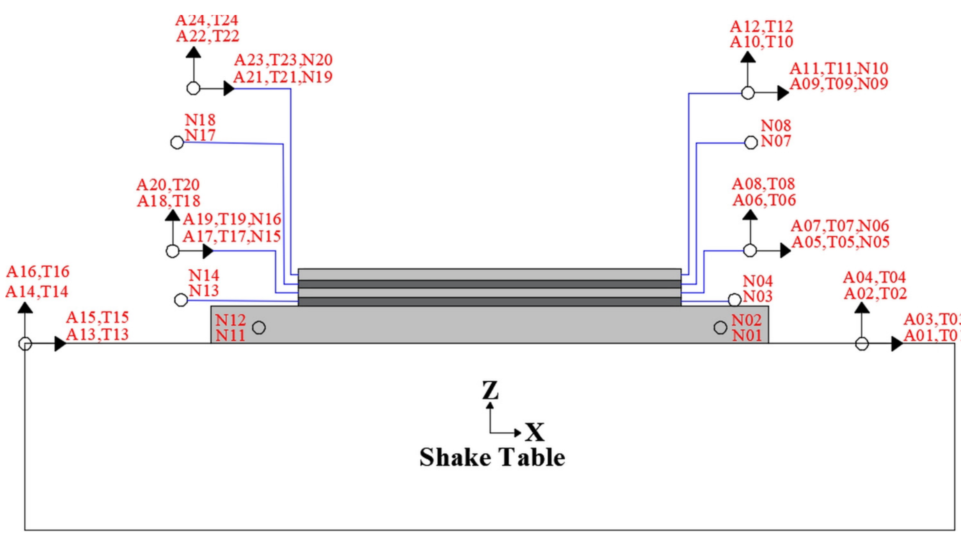

(b) Elevation view

Figure 5-121 Sensors location on Case 3

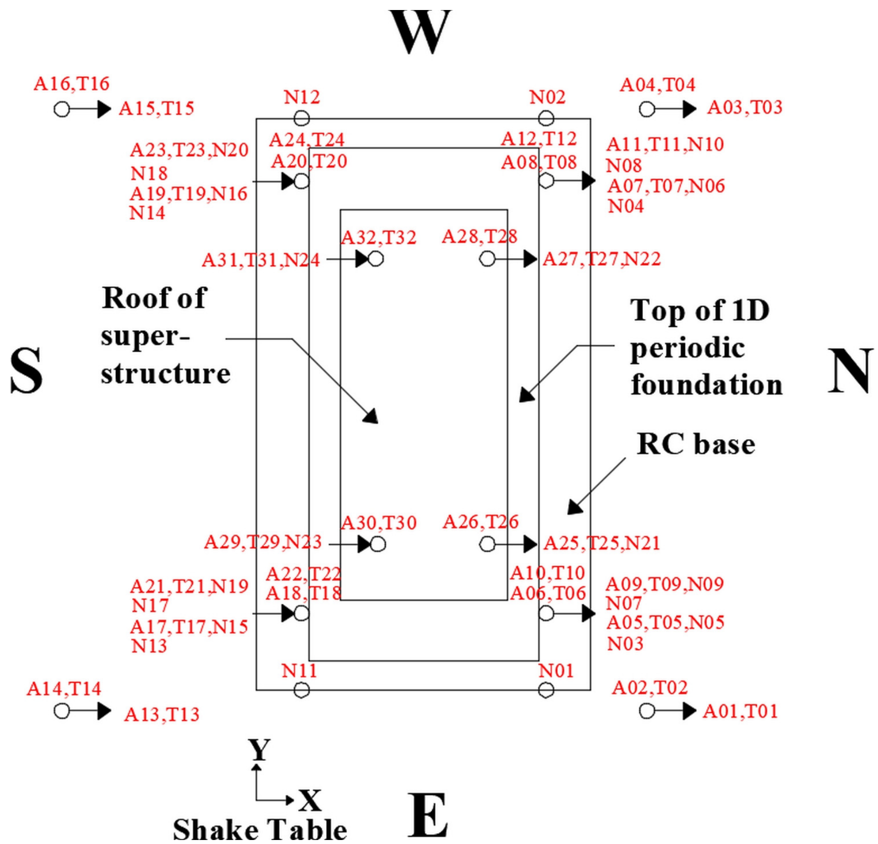

(a) Plan view

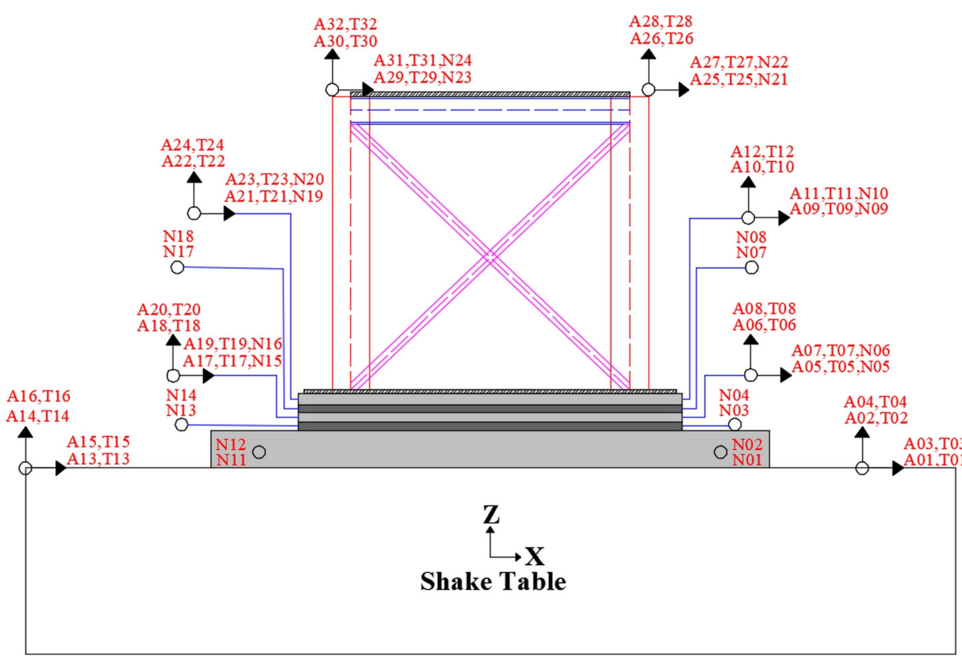

(b) Elevation view

Figure 5-122 Sensors location on Case 4

Figure 5-123 shows the schematic plan and elevation views of the location of sensors on the Case 5 specimen. In the 3D periodic foundation test, a more comprehensive observation was conducted. Accelerometers and temposonics were placed at each corner of the shake table, RC base, and the top of the 3D periodic foundation. In this way, any separation of the RC base from the shake table can be inspected from the sensors. Moreover, two additional accelerometers (A41 and A42) were placed at the middle of the top surface of the RC base inside each opening (between the blocks of the unit cells) to inspect vertical separation in the middle portion of the RC base. In addition to accelerometers and temposonics, NDI markers were placed at each corner of the RC base, the polyurethane layers, and the top of the 3D periodic foundation.

Figure 5-124 shows the location of sensors for Case 6. In general, the location of sensors on the shake table and the 3D periodic foundation are similar to those of Case 5. For the superstructure in Case 6, two accelerometers, two temposonics and one NDI marker were placed at each corner of each level of the steel floor and the roof of the superstructure. The placement of the sensors on the steel floor was to inspect any separation between the superstructure and the 3D periodic foundation.

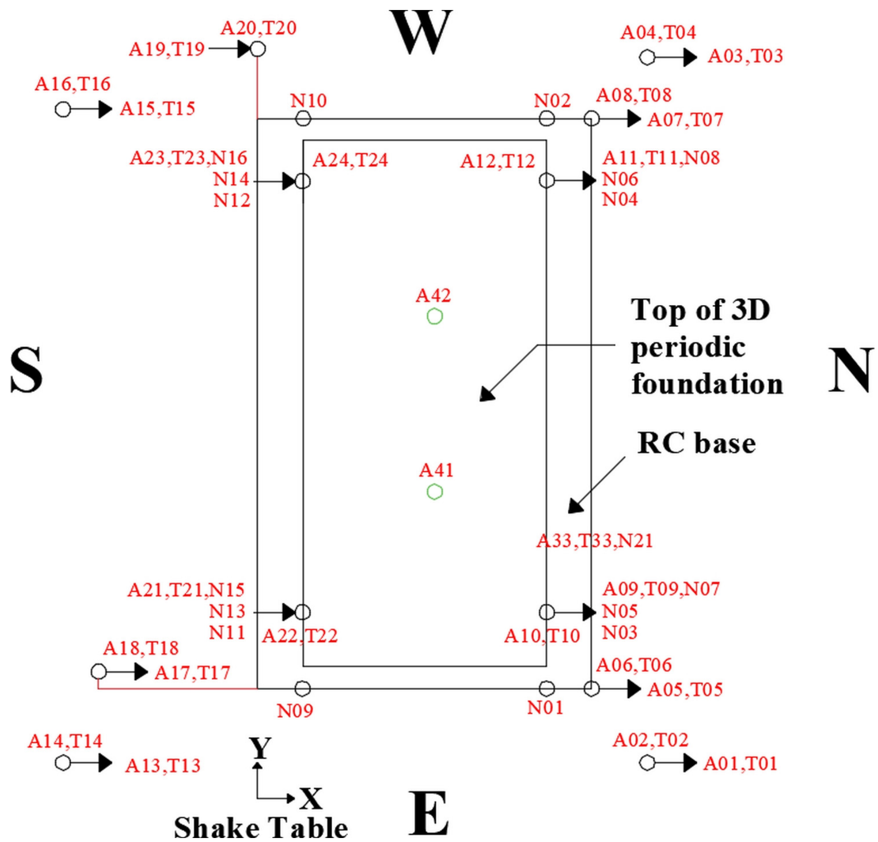

(a) Plan view

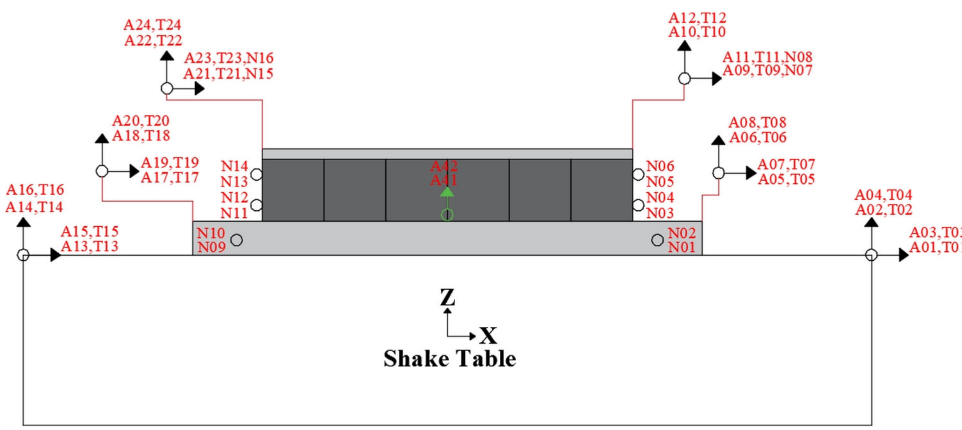

(b) Elevation view

Figure 5-123 Sensors location on Case 5

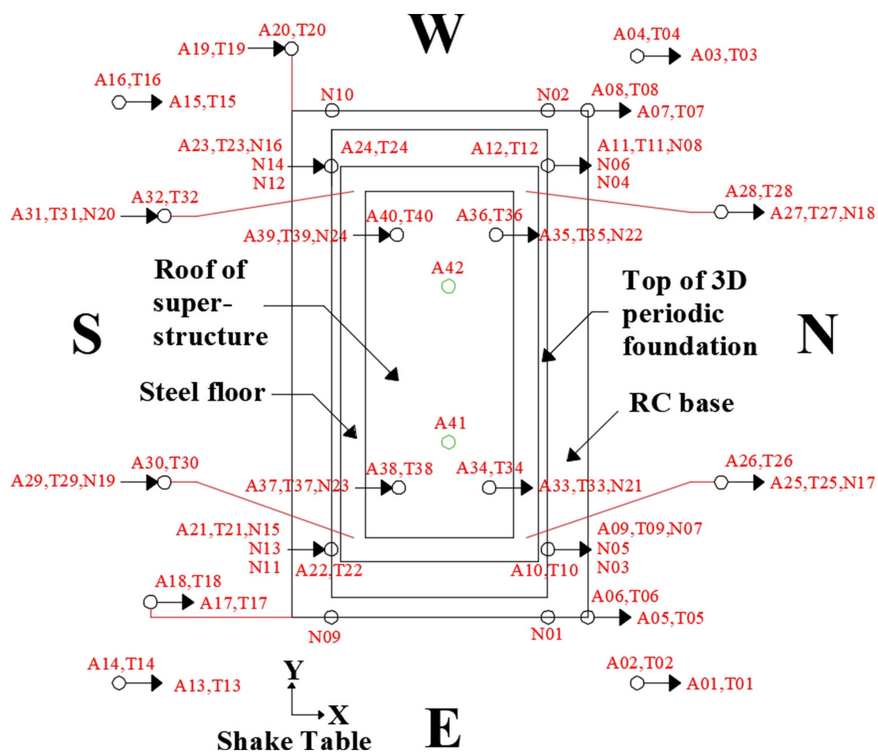

(a) Plan view

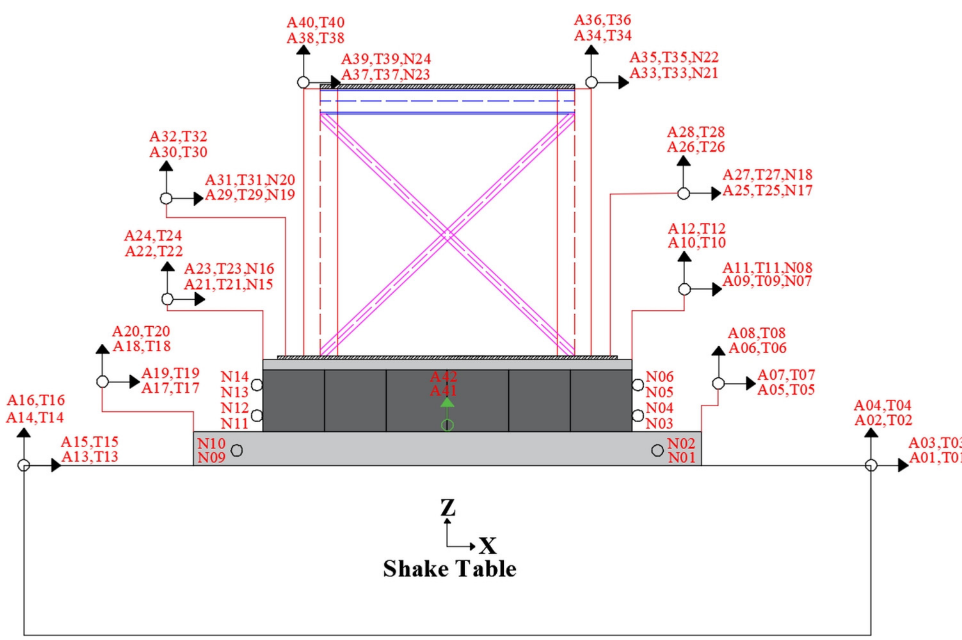

(b) Elevation view

Figure 5-124 Sensors location on Case 6

To provide a better understanding of the schematic sensors layout, pictures of a representative number of the actual sensors attached to Cases 5 and 6 are shown in Figure

5-125. Figure 5-125(a) shows the horizontal (A05) and vertical (A06) accelerometers placed at the northeast corner of the top of the RC base. Each accelerometer was placed on an angle section steel that was glued to the RC base using epoxy. Figure 5-125(b) shows the accelerometers connected to the top of the periodic foundation and the steel floor of the superstructure at the southwest corner. Figure 5-125(c) shows the horizontal (A37) and vertical (A38) accelerometers placed on the roof of the superstructure at the northwest corner. Figure 5-125(d) shows vertical temposonics at the southwest corner that were attached to the reference frames and connected to the copper rods that were extended out from the points of measurement (shake table [T16], RC base [T20], top of periodic foundation [T24], and steel floor of superstructure [T32]). Figure 5-125(e) shows the vertical accelerometers placed at the middle top surface of the RC base inside the opening or in between the unit cell blocks.

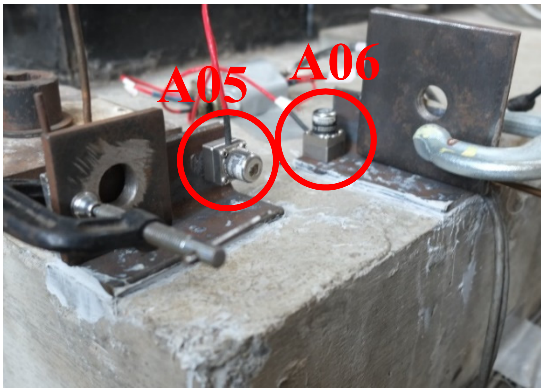

(a) Accelerometers at the northeast corner of the RC base

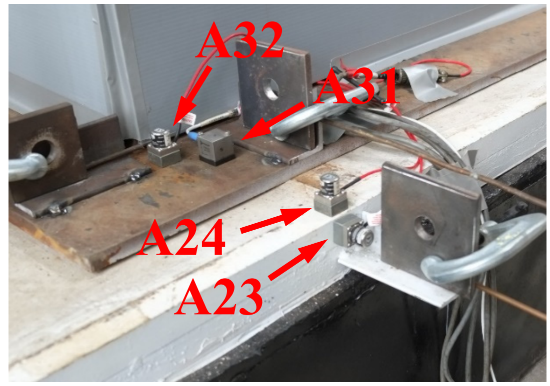

(b) Accelerometers at the southwest corner of the top of the periodic foundation and the steel floor of the superstructure

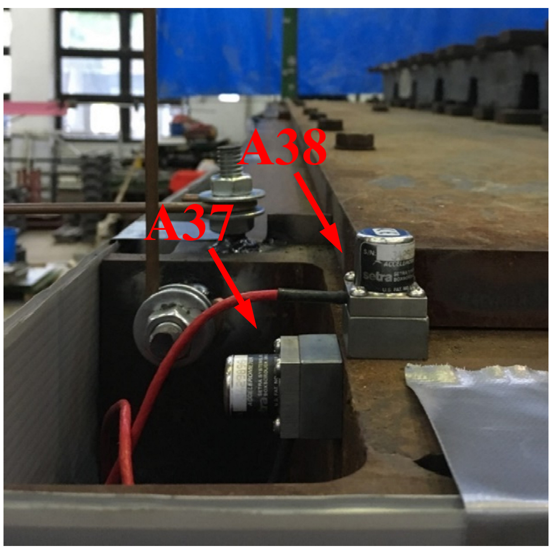

(c) Accelerometers at the northwest corner of the top of the superstructure

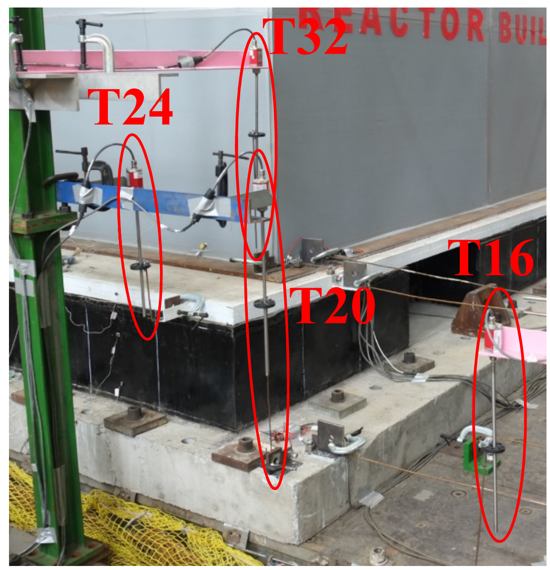

(d) Vertical temposonics at the southwest corner (minus T40 at the roof of the superstructure)

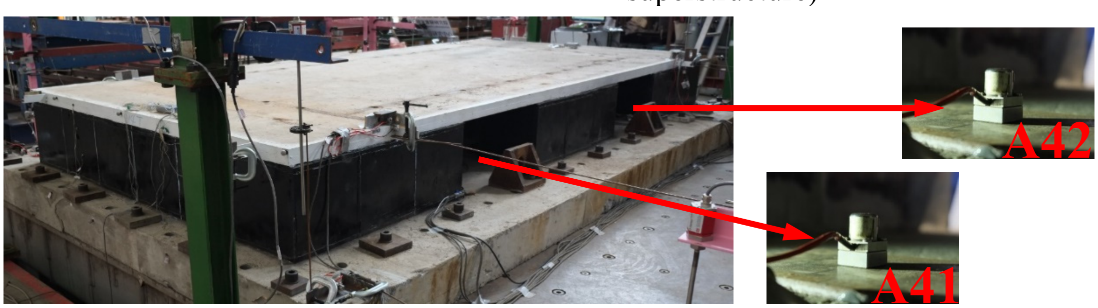

(e) A vertical accelerometer inside each opening (between the blocks of the unit cells)

Figure 5-125 Representative sensors location on Cases 5 and 6

5.4.2 Details of instrumentation

As explained in Subsection 5.4.1, three types of sensors were used to capture the response of the structural systems. Figure 5-126(a) shows the accelerometer that was used in the tests. This accelerometer is the product of Setra System, Inc., Model 141 [78]. According to the manufacturer's information, this model is a linear accelerometer that produces a high-level instantaneous DC output signal proportional to sensed accelerations (ranging from static acceleration up to 3000 Hz). The bottom side of the accelerometer cube is a strong magnet which allows the sensor to easily and firmly attach to any steel surface. Figure 5-126(b) shows two accelerometers at one corner at the top of the superstructure.

Traditional displacement measurement using displacement transducers were used in the tests. The displacement transducer type is called temposonic by MTS sensors. The temposonic senses displacement via a sonic-strain pulse which comes from momentary interaction between two magnetic fields (time-based magnetostrictive position sensing). One magnetic field comes from a moveable magnetic ring, and the other comes from an interrogation pulse applied along the waveguide [79]. The principle of magnetostrictive position sensing is shown in Figure 5-127. Figure 5-128 shows the setup of two temposonics at one corner of the roof of the superstructure. Each temposonic was attached to the reference frame. A magnetic ring fixed at the end of a copper rod was extended out from the measurement point on the specimen. The magnetic ring was inserted and positioned in the middle of the temposonic rod. The temposonic device itself is very accurate in measuring the absolute displacement of the structure. However, a small vibration on the reference frame and copper rod might contribute to some noise on the displacement record.

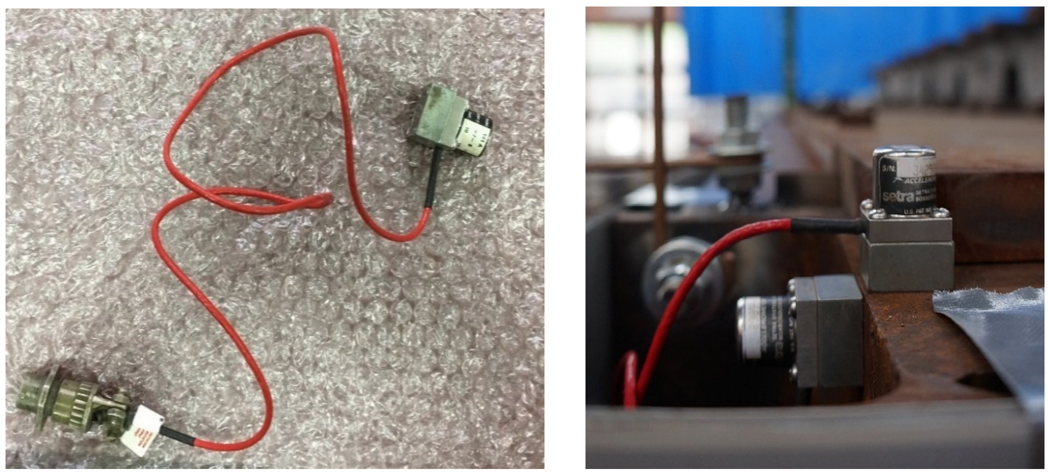

(a) (b)

Figure 5-126 (a) Single accelerometer; (b) accelerometers attached to superstructure

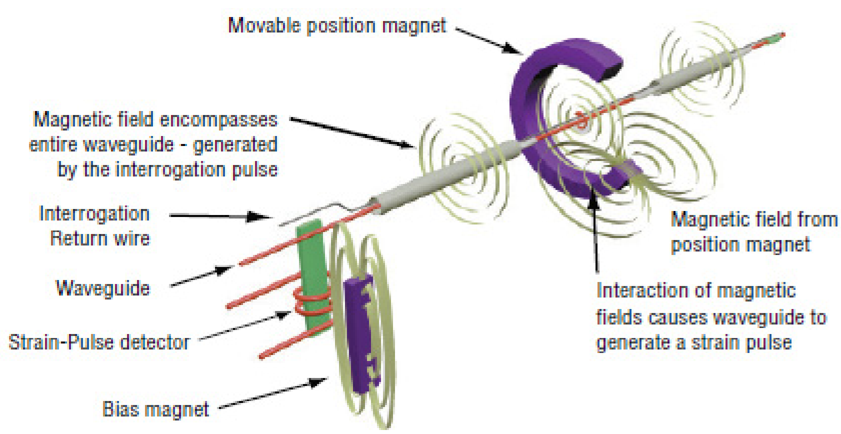

Figure 5-127 Magnetostrictive position sensing principle [79]

Figure 5-128 Temposonics on superstructure

In addition to temposonic, an optical measurement system (Optotrak Certus) by NDI [80] was used to measure displacement. The Optotrak Certus camera can track the movement of markers in three-dimensional space with a high sampling rate and excellent accuracy. The maximum sampling rate of overall markers that can be handled by a single camera is 4400 Hz. Moreover, all markers need to be visible on the camera. Since the markers were distributed on all four corners of the specimen, two Optotrak Certus cameras were used to capture the markers. The camera on the east side was set to capture the markers placed on the east side while that on the west side was set to capture the markers placed on the west side. Figure 5-129(a) shows an Optotrak Certus camera with three optical lenses. The markers attached to the 3D periodic foundation and the superstructure are shown in Figure 5-129(b) and Figure 5-129(c). The marker is very lightweight and can be easily attached to any solid surface using double-sided tape.

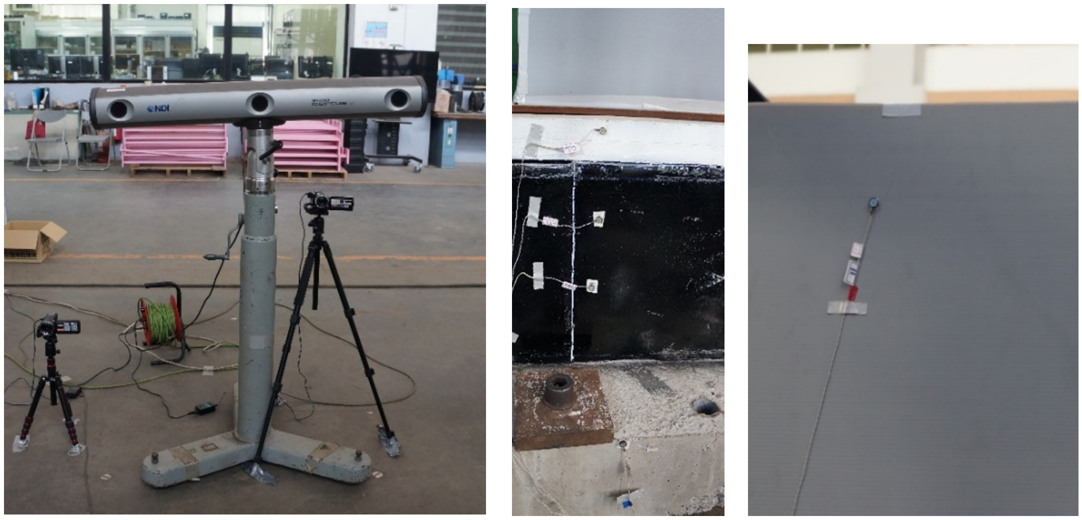

(a) (b) (c)

Figure 5-129 (a) Optotrak Certus camera; (b) Markers on 3D periodic foundation; (c) Marker on superstructure

5.4.3 Excitation types

For the tests of Cases 1, 3, and 5, the foundations were subjected to frequency sweeping tests in three directions; i.e., horizontal (X), vertical (Z), and torsional (Rz). The frequency sweeping tests were conducted to verify the existence of frequency band gaps on the 1D and 3D periodic foundations. In the frequency sweeping tests, the input wave was a continuous series of sine waves starting from 1 Hz to 50 Hz with an increment of 0.5 Hz. The amplitude of the input wave was kept constant throughout excitation. From the frequency sweeping tests, the acceleration recorded at the top of the foundations would be compared to that at the shake table. The frequency regions in which the acceleration response at the top of the periodic foundations is lower than the acceleration on the shake table correspond to the attenuation zones or frequency band gaps. For the purpose of comparison, the Case 1 specimen is also subjected to the same scanning frequency tests. Table 5-19 shows the details of the excitation types for Cases 1, 3 and 5. From the results of these three separate tests, frequency band gaps corresponding to horizontal (S-Wave), vertical (P-Wave), and torsional waves can be obtained.

Table 5-19 Excitations for frequency sweeping tests of Cases 1, 3, and 5

Excitation type	**Control Algorithm**	**Input Direction**	**Freq (Hz)**	**Amplitude (g)**	**Duration (sec)**
Frequency Sweeping	Acc	Uniaxial (X)	1-50	0.1	90
		Uniaxial (Z)	1-50	0.1	90
		Torsional (Rz)	1-50	**Amplitude (degree/sec^2)**	90
				25	

Four types of tests were conducted on Cases 2, 4, and 6, i.e., white noise, frequency sweeping, seismic, and harmonic tests. Details on each type of tests are presented in Table 5-20 to Table 5-24.

In the first type of tests, each of the structural systems was subjected to white noise in the horizontal (X) and vertical (Z) directions and the torsional (Rz) mode. White noise is a random wave with uniform main frequency content ranging from 1 Hz to 50 Hz. When a structural system is subjected to white noise in a particular direction, the response will show amplification at a specific frequency. This specific frequency is the natural frequency of the structural system in the particular direction. A white noise test is a very reliable approach in dynamic tests for obtaining fundamental natural frequencies of a structure.

Table 5-20 Excitations for white noise tests of Cases 2, 4, and 6

Excitation Type	**Control Algorithm**	**Input Direction**	**Freq (Hz)**	**Amplitude (g)**	**Duration (sec)**
White Noise	Acc	Uniaxial (X)	1-50	0.1	60
		Uniaxial (Z)	1-50	0.1	60
		Torsional (Rz)	1-50	**Amplitude (degree/sec^2)**	60
				25	

The second type of tests conducted on the structural systems was the frequency sweeping tests. These tests were conducted to investigate the frequency band gaps of the periodic foundation structural systems. These tests were to confirm that the presence of the superstructure would shift the frequency band gaps of the 1D and 3D periodic foundations to a lower frequency.

Table 5-21 Excitations for frequency sweeping tests of Cases 2, 4, and 6

<table>
<tr><th>Input Excitation</th><th>Control Algorithm</th><th>Input Direction</th><th>Freq (Hz)</th><th>Amplitude (g)</th><th>Duration (sec)</th></tr>
<tr><td rowspan="4">Frequency Sweep</td><td rowspan="4">Acc</td><td>Uniaxial (X)</td><td>1-50</td><td>0.1</td><td>90</td></tr>
<tr><td>Uniaxial (Z)</td><td>1-50</td><td>0.1</td><td>90</td></tr>
<tr><td rowspan="2">Torsional (Rz)</td><td rowspan="2">1-50</td><td>Amplitude (degree/sec^2)</td><td rowspan="2">90</td></tr>
<tr><td>25</td></tr>
</table>

One of the main purposes of this study is to evaluate the seismic performance of the periodic foundation structural systems subjected to real seismic excitation. Therefore, the third type of tests was the seismic wave tests. Seismograms from eight regular far-field earthquakes, obtained from the PEER ground motion database [81], with various main frequency contents relative to theoretical frequency band gaps were selected as the input motions. The selected earthquakes are listed in the first column of Table 5-22. As indicated in Table 5-22, all of the earthquakes had their peak ground acceleration (PGA) scaled to 0.4 g. The tests were conducted in each of the horizontal and vertical directions separately. Time scale was applied on each of the seismic excitations. Note that out of eight earthquake records, four of the records, Anza, Bishop, Gilroy, and Oroville, have most of their main frequency contents located inside the S-Wave theoretical frequency band gaps. To investigate the percentage of response reduction or filtering effect by frequency band gaps, the Case 4 and 6 specimens were also subjected to these four earthquakes with their PGAs scaled to 1 g. To study the effectiveness of the periodic foundations in isolating the torsional mode, the specimens were subjected to two torsional seismic waves. However, since the real torsional seismograms are very rare, the horizontal component of the Bishop and El Centro Earthquakes were converted into torsional waves with both PGAs scaled to 25 degrees/sec^2.

Table 5-22 Seismic tests excitations for Cases 2, 4, and 6

Earthquake event	**Seismogram Station (accelerometer orientation)**	**Control Algorithm**	**PGA**	**Input Direction**
Anza	Anza Fire Station (360)	Acc	0.4 g	Uniaxial (X)
	Anza Fire Station (UP)			Uniaxial (Z)
Bishop (Round Valley)	McGee Creek Surface (360)	Acc	0.4 g	Uniaxial (X)
	McGee Creek Surface (UP)			Uniaxial (Z)
	Modified from McGee Creek Surface (360)		25 deg/sec^2	Torsional (Rz)
Gilroy	Gilroy Array #3 (58)	Acc	0.4 g	Uniaxial (X)
	Gilroy Array #3 (UP)			Uniaxial (Z)
Oroville	Johnson Ranch (0)	Acc	0.4 g	Uniaxial (X)
	Johnson Ranch (DWN)			Uniaxial (Z)
Loma Prieta	Corralitos (90)	Acc	0.4 g	Uniaxial (X)
Imperial Valley	El Centro Array #9 (180)	Acc	0.4 g	Uniaxial (X)
	Modified from El Centro Array #9 (180)		25 deg/sec^2	Torsional (Rz)
Northridge	LA_UCLA ground (90)	Acc	0.4 g	Uniaxial (X)
San Fernando	Pacoima Dam [upper left abutment] (164)	Acc	0.4 g	Uniaxial (X)

For complete experimental studies, more seismic waves were collected and tested on Case 6. The reason to do the additional tests on Case 6 is because Case 6 possesses wide frequency band gaps in all three directions based on experimental test results. The additional seismic waves were collected and artificially generated to further investigate the response of the 3D periodic foundation structural system under different ranges of the main frequency contents of seismic waves. Table 5-23 shows the list of the additional seismograms used for the shake table tests of Case 6. The Code Anza, Code Imperial Valley, and Code San Fernando are the seismograms modified to have their acceleration response spectra match the NUREG 1.60 [82] acceleration design spectrum. The response spectra of all of the selected seismograms in comparison to the NUREG 1.60 design spectrum are shown in Figure 5-130 and Figure 5-131. These response spectra are plotted using a damping ratio of 5% with the length and time scales applied.

Table 5-23 Additional seismic tests excitations for Case 6

Earthquake event	**Seismogram Station (accelerometer orientation)**	**Control Algorithm**	**PGA**	**Input Direction**
Ancona, Italy	Ancona-Palombina (0)	Acc	0.4 g	Uniaxial (X)
	Ancona-Palombina (UP)			Uniaxial (Z)
Helena Montana	Helena Fed Building (0)	Acc	0.4 g	Uniaxial (X)
	Helena Fed Building (UP)			Uniaxial (Z)
Whittier Narrows	Riverside Airport (180)	Acc	0.4 g	Uniaxial (X)
	Riverside Airport (UP)			Uniaxial (Z)
San Fernando	Santa Anita Dam (3)	Acc	0.4 g	Uniaxial (X)
	Santa Anita Dam (DWN)			Uniaxial (Z)
Kobe, Japan	Amagasaki (0)	Acc	0.4 g	Uniaxial (X)
Anza (modified code compatible)	Anza Fire Station (360)	Acc	0.4 g	Uniaxial (X)
	Anza Fire Station (UP)			Uniaxial (Z)
Imperial Valley (modified code compatible)	El Centro Array #9 (180)	Acc	0.4 g	Uniaxial (X)
	El Centro Array #9 (UP)			Uniaxial (Z)
San Fernando (modified code compatible)	Pacoima Dam [upper left abutment] (164)	Acc	0.4 g	Uniaxial (X)
	Pacoima Dam [upper left abutment] (DWN)			Uniaxial (Z)

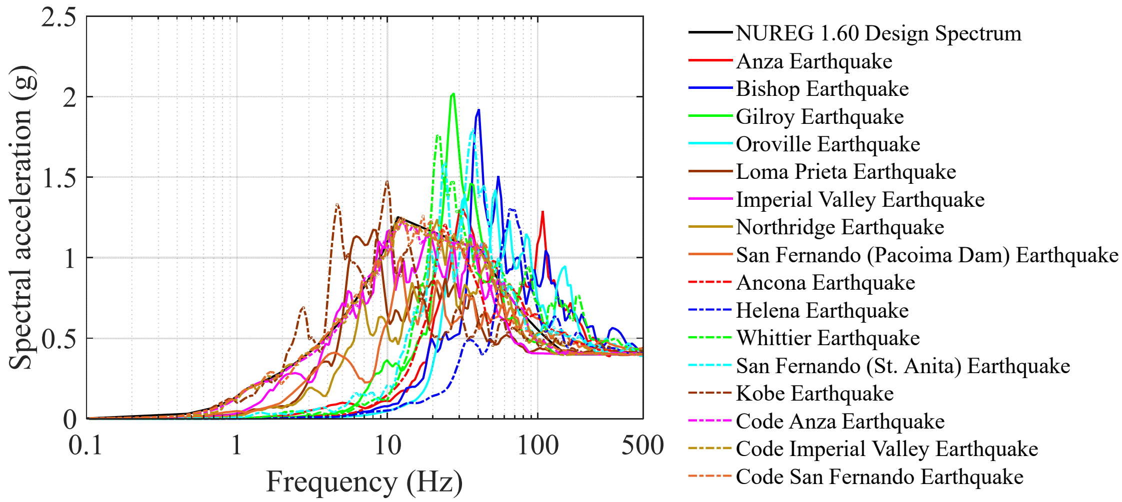

(a) In the horizontal direction

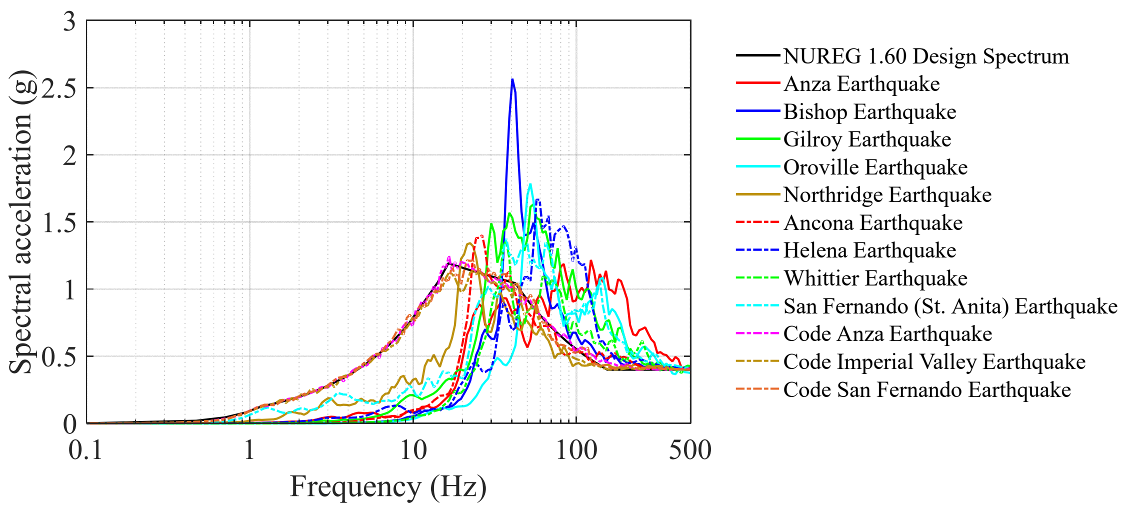

(b) In the vertical direction

Figure 5-130 Acceleration response spectra of input seismograms

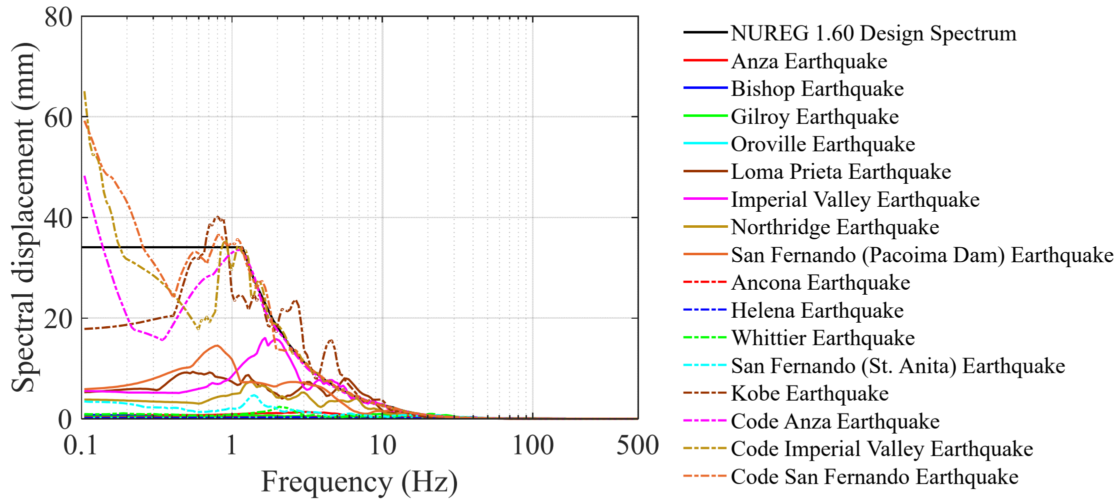

(a) In the horizontal direction

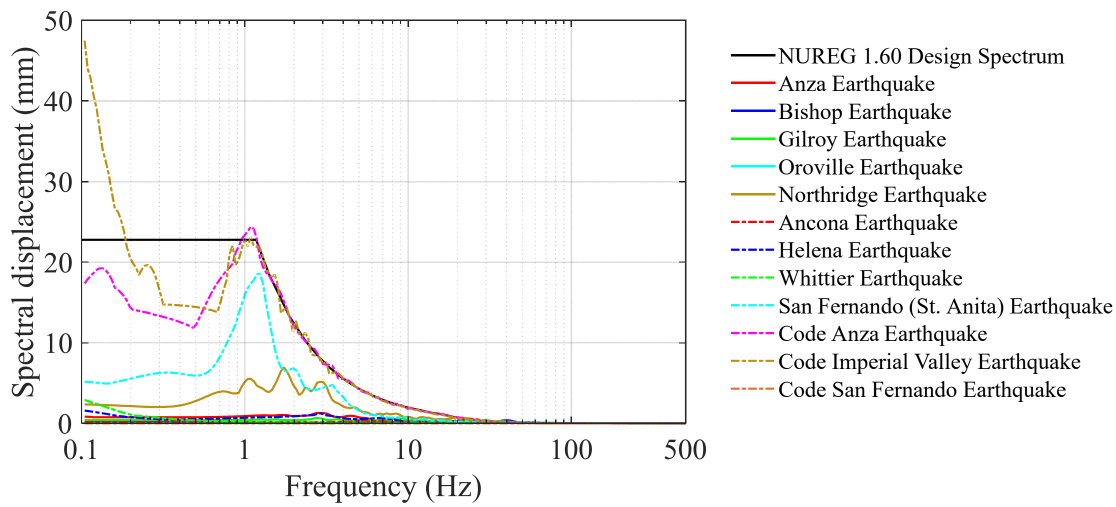

(b) In the vertical direction

Figure 5-131 Displacement response spectra of input seismograms

The fourth type of tests was the harmonic tests. In these tests, the structural systems were subjected to harmonic waves with fixed frequencies. These tests were conducted to confirm the wave attenuation when the frequencies are located inside the frequency band gaps.

Table 5-24 Harmonic tests excitations Cases 2, 4, and 6

Input Excitation	Control Algorithm	Amplitude	Input Direction
Sine Wave 5 Hz	Acc	0.1 g	Uniaxial (X)
Sine Wave 10 Hz			
Sine Wave 20 Hz			
Sine Wave 24 Hz		0.1 g	Uniaxial (Z)
Sine Wave 34 Hz			
Sine Wave 10 Hz		25 deg/sec^2	Torsional (Rz)
Sine Wave 20 Hz			
Sine Wave 30 Hz			

6 EXPERIMENTAL RESULTS

Shake table tests were performed on each of the test cases subjected to various input excitations as described in Subsection 5.4.3. This chapter discusses the response of each of the test cases as measured by the sensors. Among all of the attached sensors, many of them were placed as redundant sensors. Therefore, not all of the recorded data are shown. Only the data with significant information and of special interest are presented and discussed.

6.1 Tests of Foundations

Cases 1, 3, and 5 were subjected to frequency sweeping tests in the horizontal and vertical directions as well as the torsional mode. The frequency sweeping test results of each case in each direction are shown in Figure 6-1 to Figure 6-3. The black curves are the accelerations recorded at the shake table. These curves show the shaking generated by the shake table to the specimen. The real shaking in each test starts from 4 seconds to 94 seconds. The acceleration responses outside the time frame are low ambient waves picked up by the accelerometers. The response at the top of each specimen is shown by the blue curves.

Additional sensors placed on the RC base of the 3D periodic foundation (Case 5) recorded the actual input to the specimen. If the acceleration data recorded on the RC base (dash green curves) are the same as those recorded on the shake table (black curves), that means the specimen is firmly connected to the shake table and no separation occurs. It is observed from Figure 6-1(c) and Figure 6-3(c) that both data sets are very similar for the shaking in the horizontal direction and the torsional mode. For the shaking in the vertical direction [see Figure 6-2(c)], however, a very slight difference in the amplitude between the two acceleration records is observed. Figure 6-4 and Figure 6-5 show the enlarged portion of the acceleration response between the shake table and the RC base for the horizontal and vertical shaking, respectively. It is concluded that slight separation occurs in the vertical direction.

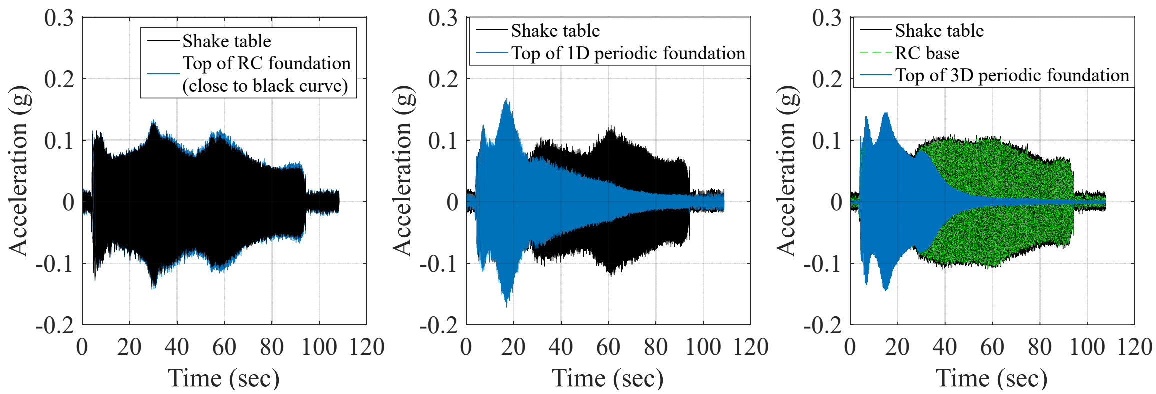

(a) Case 1 (b) Case 3 (c) Case 5

Figure 6-1 Frequency sweeping test results of foundations in the horizontal direction

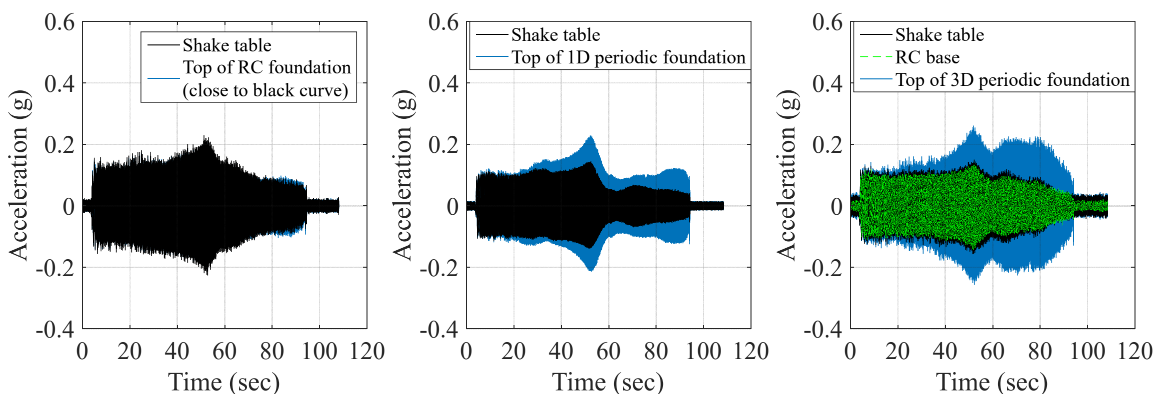

(a) Case 1 (b) Case 3 (c) Case 5

Figure 6-2 Frequency sweeping test results of foundations in the vertical direction

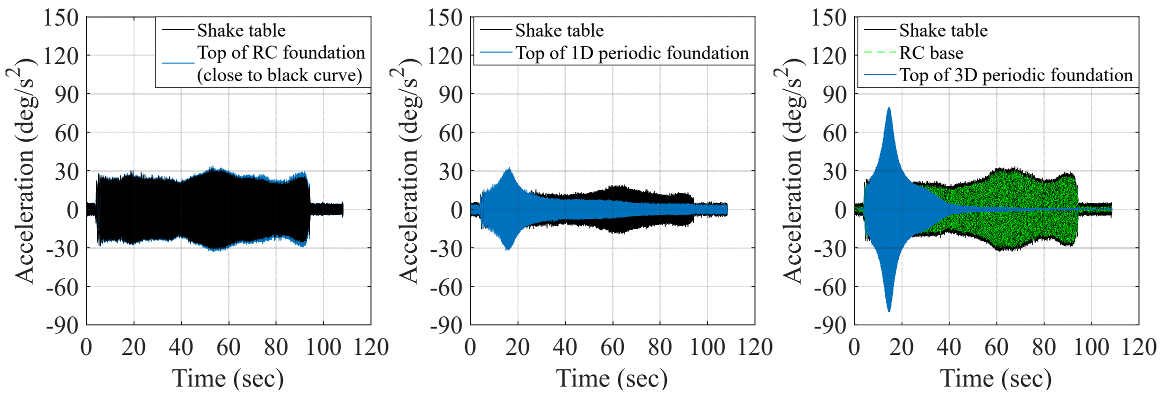

(a) Case 1 (b) Case 3 (c) Case 5

Figure 6-3 Frequency sweeping test results of foundations in the torsional mode

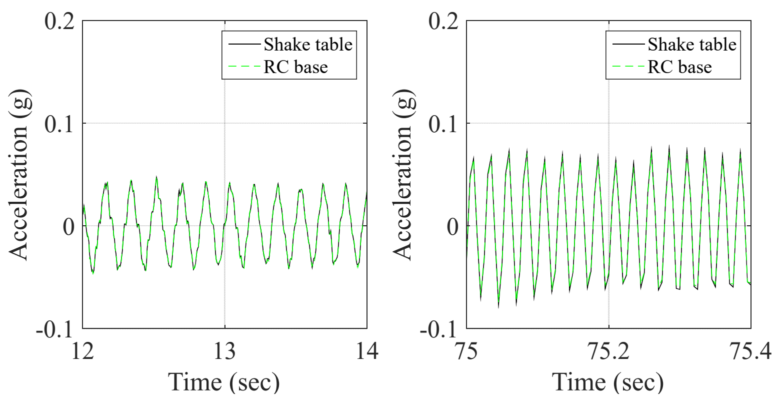

(a) At lower frequency (b) At higher frequency

Figure 6-4 Acceleration records at the shake table and the RC base of Case 5 in the horizontal direction

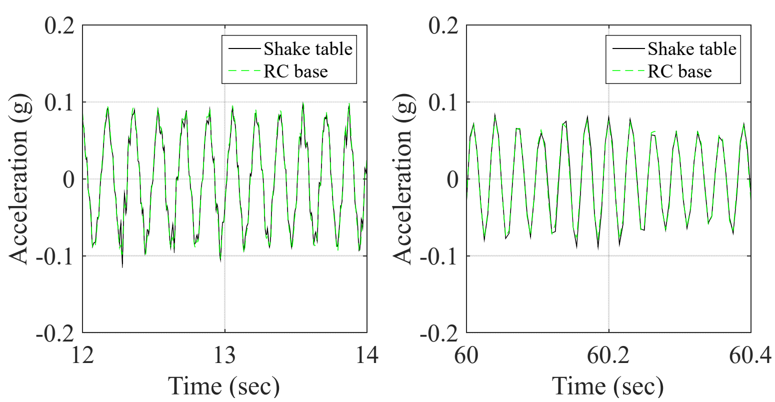

(a) At lower frequency (b) At higher frequency

Figure 6-5 Acceleration records at the shake table and the RC base of Case 5 in the vertical direction

In terms of displacement, the vertical separation is not visible from the temposonic data, as shown in Figure 6-6(b). The absolute displacement data measured at the RC base are very close to those measured at the shake table in terms of amplitude and phase angle, looking as if they are moving together. This is because the vibration at a higher frequency has a minuscule displacement.

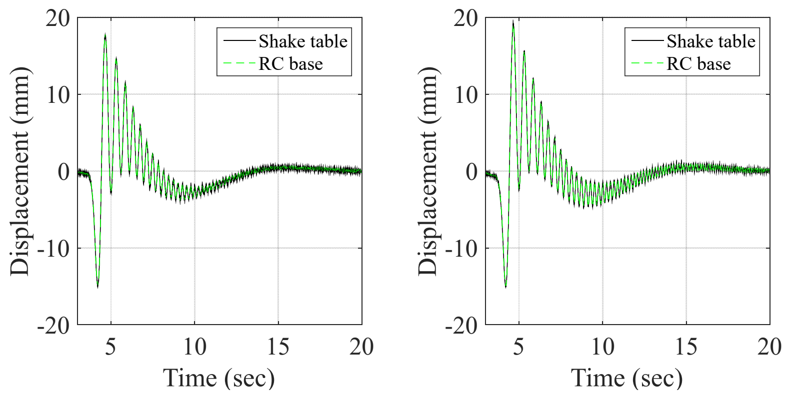

(a) In the horizontal direction (b) In the vertical direction

Figure 6-6 Displacement records at the shake table and the RC base of Case 5

The acceleration records in the time domain were transferred into the frequency domain or Fourier spectra using the Discrete Fourier Transform (Welch method [83]), as shown in Figure 6-7 to Figure 6-9. The Fourier spectra show the distribution of the main frequency content of each acceleration record. It is very evident that the incoming waves were altered by the 1D and 3D periodic foundations as indicated by the Fourier spectra curves in the results recorded at the shake table and the top of the periodic foundations. Meanwhile, the Fourier spectra curves of Case 1 show a similar frequency distribution of the accelerations recorded at both the shake table and the top of the RC foundation. This means that the RC foundation is very rigid and firmly attached to the shake table and the input waves within this frequency region pass though the relatively homogenous material.

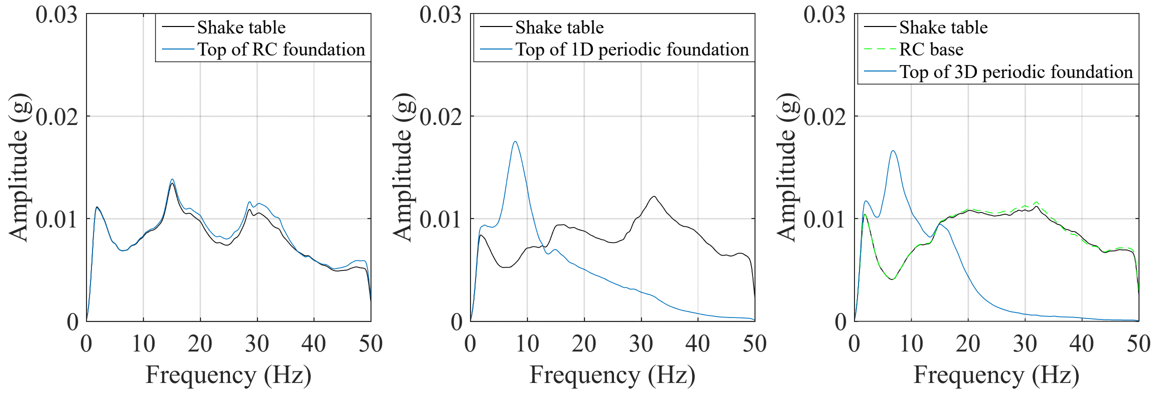

(a) Case 1 (b) Case 3 (c) Case 5

Figure 6-7 Fourier spectra of frequency sweeping test results of foundations in the horizontal direction

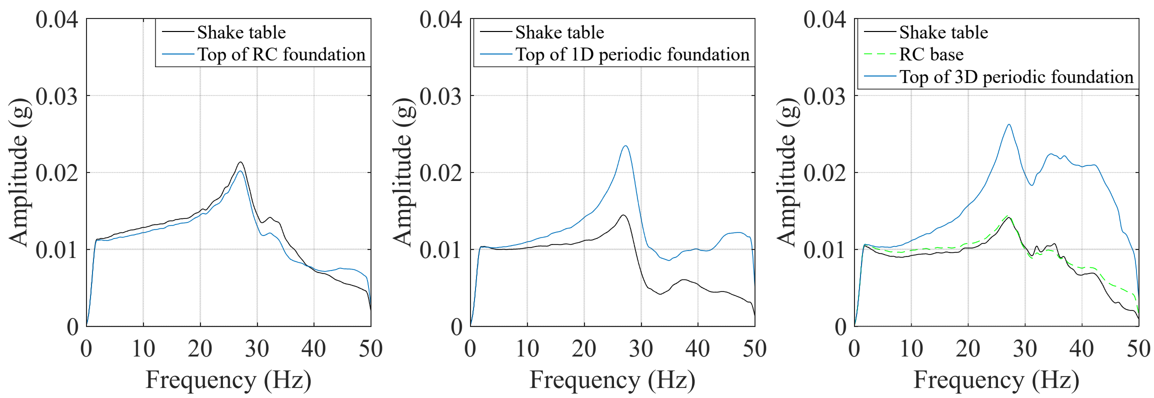

(a) Case 1 (b) Case 3 (c) Case 5

Figure 6-8 Fourier spectra of frequency sweeping test results of foundations in the vertical direction

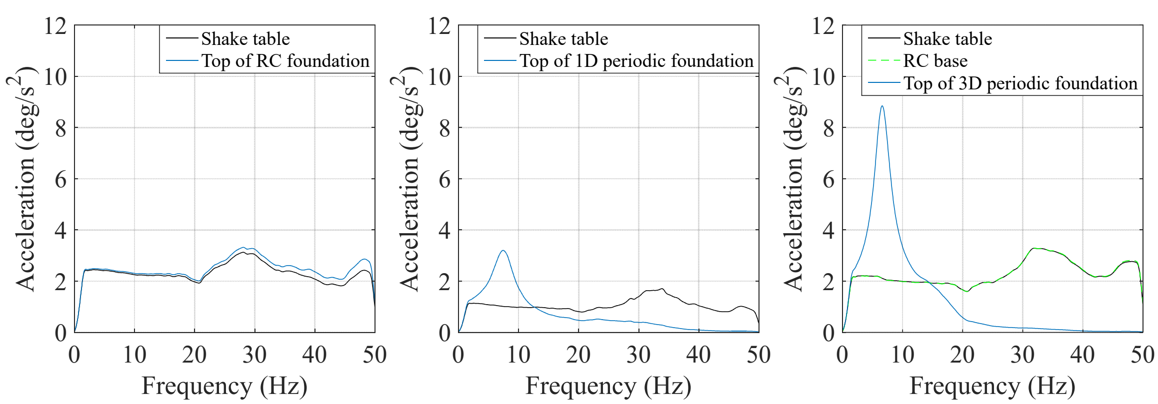

(a) Case 1 (b) Case 3 (c) Case 5

Figure 6-9 Fourier spectra of frequency sweeping test results of foundations in the torsional mode

FRF curves were subsequently generated from the Fourier spectra by following Eq. (6-1),

$$\text{FRF} = 20\log\left(\frac{a_{out}}{a_{in}}\right), \tag{6-1}$$

where a_{out} is the amplitude of output acceleration in the frequency domain measured at the location of interest, in these cases the top of the foundations, and a_{in} is the amplitude of input acceleration in the frequency domain. For Cases 1 and 3, their a_{in} uses the results recorded from the shake table, while for Case 5, it uses the results recorded from the RC base.

Figure 6-10 to Figure 6-12 show the FRF curves for each of the foundations in the horizontal and vertical directions as well as the torsional mode. The FRF curves of the RC foundation show mainly straight lines as there was no amplification nor reduction in the input waves. The attenuation zone of the 1D periodic foundation in the horizontal direction starts from 12.74–50 Hz for shaking in that direction. This attenuation zone overlaps the theoretical frequency band gaps of the S-Wave (shown in Figure 5-36) in the range of 0–50 Hz. For the shaking in the vertical direction, no attenuation zone can be found in the range of 0–50 Hz. This result also agrees with the theoretical frequency band gaps of the P-Wave. The attenuation zone in the torsional mode is found starting from 12.65–50 Hz, which is very similar to the result in the horizontal direction. This is reasonable since torsional movement is also a form of shear. Therefore, the test result is comparable and is observed to be overlapping with the theoretical frequency band gaps of the S-Wave. The tendency of FRF curves of the 3D periodic foundation is similar to that of the 1D periodic foundation. The attenuation zone in the horizontal direction is observed in 14.6–50 Hz, while that in the torsional mode is observed in 14.5–50 Hz. There is no attenuation zone observed in the vertical direction.

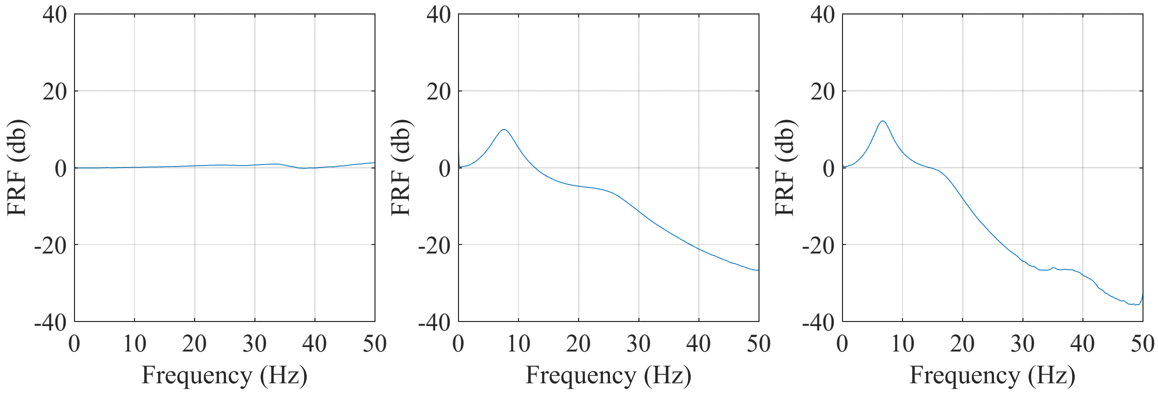

(a) Case 1 (b) Case 3 (c) Case 5

Figure 6-10 Frequency response function of frequency sweeping test results of foundations in the horizontal direction

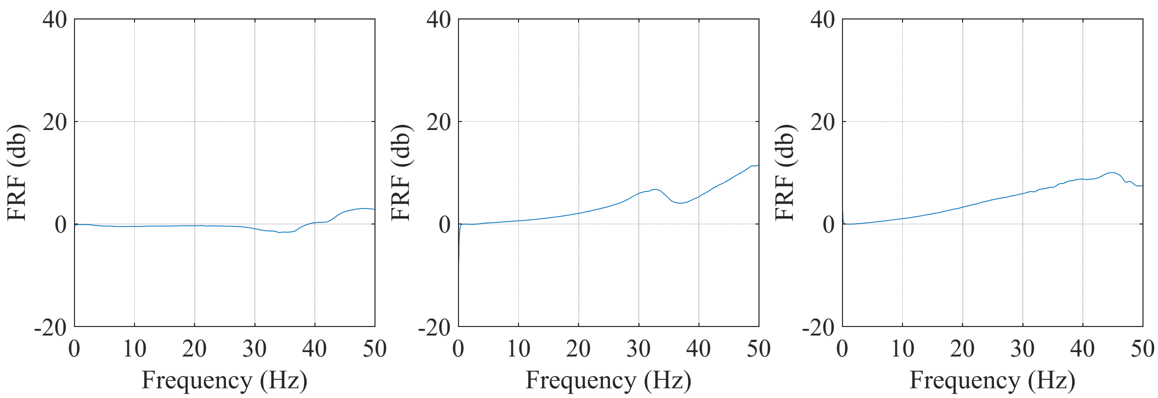

(a) Case 1 (b) Case 3 (c) Case 5

Figure 6-11 Frequency response function of frequency sweeping test results of foundations in the vertical direction

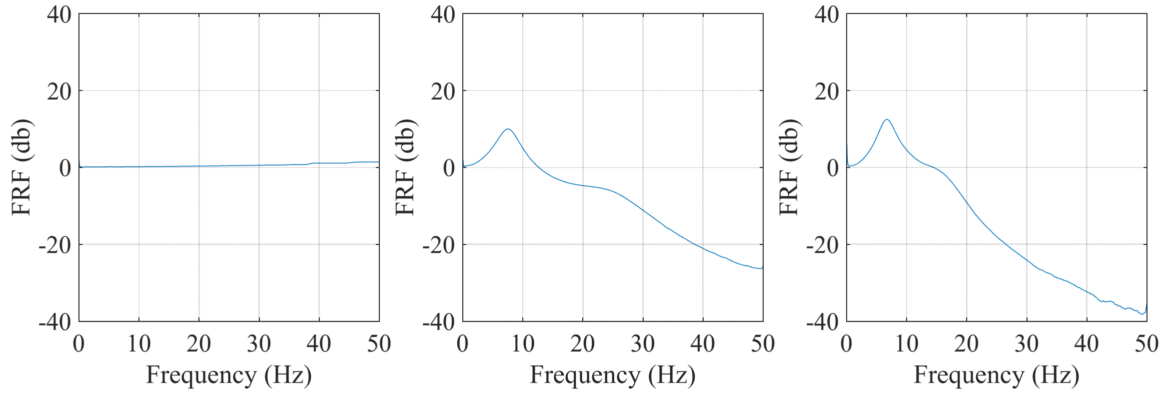

(a) Case 1 (b) Case 3 (c) Case 5

Figure 6-12 Frequency response function of frequency sweeping test results of foundations in the torsional mode

The frequency sweeping test results of the periodic foundations can be used to extract the damping ratios in the periodic foundations. The damping was evaluated using the Half Power Method. Therefore, instead of calculating the FRF based on Eq. (6-1), the dynamic magnification factor or ratio of output to input, a_{out}/a_{in}, was calculated. The frequency response curves for each of the 1D and 3D periodic foundations are shown in Figure 6-13 and Figure 6-14. Taking the bandwidth at $1/\sqrt{22}$, the damping ratio (ξ) can be calculated using Eq. (6-2),

$$\xi = \frac{f_2 - f_1}{f_2 + f_1}. \tag{6-2}$$

The border of the bandwidth frequencies (f_1 and f_2) are shown in the figures. The calculated damping ratios of the 1D periodic foundation based on the test results in the horizontal direction and the torsional mode are 23.18% and 23.28%. The damping ratio cannot be calculated from the results in the vertical direction because the frequency response curve does not have any peak in this frequency range. On the other hand, the calculated damping ratios of the 3D periodic foundation based on the test results in the horizontal and vertical directions as well as the torsional mode are 19.02%, 18.9%, and 19.12%, respectively. From the results, it is concluded that each of the 1D and 3D periodic foundations has a damping ratio of 23.18% and 19%, respectively. These damping ratios are associated with the polyurethane materials because the displacement of the periodic foundations is merely concentrated on the polyurethane layers.

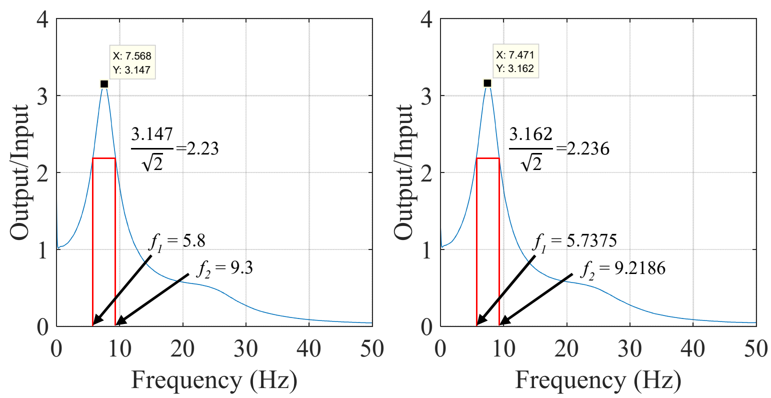

(a) In the horizontal direction (b) In the torsional mode

Figure 6-13 Frequency response curves of Case 3

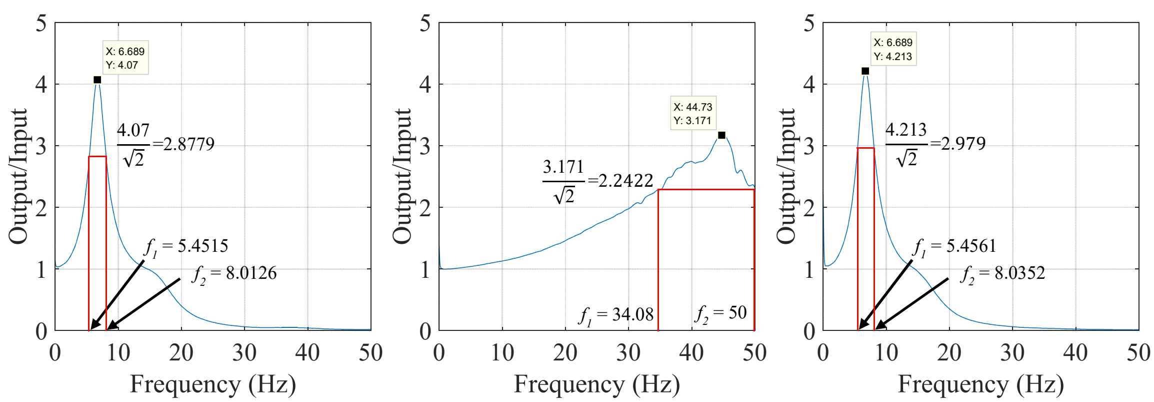

(a) In the horizontal direction (b) In the vertical direction (c) In the torsional mode

Figure 6-14 Frequency response curves of Case 5

6.2 Tests of Structural Systems

This subsection discusses the test results of the structural systems. Dynamic responses of the non-isolated SMR building model (Case 2) compare to those of the 1D and 3D periodic foundations-isolated SMR building model (Cases 4 and 6) are carefully investigated and discussed.

6.2.1 White noise test results

A typical white noise wave was used to shake Cases 2, 4, and 6 in each of the horizontal and vertical directions and the torsional mode. The recorded accelerations at the shake table (black curves), the top of the foundations (blue curves), and the roof of the superstructure (red curves) for each case in each direction are shown in Figure 6-15 to Figure 6-17. The real shaking starts from 4 seconds to 68 seconds. The acceleration responses outside the time frame are low ambient waves picked up by the accelerometers. Additional recorded accelerations at the RC base (dash green curves) and the steel floor of the superstructure (dash purple curves) of the 3D periodic foundation structural system (Case 6) are also presented.

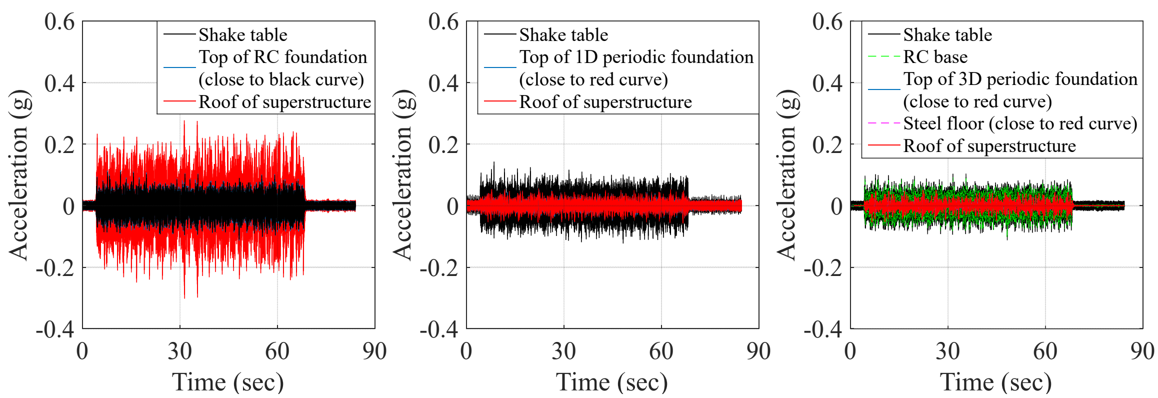

(a) Case 2 (b) Case 4 (c) Case 6

Figure 6-15 White noise test results of structural systems in the horizontal direction

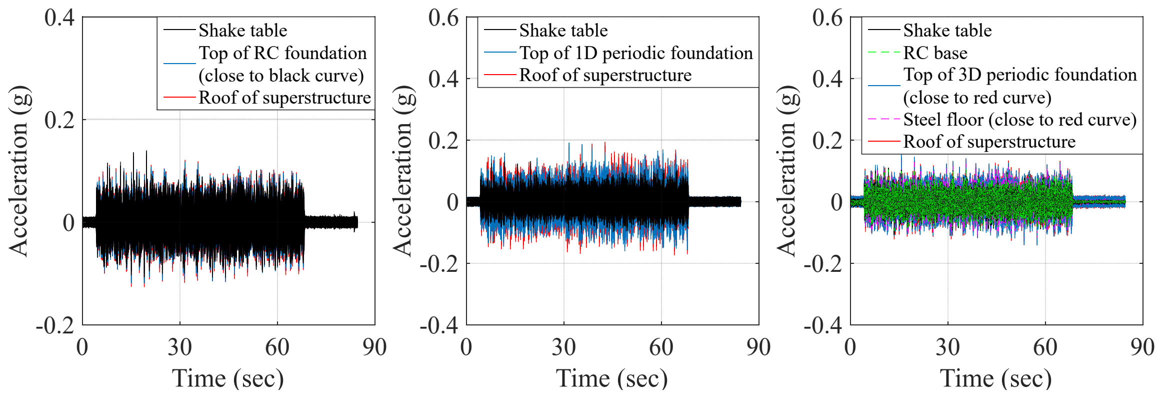

(a) Case 2 (b) Case 4 (c) Case 6

Figure 6-16 White noise test results of structural systems in the vertical direction

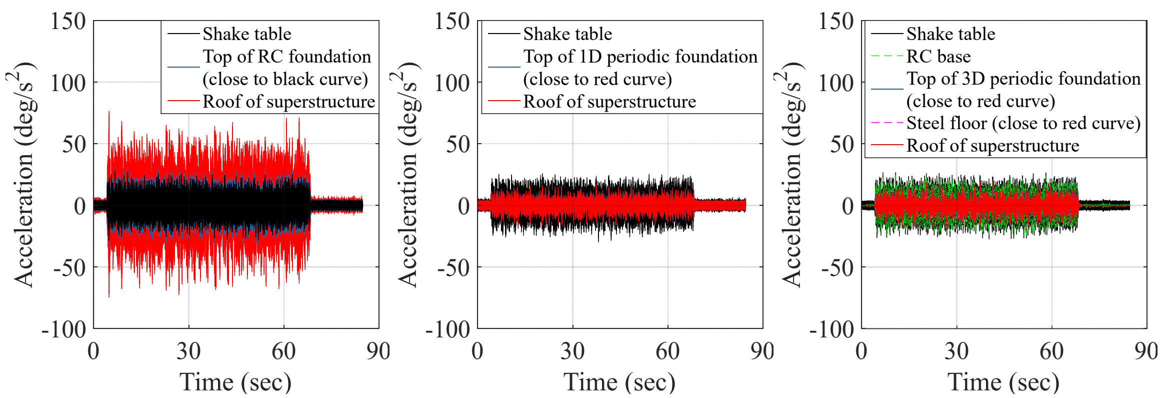

(a) Case 2 (b) Case 4 (c) Case 6

Figure 6-17 White noise test results of structural systems in the torsional mode

Figure 6-18 to Figure 6-20 show the Fourier spectrum of each of the recorded acceleration responses from white noise tests. These curves show the main frequency contents distribution of each recorded acceleration on the structural systems. Both the Fourier spectra and the time series show that there is no horizontal separation between the RC base and the shake table on Case 6 as indicated by the white noise test results in the horizontal direction and the torsional mode. The results also confirm no horizontal separation between the periodic foundation and the superstructure as shown by matching blue and dash purple curves in Figure 6-18(c) and Figure 6-20(c). The response of Case 6 in the vertical direction, however, shows that there is slight separation between the RC base (black curve) and the shake table (dash green curve) at a frequency of around 35-45 Hz. The frequency range of the separation in Case 6 is slightly lower than that in Case 5, which is 40-50 Hz, due to the presence of the superstructure's mass. Moreover, it is observed that a relatively larger vertical separation occurs between the steel frame and the 3D periodic foundation as the acceleration response at the steel floor [dash purple curve in Figure 6-19(b)] is off from that at the top of the 3D periodic foundation [blue curve in Figure 6-19(b)].

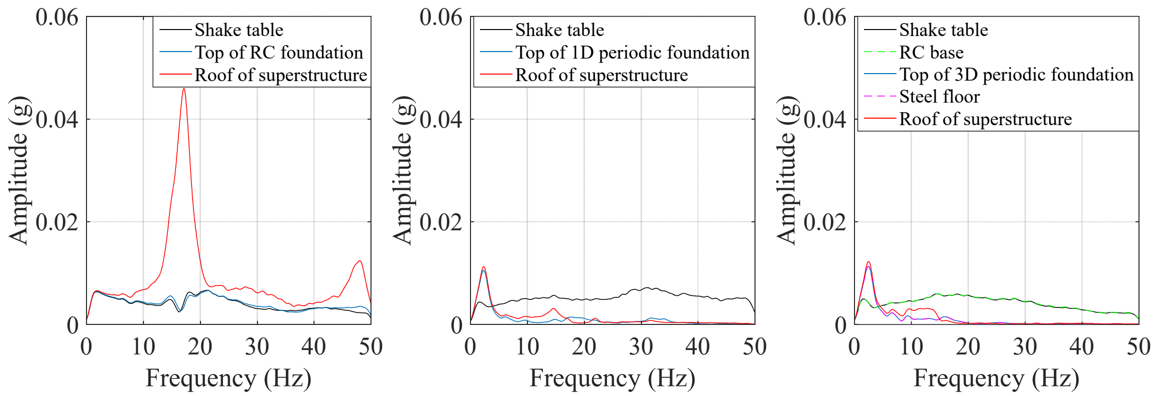

(a) Case 2 (b) Case 4 (c) Case 6

Figure 6-18 Fourier spectra of white noise test results of structural systems in the horizontal direction

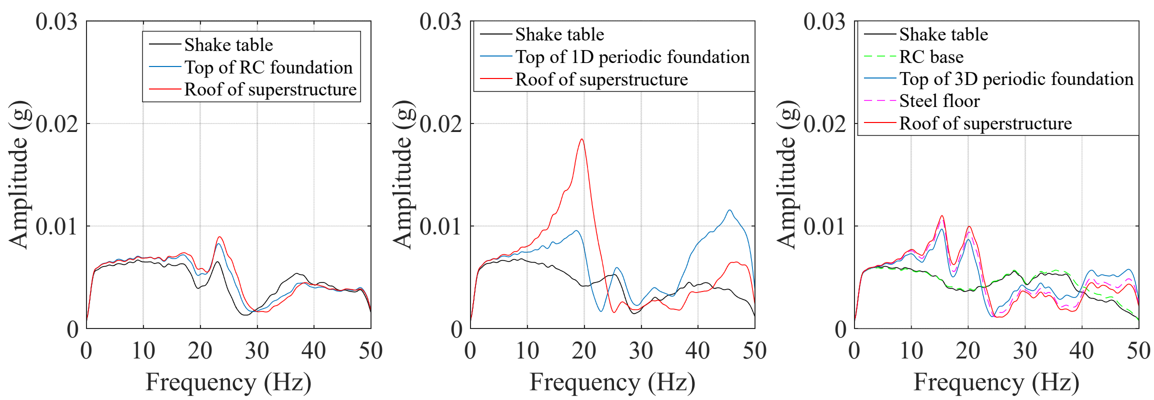

(a) Case 2 (b) Case 4 (c) Case 6

Figure 6-19 Fourier spectra of white noise test results of structural systems in the vertical direction

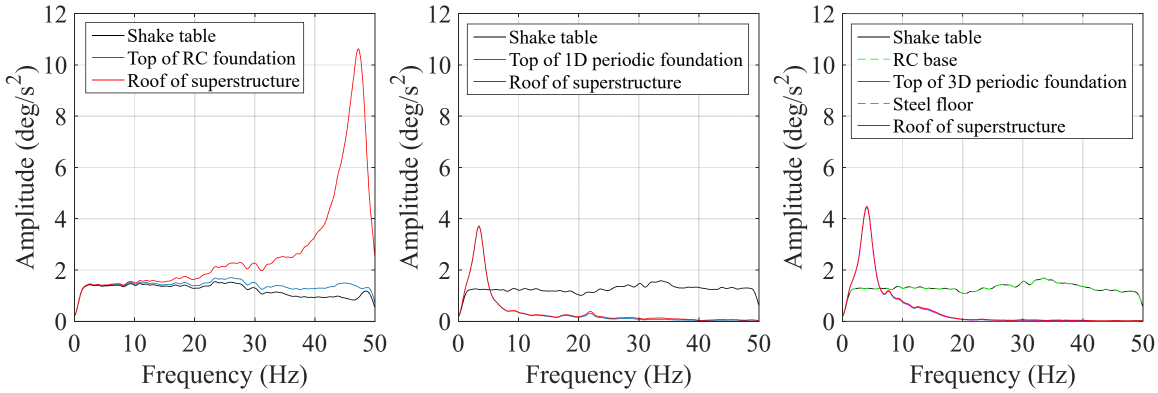

(a) Case 2 (b) Case 4 (c) Case 6

Figure 6-20 Fourier spectra of white noise test results of structural systems in the torsional mode

The vertical separation of the RC base from the shake table is also measured at the middle portion of the RC base (between the unit cell blocks by accelerometers A41 and A42). The acceleration time series, shown in Figure 6-21(a), indicate that a higher acceleration amplitude was recorded at the middle portion of the RC base in comparison to those at the corner of the RC base and the shake table. The Fourier spectra, shown in Figure 6-21(b), show a larger amplitude difference that occurs at a higher frequency (> 30 Hz).

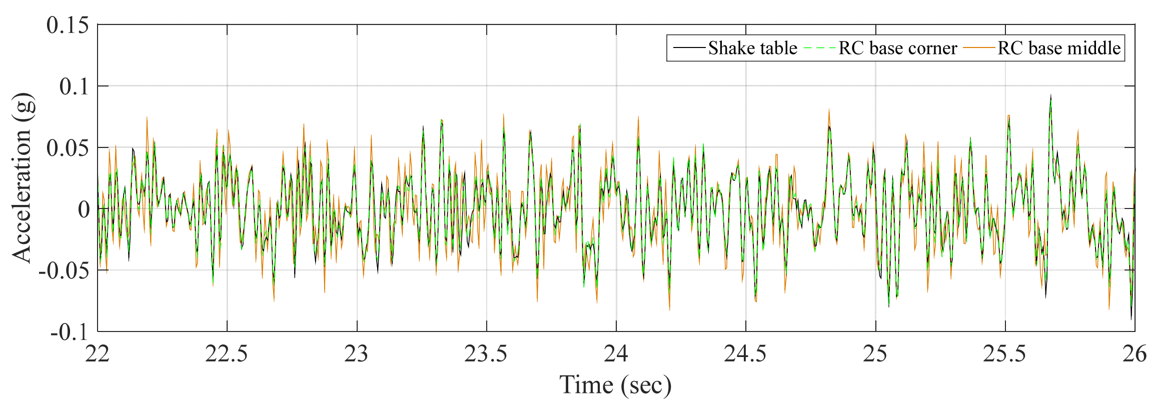

(a) Time series

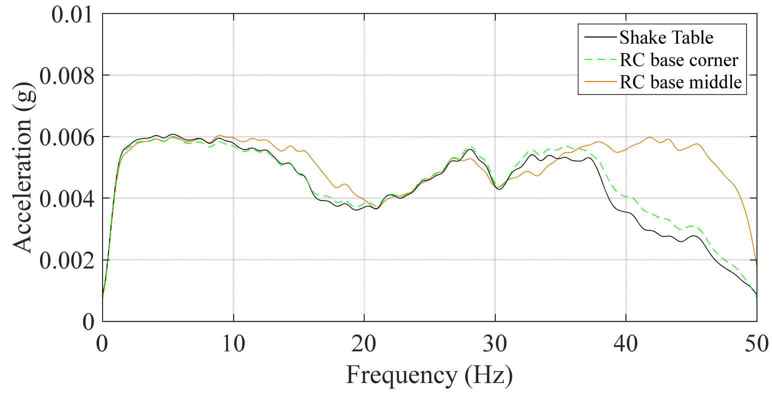

(b) Fourier spectra

Figure 6-21 Vertical acceleration of Case 6 recorded at RC base and shake table subjected to white noise

Since the vertical separation mostly occurs at a high frequency, the displacement records are not able to capture it. Figure 6-22 and Figure 6-23 show no difference in the displacement response between the two critical interfaces (between the shake table and the RC base and between the top of the 3D periodic foundation and the steel floor) in both horizontal and vertical directions.

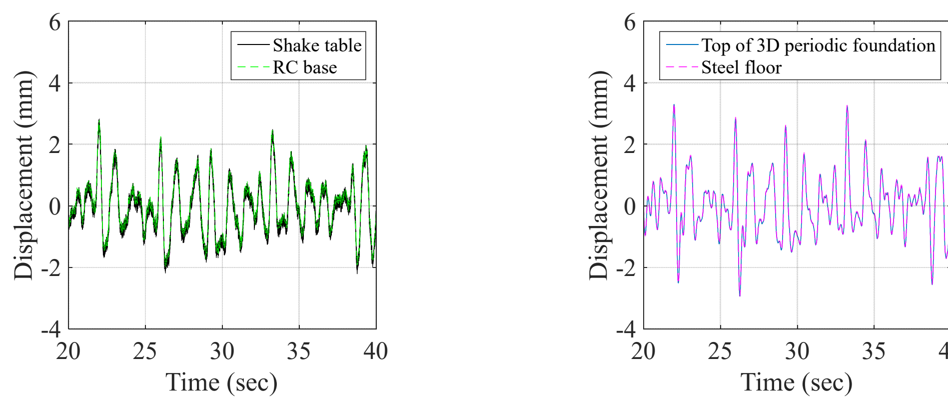

(a) At shake table and RC base (b) At top of 3D periodic foundation and steel floor

Figure 6-22 Displacement records of Case 6 in the horizontal direction

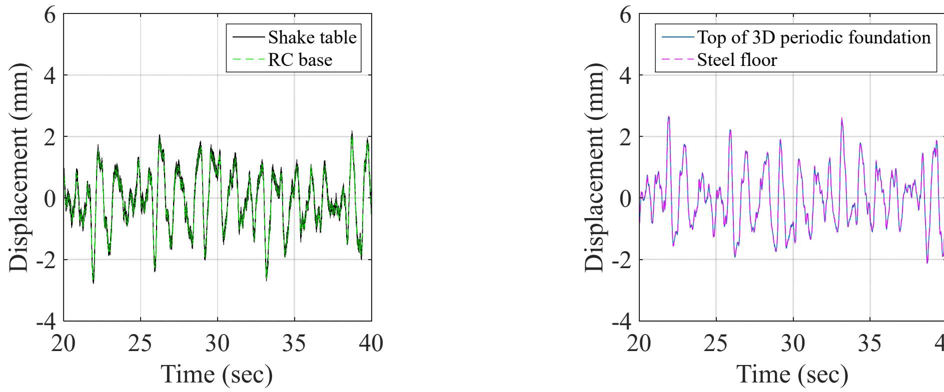

(a) At shake table and RC base

(b) At top of 3D periodic foundation and steel floor

Figure 6-23 Displacement records of Case 6 in the vertical direction

Figure 6-24 to Figure 6-26 show the dynamic magnification factor or ratio of output to input. The term “input” corresponds to the Fourier spectrum of the acceleration recorded on either the shake table (for Cases 2 and 4) or the RC base (for Case 6), while the term “output” represents the Fourier spectrum of the acceleration recorded at either the top of the periodic foundations or the roof of the superstructure. The peak ratio of output by input indicates that there exists response amplification at the particular frequency. From the white noise tests, the natural frequency of each of Cases 2, 4, and 6 in the horizontal direction is 16.41 Hz, 2.49 Hz, and 2.78 Hz, respectively. In the vertical direction, the natural frequency of each case is 26.81 Hz, 19.63 Hz, and 20.02 Hz, respectively. In the torsional mode, the natural frequency of each case is 46.88 Hz, 3.42 Hz, and 4 Hz, respectively.

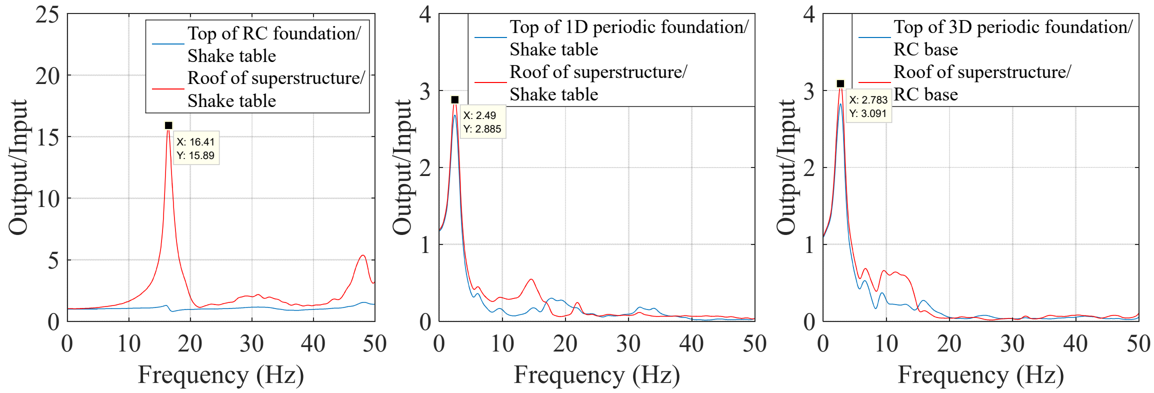

(a) Case 2 (b) Case 4 (c) Case 6

Figure 6-24 Frequency response curves of structural systems in the horizontal direction

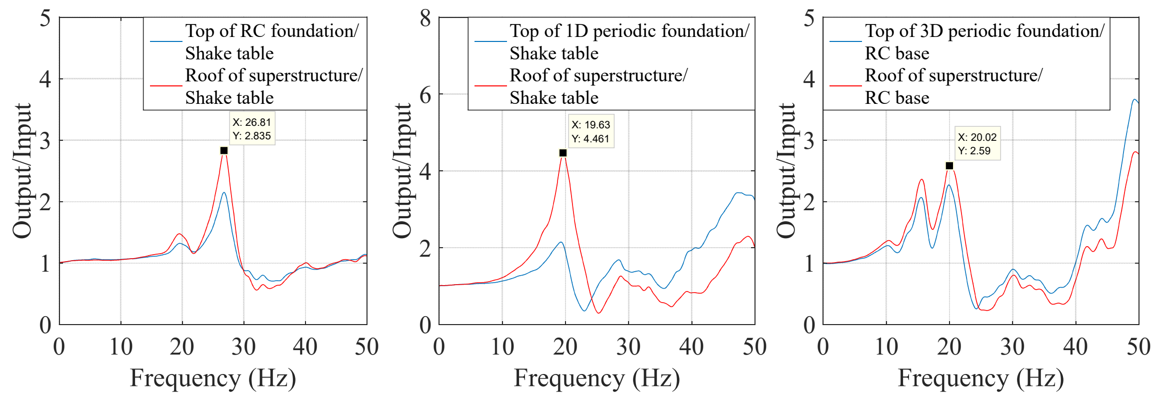

(a) Case 2 (b) Case 4 (c) Case 6

Figure 6-25 Frequency response curves of structural systems in the horizontal direction

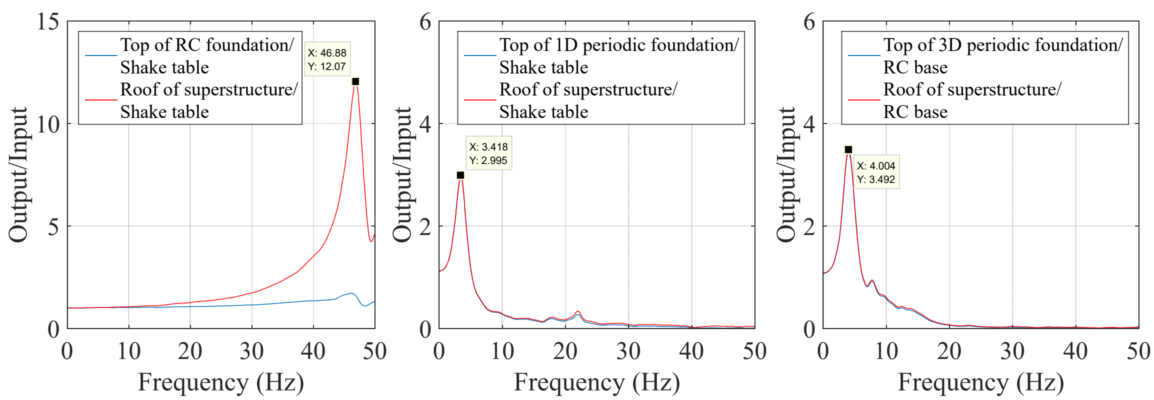

(a) Case 2 (b) Case 4 (c) Case 6

Figure 6-26 Frequency response curves of structural systems in the torsional mode

6.2.2 Frequency sweeping test results

The second type of tests conducted on the structural systems is the frequency sweeping tests. Figure 6-27 to Figure 6-29 show the results of the frequency sweeping tests in the horizontal direction, vertical direction, and torsional mode. The black curves show the recorded acceleration on the shake table. Although the amplitude was set to be 0.1 g, it is fairly difficult to maintain uniform amplitude throughout the time of shaking especially when the frequencies are changing. However, it is not a critical issue since the focus is on the ratio of the output waves (response of the structural system) to the input waves (acceleration on the shake table for Cases 2 and 4 or on the RC base for Case 6). Therefore, the attenuation zones of the structural systems can still be obtained.

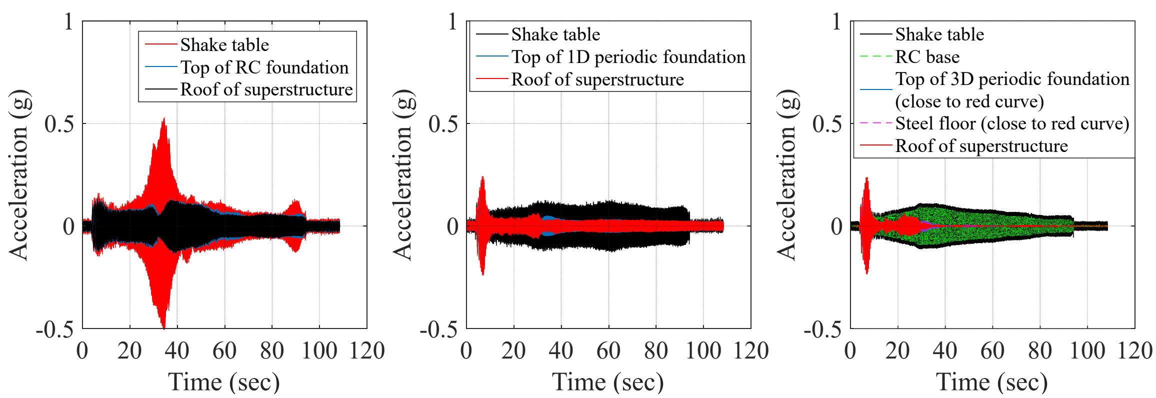

(a) Case 2 (b) Case 4 (c) Case 6

Figure 6-27 Frequency sweeping test results of structural systems in the horizontal direction

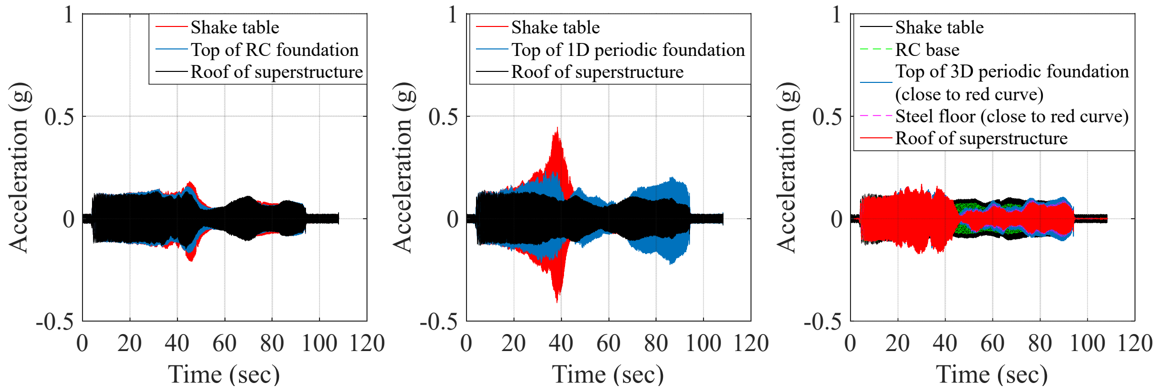

(a) Case 2 (b) Case 4 (c) Case 6

Figure 6-28 Frequency sweeping test results of structural systems in the vertical direction

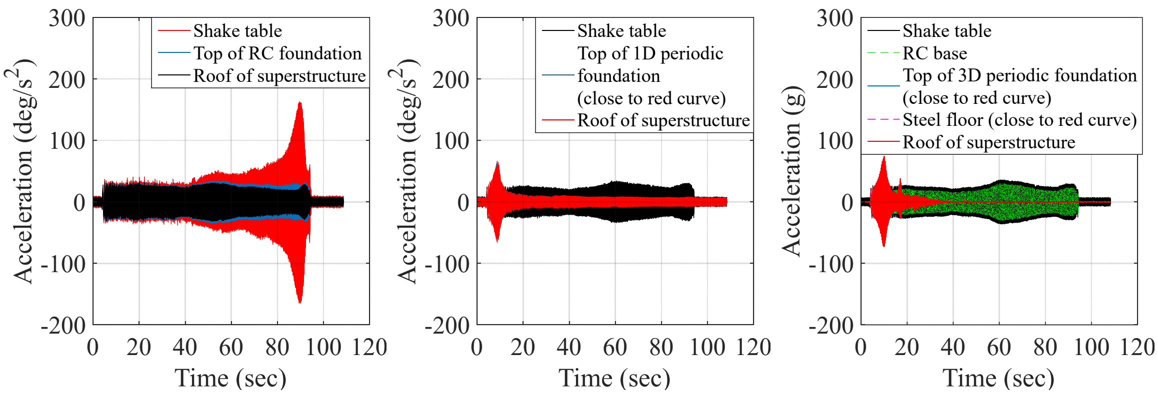

(a) Case 2 (b) Case 4 (c) Case 6

Figure 6-29 Frequency sweeping test results of structural systems in the torsional mode

The Fourier spectrum of each of the recorded accelerations is shown in Figure 6-30 to Figure 6-32. The frequency sweeping results of Cases 4 and 6 in the frequency domain show that the incoming waves are attenuated at a lower frequency in comparison to that of Cases 3 and 5. The results proved that the presence of the superstructure can shift the frequency band gaps to a lower frequency. In addition, the same vertical separation at high frequency in Case 6 is also observed at the interfaces between the RC base with the shake table and the steel floor with the 3D periodic foundation [see Figure 6-31(c)].

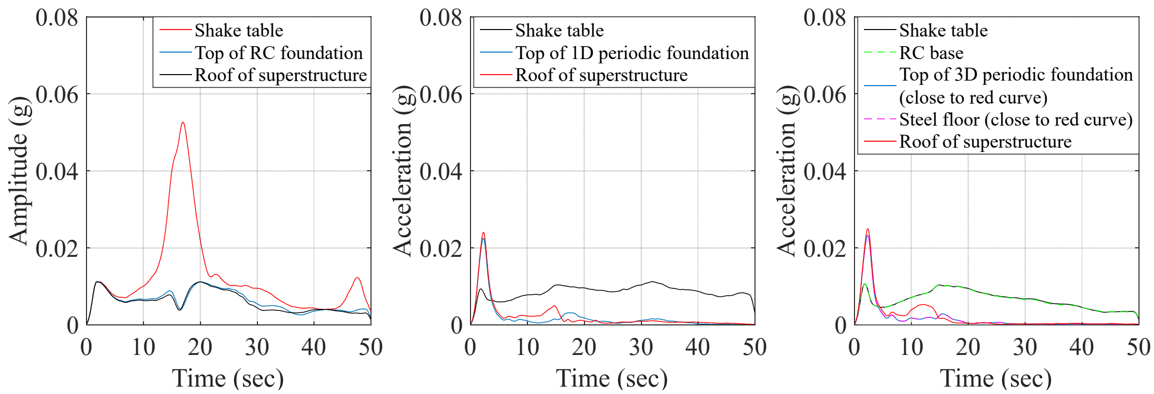

(a) Case 2 (b) Case 4 (c) Case 6

Figure 6-30 Fourier spectra of frequency sweeping test results of structural systems in the horizontal direction

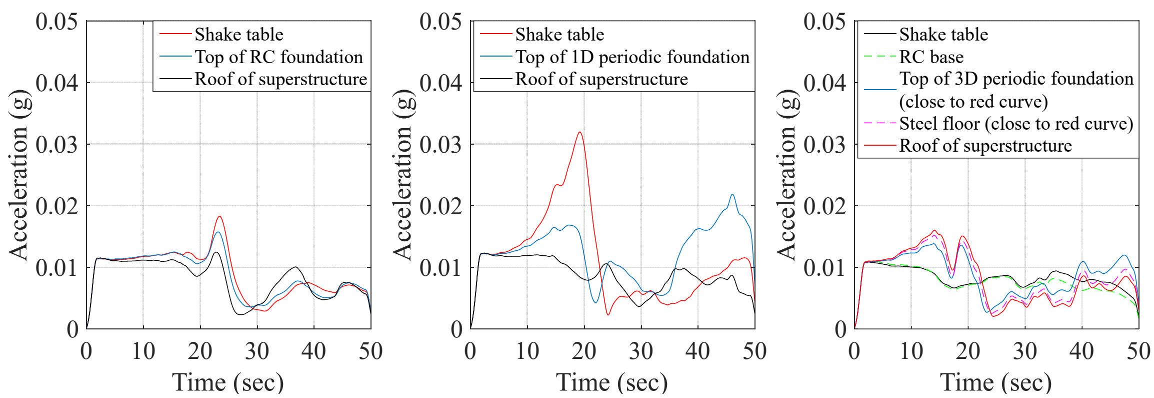

(a) Case 2 (b) Case 4 (c) Case 6

Figure 6-31 Fourier spectra of frequency sweeping test results of structural systems in the vertical direction

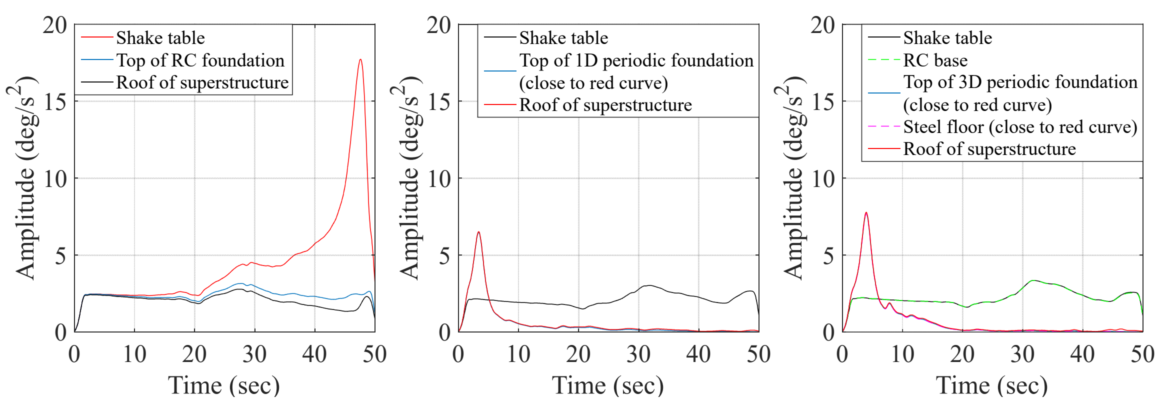

(a) Case 2 (b) Case 4 (c) Case 6

Figure 6-32 Fourier spectra of frequency sweeping test results of structural systems in the torsional mode

The FRF curves were generated [using Eq. (6-1)] to see the attenuation zones and the magnitude of the attenuation inside them. For Cases 2 and 4, their input acceleration uses the results recorded from the shake table, while for Case 6, it uses the results recorded from the RC base. Figure 6-33 to Figure 6-35 show the FRF curves of the structural systems in all three directions. From these FRF curves, one can see that the attenuation zones of the 1D and 3D periodic foundation structural systems in the horizontal direction and the torsional mode are close to their respective preliminary analysis in the horizontal direction, as presented in Sub-subsections 5.2.2.3 and 5.2.3.2. However, the attenuation zones of the 1D and 3D periodic foundation structural systems in the vertical direction are somewhat different with their respective preliminary analysis in the vertical direction. The discrepancy in the vertical direction may come from the construction errors such as an imperfect flat surface of RC layers and non-uniform glue distribution. Therefore, in some parts of the periodic foundations the polyurethane surface is not perfectly connected to the RC surface. The imperfect interface connection between each layer on the periodic foundations is affected the most when the structural systems are subjected to the waves in the vertical direction. The imperfect interface connection causes non-uniform axial stresses and load transfer between each layer making the wave propagation different from the theory. In addition, the bolt connection between the steel floor of the superstructure and the top of the periodic foundations is also not a perfect connection. The threaded bolts that tighten the connection could not provide a perfect rigid interface when they are in tension. The imperfection of the interface connection, however, has little influence when the structure is subjected to incoming waves in the horizontal direction and torsional mode. Large superstructure weight allows sufficient friction between the RC layers and polyurethane layers as well as between the periodic foundations with the superstructure to make the shear stress uniform. Therefore, the attenuation zones in the horizontal direction and torsional mode are very close to the preliminary analysis results that are consistent with the theoretical frequency band gaps. The attenuation zones of each structural system at each of the top of the foundation and roof of the superstructure is tabulated in Table 6-1. Large response reductions inside the attenuation zones are observed in all three directions, where the FRF of -10 and -20 respectively correspond to a 68.38% and 90% response reduction, respectively. There is no attenuation zone in the RC foundation as clearly shown by close to zero FRF values in Figure 6-33(a), Figure 6-34(a), and Figure 6-35(a).

Table 6-1 Attenuation zones of structural systems

Case	Direction	Attenuation zones	
		Top of foundation	Roof of superstructure
2	Horizontal	None	None
	Vertical	None	None
	Torsion	None	None
4	Horizontal	3.7–50 Hz	3.9–50 Hz
	Vertical	20.75–24.1 Hz and 32.4–35.9 Hz	22.8–27.83 Hz and 32.4–40.75 Hz
	Torsion	5.12–50 Hz	5.13 –50 Hz
6	Horizontal	4.1–50 Hz	4.5–50 Hz
	Vertical	21.63–32.96 Hz and 33.5–38.28 Hz	22.46–39.1 Hz
	Torsion	6.05–50 Hz	6.1–50 Hz

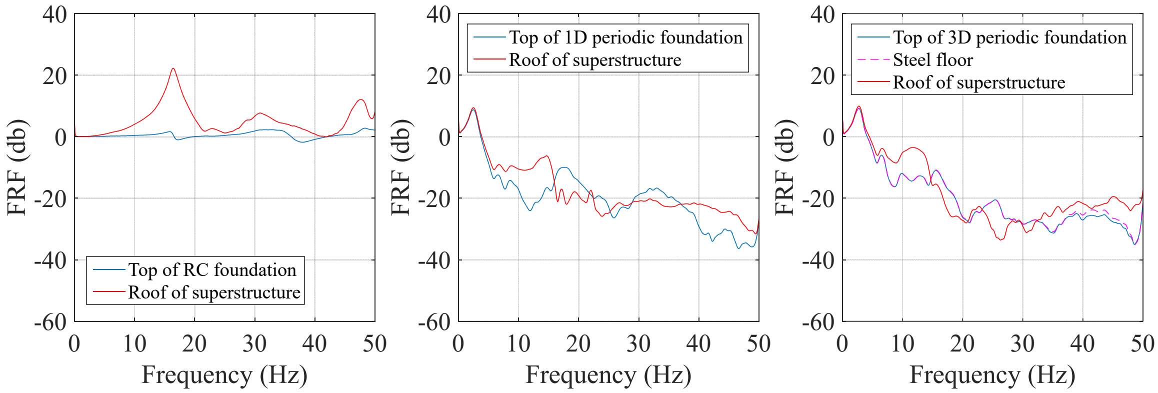

(a) Case 2 (b) Case 4 (c) Case 6

Figure 6-33 Frequency response function of frequency sweeping test results of structural systems in the horizontal direction

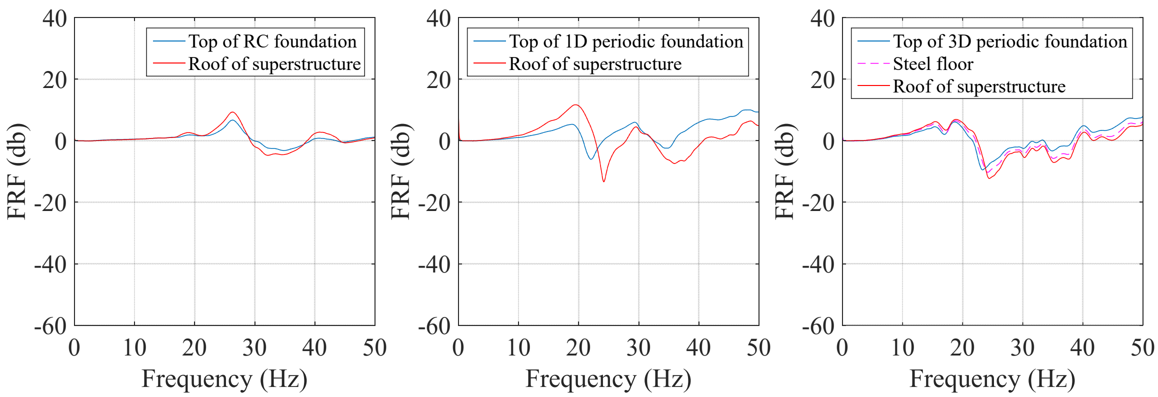

(a) Case 2 (b) Case 4 (c) Case 6

Figure 6-34 Frequency response function of frequency sweeping test results of structural systems in the vertical direction

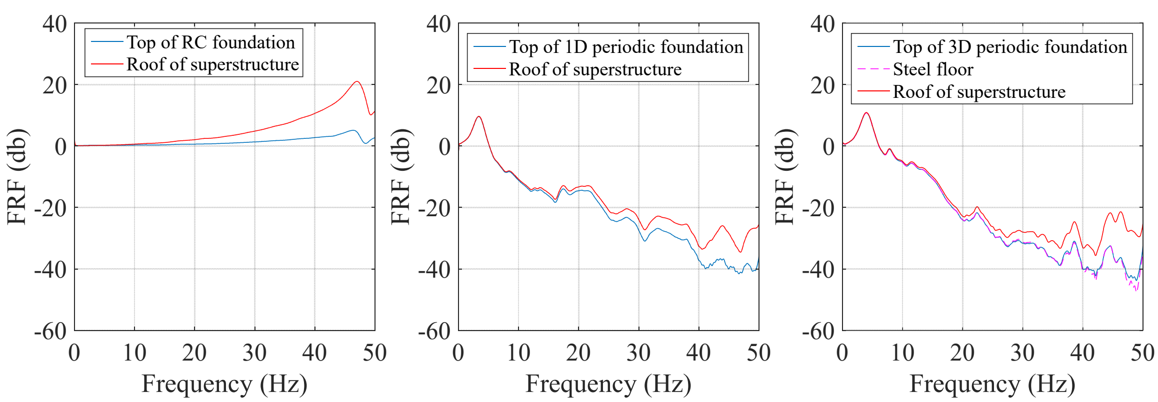

(a) Case 2 (b) Case 4 (c) Case 6

Figure 6-35 Frequency response function of frequency sweeping test results of structural systems in the torsional mode

6.2.3 Seismic test results

This Sub-subsection shows the seismic test results of the structural systems subjected to each of the seismograms presented in Table 5-22. Additional seismic test results on Case 6 using seismograms presented in Table 5-23 are also discussed. Note that the shake table capacity can only provide shaking with a maximum frequency of 50 Hz. Any frequency content larger than 50 Hz is eliminated by the shake table system. Hence, the recorded seismogram on the shake table may be different from the input (command) provided to the shake table control system due to the cutting of frequencies above 50 Hz. Therefore, all of the structural responses are compared with their respective data recorded at the shake table. The responses of the structural systems presented here are those recorded during the main shock of the input earthquakes.

6.2.3.1 Responses of structural systems subjected earthquakes in the horizontal direction

6.2.3.1.1 Acceleration responses due to earthquakes in the horizontal direction

Figure 6-36 to Figure 6-43 show the test results of all structural systems subjected to each of the horizontal earthquakes listed in Table 5-22. It can be seen that the 1D and 3D periodic foundation structural systems (Cases 4 and 6) have a much smaller acceleration response at the roof of the superstructure in comparison to that of the RC foundation structural system (Case 2). In addition, the peak acceleration responses at the top of the 1D and 3D periodic foundations are also smaller than the 0.4 g peak ground acceleration (acceleration at the shake table). The acceleration response reduction of the 1D and 3D periodic foundation structural systems is much smaller when subjected to the first four earthquakes (Anza, Bishop, Gilroy, and Oroville Earthquakes) than when they are subjected to the remaining four earthquakes [Loma Prieta, Imperial Valley, Northridge, and San Fernando (Pacoima Dam) Earthquakes]. The reason is because most of the main frequency content of each of the first four earthquakes is located completely inside the attenuation zones of the periodic foundations, therefore effectively filtering out the main frequency content, as shown in Figure 6-44 to Figure 6-47. However, the main frequency content of each of the last four earthquakes is widely distributed. A significant portion of those main frequency contents are located outside the attenuation zones and are amplified, as shown in Figure 6-48 to Figure 6-51. Moreover, due to the finite geometry of the structural systems, the structural systems also possess their own natural frequencies (which are observed to be located at the first pass bands). Therefore, more amplification is observed when the frequencies of the seismic waves correspond to the natural frequencies of the structural systems.

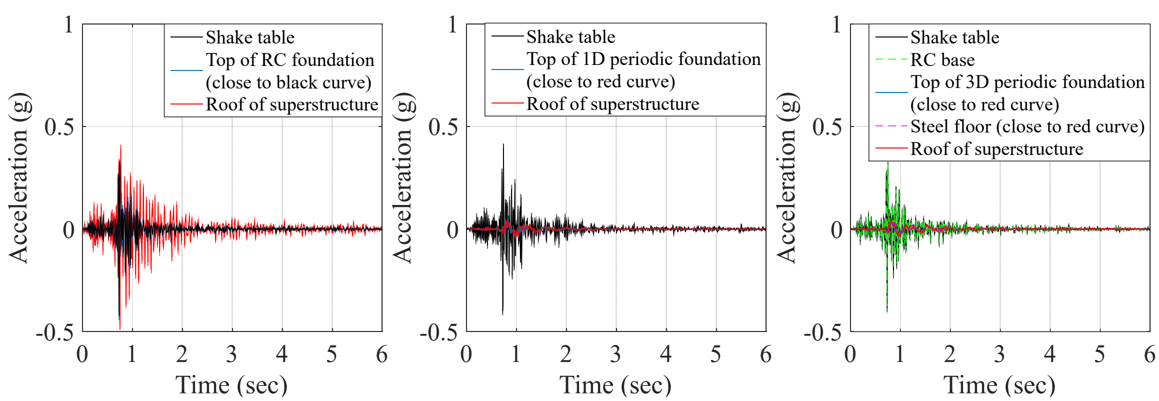

(a) Case 2 (b) Case 4 (c) Case 6

Figure 6-36 Acceleration response of structural systems subjected to Anza Earthquake in the horizontal direction

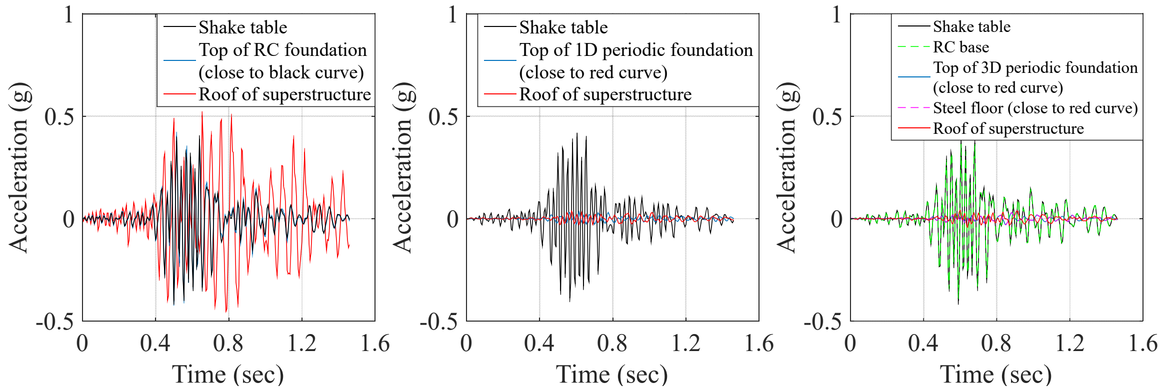

(a) Case 2 (b) Case 4 (c) Case 6

Figure 6-37 Acceleration response of structural systems subjected to Bishop Earthquake in the horizontal direction

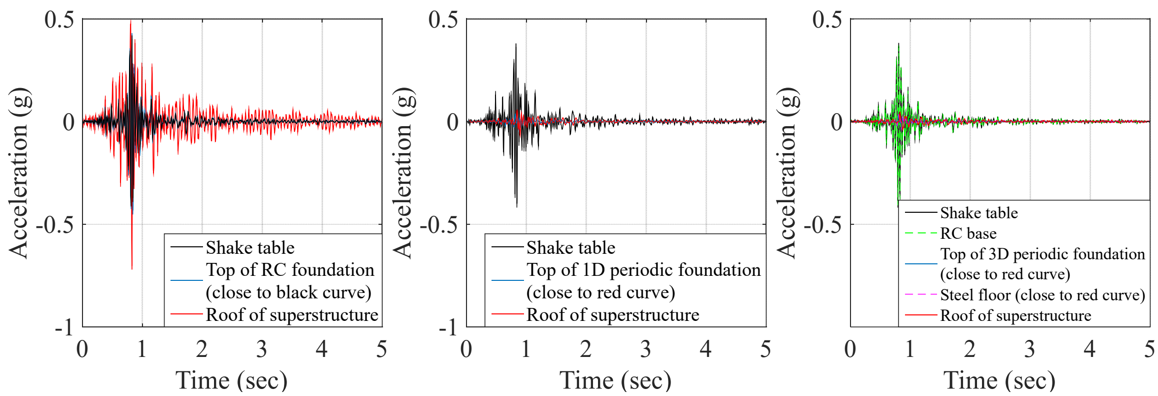

(a) Case 2 (b) Case 4 (c) Case 6

Figure 6-38 Acceleration response of structural systems subjected to Gilroy Earthquake in the horizontal direction

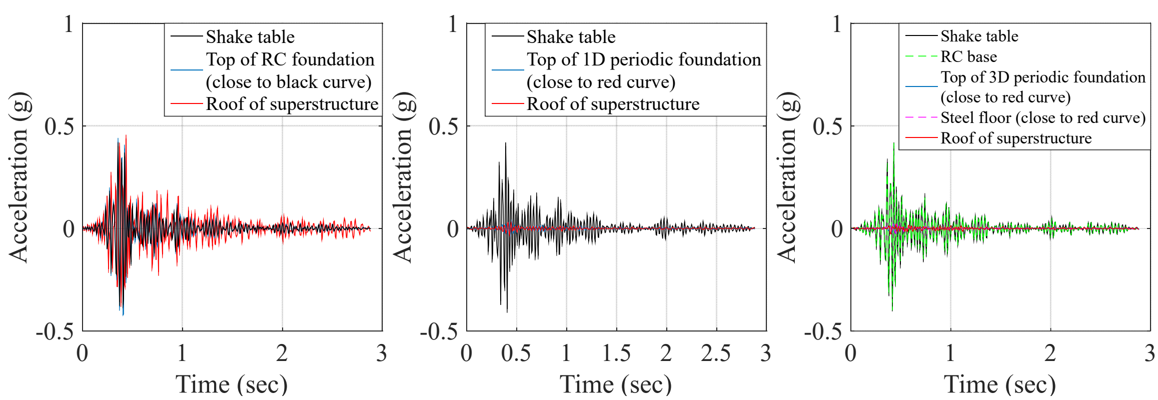

(a) Case 2 (b) Case 4 (c) Case 6

Figure 6-39 Acceleration response of structural systems subjected to Oroville Earthquake in the horizontal direction

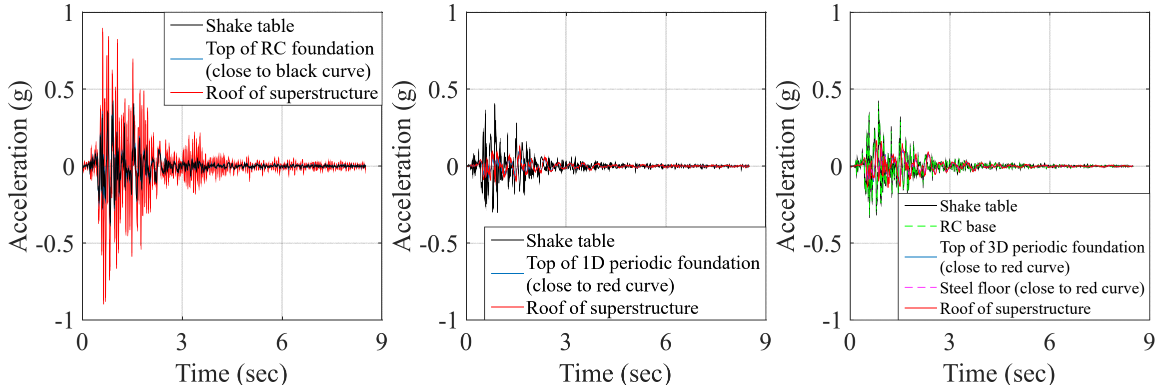

(a) Case 2 (b) Case 4 (c) Case 6

Figure 6-40 Acceleration response of structural systems subjected to Loma Prieta Earthquake in the horizontal direction

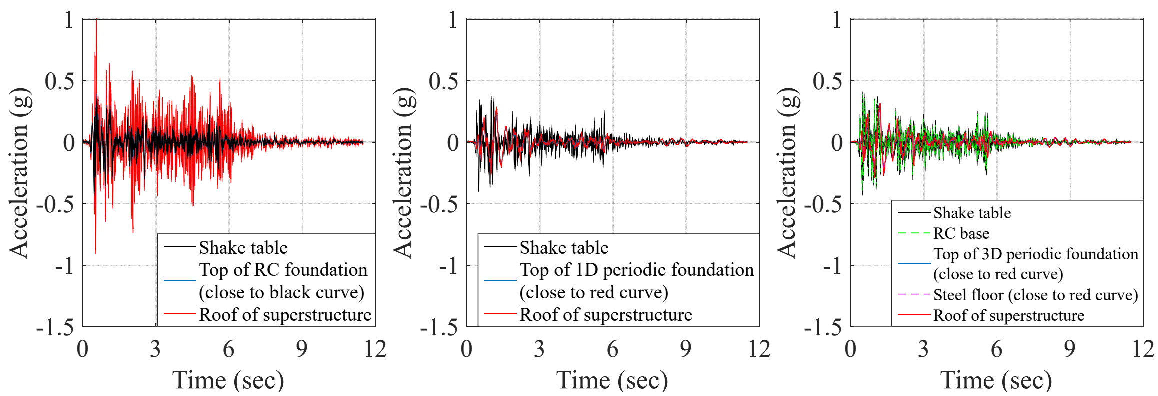

(a) Case 2 (b) Case 4 (c) Case 6

Figure 6-41 Acceleration response of structural systems subjected to Imperial Valley Earthquake in the horizontal direction

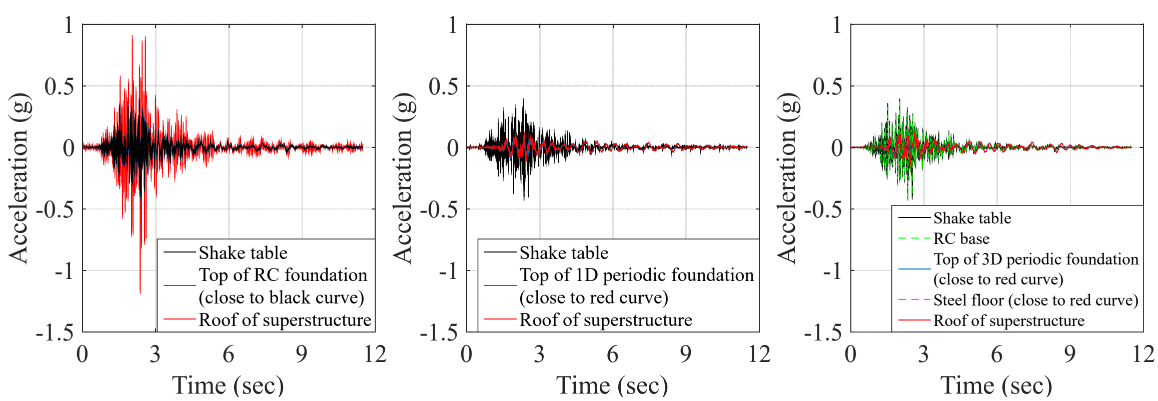

(a) Case 2 (b) Case 4 (c) Case 6

Figure 6-42 Acceleration response of structural systems subjected to Northridge Earthquake in the horizontal direction

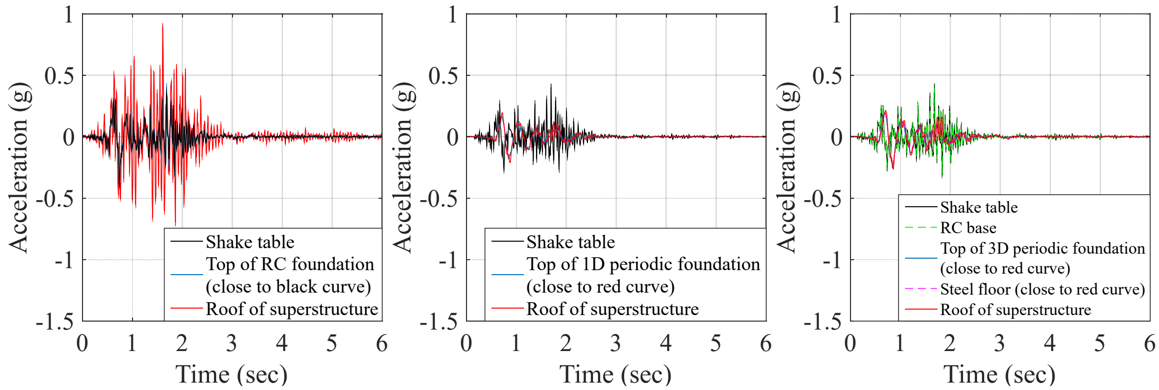

(a) Case 2 (b) Case 4 (c) Case 6

Figure 6-43 Acceleration response of structural systems subjected to San Fernando (Pacoima Dam) Earthquake in the horizontal direction

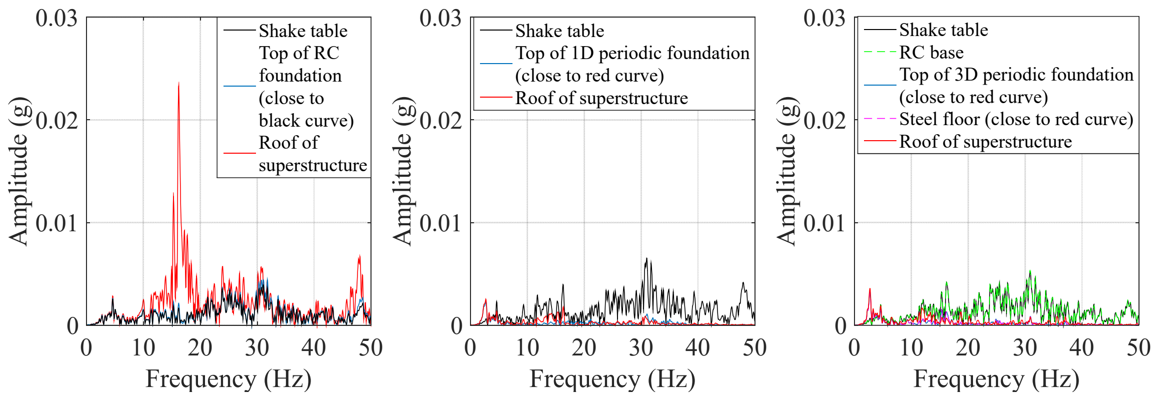

(a) Case 2 (b) Case 4 (c) Case 6

Figure 6-44 Fourier spectra of acceleration response of structural systems subjected to Anza Earthquake in the horizontal direction

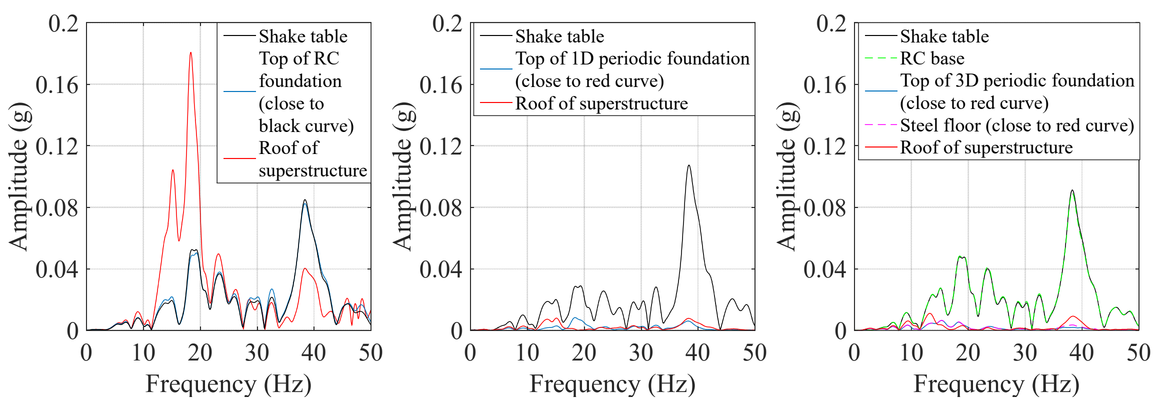

(a) Case 2 (b) Case 4 (c) Case 6

Figure 6-45 Fourier spectra of acceleration response of structural systems subjected to Bishop Earthquake in the horizontal direction

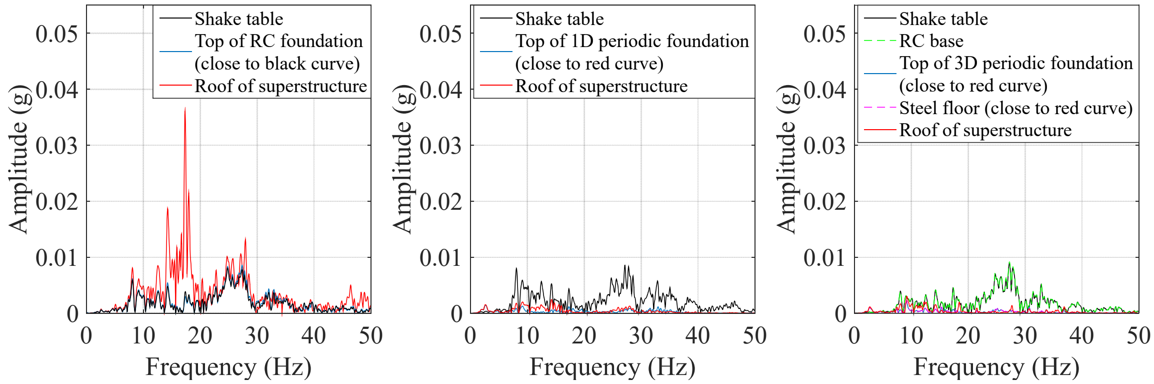

(a) Case 2 (b) Case 4 (c) Case 6

Figure 6-46 Fourier spectra of acceleration response of structural systems subjected to Gilroy Earthquake in the horizontal direction

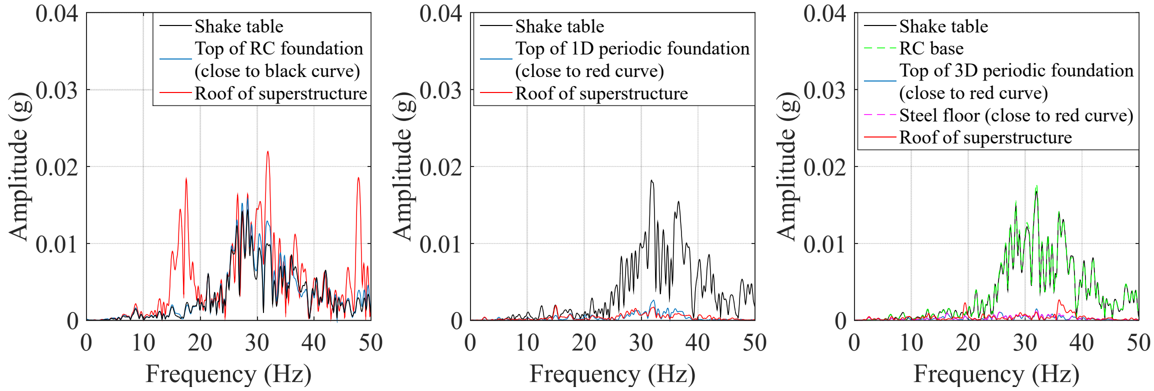

(a) Case 2 (b) Case 4 (c) Case 6

Figure 6-47 Fourier spectra of acceleration response of structural systems subjected to Oroville Earthquake in the horizontal direction

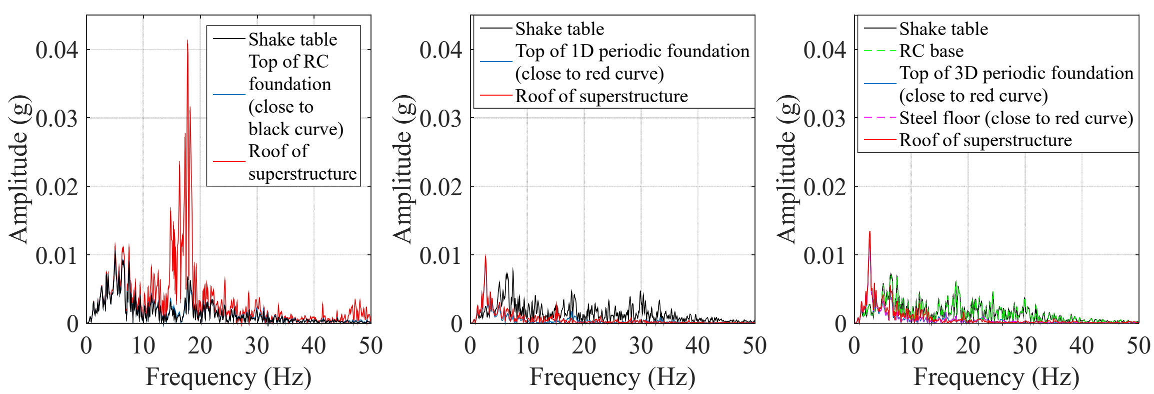

(a) Case 2 (b) Case 4 (c) Case 6

Figure 6-48 Fourier spectra of acceleration response of structural systems subjected to Loma Prieta Earthquake in the horizontal direction

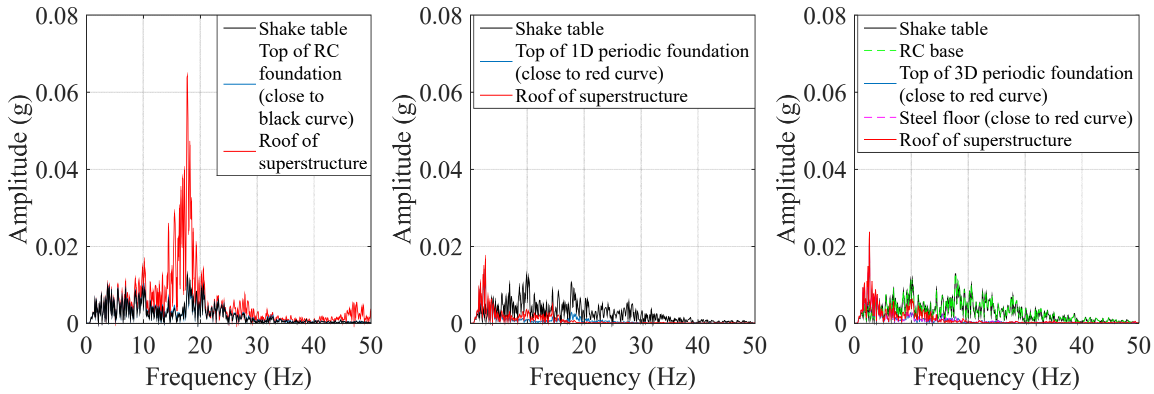

(a) Case 2 (b) Case 4 (c) Case 6

Figure 6-49 Fourier spectra of acceleration response of structural systems subjected to Imperial Valley Earthquake in the horizontal direction

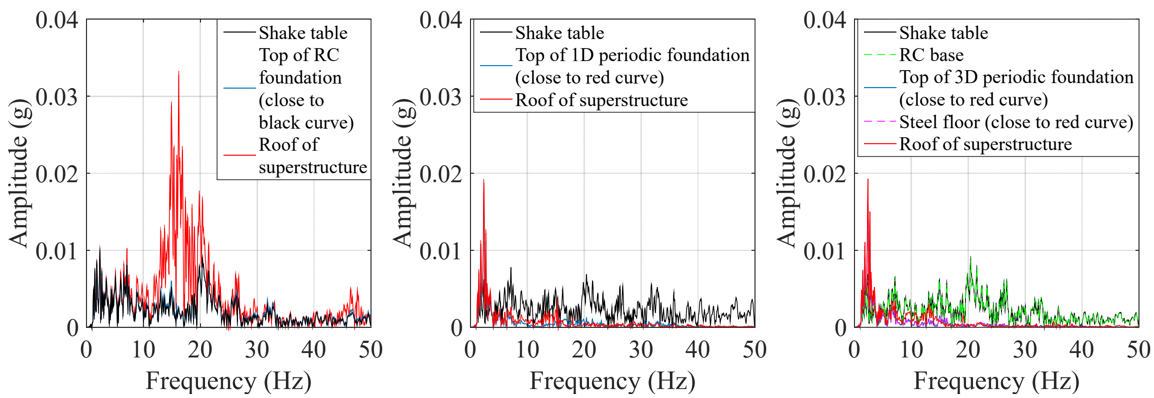

(a) Case 2 (b) Case 4 (c) Case 6

Figure 6-50 Fourier spectra of acceleration response of structural systems subjected to Northridge Earthquake in the horizontal direction

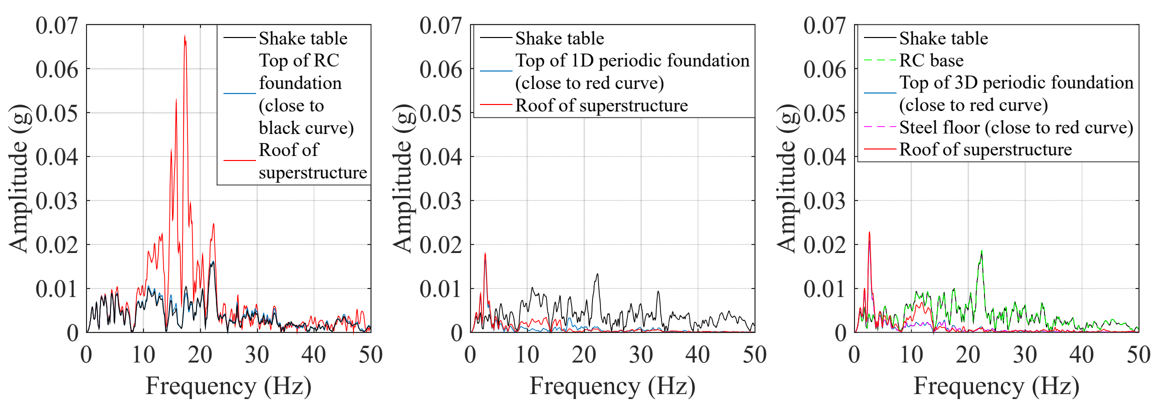

(a) Case 2 (b) Case 4 (c) Case 6

Figure 6-51 Fourier spectra of acceleration response of structural systems subjected to San Fernando (Pacoima Dam) Earthquake in the horizontal direction

Response spectra of the time series also provide information on the structural behavior and how the structural response would affect the non-structural elements on the SMR building. Figure 6-52 to Figure 6-59 show the acceleration response spectra of the time series measured during seismic tests. The response spectra of the recorded acceleration time series are slightly different from those presented in Figure 5-130(a) because of the cut-off of the main frequency contents at 50 Hz. The response spectra are drawn based on a 5% damping ratio commonly used by design engineers. It was previously reported that the horizontal attenuation zone for each of Cases 4 and 6 is located at 3.7–50 Hz and 3.9–50 Hz, respectively. As a result, the main frequency contents of the input earthquakes in these regions are attenuated. For the Bishop, Gilroy, and Oroville Earthquakes, which have their main frequency contents of the input waves completely located inside the attenuation zones, the floor response spectra of Cases 4 and 6 show almost negligible acceleration in all frequency ranges. The floor response spectra of Cases 4 and 6 for the last four earthquakes consistently show attenuation of response at frequencies inside the attenuation zones and amplification at a lower frequency region. Nevertheless, this increase occurs outside the frequency region of concern for typical non-structural components.

Similar results are observed from additional tests of Case 6. A large reduction in the acceleration responses at the top of the 3D periodic foundation and the roof of the superstructure in comparison to the acceleration at the RC base are observed when the structural system is subjected to the Ancona, Helena, Whittier, and San Fernando (St. Anita) Earthquakes [see Figure 6-60(a) to Figure 6-60(d)]. However, amplification of the acceleration response is observed when the structural system is subjected to the Kobe, Code

Anza, Code Imperial Valley, and Code San Fernando Earthquakes. The reason for these responses can be seen from the Fourier spectra shown in Figure 6-61. A significant portion of main frequency contents of the Kobe, Code Anza, Code Imperial Valley, and Code San Fernando Earthquakes are located in the low frequency region outside the attenuation zone causing amplification in that region. The response spectra of the recorded time series are shown in Figure 6-62. The peak acceleration of each of the time series is presented in Table 6-2 to Table 6-4. Response amplification and reduction percentage in comparison to the peak acceleration at the shake table (for Cases 2 and 4) and to that at the RC base (for Case 6) are also presented.

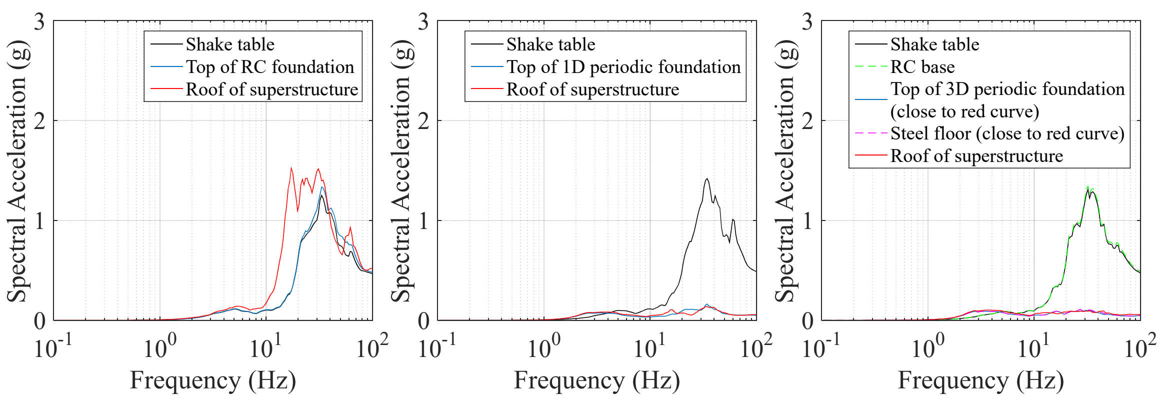

(a) Case 2 (b) Case 4 (c) Case 6

Figure 6-52 Acceleration response spectra of structural systems subjected to Anza Earthquake in the horizontal direction

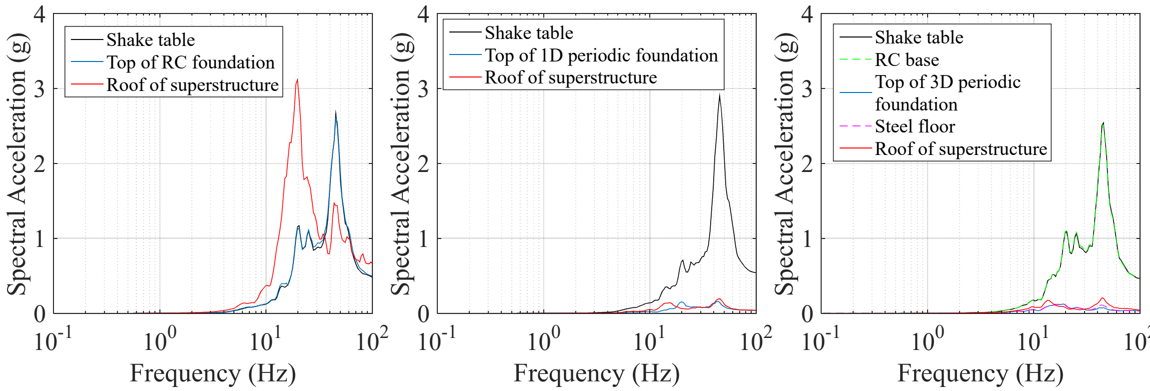

(a) Case 2 (b) Case 4 (c) Case 6

Figure 6-53 Acceleration response spectra of structural systems subjected to Bishop Earthquake in the horizontal direction

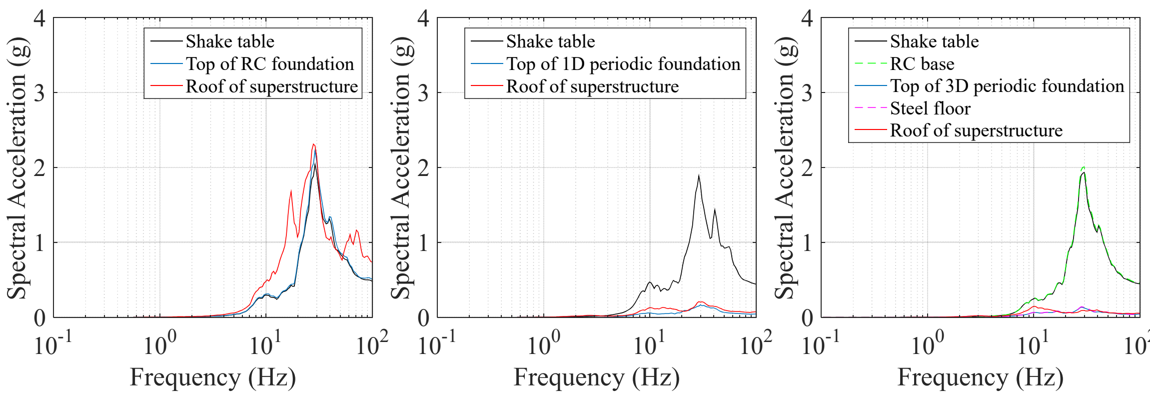

(a) Case 2 (b) Case 4 (c) Case 6

Figure 6-54 Acceleration response spectra of structural systems subjected to Gilroy Earthquake in the horizontal direction

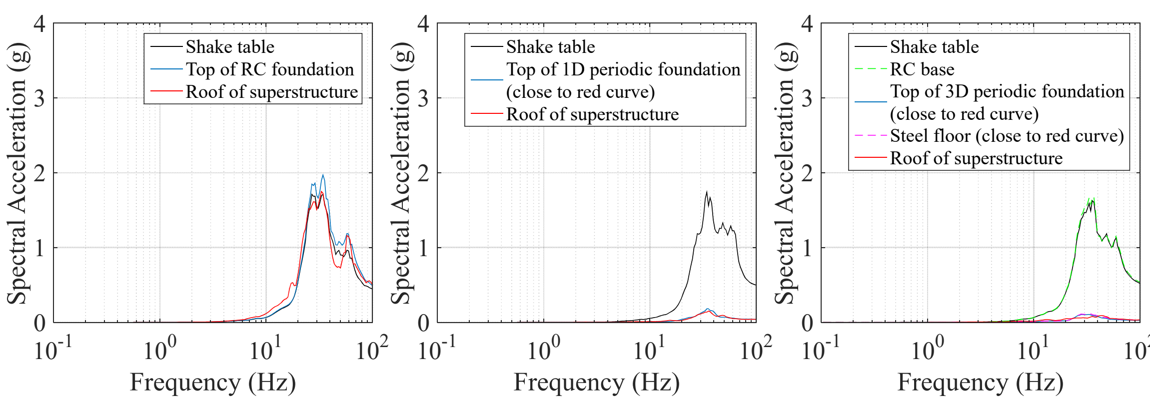

(a) Case 2 (b) Case 4 (c) Case 6

Figure 6-55 Acceleration response spectra of structural systems subjected to Oroville Earthquake in the horizontal direction

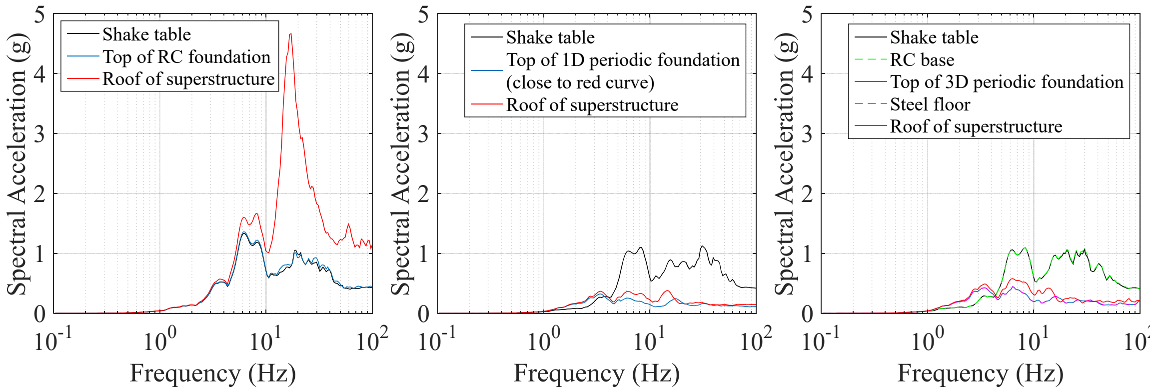

(a) Case 2 (b) Case 4 (c) Case 6

Figure 6-56 Acceleration response spectra of structural systems subjected to Loma Prieta Earthquake in the horizontal direction

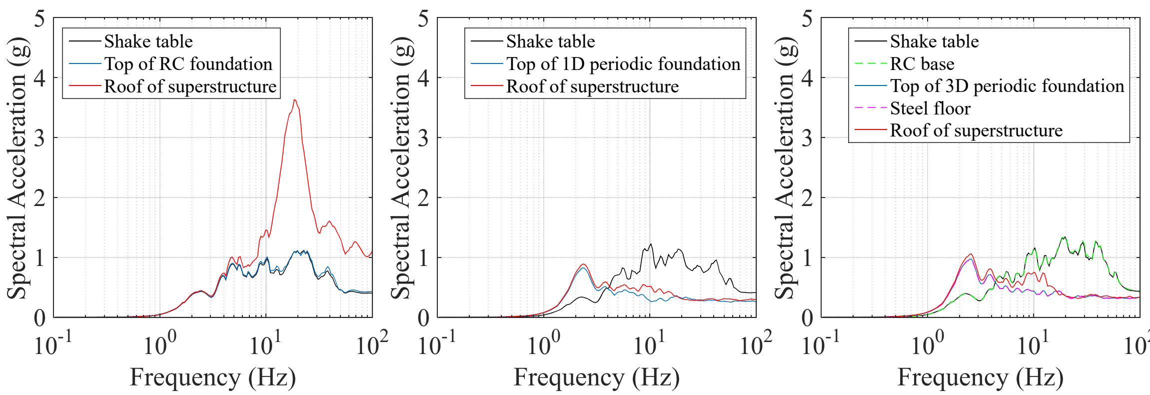

(a) Case 2 (b) Case 4 (c) Case 6

Figure 6-57 Acceleration response spectra of structural systems subjected to Imperial Valley Earthquake in the horizontal direction

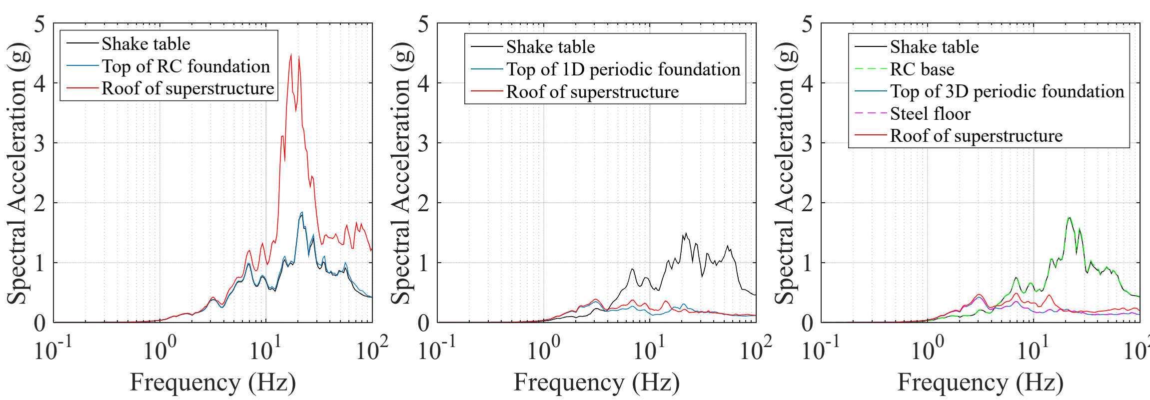

(a) Case 2 (b) Case 4 (c) Case 6

Figure 6-58 Acceleration response spectra of structural systems subjected to Northridge Earthquake in the horizontal direction

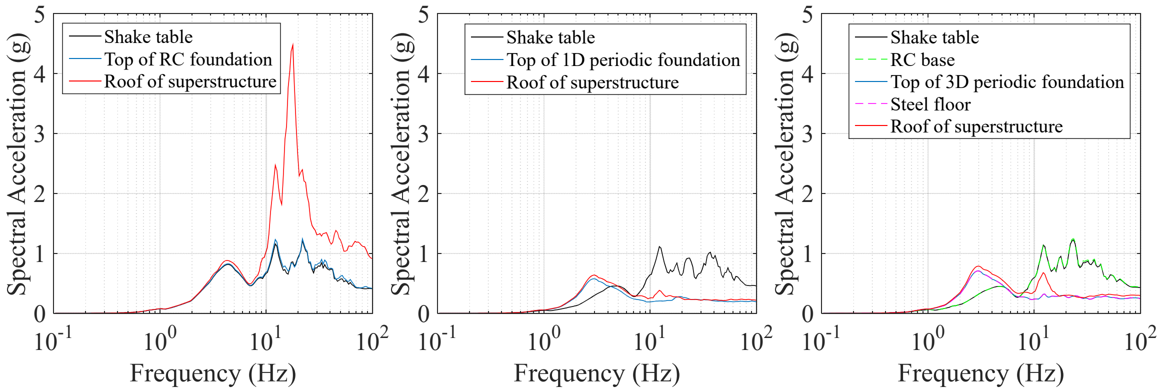

(a) Case 2 (b) Case 4 (c) Case 6

Figure 6-59 Acceleration response spectra of structural systems subjected to San Fernando (Pacoima Dam) Earthquake in the horizontal direction

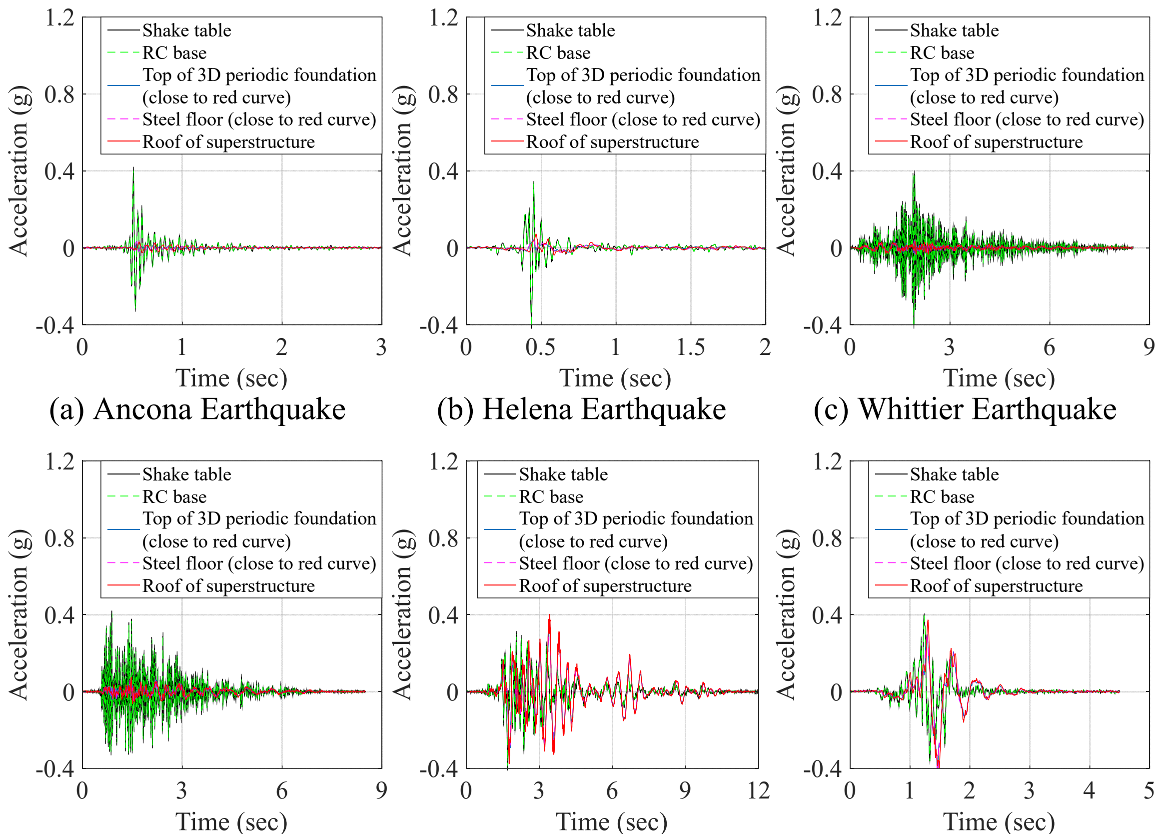

(a) Ancona Earthquake (b) Helena Earthquake (c) Whittier Earthquake

(d) San Fernando (St. Anita) Earthquake (e) Kobe Earthquake (f) Code Anza Earthquake

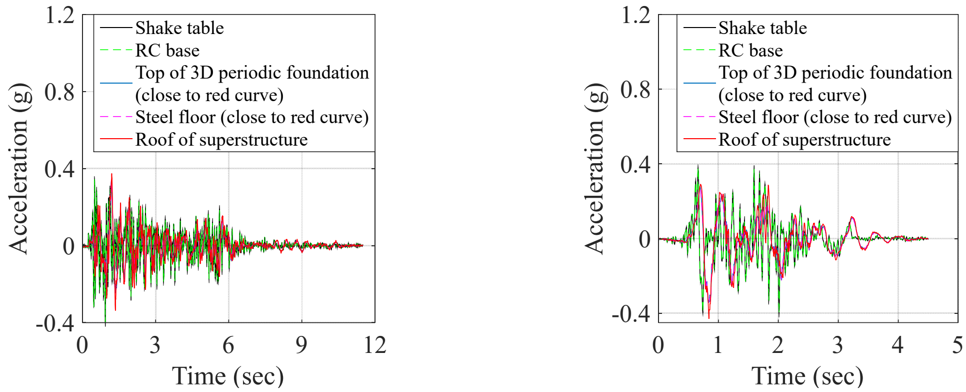

(g) Code Imperial Valley Earthquake (h) Code San Fernando Earthquake

Figure 6-60 Acceleration response of Case 6 subjected to additional earthquakes in the horizontal direction

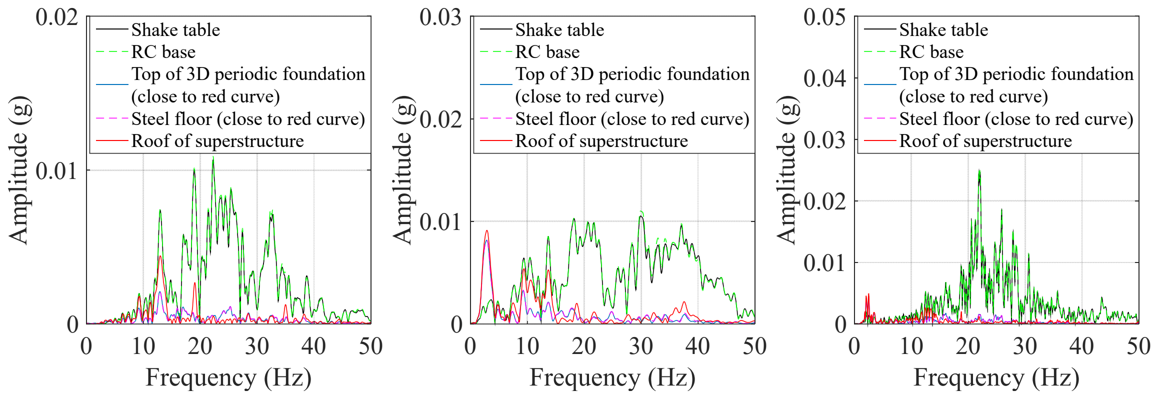

(a) Ancona Earthquake (b) Helena Earthquake (c) Whittier Earthquake

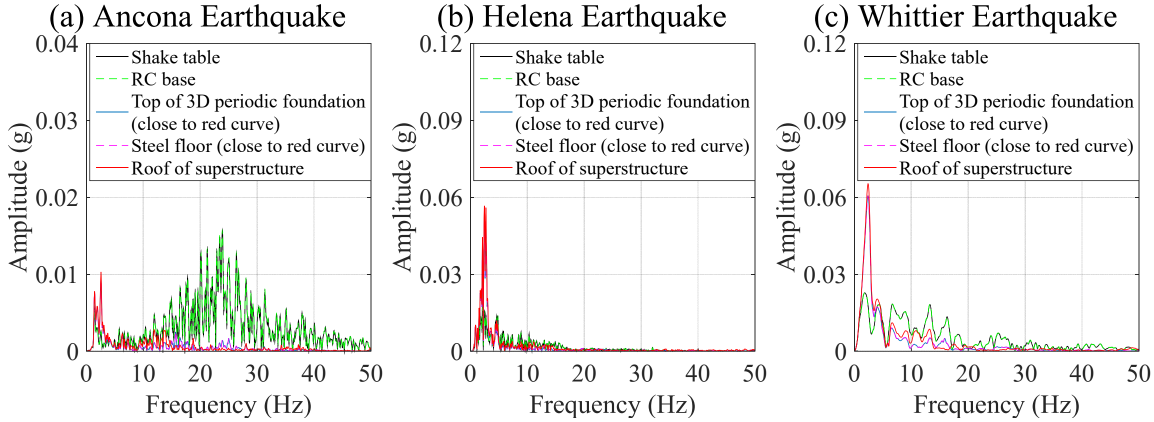

(d) San Fernando (St. Anita) Earthquake (e) Kobe Earthquake (f) Code Anza Earthquake

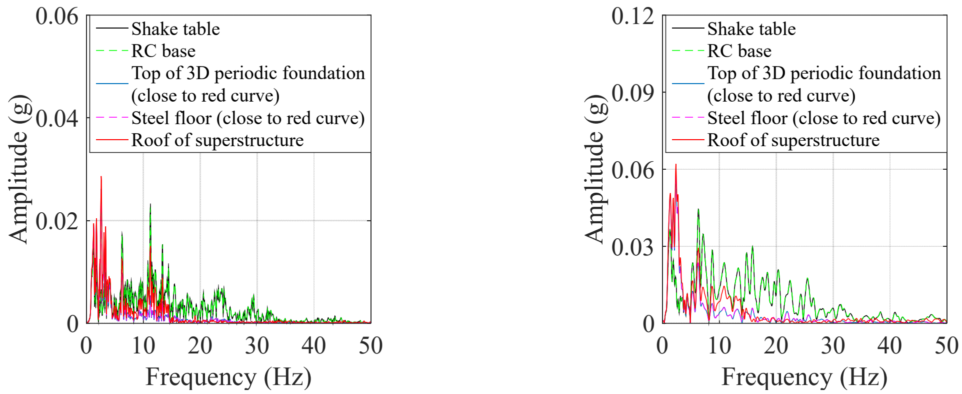

(g) Code Imperial Valley Earthquake (h) Code San Fernando Earthquake

Figure 6-61 Fourier spectra of acceleration response of Case 6 subjected to additional earthquakes in the horizontal direction

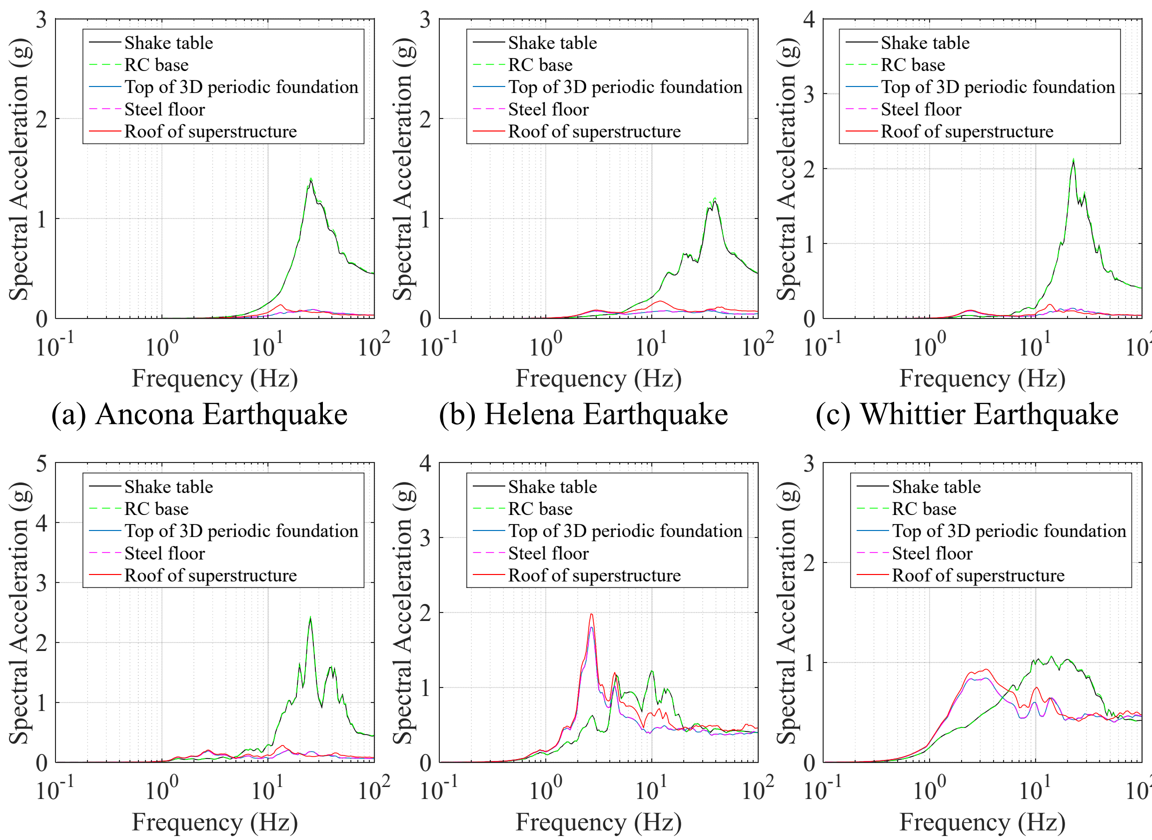

(a) Ancona Earthquake (b) Helena Earthquake (c) Whittier Earthquake

(d) San Fernando (St. Anita) Earthquake (e) Kobe Earthquake (f) Code Anza Earthquake

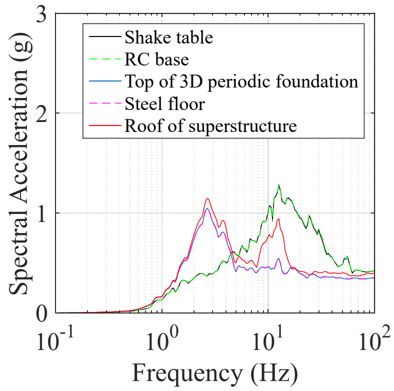

(g) Code Imperial Valley Earthquake

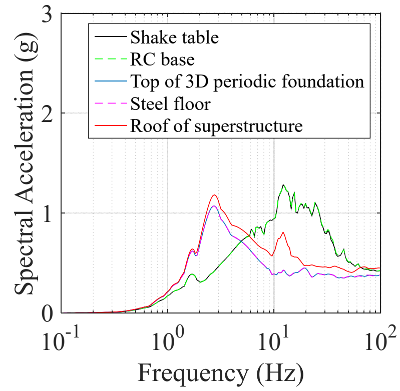

(h) Code San Fernando Earthquake

Figure 6-62 Acceleration response spectra of Case 6 subjected to additional earthquakes in the horizontal direction

Table 6-2 Peak acceleration response and response amplification percentage of Case 2 in the horizontal direction

Earthquake	RC foundation structural system				
	Shake table (g)	Top of RC foundation		Roof of superstructure	
		Acc (g)	Amplification (%)	Acc (g)	Amplification (%)
Anza	0.4	0.4249	6.23	0.4722	18.05
Bishop	0.4	0.4048	1.20	0.5041	26.02
Gilroy	0.4	0.4332	8.31	0.7011	75.28
Oroville	0.4	0.4221	5.52	0.4372	9.30
Loma Prieta	0.4	0.4067	1.68	0.8727	118.17
Imperial Valley	0.4	0.4105	2.63	0.9770	144.26
Northridge	0.4	0.3960	-1.00 (reduction)	1.1568	189.20
San Fernando (Pacoima Dam)	0.4	0.4052	1.30	0.8911	122.76

Table 6-3 Peak acceleration response and response reduction percentage of Case 4 in the horizontal direction

Earthquake	1D periodic foundation structural system				
	Shake table (g)	Top of 1D periodic foundation		Roof of superstrutcure	
		Acc (g)	Reduction (%)	Acc (g)	Reduction (%)
Anza	0.4	0.0475	88.12	0.0461	88.49
Bishop	0.4	0.0388	91.55	0.0374	90.65
Gilroy	0.4	0.0381	90.48	0.0665	83.38
Oroville	0.4	0.0351	91.23	0.0330	91.74
Loma Prieta	0.4	0.1058	73.56	0.1321	66.97
Imperial Valley	0.4	0.2546	36.34	0.2791	30.22
Northridge	0.4	0.1062	73.46	0.1175	70.63
San Fernando (Pacoima Dam)	0.4	0.1813	54.67	0.2108	47.29

Table 6-4 Peak acceleration response and response reduction percentage of Case 6 in the horizontal direction

Earthquake	3D periodic foundation structural system							
	Shake table (g)	RC base (g)	Top of 3D periodic foundation		Steel floor of superstructure		Roof of superstructure	
			Acc (g)	Reduction (%)	Acc (g)	Reduction (%)	Acc (g)	Reduction (%)
Anza	0.4	0.4120	0.0421	89.77	0.0435	89.43	0.0508	87.68
Bishop	0.4	0.3925	0.0303	92.28	0.0301	92.32	0.0439	88.82
Gilroy	0.4	0.4088	0.0397	90.28	0.0424	89.63	0.0479	88.29
Oroville	0.4	0.4154	0.0258	93.80	0.0277	93.33	0.0273	93.42
Loma Prieta	0.4	0.4057	0.1407	65.32	0.1430	64.75	0.1666	58.93
Imperial Valley	0.4	0.4010	0.3150	21.45	0.3172	20.89	0.3193	20.37
Northridge	0.4	0.4055	0.1212	70.12	0.1196	70.50	0.1730	57.32
San Fernando (Pacoima Dam)	0.4	0.4057	0.2357	41.89	0.2355	41.96	0.2656	34.53
Ancona	0.4	0.4075	0.0334	91.80	0.0349	91.44	0.0303	92.57
Helena	0.4	0.4088	0.0414	89.88	0.0391	90.44	0.0724	82.28
Whittier	0.4	0.4025	0.0400	90.05	0.0405	89.93	0.0352	91.26
San Fernando (St. Anita)	0.4	0.4057	0.0627	84.54	0.0636	84.33	0.0758	81.33
Kobe	0.4	0.3981	0.3712	6.77	0.3757	5.63	0.4026	-1.12 (amplify)
Code Anza	0.4	0.3967	0.4017	-1.27 (amplify)	0.4014	-1.19 (amplify)	0.3981	-0.35 (amplify)
Code Imperial Valley	0.4	0.3988	0.3408	14.53	0.3424	14.1371	0.3747	6.0260
Code San Fernando	0.4	0.4032	0.3436	14.7694	0.3420	15.1673	0.4292	-6.44 (amplify)

Figure 6-36 to Figure 6-39 have shown that almost all of the main frequency contents of the Anza, Bishop, Gilroy, and Oroville Earthquakes overlap with the attenuation zones of the 1D and 3D periodic foundation structural systems. Hence, large response reductions are obtained. The seismic tests using the same seismograms were conducted with the PGA of each of the seismograms scaled to 1 g. The purpose of these tests is to validate whether earthquake intensity affects the response reduction. Figure 6-63 and Figure 6-64 show the comparison of acceleration responses at the top of the periodic foundations subjected to all four earthquakes with different PGAs. It can be seen that similar response reductions can be achieved when the PGAs are scaled to 1 g. The overall test results indicate that as long as the main frequency content of an earthquake is covered by the attenuation zones, the intensity of the shaking does not affect the response reduction.

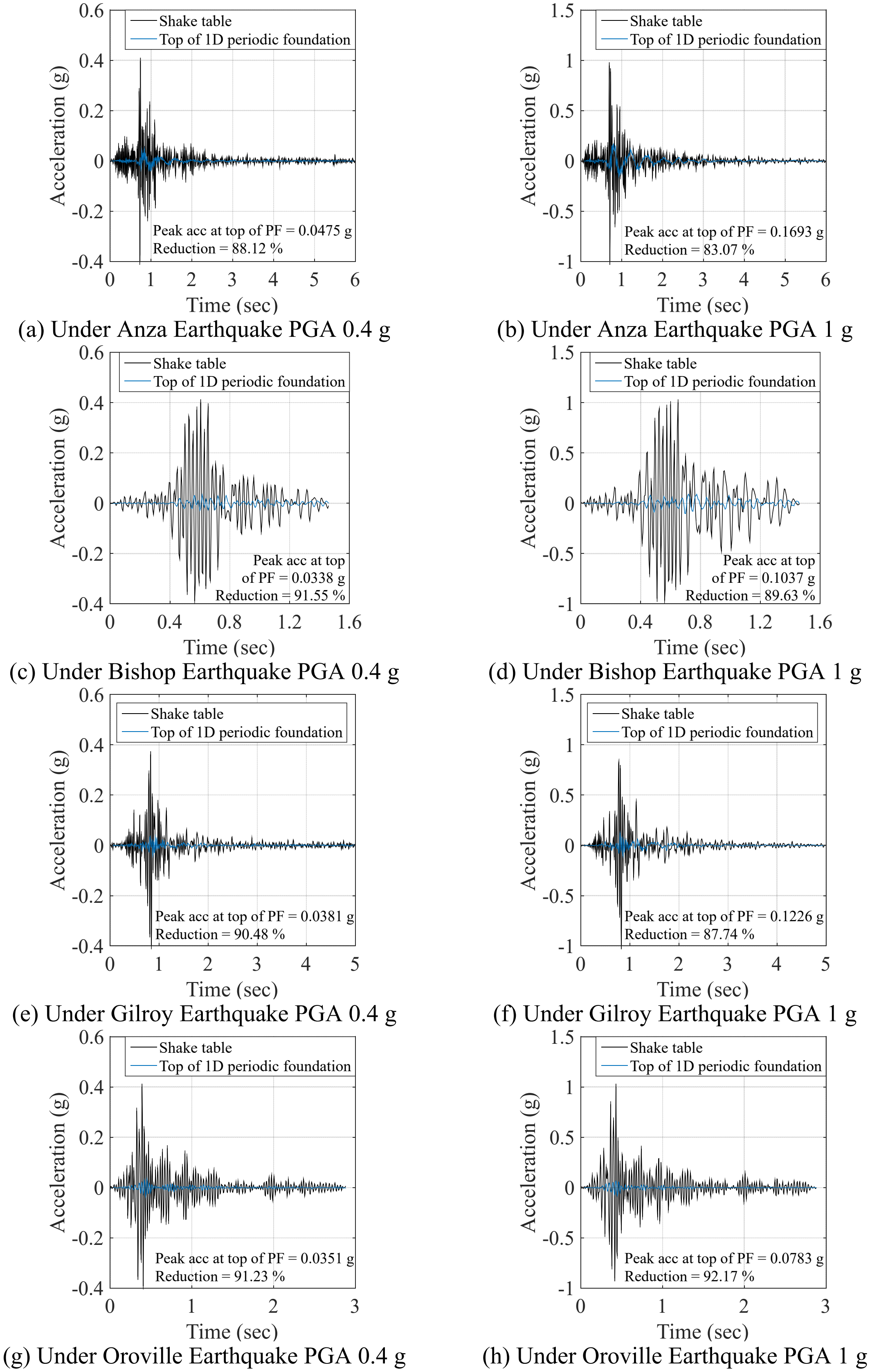

(a) Under Anza Earthquake PGA 0.4 g
(b) Under Anza Earthquake PGA 1 g
(c) Under Bishop Earthquake PGA 0.4 g
(d) Under Bishop Earthquake PGA 1 g
(e) Under Gilroy Earthquake PGA 0.4 g
(f) Under Gilroy Earthquake PGA 1 g
(g) Under Oroville Earthquake PGA 0.4 g
(h) Under Oroville Earthquake PGA 1 g

Figure 6-63 Acceleration response of Case 4 subjected to earthquakes with different PGA

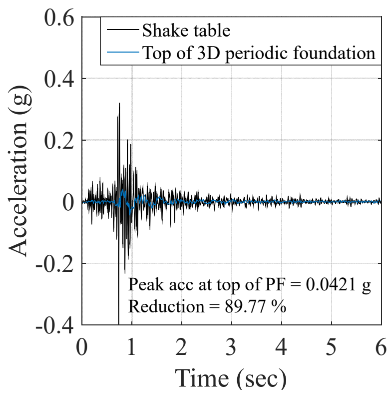

(a) Under Anza Earthquake PGA 0.4 g

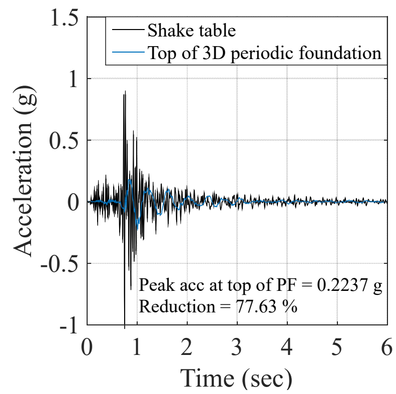

(b) Under Anza Earthquake PGA 1 g

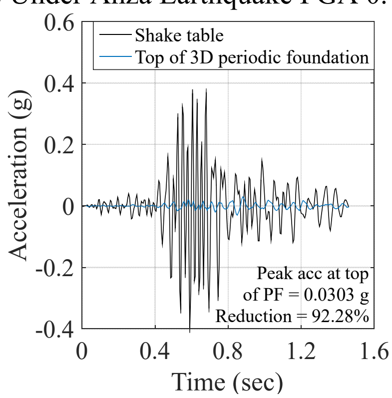

(c) Under Bishop Earthquake PGA 0.4 g

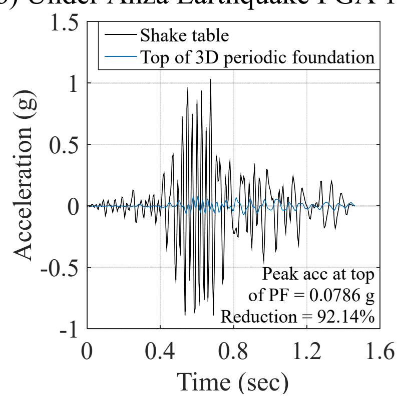

(d) Under Bishop Earthquake PGA 1 g

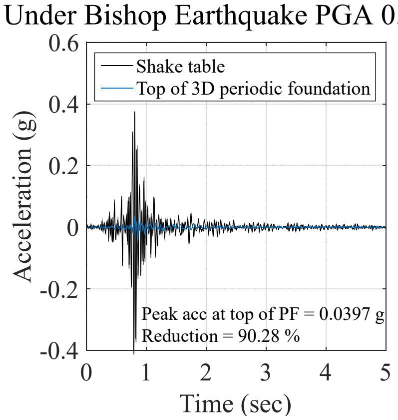

(e) Under Gilroy Earthquake PGA 0.4 g

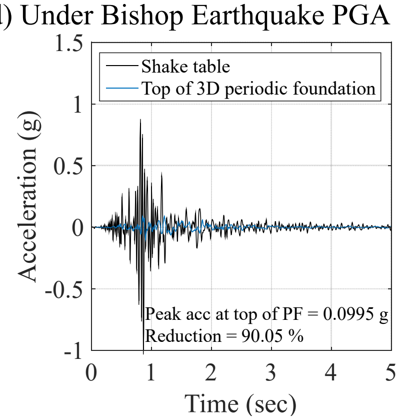

(f) Under Gilroy Earthquake PGA 1 g

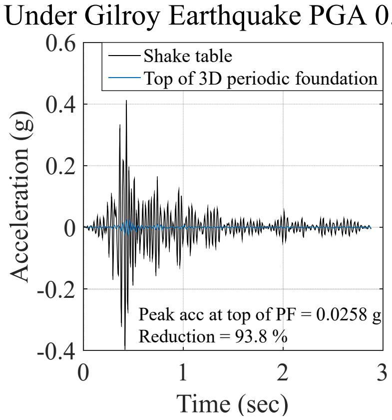

(g) Under Oroville Earthquake PGA 0.4 g

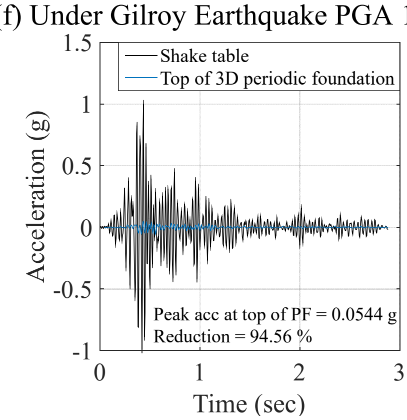

(h) Under Oroville Earthquake PGA 1 g

Figure 6-64 Acceleration response of Case 6 subjected to earthquakes with different PGA

6.2.3.1.2 Displacement and rocking responses due to earthquakes in the horizontal direction

The measured (absolute) displacement at the RC base, top of the foundation, and roof of the superstructure for each of Cases 2, 4, and 6 when subjected to each of the horizontal earthquakes is presented in Figure 6-65 to Figure 6-72. The absolute displacement response of Case 6 subjected to additional earthquakes is shown in Figure 6-73. The displacement data presented here are those recorded by the NDI systems because these systems can record displacement data with a small error margin during dynamic tests.

The measured displacement data on the structural systems are subtracted with the displacement data recorded at their respective RC bases to inspect the amount of deformation of each structural system relative to its base. The relative displacements are presented in Figure 6-74 to Figure 6-81. It is observed that the relative displacement of the roof to the RC base of Cases 4 and 6 are smaller than that of Case 2 when subjected to the Bishop and Oroville Earthquakes (see Figure 6-75 and Figure 6-77). This is because the main frequency contents of both earthquakes are located completely inside the attenuation zones as shown in Figure 6-45 and Figure 6-47. The relative displacement of Cases 4 and 6 subjected to the remaining earthquakes are observed to be larger than Case 2. This is due to some degree of amplification outside the attenuation zones. Since the amplification occurs at a lower frequency, it results in a larger displacement. Therefore, one can say that only when the main frequency content of earthquakes is located completely inside the attenuation zone will the superstructure experience very little vibration. The peak absolute and peak relative displacements of each structural system are presented in Table 6-5 to

Table 6-7. The peak relative displacements are observed to be larger than their respective difference between peak absolute displacements at the structural systems and those at their RC base. This is because the peak displacement did not happen at the exact same time.

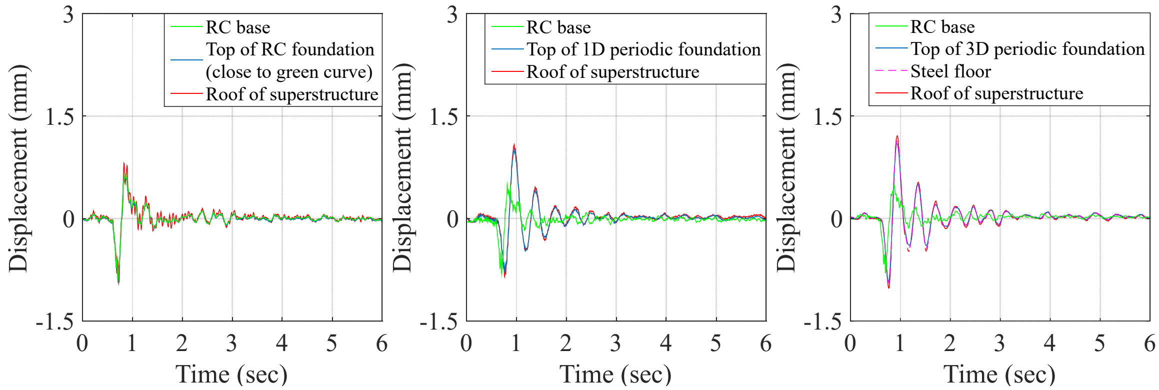

(a) Case 2 (b) Case 4 (c) Case 6

Figure 6-65 Absolute displacement response of structural systems subjected to Anza Earthquake in the horizontal direction

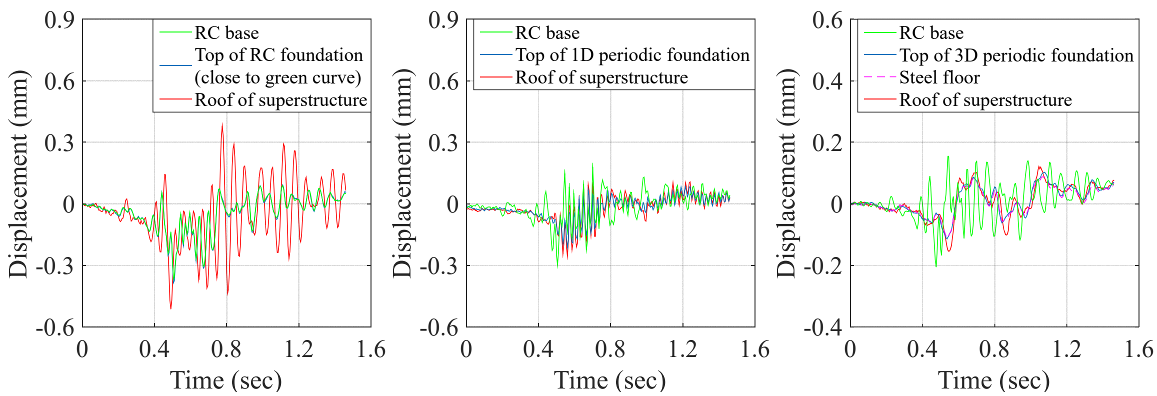

(a) Case 2 (b) Case 4 (c) Case 6

Figure 6-66 Absolute displacement response of structural systems subjected to Bishop Earthquake in the horizontal direction

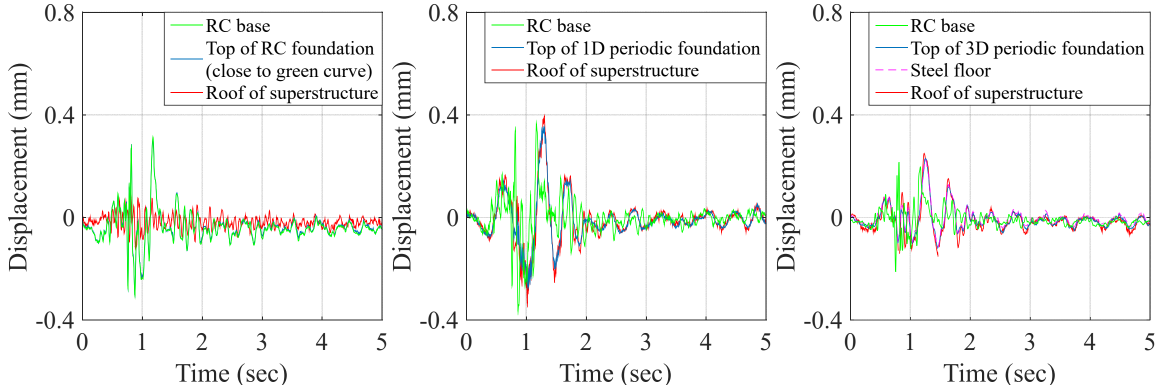

(a) Case 2 (b) Case 4 (c) Case 6

Figure 6-67 Absolute displacement response of structural systems subjected to Gilroy Earthquake in the horizontal direction

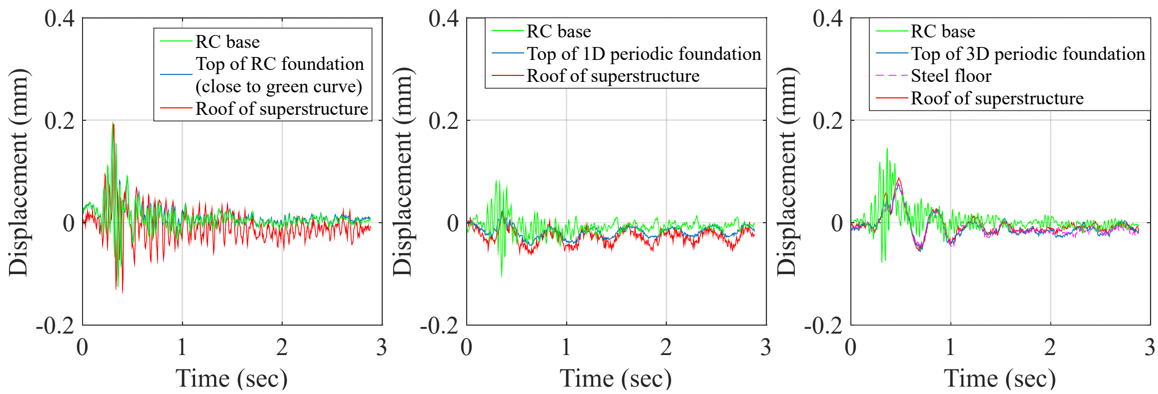

(a) Case 2 (b) Case 4 (c) Case 6

Figure 6-68 Absolute displacement response of structural systems subjected to Oroville Earthquake in the horizontal direction

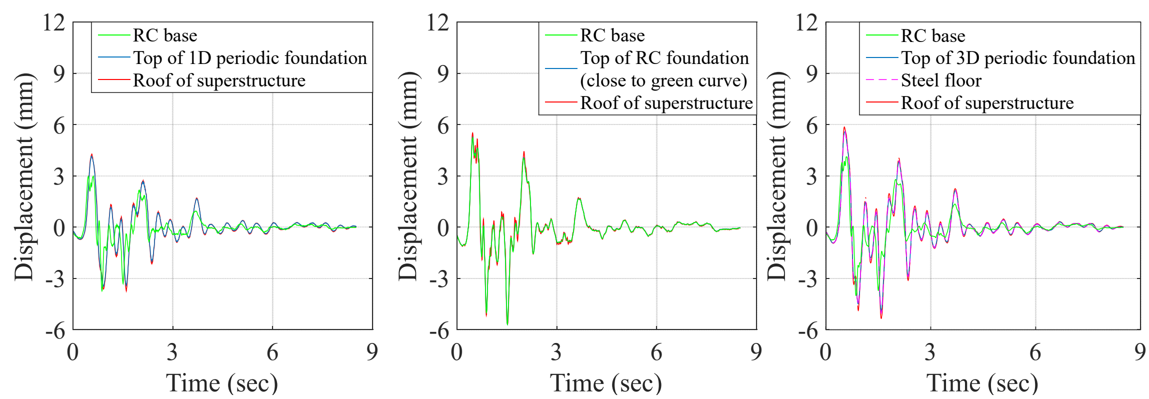

(a) Case 2 (b) Case 4 (c) Case 6

Figure 6-69 Absolute displacement response of structural systems subjected to Loma Prieta Earthquake in the horizontal direction

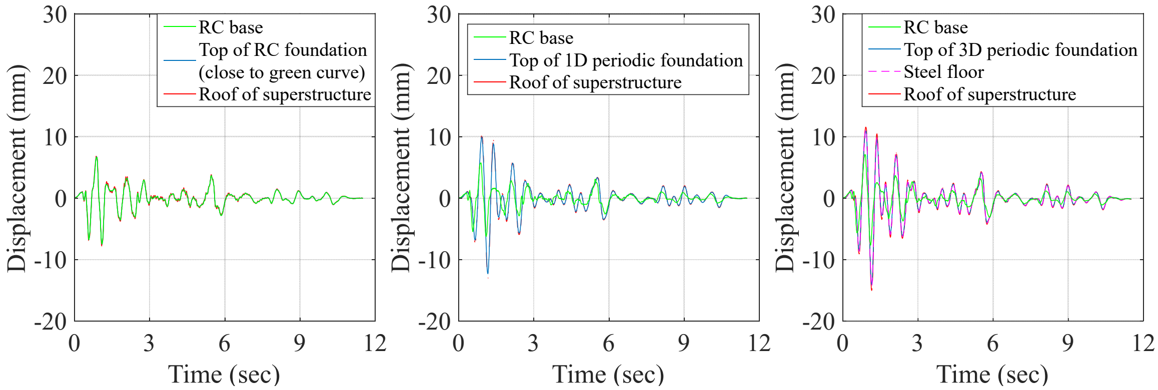

(a) Case 2 (b) Case 4 (c) Case 6

Figure 6-70 Absolute displacement response of structural systems subjected to Imperial Valley Earthquake in the horizontal direction

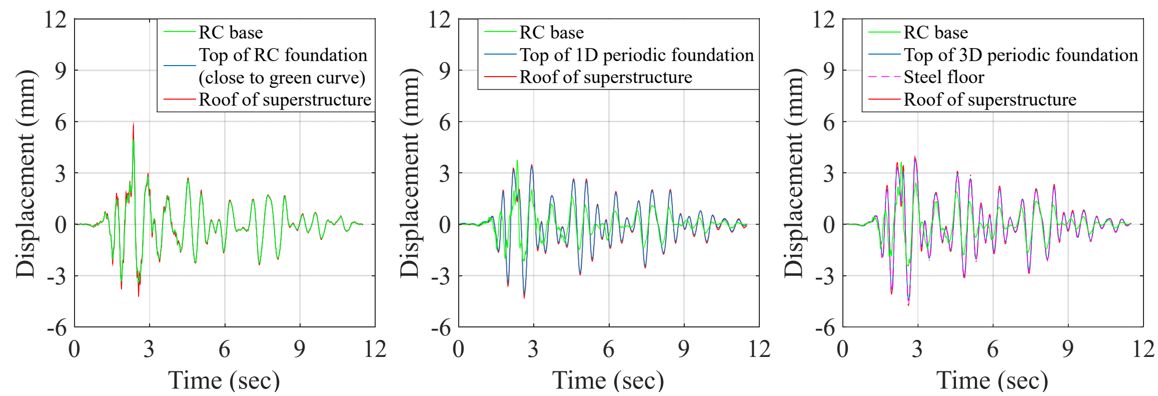

(a) Case 2 (b) Case 4 (c) Case 6

Figure 6-71 Absolute displacement response of structural systems subjected to Northridge Earthquake in the horizontal direction

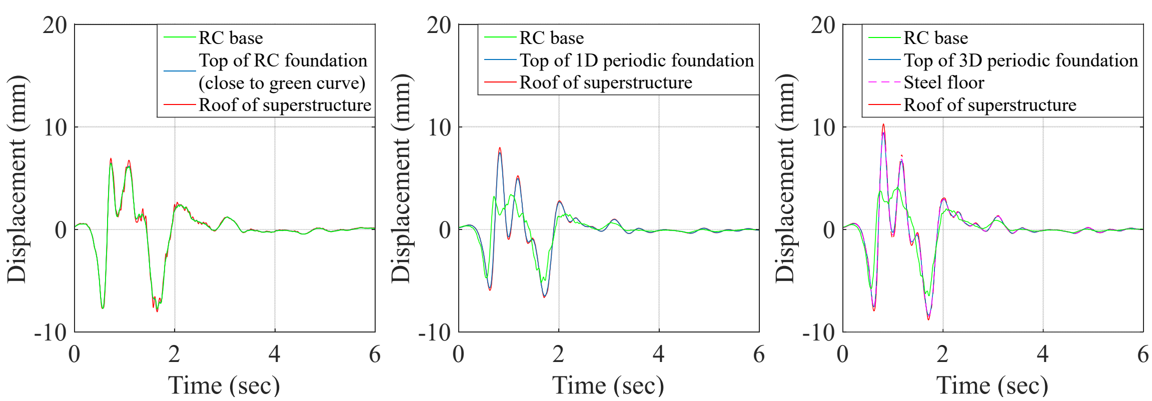

(a) Case 2 (b) Case 4 (c) Case 6

Figure 6-72 Absolute displacement response of structural systems subjected to San Fernando (Pacoima Dam) Earthquake in the horizontal direction

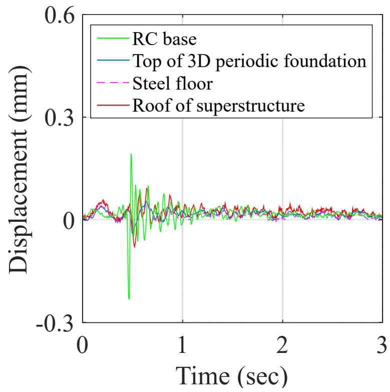

(a) Ancona Earthquake

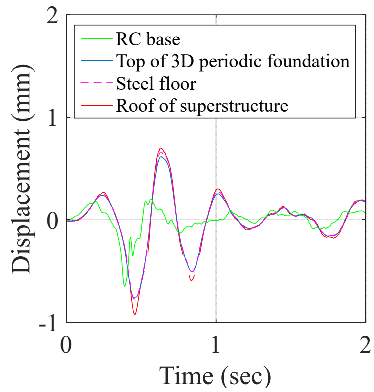

(b) Helena Earthquake

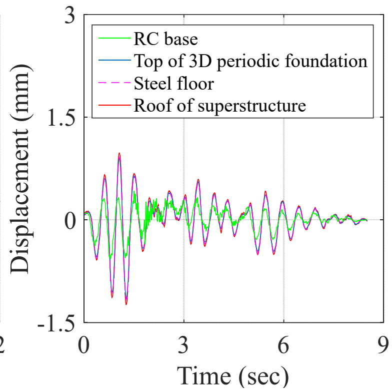

(c) Whittier Earthquake

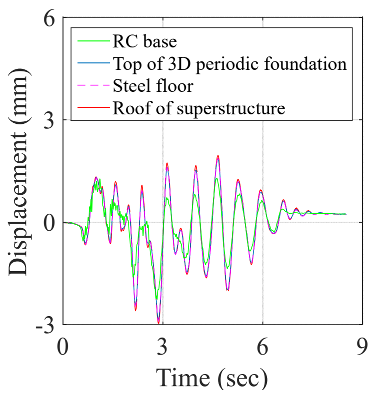

(d) San Fernando (St. Anita) Earthquake

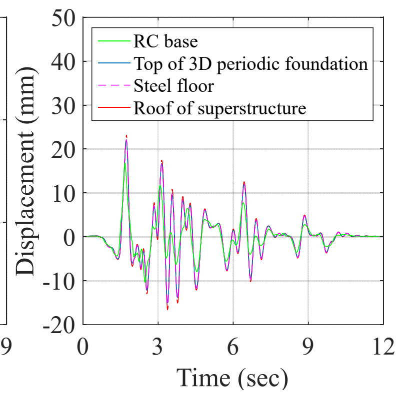

(e) Kobe Earthquake

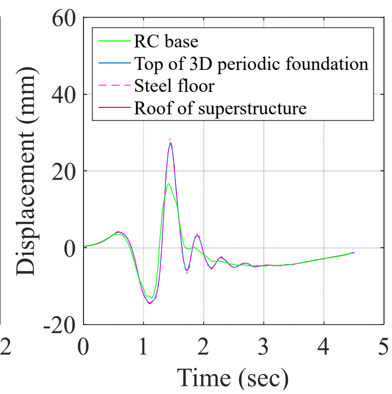

(f) Code Anza Earthquake

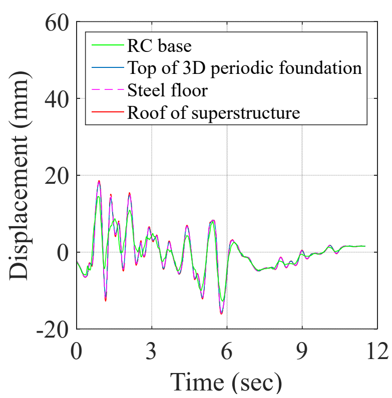

(g) Code Imperial Valley Earthquake

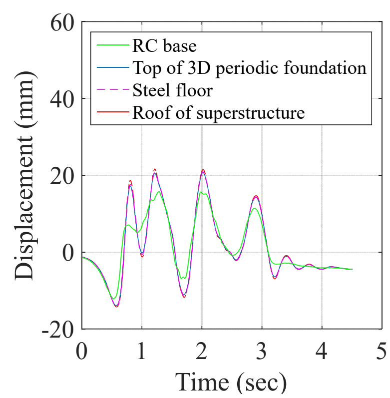

(h) Code San Fernando Earthquake

Figure 6-73 Absolute displacement response of Case 6 subjected to additional earthquakes in the horizontal direction

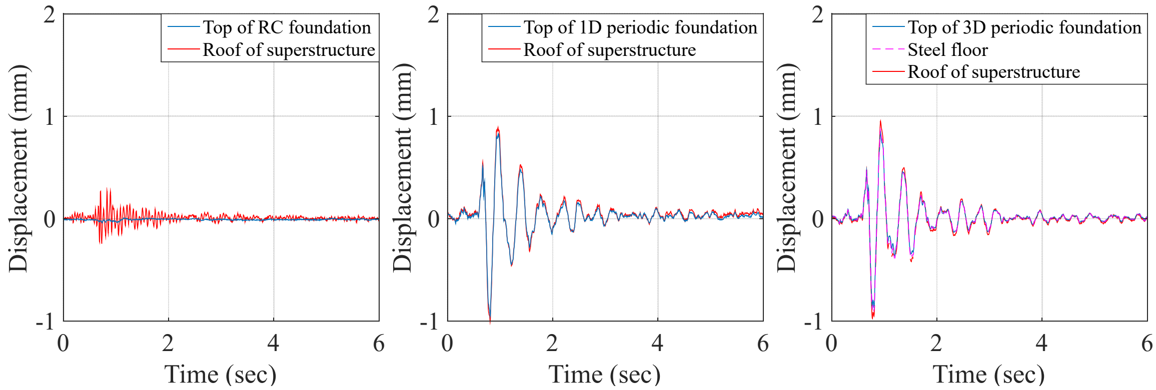

(a) Case 2 (b) Case 4 (c) Case 6

Figure 6-74 Relative displacement response of structural systems subjected to Anza Earthquake in the horizontal direction

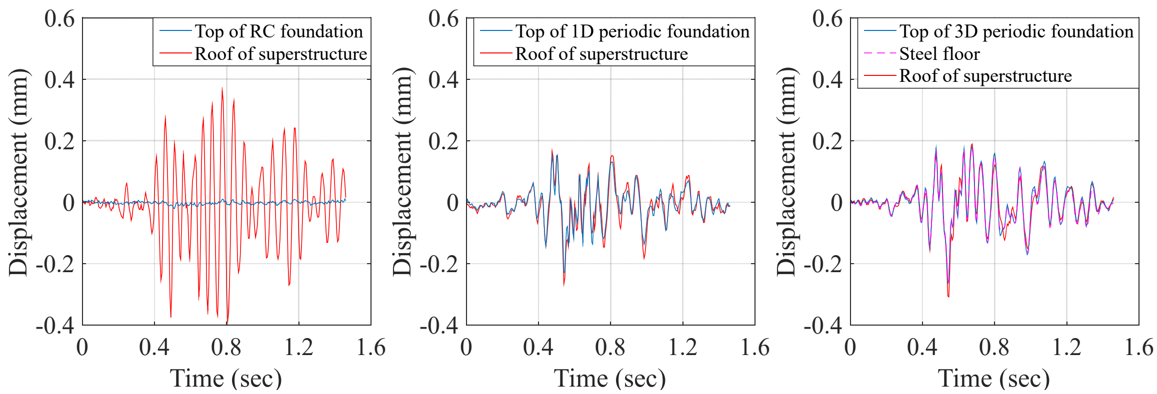

(a) Case 2 (b) Case 4 (c) Case 6

Figure 6-75 Relative displacement response of structural systems subjected to Bishop Earthquake in the horizontal direction

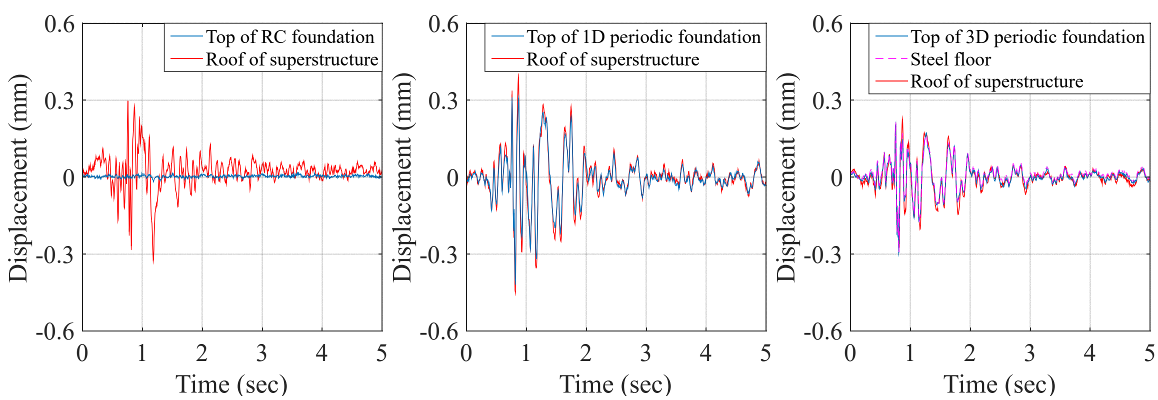

(a) Case 2 (b) Case 4 (c) Case 6

Figure 6-76 Relative displacement response of structural systems subjected to Gilroy Earthquake in the horizontal direction

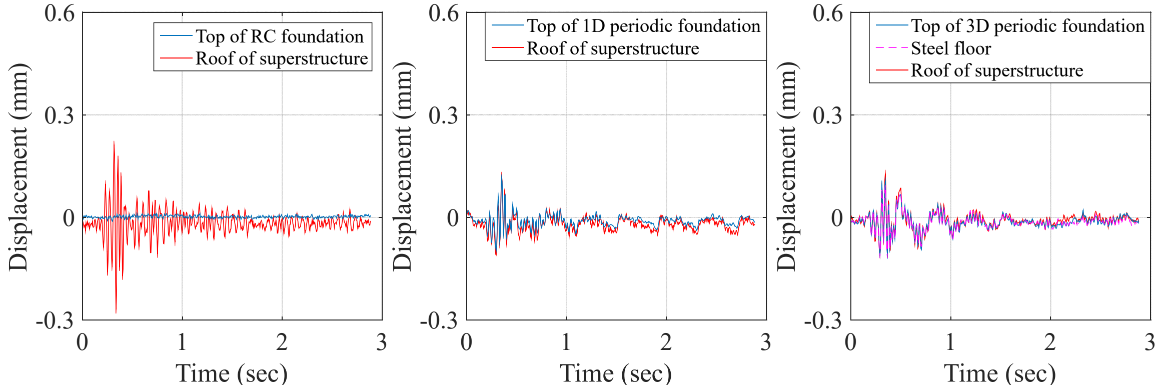

(a) Case 2 (b) Case 4 (c) Case 6

Figure 6-77 Relative displacement response of structural systems subjected to Oroville Earthquake in the horizontal direction

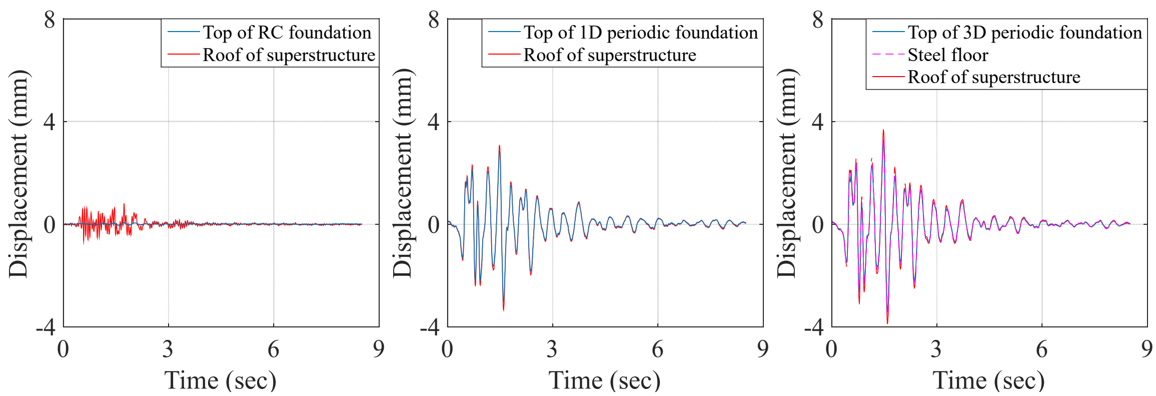

(a) Case 2 (b) Case 4 (c) Case 6

Figure 6-78 Relative displacement response of structural systems subjected to Loma Prieta Earthquake in the horizontal direction

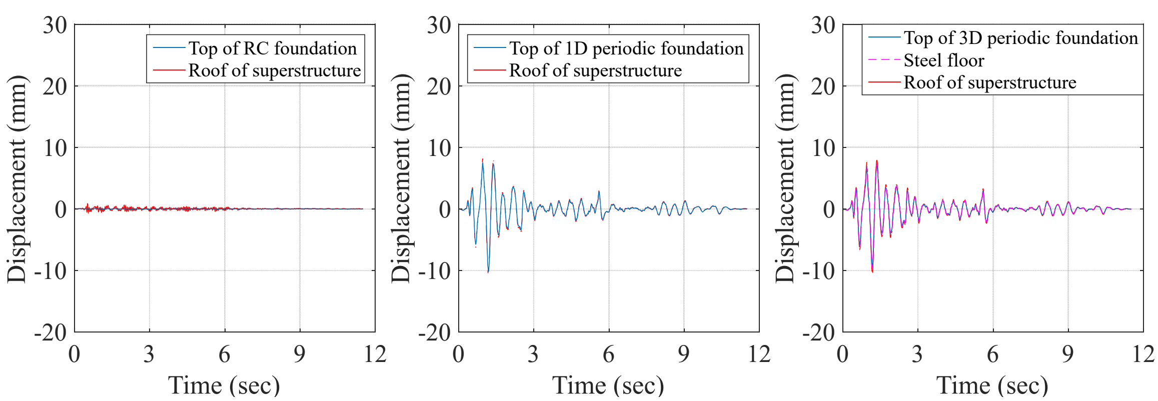

(a) Case 2 (b) Case 4 (c) Case 6

Figure 6-79 Relative displacement response of structural systems subjected to Imperial Valley Earthquake in the horizontal direction

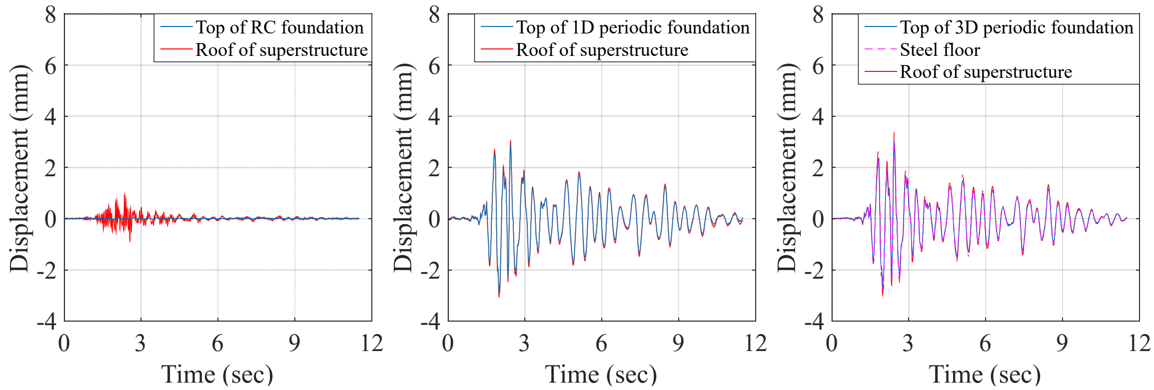

(a) Case 2 (b) Case 4 (c) Case 6

Figure 6-80 Relative displacement response of structural systems subjected to Northridge Earthquake in the horizontal direction

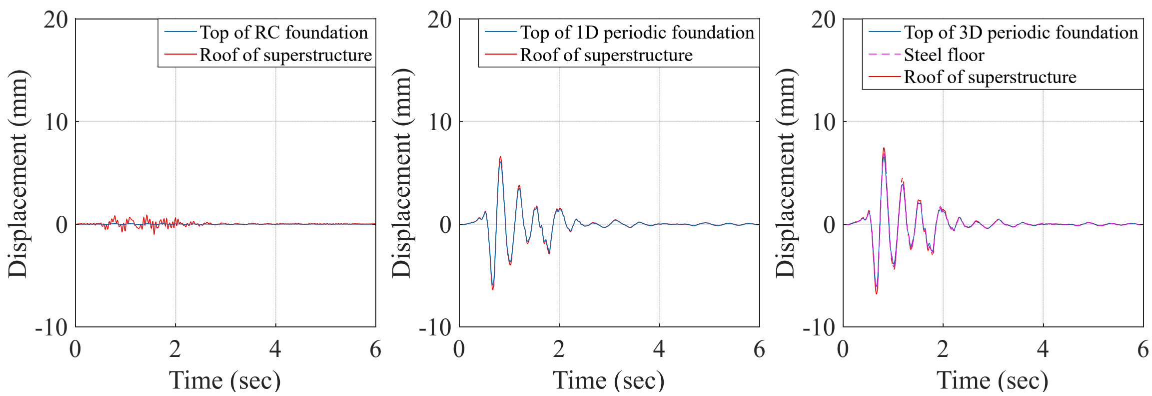

(a) Case 2 (b) Case 4 (c) Case 6

Figure 6-81 Relative displacement response of structural systems subjected to San Fernando (Pacoima Dam) Earthquake in the horizontal direction

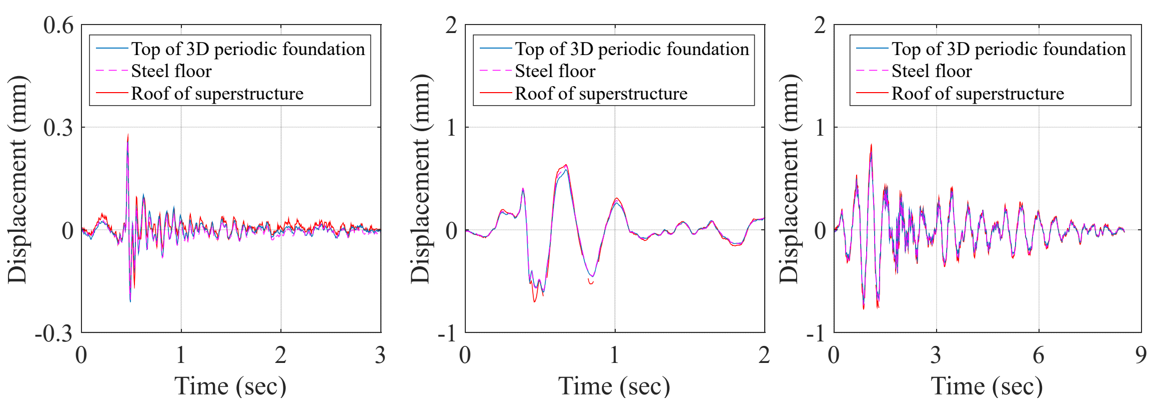

(a) Ancona Earthquake (b) Helena Earthquake (c) Whittier Earthquake

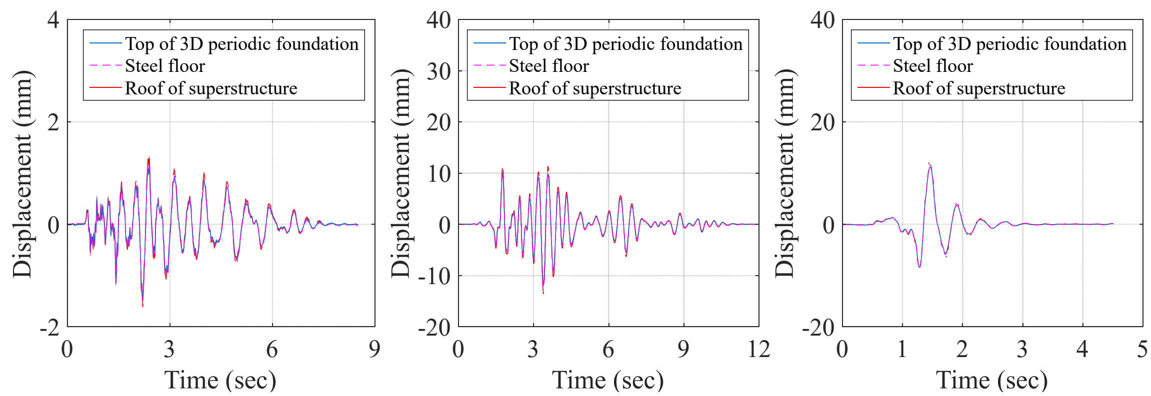

(d) San Fernando (St. Anita) Earthquake

(e) Kobe Earthquake

(f) Code Anza Earthquake

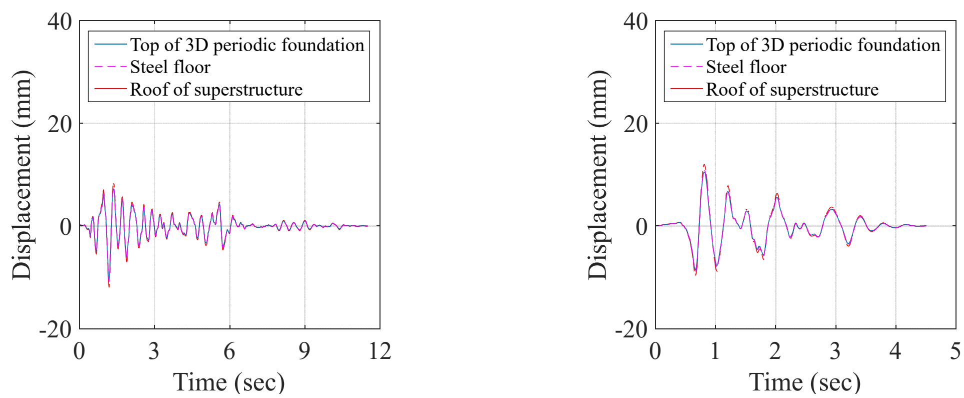

(g) Code Imperial Valley Earthquake

(h) Code San Fernando Earthquake

Figure 6-82 Relative displacement response of Case 6 subjected to additional earthquakes in the horizontal direction

Table 6-5 Peak displacement response of Case 2 in the horizontal direction

Earthquake	RC foundation structural system				
	Shake table	Top of RC foundation		Roof of superstructure	
	Absolute (mm)	Absolute (mm)	Relative to RC base (mm)	Absolute (mm)	Relative to RC base (mm)
Anza	0.8972	0.9191	0.0411	0.9434	0.2673
Bishop	0.3669	0.3853	0.0210	0.5119	0.3886
Gilroy	0.3131	0.3059	0.0181	0.1158	0.3251
Oroville	0.1898	0.1782	0.0116	0.1924	0.2694
Loma Prieta	5.6841	5.6912	0.0686	5.6695	0.7881
Imperial Valley	7.4363	7.4618	0.0606	7.7375	0.8490
Northridge	4.9037	4.9320	0.0469	5.7631	0.9163
San Fernando (Pacoima Dam)	7.7418	7.7660	0.0857	8.0306	0.9650

Table 6-6 Peak displacement response of Case 4 in the horizontal direction

Earthquake	1D periodic foundation structural system				
	RC base	Top of 1D periodic foundation		Roof of superstructure	
	Absolute (mm)	Absolute (mm)	Relative to RC base (mm)	Absolute (mm)	Relative to RC base (mm)
Anza	0.8111	1.0027	0.9480	1.0793	0.9991
Bishop	0.2978	0.2116	0.2290	0.2542	0.2651
Gilroy	0.3659	0.3526	0.4044	0.3954	0.4477
Oroville	0.0999	0.0448	0.1151	0.0612	0.1214
Loma Prieta	3.7302	4.1496	3.0125	4.2770	3.3357
Imperial Valley	6.2092	12.2787	10.1392	3.0264	10.3722
Northridge	3.7429	4.0637	2.8481	4.2816	3.0655
San Fernando (Pacoima Dam)	5.1808	7.4885	6.0803	7.9941	6.5859

Table 6-7 Peak displacement response of Case 6 in the horizontal direction

Earthquake	3D periodic foundation structural system						
	RC base	Top of 3D periodic foundation		Steel floor of superstructure		Roof of superstructure	
	Absolute (mm)	Absolute (mm)	Relative to RC base (mm)	Absolute (mm)	Relative to RC base (mm)	Absolute (mm)	Relative to RC base (mm)
Anza	0.8017	1.1007	0.8666	1.1353	0.9063	1.2119	0.9747
Bishop	0.2059	0.1137	0.2638	0.1123	0.2635	0.1544	0.3082
Gilroy	0.2160	0.2294	0.2951	0.2265	0.2942	0.2503	0.2752
Oroville	0.1457	0.0761	0.1104	0.0766	0.1180	0.0876	0.1278
Loma Prieta	4.115	5.5867	3.4121	5.6306	3.5913	5.8617	3.8744
Imperial Valley	7.6538	14.0437	9.2496	14.3366	9.6374	15.0038	10.3910
Northridge	3.6347	4.4169	2.9693	4.5364	3.0463	4.7493	3.3623
San Fernando (Pacoima Dam)	6.4732	9.4068	6.5542	9.7144	6.8752	10.2876	7.4508
Ancona	0.2327	0.0548	0.2565	0.0529	0.2592	0.0911	0.2698
Helena	0.6490	0.7574	0.6062	0.7721	0.6272	0.9207	0.7012
Whittier	0.5718	1.1517	0.7405	1.1703	0.7608	1.2373	0.8290
San Fernando (St. Anita)	2.2633	2.8497	1.4566	2.8986	1.4871	2.9657	1.6058
Kobe	16.8699	21.9362	11.8235	22.1344	12.3531	23.1023	13.5041
Code Anza	16.6996	27.0257	11.1828	27.3913	11.6118	28.2224	12.6698
Code Imperial Valley	14.4651	18.0957	10.4406	18.2445	10.8149	18.6161	11.8387
Code San Fernando	15.7581	20.7734	10.5231	20.9091	10.8933	21.6222	11.9708

The periodic foundations were designed using polyurethane layers as their component. The ultra-soft material may cause rocking of the structural systems during the shaking. To measure the amount of rocking on each of the 1D and 3D periodic foundation structural systems during horizontal seismic excitations, the data from NDI markers located at the roof of the superstructure were analyzed. The rotation on the roof of the superstructure was calculated from the difference of vertical displacements of two markers, divided by the horizontal distance between the markers, as illustrated in Figure 6-83. The calculated rotation was then converted into a degree unit. Figure 6-84 to Figure 6-86 show the roof rotation of Cases 4 and 6 subjected to the Bishop, Gilroy, and Oroville Earthquakes. The measured peak rotation data are tabulated in Table 6-8. The peak rotation of the periodic foundation structural systems is still smaller than the rotation of a building structure isolated using a combined laminated rubber bearing and air spring systems with oil dampers for rocking suppression, which has a rotation of 2.12×10^{-4} rad [10].

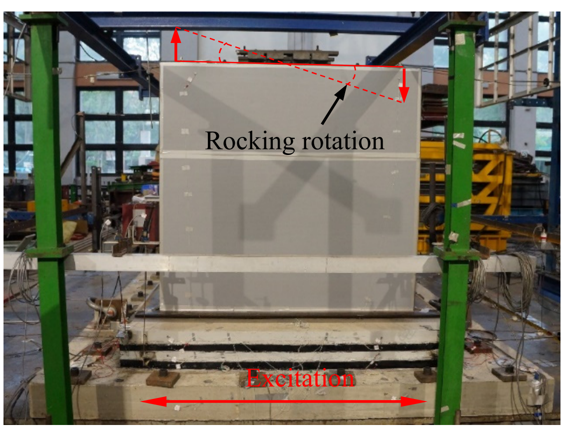

(a) Case 4

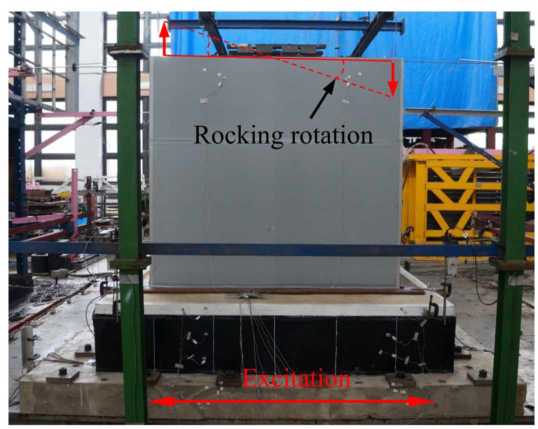

(b) Case 6

Figure 6-83 Rocking measurement on periodic foundation structural systems

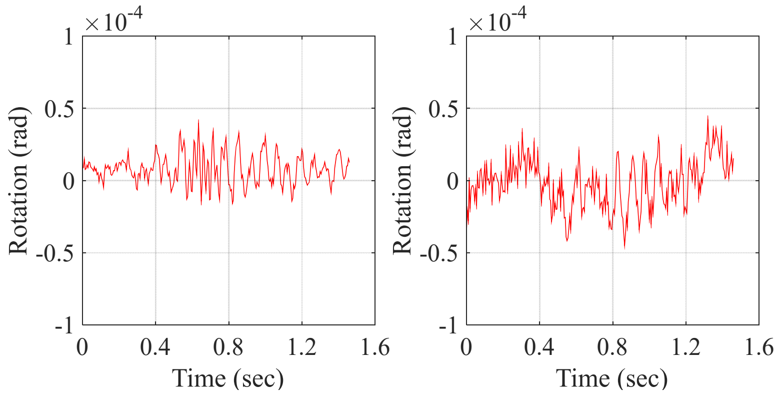

(a) Case 4 (b) Case 6

Figure 6-84 Rocking response of periodic foundation structural systems subjected to Bishop Earthquake in the horizontal direction

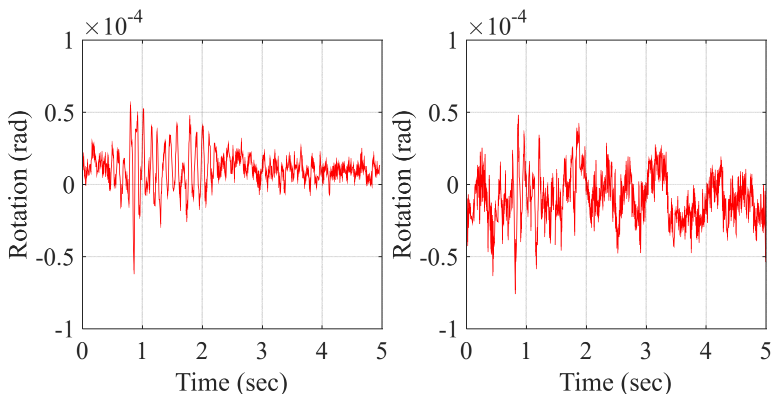

(a) Case 4 (b) Case 6

Figure 6-85 Rocking response of periodic foundation structural systems subjected to Gilroy Earthquake in the horizontal direction

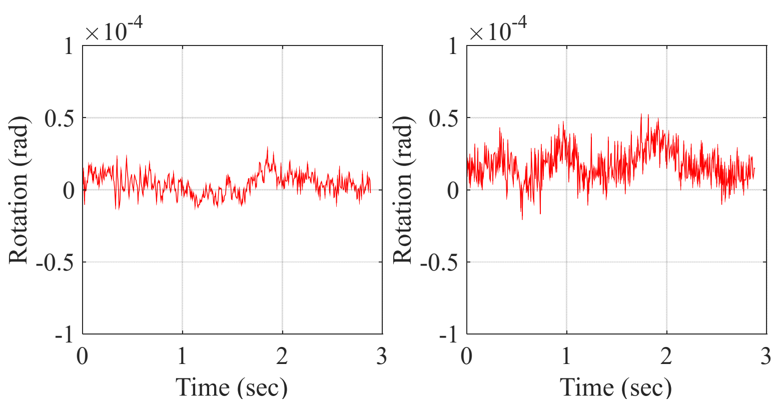

(a) Case 4 (b) Case 6

Figure 6-86 Rocking response of periodic foundation structural systems subjected to Oroville Earthquake in the horizontal direction

Table 6-8 Peak rocking response of periodic foundation structural systems

Earthquake	Rocking on Case 4 ($\times 10^{-4}$ rad)	Rocking on Case 6 ($\times 10^{-4}$ rad)
Bishop	0.3952	0.4514
Gilroy	0.5938	0.7310
Oroville	0.2740	0.5014

6.2.3.2 Responses of structural systems subjected to earthquakes in the vertical direction

6.2.3.2.1 Acceleration responses due to earthquakes in vertical direction

As obtained from the frequency sweeping tests, attenuation zones of the 1D periodic foundation structural system in the vertical direction are found to be at 20.75–24.1 Hz and 32.4–35.9 Hz (at the top of 1D periodic foundation) and 22.8–27.83 Hz and 32.4–40.75 Hz (at the roof of the superstructure). Such slim frequency band gaps are insufficient to cover the majority of the main frequency contents of the earthquakes used in these tests. Although the main frequency contents of the seismic waves falling inside the attenuation zones were attenuated, those that fall outside of the attenuation zones were amplified. Due to the fact that more regions in the main frequency contents were amplified rather than attenuated, the acceleration responses in time series at the top of the 1D periodic foundation and the roof of the superstructure were amplified. Therefore, the seismic test results of the 1D periodic foundation structural system are not suitable for use in demonstrating the theory of frequency band gaps in the vertical direction and are not presented.

On the other hand, the attenuation zones of the 3D periodic foundation structural system in the vertical direction are found to be at 21.63–32.96 Hz and 33.5–38.28 Hz, which was measured at the top of the 3D periodic foundation and 22.46–39.1 Hz, which was measured at the roof of the superstructure. These vertical attenuation zones of the 3D periodic foundation structural systems can cover more of the main frequency contents of the vertical earthquakes than those of the 1D periodic foundation structural system.

Figure 6-87 to Figure 6-90 show the response of the 3D periodic foundation structural systems in comparison to the RC foundation structural system subjected to the Anza, Bishop, Gilroy, and Oroville Earthquakes. A fair amount of acceleration reduction in comparison to the peak input acceleration is observed when the 3D periodic foundation structural system is subjected to the Anza, Bishop, and Gilroy Earthquakes. However, response amplification is observed when the periodic foundation structural system is subjected to the Oroville Earthquake. Although an amplification occurs, it is still smaller than the response of the RC periodic foundation structural system.

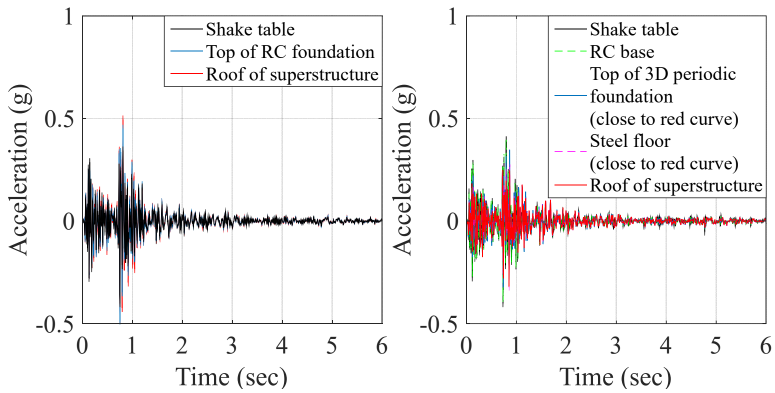

(a) Case 2 (b) Case 6

Figure 6-87 Seismic test results of structural systems subjected to Anza Earthquake in the vertical direction

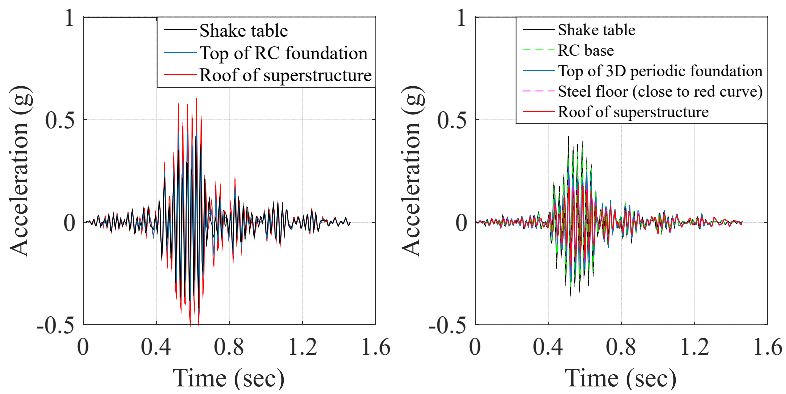

(a) Case 2 (b) Case 6

Figure 6-88 Seismic test results of structural systems subjected to Bishop Earthquake in the vertical direction

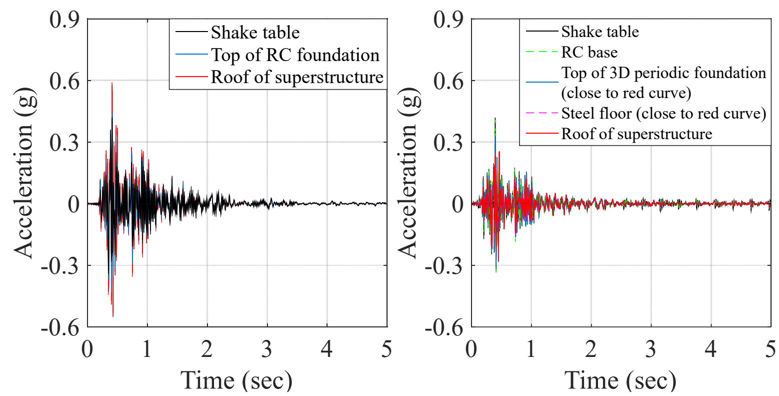

(a) Case 2 (b) Case 6

Figure 6-89 Seismic test results of structural systems subjected to Gilroy Earthquake in the vertical direction

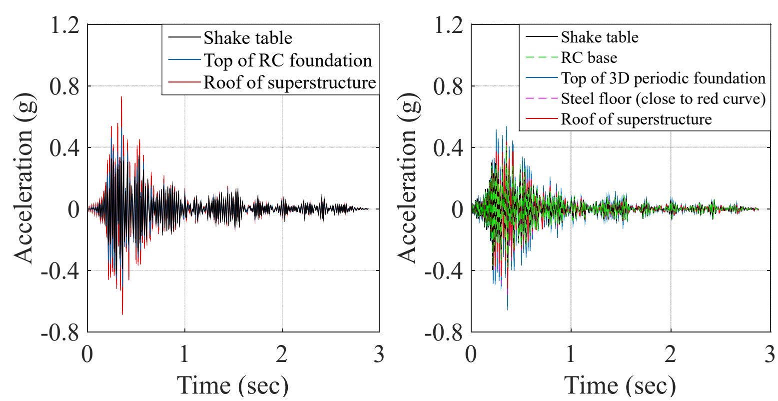

(a) Case 2 (b) Case 6

Figure 6-90 Seismic test results of structural systems subjected to Oroville Earthquake in the vertical direction

The Fourier spectra presented in Figure 6-91 to Figure 6-94 clearly demonstrate the attenuation mechanism of the 3D periodic foundation structural system. The main frequency contents of the vertical earthquakes that fall inside the attenuation zones were attenuated while those outside the frequency band gap were amplified. This mechanism is clearly different from the concept of shortening the natural frequency in the conventional isolation. Moreover, a conventional isolation system cannot isolate vertical earthquakes. In comparison to the non-isolated structure, the 3D periodic foundation structural system performed well enough. The non-isolated structure (Case 2) shows a very large response amplification on the structural system.

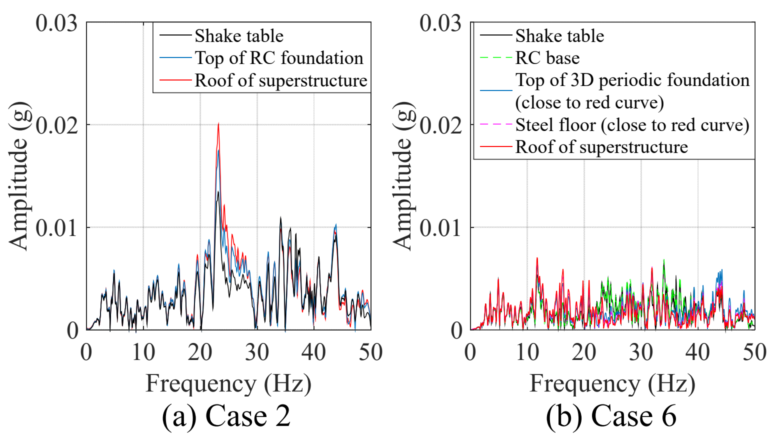

Figure 6-91 Fourier spectra of seismic test results of structural systems subjected to Anza Earthquake in the vertical direction

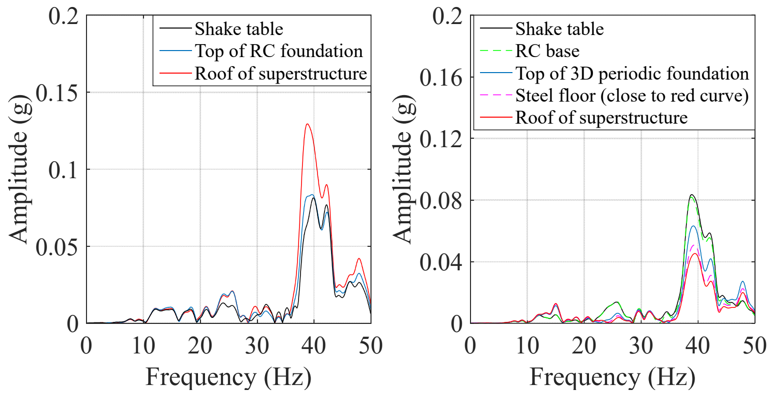

(a) Case 2 (b) Case 6

Figure 6-92 Fourier spectra of seismic test results of structural systems subjected to Bishop Earthquake in the vertical direction

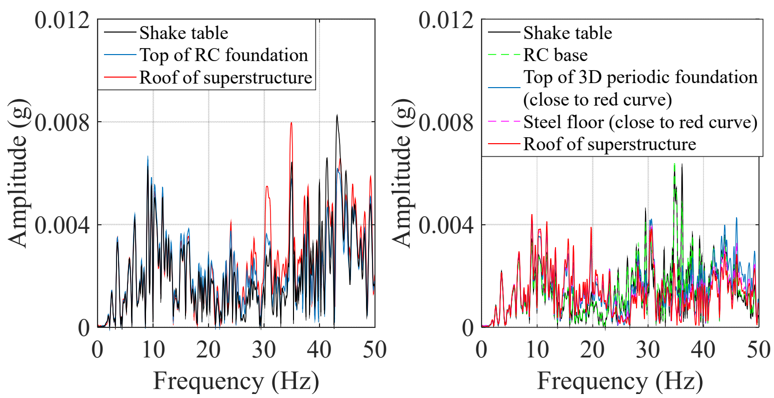

(a) Case 2 (b) Case 6

Figure 6-93 Fourier spectra of seismic test results of structural systems subjected to Gilroy Earthquake in the vertical direction

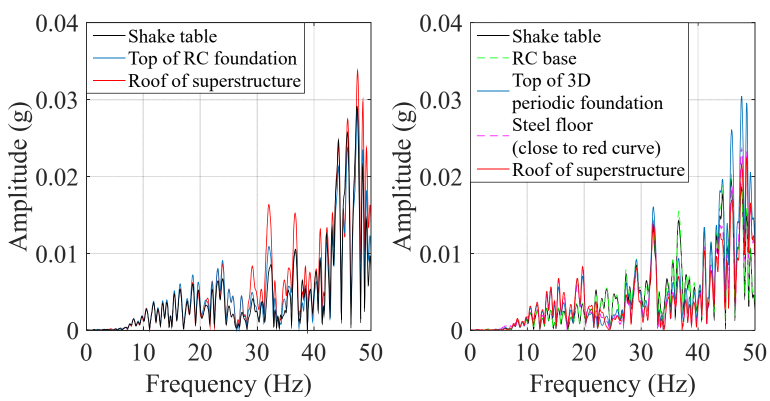

(a) Case 2 (b) Case 6

Figure 6-94 Fourier spectra of seismic test results of structural systems subjected to Oroville Earthquake in the vertical direction

The floor response spectra of Cases 2 and 6 are shown in Figure 6-95 to Figure 6-98. It is observed that the floor response spectra are very consistent with the Fourier spectra. The floor response spectra show that any non-structural elements attached to the 3D periodic foundation structural systems will experience a smaller response than when attached to a non-isolated system. These results show that the 3D periodic foundation is effective against the vertical earthquakes.

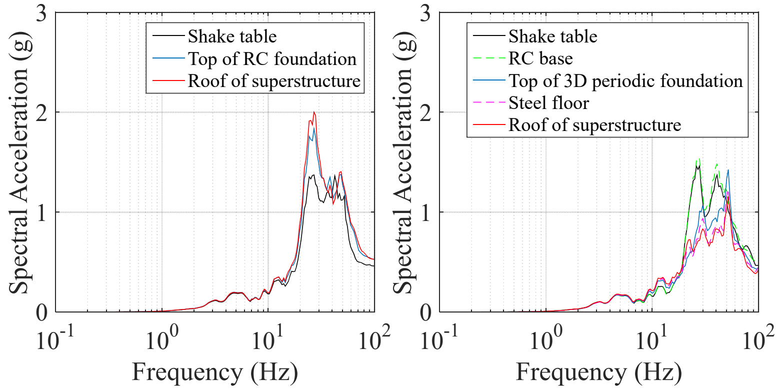

(a) Case 2 (b) Case 6

Figure 6-95 Acceleration response spectra of structural systems subjected to Anza Earthquake in the vertical direction

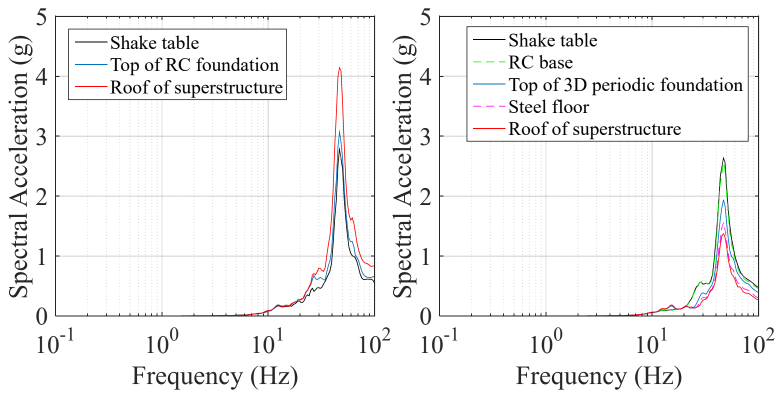

(a) Case 2 (b) Case 6

Figure 6-96 Acceleration response spectra of structural systems subjected to Bishop Earthquake in the vertical direction

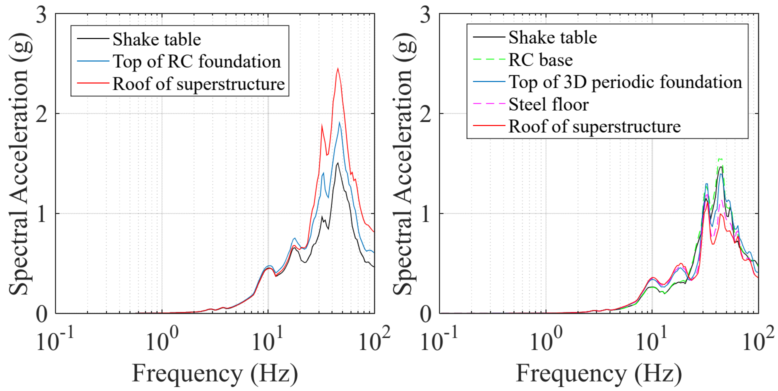

(a) Case 2 (b) Case 6

Figure 6-97 Acceleration response spectra of structural systems subjected to Gilroy Earthquake in the vertical direction

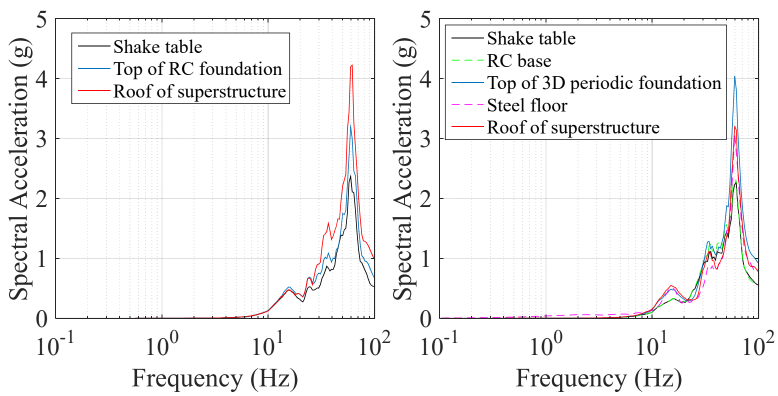

(a) Case 2 (b) Case 6

Figure 6-98 Acceleration response spectra of structural systems subjected to Oroville Earthquake in the vertical direction

Additional seismic tests on the 3D periodic foundation structural system further confirm the capability of the periodic foundation in mitigating the effect of vertical earthquakes. Acceleration response reduction in comparison to the input acceleration is observed when the structural system is subjected to the Ancona, Helena, Whittier, and San Fernando (St. Anita) Earthquakes, as shown in Figure 6-99(a) to Figure 6-99(d). Amplification of acceleration response is observed when the structural system is subjected to code compatible earthquakes. The reasons behind the response reduction or the response amplification due to different earthquakes are shown by the Fourier spectra in Figure

6-100. The distribution of the main frequency content of the input waves play a significant factor in determining the amount of response amplification or reduction.

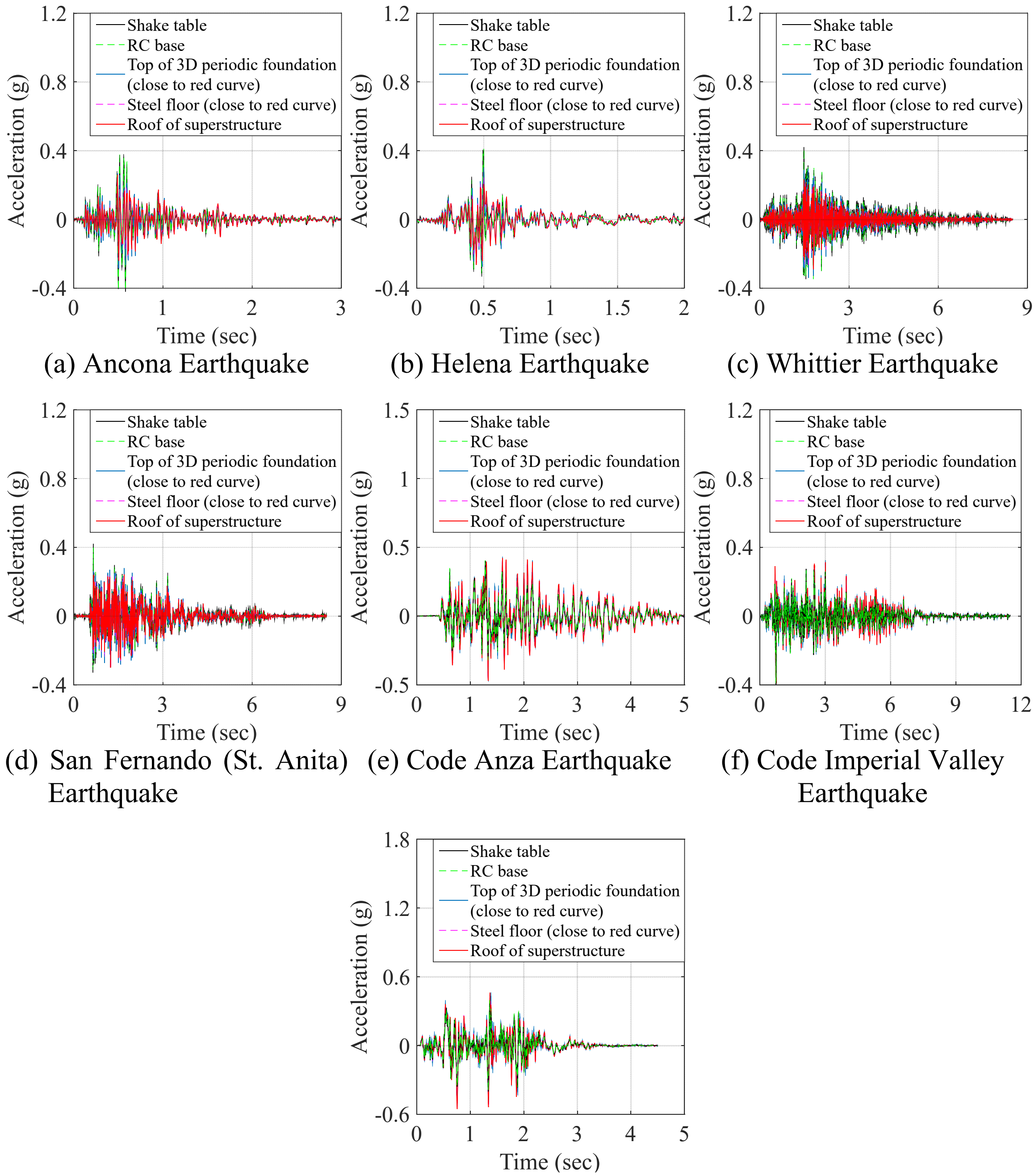

(a) Ancona Earthquake
(b) Helena Earthquake
(c) Whittier Earthquake
(d) San Fernando (St. Anita) Earthquake
(e) Code Anza Earthquake
(f) Code Imperial Valley Earthquake
(g) Code San Fernando Earthquake

Figure 6-99 Seismic test results of Case 6 subjected to additional earthquakes in the vertical direction

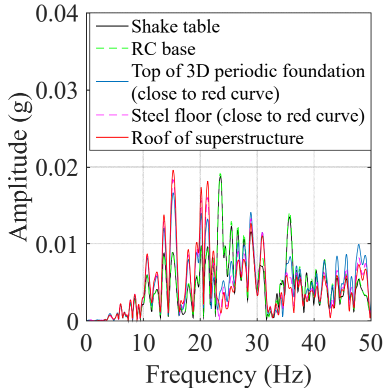

(a) Ancona Earthquake

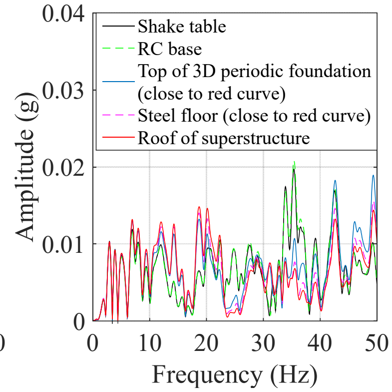

(b) Helena Earthquake

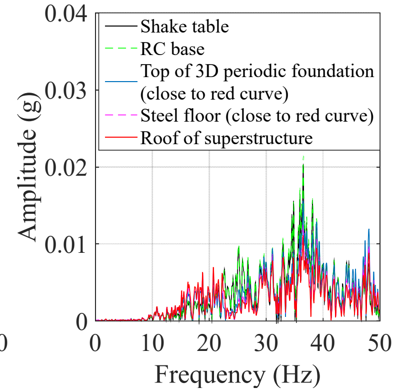

(c) Whittier Earthquake

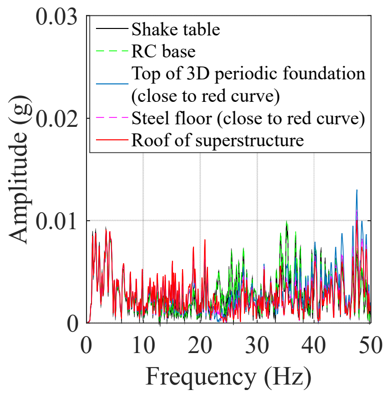

(d) San Fernando (St. Anita) Earthquake

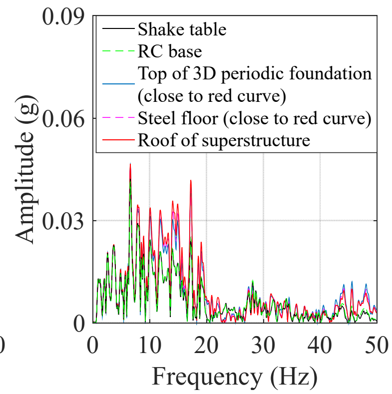

(e) Code Anza Earthquake

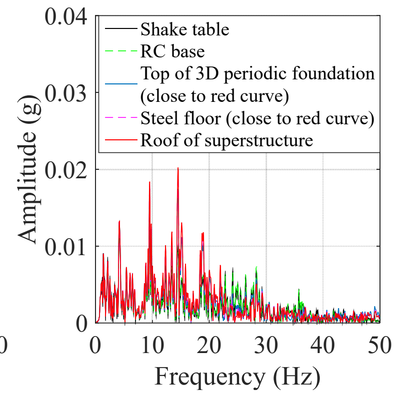

(f) Code Imperial Valley Earthquake

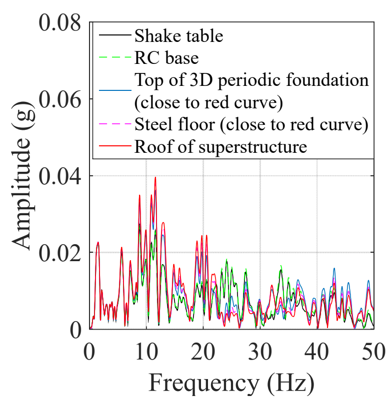

(g) Code San Fernando Earthquake

Figure 6-100 Fourier spectra of seismic test results of Case 6 subjected to additional earthquakes in the vertical direction

The response spectra of the time series from additional tests are shown in Figure 6-101. The peak acceleration of each of the time series recorded in Cases 2 and 6 is presented in Table 6-2 to Table 6-4.

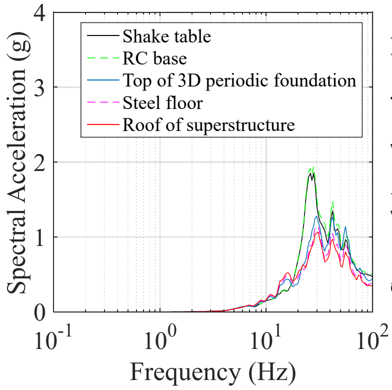

(a) Ancona Earthquake

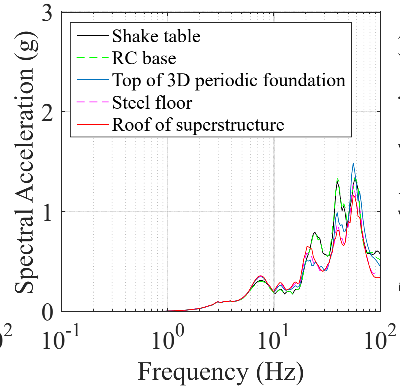

(b) Helena Earthquake

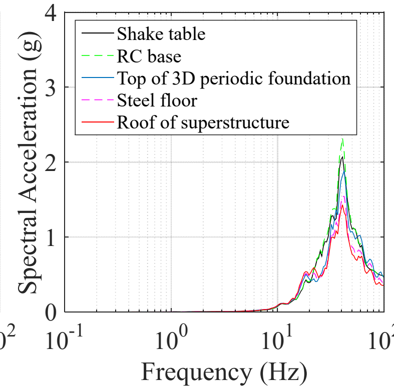

(c) Whittier Earthquake

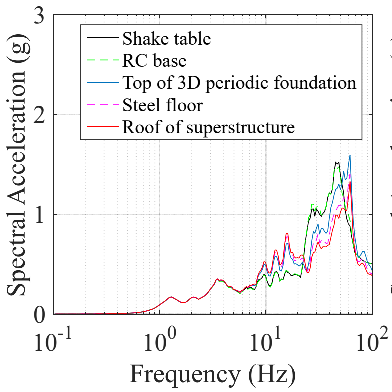

(d) San Fernando (St. Anita) Earthquake

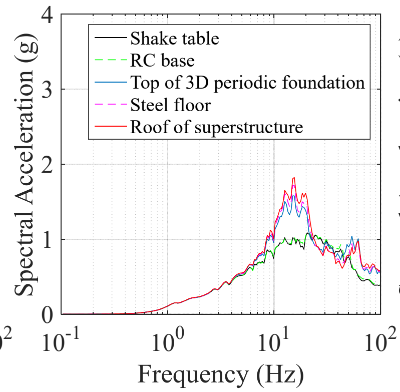

(e) Code Anza Earthquake

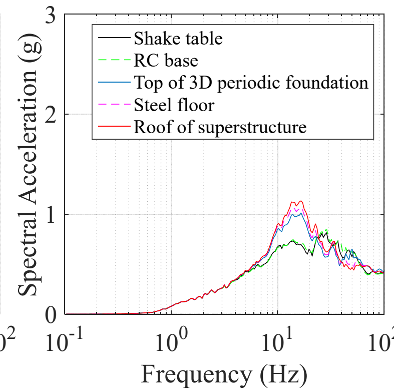

(f) Code Imperial Valley Earthquake

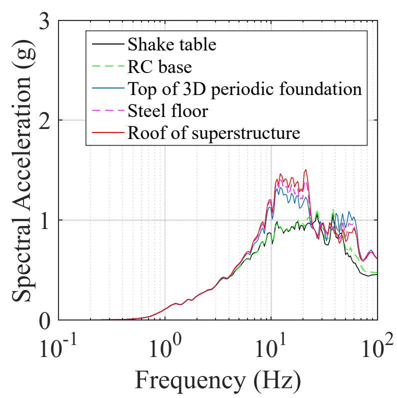

(g) Code San Fernando Earthquake

Figure 6-101 Acceleration response spectra of seismic test results of Case 6 subjected to additional earthquakes in the vertical direction

Table 6-9 Peak acceleration response and response amplification percentage of Case 2 in the vertical direction

Earthquake	RC foundation structural system				
	Shake table (g)	Top of RC foundation		Roof of superstructure	
		Acc (g)	Amplification (%)	Acc (g)	Amplification (%)
Anza	0.4	0.4849	21.22	0.4952	23.80
Bishop	0.4	0.4225	5.64	0.5852	46.29
Gilroy	0.4	0.4374	9.36	0.5714	42.85
Oroville	0.4	0.5062	26.54	0.7057	76.42

Table 6-10 Peak acceleration response and response reduction percentage of Case 6 in the vertical direction

Earthquake	3D periodic foundation structural system							
	Shake table (g)	RC base (g)	Top of 3D periodic foundation		Steel floor of superstructure		Roof of superstructure	
			Acc (g)	Reduction (%)	Acc (g)	Reduction (%)	Acc (g)	Reduction (%)
Anza	0.4	0.4027	0.3478	13.65	0.3388	15.87	0.3191	20.76
Bishop	0.4	0.3830	0.2888	24.58	0.2407	37.14	0.2168	43.38
Gilroy	0.4	0.4106	0.3209	21.84	0.2772	32.49	0.2789	32.09
Oroville	0.4	0.4154	0.6325	-52.27 (amplify)	0.5560	-33.84 (amplify)	0.5163	-24.29 (amplify)
Ancona	0.4	0.4281	0.2843	33.59	0.2575	39.85	0.2598	39.31
Helena	0.4	0.4095	0.3005	26.63	0.2525	38.33	0.2646	35.39
Whittier	0.4	0.4099	0.3394	17.21	0.2764	32.58	0.2893	29.42
San Fernando (St. Anita)	0.4	0.3999	0.2981	25.46	0.3052	23.67	0.3002	24.93
Code Anza	0.4	0.4040	0.4537	-12.29 (amplify)	0.4541	-12.38 (amplify)	0.4712	-16.63 (amplify)
Code Imperial Valley	0.4	0.3894	0.3784	2.80	0.3979	-2.19 (amplify)	0.3955	-1.57 (amplify)
Code San Fernando	0.4	0.4012	0.5026	-25.26 (amplify)	0.5368	-33.79 (amplify)	0.5541	-38.09 (amplify)

6.2.3.2.2 Displacement responses due to earthquakes in vertical direction

Figure 6-102 to Figure 6-105 show the measured vertical displacement of the RC foundation and the 3D periodic foundation structural systems under vertical earthquakes measured using the NDI systems. The displacement relative to their respective RC base is shown in Figure 6-106 to Figure 6-109. The peak absolute and relative displacements are tabulated in Table 6-11 and Table 6-12. Since the attenuation zones of the 3D periodic foundation structural system in the vertical direction do not completely cover the main frequency content of the earthquakes, it causes amplification in the lower frequency region that results in a large displacement response. Therefore, Case 6 has a larger relative displacement than Case 4.

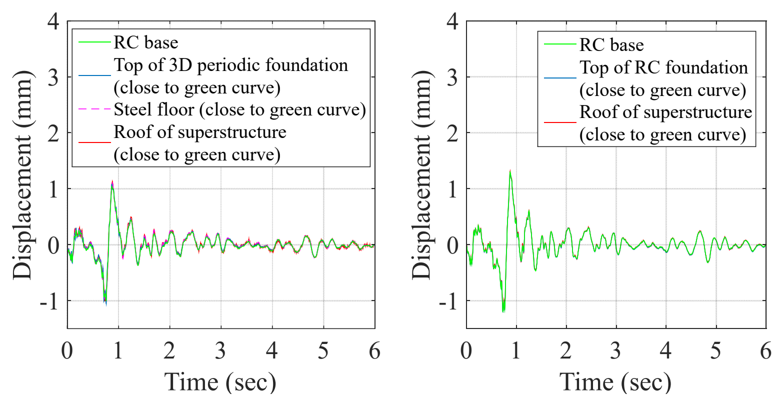

(a) Case 2 (b) Case 6

Figure 6-102 Absolute displacement response of structural systems subjected to Anza Earthquake in the vertical direction

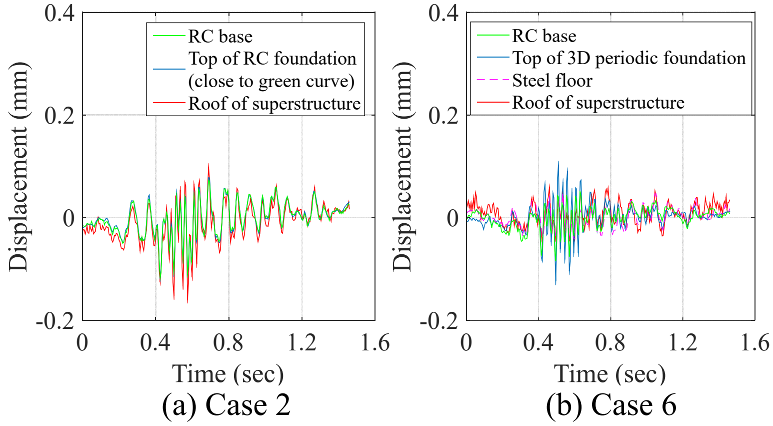

Figure 6-103 Absolute displacement response of structural systems subjected to Bishop Earthquake in the vertical direction

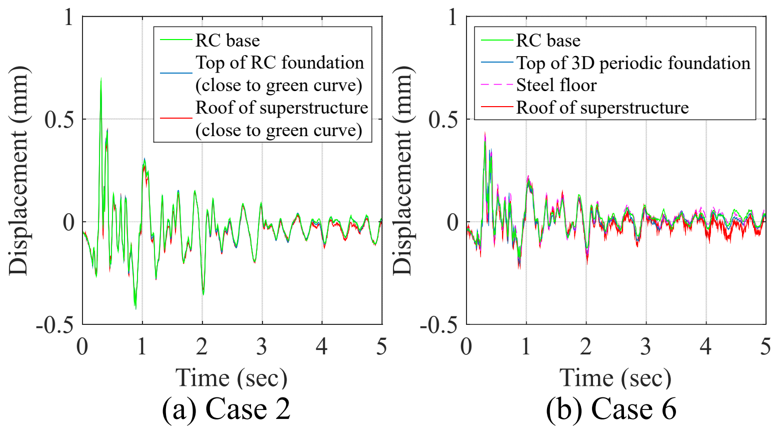

Figure 6-104 Absolute displacement response of structural systems subjected to Gilroy Earthquake in the vertical direction

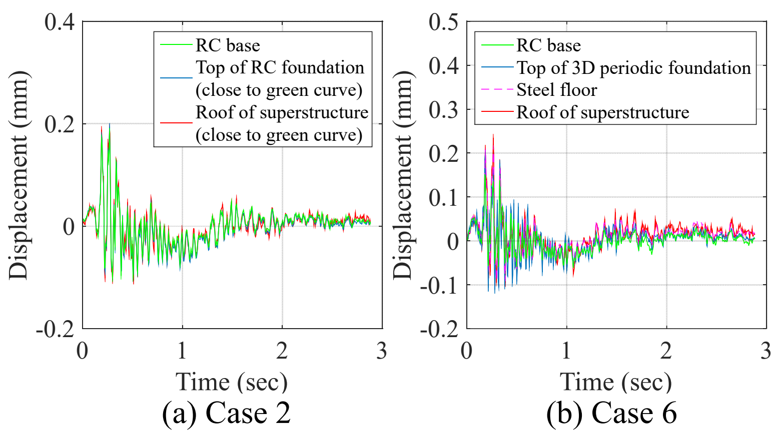

Figure 6-105 Absolute displacement response of structural systems subjected to Oroville Earthquake in the vertical direction

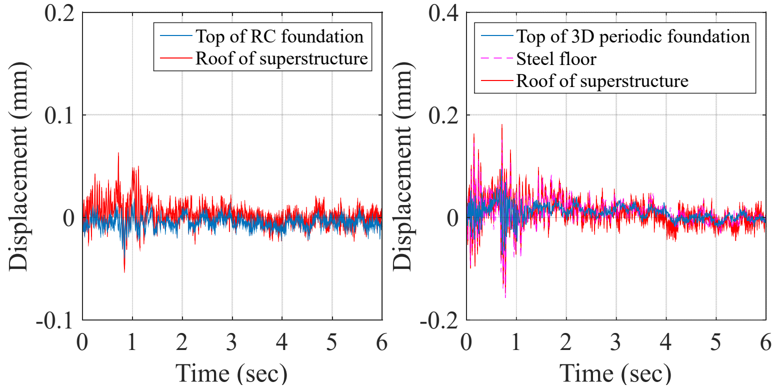

(a) Case 2 (b) Case 6

Figure 6-106 Relative displacement response of structural systems subjected to Anza Earthquake in the vertical direction

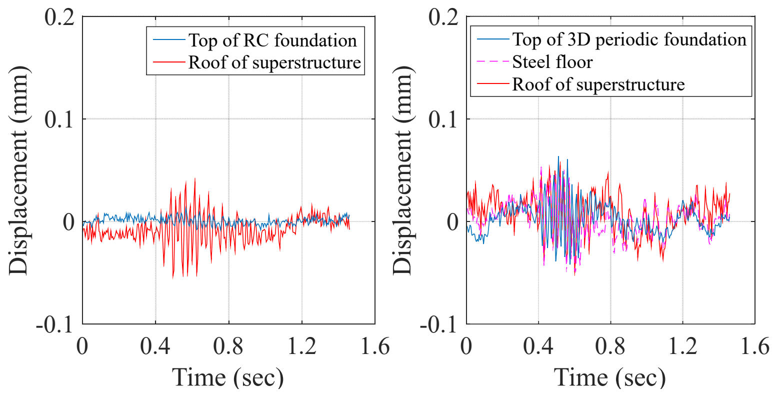

(a) Case 2 (b) Case 6

Figure 6-107 Relative displacement response of structural systems subjected to Bishop Earthquake in the vertical direction

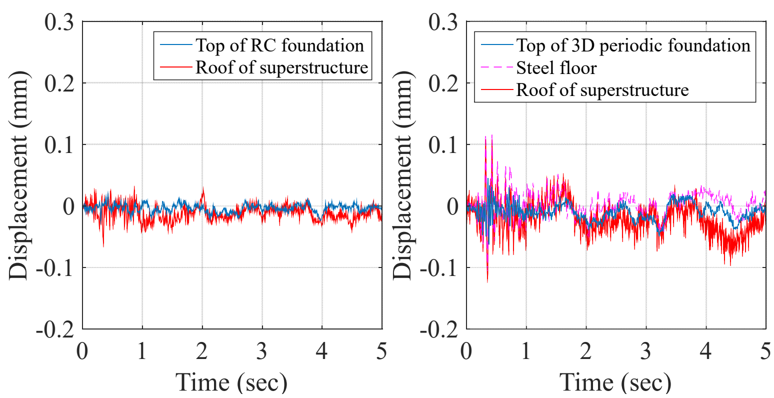

(a) Case 2 (b) Case 6

Figure 6-108 Relative displacement response of structural systems subjected to Gilroy Earthquake in the vertical direction

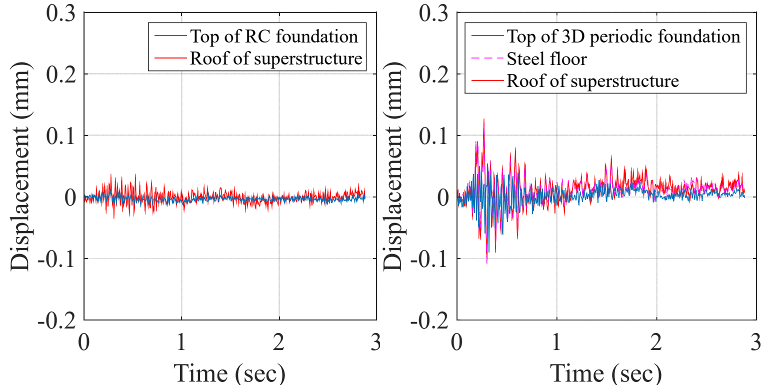

(a) Case 2 (b) Case 6

Figure 6-109 Relative displacement response of structural systems subjected to Oroville Earthquake in the vertical direction

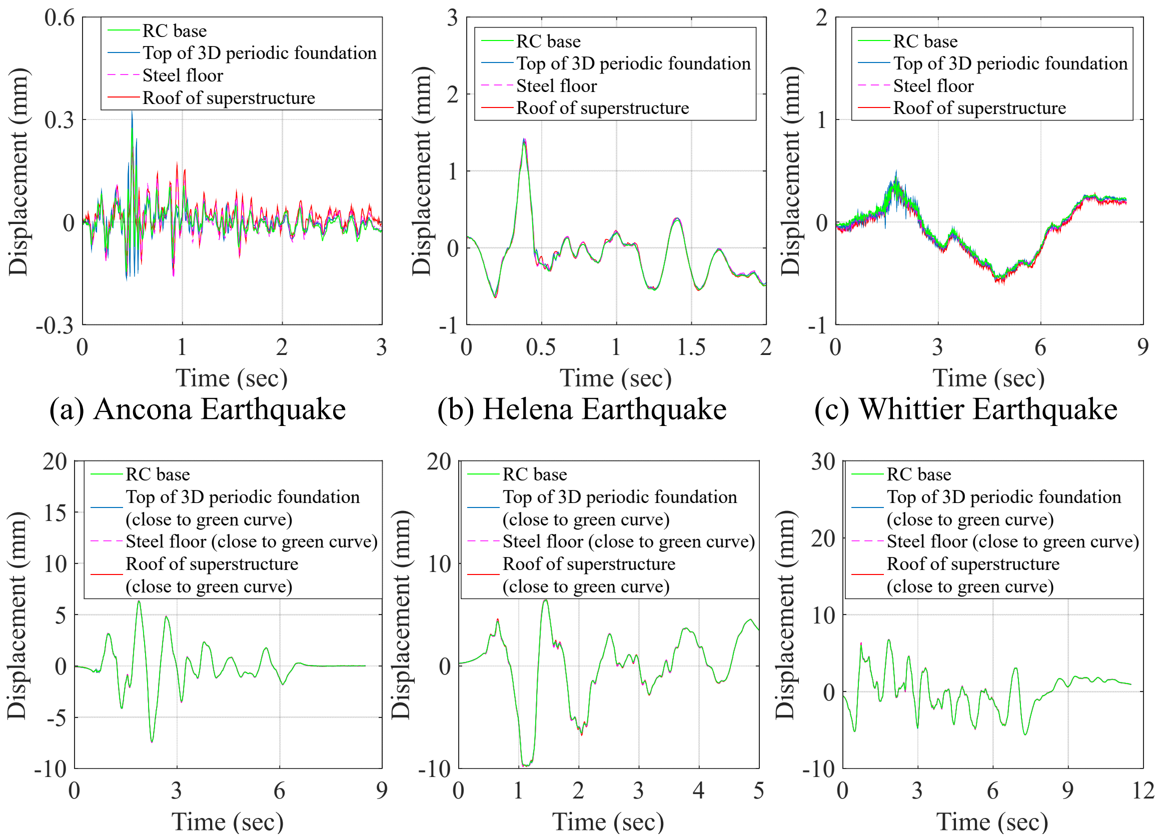

(a) Ancona Earthquake (b) Helena Earthquake (c) Whittier Earthquake

(d) San Fernando (St. Anita) Earthquake (e) Code Anza Earthquake (f) Code Imperial Valley Earthquake

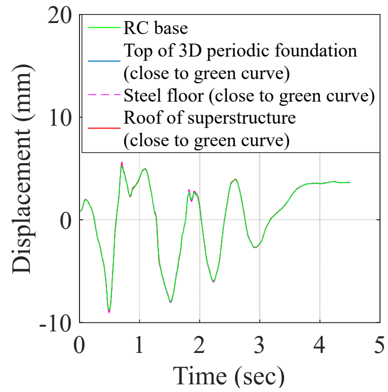

(g) Code San Fernando Earthquake

Figure 6-110 Absolute displacement response of Case 6 subjected to additional earthquakes in the vertical direction

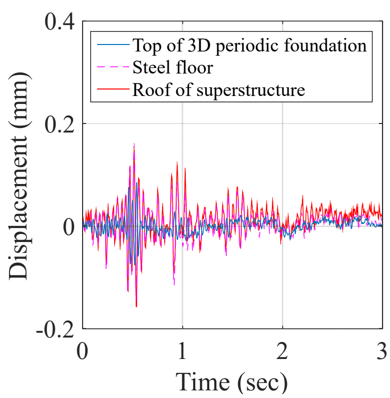

(a) Ancona Earthquake

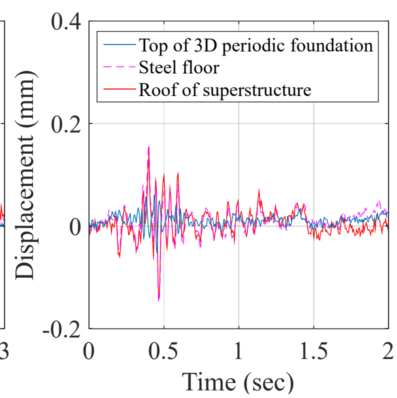

(b) Helena Earthquake

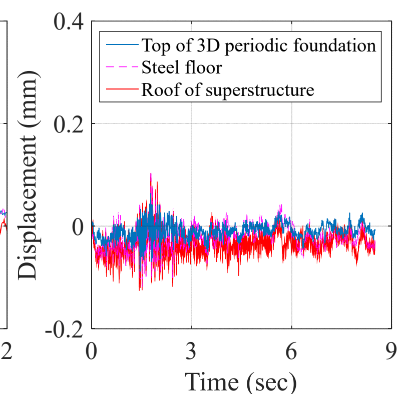

(c) Whittier Earthquake

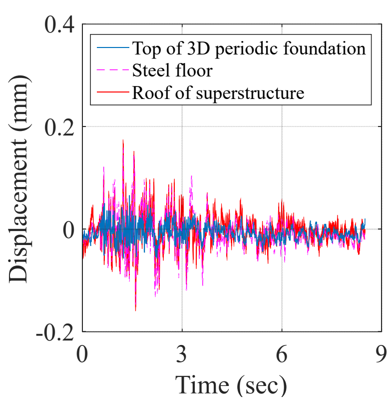

(d) San Fernando (St. Anita) Earthquake

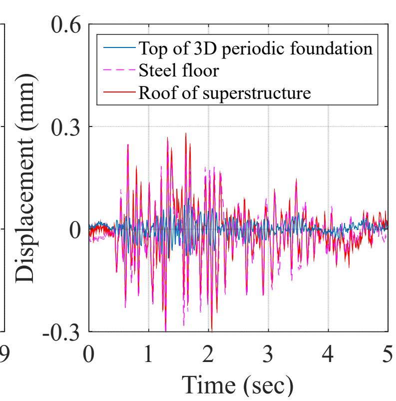

(e) Code Anza Earthquake

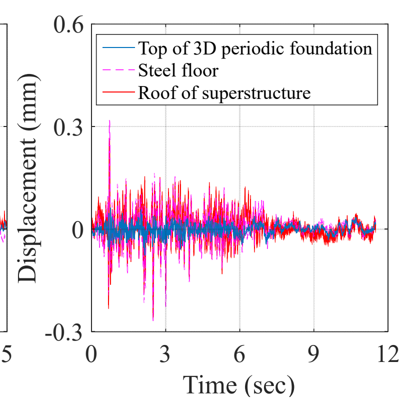

(f) Code Imperial Valley Earthquake

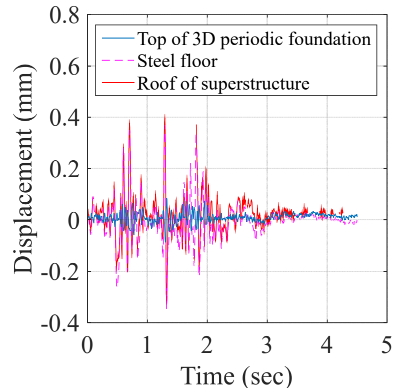

(g) Code San Fernando Earthquake

Figure 6-111 Relative displacement response of Case 6 subjected to additional earthquakes in the vertical direction

Table 6-11 Peak displacement response of Case 2 in the vertical direction

Earthquake	RC foundation structural system				
	Shake table	Top of RC foundation		Roof of superstructure	
	Absolute (mm)	Absolute (mm)	Relative to RC base (mm)	Absolute (mm)	Relative to RC base (mm)
Anza	1.2968	1.2805	0.0360	1.3112	0.0596
Bishop	0.1166	0.1183	0.0128	0.1591	0.0529
Gilroy	0.6829	0.6666	0.0242	0.6556	0.0608
Oroville	0.1840	0.1934	0.0142	0.1910	0.0314

Table 6-12 Peak displacement response of Case 6 in the vertical direction

Earthquake	3D periodic foundation structural system						
	RC base	Top of 3D periodic foundation		Steel floor of superstructure		Roof of superstructure	
	Absolute (mm)	Absolute (mm)	Relative to RC base (mm)	Absolute (mm)	Relative to RC base (mm)	Absolute (mm)	Relative to RC base (mm)
Anza	1.0479	1.0793	0.0936	1.1149	0.1591	1.1302	0.1743
Bishop	0.0847	0.1235	0.0637	0.0478	0.0551	0.0590	0.0545
Gilroy	0.3917	0.3949	0.0627	0.4283	0.1168	0.4203	0.1186
Oroville	0.1516	0.1974	0.0901	0.2175	0.1179	0.2346	0.1209
Ancona	0.2750	0.3145	0.0854	0.2280	0.1615	0.2165	0.1572
Helena	1.3557	1.4138	0.0614	1.4145	0.1595	1.3793	0.1408
Whittier	0.5488	0.5561	0.0884	0.5637	0.1209	0.5873	0.1183
San Fernando (St. Anita)	7.3708	7.4043	0.0660	7.4776	0.1585	7.4321	0.1671
Code Anza	9.7538	9.7603	0.0914	9.8274	0.3031	9.8104	0.2921
Code Imperial Valley	6.7250	6.7457	0.0762	6.7738	0.3188	6.7775	0.2645
Code San Fernando	8.8009	8.7783	0.0877	9.0627	0.3687	8.9593	0.3969

6.2.3.3 Responses of structural systems subjected to earthquakes in the torsional mode

The frequency sweeping tests confirmed a wide attenuation zone in the torsional mode. Two earthquake records were used for the rotational seismic tests. Figure 6-112 shows the torsional acceleration responses of structural systems subjected to the Bishop Earthquake. A large response reduction is observed on the structural response of Case 4. The acceleration response reduction on each of the top of the 1D periodic foundation and the roof of the superstructure is found to be 95.44% and 93.6%, respectively. A large response reduction is also observed on the structural response of Case 6. At the top of the 3D periodic foundation and the roof of the superstructure, the reductions in acceleration are found to be 93.72% and 92.97%, respectively. Figure 6-113 shows the acceleration responses of structural systems subjected to the Imperial Valley Earthquake. In Case 4, the maximum acceleration observed at the top of the periodic foundation is reduced by 38.19% from the input acceleration on the shake table, while that at the roof of the superstructure is reduced by 36.91%. In Case 6, the maximum acceleration observed at the top of the 3D periodic foundation is reduced by 1.36% from the input acceleration at the RC base, while that at the roof of the superstructure is amplified by 1.32%. Although slight amplification is observed in Case 6 when subjected to the El Centro seismic waves in the torsional mode, a much larger amplification is observed in the structural response of Case 2 when subjected to the same earthquake.

The difference in the results of the periodic foundation structural systems when subjected to the two different earthquakes can be explained by the distribution of the main frequency contents of both earthquakes. Figure 6-114 and Figure 6-115 show the Fourier spectra of the recorded rotational accelerations on Cases 4 and 6. The Bishop Earthquake has all of its main frequency content located inside the torsional attenuation zones. Hence, all of the frequency content can be seen to be greatly attenuated. The El Centro Earthquake, on the other hand, has fairly distributed main frequency content. The main frequency content with frequencies in the region outside the frequency band gap is amplified while those inside the frequency band gap are attenuated. The amplification of response outside the attenuation zones is large enough to cause amplification in the time series.

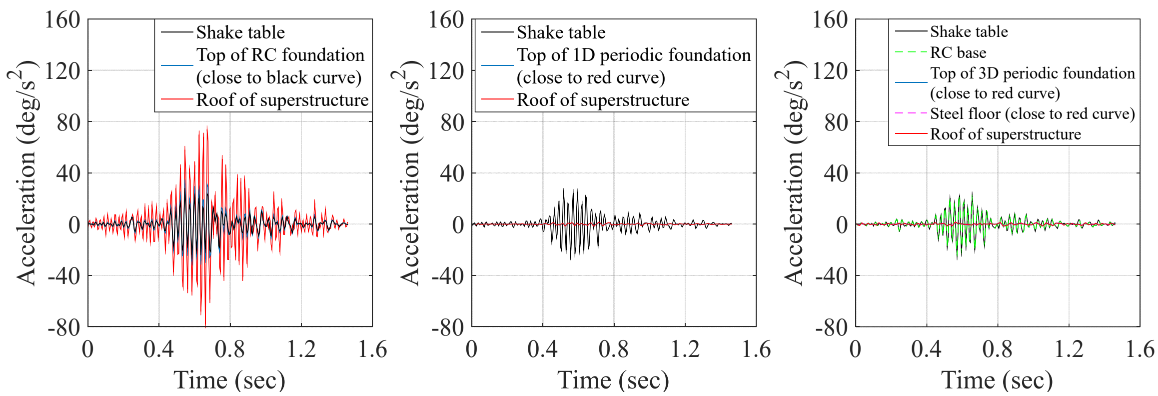

(a) Case 2 (b) Case 4 (c) Case 6

Figure 6-112 Seismic test results of structural systems subjected to Bishop Earthquake in the torsional mode

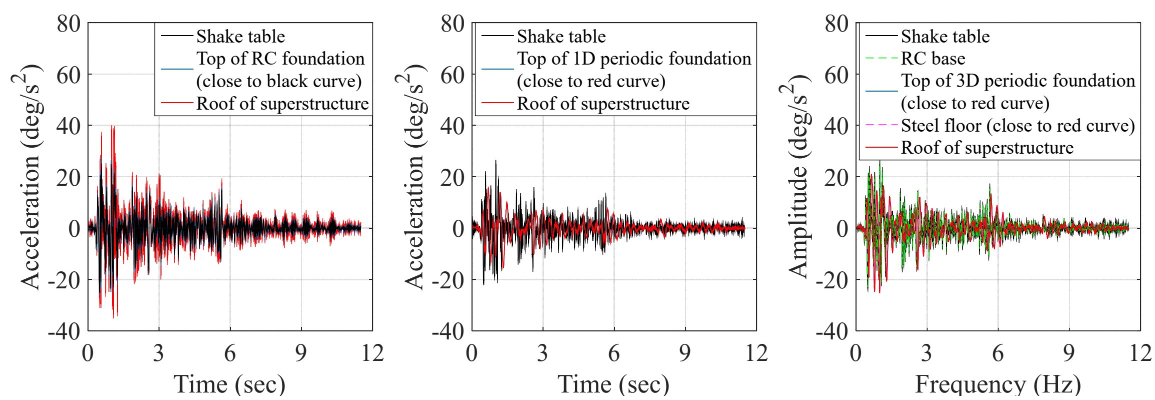

(a) Case 2 (b) Case 4 (c) Case 6

Figure 6-113 Seismic test results of structural systems subjected to Imperial Valley Earthquake in the torsional mode

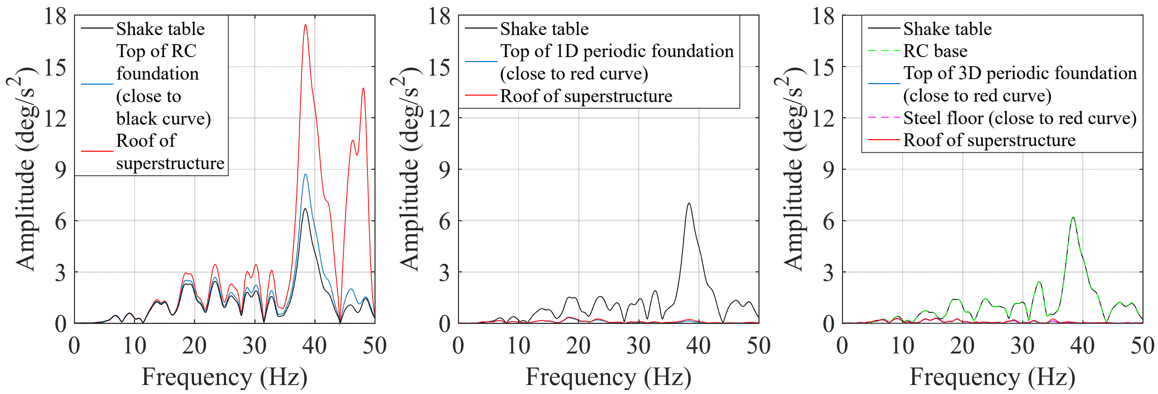

(a) Case 2 (b) Case 4 (c) Case 6

Figure 6-114 Fourier spectra of seismic test results of structural systems subjected to Anza Earthquake in the torsional mode

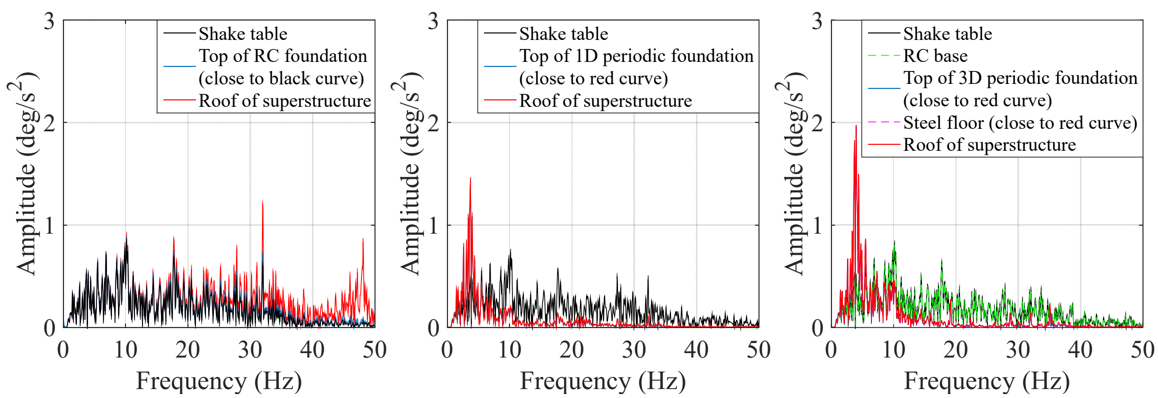

(a) Case 2 (b) Case 4 (c) Case 6

Figure 6-115 Fourier spectra of seismic test results of structural systems subjected to Imperial Valley Earthquake in the torsional mode

The response spectra of Cases 4 and 6 structural systems shown in Figure 6-116 and Figure 6-117 indicated a much lower acceleration response at higher frequency while that of Case 2 show large amplification at higher frequency especially at 46.88 Hz, which is the natural frequency of Case 2.

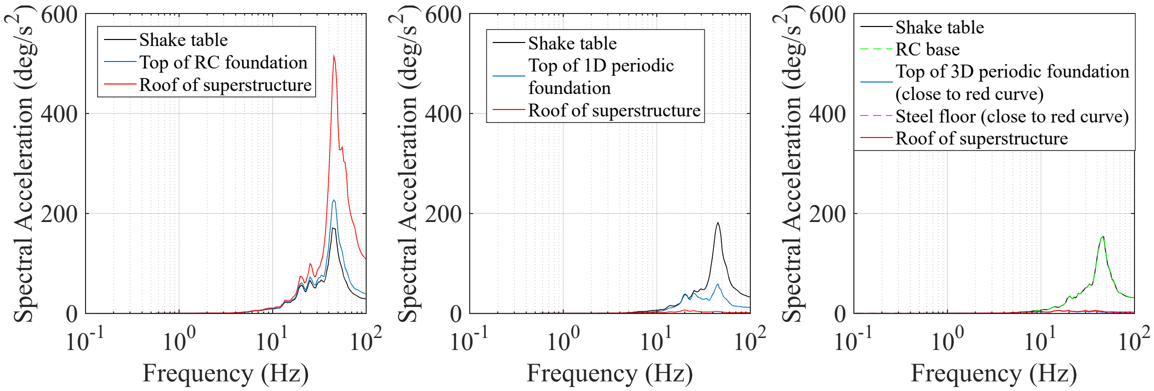

(a) Case 2 (b) Case 4 (c) Case 6

Figure 6-116 Acceleration response spectra of structural systems subjected to Bishop Earthquake in the torsional mode

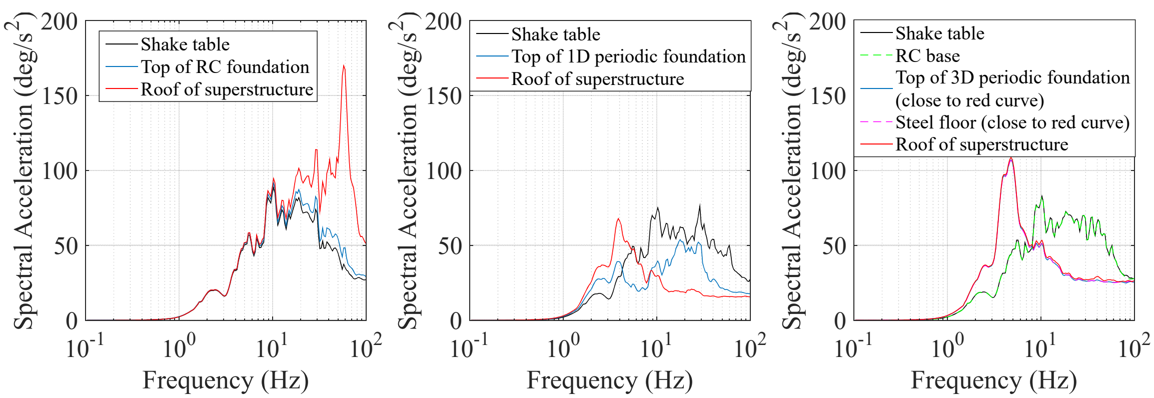

(a) Case 2 (b) Case 4 (c) Case 6

Figure 6-117 Acceleration response spectra of structural systems subjected to Imperial Valley Earthquake in the torsional mode

6.2.4 Harmonic test results

This subsection presents the results of harmonic tests on the structural systems. The input waves as presented in Table 5-24 are sine waves with fixed frequencies. These frequencies are located inside the tested attenuation zones of the 1D and 3D periodic foundation structural systems.

6.2.4.1 In the horizontal direction

For the harmonic tests in the horizontal direction, sine waves with frequencies of 5 Hz, 10 Hz, and 20 Hz were selected. Figure 6-118 to Figure 6-120 show that the acceleration response at each of the top of the periodic foundation and the roof of the superstructure in each of Cases 4 and 6 is reduced as compared to the acceleration on the shake table. On the contrary, evident amplification in structural responses is observed in Case 2.

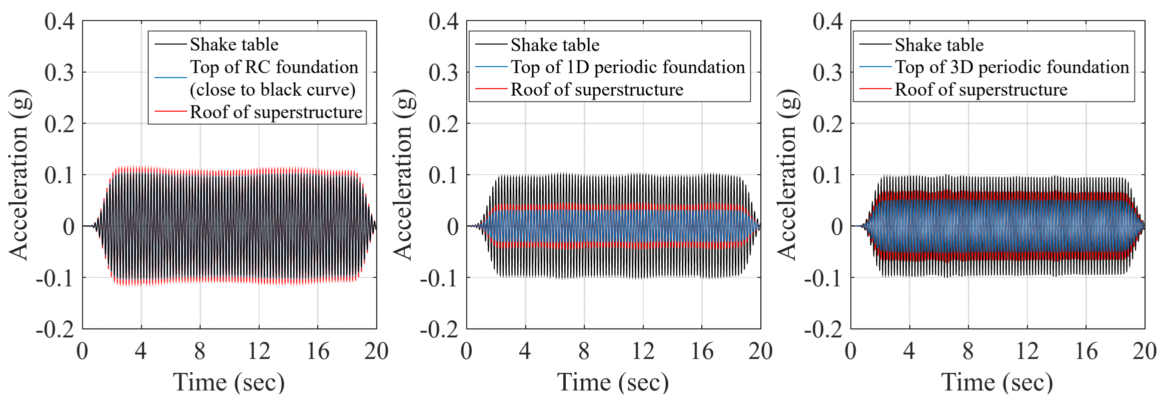

(a) Case 2 (b) Case 4 (c) Case 6

Figure 6-118 Acceleration response of structural systems subjected to Sine 5 Hz in the horizontal direction

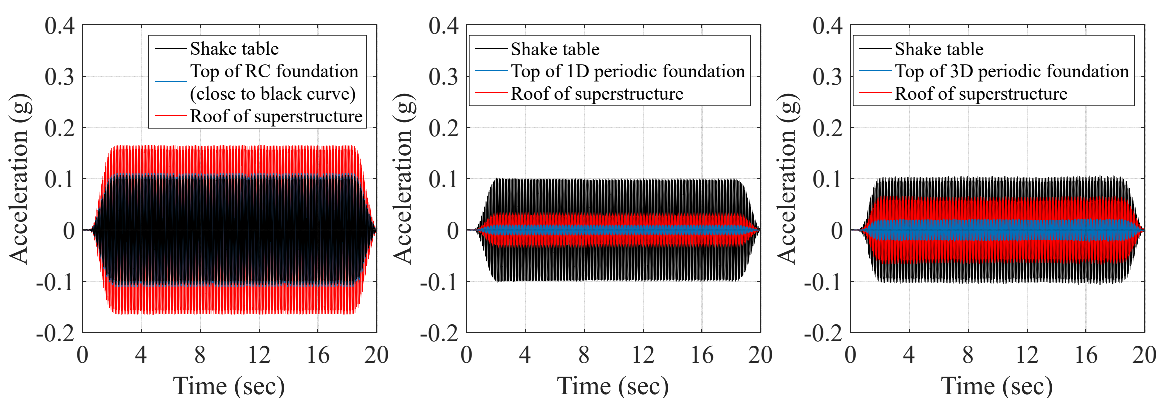

(a) Case 2 (b) Case 4 (c) Case 6

Figure 6-119 Acceleration response of structural systems subjected to Sine 10 Hz in the horizontal direction

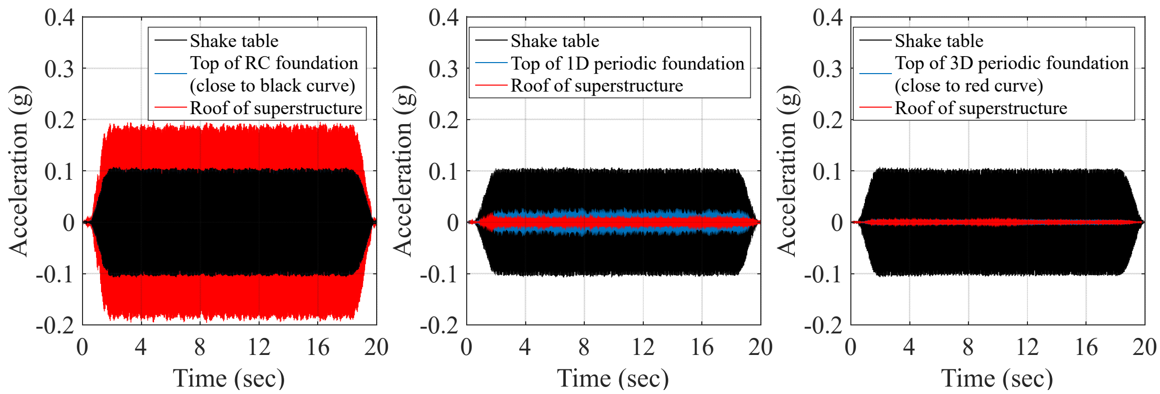

(a) Case 2 (b) Case 4 (c) Case 6

Figure 6-120 Acceleration response of structural systems subjected to Sine 20 Hz in the horizontal direction

The reduction in the harmonic wave's amplitude can be seen from the amplitude in the frequency domain. Figure 6-121 to Figure 6-123 show the Fourier spectra of the accelerations recorded on Cases 4 and 6. The curves show the corresponding amplitude and the wave frequency for each of the acceleration records. The reduction observed on each frequency is similar to the results obtained from the frequency sweeping tests.

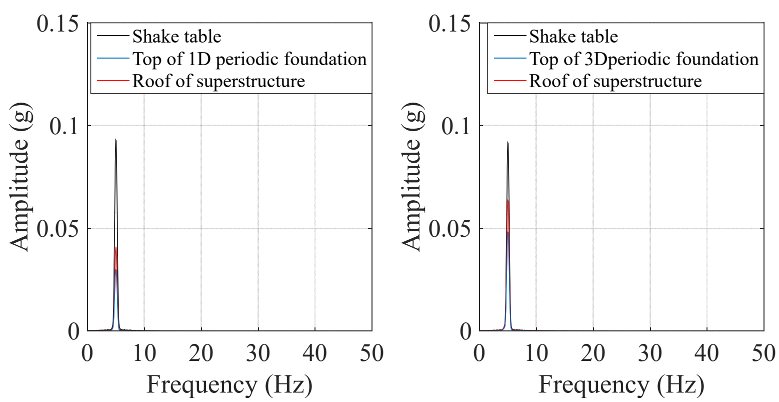

(a) Case 4 (b) Case 6

Figure 6-121 Fourier spectra of seismic test results of structural systems subjected to Sine 5 Hz in the horizontal direction

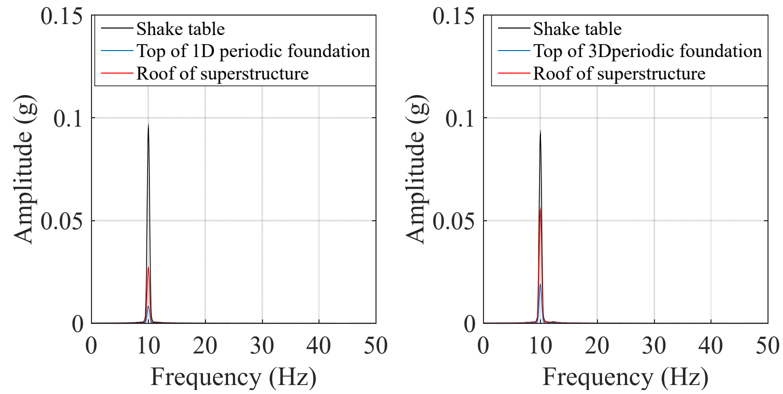

(a) Case 4 (b) Case 6

Figure 6-122 Fourier spectra of seismic test results of structural systems subjected to Sine 10 Hz in the horizontal direction

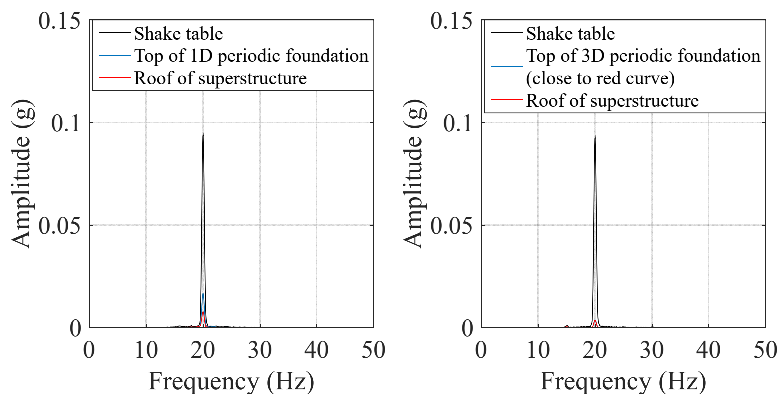

(a) Case 4 (b) Case 6

Figure 6-123 Fourier spectra of seismic test results of structural systems subjected to Sine 20 Hz in the horizontal direction

6.2.4.2 In the vertical direction

For the harmonic tests in the vertical direction, sine waves with frequencies of 24 Hz and 34 Hz were selected. Both frequencies are located inside the attenuation zones of the 1D and 3D periodic foundation structural systems in the vertical direction. Figure 6-124 and Figure 6-125 show that the acceleration response at each of the top of the periodic foundation and the roof of the superstructure in each of Cases 4 and 6 is reduced as compared to the acceleration on the shake table. On the contrary, vertical acceleration amplification at the roof of the superstructure is observed in Case 2.

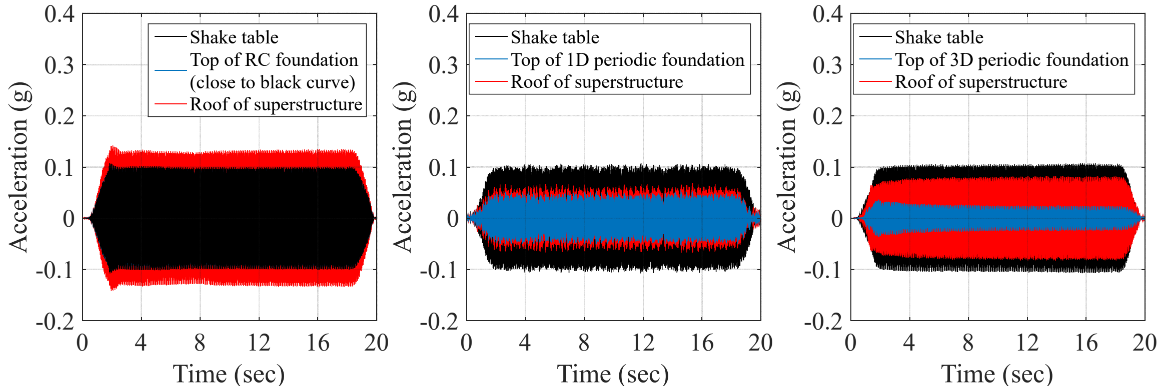

(a) Case 2 (b) Case 4 (c) Case 6

Figure 6-124 Acceleration response of structural systems subjected to Sine 24 Hz in the vertical direction

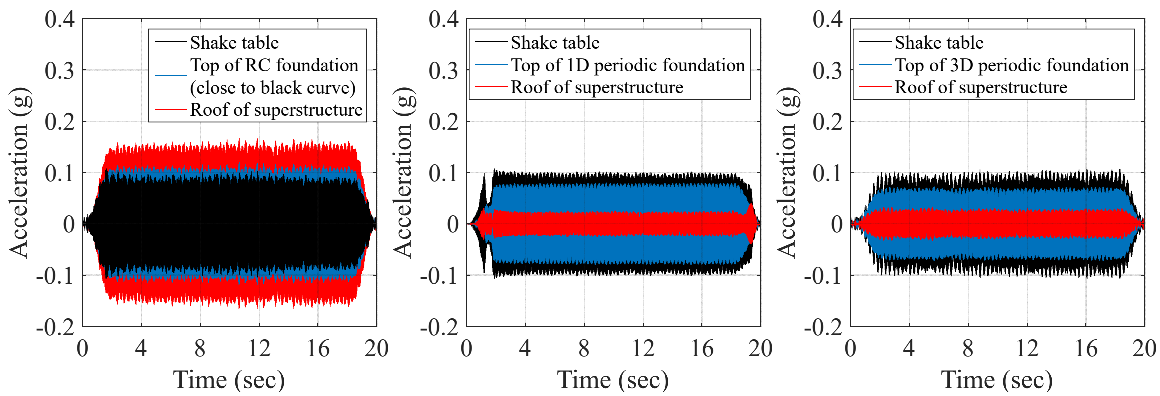

(a) Case 2 (b) Case 4 (c) Case 6

Figure 6-125 Acceleration response of structural systems subjected to Sine 34 Hz in the vertical direction

The reduction in the harmonic wave's amplitude can be seen from the amplitude in the frequency domain. Figure 6-126 and Figure 6-127 show the Fourier spectra of the recorded accelerations on Cases 4 and 6. The curves show the corresponding amplitude and the wave frequency for each of the acceleration records. The reduction observed on each frequency is similar to the results obtained from the frequency sweeping tests.

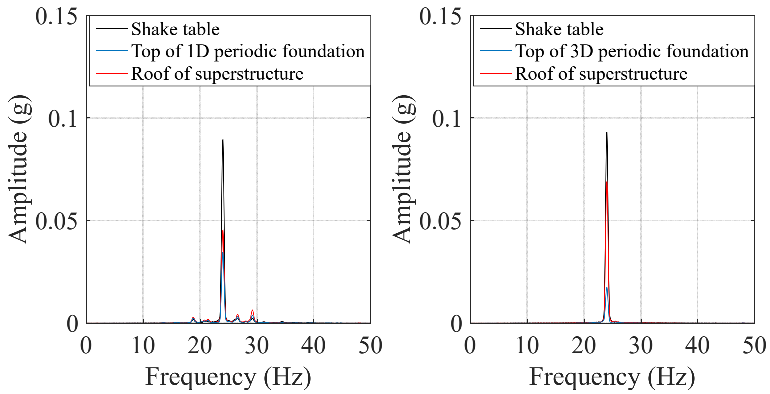

(a) Case 4 (b) Case 6

Figure 6-126 Fourier spectra of seismic test results of structural systems subjected to Sine 24 Hz in the vertical direction

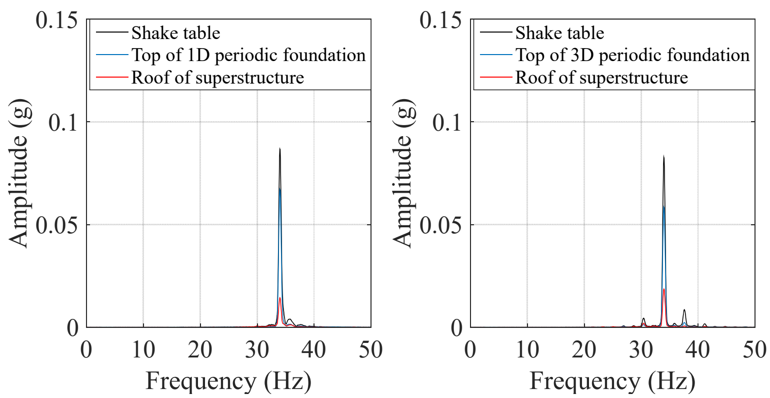

(a) Case 4 (b) Case 6

Figure 6-127 Fourier spectra of seismic test results of structural systems subjected to Sine 34 Hz in the vertical direction

6.2.4.3 In the torsional mode

For the harmonic tests in the torsional mode, sine waves with frequencies of 10 Hz, 20 Hz, and 30 Hz were selected. All three frequencies are located inside the attenuation zones of the 1D and 3D periodic foundation structural systems in the torsional mode. Figure 6-128 to Figure 6-130 show that the acceleration response at each of the top of the periodic foundation and the roof of the superstructure in each of Cases 4 and 6 is reduced as compared to the acceleration on the shake table. On the contrary, torsional amplification at the roof of the superstructure is observed in Case 2.

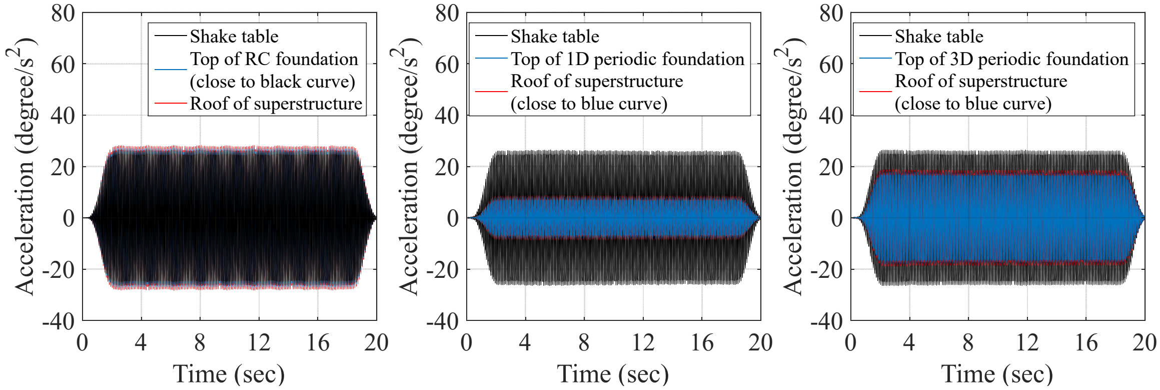

(a) Case 2 (b) Case 4 (c) Case 6

Figure 6-128 Acceleration response of structural systems subjected to Sine 10 Hz in the torsional mode

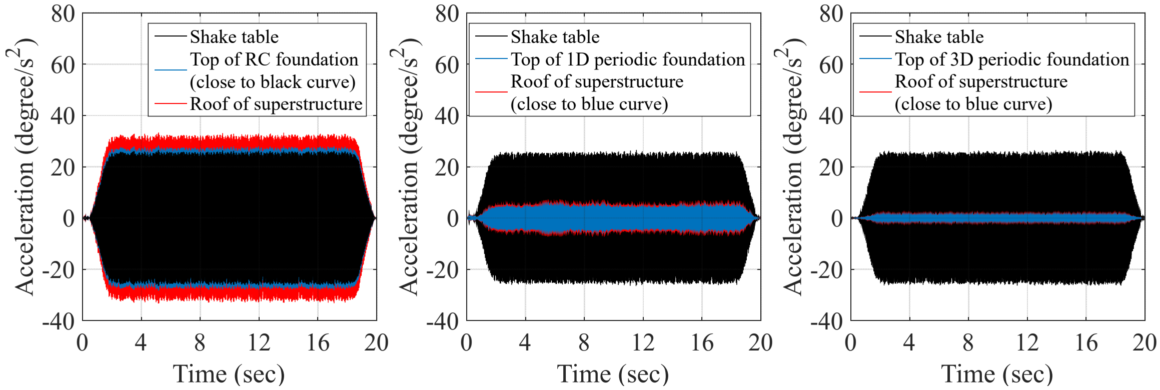

(a) Case 2 (b) Case 4 (c) Case 6

Figure 6-129 Acceleration response of structural systems subjected to Sine 20 Hz in the torsional mode

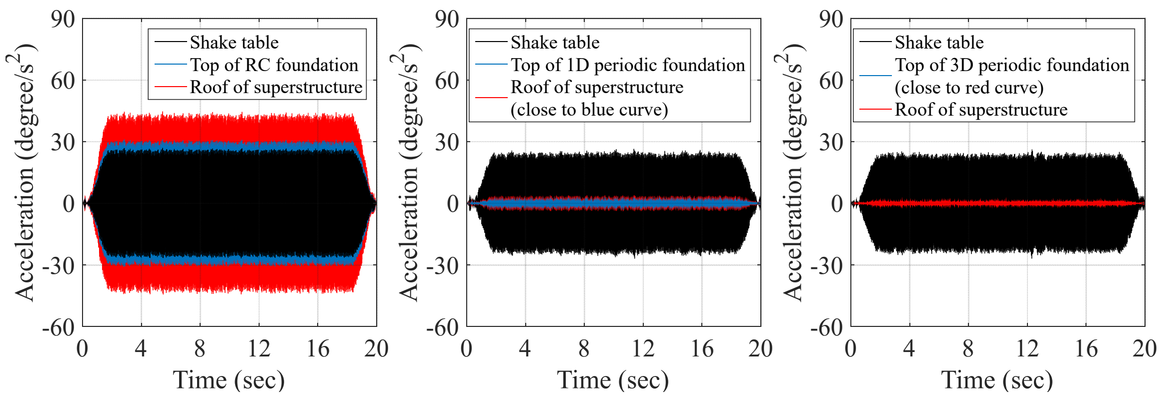

(a) Case 2 (b) Case 4 (c) Case 6

Figure 6-130 Acceleration response of structural systems subjected to Sine 30 Hz in the torsional mode

The reduction in the harmonic wave's amplitude can be seen from the amplitude in the frequency domain. Figure 6-131 to Figure 6-133 show the Fourier spectra of each acceleration recorded on Cases 4 and 6. The curves show the corresponding amplitude and the wave frequency for each of the acceleration records. The reduction observed on each frequency is similar to the results obtained from the frequency sweeping tests.

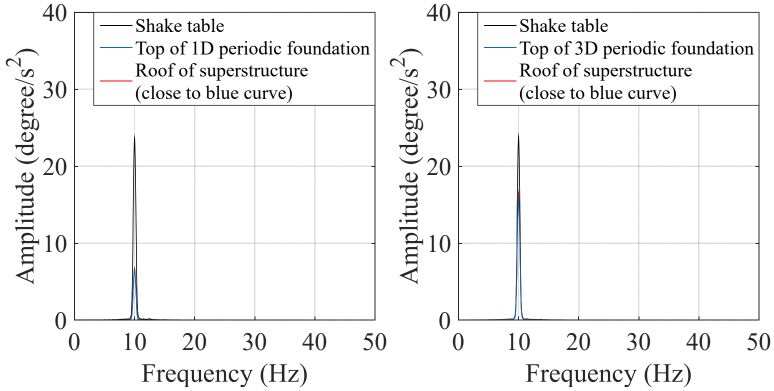

(a) Case 4 (b) Case 6

Figure 6-131 Fourier spectra of seismic test results of structural systems subjected to Sine 10 Hz in the vertical direction

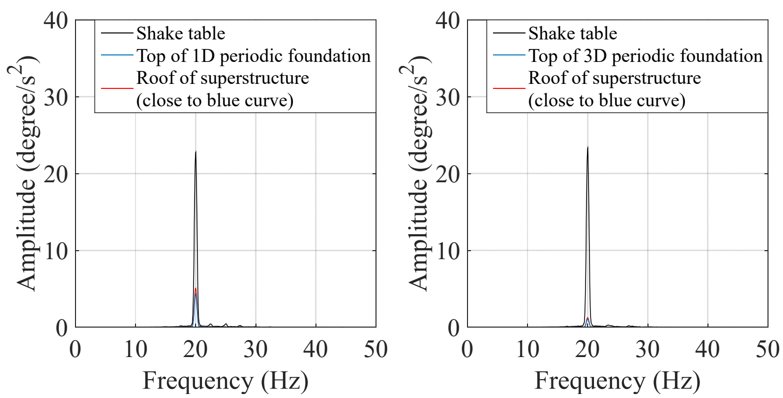

(a) Case 4 (b) Case 6

Figure 6-132 Fourier spectra of seismic test results of structural systems subjected to Sine 20 Hz in the vertical direction

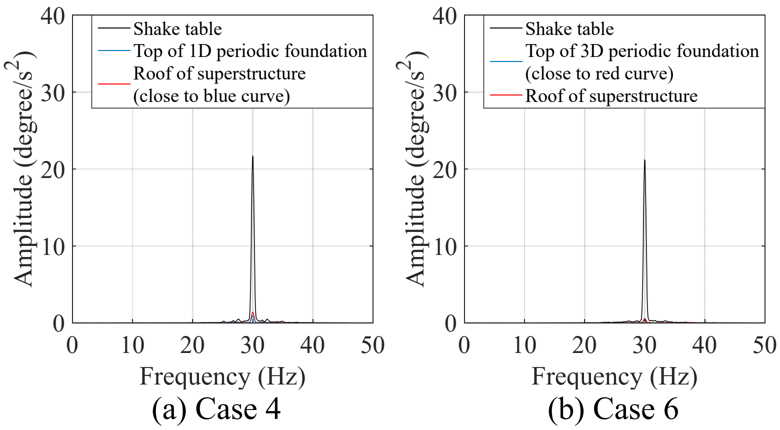

Figure 6-133 Fourier spectra of seismic test results of structural systems subjected to Sine 30 Hz in the vertical direction

7 NUMERICAL SIMULATION OF TEST SPECIMENS

The results obtained from the shake table tests have shown the capability of periodic foundations to isolate small modular reactor (SMR) buildings from incoming seismic waves in both the horizontal and vertical directions as well as the torsional mode. The test results clearly demonstrate the potential application of periodic foundations as a seismic isolator for critical infrastructures. While the periodic foundations have been experimentally proven to work, the accuracy of numerical simulation is the key factor for the design of periodic foundation structural systems in the future. An adequate degree of accuracy is required in the prediction to have a confidence in designing periodic foundations. Therefore, a comparison of the numerical simulation with the test results is needed to critically examine the numerical simulation in predicting the behavior of the real structure.

Due to differences of conditions in the actual tests, the test results are somewhat different from the preliminary analysis results presented in Sub-subsections 5.2.2.3 and 5.2.3.2. This chapter discusses a more refined finite element approach used in simulating the tested one-dimensional (1D) and three-dimensional (3D) periodic foundation structural systems and compares the finite element simulation results with the test outcomes. This chapter first presents the simulation of a hyperelastic material model of polyurethane layers. Then the finite element models based on the experimental test cases were built and analyzed. The finite element analyses involve modal analyses and steady-state frequency sweeping analyses, from which insight into the natural frequencies and frequency band gaps of the structural systems can be obtained. Furthermore, the time history analyses were performed to simulate the behavior of structural systems under various seismic and harmonic excitations.

7.1 Material Model of Polyurethane

The stress-strain curve obtained from the compression test of polyurethane samples is presented in Figure 5-49. The stress-strain curve clearly shows a hyperelastic behavior of the polyurethane material. To simulate the periodic foundations as close as possible to the reality, the finite element model needs to capture the hyperelastic behavior of the tested samples. This section presents the comparison of the stress-strain curve of the finite element and the tested polyurethane sample.

Figure 7-1 shows the real polyurethane sample with a diameter of 31.94 mm and a thickness of 12.7 mm. Figure 7-2 shows the finite element model of the sample. Hyperelastic material using the Marlow model with stress and strain values from the test results was assigned on the finite element model. The Poisson's ratio of 0.48 obtained from the sample test was also input into the finite element model. The Marlow model was selected because it is stable for all strains based on ABAQUS evaluation. Figure 7-3 shows the engineering stress and engineering strain curve of both the finite element simulation and the sample test results. The results from the finite element simulation are observed to be very close to the test results.

Figure 7-1 Polyurethane sample for compression test

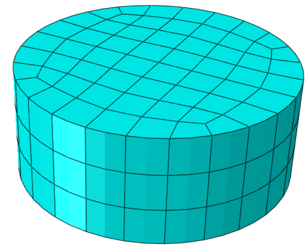

Figure 7-2 Finite element model of polyurethane sample

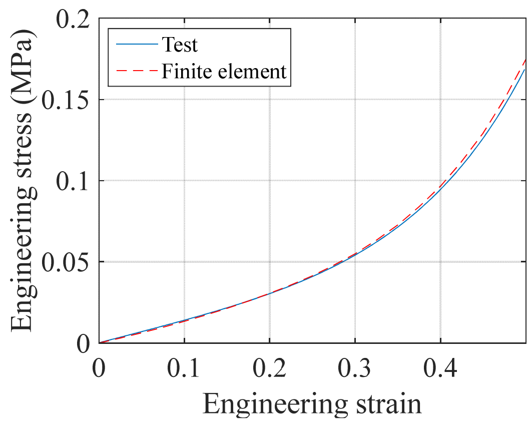

Figure 7-3 Stress-strain curve of finite element mode

7.2 Finite Element Models

Figure 7-4 shows the finite element model for each of the test cases with their respective meshes. The RC base and RC layers were modeled using 8-node linear brick elements while the polyurethane layers were modeled using 20-node quadratic brick elements. The steel floor and the roof plate were modeled using 8-node shell elements and 4-node shell elements, respectively. A reduced integration scheme to eliminate the locking problem was applied on each of the solid and shell elements. The beams and columns were meshed with an approximate length of 0.25 m for each element and were assigned with 2-node linear beam elements. Each of the longitudinal and transversal trusses was modeled with a single 2-node linear truss element. A tie constraint was assigned at the interfaces between the polyurethane layers and the RC layers for continuity. On the real cases, the steel frame structure was connected to each of the foundations using a bolt-type connection. Such connection does not provide continuity between the steel floor and the foundations; therefore, a contact condition was defined for the interaction between the steel floor and the top of the foundation in the finite element models of Cases 2, 4, and 6. The defined contact properties are rough tangential behavior (no sideway slip occurs) and linear normal behavior with a contact stiffness of 5.5×10^{8} N/m^2 pressure per 1 m overclosure. The surface stiffness was selected based on a calibration procedure to match the natural frequencies of Case 2.

The constitutive relationship of polyurethane layers was presented in Section 7.1. The density and Poisson's ratio for the polyurethane material was set as 1100 kg/m^3 and 0.48, respectively. This constitutive stress-strain relationship was assigned to Cases 3, 4, 5, and 6 for the analyses in the horizontal direction and torsional mode. For the analyses in the vertical direction, some modifications were made on the constitutive relationship. For the vertical analyses of Cases 3 and 4, the assigned stress-strain curve was cut from the curve in Figure 7-3 from strain 0.4 onward, i.e., the portion of the curve from strain 0 to 0.4 was taken out. The remaining portion was moved to origin and extrapolated. For the vertical analyses of Cases 5 and 6, the assigned stress-strain curve was cut from the curve in Figure 7-3 from strain 0.184 onward and moved to origin. The reason for such modification is because the behavior of both the 1D and 3D periodic foundations in the vertical direction were affected by the construction errors, such as an imperfect flat surface of RC layers and non-uniform glue distribution. Therefore, in some parts of the periodic foundations the polyurethane surface is not perfectly connected to the RC surface. The imperfect interface connection causes non-uniform axial stresses and load transfer between each layer making the parts of the polyurethane that carries the load receive much more stress and become much stiffer. The modification of the vertical stress-strain curve on each periodic foundation was done based on calibration with the vertical natural frequency of each structural system. The imperfection of the interface connection, however, has little influence when the structure is subjected to incoming waves in the horizontal direction and torsional mode. Large superstructure weight allows sufficient friction between each layer on the periodic foundations and makes the shear stress transfer uniform. Therefore, no modification is needed for the stress-strain relationship for analyses in the horizontal direction and torsional mode.

The A36 steel and RC materials were modeled as homogenous linear elastic material with properties shown in Table 7-1. Additional masses of 8368 kg and 1830 kg were uniformly distributed on the steel floor and roof of the superstructure, respectively. The Rayleigh damping coefficients, calculated based on Eq. (5-2), for each material on the 1D periodic foundation structural system are tabulated in Table 7-2 while those on the 3D periodic foundation structural system are tabulated in Table 7-3.

Table 7-1 Material properties of steel and reinforced concrete

Material	Young's Modulus (MPa)	Density (kg/m^3)	Poisson's ratio
A36 steel	200,000	7850	0.3
Reinforced concrete	31,400	2300	0.2

Table 7-2 Rayleigh damping coefficient for 1D periodic foundation structural system

Material	Damping ratio (ζ)	α	β
Steel A36	2%	0.6234	0.00012097
Reinforced concrete	4%	1.247	0.0002419
Polyurethane	23.18%	7.225	0.001402

Table 7-3 Rayleigh damping coefficient for 3D periodic foundation structural system

Material	Damping ratio (ζ)	α	β
Steel A36	2%	0.7425	0.0001198
Reinforced concrete	4%	1.4851	0.0002396
Polyurethane	19%	7.0541	0.0011381

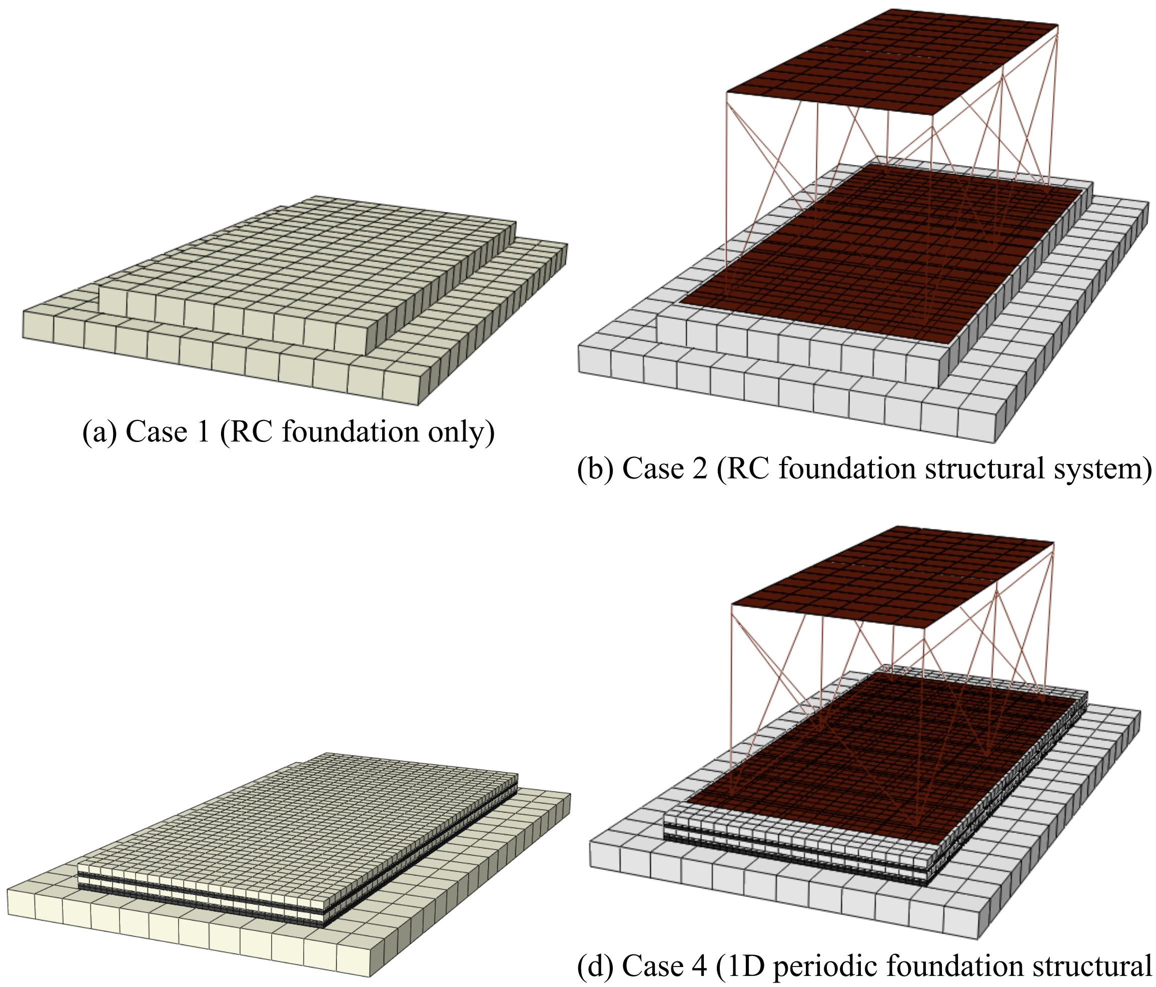

(a) Case 1 (RC foundation only)

(b) Case 2 (RC foundation structural system)

(c) Case 3 (1D periodic foundation only)

(d) Case 4 (1D periodic foundation structural system)

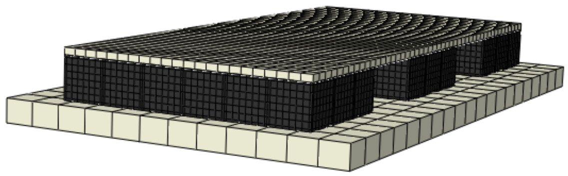

(e) Case 5 (3D periodic foundation only)

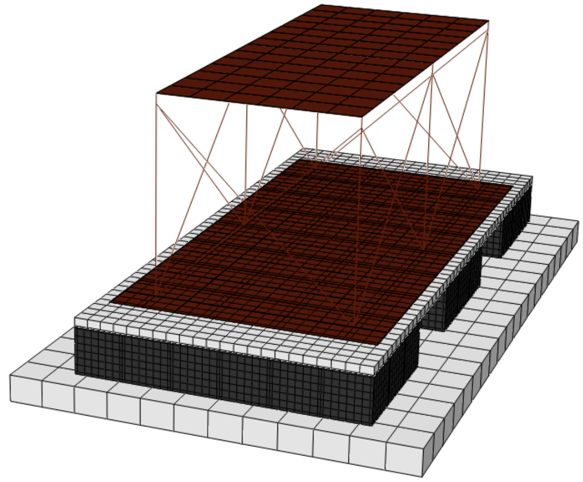

(f) Case 6 (3D periodic foundation structural system)

Figure 7-4 Finite element models for test cases

7.3 Comparison of Finite Element Simulation and Experimental Results

This section provides the comparison of finite element simulation results and test results. The items compared in this section are the natural frequencies, frequency band gaps or attenuation zones, and acceleration time history response of the structural systems.

7.3.1 Modal analysis results

Modal analysis was first conducted to obtain the natural frequencies and mode shapes of the structural systems. Figure 7-5 to Figure 7-7 show the three mode shapes (horizontal, vertical, and torsional modes) and their natural frequencies of the structural systems. Table 7-4 summarizes the obtained natural frequencies from modal analysis in comparison to their respective test results. It is observed that the natural frequencies of finite element models are very close to the test results. The largest error is 12.95% which is from the horizontal mode of Case 6. However, one must see that the finite element predicts the natural frequency to be 3.14 Hz while the test result shows 2.78 Hz. Such difference is often considered insignificant from an engineering point of view.

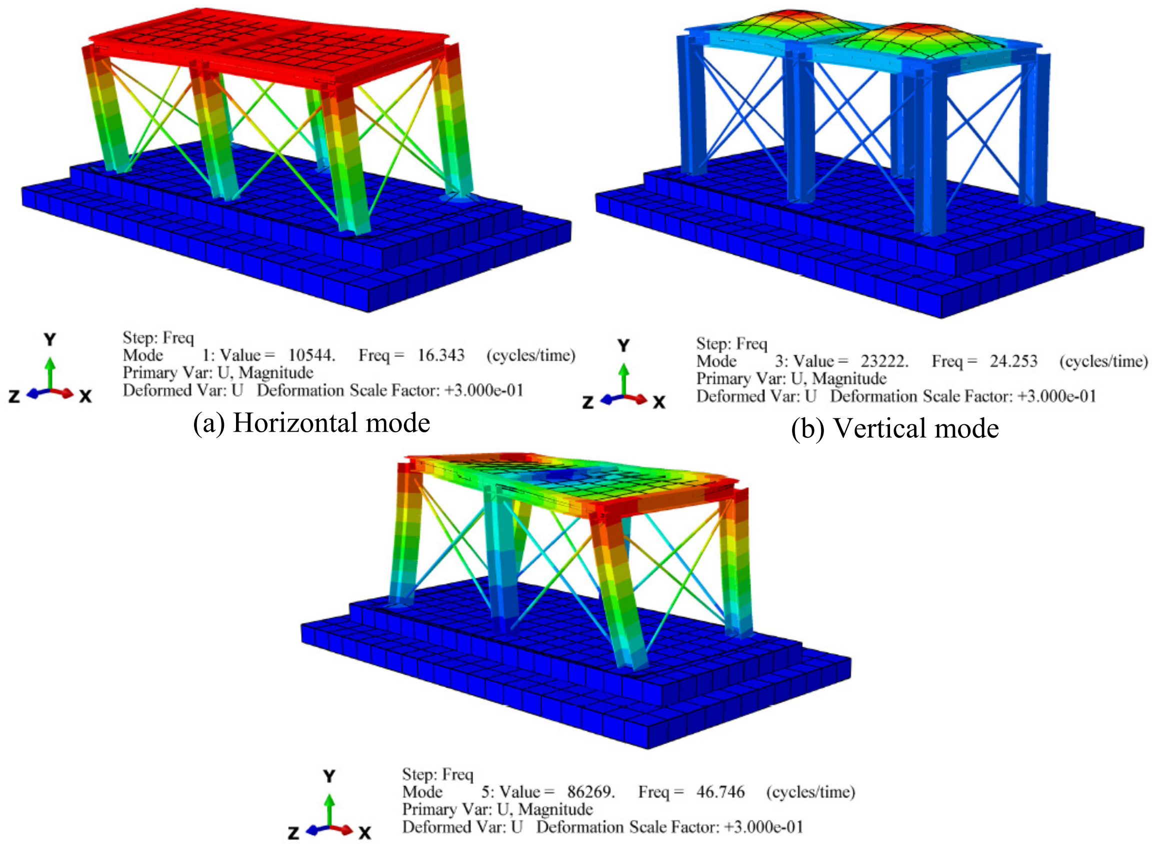

(a) Horizontal mode

(b) Vertical mode

(c) Torsional mode

Figure 7-5 Modal analysis results for Case 2

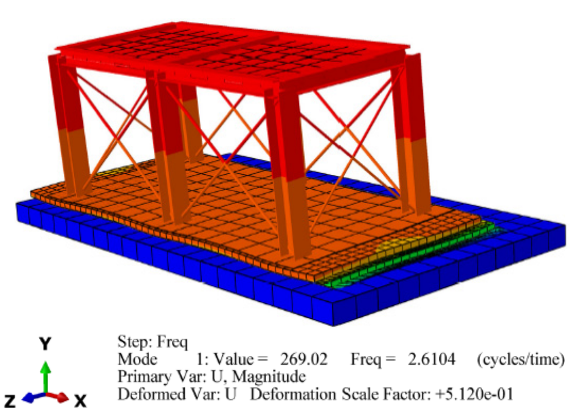

(a) Horizontal mode

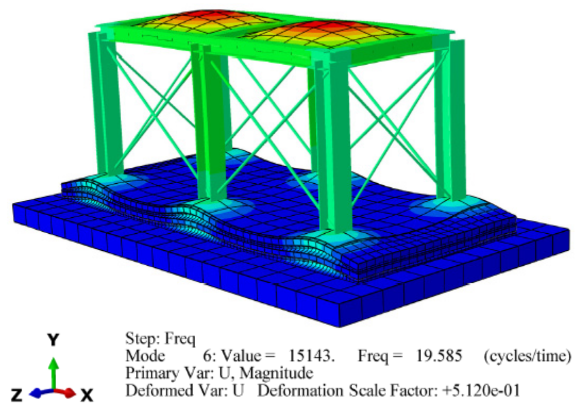

(b) Vertical mode

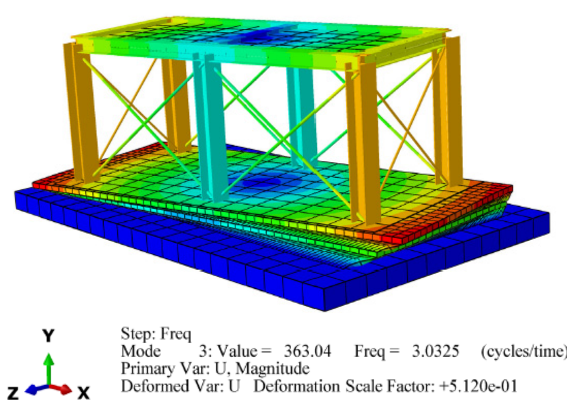

(c) Torsional mode

Figure 7-6 Modal analysis results for Case 4

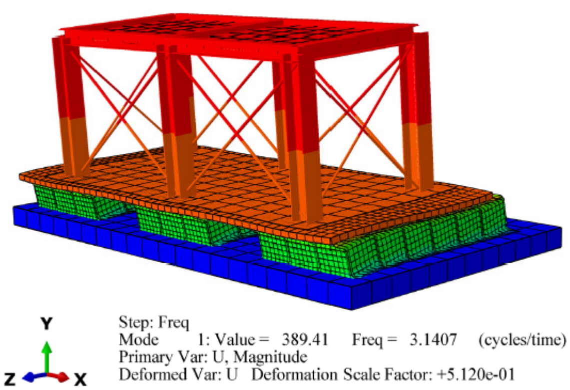

(a) Horizontal mode

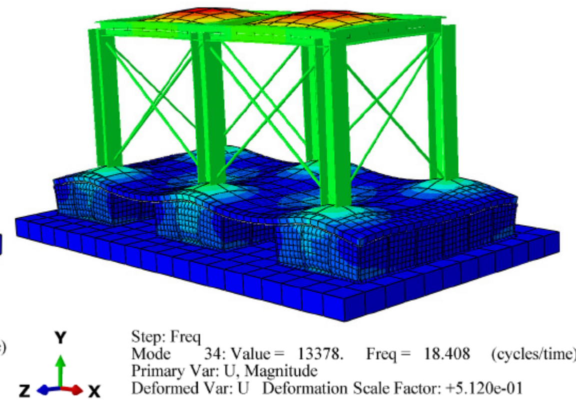

(b) Vertical mode

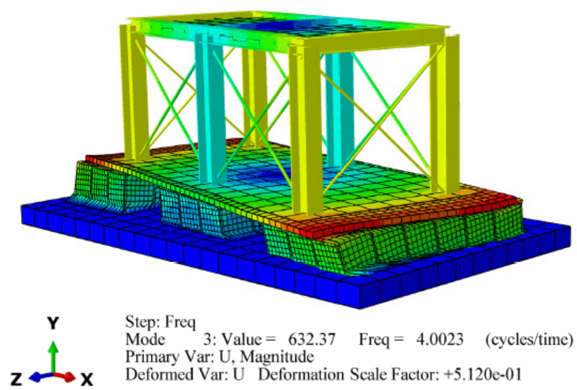

(c) Torsional mode

Figure 7-7 Modal analysis results for Case 6

Table 7-4 Comparison of natural frequencies obtained from finite element simulation and experimental tests

Specimen	Mode	Natural frequency (Hz)		Finite element to experimental error (%)
		Finite element simulation	Experimental test	
Case 2 (RC foundation structural system)	Horizontal translation	16.34	16.41	0.43
	Vertical translation	24.25	26.86	9.72
	Torsion	46.75	46.88	0.28
Case 4 (1D periodic foundation structural system)	Horizontal translation	2.61	2.49	4.82
	Vertical translation	19.59	19.63	0.20
	Torsion	3.03	3.42	11.40
Case 6 (3D periodic foundation structural system)	Horizontal translation	3.14	2.78	12.95
	Vertical translation	18.4	20.02	8.09
	Torsion	4	4	0

7.3.2 Frequency sweeping analysis results

The frequency sweeping tests of foundations presented in Section 6.1 show that the 1D and 3D periodic foundations exhibit attenuation zones in the horizontal direction and the torsional mode. However, only amplification is observed in the vertical direction for both periodic foundations. The frequency sweeping tests on the RC foundation only show that the recorded response at the top of the RC foundation is the same as the input.

Figure 7-8 shows the frequency sweeping analysis results of the finite element model of Case 1. The analysis results show that the FRF curves are all straight lines at 0 db which represent the same output response at the top of the RC foundation as the input. The results obtained from the finite element simulation are the same as the test results.

Figure 7-9 shows the steady-state frequency sweeping analysis conducted on the finite element model for Case 3. The FRF curves in the horizontal direction and torsional mode show a close tendency with the test results. The attenuation zones exhibited by the finite element results are very close with the attenuation zones of the tested specimen. The FRF curve in the vertical direction shows that the finite element model also only predicts amplification in the frequency range of 0-50 Hz.

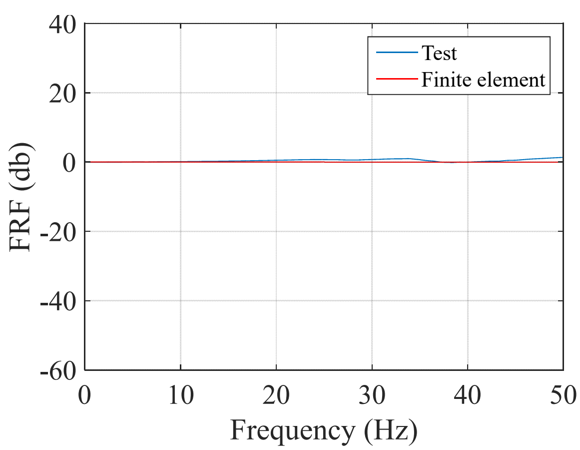

(a) In the horizontal direction

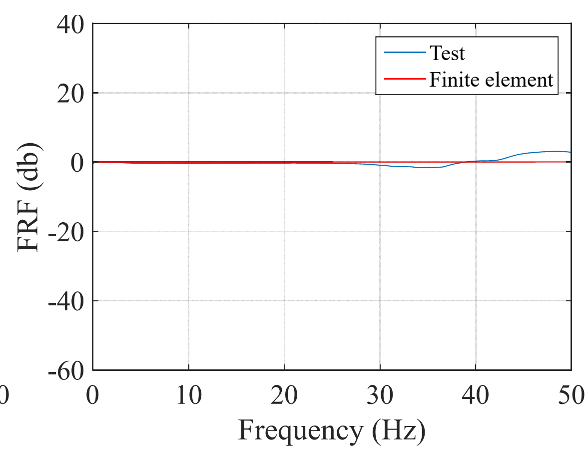

(b) In the vertical direction

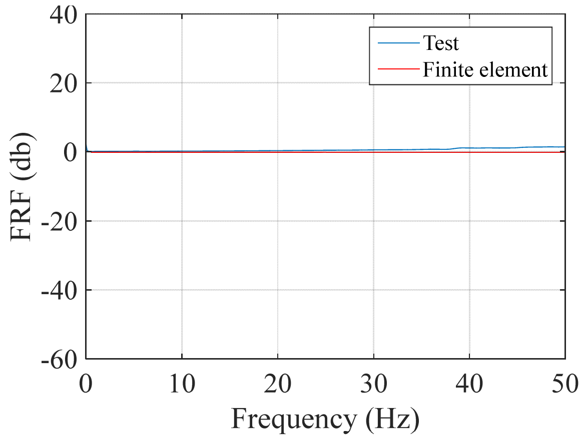

(c) In the torsional mode

Figure 7-8 Frequency sweeping analysis results for Case 1

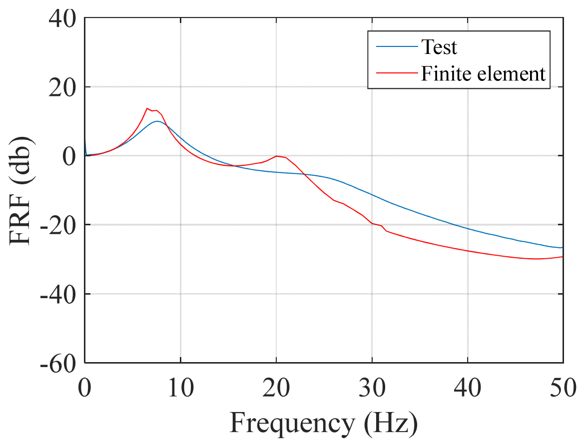

(a) In the horizontal direction

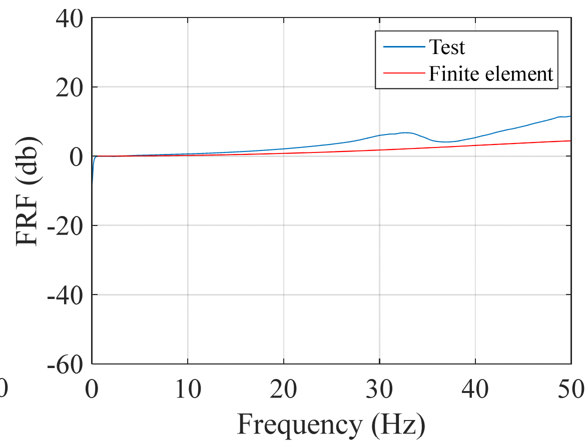

(b) In the vertical direction

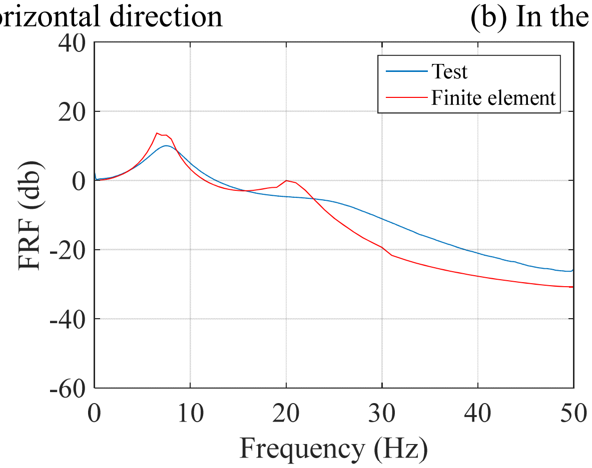

(c) In the torsional mode

Figure 7-9 Frequency sweeping analysis results for Case 3

Figure 7-10 shows the frequency sweeping test results on the finite element model of Case 5. The finite element simulation captured very close FRF curve tendencies as the test results. The analysis results in the horizontal direction and torsional mode show close attenuation zones to the test results while the analysis result in the vertical direction show a very similar amplification response.

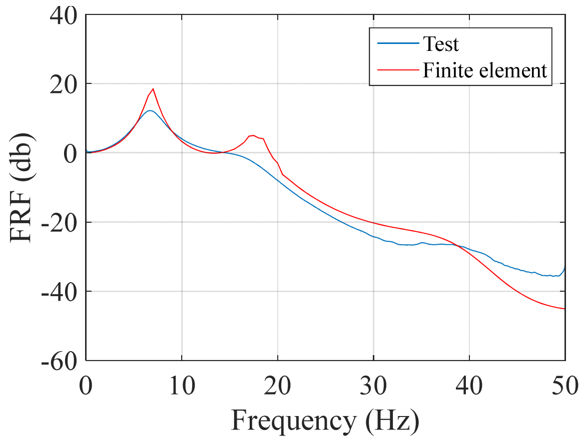

(a) In the horizontal direction

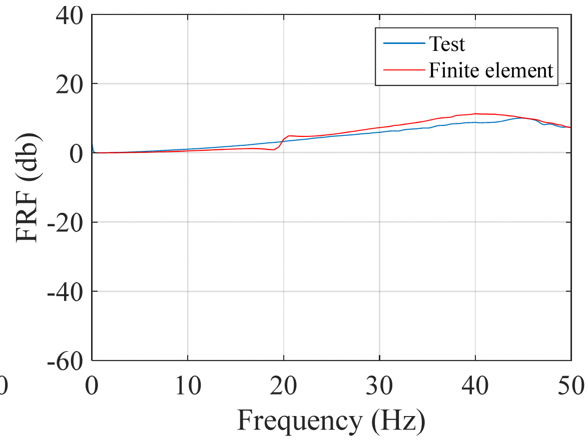

(b) In the vertical direction

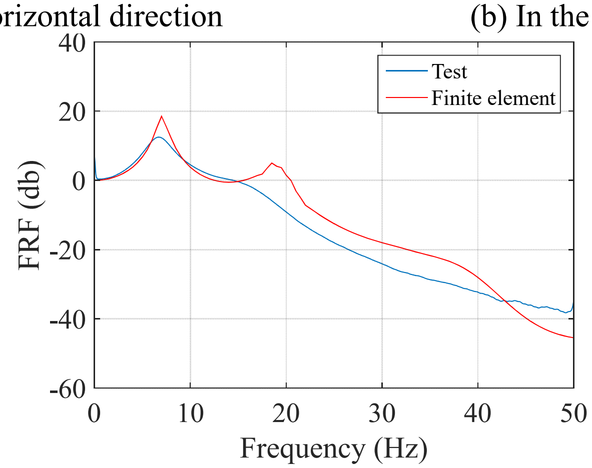

(c) In the torsional mode

Figure 7-10 Frequency sweeping analysis results for Case 5

Figure 7-11 shows the frequency sweeping analysis results on the finite element model for Case 4. The response at each of the top of the 1D periodic foundation and the roof of the superstructure is presented and compared with the test results. For the analysis in the horizontal direction the finite element model captures the amplification at frequencies near the horizontal natural frequency of Case 4. The analysis results also predict wide attenuation zones similar to the test results. However, at a higher frequency, the finite element analysis results show a much larger response reduction than the test results. For example the finite element result at the roof of superstructure at the frequency of 30 Hz shows an FRF value of -50 db while the test result shows an FRF value of -20 db. However, The FRF value of -50 corresponds to a response reduction of 99.7% while that of -20 db corresponds to a response reduction of 90%. From an engineering point of view, the prediction can be considered accurate. The FRF curves in the vertical direction show that the finite element captures the tendency of the test results. However, the simulated attenuation zones are slightly different from the test results. As mentioned in Section 7.2, construction errors cause non-uniform stress transfer at the interfaces. Since the model assumed a perfect bond between interfaces and smeared the error into the constitutive relationship, a slight difference is expected. The analysis results in the torsional mode show a very close response to the test results at each of the top the top of 1D periodic foundation and the roof of superstructure.

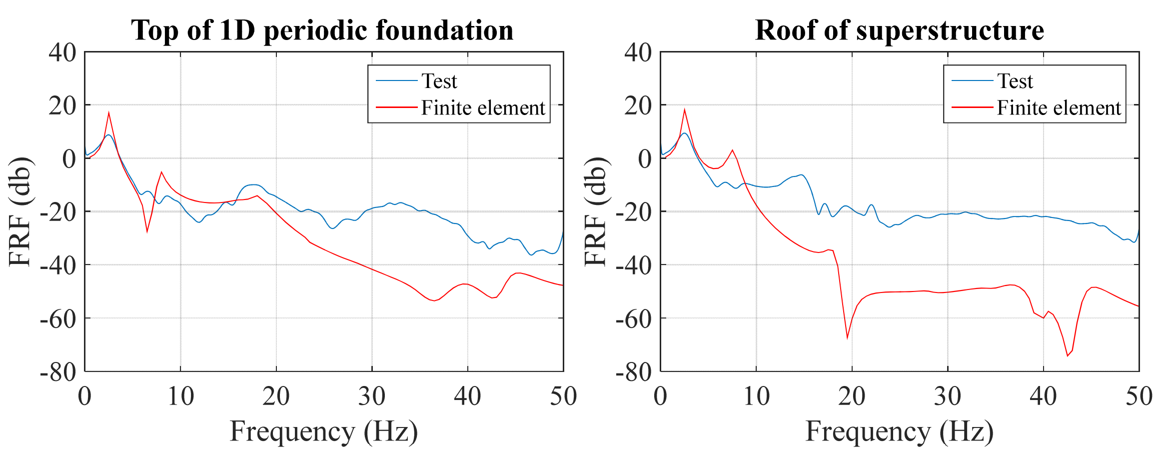

(a) In the horizontal direction

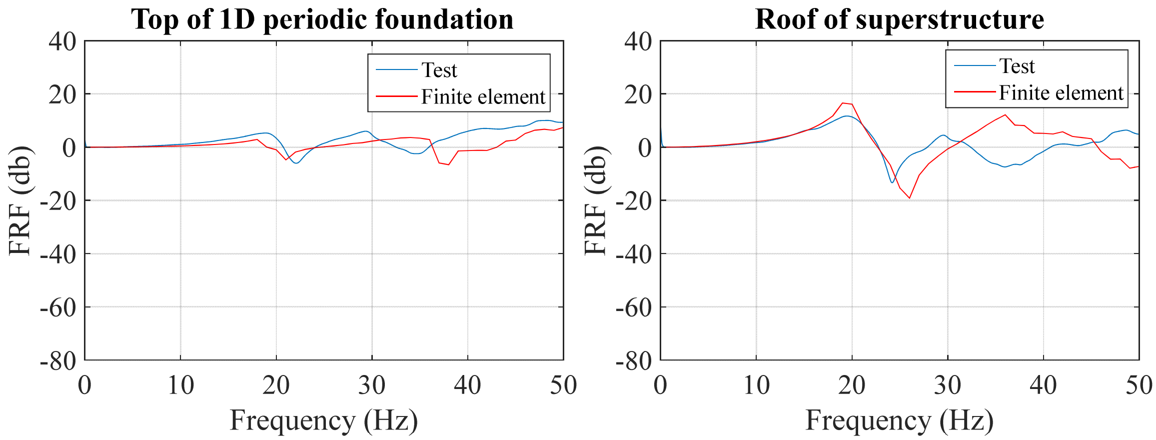

(b) In the vertical direction

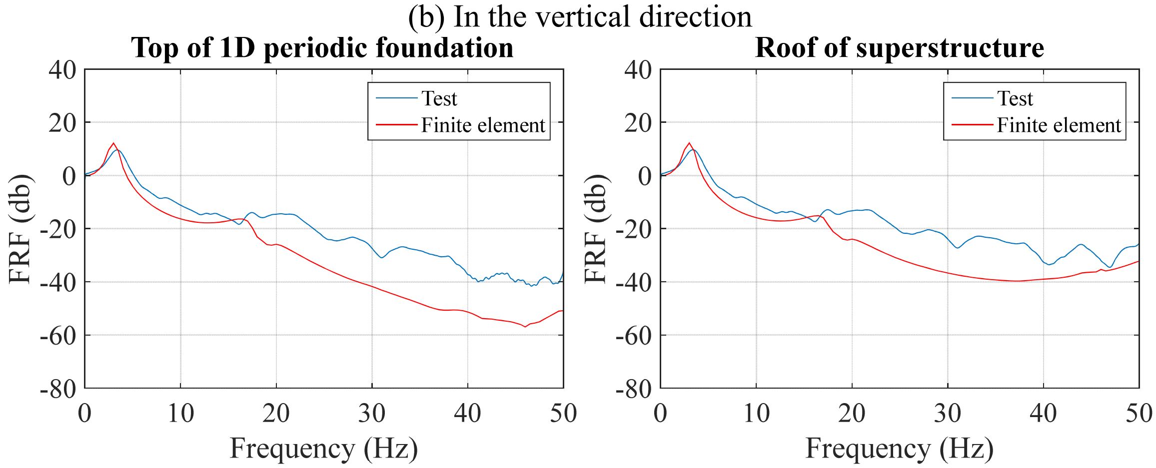

(c) In the torsional mode

Figure 7-11 Frequency sweeping analysis results for Case 4

Similar to those of Case 4, the frequency sweeping analysis results of Case 6 show that the finite element model can predict the frequency response of Case 6 in the horizontal direction and torsional mode with good accuracy. The tendency of the FRF curves, predicted attenuation zones, and the reduction inside the attenuation zones are well captured. For the case of the vertical response, the simulated frequency attenuation zones are slightly off from the tests results. However, the tendency in general is well captured.

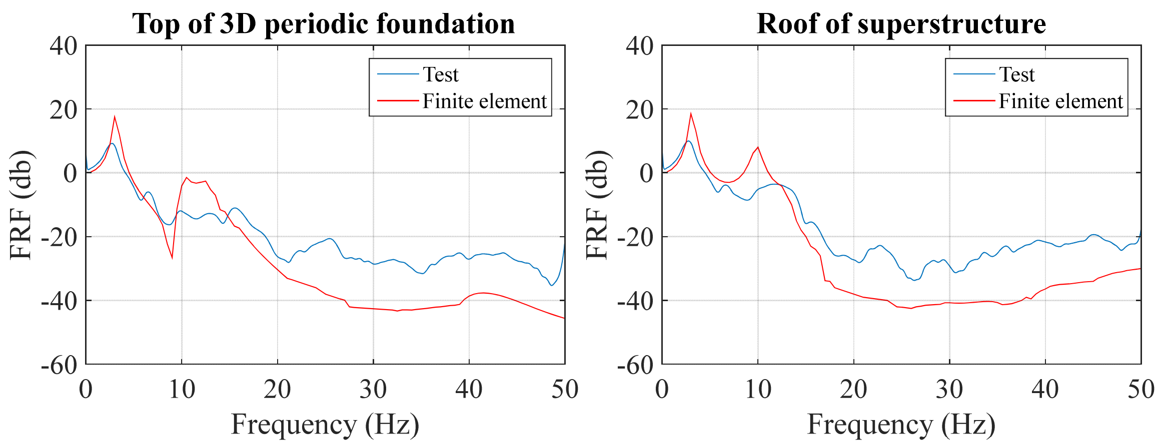

(a) In the horizontal direction

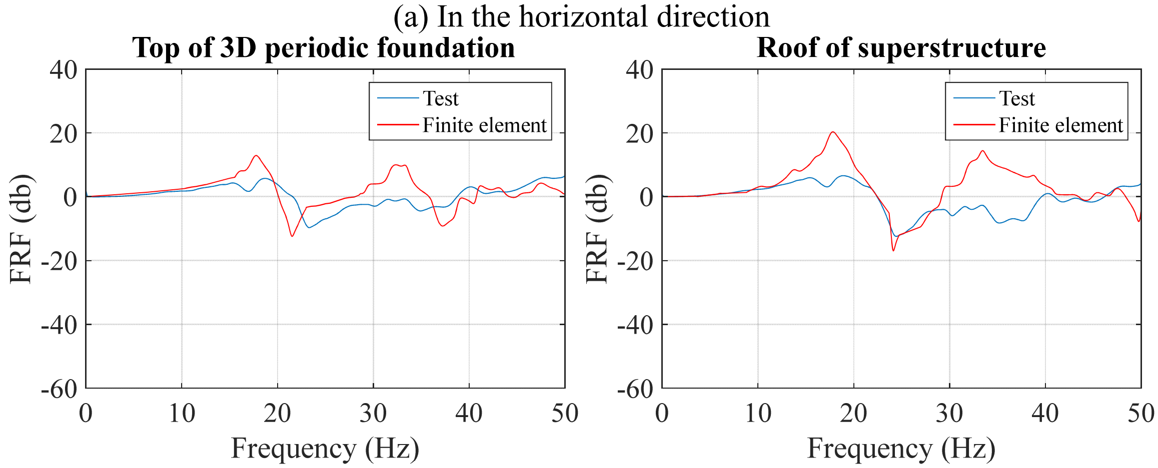

(b) In the vertical direction

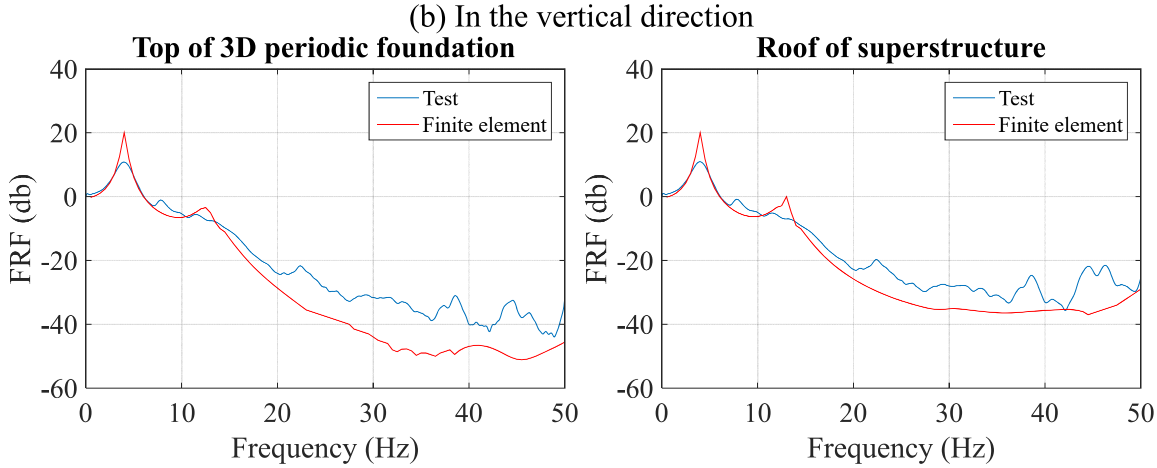

(c) In the torsional mode

Figure 7-12 Frequency sweeping analysis results for Case 6

7.3.3 Time history analysis results

This subsection presents the time history analysis results of the periodic foundation structural systems. Floor acceleration time series at the top of the periodic foundations and the roof of the superstructure from the analysis results were compared with those obtained from the shake table tests. Figure 7-13 shows the horizontal acceleration response of the finite element model of Case 4 subjected to the Anza Earthquake. It is observed that the finite element model can simulate the maximum floor acceleration at each of the top of the 1D periodic foundation and roof of the superstructure very closely to the test results. Figure 7-14 shows the acceleration response at the roof of the Case 4 specimen when subjected to harmonic wave in the vertical direction. The simulation results match the test results very well in terms of amplitude and phase angle. Figure 7-15 shows the response of the Case 4 simulation subjected to the Imperial Valley Earthquake in the torsional mode. It is observed that the floor accelerations closely match the test results.

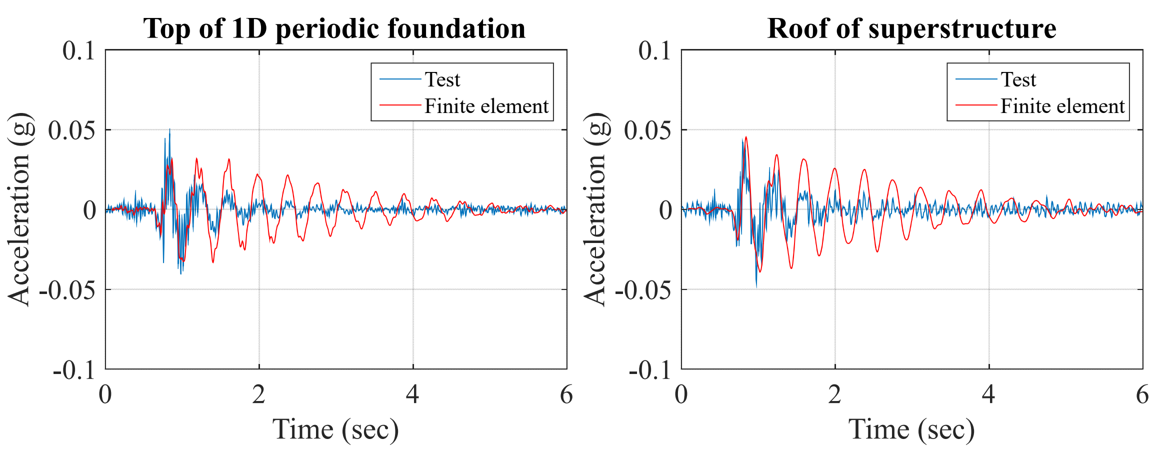

Figure 7-13 Time history analysis results of Case 4 subjected to Anza Earthquake in the horizontal direction

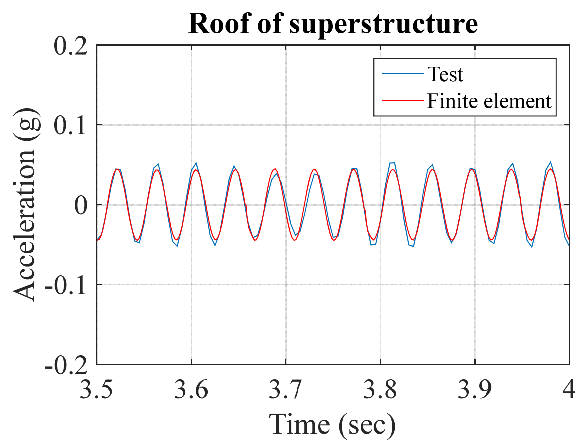

Figure 7-14 Time history analysis results of Case 4 subjected to fixed sine wave at a frequency of 24 Hz in the vertical direction

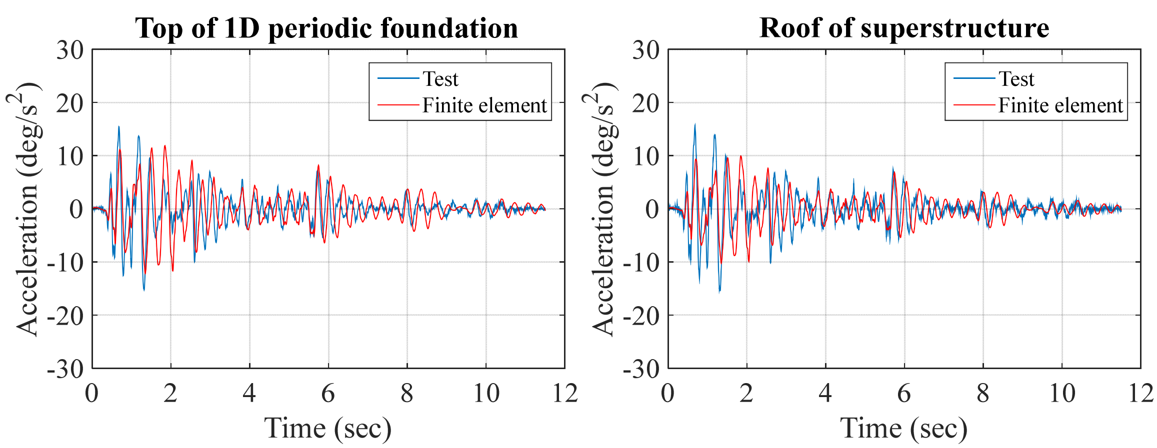

Figure 7-15 Time history analysis results of Case 4 subjected to Imperial Valley Earthquake in the torsional mode

Figure 7-16 shows the acceleration response of the finite element model of Case 6 when subjected to the Anza, San Fernando (St. Anita station), and Whittier Earthquakes in the horizontal direction. The finite element simulation results can simulate the maximum floor acceleration closely to the test results. It is worth mentioning that each of the input accelerations has a PGA of 0.4 g. Therefore, the finite element is capable of simulating the isolation effect of the periodic foundation.

Figure 7-17 shows the acceleration time history at the top of the 3D periodic foundation obtained from the finite element model of Case 6 when subjected to the Ancona, Bishop, Gilroy, and Helena Earthquakes. The time history curves are close to the test results in terms of amplitude and phase angle. Figure 7-18 shows the finite element simulation of Case 6 subjected to the Bishop Earthquake in the torsional mode. The simulation results fit the test results very well during the main shock (0.5 -1.2 sec). The test results outside the main shock show a larger amplitude than the simulation results. The larger response outside the main shock is due to ambient noise picked up by the sensors, which was observed before the seismic tests were conducted.

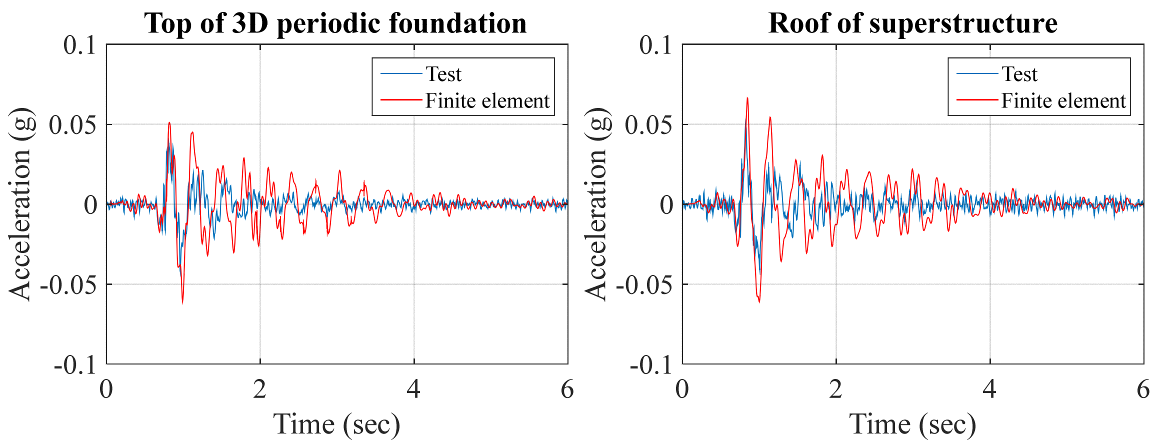

(a) Subjected to Anza Earthquake

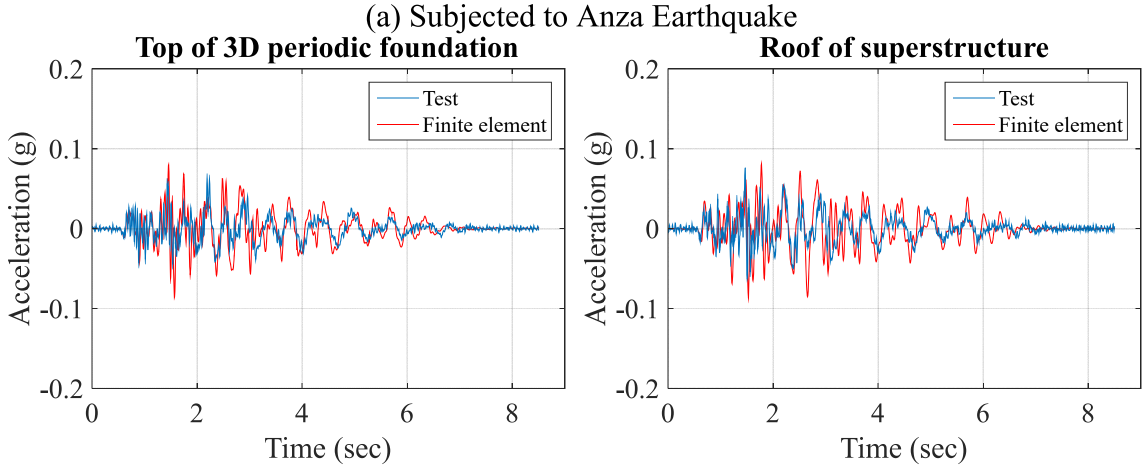

(b) Subjected to San Fernando (St. Anita station) Earthquake

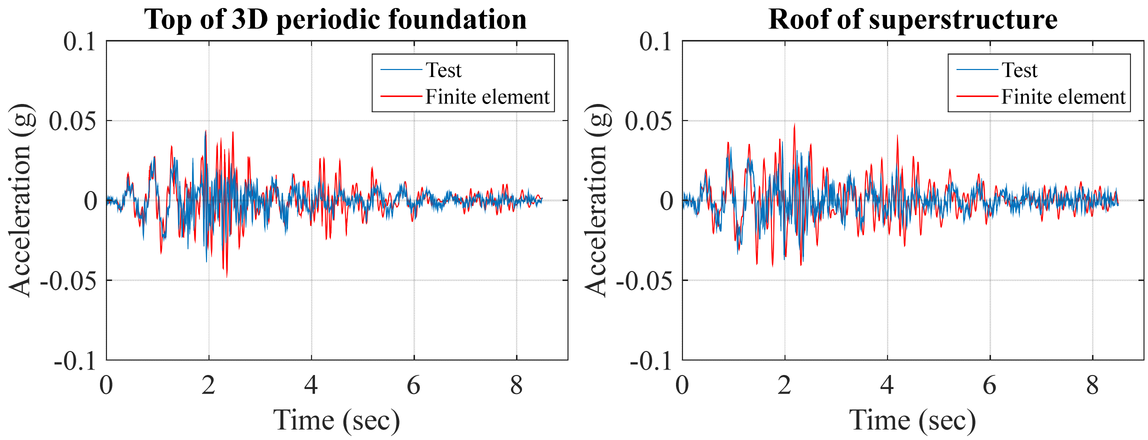

(c) Subjected to Whittier Earthquake

Figure 7-16 Time history analysis results of Case 6 in the horizontal direction

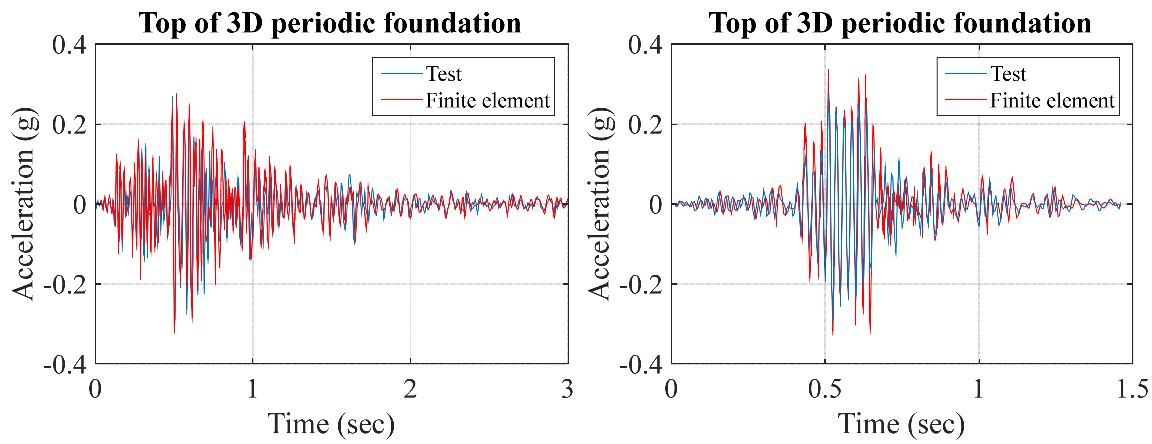

(a) Subjected to Ancona Earthquake

(b) Subjected to Bishop Earthquake

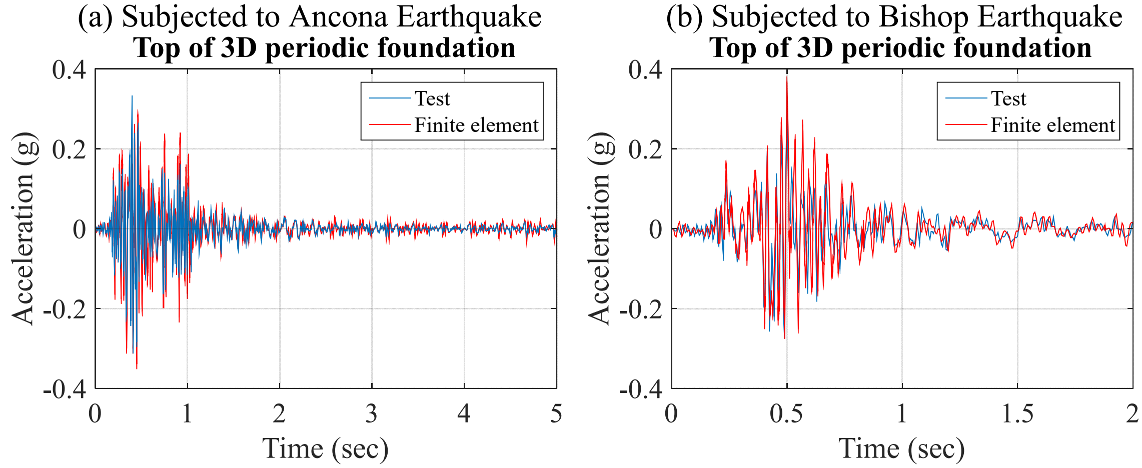

(c) Subjected to Gilroy Earthquake

(d) Subjected to Helena Earthquake

Figure 7-17 Time history analysis results of Case 6 in the vertical direction

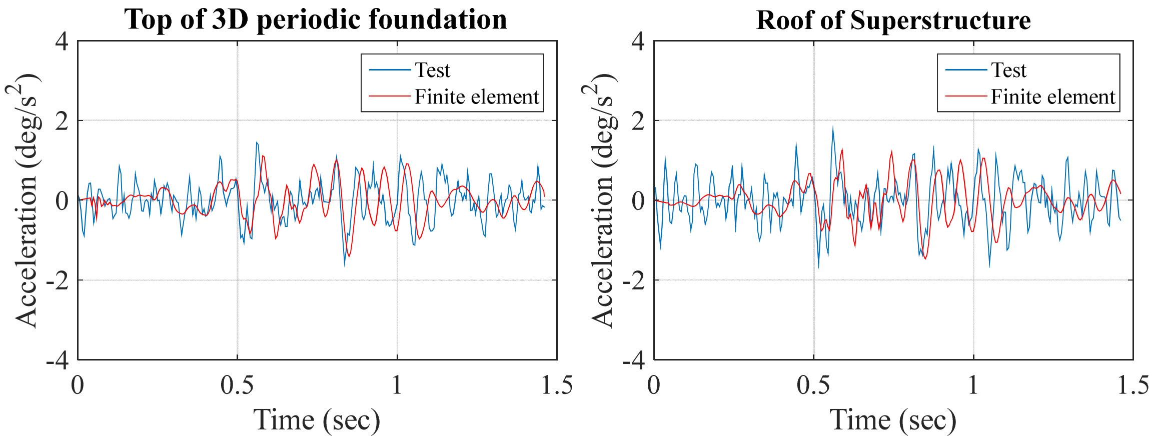

Figure 7-18 Time history analysis results of Case 6 subjected to Bishop Earthquake in the torsional mode

The overall finite element simulation results can replicate the test results well enough. The finite element can be used as a toll to perform design and preliminary analysis for the future design of periodic foundation structural systems given that the fabrication process conforms to the designed boundary conditions.

8 CONCLUSIONS AND FUTURE STUDIES

The studies presented in this dissertation are directed toward the implementation of periodic materials as seismic isolators for critical infrastructures. To this end, two scaled periodic foundations were developed, experimentally validated, and proven to effectively isolate an SMR building from incoming seismic waves. The purpose of this chapter is to recapitulate the research findings and to suggest some future research directions to enhance the application of periodic materials as seismic isolators.

8.1 Conclusions

The unique properties of frequency band gaps in periodic materials unfold countless advancements in vibration controls. This research particularly deals with isolating vibration with frequencies at the very low end of the phononic spectrum (less than 50 Hz). The newly developed periodic material-based seismic base isolation system can effectively solve inherent problems in many existing seismic isolation devices. Each of the chapters presented in this dissertation discusses and solves a specific issue starting from research motivations building up toward conceptual understanding and ultimately toward the validation of the real developed products. The key findings of this study are as follows:

- The unique frequency band gaps property of periodic materials can be obtained by deliberately arranging contrasting materials, so called unit cells, periodically. The periodicity can be applied in one, two, and three dimensions that categorize the periodic materials into 1D, 2D, and 3D types. The dispersion curve, the result of a unit cell analysis, relates the frequency and the wave vectors which can reveal the wave's characteristic oscillations over space and exponential decay of the wave amplitude inside the frequency band gaps. In the case of structures with a finite number of unit cells and finite geometry, amplifications at the natural frequencies of the structures occur. These amplifications are observed to be located in the pass bands in between frequency band gaps or attenuation zones. When material damping is considered, the damping can effectively control the amplifications in the pass bands. A small aspect ratio (length to the total thickness of all unit cells) may cause rocking modes to occur. One way to eliminate the possibility of rocking is to design the aspect ratio of the structure to be large enough.

- Investigation on the Locally resonant type 3D unit cell and Bragg scattering type 3D unit cell show that the Locally resonant type unit cell can have a relatively lower frequency band gap than the Bragg scattering unit cell. However, the response reduction of the Locally resonant unit cell is very small in comparison to that of the Bragg scattering unit cell. Therefore, the Bragg scattering unit cell is more economical for use in practical applications.
- Designing periodic materials as a foundation of the superstructure, so-called periodic foundations, can alter the attenuation zones to start at a much lower frequency. The altered attenuation zones of the 1D periodic foundation structural system can be predicted from the dispersion curve of a 1D unit cell with an equivalent superstructure layer.
- Global sensitivity analysis based on variance decomposition, or Sobol' sensitivity analysis, was conducted to characterize the most influential parameters in designing the frequency band gaps. The objective functions in this study are the first frequency band gap of two-layer 1D periodic materials subjected to each of the S-Wave and P-

Wave. The input parameters are selected as the ratio of material and geometric properties of the two layers that compose the unit cell. For the lower bound frequency or the starting of the frequency band gap subjected to the S-Wave, it is observed that the density ratio is the predominant parameter followed by the interaction of density ratio and thickness ratio parameters and the single parameter of the thickness ratio. When subjected to the P-Wave, the affecting parameters are the same as those when subjected to the S-Wave with the addition of the interaction of density ratio and first Poisson's ratio parameters and the single parameter of the first Poisson's ratio. While for the width of the frequency band gaps, more parameters and the interaction of parameters are attributed to the objective functions. In the case of the S-Wave, the dominant parameters are the thickness ratio, the interaction of Young's modulus ratio and thickness ratio, the interaction of density ratio and thickness ratio, the Young's modulus ratio, and the density ratio. In the case of the P-Wave, the dominant parameters are the same as those of the S-Wave with the addition of the first Poisson's ratio parameter. The ability of Sobol' sensitivity analysis to assess the interaction between parameters and how they affect the objective functions can provide insight and a better understanding into the uncertainty in the model, which sets this method apart from standard sensitivity analysis.

- Guided by the Sobol' indices, simplified design equations with a reduced number of input were proposed. The design equations can quickly estimate the first frequency band gap of two-layer 1D periodic materials subjected to the S-Wave and P-Wave without the need to solve the wave equation. The error analysis using 2000 input samples shows that the proposed design equation can predict the first frequency band gap with good accuracy. In fact, one may modify the proposed equation by adding more or reducing the Sobol' function terms depending on the desired level of accuracy. The proposed design equations can also be used to estimate the attenuation zones of Bragg scattering unit cells.

- As the first constructed large periodic foundations of their kind, construction errors occurred which led to the discrepancy in the designed and tested attenuation zones in the vertical direction. The behavior of both the 1D and 3D periodic foundations in the vertical direction were affected by the construction errors such as an imperfect flat surface of RC layers and non-uniform glue distribution. Therefore, in some parts of the periodic foundations the polyurethane surface is not perfectly connected to the RC surface. The imperfect interface connection causes non-uniform axial stresses and load transfer between each layer making the parts of the polyurethane that carries the load receive much more stress and become much stiffer, therefore, causing a discrepancy between the design and the test results. The imperfection of the interface connection, however, has little influence when the structure is subjected to incoming waves in the horizontal direction and torsional mode. Large superstructure weight allows sufficient friction between each layer on the periodic foundations and makes the shear stress transfer uniform. Therefore, the tested attenuation zones in the horizontal direction and the torsional mode are close to the designed attenuation zones of the S-Wave.
- Seismic performance of the 1D and 3D periodic foundations supporting an SMR building was validated through shake table tests. The experimental validation has shown that the designed periodic foundations are capable of isolating the superstructure from incoming seismic waves in the horizontal and vertical directions as well as the

torsional mode. Different from the conventional seismic isolation systems, periodic foundations utilize the inherent property of frequency band gaps to filter out the damaging frequency content of incoming seismic waves. The configuration and wave blocking mechanism allow the periodic foundations to effectively isolate incoming seismic waves without introducing rocking in the structural system. When the main frequency content of the incoming seismic waves is located inside the frequency band gaps, a significant response reduction as large as 90% can be observed. In addition to that, a small relative displacement is also achieved when the main frequency content is completely covered by the frequency band gaps. The research has shown that the technology is certainly beneficial to protect critical facilities, such as a nuclear power plant, in seismic-prone regions.

- A more realistic finite element model with the real structural conditions have shown that the finite element models can be used to replicate the response of the test specimens with a good degree of accuracy. The finite element models successfully simulate the attenuation zones of periodic foundation structural systems in both the horizontal direction and torsional mode. The simulated attenuation zones in the vertical direction were slightly off from the test results but the majority of the tendency was captured. The time history analysis results show that the finite element models can predict the acceleration response of the periodic foundation structural systems. The maximum floor acceleration as well as the phase angle of the simulated outcomes match the test results. The finite element method has been proven to be a good tool to simulate the behavior of the complex structural systems.

8.2 Future Studies

The research presented in this dissertation has proven the superior ability of periodic foundations for seismic isolation compared to existing seismic isolation systems. Several interesting issues attributed to this research offer opportunities for potential research directions.

- Typical building infrastructure including an SMR building has a life expectancy of 50 years. This long term constant gravitational loading causes creep in the materials that constitute the periodic foundations. The creep can be severe in the elastomeric materials such as rubbers and polyurethanes. In addition, exposure to environmental factors, such as changes in temperature and humidity, may also affect the properties of the materials. The changes in the material properties, such as Young's Modulus, in turn results in the changes of the frequency band gaps. Such effect is important to be addressed for devices that are intended for long term usage and exposed to the environment. Therefore, a study on long term stability of the modulus of materials in periodic materials will greatly contribute toward implementation of periodic foundations in the real world structures.
- In reality, materials carry a certain degree of defects and impurities. Up to this point, this research assumes smeared homogenous properties on the materials, for example RC layers. However, this assumption is legitimate only when the defects and impurities are relatively much smaller in size in comparison to the wavelength. In the case where the defects and impurities are large, a multiscale approach may be needed in the analysis. The effect of such defects and impurities of materials is also a particularly interesting research direction.

- The manufacturing method of large scale periodic foundations as presented in this research poses some issues on the interfaces as the different material layers are not perfectly connected. Hence, the stress transfer is not uniform across the sections. A construction method to fabricate periodic foundations can be a good future research direction. One emerging method of construction, the additive manufacturing, can be employed to fabricate the periodic foundations.
- Although periodic foundations have been proven to successfully isolate seismic waves, they do have a restricted usage. In order to block the seismic waves, the waves have to reach the periodic foundations before propagating to the superstructure. This characteristic makes periodic foundations only applicable as open foundations. However, for embedded structures or structures with basements, the periodic foundations will not be able to block the waves coming from the surrounding soil. Hence, isolating embedded structures can be a very challenging task. Future research direction using periodic material-based barriers to isolate embedded structures from laterally incoming seismic waves is also a promising area of research.
- Up to this point, the lowest frequency band gap among the two designed periodic foundation structural systems starts at 1.3 Hz. However, the near-fault earthquakes have ultra-low main frequency contents, i.e., less than 1 Hz. Therefore, to isolate important structures that are located near a fault, it is necessary to extend the frequency band gaps to cover the ultra-low frequency region.
- The theoretical frequency band gaps were derived based on the infinitesimal strain assumption. However, the measured displacement data from the experimental tests show that the deformation is not infinitesimal. Therefore, derivation of theoretical

frequency band gaps using true strain and incorporating hyperelastic material model is suggested to obtain more realistic theoretical frequency band gaps.

REFERENCES

[1] Building Seismic Safety Council and Applied Technology Council, *NEHRP guidelines for the seismic rehabilitation of buildings* vol. 1: Federal Emergency Management Agency, 1997.

[2] Ian G. Buckle and Ronald L. Mayes, "Seismic isolation: history, application, and performance—a world view," *Earthquake spectra,* vol. 6, pp. 161-201, 1990.

[3] Farzad Naeim and James M. Kelly, *Design of Seismic Isolated Structures: From Theory to Practice*: John Wiley & Sons Inc, 1999.

[4] Sachi Furukawa, Eiji Sato, Yundong Shi, Tracy Becker, and Masayoshi Nakashima, "Full-scale shaking table test of a base-isolated medical facility subjected to vertical motions," *Earthquake Engineering & Structural Dynamics,* vol. 42, pp. 1931-194, 2013.

[5] Keri L. Ryan, Siavash Soroushian, E. “Manos” Maragakis, Eiji Sato, Tomohiro Sasaki, and Taichiro Okazaki, "Seismic simulation of an integrated ceiling-partition wall-piping system at e-defense. I: Three-dimensional structural response and base isolation," *Journal of Structural Engineering,* vol. 142, p. 04015130, 2016.

[6] Junji Suhara, Tadashi Tamura, Yasuo Okada, and Katsuhiko Umeki, "Development of three dimensional seismic isolation device with laminated rubber bearing and rolling seal type air spring," in *ASME 2002 Pressure Vessels and Piping Conference*, Vancouver, BC, Canada, 2002, pp. 43-48.

[7] Junji Suhara, Ryoichiro Matsumoto, Shinsuke Oguri, Yasuo Okada, Kazuhiko Inoue, and Kenji Takahashi, "Research on 3-D base isolation system applied to new power reactor 3-D seismic isolation device with rolling seal type air spring: part 2,"

in *18th International Conference on Structural Mechanics in Reactor Technology (SMiRT 18)*, Beijing, China, 2005, pp. 3381-3391.

[8] Akihiro Kashiwazaki, Takahiro Shimada, T. Fujikawa, and Satoshi Moro, "Study on 3-dimensional base isolation system applying to new type power plant reactor (hydraulic 3-dimensional base isolation system: no. 1)," in *Transaction of the 17th International Conference on Structural Mechanics in Reactor Technology (SMiRT 17)*, Prague, Czech Republic, 2003.

[9] Shigeki Okamura, Yoshio Kamishima, Kazuo Negishi, Yoshihiko Sakamoto, Seiji Kitamura, and Shoji Kotake, "Seismic isolation design for JSFR," *Journal of Nuclear Science and Technology,* vol. 48, pp. 688-692, 2011.

[10] Osamu Takahashi, Hiromasa Aida, Junji Suhara, Ryoichiro Matsumoto, Yasuo Tsuyuki, and Takafumi Fujita, "Construction of civil building using three dimensional seismic isolation system: Part 1, design of building using three dimensional seismic isolation system," in *The 14th World Conference on Earthquake Engineering*, Beijing, China, 2008.

[11] Nicos Makris and Himanshu S. Deoskar, "Prediction of observed response of base-isolated structure," *Journal of Structural Engineering,* vol. 122, pp. 485-493, 1996.

[12] Gaofeng Jia and Zhifei Shi, "A New Seismic Isolation System and Its Feasibility Study," *Earthquake Engineering and Engineering Vibration,* vol. 9, pp. 75-82, 2010.

[13] Jing Bao, Zhifei Shi, and Hongjun Xiang, "Dynamic responses of a structure with periodic foundations," *Journal of Engineering Mechanics,* vol. 138, pp. 761–769, 2012.

[14] Zhibao Cheng and Zhifei Shi, "Novel composite periodic structures with attenuation zones," *Engineering Structures,* vol. 56, pp. 1271-1282, 2013.

[15] Yiqun Yan, Yi Lung Mo, Farn Yuh Menq, Kenneth H Stokoe II, Judy Perkins, and Yu Tang, "Development of seismic isolation systems using periodic materials," Department of Energy, Technical Report Project No. 32192014.

[16] Michael M. Sigalas and Eleftherios N. Economou, "Elastic and acoustic wave band structure," *Journal of Sound and Vibration,* vol. 158, pp. 377-382, 1992.

[17] Manvir S Kushwaha, Peter Halevi, Leonard Dobrzynski, and Bahram Djafari-Rouhani, "Acoustic band structure of periodic elastic composites," *Physical Review Letters,* vol. 71, pp. 2022-2025, 1993.

[18] Edwin L Thomas, Taras Gorishnyy, and Martin Maldovan, "Phononics: Colloidal Crystals Go Hypersonic," *Nature Materials,* vol. 5, pp. 773–774, 2006.

[19] Hong Jun Xiang, Zhi Fei Shi, Shiang Jun Wang, and Yi Lung Mo, "Periodic materials-based vibration attenuation in layered foundations: experimental validation," *Smart Materials and Structures,* vol. 21, pp. 1–10, 2012.

[20] Y Yan, A Laskar, Z Cheng, F Menq, Y Tang, Y L Mo, and Z Shi, "Seismic isolation of two dimensional periodic foundations," *Journal of Applied Physics,* vol. 116, p. 044908, 2014.

[21] Y Yan, Z Cheng, F Menq, Y L Mo, Y Tang, and Z Shi, "Three dimensional periodic foundations for base seismic isolation," *Smart Materials and Structures,* vol. 24, p. 075006, 2015.

[22] Helmut Krawinkler and Piotr D. Moncarz, "Similitude requirements for dynamic models," *ACI Special Publication,* vol. 73, 1982.

[23] W. H. Robinson and A. G. Tucker, "A lead-rubber shear damper," *Bulletin of The New Zealand National Society For Earthquake Engineering,* vol. 10, pp. 151-153, 1977.

[24] W. H. Robinson and A. G. Tucker, "Test results for lead-rubber bearings for WM. Clayton Building, Toe Toe Bridge and Waiotukupuna Bridge," *Bulletin of The New Zealand National Society For Earthquake Engineering,* vol. 14, pp. 21-33, 1983.

[25] C. J. Derham, J. M. Kelly, and A. G. Thomas, "Nonlinear natural rubber bearings for seismic isolation," *Nuclear Engineering and Design,* vol. 84, pp. 417-428, 1985.

[26] A. J. Papazoglou and A. S. Elnashai, "Analytical and field evidence of the damaging effect of vertical earthquake ground motion," *Earthquake Engineering & Structural Dynamics,* vol. 25, pp. 1109-1137, 1996.

[27] Yancheng Li, Jianchun Li, Tongfei Tian, and Weihua Li, "A highly adjustable magnetorheological elastomer base isolator for applications of real-time adaptive control," *Smart Materials and Structures,* vol. 22, p. 095020, 2013.

[28] Taiwan Pillar Industry Co. Ltd. (July 13, 2018). Available: http:// www.taiwanpillar.com.tw/en/about12c4.html?mode=3&id=14

[29] Gabriel Danila, "Seismic response control of buildings using Base Isolation," *International Journal of Mathematics and Computational Science,* vol. 1, pp. 37-49, 2015.

[30] Oiles Corporation. (July 13, 2018). Available: http://www.oiles.co.jp/en/ menshin/building/menshin/products/fps/

[31] Zhiguang Zhou, Jenna Wong, and Stephen Mahin, "Potentiality of using vertical and three-dimensional isolation systems in nuclear structures," *Nuclear Engineering and Technology,* vol. 48, pp. 1237-1251, 2016.

[32] Charles Kittel, *Introduction to Solid State Physics*. Hoboken: John Wiley & Sons, 2005.

[33] Michael Joseph Frazier, "Dissipative wave propagation in phononic crystals and metamaterials: Models and analysis," 2015.

[34] Zhengyou Liu, Xixiang Zhang, Yiwei Mao, Yongyuan Zhu, Zhiyu Yang, C. T. Chan, and Ping Sheng, "Locally Resonant Sonic Materials," *Science,* vol. 289, pp. 1734–1736, 2000.

[35] Mihail Sigalas, Manvir S. Kushwaha, Eleftherios N. Economou, Maria Kafesaki, Ioannis E. Psarobas, and Walter Steurer, "Classical vibrational modes in phononic lattices: theory and experiment," *Z. Kristallogr,* pp. 765–809, 2005.

[36] Martin Maldovan, "Sound and heat revolutions in phononics," *Nature,* vol. 503, pp. 209-217, 2013.

[37] M M Sigalas and E N Economou, "Elastic and Acoustic Wave Band Structure," *Journal of Sounda and Vibration,* vol. 158, pp. 377-382, 1992.

[38] M. M. Sigalas and C. M. Soukoulis, "Elastic-wave propagation through disordered and/or absorptive layered systems," *Physical Review B,* vol. 51, p. 2780, 1995.

[39] Gang Wang, Dianlong Yu, Jihong Wen, Yaozong Liu, and Xisen Wen, "One-dimensional phononic crystals with locally resonant structures," *Physics Letters A,* vol. 327, pp. 512-521, 2004.

[40] A-Li Chen and Yue-Sheng Wang, "Study on band gaps of elastic waves propagating in one-dimensional disordered phononic crystals," *Physica B: Condensed Matter,* vol. 392, pp. 369-378, 2007.

[41] Lin Han, Yan Zhang, Zhi Qiang Ni, Zi Ming Zhang, and Lin-Hua Jiang, "A modified transfer matrix method for the study of the bending vibration band structure in phononic crystal Euler beams," *Physica B: Condensed Matter,* vol. 407, pp. 4579-4583, 2012.

[42] Manvir S. Kushwaha, P Halevi, G Martinez, Leonard Dobrzynski, and Bahram Djafari-Rouhani, "Theory of acoustic band structure of periodic elastic composites," *Physical Review B,* vol. 49, p. 2313, 1994.

[43] Cécile Goffaux and José Sánchez-Dehesa, "Two-dimensional phononic crystals studied using a variational method: Application to lattices of locally resonant materials," *Physical Review B,* vol. 67, p. 144301, 2003.

[44] C. Goffaux and J. P. Vigneron, "Theoretical study of a tunable phononic band gap system," *Physical Review B,* vol. 64, p. 075118, 2001.

[45] Fugen Wu, Zhengyou Liu, and Youyan Liu, "Acoustic band gaps created by rotating square rods in a two-dimensional lattice," *Physical Review E,* vol. 66, p. 046628, 2002.

[46] Yukihiro Tanaka, Yoshinobu Tomoyasu, and Shin Ichiro Tamura, "Band structure of acoustic waves in phononic lattices: Two-dimensional composites with large acoustic mismatch," *Physical Review B,* vol. 62, p. 7387, 2000.

[47] Po-Feng Hsieh, Tsung-Tsong Wu, and Jia-Hong Sun, "Three-dimensional phononic band gap calculations using the FDTD method and a PC cluster system,"

IEEE transactions on ultrasonics, ferroelectrics, and frequency control, vol. 53, pp. 148-158, 2006.

[48] Tomoyuki Kurose, Kenji Tsuruta, Chieko Totsuji, and Hiroo Totsuji, "Fdtd simulations of acoustic waves in two-dimensional phononic crystals using parallel computer," *Memoirs of the Faculty of Engineering, Okayama University,* vol. 43, pp. 16-21, 2009.

[49] M. Kafesaki and Eleftherios N. Economou, "Multiple-Scattering Theory for Three-Dimensional Periodic Acoustic Composites," *Physical Review B,* vol. 60, p. 11993, 1999.

[50] Zhengyou Liu, Che Ting Chan, Ping Sheng, Andrew L. Goertzen, and John H. Page, "Elastic wave scattering by periodic structures of spherical objects: Theory and experiment," *Physical Review B,* vol. 62, p. 2446, 2000.

[51] I. E. Psarobas, N. Stefanou, and A. Modinos, "Scattering of Elastic Waves by Periodic Arrays of Spherical Bodies," *Physical Review B,* vol. 62, p. 278, 2000.

[52] Jun Mei, Zhengyou Liu, Jing Shi, and Decheng Tian, "Theory for elastic wave scattering by a two-dimensional periodical array of cylinders: An ideal approach for band-structure calculations," *Physical Review B,* vol. 24, p. 245107, 2003.

[53] Eli Yablonovitch, "Inhibited Spontaneous Emission in Solid-State Physics and Electronics," *Physical Review Letters,* vol. 58, p. 2059, 1987.

[54] Sajeev John, "Strong localization of photons in certain disordered dielectric superlattices," *Physical review letters,* vol. 58, p. 2486, 1987.

[55] Zhengyou Liu, Che Ting Chan, and Ping Sheng, "Three-Component Elastic Wave Band-Gap Material," *Physical Review B,* vol. 65, p. 165116, 2002.

[56] C. Goffaux, J. Sánchez-Dehesa, A. Levy Yeyati, Ph Lambin, A. Khelif, J. O. Vasseur, and B Djafari-Rouhani, "Evidence of Fano-Like Interference Phenomena in Locally Resonant Materials," *Physical Review Letters,* vol. 88, p. 225502, 2002.

[57] Cécile Goffaux, José Sánchez-Dehesa, and Philippe Lambin, "Comparison of the sound attenuation efficiency of locally resonant materials and elastic band-gap structures," *Physical Review B,* vol. 70, p. 184302, 2004.

[58] M. Hirsekorn, P. P. Delsanto, N. K. Batra, and P. Matic, "Modelling and Simulation of Acoustic Wave Propagation in Locally Resonant Sonic Materials," *Ultrasonics,* vol. 42, pp. 231–235, 2004.

[59] Zhengyou Liu, Che Ting Chan, and Ping Sheng, "Analytic model of phononic crystals with local resonances," *Physical Review B,* vol. 71, p. 014103, 2005.

[60] Jen-Kan Yu, Slobodan Mitrovic, Douglas Tham, Joseph Varghese, and James R. Heath, "Reduction of thermal conductivity in phononic nanomesh structures," *Nature Nanotechnology,* vol. 5, pp. 718-721, 2010.

[61] Rosa Martínez-Sala, J. Sancho, Juan V. Sánchez, Vicente Gómez, Jaime Llinares, and Francisco Meseguer, "Sound attenuation by sculpture," *Nature,* vol. 378, p. 241, 1995.

[62] Taras Gorishnyy, Chaitanya K. Ullal, Martin Maldovan, G. Fytas, and E. L. Thomas, "Hypersonic phononic crystals," *Physical review letters,* vol. 94, p. 115501, 2005.

[63] Stéphane Brûlé, E. H. Javelaud, Stefan Enoch, and Sébastien Guenneau, "Experiments on seismic metamaterials: molding surface waves," *Physical review letters* vol. 112, p. 133901, 2014.

[64] Oliver B. Wright and Osamu Matsuda. (July 15, 2018). *Watching phonons in k-space*. Available: http://kino-ap.eng.hokudai.ac.jp/ktspace.html

[65] Gaston Floquet, "Sur les equations differentielles lineaires," *Ann. ENS [2],* vol. 12, pp. 47-88, 1883.

[66] Felix Bloch, "Über die quantenmechanik der elektronen in kristallgittern," *Zeitschrift für physik,* vol. 52, pp. 555-600, 1929.

[67] William Henry Bragg and William Lawrence Bragg, "The reflection of X-rays by crystals," *Proc. R. Soc. Lond. A,* vol. 88, pp. 428-438, 1913.

[68] Witarto Witarto, S. J. Wang, Xin Nie, Y. L. Mo, Zhifei Shi, Yu Tang, and Robert P. Kassawara, "Analysis and design of one dimensional periodic foundations for seismic base isolation of structures," *International Journal of Engineering Research and Applications,* vol. 6, pp. 5-15, 2016.

[69] Ilya M. Sobol', "Sensitivity estimates for nonlinear mathematical models," *Mathematical Modelling and Computational Experiments,* vol. 1, pp. 407-414, 1993.

[70] Ilya M. Sobol', "Global sensitivity indices for nonlinear mathematical models and their Monte Carlo estimates," *Mathematics and Computers in Simulation,* vol. 55, pp. 271-280, 2001.

[71] Sanjay R. Arwade, Mohammadreza Moradi, and Arghavan Louhghalam, "Variance decomposition and global sensitivity for structural systems," *Engineering Structures,* vol. 32, pp. 1-10, 2010.

[72] P. H. Mott, J. R. Dorgan, and C. M. Roland, "The bulk modulus and Poisson's ratio of “incompressible” materials," *Journal of Sound and Vibration,* vol. 312, pp. 572-575, 2008.

[73] NuScale Power. (July 6, 2015). Available: http://www.nuscalepower.com/smr-benefits/safe/reactor-building-barriers

[74] Charles G. Salmon, John E. Johnson, and Faris A. Malhas, *Steel Structures Design and Behavior*. Upper Saddle River: Pearson Education, Inc, 2009.

[75] ACI Committee, *Building Code Requirements for Structural Concrete (ACI 318-14)*. Farmington Hills: American Concrete Institute, 2014.

[76] Thomas T. C. Hsu and Yi-Lung Mo, *Unified theory of concrete structures*: John Wiley & Sons, 2010.

[77] Sika. (June 10, 2016). Available: https://www.sika.com/

[78] Setra. (September 30, 2016). Available: http://www.setra.com/products/high-output-linear-accelerometer

[79] MTS Sensors. (September 30, 2016). Available: http://www.mtssensors.com/products/industrial-sensors/r-series-sensors/index.html

[80] NDI. (September 30, 2016). Available: http://www.ndigital.com/msci/products/optotrak-certus/

[81] Pacific Earthquake Engineering Research Center. (March 20, 2015). Available: http://peer.berkeley.edu/

[82] US Nuclear Regulatory Commission, "Regulatory guide 1.60: Design response spectra for seismic design of nuclear power plants," ed. Washington, DC: US Nuclear Regulatory Commission, 2014.

[83] Peter D. Welch, "The use of fast Fourier transform for the estimation of power spectra: A method based on time averaging over short, modified periodograms," *IEEE Transactions on Audio and Electroacoustics,* vol. 15, pp. 70-73, 1967.

APPENDIX NON-DIMENSIONAL QUANTITIES

$\hat{u}_n = u_n / L_* = u_n / h$	Non-dimensional displacement at layer n
$\hat{h}_n = h_n / L_* = h_n / h$	Non-dimensional height or thickness of layer n
$\hat{h} = h / L_* = 1$	Non-dimensional total height or thickness of unit cell
$\hat{z}_n = z_n / L_* = z_n / h$	Non-dimensional position of interest within the layer with reference to the bottom of layer n
$\hat{k}_n = k_n L_* = kh$	Non-dimensional wave number
$\hat{t} = \dfrac{t}{T_*} = \dfrac{t}{h}\sqrt{\dfrac{E_1}{\rho_1}}$	Non-dimensional time
$\hat{\omega} = \omega T_* = \omega h \sqrt{\rho_1 / E_1}$	Non-dimensional radial frequency
$\hat{\rho}_n = \rho_n L_*^3 / M_* = \rho_n / \rho_1$	Non-dimensional density of layer n
$\hat{\lambda}_n = \lambda_n L_* T_*^2 / M_* = \lambda_n / E_1$	Non-dimensional first Lamé parameter constant of layer n
$\hat{\mu}_n = \mu_n L_* T_*^2 / M_* = \mu_n / E_1$	Non-dimensional second Lamé parameter constant of layer n
$\hat{\sigma}_n = \sigma_n L_* T_*^2 / M_* = \sigma_n / E_1$	Non-dimensional normal stress at layer n
$\hat{\tau}_n = \tau_n L_* T_*^2 / M_* = \tau_n / E_1$	Non-dimensional shear stress at layer n